BEILSTEIN JOURNAL OF NANOTECHNOLOGY

Towards molecular spintronics

Edited by Georgeta Salvan and Dietrich R. T. Zahn

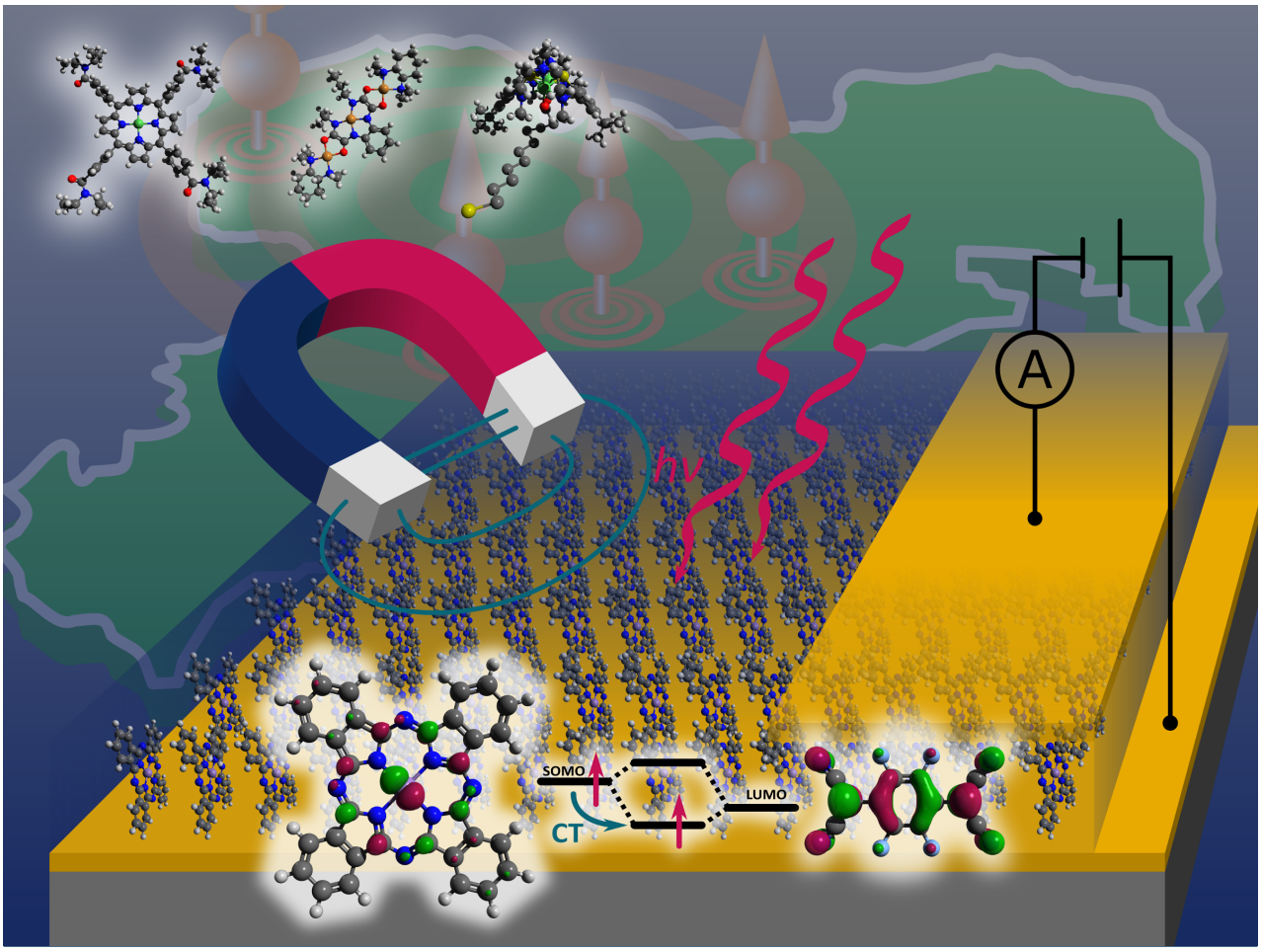

Imprint

Beilstein Journal of Nanotechnology
www.bjnano.org
ISSN 2190-4286
Email: journals-support@beilstein-institut.de

The *Beilstein Journal of Nanotechnology* is published by the Beilstein-Institut zur Förderung der Chemischen Wissenschaften.

Beilstein-Institut zur Förderung der Chemischen Wissenschaften
Trakehner Straße 7–9
60487 Frankfurt am Main
Germany
www.beilstein-institut.de

BEILSTEIN JOURNAL OF NANOTECHNOLOGY

Towards molecular spintronics

Georgeta Salvan* and Dietrich R. T. Zahn*

Editorial

Open Access

Address:
Physics Department, Semiconductor Physics, Technische Universität Chemnitz, Reichenhainer Straße 70, 09126 Chemnitz, Germany

Email:
Georgeta Salvan* - salvan@physik.tu-chemnitz.de;
Dietrich R. T. Zahn* - zahn@physik.tu-chemnitz.de

* Corresponding author

Keywords:
density functional theory; electrical and spin transport; Green's function method; interfaces; magnetic molecules; (magneto-)optical spectroscopy; molecular spintronics; photoelectron spectroscopy; surface science; thin films

Beilstein J. Nanotechnol. **2017,** *8,* 2464–2466.
doi:10.3762/bjnano.8.245

Received: 13 October 2017
Accepted: 02 November 2017
Published: 21 November 2017

This article is part of the Thematic Series "Towards molecular spintronics".

Editor-in-Chief: T. Schimmel

The discovery of tunneling and giant magnetoresistance in inorganic spin valves has led to a revolution in the field of magnetic memory and the significant increase in the storage capacity of modern hard drives. Simultaneously, given their inexpensive production, flexibility and diverse applications, molecular-based organic materials have become extremely important in electronic devices and circuitry. A combination of spintronics and organic electronics is expected to lead to a new generation of spin-based devices. These devices are expected to bring a wide range of exciting, new fields of application and products for organic/molecular spintronics.

The work of the Research Unit "Towards Molecular Spintronics" funded by the German Science Foundation (Deutsche Forschungsgemeinschaft, DFG) (DFG FOR 1154) was focused on the ultimate down-scaled functional unit which integrates the spintronic functionality into one single molecule. In our ambitious approach towards molecular spintronics we combined two interdisciplinary research fields based in otherwise disjunctive research communities: organic electronics and molecular magnetism. This required close collaboration of experts in physics (including theoretical physics), chemistry, materials science, and electrical engineering. The partners involved in this consortium are located at four Saxonian universities (Technische Universität Chemnitz, Technische Universität Dresden, Universität Leipzig, and Technische Universität Bergakademie Freiberg) as well as the Leibniz-Institut für Festkörper- und Werkstoff-Forschung (IFW) in Dresden, Germany.

The activities in this research unit were tailored to systematically address the whole research and development chain from molecule synthesis and molecular film deposition via fundamental characterization and theoretical understanding to device demonstration and integration.

Tailoring and fundamental characterization of magnetic molecules: Magnetic molecules for implementation into devices were synthesized and fundamentally investigated by theoretical density functional methods and experimental scanning probe techniques as well as optical and magnetic measurements on bulk materials. Already, at this stage, basic compatibility aspects concerning device processing had to be taken into account.

Fabrication, characterization, and optimization of molecular thin films and interfaces: Various deposition techniques to create suitable molecular films were tested for a variety of molecules. The structure, morphology, and molecular orientation of the layers were fundamentally characterized and optimized, taking into account that for device integration, the molecular layers need to obey certain boundary conditions, such as long-term stability, process compatibility, and the ability to integrate with electrode materials. Progress in this respect was only made possible by a continuous feedback from basic characterization and technology projects that allowed targeted and efficient synthesis of appropriate molecules and molecular films.

Device demonstration and on-chip integration: Rolled-up nanotechnology was used to create vertically stacked electronic devices with an organic tunnel transport layer for sensing applications. Horizontally stacked two-terminal and four-terminal devices photo sensors and magnetic field sensors were developed for large-scale integration purposes.

This complex research and development chain required various synthesis methods and theoretical approaches for prediction of molecular and devices properties. This included high-end and complementary characterization methods (ranging from static and dynamic magnetic characterization to local probe methods), as well as (magneto-)optical and electron spectroscopy, electrical measurements, new technological concepts, and sophisticated processing facilities. Such a complex chain can only become and remain successfully operational thanks to the enthusiastic cooperation between the groups, and in particular, between the young researchers. We would therefore like to express our deepest gratitude to all principal investigators, young researchers, associated researchers, and the coordinator (Jane Eisentraut) of the Research Unit for the great working atmosphere throughout the past six and a half years.

In this Thematic Series we summarize selected examples of the collaborative work in which at least two groups were involved. The range of considered molecules spans from heterotrinuclear bis(oxamato)-type and bis(oxamidato)-type complexes [1-3], to exchange-coupled dinickel complexes [4], metallo-phthalocyanines [5-7], metallo-porphyrins [8,9] and charge-transfer complexes [10,11], to metal-free molecules like pentacene-derivatives [12], fullerenes [13], trimesic acid [14], or organic ferromagnets [15]. Besides the internal cooperation, the Research Unit greatly profited from excellent talks and thorough discussions with external guests joining our scientific workshops and we are happy to host six articles from our invited guests with topics beyond the molecular systems investigated in our Research Unit, for example: theoretical predictions on metal/C_{60} interfaces [16], magneto-resistive donor/acceptor transistors [17], spin-crossover complexes [18], ferromagnetic thin films obtained from organic blends [19], and theoretical calculations on 2D porphyrin-based networks for spintronics [20]. We are also happy to host a review paper entitled "Spin-chemistry concepts for spintronics scientists" [21], which discusses the vast terminology differences and addresses the benefits that might arise from a stronger interaction between spin-chemistry and spintronics, thereby opening the horizon for future progress in both fields.

We truly appreciate the open access policy of the Beilstein-Institut, which made this Thematic Series possible. We are greatly indebted to the team at the *Beilstein Journal of Nanotechnology* for their highly professional support and always very fast feedback. We would also like to thank all referees for their effort and constructive criticism.

Georgeta Salvan and Dietrich R. T. Zahn

Chemnitz, October 2017

References

1. Aliabadi, A.; Büchner, B.; Kataev, V.; Rüffer, T. *Beilstein J. Nanotechnol.* **2017,** *8,* 2245–2256. doi:10.3762/bjnano.8.224
2. Abdulmalic, M. A.; Weheabby, S.; Meva, F. E.; Aliabadi, A.; Kataev, V.; Büchner, B.; Schleife, F.; Kersting, B.; Rüffer, T. *Beilstein J. Nanotechnol.* **2017,** *8,* 789–800. doi:10.3762/bjnano.8.82
3. Zaripov, R.; Vavilova, E.; Khairuzhdinov, I.; Salikhov, K.; Voronkova, V.; Abdulmalic, M. A.; Meva, F. E.; Weheabby, S.; Rüffer, T.; Büchner, B.; Kataev, V. *Beilstein J. Nanotechnol.* **2017,** *8,* 943–955. doi:10.3762/bjnano.8.96
4. Börner, M.; Blömer, L.; Kischel, M.; Richter, P.; Salvan, G.; Zahn, D. R. T.; Siles, P. F.; Fuentes, M. E. N.; Bufon, C. C. B.; Grimm, D.; Schmidt, O. G.; Breite, D.; Abel, B.; Kersting, B. *Beilstein J. Nanotechnol.* **2017,** *8,* 1375–1387. doi:10.3762/bjnano.8.139
5. Milekhin, A. G.; Cherkasova, O.; Kuznetsov, S. A.; Milekhin, I. A.; Rodyakina, E. E.; Latyshev, A. V.; Banerjee, S.; Salvan, G.; Zahn, D. R. T. *Beilstein J. Nanotechnol.* **2017,** *8,* 975–981. doi:10.3762/bjnano.8.99
6. Bandari, V. K.; Varadharajan, L.; Xu, L.; Jalil, A. R.; Devarajulu, M.; Siles, P. F.; Zhu, F.; Schmidt, O. G. *Beilstein J. Nanotechnol.* **2017,** *8,* 1277–1282. doi:10.3762/bjnano.8.129
7. Hahn, T.; Ludwig, T.; Timm, C.; Kortus, J. *Beilstein J. Nanotechnol.* **2017,** *8,* 2094–2105. doi:10.3762/bjnano.8.209
8. Smykalla, L.; Mende, C.; Fronk, M.; Siles, P. F.; Hietschold, M.; Salvan, G.; Zahn, D. R. T.; Schmidt, O. G.; Rüffer, T.; Lang, H. *Beilstein J. Nanotechnol.* **2017,** *8,* 1786–1800. doi:10.3762/bjnano.8.180
9. Al-Shewiki, R. K.; Mende, C.; Buschbeck, R.; Siles, P. F.; Schmidt, O. G.; Rüffer, T.; Lang, H. *Beilstein J. Nanotechnol.* **2017,** *8,* 1191–1204. doi:10.3762/bjnano.8.121
10. Waas, D.; Rückerl, F.; Knupfer, M.; Büchner, B. *Beilstein J. Nanotechnol.* **2017,** *8,* 927–932. doi:10.3762/bjnano.8.94

11. Rückerl, F.; Waas, D.; Büchner, B.; Knupfer, M.; Zahn, D. R. T.; Haidu, F.; Hahn, T.; Kortus, J. *Beilstein J. Nanotechnol.* **2017,** *8,* 1601–1615. doi:10.3762/bjnano.8.160
12. Banerjee, S.; Bülz, D.; Reuter, D.; Hiller, K.; Zahn, D. R. T.; Salvan, G. *Beilstein J. Nanotechnol.* **2017,** *8,* 1502–1507. doi:10.3762/bjnano.8.150
13. Schimmel, S.; Sun, Z.; Baumann, D.; Krylov, D.; Samoylova, N.; Popov, A.; Büchner, B.; Hess, C. *Beilstein J. Nanotechnol.* **2017,** *8,* 1127–1134. doi:10.3762/bjnano.8.114
14. Ha, N. T. N.; Gopakumar, T. G.; Yen, N. D. C.; Mende, C.; Smykalla, L.; Schlesinger, M.; Buschbeck, R.; Rüffer, T.; Lang, H.; Mehring, M.; Hietschold, M. *Beilstein J. Nanotechnol.* **2017,** *8,* 2139–2150. doi:10.3762/bjnano.8.213
15. Hu, G.; Xie, S.; Wang, C.; Timm, C. *Beilstein J. Nanotechnol.* **2017,** *8,* 1919–1931. doi:10.3762/bjnano.8.192
16. Chutora, T.; Redondo, J.; de la Torre, B.; Švec, M.; Jelínek, P.; Vázquez, H. *Beilstein J. Nanotechnol.* **2017,** *8,* 1073–1079. doi:10.3762/bjnano.8.109
17. Reichert, T.; Saragi, T. P. I. *Beilstein J. Nanotechnol.* **2017,** *8,* 1104–1114. doi:10.3762/bjnano.8.112
18. Göbel, C.; Klimm, O.; Puchtler, F.; Rosenfeldt, S.; Förster, S.; Weber, B. *Beilstein J. Nanotechnol.* **2017,** *8,* 1318–1327. doi:10.3762/bjnano.8.133
19. Robaschik, P.; Ma, Y.; Din, S.; Heutz, S. *Beilstein J. Nanotechnol.* **2017,** *8,* 1469–1475. doi:10.3762/bjnano.8.146
20. Tang, H.; Tarrat, N.; Langlais, V.; Wang, Y. *Beilstein J. Nanotechnol.* **2017,** *8,* in press.
21. Ivanov, K. L.; Wagenpfahl, A.; Deibel, C.; Matysik, J. *Beilstein J. Nanotechnol.* **2017,** *8,* 1427–1445. doi:10.3762/bjnano.8.143

License and Terms

BEILSTEIN JOURNAL OF NANOTECHNOLOGY

Probing the magnetic superexchange couplings between terminal Cu^{II} ions in heterotrinuclear bis(oxamidato) type complexes

Mohammad A. Abdulmalic[1], Saddam Weheabby[1], Francois E. Meva[2], Azar Aliabadi[3,4], Vladislav Kataev[3], Bernd Büchner[3,5], Frederik Schleife[6], Berthold Kersting[6] and Tobias Rüffer[*1,§]

Full Research Paper

Open Access

Address:
[1]Department of Inorganic Chemistry, Faculty of Natural Sciences, Chemnitz University of Technology, Strasse der Nationen 62, D-09111 Chemnitz, Germany, [2]Department of Pharmaceutical Sciences, Faculty of Medicine and Pharmaceutical Sciences, University of Douala, BP 2701, Cameroon, [3]Leibniz Institute for Solid State and Materials Research IFW Dresden, D-01171 Dresden, Germany, [4]Institut für Nanospektroskopie (EM-ISPEK), Helmholtz-Zentrum Berlin für Materialien und Energie, Kekuléstr. 5, D-12489 Berlin, Germany, [5]Institute for Solid State Physics, Technical University Dresden, D-01062 Dresden, Germany and [6]Department of Inorganic Chemistry, Faculty of Chemistry and Mineralogy, University of Leipzig, Johannisallee 29, D-04103 Leipzig, Germany

Email:
Tobias Rüffer* - tobias.rueffer@chemie.tu-chemnitz.de

* Corresponding author
§ Phone: +49 (0)371-531-31836

Keywords:
bis(oxamidato); crystallographic characterization; diamagnetic; heteronuclear complexes; magnetic superexchange coupling; molecular structure

Beilstein J. Nanotechnol. **2017,** *8,* 789–800.
doi:10.3762/bjnano.8.82

Received: 25 January 2017
Accepted: 14 March 2017
Published: 06 April 2017

This article is part of the Thematic Series "Towards molecular spintronics".

Guest Editor: G. Salvan

Abstract

The reaction of one equivalent of $[n\text{-}Bu_4N]_2[Ni(opboR_2)]$ with two equivalents of $[Cu(pmdta)(X)_2]$ afforded the heterotrinuclear $Cu^{II}Ni^{II}Cu^{II}$ containing bis(oxamidato) type complexes $[Cu_2Ni(opboR_2)(pmdta)_2]X_2$ (R = Me, X = NO_3^- (**1**); R = Et, X = ClO_4^- (**2**); R = *n*-Pr, X = NO_3^- (**3**); $opboR_2$ = *o*-phenylenebis(NR-substituted oxamidato); pmdta = *N*,*N*,*N*',*N*",*N*"-pentamethyldiethylenetriamine). The identities of the heterotrinuclear complexes **1**–**3** were established by IR spectroscopy, elemental analysis and single-crystal X-ray diffraction studies, which revealed the cationic complex fragments $[Cu_2Ni(opboR_2)(pmdta)_2]^{2+}$ as not involved in any further intermolecular interactions. As a consequence thereof, the complexes **1**–**3** possess terminal paramagnetic $[Cu(pmdta)]^{2+}$ fragments separated by $[Ni^{II}(opboR_2)]^{2-}$ bridging units representing diamagnetic $S_{Ni} = 0$ states. The magnetic field dependence of the magnetization $M(H)$ of **1**–**3** at $T = 1.8$ K has been determined and is shown to be highly reproducible with the Brillouin func-

tion for an ideal paramagnetic spin = $^1/_2$ system, verifying experimentally that no magnetic superexchange couplings exists between the terminal paramagnetic $[Cu(pmdta)]^{2+}$ fragments. Susceptibility measurements versus temperature of **1**–**3** between 1.8–300 K were performed to reinforce the statement of the absence of magnetic superexchange couplings in these three heterotrinuclear complexes.

Introduction

Significant synthetic efforts have been directed to the synthesis of polynuclear species in which the metal ions are bridged by oxamato, oxamido, oxalato or dithiooxalato ligand [1-4]. In this context, the so-called bis(oxamato) type transition metal complexes as mononuclear species (Figure 1, type **I**) have received very special attention, as they allow the synthesis of multidimensional *n*D (*n* = 0–3) products, of which the magnetic properties were of specific interest [5]. Bis(oxamidato) type complexes (Figure 1, type **II**) have, on the other hand, received much less attention [6-9], although the flexidentate properties of these as well as type **I** complexes allows the convenient synthesis of the trinuclear type **III** and **IV** complexes, cf. Figure 1 [5,10,11].

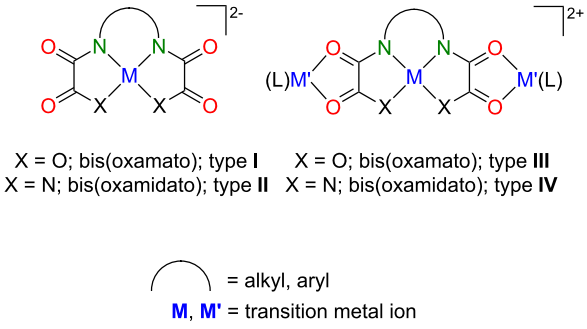

Figure 1: Chemical structures of type **I**–**IV** complexes.

The magnetic characterization of type **III** complexes has already significantly contributed to a better understanding of the origin of magnetic exchange interactions in polynuclear complexes [5,12]. One could expect that due to the lower electronegativity of the nitrogen atoms of type **III** (compared to the oxygen atoms of type **IV** complexes), the magnetic exchange couplings should increase [1]. These are studies to which we have already contributed [13-18].

Basically, one can expect different magnetic exchange pathways between the paramagnetic metal ions of type **III** and **IV** complexes as depicted in Figure 2a and consequently these complexes might possess three different pathways in case that they are composed of three nonequivalent metal ions. To some extent, that has been already shown for heterotrinuclear $Mn^{II}Cu^{II}Mn^{II}$ ($S = {}^9/_2$) and $Ni^{II}Cu^{II}Ni^{II}$ ($S = {}^3/_2$) type **III** complexes [19-21]. Thus, by locating a small local between two large spins (Figure 2b), complexes with high-spin ground states can been obtained.

If we follow this idea further we could replace the middle local spin, cf. Figure 2b, by a diamagnetic fragment. This would allow unambiguous verification of whether type **III**/**IV** complexes might have $J_{1,3}$ magnetic couplings (Figure 2a) or not. There is already a first study of Sanada et al. [11], who reported for the heterotrinuclear $Gd^{III}Ni^{II}Gd^{III}$ type **IV** complex ($S = {}^7/_2$) a very small $J_{1,3}$ coupling of -0.002 cm^{-1}. However, this small coupling might be attributed to the shielding effect of the outer-shell electrons on the 4f electron of the Gd^{III} ions [11]. On the other hand, for homotrinuclear $Cu^{II}Cu^{II}Cu^{II}$ type **III** complexes, $J_{1,3}$ couplings were either assumed to be zero or negligible [14-16,22]. One can thus conclude that $J_{1,3}$ couplings are very small.

In our earlier work, we previously reported on the magnetic characterization of homotrinuclear $Cu^{II}Cu^{II}Cu^{II}$ type **IV** complexes [15]. We noticed, unexpectedly, that the central Cu^{II} ions

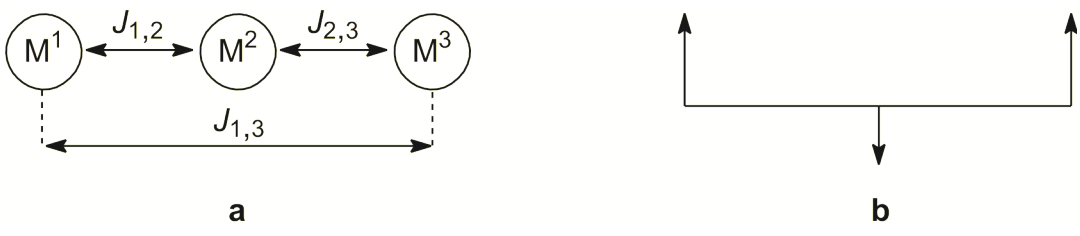

Figure 2: Expected *J* couplings between the central and terminal paramagnetic metal ions in type **III**/**IV** complexes (a). Approach of a small local spin located between two large local spins (b).

of these complexes were not coordinated by any counter ions or solvents. It is this finding which gave birth to the idea to report here on the synthesis of heterotrinuclear $Cu^{II}Ni^{II}Cu^{II}$ type **IV** complexes. Their central $[Ni^{II}(opboR_2)]^{2-}$ fragments were anticipated to be free of any further co-ligands. That would make these central fragments purely diamagnetic and thus these heterotrinuclear $Cu^{II}Ni^{II}Cu^{II}$ type **IV** complexes, possessing terminal paramagnetic Cu^{II} ions, appear as ideal candidates to study the magnitude of the $J_{1,3}$ coupling of type **III**/**IV** complexes.

Results and Discussion

Synthesis

The synthesis of the heterotrinuclear $Cu^{II}Ni^{II}Cu^{II}$ complexes **1**–**3** out of literature-known precursors is shown in Scheme 1.

Under anaerobic working conditions one equivalent of the non-hygroscopic $[n\text{-}Bu_4N]^+$ salts of mononuclear $[Ni^{II}(opboR_2)]^{2-}$ complexes were treated with two equivalents of $[Cu(pmdta)(X)_2]$ (X = NO_3^- for **1** and **3**, X = ClO_4^- for **2**) in MeCN solutions of to give $[NiCu_2(opboR)(pmdta)_2](X)_2$ (**1**–**3**, cf. Scheme 1) in yields exceeding 60%. The reaction side products $[n\text{-}Bu_4N][NO_3]$ and $[n\text{-}Bu_4N][ClO_4]$, respectively, could be smoothly separated as they are soluble in 4:1 THF/Et_2O mixtures, while the desired complexes **1**–**3** are insoluble in such mixtures. The isolated powders of **1**–**3** had to be stored under inert gas atmosphere, as they are hygroscopic. Single crystals of **1**–**3** could be obtained as described next by crystallisation experiments performed under inert atmosphere.

Single crystal X-ray diffraction studies

Slow diffusion of Et_2O vapour into CH_2Cl_2 solutions of **1** and **3** and into a MeCN solution of **2** afforded single crystals suitable for crystallographic studies of the compositions $[\{NiCu_2(opboMe_2)(pmdta)_2\}_2][NO_3]_4\cdot 3.75CH_2Cl_2$ (**1'**), $[NiCu_2(opboMe_2)(pmdta)_2][ClO_4]_2\cdot 2MeCN$ (**2'**) and $[NiCu_2(opboMe_2)(pmdta)_2][NO_3]_2\cdot 2CH_2Cl_2$ (**3'**). In case of **1'**, the asymmetric unit comprises two crystallographically independent complexes of **1**. Their dicationic complex fragments $[Cu_2Ni(opboMe_2)(pmdta)_2]^{2+}$ are denoted in the following as **1A** (comprising Ni1) and **1B** (comprising Ni2). The related bond lengths and angles of **1A**/**1B** show differences of up to 1.5% and ca. 2%, respectively, whereby only bond lengths and angles of **1A** will be discussed, although Table 1 and Table 2 displays them for both **1A** and **1B**. In analogy, the cationic complex fragments $[NiCu_2(opboMe_2)(pmdta)_2]^{2+}$ of **2'** and $[NiCu_2(opboMe_2)(pmdta)_2]^{2+}$ of **3'** are denoted in the following as **2A** and **3A**. It should be highlighted and emphasized that in the crystal structures of **1'**–**3'** no unusual short intermolecular interactions were observed and that the complex fragments **1A**–**3A** are indeed discrete.

The molecular structures of **1A**–**3A** are similar to each other and thus structural features of all three complex fragments will be discussed together. A collective plot of the molecular structures of **1A**–**3A** in an analogous perspective view is shown in Figure 3. Selected bond lengths and angles of the $[Ni(opboR_2)]^{2-}$ and of the $[Cu(pmdta)]^{2+}$ complex fragments of **1A**–**3A** are given in Table 1 and Table 2, respectively. Crystal and structural refinement data are summarized in Table 3.

The Ni^{II} ions of **1A**–**3A** are coordinated by four deprotonated amide N donor atoms to form a planar-quadratic NiN_4 coordination environment. Two of them belong to the *N*,*N*'-*o*-phenylene bridges of **1A**–**3A** (**1A**/**2A**: N1 and N3. **3A**: N1 and N1A) and are referred to in the following as N_{aryl} donor atoms. The other two belong to the alkyl-substituted amide functions of **1A**–**3A** (**1A**/**2A**: N2 and N4. **3A**: N2 and N2A) and are further referred to as N_{alkyl} donor atoms. The planarity of the NiN_4 units is revealed, for example, by calculations of mean planes of its atoms and gives the following root-mean-square deviations from planarity (rmsd) together with values for the atom with the highest deviation from planarity (hdp) as follows: **1A**/**2A**/**3A** (rmsd, hdp) = 0.035 Å, N1 with 0.046(3) Å /0.030 Å, N1 with 0.035(8) Å/0.082 Å, N1 with 0.100(4) Å, respectively. Moreover, the sum of bond angles of the NiN_4 units amounts to 360.1(4)° (**1A**), 360.1(6)° (**2A**) and 360.5(5)° (**3A**). For the mononuclear Ni^{II}-containing bis(oxamato) complex

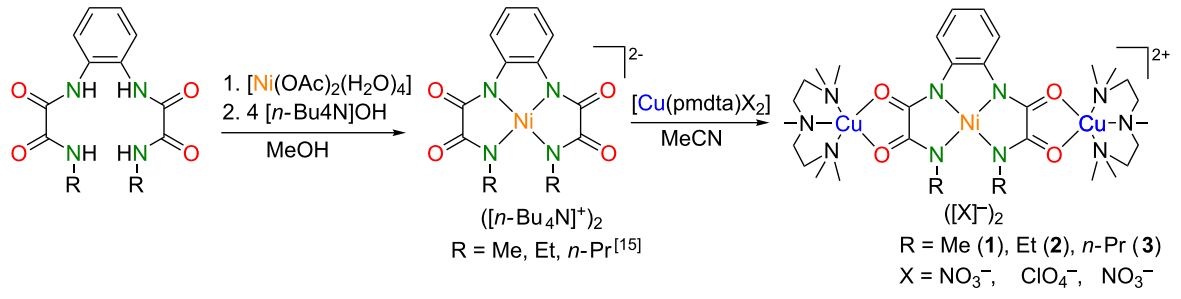

Scheme 1: Synthesis of the heterotrinuclear $Cu^{II}Ni^{II}Cu^{II}$ type **IV** complexes **1**–**3**.

Table 1: Selected bond lengths (Å) and angles (°) of the $[Ni(opboR_2)]^{2-}$ fragments of **1A**/**1B** (R = Me), **2A** (R = Et) and **3A** (R = *n*-Pr).

	1A/1B	2A	3A
Bond lengths			
N1–Ni1	1.865(6)/1.862(6)	1.869(6)	1.847(5)
N2–Ni1	1.915(6)/1.912(7)	1.922(6)	1.904(6)
N3–Ni1(N1A–Ni1)[a]	1.866(6)/1.867(6)	1.860(6)	1.847(5)
N4–Ni1(N2A–Ni1)[a]	1.923(6)/1.922(7)	1.923(6)	1.904(6)
C1–O1	1.260(8)/1.238(9)	1.259(10)	1.264(8)
C2–O2	1.280(8)/1.300(9)	1.261(9)	1.289(8)
C3–O3(C1A–O1A)[a]	1.255(8)/1.248(9)	1.237(9)	1.264(8)
C4–O4 (C2A–O2A)[a]	1.279(8)/1.280(9)	1.278(9)	1.289(8)
C1–N1	1.316(9)/1.325(10)	1.315(10)	1.317(8)
C2–N2	1.280(9)/1.288(10)	1.333(10)	1.326(9)
C3–N3(C1A–N1A)[a]	1.308(9)/1.303(10)	1.331(10)	1.317(8)
C4–N4(C2A–N2A)[a]	1.304(9)/1.281(11)	1.298(10)	1.326(9)
C1–C2	1.535(9)/1.522(10)	1.492(11)	1.487(11)
C3–C4(C1A–C2A)[a]	1.514(9)/1.533(10)	1.515(11)	1.487(11)
Bond angles			
N1–Ni1–N3(N1–Ni1–N1A)[a]	83.7(2)/83.7(3)	83.7(3)	83.5(3)
N2–Ni1–N4(N2–Ni1–N2A)[a]	107.1(2)/107.5(3)	107.5(3)	107.0(4)
N1–Ni1–N2	84.6(2)/84.4(3)	84.4(3)	85.0(2)
N3–Ni1–N4(N1A–Ni1–N2A)[a]	84.7(2)/84.3(3)	84.5(3)	85.0(2)
N1–Ni1–N4(N1–Ni1–N2A)[a]	167.8(2)/167.6(3)	168.0(3)	166.9(2)
N2–Ni1–N3(N2–Ni1–N1A)[a]	168.2(2)/168.0(3)	167.9(3)	166.9(2)
N1–C1–O1	129.7(6)/129.9(7)	128.7(8)	128.2(7)
N2–C2–O2	127.1(6)/126.7(7)	125.0(7)	126.3(7)
N3–C3–O3(N1A–C1A–O1A)[a]	129.6(6)/129.5(7)	128.7(7)	128.2(7)
N4–C4–O4(N2A–C2A–O2A)[a]	126.1(6)/127.8(7)	126.9(7)	126.3(7)

[a]Data in brackets refer to respective bond lengths and angles of **10A**. Symmetry operation used to generate equivalent atoms 'A' for **10A**: –x, y, –z + $^3/_2$.

$[n\text{-}Bu_4N]_2[Ni(opba)]$ (**11**) [23] and the related bis(oxamidato) type complex $[Ph_4P]_2[Ni(opboMe_2)]$ (**12**) [9] the following observation has been made: Three of bond angles of the central NiN_2O_2/NiN_4 coordination units are small (**11**: 85.79(8)–86.18(5)°; **12**: 82.7(3)–84.7(3)°), while the fourth one is significantly larger (**11**: 101.97(7)°; **12**: 108.8(3)°). Thereby, the latter bond angle is the one created of the two carboxylate oxygen atoms of **11** or the two N_{alkyl} donor atoms of **12**. This feature is due to the presence of 5-5-5 fused chelate rings around the Ni^{II} ion [17,24]. In case of **1A**–**3A** this feature is observed as well, cf. Table 1.

The Ni–N bond lengths of the NiN_4 units of **1A**–**3A** fall into two categories: The Ni–N_{aryl} bond lengths are significantly shorter compared to the Ni–N_{alkyl} ones [25]. For example, the Ni–N_{aryl} bond lengths of **1A** (Ni1–N1 and Ni1–N3, $\bar{d}$ = 1.864(8) Å) are substantially shorter compared to the Ni–N_{alkyl} bond lengths (Ni1–N2 and Ni1–N4, $\bar{d}$ = 1.912(8) Å). This fact is in principal in agreement with the observations made for **12** [9] and could be explained in analogy to statements made for mononuclear Cu^{II}-containing bis(oxamato) complexes by the greater basicity of the N_{aryl} vs the N_{alkyl} donor atoms [24].

In the following the geometries of the terminal $[Cu(pmdta)]^{2+}$ fragments will be briefly described. It should be emphasized that the findings described in the following have been made analogously for our previously reported homotrinuclear $Cu^{II}Cu^{II}Cu^{II}$ complexes as described in [15]. Thus, the terminal Cu^{II} ions of **1A**–**3A** are each coordinated by two O donor atoms of the oxamidato groups as well as three N donor atoms of the pmdta ligands to form CuN_3O_2 coordination units closer to the ideal square-pyramidal compared to the ideal trigonal-bipyramidal coordination geometry with respect to their τ parameters [26], cf. Table 2. One feature, commonly observed for all CuN_3O_2 units, deserves specific attention. The largest bond angle of all CuN_3O_2 units always involves the O donor atom of

Table 2: Selected bond lengths (Å), angles (°) and τ parameters of the terminal $[Cu(pmdta)]^{2+}$ fragments of **1A**/**1B** (R = Me), **2A** (R = Et) and **3A** (R = *n*-Pr).

	1A/1B	**2A**	**3A**
Bond lengths			
Cu1–O1	2.243(5)/2.218(5)	2.210(5)	2.192(5)
Cu1–O2	1.957(5)/1.953(5)	1.998(6)	1.982(5)
Cu1–N5	2.047(6)/2.061(6)	2.070(8)	2.077(6)
Cu1–N6	2.028(7)/1.997(7)	2.015(7)	2.010(6)
Cu1–N7	2.072(6)/2.090(6)	2.035(7)	2.029(6)
Cu2–O3	2.198(5)/2.203(5)	2.198(5)	–[a]
Cu2–O4	1.962(5)/1.957(6)	1.994(5)	–[a]
Cu2–N8	2.042(6)/2.044(7)	2.056(6)	–[a]
Cu2–N9	2.010(6)/2.007(10)	2.014(6)	–[a]
Cu2–N10	2.091(6)/2.082(9)	2.072(7)	–[a]
Bond angles			
O1–Cu1–O2	81.78(17)/82.2(2)	81.1(2)	81.80(19)
O1–Cu1–N5	99.1(2)/98.7(3)	99.5(3)	99.5(2)
O1–Cu1–N6	105.9(2)/104.1(2)	104.3(3)	101.6(2)
O1–Cu1–N7	103.7(2)/105.6(2)	106.4(3)	107.6(2)
O2–Cu1–N5	94.0(2)/95.0(3)	92.8(3)	92.9(2)
O2–Cu1–N6	172.0(2)/173.1(2)	174.6(3)	176.6(3)
O2–Cu1–N7	90.4(2)/89.7(3)	91.8(3)	92.6(2)
N5–Cu1–N6	87.0(3)/86.9(3)	86.3(3)	86.3(3)
N5–Cu1–N7	157.2(3)/155.6(3)	154.1(3)	152.8(3)
N6–Cu1–N7	85.6(3)/86.0(3)	86.7(3)	86.7(3)
O3–Cu2–O4	81.75(18)/81.9(2)	81.4(2)	–[a]
O3–Cu2–N8	101.0(2)/102.0(3)	104.2(2)	–[a]
O3–Cu2–N9	104.4(2)/105.3(3)	102.8(2)	–[a]
O3–Cu2–N10	101.8(2)/100.5(3)	100.2(2)	–[a]
O4–Cu2–N8	92.4(2)/91.3(3)	92.5(2)	–[a]
O4–Cu2–N9	173.8(2)/172.8(3)	175.8(3)	–[a]
O4–Cu2–N10	92.4(2)/90.3(4)	93.0(2)	–[a]
N8–Cu2–N9	86.5(2)/86.5(4)	86.2(3)	–[a]
N8–Cu2–N10	157.1(3)/157.4(3)	155.6(3)	–[a]
N9–Cu2–N10	86.3(3)/89.1(5)	86.6(3)	–[a]
τ parameter Cu1	0.247/0.292	0.342	0.397
Cu2	0.278/0256	0.337	–[a]

[a]Data of this $[Cu(pmdta)]^{2+}$ fragment corresponds to those of the $[Cu(pmdta)]^{2+}$ fragment comprising the atom Cu1, due to the crystallographically imposed C_2 symmetry of **3A**.

the $O{=}C{-}N_{alkyl}$ function and the middle N donor atom of the pmdta ligands, cf. Figure 1 and Table 2. A related observation was made recently for the asymmetric trinuclear complex $[Cu_3(opooMe)(pmdta)_2](NO_3)_2$ (**13**, opooMe = *o*-phenylene-(*N'*-methyl oxamidato)(oxamato)) [13] and has been compared to observations made for bis(oxamato) type entities. As observed for the CuN_3O_2 units of **1A**–**3A**, even in the case of **13**, the largest O–Cu–N bond angle involves the O donor atom of the $O{=}C{-}N_{alkyl}$ function for the oxamidato side, whereas in case of the oxamato side the largest bond angle involves the O donor atom of the $O{=}C{-}N_{aryl}$ function. Consequences of this observation to magnetic exchange couplings have been discussed [13]. Thus, it seems that for polynuclear complexes comprising one or two oxamidato groups, cf. [13] and [15], this specific feature of the terminal CuN_3O_2 units is of broader validity.

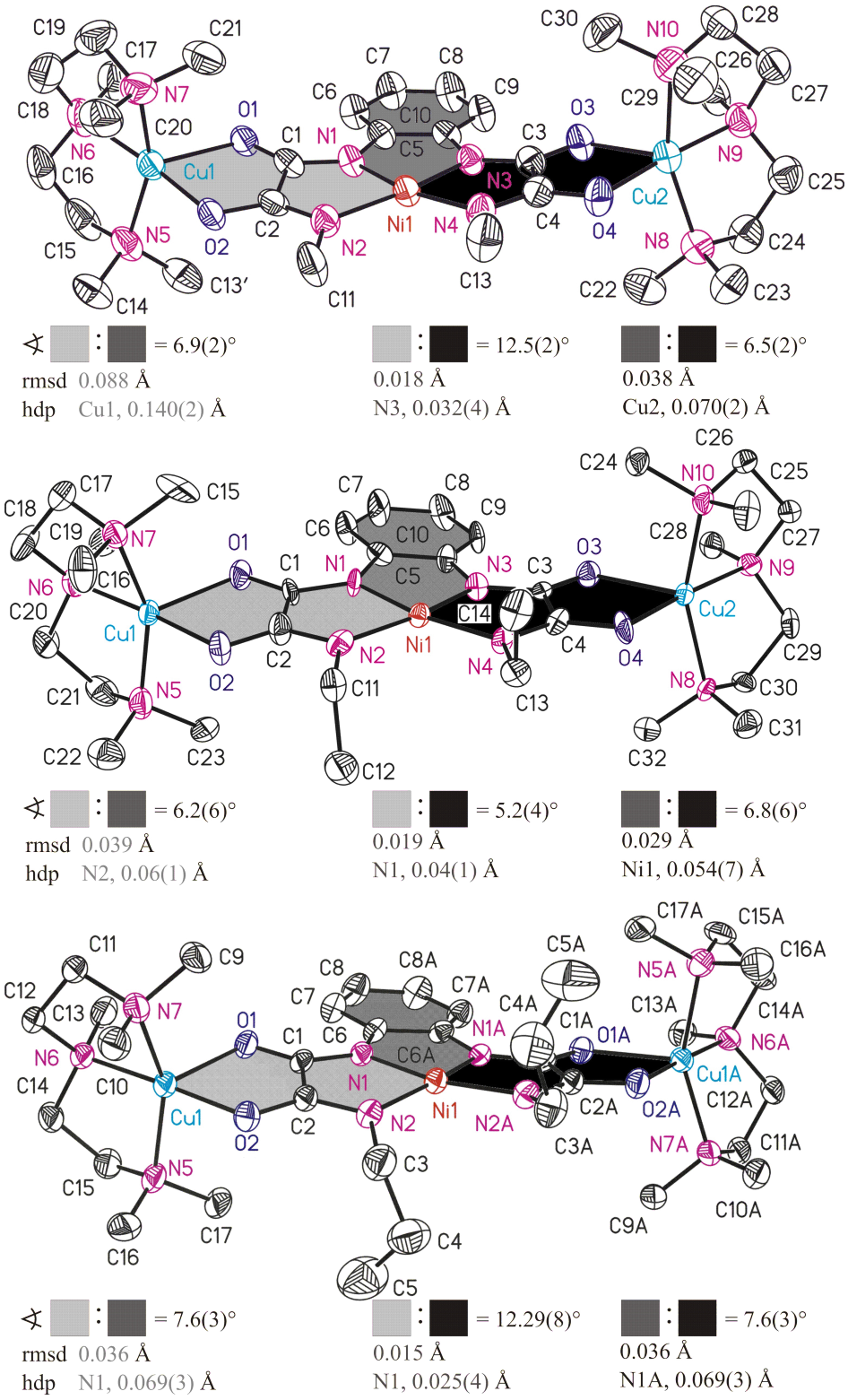

Figure 3: ORTEP diagrams (50% ellipsoid probability) of the molecular structures of **1A** (top), **2A** (middle) and **3A** (down), respectively. All hydrogen atoms are omitted for clarity. The sign ∢ refers to the interplanar angle, rmsd to the root-mean-square deviation from planarity and hdp to the highest deviation from planarity of calculated mean planes of atoms adjoining differently coloured areas. Symmetry code 'A' for 10A: –x, y, –z + $^{3}/_{2}$. The rmsd/hdp of atoms adjoining light gray and black coloured areas amounts as follows: 8A, 0.118 Å/Cu1 with 0.410 Å. 9A, 0.064 Å/O2 with 0.135 Å. 10A, 0.107 Å/O2 with 0.207 Å.

Table 3: Crystal and structural refinement data of **1'**, **2'**and **3'**.

	1'	**2'**	**3'**
Empirical formula	$C_{255}H_{478}Cl_{30}Cu_{16}N_{96}Ni_8O_{80}$	$C_{36}H_{66}Cl_2Cu_2N_{12}NiO_{12}$	$C_{36}H_{68}Cl_4Cu_2N_{12}NiO_{10}$
Formula weight ($g·mol^{-1}$)	8719.15	1115.69	1156.61
Crystal system	orthorhombic	triclinic	orthorhombic
Space group	*Pbca*	*P−1*	*Pbcn*
a (Å)	35.6630(14)	8.2749(3)	29.485(2)
b (Å)	14.0366(7)	10.9892(3)	11.2595(13)
c (Å)	37.5448(16)	30.1863(10)	16.0310(13)
α (°)	90.0	83.352(3)	90.0
β (°)	90.0	82.706(3)	90.0
γ (°)	90.0	70.178(3)	90.0
V ($Å^{-3}$)	18810.3(14)	2553.65(15)	5322.1(8)
Measurement temperature (K)	110	115	110
Radiation source	Cu Kα	Cu Kα	Cu Kα
Wavelength (Å)	1.54184	1.54184	1.54184
Z	2	2	4
Density (calculated) ($Mg·m^{-3}$)	1.539	1.451	1.443
Absorption coefficient (mm^{-1})	4.008	2.912	3.687
F(000)	9036	1164	2408
Reflections collected	53695	10264	10911
Reflections unique /R_{int}[a]	15422, 0.0475	10264, 0.0412	4212, 0.0462
Limiting indices	$-23 \le h \le 41$, $-16 \le k \le 11$, $-43 \le l \le 42$	$-9 \le h \le 9$, $-12 \le k \le 12$, $-34 \le l \le 31$	$-32 \le h \le 34$, $-12 \le k \le 12$, $-18 \le l \le 15$
θ range for data collection (°)	3.417 to 62.981	4.290 to 62.706	4.203 to 62.744
Data/restraints/parameters	15422/1164/1126	10264/662/645	4212/289/292
Goodness-of-fit on F^2 [b]	0.938	1.101	0.830
Final *R* indices [$I > 2\sigma(I)$][c]	R_1 = 0.0816, wR_2 = 0.2279	R_1 = 0.0777, wR_2 = 0.2073	R_1 = 0.0810, wR_2 = 0.2120
R indices (all data)[c]	R_1 = 0.1234, wR_2 = 0.2460	R_1 = 0.0816, wR_2 = 0.2097	R_1 = 0.1364, wR_2 = 0.2337
Largest diff. peak/hole ($e·Å^{-3}$)	1.988/−1.311	1.132/−0.549	0.925/−0.868

[a] $R_{int} = \Sigma\left|F_o^2 - F_o^2(\text{mean})\right| / \Sigma F_o^2$, where F_o^2(mean) is the average intensity of symmetry equivalent diffractions. [b] $S = [\sum w(F_o^2 - F_c^2)^2]/(n-p)^{1/2}$, where *n* = number of reflections, *p* = number of parameters. [c] $R = [\sum(||F_o| - |F_c||)/\sum|F_o|)$; $wR = [\sum(w(F_o^2 - F_c^2)^2)/\sum(wF_o^4)]^{1/2}$.

It is recalled that the Ni^{II} ions of **1A**–**3A** are not coordinated further by any counter anions and/or solvent molecules. In contrast, in $Cu^{II}Cu^{II}Cu^{II}$ type **III** complexes (Figure 1) the central Cu^{II} ions are commonly further coordinated, even by BF_4^- ions [14]. Hence, the Ni^{II} ions of **1A**–**3A** indeed represent diamagnetic $S_{Ni} = 0$ states. Specifically, this property makes them excellently suited candidates to experimentally verify whether long-range magnetic superexchange interactions along two consecutively aligned oxamidato and even oxamato bridges are possible.

Magnetic properties

The results of the measurements of the magnetic field dependence of the magnetization $M(H)$ for samples **1**, **2** and **3** at T = 1.8 K are shown in Figure 4, Figure 5 and Figure 6. All curves can be very well fitted with the Brillouin function for spin $S = {}^1/_2$ and the spectroscopic *g*-factor g = 2.1 determined from the electron spin resonance (ESR) spectra (not shown):

$$M(H) = N_{S=1/2} g S \mu_B \tanh\left(gS\mu_B H / k_B T\right) \quad (1)$$

Here, $N_{S=1/2}$ is the number of spins $^1/_2$ in the molecule, μ_B is the Bohr magneton, and k_B is the Boltzmann constant. Considering that Equation 1 describes the behavior of an ideal paramagnet comprising non-interacting spins and that Equation 1 nicely reproduces the shape of the measured $M(H)$ dependences, one can safely conclude that at T = 1.8 K and (within the experimental uncertainty) there is no magnetic interaction between the Cu^{II} spins of the terminal $[Cu(pmdta)]^{2+}$ complex fragments in all three samples. At fields above 5 T, all $M(H)$ curves saturate, cf. Figure 4–6. Under these experimental condi-

tions one has $gS\mu_B H/k_B T >> 1$ and Equation 1 thus reduces to $M_{sat}(H) = N_{S=1/2} g S \mu_B$ for the heterotrinuclear **1**–**3** with $N_{S=1/2} = 2$. Therefore, the expected saturation magnetization for $S = {}^1/_2$ and $g = 2.1$ should amount to $M_{sat}(H) = 2.1\mu_B$ per formula unit (f.u.). The experimentally observed values of $M_{sat}(H)$ are somewhat smaller, amounting to $1.91\mu_B$, $1.79\mu_B$, and $1.85\mu_B$ for **1**, **2** and **3**, respectively. This implies that the effective number of non-interacting Cu^{II} spins per f.u. which contribute to the magnetization signal is smaller than $N_{S=1/2} = 2$ and amounts to $N^{eff}_{s=1/2} = 1.82$, 1.7, and 1.76 for **1**, **2** and **3**, respectively. This discrepancy of the order of ≈10% in average could be attributed to remaining amounts of packing solvent molecules and thus errors in the determination of the molecular weight. It could be attributed furthermore to the hygroscopic nature of vacuum-dried single crystals of **1'**–**3'** and as the sample preparation was performed under aerobic conditions, cf. Experimental Section and Supporting Information File 1, giving thus errors in the determination of the molecular weight of the samples.

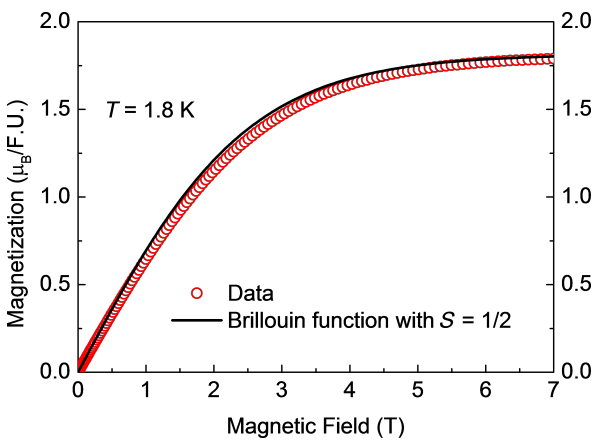

Figure 5: Magnetization versus magnetic field $M(H)$ of **2** at $T = 1.8$ K (symbols) together with the fit of $M(H)$ to the Brillouin function with $S = {}^1/_2$ according to Equation 1 (solid line).

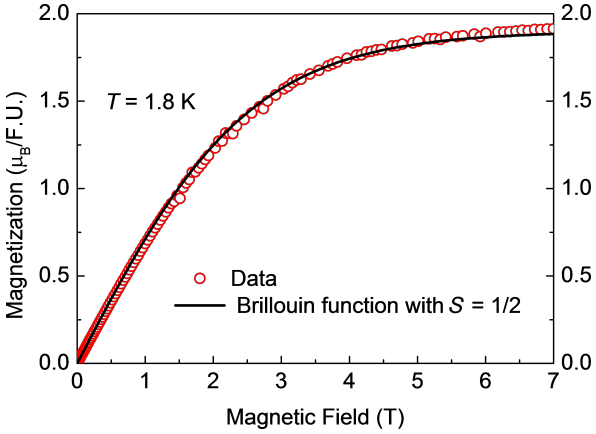

Figure 4: Magnetization versus magnetic field $M(H)$ of **1** at $T = 1.8$ K (symbols) together with the fit of $M(H)$ to the Brillouin function with $S = {}^1/_2$ according to Equation 1 (solid line).

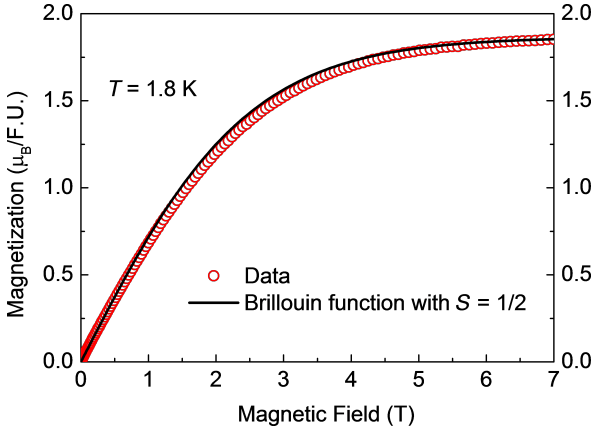

Figure 6: Magnetization versus magnetic field $M(H)$ of **3** at $T = 1.8$ K (symbols) together with the fit of $M(H)$ to the Brillouin function with $S = {}^1/_2$ according to Equation 1 (solid line).

Further insights into the magnetism of the studied samples can be obtained from the analysis of the temperature dependence of the static magnetic susceptibility $\chi = M/H$. The curves $\chi(T)$ and the corresponding inverse susceptibility $\chi^{-1}(T)$ for **1**, **2** and **3** are presented in Figure 7–9. These dependences for **1** and **2** can be very well understood in terms of the Curie–Weiss law:

$$\chi(T) = \chi_0 + N_{S=1/2} N_A g^2 S(S+1)\mu_B^2 / \left[3k_B(T+\theta)\right] \quad (2)$$

Here, χ_0 is a temperature independent term comprising the van Vleck and diamagnetic susceptibilities, N_A is the Avogadro number, and θ is the Curie–Weiss temperature which is a measure of the magnetic interaction between the spins. Since the analysis of the $M(H)$ curves reveal no interaction between Cu^{II} spins, θ can be assumed zero. With $S = {}^1/_2$, $g = 2.1$ and the values of $N^{eff}_{s=1/2}$ from the saturation magnetization $M_{sat}(H)$ one can calculate the dependence (Equation 2) versus $\chi^{-1}_{cal}(T)$ as plotted in black in Figure 7 and Figure 8. Obviously, the plots agree well with the experimental dependence $\chi^{-1}(T)$ for **1** and **2**. Here, the values $\chi_0 = 5{\cdot}10^{-5}$ erg/G^2/mol and $1{\cdot}10^{-4}$ erg/G^2/mol were chosen for samples **1** and **2**, respectively. From the above discussion one can therefore conclude that the self-consistent analysis of the $M(H)$ and $\chi(T)$ dependences gives evidence for the absence of magnetic interaction between the terminal Cu^{II} ions in the heterotrinuclear $Cu^{II}Ni^{II}Cu^{II}$ complexes **1** and **2**.

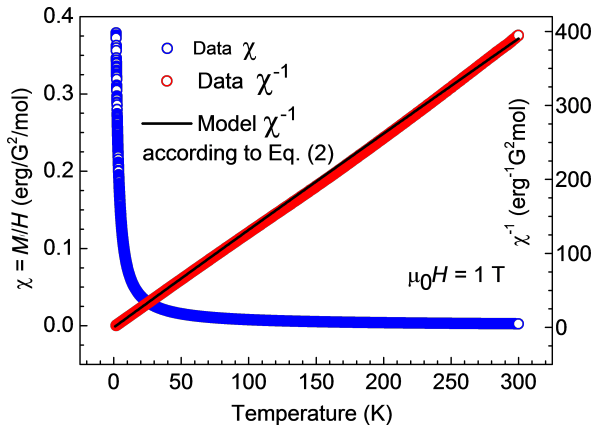

Figure 7: Temperature dependence of the magnetic susceptibility $\chi = M/H$ and of the corresponding inverse susceptibility χ^{-1} for **1** (symbols). The black line represents a model curve $\chi_{cal}^{-1}(T)$ according to Equation 2 (see the text).

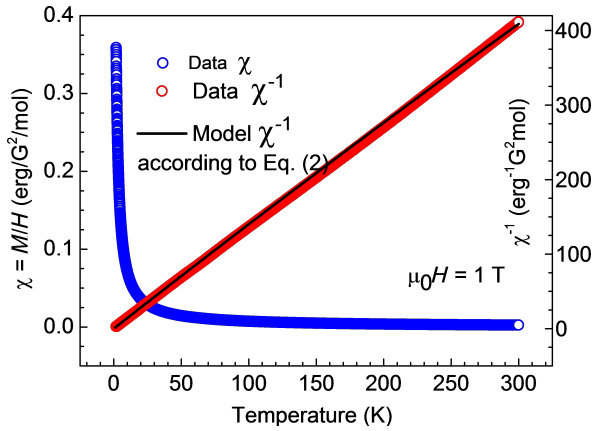

Figure 8: Temperature dependence of the magnetic susceptibility $\chi = M/H$ and of the corresponding inverse susceptibility χ^{-1} for **2** (symbols). The black line represents a model curve $\chi_{cal}^{-1}(T)$ according to Equation 2 (see the text).

Unfortunately, no definite conclusion can be drawn for complex **3**. The similarly calculated curve $\chi_{cal}^{-1}(T)$ according to Equation 2 is shown by the black solid curve in Figure 9. It strongly deviates from the measured $\chi^{-1}(T)$ dependence. Correspondingly, the product $\chi(T)T$ increases with temperature (Figure 10, inset). There is obviously an additional contribution to the static susceptibility, leading to lower values of the inverse susceptibility $\chi_{exp}^{-1}(T)$ of the sample. This contribution is absent in the magnetization data at $T = 1.8$ K, suggesting that it may originate from some species in a concentration of the order of 10% with thermally activated magnetism. The difference $\Delta\chi = \chi_{exp} - \chi_{cal}$ is plotted in Figure 10, main panel, and might originate from paramagnetic impurities, cf. [16]. On the other hand, vacuum-dried powders of **3'** appeared as more hygroscopic compared to the ones of **1'** and **2'**, cf. above and Supporting Information File 1. As the sample preparation was performed under aerobic conditions, it is imaginable that air moisture had an impact on these measured as it is shown for the IR spectroscopically characterized **3**. Attempts to model this contribution with some specific models invoking possible exchange interactions between the two Cu centers (e.g., [13,15,27]) were not successful.

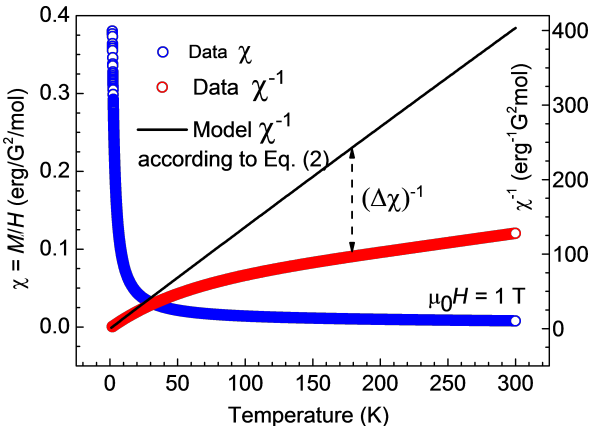

Figure 9: Temperature dependence of the magnetic susceptibility $\chi = M/H$ and of the corresponding inverse susceptibility χ^{-1} for **3**. The black line represents a model curve $\chi_{cal}^{-1}(T)$ according to Equation 2 (see the text). The dashed arrow indicates the discrepancy between the model curve and the experimental dependence.

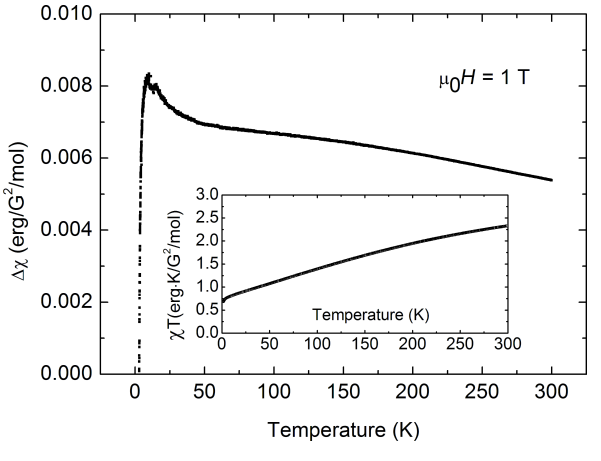

Figure 10: Main panel: Difference between the calculated and measured static susceptibility for **3**. Inset: Temperature dependence of the product χT for **3** (see the text).

Conclusion

The three heterotrinuclear bis(oxamidato) type complexes comprising $[Cu_2Ni(opboR_2)]^{2+}$ fragments (R = Me (**1**), Et (**2**), *n*-Pr

(**3**)) could be successfully synthesized and their identities have been unambiguously established by single-crystal X-ray diffraction studies. These studies revealed that all $[Cu_2Ni(opboR_2)]^{2+}$ fragments are not involved in any intermolecular interactions and are thus discrete in the solid state. That made these three complexes especially well-suited to experimentally verify that there are no magnetic superexchange couplings between their terminal $[Cu(pmdta)]^{2+}$ fragments. Thus, we can conclude that for trinuclear type **IV** as well as type **III** complexes incorporating exclusively 3d transition metal ions, no long-range magnetic couplings across two consecutively aligned oxamidato or oxamato bridges can occur.

Experimental

General methods and materials

All chemicals were purchased from commercial sources and used as received unless stated otherwise. All reactions were carried out under an atmosphere of dry argon using standard Schlenk techniques and vacuum-line manipulations unless stated otherwise. All solvents were distilled prior to use and were purified/dried according to standard procedures [28]. NMR spectra were recorded at room temperature with a Bruker Avance III 500 Ultra Shield Spectrometer (^{1}H at 500.300 MHz and $^{13}C\{^1H\}$ at 125.813 MHz) in the Fourier transform mode. Chemical shifts are reported in δ (ppm) versus $SiMe_4$ with the solvent as the reference signal ([D_6]-DMSO: ^{1}H NMR, δ = 2.54; and $^{13}C\{^1H\}$NMR, δ = 40.45). FTIR spectra were recorded in the range of 400–4000 cm^{-1} on a Perkin-Elmer Spectrum 1000 FTIR spectrophotometer as KBr pellets. Elemental analysis for C, H and N were performed on a Thermo FlashAE 1112 series. The mononuclear Ni^{II}-containing complexes $[n\text{-}Bu_4N]_2[Ni(opboR_2)]$ (R = Me, Et, *n*-Pr) were synthesized according to the literature [15]. Static magnetization measurements at T = 1.8 K and in magnetic fields μ_0H up to 7 T were carried out with a 7 T VSM-SQUID magnetometer from Quantum Design. The temperature dependence of the static magnetization was measured in a temperature range T = 1.8–300 K and at μ_0H = 1 T with this device. For these magnetic measurements, single crystals of the individual complexes were taken and gently heated (ca. 35 °C) overnight in vacuum to obtain materials free of packing solvents. Unfortunately, no inspection of the vacuum-dried crystals under the microscope was possible due to the hygroscopic nature of the materials, cf. below and Supporting Information File 1.

Singe-crystal X-ray crystallographic studies. Intensity data of **1'**, **2'** and **3'**, respectively, were collected on an Oxford Gemini S diffractometer with Cu Kα radiation. The structures were solved by direct methods and refined by full-matrix least-squares methods on F^2 with the SHELX-2013 software [29]. All non-hydrogen atoms were refined anisotropically, and riding models were employed in the treatment of the hydrogen atom positions. Crystallographic data have been deposited at the Cambridge Crystallographic Data Center under the CCDC numbers 923899 (**1'**), 923898 (**2'**) and 923900 (**3'**). In case of **1'** one CH_2Cl_2 packing solvent molecule has been refined to an occupation factor of 0.75 (Cl7, Cl8, C61) and another CH_2Cl_2 packing solvent molecule (Cl5, Cl6, C64) has been refined disordered on two position with occupation factors of 0.75/0.25. In case of **2'** the two ClO_4^- counter ions were both refined disordered on two position with occupation factors of 0.61/0.39 (Cl1, O5–O8) and 0.50/0.50 (Cl2, O9–O12), respectively. Crystals of **2'** were all twinned. The selected one was composed of two nearly equally populated domains covering ca. 98% of all measured reflections, which were simultaneously integrated to generate a hklf 5 file with the diffractometer software [30]. In the case of **3'**, the CH_2Cl_2 packing solvent molecule (Cl1, Cl2, C18) has been refined disordered on two position with occupation factors of 0.67/0.33.

Synthesis of $[NiCu_2(opboR_2)(pmdta)_2][X]_2$, R = Me, X = NO_3 (1); R = Et, X = ClO_4 (2), R = *n*-Pr, X = NO_3 (3). To a solution of $[n\text{-}Bu_4N]_2[Ni(opboR_2)]$ (R = Me, ^{n}Pr) or $[n\text{-}Bu_4N]_2[Ni(opboEt_2)]$ (0.0006 mol) in MeCN (50 mL) a solution of $[Cu(pmdta)(NO_3)_2]$ (0.0012 mol) in MeCN (25 mL) or $[Cu(pmdta)(ClO_4)_2]$ (0.0012 mol) in MeCN (25 mL) was added, respectively. After stirring for 1 h, the resulting reaction mixture was concentrated to approximately 5 mL and Et_2O (100 mL) was added to give a green precipitate. The overlaying solvent mixture was removed via a Teflon tube and MeCN (5 mL) was added to dissolve the residue. A mixture of THF/Et_2O 4:1 (100 mL) was added to precipitate a green powder, which was washed twice with the same solvents mixture (50 mL). After removal of the supernatant, the remaining solid was dried in vacuum. Crystals suitable for X-ray crystallographic studies were grown by slow diffusion of Et_2O vapour in CH_2Cl_2 solutions of **1** and **3** and in a MeCN solution of **2**. Supporting Information File 1 gives the IR spectra of **1**–**3**, respectively.

1. Yield: 0.35 g (63%); anal. calcd for $C_{30}H_{56}Cu_2N_{12}NiO_{10}$ (930.63 g·mol^{-1}): C, 38.72; H, 6.07; N, 18.06; found: C, 38.22; H, 5.85; N, 17.92%; IR: ν = 2958 (m), 2946 (m) (CH); 1630 (s), 1602 (m) (CO); (1383) (s) (N=O).

2. Yield: 0.44 g (77%); anal. calcd for $C_{32}H_{60}Cl_2Cu_2N_{10}NiO_{12}$ (1033.57 g·mol^{-1}): C, 37.19; H, 5.85; N, 13.55; found: C, 37.22; H 5.74; N, 13.28%; IR: ν = 2983 (m), 2960 (m) (CH); 1653 (m), 1614 (m) (CO); (1061) (s) (Cl=O).

3. Yield: 0.43 g (74%); anal. calcd for $C_{34}H_{64}Cu_2N_{12}NiO_{10}$ (986.73 g·mol^{-1}): C, 41.39; H, 6.54; N, 17.03; found: C, 41.11;

H, 6.39; N, 16.89%; IR: ν = 2977 (m), 2951 (m) (CH); 1647 (s), 1614 (m) (CO); (1389) (s) (N=O).

Supporting Information

Supporting Information File 1

IR spectra of **1**–**3**.
[http://www.beilstein-journals.org/bjnano/content/supplementary/2190-4286-8-82-S1.pdf]

Acknowledgements

This work has been supported by the Deutsche Forschungsgemeinschaft through project FOR 1154 “Towards Molecular Spintronics”. M. A. A. thanks the DAAD for a scholarship. We thank Janine Freytag and Ute Stöß for measuring elemental analysis.

References

1. Kahn, O. *Angew. Chem., Int. Ed. Engl.* **1985,** *24,* 834–850. doi:10.1002/anie.198508341
2. Pei, Y.; Kahn, O.; Sletten, J. *J. Am. Chem. Soc.* **1986,** *108,* 3143–3145. doi:10.1021/ja00271a075
3. Stumpf, H. O.; Pei, Y.; Kahn, O.; Sletten, J.; Renard, J. P. *J. Am. Chem. Soc.* **1993,** *115,* 6738–6745. doi:10.1021/ja00068a034
4. Okawa, H.; Mitsumi, M.; Ohba, M.; Kodera, M.; Matsumoto, N. *Bull. Chem. Soc. Jpn.* **1994,** *67,* 2139–2144. doi:10.1246/bcsj.67.2139
5. Pardo, E.; Ruiz-García, R.; Cano, J.; Ottenwaelder, X.; Lescouëzec, R.; Journaux, Y.; Lloret, F.; Julve, M. *Dalton Trans.* **2008,** 2780–2805. doi:10.1039/b801222a
6. Estrada, J.; Fernandez, I.; Pedro, J. R.; Ottenwaelder, X.; Ruiz, R.; Journaux, Y. *Tetrahedron Lett.* **1997,** *38,* 2377–2380. doi:10.1016/S0040-4039(97)00354-7
7. Journaux, Y.; Ruiz, R.; Aukauloo, A.; Pei, Y. *Mol. Cryst. Liq. Cryst.* **1997,** *305,* 193–202. doi:10.1080/10587259708045056
8. Ruiz, R.; Surville-Barland, C.; Aukauloo, A.; Anxolabehere-Mallart, E.; Journaux, Y.; Cano, J.; Muñoz, M. C. *J. Chem. Soc., Dalton Trans.* **1997,** 745–752. doi:10.1039/A607572J
9. Ottenwaelder, X.; Aukauloo, A.; Journaux, Y.; Carrasco, R.; Cano, J.; Cervera, B.; Castro, I.; Curreli, S.; Muñoz, M. C.; Roselló, A. L.; Soto, B.; Ruiz-García, R. *Dalton Trans.* **2005,** 2516–2526. doi:10.1039/b502478a
10. Ruiz, R.; Surville-Barland, C.; Journaux, Y.; Colin, J. C.; Castro, I.; Cervera, B.; Julve, M.; Lloret, F.; Sapiña, F. *Chem. Mater.* **1997,** *9,* 201–209. doi:10.1021/cm9602961
11. Sanada, T.; Suzuki, T.; Kaizaki, S. *J. Chem. Soc., Dalton Trans.* **1998,** 959–966. doi:10.1039/A706834D
12. Kahn, O. *Molecular Magnetism;* VCH: New York, 1993. doi:10.1002/bbpc.19940980935
13. Abdulmalic, M. A.; Aliabadi, A.; Petr, A.; Krupskaya, Y.; Kataev, V.; Büchner, B.; Hahn, T.; Kortus, J.; Rüffer, T. *Dalton Trans.* **2012,** *41,* 14657–14670. doi:10.1039/c2dt31802d
14. Rüffer, T.; Bräuer, B.; Powell, A. K.; Hewitt, I.; Salvan, G. *Inorg. Chim. Acta* **2007,** *360,* 3475–3483. doi:10.1016/j.ica.2007.03.037
15. Abdulmalic, M. A.; Aliabadi, A.; Petr, A.; Krupskaya, Y.; Kataev, V.; Büchner, B.; Zaripov, R.; Vavilova, E.; Voronkova, V.; Salikov, K.; Hahn, T.; Kortus, J.; Meva, F. E.; Schaarschmidt, D.; Rüffer, T. *Dalton Trans.* **2015,** *44,* 8062–8079. doi:10.1039/c4dt03579h
16. Rüffer, T.; Bräuer, B.; Meva, F. E.; Sorace, L. *Inorg. Chim. Acta* **2009,** *362,* 563–569. doi:10.1016/j.ica.2008.05.005
17. Abdulmalic, M. A.; Rüffer, T. *Bull. Chem. Soc. Jpn.* **2013,** *86,* 724–728. doi:10.1246/bcsj.20130031
18. Abdulmalic, M. A. A Tailor-Made Approach for Thin Films and Monolayer Assemblies of bis (oxamato) and bis (oxamidato) Transition Metal Complexes. Ph.D. Thesis, Chemnitz University of Technology, Faculty of Natural Sciences, 2013.
19. Pei, Y.; Journaux, Y.; Kahn, O. *Inorg. Chem.* **1988,** *27,* 399–404. doi:10.1021/ic00275a031
20. Ribas, J.; Diaz, C.; Costa, R.; Journaux, Y.; Mathoniere, C.; Kahn, O.; Gleizes, A. *Inorg. Chem.* **1990,** *29,* 2042–2047. doi:10.1021/ic00336a003
21. Wang, Q.-L.; Zhu, L.-N.; Liao, D.-Z.; Yan, S.-P.; Jiang, Z.-H.; Cheng, P.; Yang, G.-M. *J. Mol. Struct.* **2005,** *754,* 10–15. doi:10.1016/j.molstruc.2005.05.032
22. Gao, E.-Q.; Zhao, Q.-H.; Tang, J.-K.; Liao, D.-Z.; Jiang, Z.-H.; Yan, S.-P. *J. Chem. Soc., Dalton Trans.* **2001,** 1537–1540. doi:10.1039/B100142F
23. Abdulmalic, M. A.; Aliabadi, A.; Petr, A.; Kataev, V.; Rüffer, T. *Dalton Trans.* **2013,** *42,* 1798–1809. doi:10.1039/C2DT32259E
24. Cervera, B.; Sanz, J. L.; Ibáñez, M. J.; Vila, G.; Lloret, F.; Julve, M.; Ruiz, R.; Ottenwaelder, X.; Aukauloo, A.; Poussereau, S.; Journaux, Y.; Muñoz, M. C. *J. Chem. Soc., Dalton Trans.* **1998,** 781–790. doi:10.1039/A706964B
25. Cruickshank, D. W. J. *Acta Crystallogr.* **1949,** *2,* 65–82. doi:10.1107/S0365110X49000175
26. Addison, A. W.; Rao, T. N.; Reedijk, J.; van Rijn, J.; Verschoor, G. C. *J. Chem. Soc., Dalton Trans.* **1984,** 1349–1356. doi:10.1039/DT9840001349
27. Krupskaya, Y.; Alfonsov, A.; Parameswaran, A.; Kataev, V.; Klingeler, R.; Steinfeld, G.; Beyer, N.; Gressenbuch, M.; Kersting, B.; Büchner, B. *ChemPhysChem* **2010,** *11,* 1961–1970. doi:10.1002/cphc.200900935
28. Perin, D. D.; Armarego, W. L. F. *Purification of Laboratory Chemicals,* 3rd ed.; Pergamon: New York, 1988.
29. Sheldrick, G. M. *Acta Crystallogr., Sect. A* **2008,** *A64,* 112–122. doi:10.1107/S0108767307043930
30. *Data collection, refinement and reduction software: CrysAlisPro,* 1.171.38.41l ; Rigaku OD, 2015.

BEILSTEIN JOURNAL OF NANOTECHNOLOGY

Energy-level alignment at interfaces between manganese phthalocyanine and C_{60}

Daniel Waas*, Florian Rückerl, Martin Knupfer* and Bernd Büchner

Full Research Paper

Open Access

Address:
IFW Dresden, P.O. Box 270116, D-01171 Dresden, Germany

Email:
Daniel Waas* - d.waas@ifw-dresden.de; Martin Knupfer* - m.knupfer@ifw-dresden.de

* Corresponding author

Keywords:
C_{60}; manganese phthalocyanine (MnPc); organic interfaces; photoelectron spectroscopy (PES)

Beilstein J. Nanotechnol. **2017,** *8,* 927–932.
doi:10.3762/bjnano.8.94

Received: 23 November 2016
Accepted: 22 March 2017
Published: 25 April 2017

This article is part of the Thematic Series "Towards molecular spintronics".

Guest Editor: G. Salvan

Abstract

We have used photoelectron spectroscopy to determine the energy-level alignment at organic heterojunctions made of manganese phthalocyanine (MnPc) and the fullerene C_{60}. We show that this energy-level alignment depends upon the preparation sequence, which is explained by different molecular orientations. Moreover, our results demonstrate that MnPc/C_{60} interfaces are hardly suited for application in organic photovoltaic devices, since the energy difference of the two lowest unoccupied molecular orbitals (LUMOs) is rather small.

Introduction

Within the last decades we have witnessed considerable progress in the development and understanding of organic (opto-)electronic devices [1-10]. A key issue in any device is the energetics at the device interfaces as it determines charge transport across or charge separation at the corresponding interface [11,12]. Thus, it is not surprising that the investigation of organic semiconductor interfaces has a rather long history, and a large number of studies has resulted in an advanced understanding of such interfaces [11,13-25]. A significant step forward was achieved recently by the development of a theoretical framework which is able to reproduce previous experimental results and to provide a comprehensive overview over the possible energy level alignments [26].

One class of materials that has been considered as constituents of organic devices quite often is the family of transition-metal phthalocyanines [27]. Indeed, several phthalocyanine-based (model) devices have been realized [28-33]. In particular, organic photovoltaic cells containing, e.g., copper phthalocyanine (CuPc) can be found rather frequently in the literature [28,30,34-36]. There, the charge separation at interfaces between the phthalocyanine and an appropriate electron acceptor is a crucial process. Often, fullerenes (C_{60}) and their derivatives are used as acceptor materials.

Amongst the transition-metal phthalocyanines MnPc is exceptional in some respects. Due to the participation of manganese

3d orbitals to the molecular electronic states close to the Fermi energy, MnPc differs significantly from other transition-metal phthalocyanines, as it is characterized by the smallest ionization potential, the largest electron affinity, the smallest band gap and the largest exciton-binding energy [37-42]. Furthermore, it has an unusual spin-state of the Mn^{2+} ion of $S = 3/2$ and shows a weak ferromagnetic interaction in the bulk [43]. In this respect, thorough studies of MnPc in comparison to other transition-metal phthalocyanines (e.g., CuPc) widens our knowledge and understanding of these systems and beyond.

In this contribution we present an investigation of the energy level alignment at MnPc/C_{60} interfaces using photoelectron spectroscopy (PES). We show that this alignment depends on the preparation sequence and that the lowest unoccupied molecular orbitals (LUMOs) of the two molecules lie energetically very close at the interfaces, which is disadvantageous for applications in organic solar cells.

Experimental

We have carried out valence-band and core-level photoelectron spectroscopy studies of MnPc/C_{60} interfaces at room temperature. The preparation and the analysis chamber had a base pressure of about $3 \cdot 10^{-10}$ mbar. For the measurements an X-ray tube XR-50-M with a monochromator Focus-500, a gas-discharge lamp UVS-300 and a hemispherical electron-energy analyzer PHOIBOS-150 (SPECS) were used. The energy scales were calibrated with the Au $4f_{7/2}$ core level emission feature of the substrate at 84.0 eV binding energy and the Fermi cutoff (0 eV binding energy) in the valence-band region. Furthermore, the valence-band spectra were corrected accounting for contributions of He I_β and HeI_γ satellites, assuming they had the same shape, and intensities of 1.8% (He I_β) and 0.5% (He I_γ) of the He I_α signal with an energy shift towards lower binding energies of 1.87 eV (He I_β) and 2.52 eV (He I_γ), respectively. To obtain the correct secondary-electron cutoff a sample bias of −5 eV was applied. The total energy resolution of the spectrometer was 0.35 eV for XPS and 0.15 eV for the UPS measurements.

For our investigations a pre-cleaned Au(100) crystal, controlled by core-level PES spectra, was used as a substrate, on which the MnPc/C_{60} heterojunctions were prepared. The fullerene and manganese phthalocyanine films were grown step by step at room temperature via evaporation of the two materials from home-built evaporators. The film thickness was monitored by a quartz crystal microbalance and additionally determined using the intensity change of the Au $4f_{7/2}$ core level peak according to the method established by Seah and Dench [44]. We have grown the interfaces under investigation by both deposition sequences, MnPc on C_{60} and vice versa. After each MnPc or C_{60} deposition step C1s, N1s, Mn2p and Au4f core-level and valence-band photoelectron spectra were measured in order to follow changes of the electronic structure and to determine the energy level alignment at the interfaces.

Results and Discussion

In Figure 1a and Figure 1b, we present the valence-band data as obtained from the freshly prepared gold substrate, from the starting layers of C_{60} and MnPc, respectively, and from the organic heterojunctions MnPc/C_{60} and C_{60}/MnPc as a function of the respective layer thickness of the organic material on top. The corresponding layer thicknesses are displayed in these two figures. The spectra of pristine C_{60} and MnPc agree very well with those published earlier [39,41,45-49]. Upon deposition of the second organic material, the valence-band spectra change

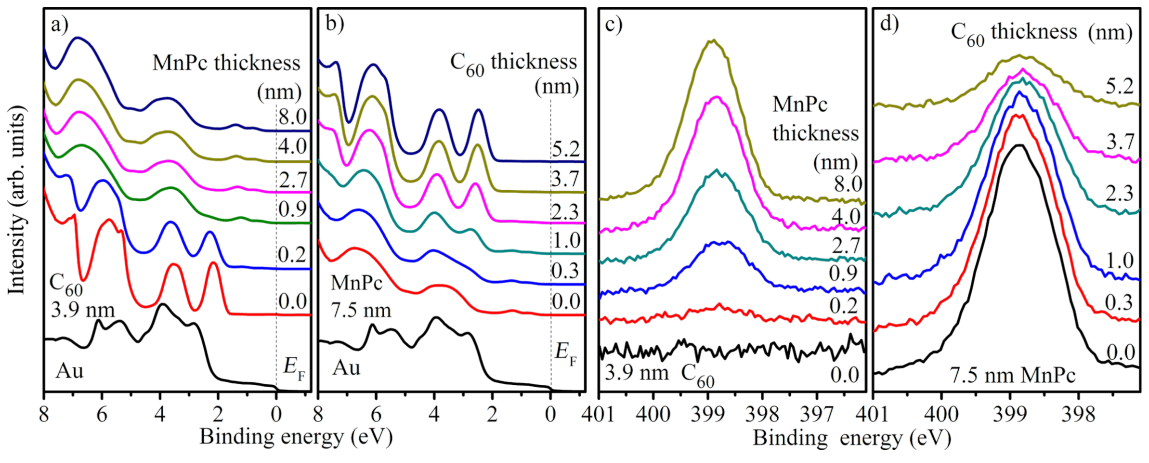

Figure 1: Evolution of the valence-band PES data (He I_α) as a function of a) MnPc deposition onto C_{60} and b) C_{60} deposition onto MnPc. Additionally, the bottom spectrum represents the freshly prepared Au(100) surface. N1s core-level data of MnPc as a function of c) MnPc deposition onto C_{60} and d) C_{60} deposition onto MnPc. The corresponding layer thicknesses are indicated.

characteristically, the valence-band features of the second material, MnPc (Figure 1a) and C_{60} (Figure 1b), are observed and increase with increasing top-layer thicknesses until they are fully developed. In addition, there are energy shifts as a function of layer thickness, which indicate a change of the electrostatic potential at these interfaces as discussed below. There is no evidence for any additional contribution to the spectra and all spectra can be well described by a superposition of the spectra of pure C_{60} and MnPc. This clearly indicates the absence of chemical reactions at the interface studied here, as otherwise additional features or energy shifts would be expected.

We now turn to the discussion of the N1s core level data as obtained from the two deposition series, which are depicted in Figure 1c and Figure 1d. These data stem from MnPc only and, thus, allow insight into the behavior of one side of the interface under investigation. As a function of the corresponding overlayer thickness, the N1s core levels shift in energy, similar to what has been observed for the valence band data (see above). Apart from this energy shift, there are no significant changes in the measured line shapes except some broadening, which can be assigned to positional disorder right at the interface. This again indicates that the interface between C_{60} and MnPc is free of chemical reaction.

Unfortunately, the information that can be obtained from the C1s core levels (see Supporting Information File 1) is less clear, since the contributions of the two materials overlap. We therefore have analyzed only the peak positions from those data sets in which the assignment to the corresponding MnPc or C_{60} structures is clear. Moreover, potential (energy) changes occurring at the interface can also be followed looking at the secondary-electron cutoff, which represents the work function of the actual sample (see Supporting Information File 1). In Figure 2 we summarize all the energy shifts that are observed in valence-band, core-level and secondary-cutoff data for both deposition series in a relative manner. Inspection of this figure makes clear that going across the MnPc/C_{60} interface, all available data shift in a very similar way. This is a strong indication for a common electrostatic potential for all electrons, in good agreement to our conclusions above that the MnPc/C_{60} is free from chemical interactions at the interface.

From our data, we determined the energy-level alignments at the MnPc/C_{60} interface for both deposition sequences, which are shown in Figure 3. The according energies for the highest occupied molecular orbitals (HOMOs) have been taken from those thicknesses of the respective overlayers, for which the energy changes as seen in Figure 2 are virtually saturated. Moreover, we also included the energy position of the lowest unoccupied orbitals (LUMOs), which are derived taking into account the energy gap of the two materials (2.3 eV for C_{60} [46,50] and 1.2 eV for MnPc [41]). Figure 3 indicates a rather large offset of the HOMOs of more than 1 eV at the interface, while the energy positions of the LUMOs are much closer. These values are significantly different from those found for the interface between copper phthalocyanine (CuPc) and C_{60}, where the HOMO offset was reported to be about 0.9 eV [51],

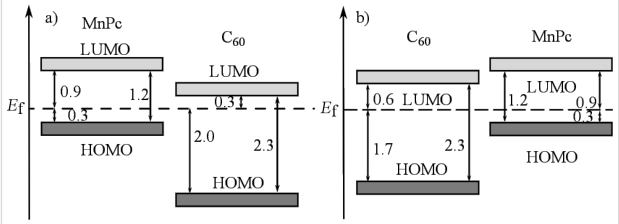

Figure 3: Schematic energy level diagrams of a) MnPc/C_{60}, when C_{60} is deposited onto MnPc and b) C_{60}/MnPc, when MnPc is deposited onto C_{60}. All values are given in electronvolts.

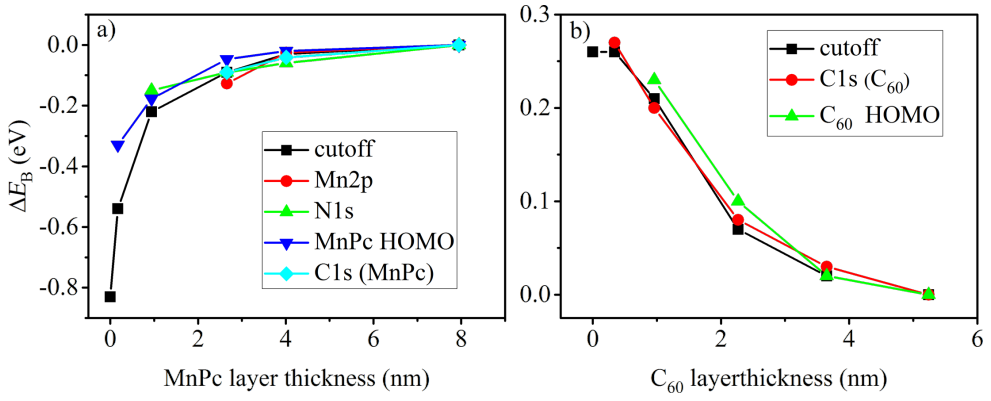

Figure 2: Comparison of the energy shifts of core levels, valence-band features and the secondary-electron cutoff (work function) of a) the C_{60}/MnPc interface and b) the MnPc/C_{60} interface studied in this work.

while the LUMO offset can be estimated to about 0.8 eV. This difference is predominantly due to the rather different energy gaps in CuPc (about 2.2 eV [52]) and MnPc (1.2 eV). As a consequence, MnPc/C_{60} junctions are less suited for the application in organic photovoltaic devices since the energy gain associated with the charge separation at the interface is significantly reduced.

Interestingly, the energy-level alignment at the interface between MnPc and C_{60}, prepared on a gold substrate depends on the deposition sequence. The HOMO offset differs by about 0.3 eV. Furthermore, the position of the Fermi level in MnPc is identical for the two cases (Figure 3). This is in contrast to the CuPc/C_{60} interface where the results were independent of the deposition sequence [51]. Following a recently introduced model [26], such a difference in the energy-level alignment would be expected, if the interaction of the organic layer deposited first and the metal substrate (gold) varies going from MnPc to C_{60} with the consequence of a different Fermi-level position in the layer stack. Moreover, in previous studies [25,53] the importance of interface morphologies, molecular orientations and the resulting density of states on the energy-level alignment has been demonstrated. For instance, at the interface between CuPc and F_{16}CuPc a significant change in the ionization potential and work function due to the molecular orientation was observed [54]. Also, the orientation of phthalocyanine molecules has been used to influence the C_{60} energy levels at respective junctions [55]. It is further known that MnPc and other transition-metal-phthalocyanine molecules grow in a flat lying manner on Au(100) [49,56], while on top of C_{60} they exhibit an edge-on orientation (i.e., they stand up) [57,58]. This then can cause a different energy-level alignment as the ionization depends on the molecular orientation in the layers [53].

Finally, comparing our results to those from an associated measurement of co-evaporated mixtures of MnPc and C_{60} [59] one can find many similarities. The behavior of the valence-band features upon changing the mixing ratio was found to be equivalent to the observed changes with increasing the layer thickness as shown above. Relative energy shifts parallel the behavior as seen in Figure 3.

Conclusion

We have determined the energy-level alignment at interfaces between MnPc and C_{60} using photoelectron spectroscopy studies. The relative energies at the interface depend on the deposition sequence. This is most likely a consequence of different growth modes of MnPc on either Au or C_{60} thin films. Moreover, our results show that at this interface the LUMO levels of MnPc and C_{60} lie energetically too close to render MnPc an appropriate absorber material in organic photovoltaic cells in contrast to, e.g., CuPc.

Supporting Information

Supporting Information File 1

Additional spectra.
[http://www.beilstein-journals.org/bjnano/content/supplementary/2190-4286-8-94-S1.pdf]

Acknowledgements

We thank M. Naumann, R. Hübel and S. Leger for technical assistance. Financial support by the Deutsche Forschungsgemeinschaft (Grant Nos. KN393/14, and KN393/25) is gratefully acknowledged.

References

1. Van Slyke, S.; Chen, C. H.; Tang, C. W. *Appl. Phys. Lett.* **1996,** *69,* 2160–2162. doi:10.1063/1.117151
2. Cicoira, F.; Santato, C. *Adv. Funct. Mater.* **2007,** *17,* 3421–3434. doi:10.1002/adfm.200700174
3. Dodabalapur, A. *Mater. Today* **2006,** *9,* 24–30. doi:10.1016/S1369-7021(06)71444-4
4. Rand, B. P.; Genoe, J.; Heremans, P.; Poortmans, J. *Prog. Photovoltaics* **2007,** *15,* 659–676. doi:10.1002/pip.788
5. Reineke, S.; Lindner, F.; Schwartz, G.; Seidler, N.; Walzer, K.; Lüssem, B.; Leo, K. *Nature* **2009,** *459,* 234–238. doi:10.1038/nature08003
6. Brabec, C. J.; Gowrisanker, S.; Halls, J. J. M.; Laird, D.; Jia, S.; Williams, S. P. *Adv. Mater.* **2010,** *22,* 3839–3856. doi:10.1002/adma.200903697
7. Klauk, H. *Chem. Soc. Rev.* **2010,** *39,* 2643–2666. doi:10.1039/b909902f
8. Sasabe, H.; Kido, J. *Chem. Mater.* **2011,** *23,* 621–630. doi:10.1021/cm1024052
9. Lüssem, B.; Tietze, M. L.; Kleemann, H.; Hoßbach, C.; Bartha, J. W.; Zakhidov, A.; Leo, K. *Nat. Commun.* **2013,** *4,* 2775. doi:10.1038/ncomms3775
10. Lu, L.; Zheng, T.; Wu, Q.; Schneider, A. M.; Zhao, D.; Yu, L. *Chem. Rev.* **2015,** *115,* 12666–12731. doi:10.1021/acs.chemrev.5b00098
11. Koch, N. *ChemPhysChem* **2007,** *8,* 1438–1455. doi:10.1002/cphc.200700177
12. Vandewal, K.; Albrecht, S.; Hoke, E. T.; Graham, K. R.; Widmer, J.; Douglas, J. D.; Schubert, M.; Mateker, W. R.; Bloking, J. T.; Burkhard, G. F.; Sellinger, A.; Fréchet, J. M. J.; Amassian, A.; Riede, M. K.; McGehee, M. D.; Neher, D.; Salleo, A. *Nat. Mater.* **2014,** *13,* 63–68. doi:10.1038/nmat3807
13. Ishii, H.; Sugiyama, K.; Ito, E.; Seki, K. *Adv. Mater.* **1999,** *11,* 605–625. doi:10.1002/(SICI)1521-4095(199906)11:8<605::AID-ADMA605>3.0.CO;2-Q
14. Scott, J. C. *J. Vac. Sci. Technol., A* **2003,** *21,* 521–531. doi:10.1116/1.1559919
15. Kahn, A.; Koch, N.; Gao, W. *J. Polym. Sci., Part B: Polym. Phys.* **2003,** *41,* 2529–2548. doi:10.1002/polb.10642

16. Knupfer, M.; Paasch, G. *J. Vac. Sci. Technol., A* **2005,** *23,* 1072–1077. doi:10.1116/1.1885021
17. Braun, S.; Salaneck, W. R.; Fahlman, M. *Adv. Mater.* **2009,** *21,* 1450–1472. doi:10.1002/adma.200802893
18. Vázquez, H.; Gao, W.; Flores, F.; Kahn, A. *Phys. Rev. B* **2005,** *71,* 041306. doi:10.1103/PhysRevB.71.041306
19. Vázquez, H.; Dappe, Y. J.; Ortega, J.; Flores, F. *Appl. Surf. Sci.* **2007,** *254,* 378–382. doi:10.1016/j.apsusc.2007.07.047
20. Greiner, M. T.; Helander, M. G.; Tang, W.-M.; Wang, Z.-B.; Qiu, J.; Lu, Z.-H. *Nat. Mater.* **2012,** *11,* 76–81. doi:10.1038/nmat3159
21. Koch, N. *Phys. Status Solidi RRL* **2012,** *6,* 277–293. doi:10.1002/pssr.201206208
22. Ley, L.; Smets, Y.; Pakes, C. I.; Ristein, J. *Adv. Funct. Mater.* **2013,** *23,* 794–805. doi:10.1002/adfm.201201412
23. Oehzelt, M.; Koch, N.; Heimel, G. *Nat. Commun.* **2014,** *5,* 4174. doi:10.1038/ncomms5174
24. Akaike, K.; Koch, N.; Heimel, G.; Oehzelt, M. *Adv. Mater. Interfaces* **2015,** *2,* 2196–7350. doi:10.1002/admi.201500232
25. Opitz, A.; Wilke, A.; Amsalem, P.; Oehzelt, M.; Blum, R.-P.; Rabe, J. P.; Mizokuro, T.; Hörmann, U.; Hansson, R.; Moons, E.; Koch, N. *Sci. Rep.* **2016,** *6,* 21291. doi:10.1038/srep21291
26. Oehzelt, M.; Akaike, K.; Koch, N.; Heimel, G. *Sci. Adv.* **2015,** *1,* e1501127. doi:10.1126/sciadv.1501127
27. McKeown, N. B. *Phthalocyanine materials: synthesis, structure and function;* Cambridge University Press: Cambridge, United Kingdom, 1998.
28. Uchida, S.; Xue, J.; Rand, B. P.; Forrest, S. R. *Appl. Phys. Lett.* **2004,** *84,* 4218. doi:10.1063/1.1755833
29. Rand, B. P.; Cheyns, D.; Vasseur, K.; Giebink, N. C.; Mothy, S.; Yi, Y.; Coropceanu, V.; Beljonne, D.; Cornil, J.; Brédas, J.-L.; Genoe, J. *Adv. Funct. Mater.* **2012,** *22,* 2987–2995. doi:10.1002/adfm.201200512
30. Sullivan, P.; Jones, T. S.; Ferguson, A. J.; Heutz, S. *Appl. Phys. Lett.* **2007,** *91,* 233114. doi:10.1063/1.2821229
31. Ren, J.; Meng, S.; Kaxiras, E. *Nano Res.* **2012,** *5,* 248–257. doi:10.1007/s12274-012-0204-7
32. Kim, H. J.; Kim, J. W.; Lee, H. H.; Lee, B.; Kim, J.-J. *Adv. Funct. Mater.* **2012,** *22,* 4244–4248. doi:10.1002/adfm.201200778
33. Holzmueller, F.; Wilde, L.; Wölzl, F.; Koerner, C.; Vandewal, K.; Leo, K. *Org. Electron.* **2015,** *27,* 133–136. doi:10.1016/j.orgel.2015.08.031
34. Rusu, M.; Wiesner, S.; Lauermann, I.; Fischer, C.-H.; Fostiropoulos, K.; Audinot, J. N.; Fleming, Y.; Lux-Steiner, M. C. *Appl. Phys. Lett.* **2010,** *97,* 073504. doi:10.1063/1.3481395
35. Jeong, W.-I.; Lee, Y. E.; Shim, H.-S.; Kim, T.-M.; Kim, S.-Y.; Kim, J.-J. *Adv. Funct. Mater.* **2012,** *22,* 3089–3094. doi:10.1002/adfm.201200069
36. Lo, M. F.; Ng, T. W.; Liu, T. Z.; Roy, V. A. L.; Lai, S. L.; Fung, M. K.; Lee, C. S.; Lee, S. T. *Appl. Phys. Lett.* **2010,** *96,* 113303. doi:10.1063/1.3360336
37. Fielding, P. E.; MacKay, A. G. *Aust. J. Chem.* **1964,** *17,* 750–758. doi:10.1071/CH9640750
38. Grobosch, M.; Aristov, V. Yu.; Molodtsova, O. V.; Schmidt, C.; Doyle, B. P.; Nannarone, S.; Knupfer, M. *J. Phys. Chem. C* **2009,** *113,* 13219–13222. doi:10.1021/jp901731y
39. Grobosch, M.; Mahns, B.; Loose, C.; Friedrich, R.; Schmidt, C.; Kortus, J.; Knupfer, M. *Chem. Phys. Lett.* **2011,** *505,* 122–125. doi:10.1016/j.cplett.2011.02.039
40. Kraus, R.; Grobosch, M.; Knupfer, M. *Chem. Phys. Lett.* **2009,** *469,* 121–124. doi:10.1016/j.cplett.2008.12.090
41. Haidu, F.; Fechner, A.; Salvan, G.; Gordan, O. D.; Fronk, M.; Lehmann, D.; Mahns, B.; Knupfer, M.; Zahn, D. R. T. *AIP Adv.* **2013,** *3,* 062124. doi:10.1063/1.4812230
42. Lever, A. B. P.; Milaeva, E. R.; Speier, G. In *Phthalocyanines Properties and Applications;* Leznoff, C. C.; Lever, A. B. P., Eds.; VCH Publishers: Weinheim, Germany, 1993.
43. Barraclough, C. G.; Martin, R. L.; Mitra, S.; Sherwood, R. C. *J. Chem. Phys.* **1970,** *53,* 1638–1642. doi:10.1063/1.1674236
44. Seah, M. P.; Dench, W. A. *Surf. Interface Anal.* **1979,** *1,* 2–11. doi:10.1002/sia.740010103
45. Benning, P. J.; Poirier, D. M.; Troullier, N.; Martins, J. L.; Weaver, J. H.; Haufler, R. E.; Chibante, L. P. F.; Smalley, R. E. *Phys. Rev. B* **1991,** *44,* 1962. doi:10.1103/PhysRevB.44.1962
46. Lof, R. W.; van Veenendaal, M. A.; Koopmans, B.; Jonkman, H. T.; Sawatzky, G. A. *Phys. Rev. Lett.* **1992,** *68,* 3924. doi:10.1103/PhysRevLett.68.3924
47. Knupfer, M. *Surf. Sci. Rep.* **2001,** *42,* 1–74. doi:10.1016/S0167-5729(00)00012-1
48. Veenstra, S. C.; Heeres, A.; Hadziioannou, G.; Sawatzky, G. A.; Jonkman, H. T. *Appl. Phys. A* **2002,** *75,* 661–666. doi:10.1007/s003390201311
49. Petraki, F.; Peisert, H.; Hoffmann, P.; Uihlein, J.; Knupfer, M.; Chassé, T. *J. Phys. Chem. C* **2012,** *116,* 5121–5127. doi:10.1021/jp211445n
50. Benning, P. J.; Poirier, D. M.; Ohno, T. R.; Chen, Y.; Jost, M. B.; Stepniak, F.; Kroll, G. H.; Weaver, J. H.; Fure, J.; Smalley, R. E. *Phys. Rev. B* **1992,** *45,* 6899. doi:10.1103/PhysRevB.45.6899
51. Molodtsova, O. V.; Knupfer, M. *J. Appl. Phys.* **2006,** *99,* 3704. doi:10.1063/1.2175468
52. Zahn, D. R. T.; Gavrila, G. N.; Gorgoi, M. *Chem. Phys.* **2006,** *325,* 99–112. doi:10.1016/j.chemphys.2006.02.003
53. Duhm, S.; Heimel, G.; Salzmann, I.; Glowatzki, H.; Johnson, R. L.; Vollmer, A.; Rabe, J. P.; Koch, N. *Nat. Mater.* **2008,** *7,* 326–332. doi:10.1038/nmat2119
54. Chen, W.; Huang, H.; Chen, S.; Huang, Y. L.; Gao, X. Y.; Wee, A. T. S. *Chem. Mater.* **2008,** *20,* 7017–7021. doi:10.1021/cm8016352
55. Mao, H. Y.; Wang, R.; Huang, H.; Wang, Y. Z.; Gao, X. Y.; Bao, S. N.; Wee, A. T. S.; Chen, W. *J. Appl. Phys.* **2010,** *108,* 053706. doi:10.1063/1.3475716
56. Lindner, S.; Mahns, B.; Treske, U.; Vilkov, O.; Haidu, F.; Fronk, M.; Zahn, D. R. T.; Knupfer, M. *J. Chem. Phys.* **2014,** *141,* 094706. doi:10.1063/1.4894757
57. Huang, H.; Chen, W.; Chen, S.; Qi, D. C.; Gao, X. Y.; Wee, A. T. S. *Appl. Phys. Lett.* **2009,** *94,* 163304. doi:10.1063/1.3122940
58. Schünemann, C.; Wynands, D.; Wilde, L.; Hein, M. P.; Pfützner, S.; Elschner, C.; Eichhorn, K.-J.; Leo, K.; Riede, M. *Phys. Rev. B* **2012,** *85,* 245314. doi:10.1103/PhysRevB.85.245314
59. Roth, F.; Herzig, M.; Lupulescu, C.; Darlatt, E.; Gottwald, A.; Knupfer, M.; Eberhardt, W. *J. Appl. Phys.* **2015,** *118,* 185310. doi:10.1063/1.4935623

BEILSTEIN JOURNAL OF NANOTECHNOLOGY

Tuning the spin coherence time of Cu(II)−(bis)oxamato and Cu(II)−(bis)oxamidato complexes by advanced ESR pulse protocols

Ruslan Zaripov[1], Evgeniya Vavilova[1], Iskander Khairuzhdinov[1], Kev Salikhov[1], Violeta Voronkova[1], Mohammad A. Abdulmalic[2], Francois E. Meva[3], Saddam Weheabby[2], Tobias Rüffer[2], Bernd Büchner[4,5] and Vladislav Kataev*[4]

Full Research Paper

Open Access

Address:
[1]Kazan E. K. Zavoisky Physical -Technical Institute, Russian Academy of Sciences, 420029 Kazan, Russia, [2]Technische Universität Chemnitz, Fakultät für Naturwissenschaften, Institut für Chemie, Straße der Nationen 62, D-09111 Chemnitz, Germany, [3]Department of Pharmaceutical Sciences, Faculty of Medicine and Pharmaceutical Sciences, University of Douala, BP 2701, Cameroon, [4]Leibniz Institute for Solid State and Materials Research IFW Dresden, D-01171 Dresden, Germany and [5]Institut für Festkörperphysik, Technische Universität Dresden, D-01062 Dresden, Germany

Email:
Vladislav Kataev* - v.kataev@ifw-dresden.de

* Corresponding author

Keywords:
electron spin echo; ESR; hyperfine interaction; molecular complexes; spin coherence

Beilstein J. Nanotechnol. **2017,** *8,* 943–955.
doi:10.3762/bjnano.8.96

Received: 31 January 2017
Accepted: 29 March 2017
Published: 27 April 2017

This article is part of the Thematic Series "Towards molecular spintronics".

Guest Editor: G. Salvan

Abstract

We have investigated with the pulsed ESR technique at X- and Q-band frequencies the coherence and relaxation of Cu spins $S = 1/2$ in single crystals of diamagnetically diluted mononuclear $[n\text{-Bu}_4\text{N}]_2[\text{Cu(opba)}]$ (1%) in the host lattice of $[n\text{-Bu}_4\text{N}]_2[\text{Ni(opba)}]$ (99%, opba = *o*-phenylenebis(oxamato)) and of diamagnetically diluted mononuclear $[n\text{-Bu}_4\text{N}]_2[\text{Cu(opbo}n\text{-Pr}_2)]$ (1%) in the host lattice of $[n\text{-Bu}_4\text{N}]_2[\text{Ni(opbo}n\text{-Pr}_2)]$ (99%, opbo$n$-Pr_2 = *o*-phenylenebis(*N*(propyl)oxamidato)). For that we have measured the electron spin dephasing time T_m at different temperatures with the two-pulse primary echo and with the special Carr–Purcell–Meiboom–Gill (CPMG) multiple microwave pulse sequence. Application of the CPMG protocol has led to a substantial increase of the spin coherence lifetime in both complexes as compared to the primary echo results. It shows the efficiency of the suppression of the electron spin decoherence channel in the studied complexes arising due to spectral diffusion induced by a random modulation of the hyperfine interaction with the nuclear spins. We argue that this method can be used as a test for the relevance of the spectral diffusion for the electron spin decoherence. Our results have revealed a prominent role of the opba^{4-} and opbo$n$-Pr_2^{4-} ligands for the dephasing of the Cu spins. The presence of additional ^{14}N nuclei and protons in $[\text{Cu(opbo}n\text{-Pr}_2)]^{2-}$ as compared to $[\text{Cu(opba)}]^{2-}$ yields significantly shorter T_m times. Such a detrimental effect of the opbo$n$-Pr_2^{4-} ligands has to be

considered when discussing a potential application of the Cu(II)−(bis)oxamato and Cu(II)−(bis)oxamidato complexes as building blocks of more complex molecular structures in prototype spintronic devices. Furthermore, in our work we propose an improved CPMG pulse protocol that enables elimination of unwanted echoes that inevitably appear in the case of inhomogeneously broadened ESR spectra due to the selective excitation of electron spins.

Introduction

Cu(II)−(bis)oxamato and Cu(II)−(bis)oxamidato complexes have attracted in the recent past substantial attention as precursor materials for the synthesis of the corresponding polynuclear complexes which in their turn have been investigated with regard to the magnetic superexchange interactions between the Cu spins mediated by the O and N ligands [1-8]. In this context, the transfer of the spin density from the central metal ion to the ligands and next via the oxamato or oxamidato unit bridging two neighbored paramagnetic transition metal ions is important for the maintaining of the superexchange interaction. This transfer also gives rise to the hyperfine (HF) coupling between the Cu electron spin $S = 1/2$ and ^{14}N nuclear spins $I = 1$ which has been studied with ESR techniques in some detail [8-11]. On the other hand, the dynamics of electron spins, the spin coherence and spin relaxation processes in such complexes have been scarcely addressed so far. Such knowledge is however equally important from the fundamental point of view and also by considering possible applications of mono- and polymetallic Cu(II)−(bis)oxamato and Cu(II)−(bis)oxamidato complexes in molecular electronic devices.

Pulse methods of electron spin resonance (ESR) have been shown to be very informative in assessing the magnetically active molecular complexes for the purpose of quantum information processing. With these techniques, one can directly measure the electron spin coherence times and, moreover, can manipulate the spin states in order to perform quantum logical operations [12-23]. For measurements of the electron spin dephasing time T_m most commonly the simple primary Hahn echo method employing two pulses that rotate the spins at resonance by 90° (π/2) and 180° (π) was used: $\pi/2 - \tau - \pi - \tau -$ echo. Recently we have shown that the application of a more sophisticated, so-called Carr–Purcell–Meiboom–Gill (CPMG) multiple microwave pulse sequence [24,25] can boost the T_m time in molecular complexes up to one order of magnitude [20]. The CPMG pulse protocol can efficiently reduce the manifestation of the unwanted decoherence channel, referred to as spectral diffusion, that arises due to the random modulation of the HF interaction of electron spins with surrounding nuclear spins. It should be noted that the slowing down of the spin decoherence in the multi-pulse CPMG experiments is of special interest with regard to quantum computation on molecular electron spins (see, e.g., [26]), since the realization of the logical operations requires special pulse sequences. For example, it has been shown in [27] that for the realization of the quantum logical operation CNOT on two electron spins it is necessary to apply about twenty microwave pulses. Thus, it is obviously important to take into account the influence of the multiple pulse protocols on the decoherence of spins on which the quantum logical operations are performed.

In the present work, we have investigated the temperature and magnetic field/frequency dependence of the spin dephasing time T_m in the single-crystalline samples of Cu(II)−(bis)oxamato and Cu(II)−(bis)oxamidato molecular complexes with pulse ESR at the X- and Q-band frequencies. The first complex is the diamagnetically diluted mononuclear [*n*-Bu_4N]$_2$[Cu(opba)] complex (1%) in the host lattice of [*n*-Bu_4N]$_2$[Ni(opba)] (99%, opba = *o*-phenylenebis(oxamato)), and the second one is the diamagnetically diluted mononuclear [*n*-Bu_4N]$_2$[Cu(opbo*n*-Pr_2)] complex (1%) in the host lattice of [*n*-Bu_4N]$_2$[Ni(opbo*n*-Pr_2)] (99%, opbo*n*-Pr_2 = *o*-phenylenebis(*N*(propyl)oxamidato)) (Figure 1). We have shown that the CPMG pulse sequence can maintain the spin coherence on the time scale of up to ≈10 μs at low temperatures in the first complex whereas the spin dephasing in the second complex occurs on a shorter time scale. We relate this difference with the detrimental influence of the HF interaction with additional ^{14}N nuclei and protons in the Cu(II)−(bis)oxamidato complex whereas this unwanted effect is reduced in the Cu(II)−(bis)oxamato complex containing less ^{14}N nuclei and protons. In fact, a multi-pulse CPMG sequence which can slow down the phase relaxation of electron spins as compared to the primary echo, the effect which we earlier suggested to be a manifestation of the quantum Zeno effect in multi-pulse experiments [20], can be proposed as a method to reveal on a phenomenological level the contribution of the spectral diffusion to the electron spin phase relaxation. Furthermore, in our experiments we were confronted with the situation that required a modification of the CPMG pulse protocol. The common CPMG theory assumes that all pulses in the sequence unselectively rotate all spins by the same angle of π/2 for the first pulse and of π for the other pulses. However, often in reality the spins are rotated selectively so that the different sub-ensembles of isochromatic spins are turned by the microwave pulses by different angles, yielding additional echoes such as the stimulated echo. Indeed, by applying the standard CPMG pulse protocol we have observed that the CPMG echoes are distorted by additional echoes

arising due to the selective excitation of electron spins by the pulses. We have proposed a modified CPMG pulse protocol, applying which we could successfully eliminate these contributions.

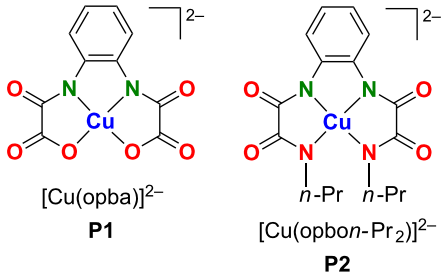

Figure 1: Chemical structures of the anionic complex fragments $[Cu(opba)]^{2-}$ (**P1**, left) and $[Cu(opbo\textit{n}\text{-}Pr_2)]^{2-}$ (**P2**, right).

Experimental Results

In this work two single-crystalline samples of $[n\text{-}Bu_4N]_2[Cu(opba)]$ and $[n\text{-}Bu_4N]_2[Cu(opbo\textit{n}\text{-}Pr_2)]$, denoted in the following as **P1** and **P2** (Figure 1), diamagnetically diluted in the host lattices of their corresponding and diamagnetic Ni(II)-containing complexes $[n\text{-}Bu_4N]_2[Ni(opba)]$ and $[n\text{-}Bu_4N]_2[Ni(opbo\textit{n}\text{-}Pr_2)]$ have been studied with pulse ESR techniques at X- and Q-band microwave frequencies of ≈9.8 GHz and 33.9 GHz, respectively. The accessibility of such diamagnetically diluted single crystals has been recently described by some of us [10,28]. Due to the coordination of two deprotonated amido nitrogen atoms and two carboxylate oxygen atoms for **P1** the formation of a CuO_2N_2 coordination unit was observed [28], cf. Figure 1. It is to note, that not only the CuO_2N_2 unit but the whole complex fragment **P1** was observed as nearly ideally planar [28]. Moreover, the complex fragment **P1** in the diamagnetically diluted single crystals described here is expected to have crystallographically imposed C_2 symmetry, as $[n\text{-}Bu_4N]_2[Cu(opba)]$ and $[n\text{-}Bu_4N]_2[Ni(opba)]$ are structurally isomorphic and possess C_2 symmetric complex fragments as well [28]. For **P2**, due to the coordination of four deprotonated amino nitrogen atoms, the formation of a CuN_4 coordination unit was observed [10], cf. Figure 1. Compared to **P1**, deviations from planarity of the CuN_4 unit and of **P2** are significantly larger [10]. Furthermore, **P2** should be C_1 symmetric in the here described diamagnetically diluted single crystals, cf. crystallographic data and descriptions in [10].

Measurement details

ESR measurements were performed with an Elexsys E580 spectrometer from Bruker operating at X- and Q-bands. The spectrometer is equipped with the standard cavities (ER4118MD5-W1 for X-band and EN5107D2 for Q-band measurements). For the temperature dependent measurements the cavities are inserted into the CF935 cryostat. The temperature is controlled with the ITC503 temperature controller from Oxford Ins.

Echo-detected ESR spectra were recorded by using the standard primary echo method with the subsequent integration of the echo signal during the magnetic field sweep at each field point.

For the measurements of the phase memory time T_m two pulse protocols were used: the primary echo decay and the decay of the Carr–Purcell–Meiboom–Gill echoes [24,25]. With the first protocol, $\pi/2 - \tau - \pi -$ echo, the echo intensity was measured as a function of the time interval τ. The initial τ value of 200 ns was always used, and the increment of τ amounted to 20 ns for both X- and Q-band measurements. The length of the $\pi/2$-pulse amounted to 100 ns and 26 ns for X- and Q-bands, respectively. The long selective $\pi/2$-pulse of 100 ns was used to avoid the modulation of the echo envelope due to the interaction of electron spins with protons (the so-called ESEEM effect) [29-31].

In the CPMG sequence $(\pi/2)_x - \{ \tau - (\pi)_y - \tau -$ echo $-\}^n$- the length of the $\pi/2$-pulse was set to 16 ns and 26 ns at X- and Q-bands, respectively. Due to technical limitations the delay time τ cannot be set shorter as 300 ns. To enable measurements of both complexes in a broad temperature range and at two frequencies with the same value of τ, we have fixed it at 400 ns. The number n of the π-pulses was chosen such, so that the last n-th echo could not be observed anymore above the noise level. For example, at $T = 10$ K it was possible to apply 250 π-pulses, whereas the number of echoes reduced down to $n = 25$ at 80 K. To evaluate the longitudinal relaxation time the stimulated echo (SE) decay was measured at the Q-band. The SE pulse protocol reads: $\pi/2 - \tau - \pi/2 - t - \pi/2 - \tau -$ SE. With this protocol, the SE intensity is measured as a function of time t. The length of the $\pi/2$-pulse amounted to 20 ns, the τ value was equal to 200 ns, and the initial value of t started from 800 ns.

X-band results

Representative spin echo detected ESR spectra of **P1** are shown in Figure 2 for two orientations of the magnetic field $\boldsymbol{H}$. For $\boldsymbol{H}$ normal to the molecular plane ($\boldsymbol{H}||z$-axis) the spectrum consists of four groups of lines arising due to the on-site hyperfine (HF) interaction between the Cu spin $S = 1/2$ with the ^{63,65}Cu nuclear spins $I = 3/2$. Each group is further structured due to the HF-coupling with the ^{14}N nuclear spins $I = 1$ of the two N ligands (Figure 2). For the in-plane orientation ($\boldsymbol{H}||xy$-plane) this group of lines collapses into an only partially resolved spectrum. Similar ESR spectra, though with the less resolved ^{14}N HF structure due to the presence of four instead of two N-donor ligands, were obtained for **P2** (not shown).

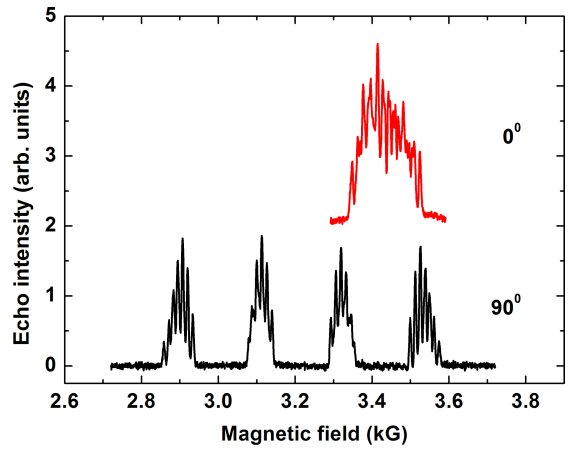

Figure 2: Echo detected ESR spectra of **P1** at a frequency ν = 9.85 GHz (X-band) and at T = 20 K for the magnetic field oriented normal (90°) and parallel (0°) to the molecular plane.

Measurements of the phase relaxation time T_m of both complexes with the primary echo and CPMG pulse sequences have revealed that T_m does not depend on the choice of the peak of the ESR spectrum where the pulse sequences were applied and on the orientation of the field.

Typical time dependences of the spin echo decay for complex **P1** obtained with the primary echo and CPMG pulse sequences are shown in Figure 3a. The primary echo decay is modulated for both, X- and Q-band, measurements (Figure 3), and the modulation frequency is rather low ≈0.3 MHz. We suppose that this modulation effect occurs due to the non-secular part of a type S_zI_x of the HF interaction between the Cu electron spin and the nitrogen nuclei [32]. Note that this particular part of the HF interaction is responsible for the excitation of the forbidden transitions induced by the microwave pulses which produce the electron spin echo signal, so that allowed and forbidden ESR transitions manifest the coherence in their excitation by the microwave pulses. This spin coherence is manifested as the ESEEM effect [29-31].

The spin echo decay curves were fitted with the stretched exponential function $y = y_0 + A\cdot\exp(-2\tau/T_m)^b$, where b is the exponent index characterizing the spread of the relaxation times. For **P1**, the fit reveals $b \approx 2$ for the primary echo decay indicating the effect of the spectral diffusion [33-35], whereas a smaller value of the exponent $b \approx 0.8 - 1$ characterizes the primary echo decay of **P2**. The exponent $b \approx 1$ was found for the decay of the CPMG echoes for both complexes revealing their mono-exponential character. Representative T-dependences of T_m for **P1** and **P2** are shown in Figure 4. Evidently, an application of the CPMG pulse protocol leads to a significant enhancement of the T_m time, by a factor of ≈6 and ≈4 at the lowest temperature for complexes **P1** and **P2**, respectively. On the absolute scale, however, the spin decoherence of **P2** is sigificantly faster as compared to **P1** regardelss the applied pulse sequence.

Q-band results

Echo detected ESR spectra of complexes **P1** and **P2** in the Q-band frequency range have revealed similar features as the X-band spectra. The quartet group of peaks due to the on-site HF coupling with the ^{63,65}Cu nuclear spins is most extended for the magnetic field applied normal to the molecular plane (90° orientation). The structure of each peak due to the HF-coupling with the ^{14}N nuclear spins is visible only for complex **P1** with two N-donor ligands only. Representative spectra for $\boldsymbol{H}||z$-axis are shown in Figure 5. The small shoulders visible at the two high-field peaks in the spectrum of **P2** are presumably related to a small amount of powder inclusions in the sample. It appears that unavoidable thermal cycling of the sample between 10 K and room temperature during the experiments yields microcracks and partial crumbling of some parts of the crystal.

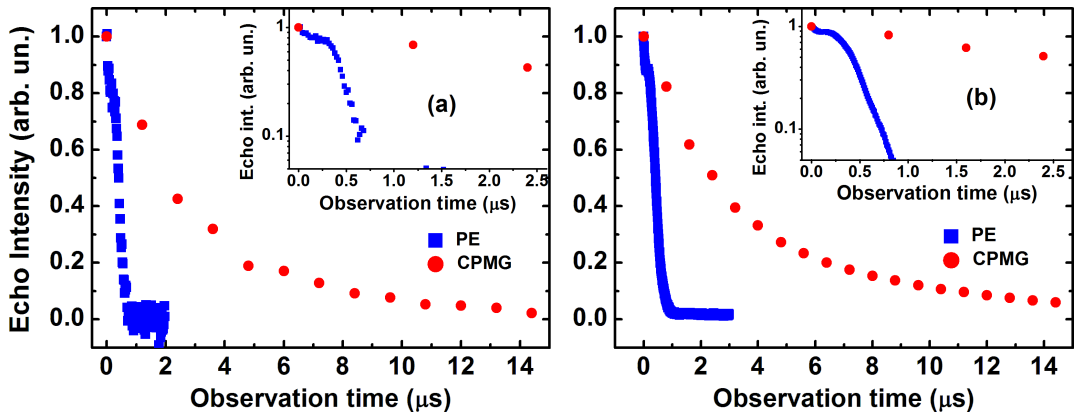

Figure 3: Time dependence of the intensity of the echo signal for complex **P1** at T = 30 K on a linear (main panel) and on a logarithmic scale (inset) measured with the primary echo (blue squares) and CPMG (red circles) protocols at X-band (a) and at Q-band (b).

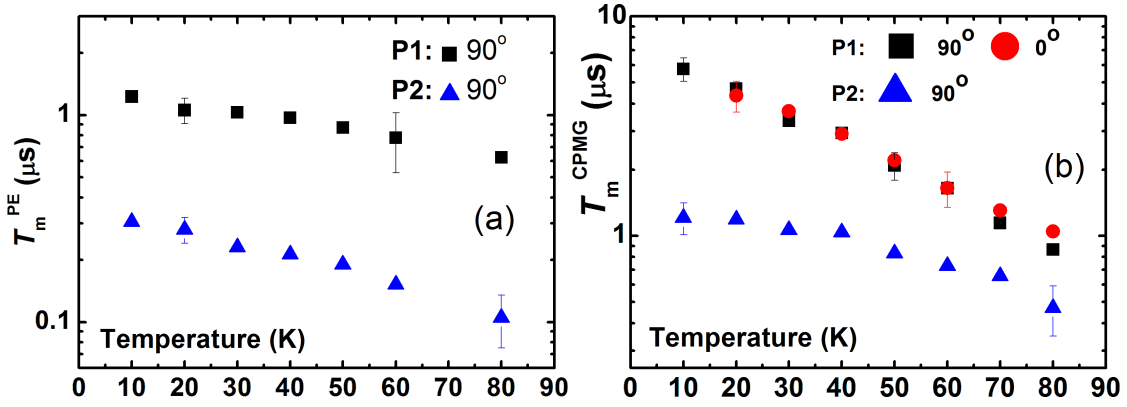

Figure 4: Temperature dependence of the phase relaxation time T_m of **P1** and **P2** at a frequency ν = 9.85 GHz measured with the primary echo sequence for the 90° field orientation (a) and with the CPMG pulse sequence for 0° and 90° orientations of the magnetic field (b).

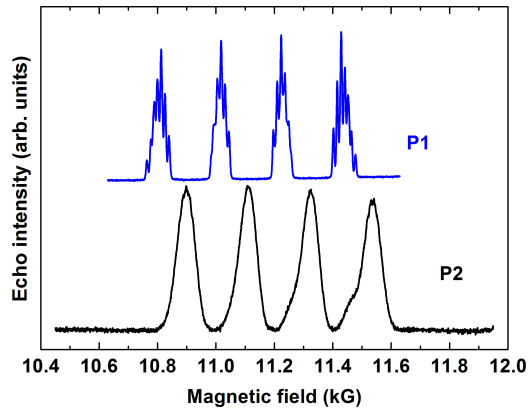

Figure 5: Echo detected ESR spectra of **P1** (top) and **P2** (bottom) at a frequency ν = 33.899 GHz (P1) and 33.915 GHz (P2) (Q-band) and at T = 20 K for the magnetic field oriented normal (90°) to the molecular plane. The difference of the line positions of the two spectra is due to the different g-factor of Cu for the studied samples g_z(P1) = 2.184 [9] and g_z(P2) = 2.159 [10].

Similar to the X-band results, the T_m spin dephasing time for both complexes did not depend on the magnetic field orientation and on the choice of the spectral peak where the measurement took place. Typical spin echo decay curves are shown in Figure 3b. Temperature dependences of T_m measured with the primary echo and CPMG pulse sequences are presented in Figure 6.

The spin coherence time T_m^{CPMG} obtained with the CPMG pulse protocol is enhanced by a factor of ≈2 at the lowest temperature as compared to the T_m^{CPMG} time in the X-band measurements.

Finally, to ensure that the longitudinal relaxation does not influence the electron spin decoherence, the T_1 time was measured for both complexes. As can be seen in Figure 7, at all studied temperatures T_1 is always longer than the respective T_m times, cf. Figure 4 and Figure 6.

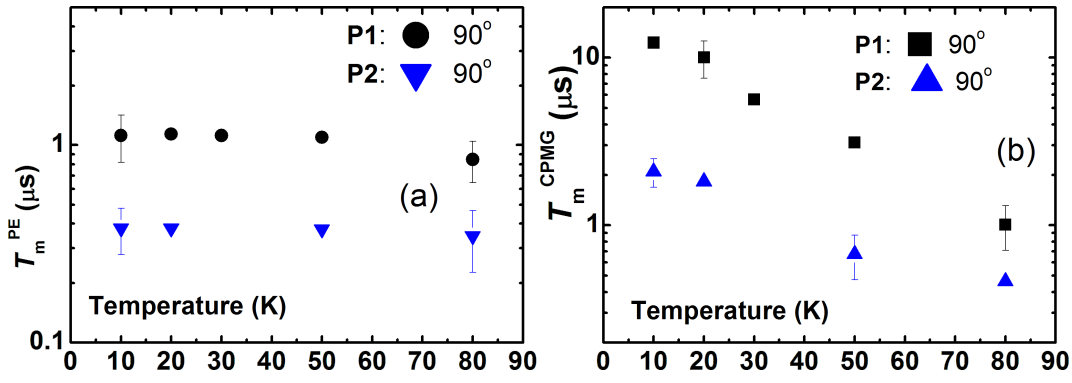

Figure 6: Temperature dependence of the phase relaxation time T_m of **P1** and **P2** at a frequency ν = 33.9 GHz for the 90° field orientation measured with the primary echo sequence (a) and with the CPMG pulse sequence (b).

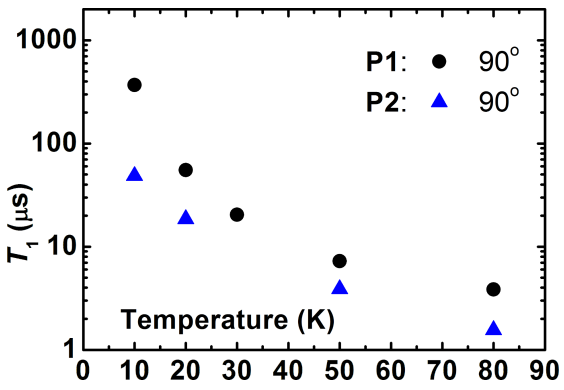

Figure 7: Temperature dependence of the longitudinal relaxation time T_1 of **P1** and **P2** at a frequency ν = 33.9 GHz for the 90° field orientation.

Peculiarities of the CPMG spin echoes

Application of the conventional CPMG pulse protocol $(\pi/2)_x - \tau - (\pi)_y - \tau -$ echo $- \{\tau - (\pi)_y - \tau -$ echo$\}^{(n-1)}$ enhances the spin coherence lifetime of the studied complexes. In addition, the experiments have revealed a dependence of the CPMG echoes on the applied microwave power. At small power levels, the second echo appears larger in amplitude than the first primary echo (Figure 8). In the ideal CPMG experiment, each echo generated by the *n*-th π pulse is the *n*-th refocused primary echo (RPE) which amplitude decreases with *n* due to the inevitable spin decoherence. Thus, the observed nonmonotonous behavior suggests that in addition to the RPE other unwanted echoes contribute to the signal. To separate the RPE from those contributions, a modified pulse sequence $(\pi/2)_x - \tau_1 - (\pi)_y - \tau_1 -$ echo $- \{\tau_2 - (\pi)_y - \tau_2 -$ echo$\}^{(n-1)}$ has been applied. As a result, the RPEs occur always at the time delay τ_2 after the *n*-th π pulse, whereas, for instance the stimulated echo, which can occur due to the incomplete rotation by the pulses of the spins that are slightly off the resonance, has an offset from the RPE by $|\tau_2 - \tau_1|$ (Figure 9). In this way, the "parasitic" contributions to the true CPMG echoes can be identified and separated. Furthermore, they can be successfully eliminated by applying the phase cycling, following the general rules of the cycling of the phases of microwave pulses (see, e.g., [31,36]). In the first run, the first π pulse in the CPMG sequence is applied about the $+y$-axis, $(\pi)_y$, whereas in the second run it is applied about the $-y$-axis $(\pi)_{-y}$, and the two runs are summed up. As a result, an almost perfect sequence of RPEs has been obtained (Figure 9).

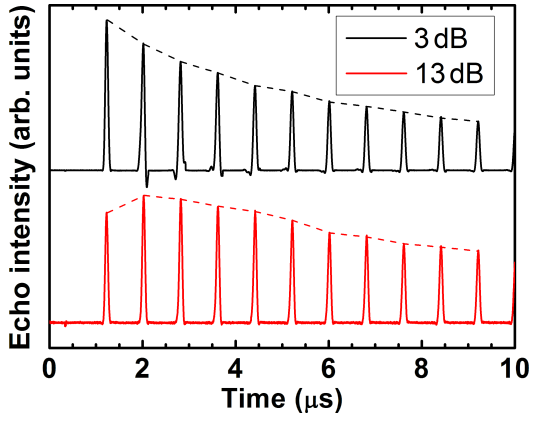

Figure 8: CPMG echoes for complex **P1** for two levels of the microwave power attenuation of 3 dB and 13 dB. Note that in the latter case the 2nd and not the 1st echo has the strongest amplitude.

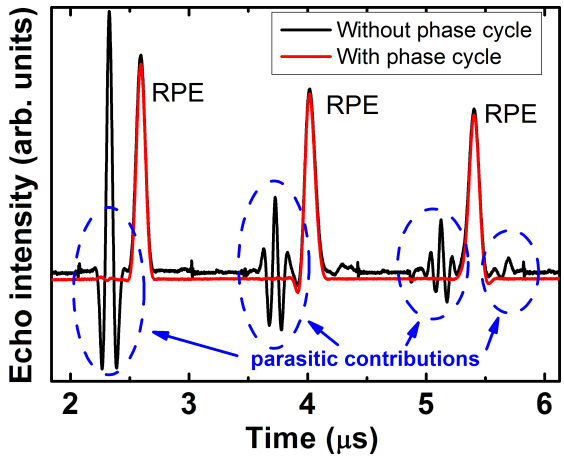

Figure 9: CPMG experiment on complex **P1** at ν = 33.9 GHz, T = 20 K, and $\boldsymbol{H}\|z$-axis: Separation of the refocused primary echoes (RPE) from other parasitic contributions by applying the modified CPMG pulse $(\pi/2)_x - \tau_1 - (\pi)_y - \tau_1 -$ echo $- \{\tau_2 - (\pi)_y - \tau_2 -$ echo$\}^{(n-1)}$ with τ_1 = 400 ns and τ_2 = 700 ns (black line). The signal plotted in red is the result of the phase cycling of the first π pulse that effectively suppresses the "parasitic" contributions to the true CPMG echoes (see the text).

Discussion

Our experiments on the molecular complexes **P1** and **P2** demonstrate clearly that the dephasing time of the Cu spins S = 1/2 can be significantly enhanced by the application of the CPMG pulse protocol. Analogous effect of a drastic increase of the spin coherence time in molecular magnets with the CPMG protocol was observed and comprehensively discussed in our previous work on pulse ESR on model binuclear 1,2-diphosphacyclopentadienyl manganese complexes [20]. There we have studied in detail the slowing down of the electron spin decoherence in a CPMG experiment if the decoherence is caused by the stochastic process of the spectral diffusion. In that our work [20] we have interpreted such slowing down as a manifestation of the quantum Zeno effect in multi-pulse experiments. Thus the occurrence of this effect signifies that the spin decoherence is related to some process of spectral diffusion.

Generally, electron spin decoherence can be due to spin-lattice interaction, spin-rotation interaction, HF interaction with magnetic nuclei as well as spin-spin interaction. On a specific example we considered in [20] the situation when stochastic changes of the resonance frequency of an electron spin are caused by stochastic modulation of the HF interaction of an electron with magnetic nuclei. Also in the present work, considering the above described experimental results on the magnetically diluted Cu(II)–(bis)oxamato and Cu(II)–(bis)oxamidato complexes, it is reasonable to conclude that the major contribution to the decoherence of the Cu(II) electron spins is given by the HF interaction with the nuclear spins of the host lattice.

Electron spin decoherence due to the HF interaction with surrounding nuclei has been studied in a number of works beginning with the pioneering work by Gordon and Bowers [37]. In [30,33,38] a detailed theoretical and experimental investigation of the kinetics of the decay of the envelope of the primary spin echo of hydrogen atoms in frozen solutions of H_2SO_4 and in fused quartz has been made. The shift of the ESR resonance frequency can be written in the form $\Delta\omega = \sum A_k M_k$, where A_k and M_k are the HF constant and the projection of the k-th nuclear spin on the direction of the external magnetic field. For a number of reasons the projection M_k can stochastically change in time. This can be due to the spin-lattice relaxation. The parameters A_k can also randomly change due to molecular motion, lateral and rotational diffusion. One expects that in solids at low temperatures the more effective mechanism of the spectral diffusion arises from the stochastic variations of M_k due to the spin diffusion, i.e., the stochastic mutual flip-flops of two nuclear spins induced by the nuclear dipole–dipole interaction. For example, a characteristic flip-flop frequency of the neighboring protons in a lattice is of the order 10^4–10^5 1/s, i.e., flip-flops occur on the time scale 10^{-4}–10^{-5} s. Thus, the shift of the ESR frequency of the electron spin is a stochastic process $\omega(t)$. A stationary distribution of these frequencies determines the HF structure of an ESR spectrum. The theory in [30,33,38] shows that the primary electron spin echo signal decay resulting from the random modulation of the hyperfine interaction by nuclear spin diffusion obeys the expression

$$V(2\tau) = V_0 e^{\left(-m\tau^k\right)}, \tag{1}$$

where $7/4 \le k \le 3$. In the region of a comparatively small τ, $k = 3$, whereas for large τ the exponent k in Equation 1 takes the value $k = 7/4$.

For the nuclear spins $I = 1/2$ in the limit of large τ one has [30,33,38]:

$$m \approx 2\pi W_n C_n \left(3 r_n \gamma_e \gamma_n \hbar\right)^{3/4}. \tag{2}$$

Here, C_n is the concentration of magnetic nuclei, γ_e and γ_n are the electron and nuclear gyromagnetic ratios, respectively, $\hbar$ is the reduced Planck constant, r_n is the distance between the neighboring magnetic nuclei, and W_n is the nuclear flip-flop rate [39]:

$$W_n = 0.1\hbar\gamma_n^2 C_n. \tag{3}$$

In fact, the parameter m depends on the diffusion barrier for nuclear spins in the vicinity of the unpaired electron. The dipolar magnetic field of the unpaired electron is differently shifting the resonance frequencies of the nuclear spins at different spatial positions. At close distances, the difference of the nuclear spins' frequencies exceeds the strength of their mutual nuclear dipole–dipole interaction so that their mutual flip-flop process is inhibited. Thus, nuclear spin diffusion stops close to the unpaired electron, at a distance which is referred to as a diffusion barrier for nuclear spins. The radius of the spin diffusion barrier d is estimated to be about $d \approx 1$ nm [38]. The parameter m (Equation 2) is expected to be larger if d is reduced. This point has to be kept in mind when studying the electron spin decoherence for different paramagnetic centers.

For complexes **P1** and **P2** studied in the present work we do not expect significantly different radii of the nuclear spin diffusion barrier. From Equation 2 and Equation 3 it follows that $m \sim C_n^2$. The concentration of protons and nitrogen nuclei in **P1** is smaller than in **P2** (Figure 1). Thus, from the above considerations, the electron spin decoherence rate in complex **P1** is expected to be smaller than in complex **P2** which agrees qualitatively very well with the experimental observations (Figure 3 and Figure 6).

Though the kinetics of the decay of the primary and stimulated echoes due to the spectral diffusion induced by the stochastic modulation of the HF interaction in the presence of the nuclear spin diffusion was theoretically elaborated in [38], the manifestation of this mechanism for a CPMG pulse protocol was first theoretically addressed in [20] in the framework of the model of a normal stochastic process. If the number of magnetic nuclei that effectively interact with an electron is sufficiently large (e.g., larger than 5), then in a good approximation the respective frequency distribution can be described by the Gaussian with the dispersion

$$\sigma \equiv \left\langle \omega^2 \right\rangle = (1/3) \sum I_k \left(I_k + 1\right) A_k^2, \tag{4}$$

where I_k is the spin of the k-th nucleus. It should be noted that the magnetic nuclei nearest to the electron, i.e., those located closer than the radius of the diffusion barrier d, do not contribute to the spectral diffusion. Therefore, in Equation 4 the dispersion σ is determined by the HF interaction with the nuclear spins at distances larger than d. Thus, in complexes **P1** and **P2** studied in the present work the HF interaction of the Cu(II) electron spin with its own ^{63,65}Cu nucleus and with the ^{14}N nuclei of the nearest ligands most likely do not contribute to the spectral diffusion whereas distant ^{63,65}Cu and ^{14}N nuclei can contribute to this process. This means that, unfortunately, the parameter σ in Equation 4 cannot be calculated simply as a dispersion of a usual continuous wave ESR spectrum that contains contribution of all magnetic nuclei, both within and outside the diffusion barrier sphere of the radius d.

For quantitative estimates, it is necessary to describe the stochastic process ω(t). In [20] a phenomenological model of the normal stochastic process has been considered for the description of the spectral diffusion. In this model such a process can be fully described by the dispersion of the frequency distribution and the frequency correlation function

$$g(\tau) = \left(1/\left\langle \omega^2 \right\rangle\right)\left\langle \omega(t)\omega(t-\tau)\right\rangle. \quad (5)$$

We can define a characteristic time of the decay of the frequency correlation as τ_c, and assume that the correlation function $g(\tau)$ (Equation 5) has an exponential form:

$$g(\tau) = \exp\left(-|\tau|/\tau_c\right). \quad (6)$$

In the case of the spectral diffusion induced by the nuclear spin diffusion τ_c is of the order of the flip-flop time of the neighboring nuclear spins. If those spin-flops are caused by the nuclear dipole–dipole interaction, then $\tau_c \approx 10^{-4}$–10^{-5} s [39]. According to [20], the expression for the n-th signal in a CPMG experiment in the presence of spectral diffusion reads:

$$\begin{aligned} V_n = \exp\Big\{-\Big[&2f(\tau)+(n-1)f(2\tau)+ \\ &\sigma\tau_c^2\Bigg((-1)^n\exp\left(-\frac{2(n-1)\tau}{\tau_c}\right)g^2(\tau)- \\ &2\sum_{k=0}^{n-2}(-1)^k\exp\left(-\frac{2k\tau}{\tau_c}\right)g(\tau)g(2\tau)- \\ &\sum_{k=0}^{n-3}(-1)^k(n-2-k)\exp\left(-\frac{2k\tau}{\tau_c}\right)g^2(2\tau)\Bigg)\Big]\Big\} \end{aligned} \quad (7)$$

In Equation 7 the functions $f(t)$ and $g(t)$ are defined as:

$$f(t) = \sigma\left[t\tau_c - \tau_c^2 g(t)\right],\ g(t) = 1-\exp\left(-t/\tau_c\right). \quad (8)$$

Setting n = 1 in Equation 7 yields the expression for the amplitude of the primary echo

$$V(2\tau) = \exp\left\{-\left[2f(\tau)-\sigma\tau_c^2 g^2(\tau)\right]\right\}. \quad (9)$$

For short observation times $\tau << \tau_c$, Equation 9 reduces to

$$V(2\tau) = \exp\left(-\left(2/3\right)\sigma\tau^3/\tau_c\right). \quad (10)$$

(Note that in [20] Equation 10 was mistakenly written as $V(2\tau) = \exp(-2\sigma\tau^2)$, cf. Eq. (11) in [20]). For long observation times $\tau >> \tau_c$, it follows from Equation 9 that the primary echo signal exponentially depends on τ:

$$V(2\tau) = \exp\left(-4\sigma\tau_c\left(\tau-1.5\tau_c\right)\right). \quad (11)$$

It can be concluded from Equation 10 and Equation 11 that in the framework of the phenomenological model of the normal stochastic process for the description of the spectral diffusion due to the stochastic modulation of the HF interaction by the nuclear spin diffusion, the dependence of the decay of the primary echo signal has the form $\exp(-m\tau^k)$ where the index k changes from 3 to 1 by increasing the observation time 2τ. This agrees qualitatively with the earlier result in [38].

The phenomenological model of the spectral diffusion describes correctly also the manifestation of the spectral diffusion in a CPMG experiment. Indeed, as has been shown in [20] the electron spin decoherence in this case slows down according to Equation 7 and Equation 8. The decay of the CPMG echoes with $n >> 1$ occurs slower than for the primary echo if one compares the echo amplitudes with the same total time interval of the observation, i.e., the time 2τ in the primary echo experiment should be equal to the time $2n\tau$ in the CPMG experiment.

The decay of the primary echo signal and the decay of the echo signal in the CPMG pulse protocol with 6 and 12 π-pulses calculated with Equation 7 and Equation 8 are shown in Figure 10 and Figure 11, respectively. In numerical calculations the time τ is given in units of the correlation time τ_c for the normal stochastic process of the spectral diffusion and the dispersion of the resonance frequency σ is given in units of $1/\tau_c^2$. In Figure 11 the decay of the CPMG echo signal is

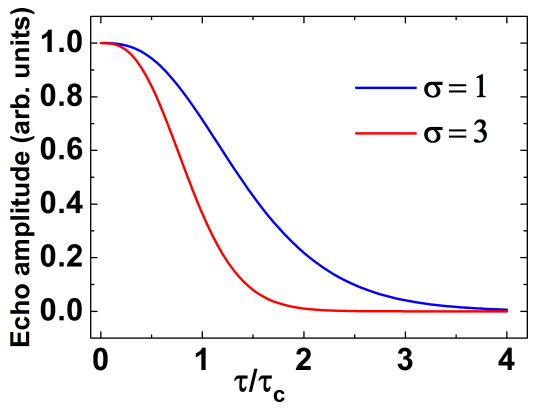

Figure 10: The calculated decay of the primary echo signal as a function of the time delay τ between the two pulses. τ is measured in units of the correlation time τ_c for the normal stochastic process of the spectral diffusion and the dispersion of the resonance frequency σ is given in units of $1/\tau_c^2$. The calculations were made for the two values of the dispersion σ = 1 (blue) and σ = 3 (red).

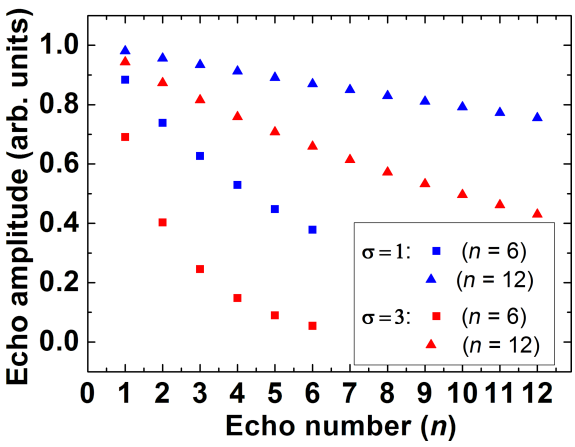

Figure 11: The calculated decay of the echo signal in the CPMG experiment as a function of the number *n* of the π-pulses in the CPMG protocol. The results of the modeling are presented for the same values of the dispersion σ as in Figure 10, σ = 1 (blue symbols) and σ = 3 (red symbols). The calculations were made for *n* = 6 (squares) and *n* = 12 (triangles). The total observation time of $10\tau_c$ is the same as in Figure 10.

plotted as a function of the number *n* of the CPMG echo. Obviously, Figure 10 demonstrates a rather complicated kinetics of the decay of the signal of the primary echo due to the spectral diffusion (see also Equations 9, 10 and 11). As can be seen there, with increasing the dispersion the contribution of the spectral diffusion to the spin decoherence increases and the echo signal decays faster. It should be noted that for sufficiently large time intervals between the pulses the decay of this signal can be described by the simple exponent (see, Equation 10) albeit this simple dependence holds only for the tail of the spin echo signal decay (Figure 10).

From these calculations the following conclusions can be drawn. Similar to the situation with the primary echo the intensity of the CPMG echo signals decays faster with increasing the dispersion σ (cf. squares and triangles in Figure 11). The dependence of the decay of the intensity of the CPMG echo as a function of its number *n* can be described by a simple exponent, in contrast to a more complicated behavior in the case of the primary echo. Note that the total observation time in Figure 10 and Figure 11 is equal and amounts to$10\tau_c$. From the point of view of potential application of electron spins as qubits, the slowing down of the spin decoherence as compared to the primary echo is certainly an interesting effect. Furthermore, for a given time interval of the observation the slowing down of the spin decoherence increases with the increase of the number of refocusing π-pulses in the CPMG protocol.

Thus the calculations presented above allow one to interpret qualitatively a drastic difference between the experimentally observed fast decay of the primary echo signal and the much slower decay of the CPMG echoes as shown in Figure 3 which demonstrates the efficiency of the CPMG protocol for the elimination of the effect of spectral diffusion on the electron spin decoherence in the studied molecular complexes. We have attempted to fit experimentally observed kinetic curves of the echo signal decay using Equation 7. Two examples with different fit parameters are presented in Figure 12a,b and Figure 12c,d, respectively.

The results shown in Figure 12 demonstrate that by varying parameters of the theoretical model, namely, the dispersion of the frequency σ and the frequency correlation time τ_c one can, in principle, fit the experimental data using Equation 7 reasonably well (see Figure 12c,d). However, such a good agreement with experiment is achieved by using a rather unrealistic value of τ_c = 120 ns. This correlation time is at least an order of magnitude smaller than that expected for a mutual flip-flop process responsible for the nuclear spin diffusion. Taking a more realistic value of τ_c = 2000 ns worsens the agreement substantially (see Figure 12a,b). This implies that although the theoretical model described above can provide a reasonably good qualitative description of the experimentally observed echo decay kinetic curves, but, on the quantitative level, in addition to the spin diffusion one has to take into account also other sources of stochastic modulation of the HF interaction.

Indeed, there are also other experimental observations which indicate that the nuclear spin diffusion is not only one source of a random modulation of the HF interaction in the studied materials. It should be noted that the electron spin dephasing time T_m obtained both with the primary echo and the CPMG pulse protocol is generally longer at the Q-band than at the X-band

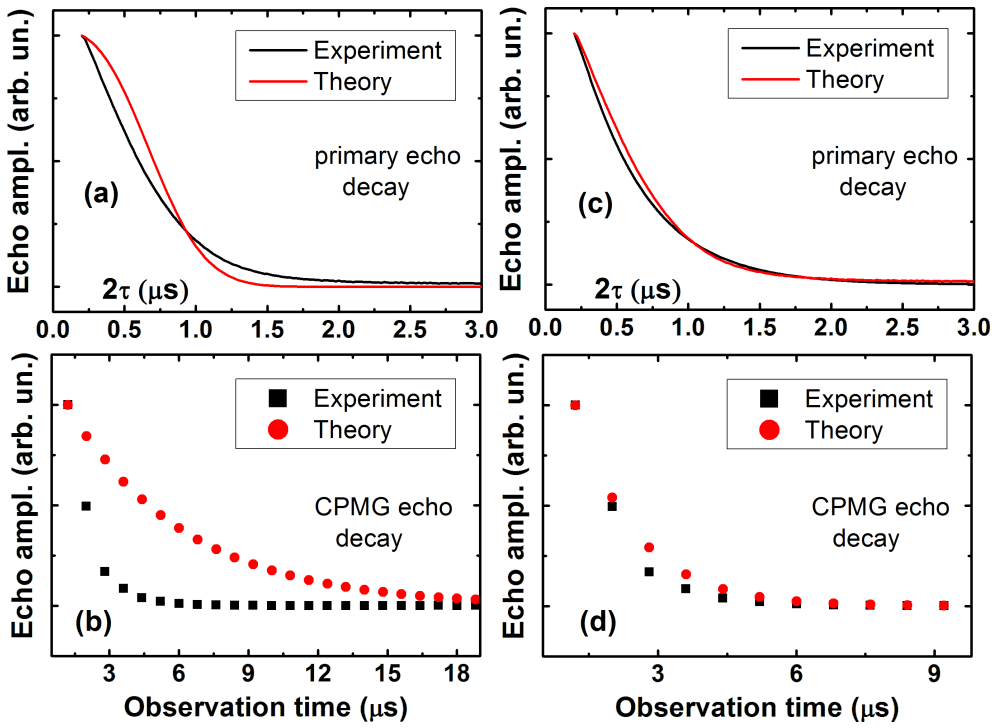

Figure 12: Comparison of the experimental and model dependences of the decay of the primary (a,c) and CPMG echoes (b,d) for complex **P1** at T = 80 K. The model curves in (a,b) were calculated according to Equation 7 with the correlation time τ_c = 2 μs, the diffusion barrier d = 0.7 nm, and $\sigma\tau_c^2 \sim 32$, and in (c,d) with τ_c = 120 ns, d = 0.68 nm, and $\sigma\tau_c^2 \sim 0.13$, respectively.

(Figure 4 and Figure 6). At both ESR frequencies the T_m time is systematically shorter for complex **P2** as compared to complex **P1** due to a larger number of magnetic nuclei (^{14}N and ^{1}H) in the former complex as compared to the latter one. The difference of the decoherence rate in the X- and Q-band measurements possibly indicates that the stochastic modulation of the HF interaction is caused not only by the nuclear spin diffusion but also by the stochastic changes of the nuclear spin projections due to the nuclear spin-lattice relaxation. Since the latter slows down with increasing the field strength [39], its possible effect on T_m should decrease too, which could qualitatively explain the difference of the electron spin dephasing rates in the two ESR frequency bands. Furthermore, the rate of the nuclear mutual flip-flops may be magnetic field dependent. In particular, the field-induced inhomogeneous broadening of the NMR line could make flip-flop processes less efficient. In any case, on the quantitative level, this interesting problem requires a special theoretical treatment to be addressed separately.

There is one more experimental observation which indicates a possible contribution of the nuclear spin-lattice relaxation to the electron spin dephasing induced by the HF interaction. Indeed, the spectral diffusion induced by random changes of the HF interaction caused by the nuclear spin diffusion is expected to be independent of temperature. Experimentally, the electron spin dephasing time T_m decreases with increasing temperature (Figure 4). This suggests additional temperature dependent contributions to the stochastic modulation of the HF interaction in the studied complexes. Such contributions, which could explain the observed temperature dependence of T_m, may arise due to a random modulation of the HF interaction by a temperature dependent nuclear spin-lattice relaxation and/or by molecular mobility, e.g., by rotation of the CH_3, CH_2CH_3 or other groups. Arguably, at low temperatures the local HF magnetic field acting on the electron spin is most effectively modulated by the nuclear spin diffusion. With increasing temperature a contribution of the nuclear spin-lattice relaxation to the stochastic modulation of the HF interaction, i.e., to the spectral diffusion, may become significant. As has been shown in [30,33], these two spectral diffusion mechanisms lead to different kinetics of the electron spin phase relaxation. The difference originates from the fact that in the case of the nuclear spin diffusion in an elementary act two spins are involved into the flip-flop process, while in the case of the spin-lattice relaxation each nuclear spin flips (or flops) independently. It should be noted that there are further significant differences between the two above discussed mechanisms. In the case of the nuclear spin diffusion its contribution to the electron spin dephasing is determined by the HF coupling to the nuclear spins at distances larger that the diffusion barrier. In the case of the nuclear spin

relaxation all nuclei, including those inside the diffusion barrier, contribute to the shortening of T_m. In addition, also the nuclear spin-lattice relaxation time depends on the distance between a particular nucleus and the paramagnetic center. This circumstance, as well freezing of the motion of the propyl groups may be responsible for the reduction of the stretching exponent $b < 1$ of the spin echo decay of complex **P2**.

Finally, we note on the specifics of the use of the CPMG pulse sequences in an ESR experiment. As it was originally pointed out in [40], unlike in an NMR experiment on non-magnetic substances where the first pulse excites the complete absorption line of the nuclear spins under study, it is often not the case for the inhomogeneously broadened ESR line. Due to a selective excitation of this line, the electron spins are turned by the first microwave pulse by different angles depending on their offset from the resonance frequency. As a result, in addition to the CPMG echoes which are basically the refocused primary echo, other unwanted echoes appear. Complications due to a selective excitation of spins in CPMG ESR experiments were later observed in several works [41-45]. However, up to now a detailed analysis of the underlying mechanisms giving rise to these complications, their impact on the determination of the spin dephasing time and the ways of elimination of unwanted effects were not elaborated sufficiently. The phase cycling which we use in our work as well as other cycling protocols [44] are definitely helpful in improving the quality of a CPMG ESR experiment. A more detailed theoretical and experimental treatment of this very interesting problem will be published elsewhere.

Conclusion

We have experimentally studied the dephasing time T_m of Cu(II) spins in single crystals of diamagnetically diluted mononuclear $[n\text{-}Bu_4N]_2[Cu(opba)]$ (1%) in the host lattice of $[n\text{-}Bu_4N]_2[Ni(opba)]$ (**P1**) and of diamagnetically diluted mononuclear $[n\text{-}Bu_4N]_2[Cu(opbo\textit{n}\text{-}Pr_2)]$ (1%) in the host lattice of $[n\text{-}Bu_4N]_2[Ni(opbo\textit{n}\text{-}Pr_2)]$ (**P2**) by pulse ESR measurements at X- and Q-band frequencies. We have found that application of the special Carr–Purcell–Meiboom–Gill (CPMG) pulse protocol significantly increase the T_m time of both complexes as compared to the results of the standard two-pulse primary echo measurements. Our theoretical analysis shows that this effect is related to an efficient suppression by the CPMG multi-pulse sequence of the detrimental influence on the spin coherence lifetime of the spectral diffusion induced by the stochastic modulation of the HF interaction. This stochastic modulation can be caused by several random processes such as the nuclear spin diffusion, the nuclear spin-lattice relaxation, molecular mobility, e.g., the random rotation of CH_3, CH_2CH_3 groups, etc. At low temperatures the first mechanism is dominating whereas with increasing temperature the other two may become relevant, thus explaining the experimentally observed decrease of the electron spin dephasing time T_m. The systematically shorter T_m times at all temperatures found for complex **P2** as compared to **P1** can be obviously related to a larger number of magnetic nuclei in the former complex that additionally contribute to the spectral diffusion mechanism of the electron spin dephasing. It is likely for this reason the T_m times of both complexes measured by the primary spin echo appear shorter as in a number of other copper, vanadyl and chromium complexes reported and discussed in recent literature in the context of quantum information processing (see, e.g., [23,45-48]). This has to be kept in mind while considering possible applications of Cu(II)–(bis)oxamato and Cu(II)–(bis)oxamidato complexes in molecular electronic devices. Our experimental results show that this drawback can be to a large extent overcome by application of the multi-pulse CPMG sequences. Additionally, this approach offers a possibility to assess if some mechanism of the spectral diffusion affects the electron spin coherence by measuring the T_m time with primary and CPMG echoes which in this case should be substantially different. What specific mechanism of the spectral diffusion is active can be concluded from the analysis of the kinetics of the phase relaxation and its dependence on temperature, HF interaction, etc.

Finally, on the experimental level, we have suggested a modification of the standard CPMG pulse protocol that enabled an effective elimination of additional unwanted echoes arising due to a selective excitation of electron spins.

Acknowledgements

This work was supported by the Deutsche Forschungsgemeinschaft through the Focused Research Unit FOR1154 “Towards Molecular Spintronics” and through the Program of Fundamental Research of the Presidium RAS No. 1.26П.

References

1. Pardo, E.; Ruiz-García, R.; Cano, J.; Ottenwaelder, X.; Lescouëzec, R.; Journaux, Y.; Lloret, F.; Julve, M. *Dalton Trans.* **2008,** 2780–2805. doi:10.1039/b801222a
2. Kahn, O. *Molecular Magnetism;* Wiley-VCH: Weinheim, Germany, 1993.
3. Ruiz, R.; Surville-Barland, C.; Aukauloo, A.; Anxolabehere-Mallart, E.; Journaux, Y.; Cano, J.; Muñoz, M. C. *J. Chem. Soc., Dalton Trans.* **1997,** *27,* 745–752. doi:10.1039/a607572j
4. Ruiz, R.; Surville-Barland, C.; Journaux, Y.; Colin, J. C.; Castro, I.; Cervera, B.; Julve, M.; Lloret, F.; Sapiña, F. *Chem. Mater.* **1997,** *9,* 201–209. doi:10.1021/cm9602961
5. Ottenwaelder, X.; Aukauloo, A.; Journaux, Y.; Carrasco, R.; Cano, J.; Cervera, B.; Castro, I.; Curreli, S.; Muñoz, M. C.; Roselló, A. L.; Soto, B.; Ruiz-García, R. *Dalton Trans.* **2005,** *15,* 2516–2526. doi:10.1039/b502478a

6. Fernández, I.; Pedro, J. R.; Roselló, A. L.; Ruiz, R.; Castro, I.; Ottenwaelder, X.; Journaux, Y. *Eur. J. Org. Chem.* **2001,** *2001,* 1235–1247. doi:10.1002/1099-0690(200104)2001:7<1235::aid-ejoc1235>3.0.co;2-4
7. Sanada, T.; Suzuki, T.; Kaizaki, S. *J. Chem. Soc., Dalton Trans.* **1998,** *68,* 959–965. doi:10.1039/a706834d
8. Abdulmalic, M. A.; Aliabadi, A.; Petr, A.; Krupskaya, Y.; Kataev, V.; Büchner, B.; Hahn, T.; Kortus, J.; Rüffer, T. *Dalton Trans.* **2012,** *41,* 14657–14670. doi:10.1039/c2dt31802d
9. Bräuer, B.; Weigend, F.; Fittipaldi, M.; Gatteschi, D.; Reijerse, E. J.; Guerri, A.; Ciattini, S.; Salvan, G.; Rüffer, T. *Inorg. Chem.* **2008,** *47,* 6633–6644. doi:10.1021/ic702460t
10. Abdulmalic, M. A.; Aliabadi, A.; Petr, A.; Krupskaya, Y.; Kataev, V.; Buchner, B.; Zaripov, R.; Vavilova, E.; Voronkova, V.; Salikov, K.; Hahn, T.; Kortus, J.; Eya'ane Meva, F.; Schaarschmidt, D.; Rüffer, T. *Dalton Trans.* **2015,** *44,* 8062–8079. doi:10.1039/C4DT03579H
11. Aliabadi, A.; Zaripov, R.; Salikhov, K.; Voronkova, V.; Vavilova, E.; Abdulmalic, M. A.; Rüffer, T.; Büchner, B.; Kataev, V. *J. Phys. Chem. B* **2015,** *119,* 13762–13770. doi:10.1021/acs.jpcb.5b03987
12. Ardavan, A.; Rival, O.; Morton, J. J. L.; Blundell, S. J.; Tyryshkin, A. M.; Timco, G. A.; Winpenny, R. E. P. *Phys. Rev. Lett.* **2007,** *98,* 057201. doi:10.1103/PhysRevLett.98.057201
13. Schlegel, C.; van Slageren, J.; Manoli, M.; Brechin, E. K.; Dressel, M. *Phys. Rev. Lett.* **2008,** *101,* 147203. doi:10.1103/PhysRevLett.101.147203
14. Takahashi, S.; van Tol, J.; Beedle, C. C.; Hendrickson, D. N.; Brunel, L.-C.; Sherwin, M. S. *Phys. Rev. Lett.* **2009,** *102,* 087603. doi:10.1103/PhysRevLett.102.087603
15. Krupskaya, Y.; Zaripov, R.; Vavilova, E.; Miluykov, V.; Bezkishko, I.; Krivolapov, D.; Kataeva, O.; Sinyashin, O.; Hey-Hawkins, E.; Voronkova, V.; Salikhov, K.; Kataev, V.; Büchner, B. *Phys. Rev. B* **2011,** *84,* 092402. doi:10.1103/PhysRevB.84.092402
16. Choi, K.-Y.; Wang, Z.; Nojiri, H.; van Tol, J.; Kumar, P.; Lemmens, P.; Bassil, B. S.; Kortz, U.; Dalal, N. S. *Phys. Rev. Lett.* **2012,** *108,* 67206. doi:10.1103/PhysRevLett.108.067206
17. Wedge, C. J.; Timco, G. A.; Spielberg, E. T.; George, R. E.; Tuna, F.; Rigby, S.; McInnes, E. J. L.; Winpenny, R. E. P.; Blundell, S. J.; Ardavan, A. *Phys. Rev. Lett.* **2012,** *108,* 107204. doi:10.1103/PhysRevLett.108.107204
18. Yang, J.; Wang, Y.; Wang, Z.; Rong, X.; Duan, C.-K.; Su, J.-H.; Du, J. *Phys. Rev. Lett.* **2012,** *108,* 230501. doi:10.1103/PhysRevLett.108.230501
19. Shim, J. H.; Bertaina, S.; Gambarelli, S.; Mitra, T.; Müller, A.; Baibekov, E. I.; Malkin, B. Z.; Tsukerblat, B.; Barbara, B. *Phys. Rev. Lett.* **2012,** *109,* 050401. doi:10.1103/PhysRevLett.109.050401
20. Zaripov, R.; Vavilova, E.; Miluykov, V.; Bezkishko, I.; Sinyashin, O.; Salikhov, K.; Kataev, V.; Büchner, B. *Phys. Rev. B* **2013,** *88,* 094418. doi:10.1103/PhysRevB.88.094418
21. Lutz, P.; Marx, R.; Dengler, D.; Kromer, A.; van Slageren, J. *Mol. Phys.* **2013,** *111,* 2897–2902. doi:10.1080/00268976.2013.826421
22. Moro, F.; Kaminski, D.; Tuna, F.; Whitehead, G. F. S.; Timco, G. A.; Collison, D.; Winpenny, R. E. P.; Ardavan, A.; McInnes, E. J. L. *Chem. Commun.* **2014,** *50,* 91–93. doi:10.1039/C3CC46326E
23. Bader, K.; Dengler, D.; Lenz, S.; Endeward, B.; Jiang, S.-D.; Neugebauer, P.; van Slageren, J. *Nat. Commun.* **2014,** *5,* 5304. doi:10.1038/ncomms6304
24. Carr, H. Y.; Purcell, E. M. E. *Phys. Rev.* **1954,** *94,* 630–638. doi:10.1103/PhysRev.94.630
25. Meiboom, S.; Gill, D. *Rev. Sci. Instrum.* **1958,** *29,* 688–691. doi:10.1063/1.1716296
26. Troiani, F.; Affronte, M. *Chem. Soc. Rev.* **2011,** *40,* 3119–3129. doi:10.1039/c0cs00158a
27. Volkov, M. Yu.; Salikhov, K. M. *Appl. Magn. Reson.* **2011,** *41,* 145–154. doi:10.1007/s00723-011-0297-2
28. Abdulmalic, M. A.; Aliabadi, A.; Petr, A.; Kataev, V.; Rüffer, T. *Dalton Trans.* **2013,** *42,* 1798–1809. doi:10.1039/C2DT32259E
29. Mims, W. B. *Phys. Rev. B* **1972,** *5,* 2409. doi:10.1103/PhysRevB.5.2409
30. Salikhov, K. M.; Semenov, A. G.; Tsvetkov, Yu. D. *Electron Spin Echoes and Their Applications;* Nauka: Novosibirsk, Russia, 1976.
31. Schweiger, A.; Jeschke, G. *Principles of Pulse Electron Paramagnetic Resonance;* Clarendon Press: Oxford, United Kingdom, 2001.
32. Deligiannakis, Y.; Louloudi, M.; Hadjiliadis, N. *Coord. Chem. Rev.* **2000,** *204,* 1–112. doi:10.1016/S0010-8545(99)00218-0
33. Salikhov, K. M.; Tsvetkov, Yu. D. Electron spin studies of spin-spin interactions in solids. In *Time Domain Electron Spin Resonance;* Kevan, L.; Schwartz, R., Eds.; Wiley: New York, NY, U.S.A., 1979; pp 231–278.
34. Zecevic, A.; Eaton, G. R.; Eaton, S. S.; Lindgren, M. *Mol. Phys.* **1998,** *95,* 1255–1263. doi:10.1080/00268979809483256
35. Sato, H.; Kathirvelu, V.; Spagnol, G.; Rajca, S.; Rajca, A.; Eaton, S. S.; Eaton, G. R. *J. Phys. Chem. B* **2008,** *112,* 2818–2828. doi:10.1021/jp073600u
36. Stoll, S.; Kasumaj, B. *Appl. Magn. Reson.* **2008,** *35,* 15–32. doi:10.1007/s00723-008-0140-6
37. Gordon, J. P.; Bowers, K. D. *Phys. Rev. Lett.* **1958,** *1,* 368. doi:10.1103/PhysRevLett.1.368
38. Milov, A.; Salikhov, K.; Tsvetkov, Y. *Fiz. Tverd. Tela (S.-Peterburg)* **1973,** *15,* 1187.
39. Abragam, A. *The Principles of Nuclear Magnetism;* Clarendon Press: Oxford, United Kingdom, 1961.
40. Kurshev, V. V.; Raitsimring, A. M. *J. Magn. Reson.* **1990,** *88,* 126–129. doi:10.1016/0022-2364(90)90113-n
41. Schweiger, A. *Angew. Chem.* **1991,** *103,* 223–250. doi:10.1002/ange.19911030304
42. Harbridge, J. R.; Eaton, S. S.; Eaton, G. R. *J. Magn. Reson.* **2003,** *164,* 44–53. doi:10.1016/S1090-7807(03)00182-4
43. Mentink-Vigier, F.; Collauto, A.; Feintuch, A.; Kaminker, I.; Tarle, V.; Goldfarb, D. *J. Magn. Reson.* **2013,** *236,* 117–125. doi:10.1016/j.jmr.2013.08.012
44. Mitrikas, G.; Prokopiou, G. *J. Magn. Reson.* **2015,** *254,* 75–85. doi:10.1016/j.jmr.2015.03.002
45. Atzori, M.; Morra, E.; Tesi, L.; Albino, A.; Chiesa, M.; Sorace, L.; Sessoli, R. *J. Am. Chem. Soc.* **2016,** *138,* 11234–11244. doi:10.1021/jacs.6b05574
46. Zadrozny, J. M.; Niklas, J.; Poluektov, O. G.; Freedman, D. E. *ACS Cent. Sci.* **2015,** *1,* 488–492. doi:10.1021/acscentsci.5b00338
47. Fataftah, M. S.; Zadrozny, J. M.; Coste, S. C.; Graham, M. J.; Rogers, D. M.; Freedman, D. E. *J. Am. Chem. Soc.* **2016,** *138,* 1344–1348. doi:10.1021/jacs.5b11802
48. Hoffmann, S. K.; Goslar, J.; Lijewski, S.; Zalewska, A. *J. Magn. Reson.* **2013,** *236,* 7–14. doi:10.1016/j.jmr.2013.08.009

BEILSTEIN JOURNAL OF NANOTECHNOLOGY

Nanoantenna-assisted plasmonic enhancement of IR absorption of vibrational modes of organic molecules

Alexander G. Milekhin*[1,2], Olga Cherkasova[2,3], Sergei A. Kuznetsov[2,4], Ilya A. Milekhin[1,2], Ekatherina E. Rodyakina[1,2], Alexander V. Latyshev[1,2], Sreetama Banerjee[5], Georgeta Salvan[5] and Dietrich R. T. Zahn[5]

Full Research Paper

Open Access

Address:
[1]A.V. Rzhanov Institute of Semiconductor Physics, Novosibirsk, 630090, Russia, [2]Novosibirsk State University, Novosibirsk, 630090, Russia, [3]Institute of Laser Physics of SB RAS, Novosibirsk, 630090, Russia, [4]A.V. Rzhanov Institute of Semiconductor Physics RAS, Novosibirsk Branch "TDIAM", Lavrentiev Ave. 2/1, Novosibirsk, 630090, Russia, and [5]Semiconductor Physics, Technische Universität Chemnitz, D-09107 Chemnitz, Germany

Email:
Alexander G. Milekhin* - milekhin@isp.nsc.ru

* Corresponding author

Keywords:
cobalt phthalocyanine; cortisol; localized surface plasmon resonance; metal nanoantennas; Raman scattering; surface-enhanced infrared absorption (SEIRA)

Beilstein J. Nanotechnol. **2017,** *8,* 975–981.
doi:10.3762/bjnano.8.99

Received: 24 November 2016
Accepted: 07 April 2017
Published: 03 May 2017

This article is part of the Thematic Series "Towards molecular spintronics".

Associate Editor: P. Leiderer

Abstract

Nanoantenna-assisted plasmonic enhancement of IR absorption and Raman scattering was employed for studying the vibrational modes in organic molecules. Ultrathin cobalt phthalocyanine films (3 nm) were deposited on Au nanoantenna arrays with specified structural parameters. The deposited organic films reveal the enhancement of both Raman scattering and IR absorption vibrational modes. To extend the possibility of implementing surface-enhanced infrared absorption (SEIRA) for biological applications, the detection and analysis of the steroid hormone cortisol was demonstrated.

Introduction

Organic semiconductors have been extensively investigated during the past few decades due to their wide range of applications in various organic–inorganic hybrid devices [1]. The ability to tailor the chemical structure of the organic molecules according to the device requirements, in addition to the light weight, flexibility and easy processing of these materials, open up the possibility of fabricating novel hybrid devices [2]. In the last decade, organic semiconductors gained the attention of the spintronics community as these organic semiconductors have been considered as good candidates for spin transport. The most interesting property of organic semiconductors for spintronic applications is the weak spin–scattering mechanism [3], which means that the spin polarization of the carriers can continue for an extended time (in the range from microseconds to millisec-

onds) [4]. This feature is caused by very low spin–orbit coupling and weak hyperfine interaction.

Phthalocyanines (Pcs) are a class of stable, planar small molecules, often investigated as promising candidates for molecular spintronics [5,6]. There have been studies on molecule/metal interfaces [7], magnetic coupling in the metal phthalocyanine layers [8], spin transport or magnetic properties through single molecules or even thin layers [6,9,10] of phthalocyanines. These molecules also offer the possibility of changing the spin-dependent transport mechanism by slightly modifying the molecular structure [6]. It has been previously shown that the molecular structure of a magnetic material can be probed by various spectroscopic techniques [11]. Under conditions of plasmonic enhancement, a magnetic material can be employed for a wide range of applications [11].

A relatively low optical signal from the vibrational modes of organic molecules using conventional spectroscopic techniques such as infrared (IR) and Raman spectroscopy restricts their detection limit, which is crucial for sensor applications. The sensitivity of these optical methods can be drastically increased by implementation of nanoantenna-assisted plasmonic-enhanced spectroscopy techniques such as surface-enhanced IR absorption (SEIRA) [12] or surfaced-enhanced Raman scattering (SERS) [13]. The principle of SEIRA and SERS is based on specially designed, resonant, metal nanoantennas, providing a high electromagnetic field intensity in close proximity to the plasmonic nanostructure when resonantly excited in the IR or optical regime [14,15]. It was shown that elongated nanoantennas can enhance the SEIRA signal by molecular vibrations in model adsorbates such as octadecanthiol (ODT) [16] and 4,4'-bis(*N*-carbazolyl)-1,1'-biphenyl (CBP) by up to five orders of magnitude [17]. The IR absorption bands of these molecules become pronounced, even for molecular monolayers, by tuning the localized surface plasmon energy of the nanoantennas to the energy of the molecular vibrations. Along with SEIRA, SERS is also traditionally used to study the vibrational spectra of various organic and biological substances [18], which may be present in very low quantities down to single molecules [19]. Raman enhancement up to 10^{14} can be achieved.

Although SEIRA is a relatively new tool for detection of organic and biological substances, it is found to be very effective for probing extremely low concentrations. Adato et al. demonstrated detection of 3×10^{-19} moles of silk protein for the entire nanoantenna array, corresponding to only 145 molecules per antenna [20]. A similar approach is used for the terahertz (or far-IR) spectral range for which special nanoscale slot-antenna arrays were designed to determine glucose and fructose in solutions, including market beverages [21]. Terahertz transmittance measurements were made in the frequency range of 0.5–2.5 THz for concentrations from 10 to 4168 mg/dL. Similar structures have been used for the determination of pesticide concentration in solution and on the surface of fruit. The detection limit was 8 μmol [22].

Here, we demonstrate the application of SEIRA for the detection and analysis of vibrational modes of cobalt phthalocyanine deposited on Au nanoantenna arrays. The estimation of the plasmonic enhancement of the fabricated nanoantenna arrays was performed by analyzing the SEIRA and SERS spectra of homogeneous, ultrathin Co Pc films. We also demonstrate SEIRA by detection of the steroid hormone cortisol deposited on Au nanoantenna arrays to extend the possibility of using the method also for biological applications.

Results and Discussion

Applications of SEIRA for organic compounds

Representative SEM images of the Au nanoantenna arrays (length 900 nm; width 60 nm) employed for the IR investigation are shown in Figure 1. The period of the array is 5 μm and the distance between nanoantenna edges is about 100 nm.

For the quantitative estimation of the nanoantenna-assisted plasmonic enhancement of the fabricated arrays, ultrathin CoPc films (with a thickness up to 3 nm) were deposited on the

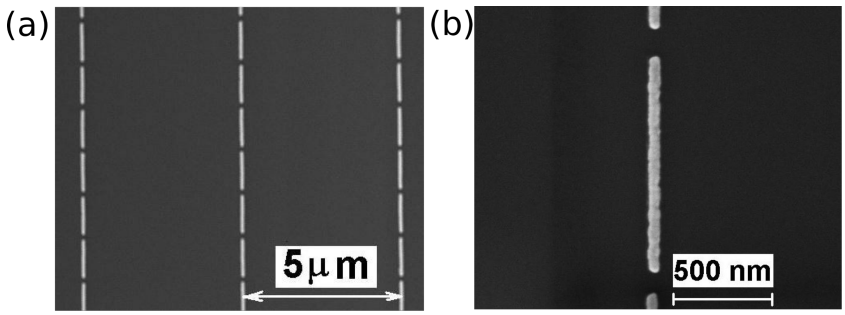

Figure 1: (a) Representative SEM image of Au nanoantenna array; nanoantenna length 900 nm. (b) Detailed image of a nanoantenna.

antenna arrays and a Si substrate. The homogeneity of the CoPc films deposited on the arrays was probed using micro-Raman mapping. The Raman spectra of the CoPc films deposited on a Si substrate (Figure 2a) reveal a rich spectrum of CoPc vibrational modes similar to that observed previously [23]. Note that the excitation energy was 1.96 eV (632.8 nm), which matches well with the HOMO–LUMO gap energy of CoPc (1.9 eV). The coincidence of the excitation energy with that of the electronic transitions in CoPc defines the conditions for resonant Raman scattering (RRS) in CoPc. In addition to the most intense mode of the Si substrate (observed at 520.5 cm^{-1}), the RRS spectrum (Figure 2) is dominated by the vibrational mode at 1543 cm^{-1} assigned to the C=N stretching mode [23]. The chemical structure of CoPc is shown in the inset of Figure 2a. The mode frequencies observed at 683, 750, 958, 1307, 1340, and 1465 cm^{-1} are in accordance with the literature data [23].

The Raman spectra measured from CoPc deposited on the Au nanoantennas demonstrate the enhancement of the Raman scattering (a factor of about 9) without noticeable shift of the mode frequencies, manifesting a SERS effect by CoPc. In the case of nanoantennas, the SERS enhancement is much weaker than that determined for CoPc on Au nanocluster arrays (enhancement factor of 2×10^4) observed in our previous experiments [24]. Much stronger SERS enhancement of CoPc on Au nanocluster arrays with respect to that for nanoantennas can be explained by the resonant SERS effect, as the energy of the local surface plasmon resonance (LSPR) of nanoclusters is located in the red spectral region, which is in resonance with the excitation energy. In the case of nanoantennas, the energy of longitudinal LSPR modes polarized along the antennas shifts in the IR spectral range, which leads to off-resonant SERS conditions. The transverse LSPR modes polarized perpendicular to the nanoantennas undergo a small blue shift along with a decrease in the mode intensity [25], which leads to reduced SERS enhancement. Despite this, the SERS effect in CoPc on nanoantenna arrays allows the homogeneity of the CoPc coverage on a nanoantenna array to be investigated using Raman mapping. The intensity of the C=N stretching mode at 1543 cm^{-1} was monitored. The Raman map obtained for a Au nanoantenna array with a 3 nm thick CoPc film shown in Figure 2b,c agrees well with the SEM image of the same structure. One can see from Figure 2c that the Raman mapping indicates the position of the nanoantennas by the stronger Raman (SERS) intensity (brighter regions), which reproduces the 5 μm periodicity of the

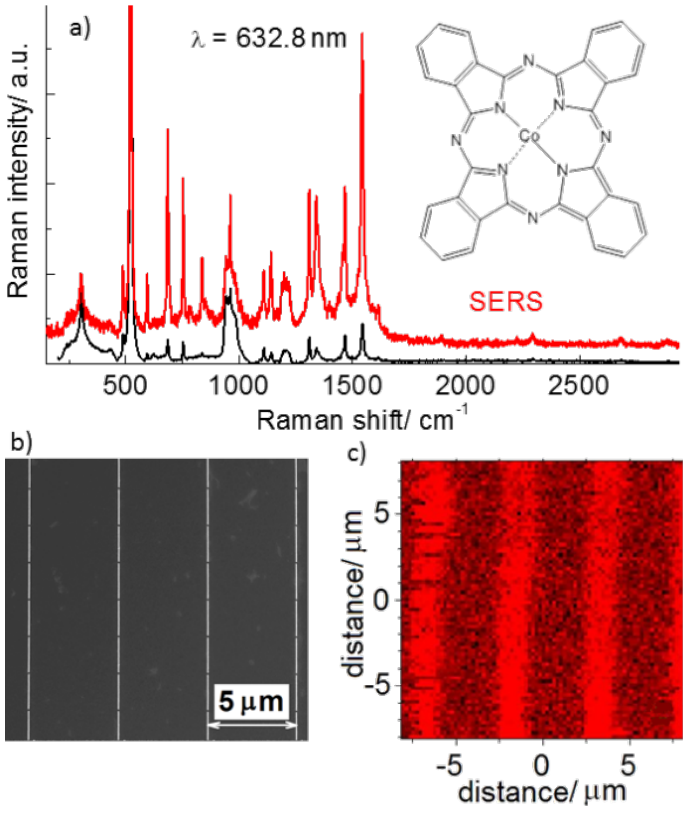

Figure 2: (a) Raman and SERS spectra of a cobalt phthalocyanine (CoPc) film with thickness of 3 nm deposited on a nanoantenna array. The chemical structure of CoPc is shown in the inset. (b) SEM image of the nanoantenna array with antenna length of 1900 nm. (c) Raman mapping (100 × 100 pixels) of the C=N mode (1543 cm^{-1}) intensity.

nanoantenna array and evidences the homogeneous coverage of CoPc over the sample.

The IR spectrum of a 10 nm thick CoPc film is presented in Figure 3 in the spectral range of 500–2000 cm^{-1}, where most absorption lines of CoPc are located. The vibrational spectrum of the CoPc film is similar to that defined for CoPc earlier [26-31] by means of IR absorption. The absorption line at 726 cm^{-1} attributed to nonplanar deformation of C–H bonds of benzene rings [26-28] has the strongest intensity and, therefore, was chosen for further SEIRA experiments. It is accompanied by a weaker mode at 755 cm^{-1}, referred to as the nonplanar (out-of-plane) bending of C–H bonds and the Co–N bond vibrations [26-28].

Au nanoantenna arrays with structural parameters (nanoantenna length and period) designed to ensure the LSPR band energy from 600 to 1000 cm^{-1} were fabricated (Figure 4a). In order to determine the structural parameters of the arrays with the targeted LSPR energy and a maximal SEIRA enhancement, 3D full-wave simulations were carried out and the distribution of the electromagnetic field near Au nanoantennas on a silicon substrate was simulated as described in [32]. In the simulations, the same nominal values of nanoantenna width, height, and the spacing between nanoantennas were assumed as imposed by the nanofabrication technology.

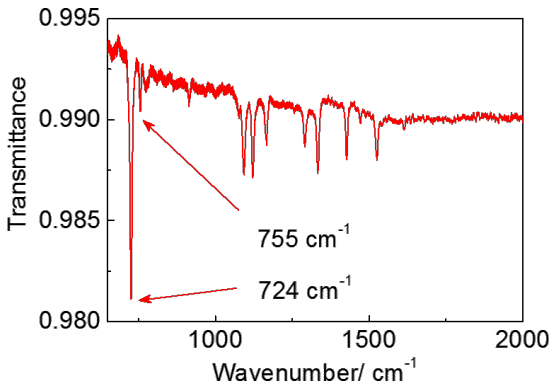

Figure 3: IR transmission spectrum of a 10 nm thick CoPc film deposited on a Si substrate normalized to the IR spectrum of a Si substrate.

Except for the fundamental LSPR mode, the third-order resonance centered at about 2400 cm^{-1} occurs in the IR spectra. A weaker feature near 1200 cm^{-1} is assigned to the surface optical mode from natural silicon oxide covering the Si substrate [33]. The deposition of thin CoPc films on the nanoantenna arrays leads to intensity enhancement for the vibrational modes at 724 and 755 cm^{-1}, which are inherent to CoPc in the spectral range of the LSPR band. Note that for the 3 nm thick CoPc film, the mode at 755 cm^{-1} is observed only in the case of the CoPc film deposited on the nanoantenna array (Figure 4a,b). Weak oscillations seen in Figure 4a,b are the interference fringes at the sample thickness (about 400 µm). The overall enhancement factor (EF) for the 10 nm thick CoPc film amounts to 2 and is within the range of 4–5 for a 3 nm thick film. The increase of the EF with decreasing CoPc film thickness is due to the strong electric filed localization near the Si surface in the nanogap between the nanoantenna edges. Using the approach similar to that described in [34], one can quantitatively estimate the enhancement induced by nanoantennas (EF_N). It can be calculated as the ratio of the areas covered by the nanogaps to the entire nanoantenna array and amounts to about 1/1200. Here, we suppose that the IR absorption predominantly takes place in the nanogap. Taking the maximum EF = 5 for the 3 nm thick CoPc film, the enhancement induced by nanogaps in the array reaches the value of EF_N = 6000.

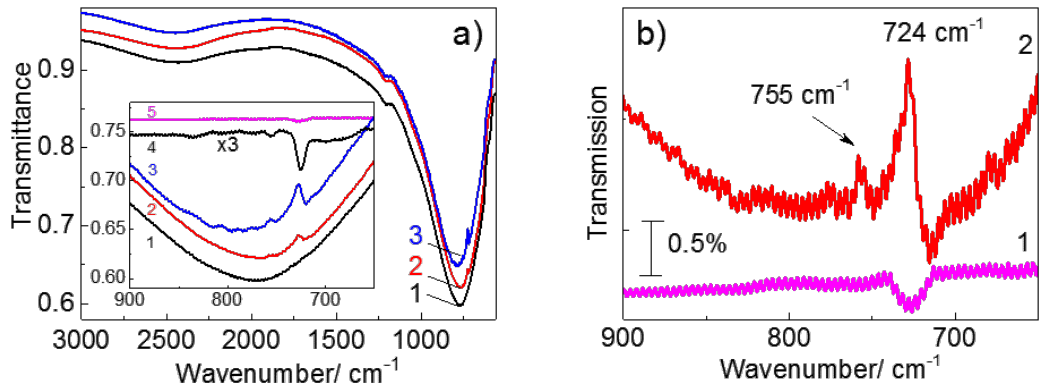

Figure 4: (a) IR spectrum of bare nanoantennas (curve 1) and IR spectra of nanoantennas with deposited 3 nm and 10 nm thick CoPc films (curves 2 and 3, respectively). The inset shows a comparison of the same spectra with the IR spectra of 3 nm and 10 nm thick CoPc films on a Si substrate without nanoantennas (curves 4 and 5, respectively). (b) Comparison of IR spectrum of bare nanoantennas (curve 1) and with the spectrum of the structure with the 3 nm thick CoPc film (curve 2) after background subtraction.

In accordance with previous studies [18,20,35], the vibrational modes observed in the SEIRA spectra exhibit a clear Fano line shape.

Further applications of SEIRA for biological compounds

A similar approach was used for the investigation of cortisol using SEIRA. Among other organic compounds, the steroid hormones are of great importance because they influence many physiological processes in humans and animals.

Cortisol is the major glucocorticoid hormone produced in the adrenal gland and in several tissues and regulates blood glucose levels. Cortisol production disorders lead to the development of diabetes, Cushing's syndrome and other pathologies [36]. Therefore, the determination of the cortisol concentration in blood and tissue is important. The immunoassay methods are predominantly performed in clinical practice [37]. Other methods, such as chromatography [38-40] and surface plasmon resonance [41], are used in fundamental research. Each of these methods of cortisol detection has advantages and drawbacks. Conventional Raman scattering, which is widely used for the investigation of organic and inorganic materials, cannot be applied for investigation of cortisol in blood and tissues due to its low Raman signal response. Therefore, SEIRA is considered as a complementary method for enhanced cortisol detection. Cortisol is the derivative of 1,2-cyclopentanephenanthrene. The molecule core of cortisol consists of four fused carbon rings: three cyclohexane rings (denoted as A, B, and C in the Figure 5a) and one cyclopentane ring (the D ring).

The IR spectrum of cortisol reveals the most pronounced absorption bands associated with valence vibrations of C=O groups [42,43]. According to [44] the calculated (experimental) frequency positions of the bands are located at 1686 (1660) cm^{-1} and 1725 (1735) cm^{-1} and demonstrate the highest intensities. Therefore, the structural parameters of the nanoantennas were chosen in such a way to ensure the LSPR absorption band close to the energy of the most pronounced vibrational modes in cortisol. The deposition of cortisol on a solid substrate implies, as a general rule, the use of the drop-casting method, which results in inhomogeneous coverage. The dielectric function of the media surrounding the nanoantennas is changed after deposition of cortisol solution onto the surface. This results in an LSPR energy shift from 1535 cm^{-1} towards lower energy (near 1500 cm^{-1}). Three characteristic vibrational modes of cortisol are also seen in the IR spectrum after subtraction of the envelope line (Figure 5b). These modes can be assigned as deformation vibrations of C–H bonds (1470 cm^{-1}), stretching vibrations C3=O3 (1660 cm^{-1}) and C20=O20 bonds (1735 cm^{-1}). The detection limit of the cortisol concentration determined from the IR spectra was 40 ng. With increasing cortisol concentration (up to 100 ng) the intensity of the modes increases and remains unchanged with further concentration increase. The most probable explanation is that the thickness of the cortisol film reaches the value of the nanoantenna height, which prevents further increase of the optical response. The determined detection limit of the cortisol concentration from the analysis of the SEIRA spectra corresponds to the concentration of the steroid in real biological assays.

Conclusion

In this work, we characterized the nanoantenna-assisted plasmonic enhancement of IR absorption and Raman scattering from vibrational modes of organic molecules. Au nanoantenna arrays with specified structural parameters were employed to enhance the absorption signatures from the vibrational modes of cobalt phthalocyanine ultrathin films and cortisol molecules. This work may have a wide range of applications as it opens up the possibility to spectroscopically study a magnetic material

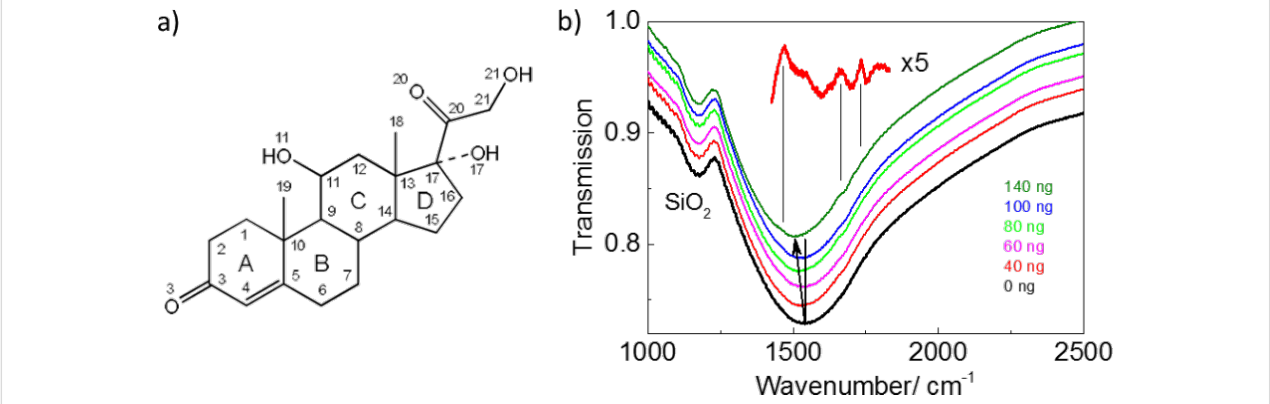

Figure 5: (a) The cortisol chemical structure and numeration of atoms in the cortisol molecule. (b) IR spectrum of a bare Au nanoantenna array and cortisol deposited from the solution with concentration 10ng/μL on the array. Inset shows the detailed fragmentary IR spectrum of 40 ng of cortisol after subtraction of the envelope line.

under the influence of localized plasmonic enhancements, thus increasing the sensitivity limit. As a proposed further application of SEIRA, it was also shown that the detection limit of cortisol using SEIRA corresponds to 40 ng – this opens up the possibility for determination of steroid concentrations in real biological assays.

Experimental

The uniform periodic arrays of linear Au nanoantennas with length 900 and 1900 nm and period of 5 μm were fabricated on (001)-oriented Si substrates by a direct writing nanolithographic machine (Raith-150, Raith GmbH, Germany) and covers an area of 3 × 3 mm^2, providing the LSPR band energies in the range from 1580–800 cm^{-1}. To avoid interference in the SEIRA spectra, 400 μm thick Si substrates were used. The fabrication process of nanoantenna arrays is very similar to that described in [24] for Au nanocluster arrays.

The structural parameters of nanoantenna arrays were controlled by a scanning electron microscopy (SEM) using the same Raith-150 system at 10 kV acceleration voltage, 30 μm aperture, and 6 mm working distance.

Ultrathin CoPc films with thickness 3 and 10 nm were formed using organic molecular beam vapor deposition onto arrays of Au nanoantennas. The thermal evaporation of the organic molecule was performed in a vacuum chamber at a pressure of ≈5 × 10^{-8} mbar. The evaporation temperature was approximately 400 °C and the deposition rate was ≈0.5 nm/min. During the organic film growth, the substrate was kept at room temperature.

Cortisol (11β)-11,17,21-trihydroxypregn-4-ene-3,20-dione) was purchased from Calbiochem (USA) and was used without further purification. Cortisol dissolved in ethanol at concentration of 10 ng/mL (27.6 μM) was deposited onto arrays of Au nanoantennas by drop-casting. The drop volume was 2 μL.

The LSPR energy on Au nanoantenna arrays with and without organic material was determined from the IR transmission measurements carried out by using a Bruker Vertex 80v Fourier transform infrared spectrometer in the spectral range of 600–4000 cm^{-1}. The spectral resolution was 2 cm^{-1} over the whole spectra range. The ratio of the transmission spectra polariszed along and perpendicular to the long axis of the bare nanoantennas and with deposited organic films was analyzed. The noise level was below 0.1% in the IR experiments. The measurements were carried out at room temperature.

Non-polarized Raman spectra were measured using Labram spectrometers equipped with a Renishaw InVia Raman microscope (the laser beam was focused to a spot with a diameter of about 1 μm) in a backscattering geometry at room temperature. A HeNe laser was used as an excitation source at the wavelength of 632.8 nm (2.41 eV). A laser power of less than 100 μW (before the microscope) was used to avoid possible effects of local heating. The spectral resolution was below 2.5 cm^{-1} over the whole spectral range.

Acknowledgements

The authors gratefully acknowledge financial support from Volkswagen Foundation, TMS project (TU Chemnitz), Russian Science Foundation (project n.14-12-01037) in part of simulation and fabrication of Au nanoantenna arrays and SEIRA measurements, and the Ministry of Education and Science of the Russian Federation. The authors are thankful to L.L. Sveshnikova and A.S. Medvedev for technical assistance.

References

1. Wang, L.; Yoon, M.-H.; Lu, G.; Yang, Y.; Facchetti, A.; Marks, T. J. *Nat. Mater.* **2006,** *5,* 893–900. doi:10.1038/nmat1755
2. Zhang, C.; Chen, P.; Hu, W. *Chem. Soc. Rev.* **2015,** *44,* 2087–2107. doi:10.1039/C4CS00326H
3. Dediu, V. A.; Hueso, L. E.; Bergenti, I.; Taliani, C. *Nat. Mater.* **2009,** *8,* 707–716. doi:10.1038/nmat2510
4. Gu, H.; Zhang, X.; Wei, H.; Huang, Y.; Wei, S.; Guo, Z. *Chem. Soc. Rev.* **2013,** *42,* 5907–5943. doi:10.1039/c3cs60074b
5. Robaschik, P.; Siles, P. F.; Bülz, D.; Richter, P.; Monecke, M.; Fronk, M.; Klyatskaya, S.; Grimm, D.; Schmidt, O. G.; Ruben, M.; Zahn, D. R. T.; Salvan, G. *Beilstein J. Nanotechnol.* **2014,** *5,* 2070–2078. doi:10.3762/bjnano.5.215
6. Barraud, C.; Bouzehouane, K.; Deranlot, C.; Kim, D. J.; Rakshit, R.; Shi, S.; Arabski, J.; Bowen, M.; Beaurepaire, E.; Boukari, S.; Seneor, P.; Mattana, R. *Dalton Trans.* **2016,** *45,* 16694–16699. doi:10.1039/C6DT02467J
7. Lach, S.; Altenhof, A.; Tarafder, K.; Schmitt, F.; Ali, M. E.; Vogel, M.; Sauther, J.; Oppeneer, P. M.; Ziegler, C. *Adv. Funct. Mater.* **2012,** *22,* 989–997. doi:10.1002/adfm.201102297
8. Serri, M.; Wu, W.; Fleet, L. R.; Harrison, N. M.; Hirjibehedin, C. F.; Kay, C. W. M.; Fisher, A. J.; Aeppli, G.; Heutz, S. *Nat. Commun.* **2014,** *5,* No. 3079. doi:10.1038/ncomms4079
9. Schmaus, S.; Bagrets, A.; Nahas, Y.; Yamada, T. K.; Bork, A.; Bowen, M.; Beaurepaire, E.; Evers, F.; Wulfhekel, W. *Nat. Nanotechnol.* **2011,** *6,* 185–189. doi:10.1038/nnano.2011.11
10. Annese, E.; Fujii, J.; Vobornik, I.; Panaccione, G.; Rossi, G. *Phys. Rev. B* **2011,** *84,* 174443. doi:10.1103/PhysRevB.84.174443
11. Larson, T. A.; Bankson, J.; Aaron, J.; Sokolov, K. *Nanotechnology* **2007,** *18,* 325101. doi:10.1088/0957-4484/18/32/325101
12. de la Chapelle, M. L.; Pucci, A., Eds. *Nanoantenna: Plasmon-Enhanced Spectroscopies for Biotechnological Applications;* Pan Stanford Publishing Pte. Ltd.: Singapore, 2013. doi:10.1201/b14594
13. Aroca, R. *Surface-enhanced Vibrational Spectroscopy;* John Wiley & Sons: New Jersey, U.S.A., 2006. doi:10.1002/9780470035641
14. Steinle, T.; Neubrech, F.; Steinmann, A.; Yin, X.; Giessen, H. *Opt. Express* **2015,** *23,* 11105–11113. doi:10.1364/OE.23.011105

15. Schatz, G. C.; Young, M. A.; Van Duyne, R. P. Electromagnetic Mechanism of SERS. In *Surface–Enhanced Raman Scattering: Physics and Applications;* Kneipp, K.; Moskovits, M.; Kneipp, H., Eds.; Topics in Applied Physics, Vol. 103; Springer: Berlin, Germany, 2006; pp 19–45. doi:10.1007/3-540-33567-6_2
16. Neubrech, F.; Pucci, A.; Cornelius, T. W.; Karim, S.; García-Etxarri, A.; Aizpurua, J. *Phys. Rev. Lett.* **2008,** *101,* 157403. doi:10.1103/PhysRevLett.101.157403
17. Huck, C.; Neubrech, F.; Vogt, J.; Toma, A.; Gerbert, D.; Katzmann, J.; Härtling, T.; Pucci, A. *ACS Nano* **2014,** *8,* 4908–4914. doi:10.1021/nn500903v
18. Moskovits, M. *Rev. Mod. Phys.* **1985,** *57,* 783–826. doi:10.1103/RevModPhys.57.783
19. Kneipp, K.; Wang, Y.; Kneipp, H.; Perelman, L. T.; Itzkan, I.; Dasari, R. R.; Feld, M. S. *Phys. Rev. Lett.* **1997,** *78,* 1667–1670. doi:10.1103/PhysRevLett.78.1667
20. Adato, R.; Yanik, A. A.; Amsden, J. J.; Kaplan, D. L.; Omenetto, F.; Hong, M. K.; Erramilli, S.; Altug, H. *Proc. Natl. Acad. Sci. U. S. A.* **2009,** *106,* 19227–19232. doi:10.1073/pnas.0907459106
21. Lee, D.-K.; Kang, J.-H.; Lee, J.-S.; Kim, H.-S.; Kim, C.; Kim, J. H.; Lee, T.; Son, J.-H.; Park, Q.-H.; Seo, M. *Sci. Rep.* **2015,** *5,* 15459. doi:10.1038/srep15459
22. Lee, D.-K.; Kim, G.; Son, J.-H.; Seo, M. *Proc. SPIE* **2016,** *9747,* 97470S. doi:10.1117/12.2212055
23. Aroca, R.; Pieczonka, N.; Kam, A. P. *J. Porphyrins Phthalocyanines* **2001,** *5,* 25–32. doi:10.1002/1099-1409(200101)5:1<25::AID-JPP301>3.0.CO;2-A
24. Milekhin, A. G.; Yeryukov, N. A.; Sveshnikova, L. L.; Duda, T. A.; Rodyakina, E. E.; Sheremet, E. S.; Ludemann, M.; Gordan, O. D.; Latyshev, A. V.; Zahn, D. R. T. *Thin Solid Films* **2013,** *543,* 35–40. doi:10.1016/j.tsf.2013.03.070
25. Oraevsky, A. A.; Oraevsky, A. N. *Quantum Electron.* **2002,** *32,* 79–82. doi:10.1070/QE2002v032n01ABEH002131
26. Sidorov, A. N. *Opt. Spectrosc.* **1976,** *40,* 280–283.
27. Meshkova, G. N.; Vartanyan, A. T.; Sidorov, A. N. *Opt. Spectrosc.* **1977,** *43,* 151–154.
28. El-Nahass, M. M.; Abd-El-Rahman, K. F.; Darwish, A. A. A. *Mater. Chem. Phys.* **2005,** *92,* 185–189. doi:10.1016/j.matchemphys.2005.01.008
29. Zeman, E. J.; Carron, K. T.; Schatz, G. C.; Van Duyne, R. P. *J. Chem. Phys.* **1987,** *87,* 4189–4200. doi:10.1063/1.452923
30. Kötz, R.; Yeager, E. *J. Electroanal. Chem. Interfacial Electrochem.* **1980,** *113,* 113–125. doi:10.1016/S0022-0728(80)80515-8
31. Toman, P.; Nešpůrek, S.; Yakushi, K. *J. Porphyrins Phthalocyanines* **2002,** *6,* 556–562. doi:10.1142/S1088424602000695
32. Milekhin, I. A.; Kuznetsov, S. A.; Rodyakina, E. E.; Milekhin, A. G.; Latyshev, A. V.; Zahn, D. R. T. *Beilstein J. Nanotechnol.* **2016,** *7,* 1519–1526. doi:10.3762/bjnano.7.145
33. Neubrech, F.; Weber, D.; Enders, D.; Nagao, T.; Pucci, A. *J. Phys. Chem. C* **2010,** *114,* 7299–7301. doi:10.1021/jp908921y
34. Toma, A.; Tuccio, S.; Prato, M.; De Donato, F.; Perucchi, A.; Di Pietro, P.; Marras, S.; Liberale, C.; Zaccaria, R. P.; De Angelis, F.; Manna, L.; Lupi, S.; Di Fabrizio, E.; Razzari, L. *Nano Lett.* **2015,** *15,* 386–391. doi:10.1021/nl503705w
35. D'Andrea, C.; Bochterle, J.; Toma, A.; Huck, C.; Neubrech, F.; Messina, E.; Fazio, B.; Maragò, O. M.; Di Fabrizio, E.; de La Chapelle, M. L.; Gucciardi, P. G.; Pucci, A. *ACS Nano* **2013,** *7,* 3522–3531. doi:10.1021/nn4004764
36. Cherkasova, O. P. *Biochemistry (Moscow)* **2007,** *1,* 172–175. doi:10.1134/S1990750807020126
37. Holder, G. Measurement of Glucocorticoids in Biological Fluids. In *Hormone Assays in Biological Fluids;* Wheeler, M. J.; Hutchinson, J. S. M., Eds.; Methods in Molecular Biology, Vol. 324; Humana Press: Totowa, NJ, U.S.A.; pp 141–157. doi:10.1385/1-59259-986-9:141
38. Cherkasova, O. P.; Selyatitskaya, V. G. *Biochemistry (Moscow)* **2013,** *7,* 90–94. doi:10.1134/S1990750813010034
39. Al Sharef, O.; Feely, J.; Kavanagh, P. V.; Scott, K. R.; Sharma, S. C. *Biomed. Chromatogr.* **2007,** *21,* 1201–1206. doi:10.1002/bmc.877
40. Lee, S.; Lim, H.-S.; Shin, H.-J.; Kim, S.-A.; Park, J.; Kim, H.-C.; Kim, H.; Kim, H. J.; Kim, Y.-T.; Lee, K.-R.; Kim, Y.-J. *J. Anal. Methods Chem.* **2014,** *2014,* 787483. doi:10.1155/2014/787483
41. Mitchell, J. S.; Lowe, T. E.; Ingram, J. R. *Analyst* **2009,** *134,* 380–386. doi:10.1039/B817083P
42. Kasal, A.; Budesinsky, M.; Griffiths, W. J. Spectroscopic Methods of Steroid Analysis. In *Steroid Analysis;* Makin, H. L. J.; Gower, D. B., Eds.; Springer: Berlin, Germany, 2010; pp 27–161. doi:10.1023/b135931_2
43. Spectral Database for Organic Compounds (SDBS), http://sdbs.db.aist.go.jp/sdbs/cgi-bin/direct_frame_top.cgi, SDBS No. 10001, hydrocortisone.
44. Rojek, B.; Wesolowski, M. *J. Therm. Anal. Calorim.* **2017,** *127,* 543–553. doi:10.1007/s10973-016-5441-7

License and Terms

BEILSTEIN JOURNAL OF NANOTECHNOLOGY

Stable Au–C bonds to the substrate for fullerene-based nanostructures

Taras Chutora[1,2], Jesús Redondo[1], Bruno de la Torre[1], Martin Švec[1], Pavel Jelínek[*1] and Héctor Vázquez[*1]

Full Research Paper

Open Access

Address:
[1]Institute of Physics, Academy of Sciences of the Czech Republic, Cukrovarnicka 10, Prague, Czech Republic and [2]Palacký University, RCPTM, Joint Laboratory of Optics, 17. listopadu 12, Olomouc, Czech Republic

Email:
Pavel Jelínek[*] - jelinekp@fzu.cz; Héctor Vázquez[*] - vazquez@fzu.cz

* Corresponding author

Keywords:
Au–C bonds; density functional theory (DFT); fullerenes; scanning tunneling microscopy (STM); sputtering

Beilstein J. Nanotechnol. **2017,** *8,* 1073–1079.
doi:10.3762/bjnano.8.109

Received: 15 February 2017
Accepted: 26 April 2017
Published: 17 May 2017

This article is part of the Thematic Series "Towards molecular spintronics".

Guest Editor: G. Salvan

Abstract

We report on the formation of fullerene-derived nanostructures on Au(111) at room temperature and under UHV conditions. After low-energy ion sputtering of fullerene films deposited on Au(111), bright spots appear at the herringbone corner sites when measured using a scanning tunneling microscope. These features are stable at room temperature against diffusion on the surface. We carry out DFT calculations of fullerene molecules having one missing carbon atom to simulate the vacancies in the molecules resulting from the sputtering process. These modified fullerenes have an adsorption energy on the Au(111) surface that is 1.6 eV higher than that of C_{60} molecules. This increased binding energy arises from the saturation by the Au surface of the bonds around the molecular vacancy defect. We therefore interpret the observed features as adsorbed fullerene-derived molecules with C vacancies. This provides a pathway for the formation of fullerene-based nanostructures on Au at room temperature.

Introduction

In single-molecule electronics, the active element in an electronic circuit is a small molecule connected to two nanoelectrodes, and molecular chemical properties determine the characteristics of current flow. The reliable preparation and characterization of such nanostructures has been made possible by state-of-the-art scanning probe methods with which individual atoms and molecules can be manipulated. In parallel, the use of atomistic simulations, mainly based on density functional theory (DFT), has allowed for a detailed understanding of the basic mechanisms that determine the electronic and nanoscale transport properties [1]. For spintronics, small organic molecules are appealing since they feature weak spin–orbit interaction and long spin lifetimes [2,3].

The large pool of organic molecules opens the possibility of almost unlimited functionalities given the right molecular

design [4]. Fullerenes are particularly well-studied molecules. Since their discovery in 1985 [5], fullerenes have played an important role in molecular surface science, organic photovoltaics and single-molecule electronics. Fullerenes can be deposited on a series of metallic and semiconducting substrates [6-8]. In molecular transport, they have been used both as target molecules as well as anchoring groups [9-12]. They have featured in spin transport studies, where spin currents can be achieved by encapsulating magnetic atoms or impurities inside the fullerene cage [13-18]. The adsorption of C_{60} on the metal surface determines the strength and spread of electronic coupling and conductance values [9-12]. For an archetypal electrode material in single molecule transport studies such as Au, however, their high mobility at room temperature can lead to a large spread in conductance or to problems in trapping the molecule at the interface [19,20]. It might therefore be desirable to achieve strong metal–molecule bonds that result are electronically transparent or exhibit a well-defined conductance. Au–C metal–molecule bonds were found to be highly conducting [21,22].

Here we report on the formation of stable fullerene-based nanostructures on Au(111) at room temperature in ultra-high vacuum (UHV) environment. These structures were realized by soft sputtering of fullerene films on the surface with Ar^+ ions and were studied using scanning tunneling microscopy (STM). After sputtering, bright spots on the herringbone corners are observed, which we show to be adsorbed fullerenes with defects created by the sputtering process. The sputtering process is expected to result in the formation of vacancies in the fullerene molecules, where C atoms are knocked out. A series of fullerene fragments can be formed in the collision with high-energy atoms and ions. In our work, we gradually increased the energy of the incident ions starting from a low value until changes in the film morphology (in particular the spots on the herringbone elbows) were observed. We therefore hypothesize that the damaged fullerenes in our study are C_{59} molecules, an assumption discussed below. C_{59} molecules have the highest energetic stability (difference between the cluster energy and the sum of the energy of the individual C atoms) after C_{60} [23-25]. These findings are corroborated by total-energy DFT simulations.

Since the diffusion of fullerenes on Au is very fast at room temperature, individual molecules cannot be stabilized and contacted outside islands. This has important consequences for single-molecule transport, where it would be desirable to have reliable and stable metal–molecule contacts. In the case of molecular spintronics, the stable fullerene-based structures proposed here might be useful for transport studies on magnetic atoms and impurities encapsulated inside molecules based on fullerenes.

Results and Discussion

STM room-temperature measurements

Figure 1a shows a constant-current STM image acquired at room temperature after the deposition of C_{60} molecules on the reconstructed Au(111) surface [26-28]. The deposition process was performed at room temperature. In this initial state of adsorption, we observe that almost all the C_{60} molecules are adsorbed at the terrace edges of the monoatomic steps. Molecules are assembled into one-dimensional islands or short chains along the steps. This can be attributed to the increased local reactivity of the step edges [29-31]. STM images taken after Ar^+ bombardment (120 eV, 5 min) [32-34] of the system (Figure 1b) show single bright dots on the surface, which correspond to individual molecules disjoined from islands as a result of the sputtering process. Line profiles (indicated by blue lines in Figure 1b) reveal an apparent height difference of approximately 0.15 nm between the individual molecules and those inside the island.

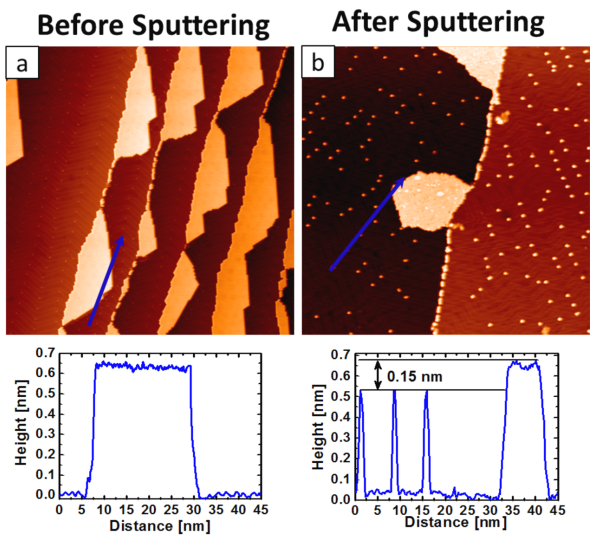

Figure 1: (a) (200 × 200 nm^2) High-resolution STM image (U_b = −0.5 V, I_s = 0.3 nA) of Au (111) after deposition of C_{60}. The molecules formed self-assembled islands, attached to the surface-terrace edges as expected. (b) (200 × 200 nm^2) High-resolution STM image (U_b = −0.6 V, I_s = 0.3 nA) of the system after sputtering with 120 eV Ar^+ ions for 5 min. Single molecules were detached from the islands as the result of the sputtering process. Profiles measured along the indicated blue arrows reveal the apparent height differences between isolated molecules and those inside the island.

Figure 2a shows a high-resolution STM image of the close-packed arrangement of C_{60} inside the island after deposition [35-37]. In addition, we observe dim molecules (indicated by green arrows), which can be attributed to C_{60} molecules above gold vacancies [29,37]. Closer inspection of molecules inside the island after Ar^+ ion bombardment (Figure 2b) enables the sorting of the molecules in the island according to their appear-

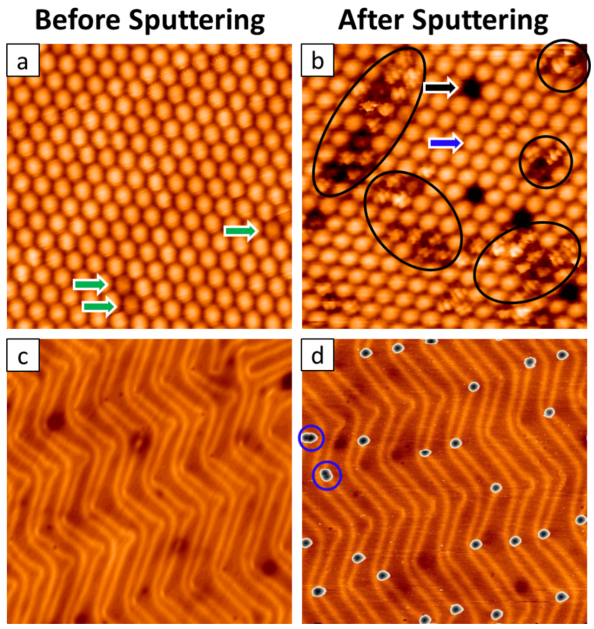

Figure 2: (a) (14 × 14 nm^2) STM image (U_b = −2.5 V, I_s = 0.3 nA) of a fullerene island before Ar^+ bombardment. (b) (14 × 14 nm^2) STM image (U_b = 0.6 V, I_s = 0.3 nA) of the fullerene island after Ar^+ bombardment. The blue arrow indicates a pristine C_{60} molecule. The black arrow points to a vacancy inside the island. Black circles mark regions with modified molecules. (c) (65 × 65 nm^2) STM image (U_b = 1.8 V, I_s = 0.3 nA) of the herringbone reconstruction before Ar^+ bombardment. (d) (65 × 65 nm^2) STM image (U_b = 0.5 V, I_s = 0.09 nA) of single molecules attached to the herringbone elbow sites. Two dimers are enclosed by blue circles.

ance. We can easily identify pristine C_{60} (blue arrow). Also, we observe regions in the island (indicated by black circles) corresponding to modified molecules, with a variation in the topographic heights. We assume that the varying apparent heights of these molecules inside the island stem from different adsorption geometries and possibly the local influence of neighboring molecules. Finally, we observe dark spots in the islands (black arrows in Figure 2b), which we can attribute to holes formed due to the ion bombardment and subsequent departure of the fullerenes from the islands.

Figure 2c shows a high-resolution STM image of reconstructed Au(111) after C_{60} deposition prior to the Ar^+ ion bombardment. From this image, it is clear that no molecules are seen at the elbow sites before soft sputtering. In Figure 2d we observe the adsorption pattern of isolated molecules that were disjoined from the islands after sputtering. Importantly, these molecules bind to the elbow sites of the herringbone reconstruction of the substrate. This can be explained by the increased reactivity of the elbow sites, so-called Shockley partial dislocations of the Au bulk [38,39]. The faulty structure of the elbow site makes it a favorable nucleation site for the functionalized molecules to bind. STM images also show the presence of dimer structures bound at the elbow sites (indicated by blue circles). We attribute these features to be dimers of molecules damaged during the sputtering. The number of observed dimers was very limited.

We turn to the features on the herringbone corners. Given the higher reactivity of these elbow sites, we consider the possibility of the bright spots being normal C_{60} molecules and for the structures on the herringbone corners being unrelated to the formation of molecular defects. However, this scenario can be ruled out since these spots are only observed after sputtering of the fullerene film. First, without sputtering, C_{60} molecules are highly mobile on terraces at room temperature and form islands that are adsorbed at step edges. Second, the creation of reactive sites in the Au surface due to sputtering and to which normal C_{60} molecules could bind, can also be excluded: no features on the elbow sites were observed when sputtering the clean Au surface prior to C_{60} deposition. Molecules bound to the herringbone corner sites were only observed after soft sputtering of the fullerene films, implying that these adsorbates result from an increased reactivity of the molecules after sputtering.

Isolated fullerenes with C vacancies

In order to understand the STM measurements, we carried out electronic-structure calculations based on DFT, focusing on fullerene molecules with vacancy defects where the missing C atoms result in increased reactivity and stronger binding with the substrate. We consider C_{59} molecules, resulting from the removal of a single C atom. While high-energy collisions can result in a wide range of products after removal of a series of fragments [23], it has been shown that sputtering of carbon materials with such low energies as in our case results in predominantly single vacancies [32-34]. C_{59} molecules also have the highest energetic stability after C_{60} [24,25] and, as described below, result in strong and stable bonds to the Au(111) surface, in particular stronger than those of C_{58}. We therefore study the binding of C_{59} species to the substrate which, as detailed below, explains the STM observations.

We start by discussing the structure of isolated C_{59} molecules. From the equilibrium C_{60} molecule, we remove a C atom and explore low-energy structures by optimizing the geometry. The removal of an atom from the C_{60} molecule results in many unsaturated bonds that induce a geometric rearrangement of the molecule. In the calculations, we find two different structural isomers (Figure 3), depending on how the fullerene vacancy is healed. In the first isomer, the atoms surrounding the vacancy rearrange to form two rings, one consisting of four atoms, and the other of nine atoms. In the other one, the C atoms around the vacancy assemble into a ring of eight atoms, and another ring of five atoms. Notice that in both structural isomers two

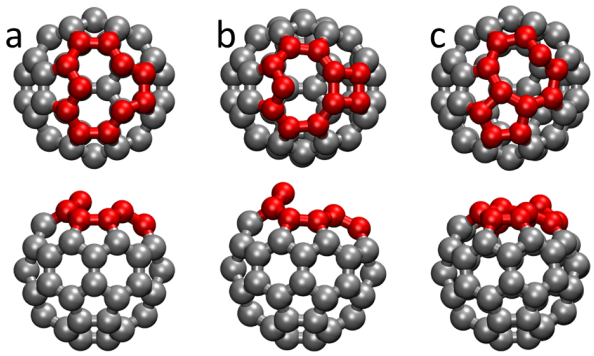

Figure 3: Top and side views of the computed structure of C_{59} structural isomers. Carbon atoms around the vacancy are shown in red. (a) Initial structure for geometry optimization, obtained from a C_{60} molecule by removing one atom. (b) Isomer where the atoms around the vacancy form one four- and one nine-membered ring. (c) More stable isomer having eight- and five-membered rings.

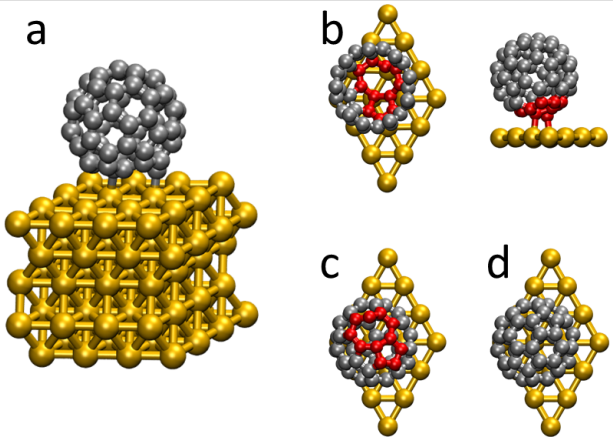

Figure 4: (a) Unit cell used in the calculations. (b) Top and side views of the 8,5-isomer with the single vacancy close to the metal surface. In the top view, the upper C atoms have been removed for clarity. (c) Top view of the 8,5-isomer with the vacancy away from the surface. (d) Fullerene with no defects (C_{60}). Carbon atoms around the vacancy are shown in red.

C atoms belong to both rings, but for clarity we choose to name them according to the total number of atoms in each ring. At the optimized structures, both C_{59} isomers have a carbon atom protruding from the shape of a C_{60} molecule or that of a C_{60} molecule with one missing C atom (the starting geometry of the structural optimizations). Despite the structural rearrangement, interatomic C–C bond distances are not dramatically altered. Calculated interatomic bond distances for C_{60} are 1.42 and 1.47 Å, to be compared to the reported values of 1.40 and 1.46 Å [40,41]. For the 4,9- isomer, C–C distances around the vacancy are in the range of 1.42–1.49 Å, while for the 8,5-isomer the calculated values are between 1.40 and 1.51 Å. When comparing the total energy of both species we find the isomer with 8- and 5-atom rings to be more stable by ca. 0.9 eV than the 4,9-isomer, consistent with previous quantum chemical calculations [25]. Therefore, when considering the adsorbed defected fullerenes on the surface we study the 8,5-isomer only.

Fullerenes with defects adsorbed on the Au(111) surface

We now describe the adsorption of this 8,5-fullerene with vacancy defect on the (111) surface of Au using DFT simulations. The herringbone reconstruction arises from the $22\times\sqrt{3}$ reconstruction of the Au(111) surface. However, the calculation of the very large supercells needed to explicitly describe this reconstruction would require a huge computational effort [42]. We therefore follow previous works and study the adsorption on the ideal (111) surface. Figure 4a shows the unit cell used in the calculations, illustrated for pristine fullerene (C_{60}). There are five Au layers, each consisting of 16 atoms. We calculate the fullerene molecule before and after sputtering, where we model it as having 60 and 59 atoms, respectively. In both cases, above the molecule there is a large vacuum gap. Technical details of the calculations are given in the Experimental section at the end of the paper.

We first screen the possible adsorption geometries by carrying out structural optimizations starting from a series of initial metal–molecule structures. We investigated several initial geometries where the C_{59} molecule was rotated or its center of mass had been shifted, in order to explore the metal–molecule interaction. We considered geometries where the fullerene vacancy was oriented towards the Au substrate ("defect-down" structure) as well as towards the vacuum ("defect-up" structure). Figure 4b–d show the optimized geometries for the fullerene molecules with vacancy defect having the vacancy towards the interface or towards the vacuum, and for the adsorbed pristine C_{60} molecule. We find that, upon adsorption, the calculated interatomic C–C bond distances are only slightly changed compared to the isolated 8,5-isomer. When the vacancy is oriented towards the vacuum, the changes in the C–C bond distances are negligible. In the defect-down geometry they are larger, as expected, with the smaller five-atom ring exhibiting smaller bond distance variations upon adsorption (mean change less than 0.005 Å) than the eight-atom ring (mean change of ca. 0.025 Å). This is consistent with the intuitive idea that the eight-atom ring is more reactive, and in fact is found to be closer to the metal surface in the optimized geometry. From the calculations, the binding energy of the defect-down geometry (Figure 4b) is ca. 1.6 eV. This is much higher than that of the defect-up (Figure 4c) and the pristine C_{60} (Figure 4d) structures. The calculated binding energies of these two structures is (in the absence of van der Waals forces) close to zero. This indicates that changes in the electronic structure arising from the vacancy when it is oriented towards vacuum do not significant-

ly affect the metal–molecule contact. In contrast to the value of the defect-down structure, previous calculations on C_{60}/Au(111) have established that the binding energy results almost solely from van der Waals interactions [43]. Finally, we also considered the case of a double vacancy. Calculations for the binding of a C_{58} molecule with the defect pointing towards the metal result in a binding energy close to 0.6 eV. This value is significantly smaller than that of C_{59}, further supporting the idea that the bright spots observed in STM are fullerenes with single vacancies.

The optimized geometry of the defect-down C_{59} structure has three different C atoms separated by less than 2.5 Å from an Au atom in the surface layer. As expected, one of these atoms is the C atom protruding from the eight-atom ring, consistent with the intuitive notion of its high reactivity and readiness to form bonds with the substrate. As seen in Figure 4b, these small Au–C distances result from the three C atoms being close to an atop position with respect to the Au layer. For comparison, these values are slightly larger than the Au–C distances of ca. 2.1 Å found in other molecular nanostructures [21,22]. In our simulations, we found another local minimum of the C_{59} defect-down configuration with a smaller binding energy of 1.2 eV. In this geometry, the protruding C atom in the eight-atom ring is also close to a surface Au atom, while other C atoms in the eight- and five-membered rings are further away. This shows that, although several atoms around the fullerene vacancy contribute to the binding energy at the interface, the most important contribution comes from the apical C atom sticking out of the former icosahedral structure. In the case of the defect-up and the pristine structures (Figure 4c,d), a C–C bond shared by two hexagons relaxed to a position above a Au surface atom. This was previously found to be a favorable binding site for C_{60}/Au(111) [37]. Changes in the orientation of the defect-up structure resulted in minor variations in the calculated binding energy [43]. This is again consistent with the notion that when the vacancy is oriented towards vacuum, the carbon atoms close to the Au surface are relatively unaffected and the binding to the metal is similar to that of pristine C_{60}.

To sum up, the passivation of the bonds of the C atoms around the vacancy defect by the Au surface results in the formation of metal–molecule bonds and an energy gain of 1.6 eV. On the other hand, a vacancy exposed towards the vacuum would by very unstable and energetically unfavorable and it is unlikely that it would be present in experiment. Finally, from the calculations, the height of the defect-down fullerene is ca. 0.9 Å lower than that of the pristine C_{60} molecule.

Finally, we turn to the electronic properties of the adsorbed fullerenes with vacancy defect, and compare them to those of the C_{60}/Au(111) system. Figure 5 shows the calculated density of states (DOS) of the isolated molecule (dashed lines) and junction (solid lines) projected onto the molecular atoms. Upon adsorption, the calculated spectrum of C_{60} is not appreciably modified, nor is that of C_{59} for the defect-up geometry. When the defect is adsorbed facing the substrate, however, significant changes are seen with respect to the isolated molecule. Spectral features, especially in the empty part of the spectrum, are broadened due to hybridization with metal states. Three scenarios at the interface are compared: the C_{59} molecules adsorbed with the vacancy towards the Au substrate or away from it, and the case of C_{60} for comparison. The spectrum of C_{60} on Au is well known [29,44-46]. Fullerene has a three-fold degenerate LUMO and a five-fold degenerate HOMO. In Figure 5 these are the peaks at about 0.8 and about −0.9 eV. The vacancy defect in the fullerene is related to the existence of states in the former gap of the molecule. For the defect-up geometry this is clearly seen in the peaks at 0.2 and around −0.5 eV, which can be explained by the breaking of degeneracy of one empty and two occupied states. Other molecular states are relatively unaffected compared to C_{60}/Au(111). When the vacancy is adsorbed towards the substrate, the Au–C bonds result in the broadening of the molecular spectrum, and there are broad features in the former energy gap. Identifying individual peaks and comparing them with C_{60} is more difficult but the occupied part of the spectrum seems to have changed more than the empty states upon adsorption. Unfortunately, attempts to reliably measure at room temperature the dI/dV spectrum of molecules adsorbed at the herringbone elbow sites or in islands were unsuccessful.

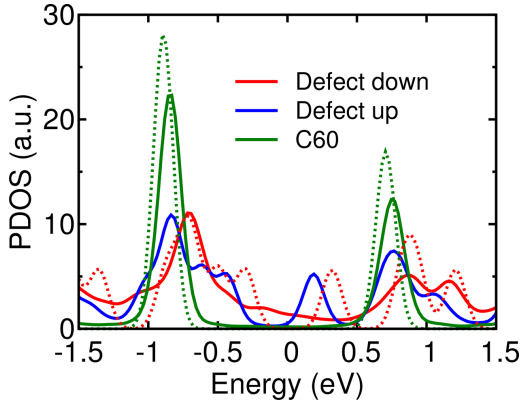

Figure 5: Calculated DOS of fullerenes with and without vacancy defects adsorbed on Au(111). In the case of defects, the molecule was adsorbed with the vacancy close to the surface ("defect-down") or towards the vacuum layer ("defect-up"). The DOS of isolated molecules are shown as dashed lines.

Conclusion

To summarize, we presented a combined theoretical–experimental study of sputtered fullerene-based films on Au(111). We

carried out STM measurements at room temperature in UHV. Initially we observed C_{60} molecules forming islands or chains at terrace edges of monoatomic Au steps. After soft sputtering, bright spots were visible at the Au herringbone corners. Line scans revealed these spots to have an apparent height difference of 1.5 Å with respect to fullerenes in islands. We interpret these bright spots as fullerene molecules with vacancies created by the sputtering process. DFT-based calculations show that C_{59} fullerenes with single defects are consistent with experimental findings. The vacancy created by the removal of a C atom from a fullerene molecule results in structural rearrangement and increased molecular reactivity. We showed that C_{59} molecules adsorbed with the defect close to the surface have a binding energy on Au that is 1.6 eV higher than that of C_{60}. This results from the passivation of C unsaturated bonds around the defect by the Au surface atoms. The calculated metal–molecule structure has several Au–C bond distances below 2.5 Å at the interface. This favorable binding configuration of the fullerene defect is consistent with the stable isolated molecules observed experimentally at the herringbone corners after sputtering. Our work thus provides a pathway for the formation of strong metal–molecule anchors for fullerene-based nanostructures at room temperature.

Experimental

Deposition and sputtering of C_{60}

Experiments were performed in ultrahigh vacuum, variable temperature STM (VT-STM), with base pressure below 5×10^{-10} mbar. Typically, six cycles of Ar^+ ion sputtering (1 kV, 10 min) and annealing (600 °C, 5 min) were required to obtain samples with overall cleanliness suitable for achieving the atomic resolution by means of STM. For deposition, we employed a custom-made thermal evaporation source, which contained a pocket made of tantalum, suitable for the evaporation of molecules such as C_{60}. During the deposition, the evaporation source and substrate were placed inside a vacuum chamber with a base pressure around 5×10^{-10} mbar. Before every deposition, the C_{60} source was preheated to 360 °C and degassed for 5 min to remove contaminations. After this procedure the sample was transferred into the STM head for the deposition of C_{60} by heating the evaporation source at 420 °C. In order to remove C atoms from the C_{60} molecules, the sample was bombarded with Ar^+ ions (120 eV, 5 min).

DFT-based calculations

We use the DFT code Siesta [47] for the calculation of the adsorption and electronic properties. We used single-zeta polarized orbitals for gold and a double-zeta polarized basis for carbon atoms. Exchange–correlation was described with the Perdew–Burke–Ernzerhof implementation of the Generalized Gradient Approximation (GGA) [48]. Each Au layer consisted of 16 atoms and five layers were used in the calculations. A vacuum gap of about 10 Å was introduced above the topmost molecular atom to avoid interaction with the cell images in the *z*-direction. Interface geometries were optimized using the Conjugated Gradient algorithm. We used a 2 × 2 Monkhorst–Pack grid for the *k*-point sampling of the Brillouin zone. The position of Au atoms in the surface layer and C atoms was relaxed until the forces acting on these atoms were smaller than 0.02 eV/Å. Projected DOS curves were calculated using a denser 15 × 15 Monkhorst–Pack *k*-point grid at optimized geometries. For the calculation of fullerene binding energies, ghost orbitals were used to correct for basis set superposition errors [49].

Acknowledgements

We gratefully acknowledge financial support from the Czech Science Foundation (GAČR) under project 15-19672S and the Purkyně Fellowship program of the Academy of Sciences of the Czech Republic. T.C. acknowledges support by the project LO1305 of the Ministry of Education, Youth and Sports of the Czech Republic. H.V. thanks the National Grid Infrastructure MetaCentrum for access to computing and storage facilities provided by the "Projects of Large Research, Development, and Innovations Infrastructures" (CESNET LM2015042) program.

References

1. Cuevas, J. C.; Scheer, E. *Molecular Electronics: An Introduction to Theory and Experiment;* World Scientific Series in Nanoscience and Nanotechnology, Vol. 1; World Scientific Publishing Co. Pte. Ltd: Singapore, 2010. doi:10.1142/7434
2. Sanvito, S. *Chem. Soc. Rev.* **2011,** *40,* 3336–3355. doi:10.1039/c1cs15047b
3. McCamey, D. R.; Seipel, H. A.; Paik, S.-Y.; Walter, M. J.; Borys, N. J.; Lupton, J. M.; Boehme, C. *Nat. Mater.* **2008,** *7,* 723–728. doi:10.1038/nmat2252
4. Su, T. A.; Neupane, M.; Steigerwald, M. L.; Venkataraman, L.; Nuckolls, C. *Nat. Rev. Mater.* **2016,** *1,* 16002. doi:10.1038/natrevmats.2016.2
5. Kroto, H. W.; Heath, J. R.; O'Brien, S. C.; Curl, R. F.; Smalley, R. E. *Nature* **1985,** *318,* 162–163. doi:10.1038/318162a0
6. Rosei, F.; Schunack, M.; Naitoh, Y.; Jiang, P.; Gourdon, A.; Laegsgaard, E.; Stensgaarda, I.; Joachim, C.; Besenbacher, F. *Prog. Surf. Sci.* **2003,** *71,* 95–146. doi:10.1016/S0079-6816(03)00004-2
7. Bonifazi, D.; Enger, O.; Diederich, F. *Chem. Soc. Rev.* **2007,** *36,* 390–414. doi:10.1039/B604308A
8. Moriarty, P. J. *Surf. Sci. Rep.* **2010,** *65,* 175–227. doi:10.1016/j.surfrep.2010.08.001
9. Kiguchi, M.; Kaneko, S. *Phys. Chem. Chem. Phys.* **2013,** *15,* 2253–2267. doi:10.1039/C2CP43960C
10. Schwarz, F.; Lörtscher, E. *J. Phys.: Condens. Matter* **2014,** *26,* 474201. doi:10.1088/0953-8984/26/47/474201
11. Sun, L.; Diaz-Fernandez, Y. A.; Gschneidtner, T. A.; Westerlund, F.; Lara-Avila, S.; Moth-Poulsen, K. *Chem. Soc. Rev.* **2014,** *43,* 7378–7411. doi:10.1039/C4CS00143E

12. Leary, E.; La Rosa, A.; González, M. T.; Rubio-Bollinger, G.; Agraït, N.; Martín, N. *Chem. Soc. Rev.* **2015,** *44,* 920. doi:10.1039/C4CS00264D
13. Yagi, Y.; Briere, T. M.; Sluiter, M. H. F.; Kumar, V.; Farajian, A. A.; Kawazoe, Y. *Phys. Rev. B* **2004,** *69,* 075414. doi:10.1103/PhysRevB.69.075414
14. Sakai, S.; Yakushiji, K.; Mitani, S.; Takanashi, K.; Naramoto, H.; Avramov, P. V.; Narumi, K.; Lavrentiev, V.; Maeda, Y. *Appl. Phys. Lett.* **2006,** *89,* 113118. doi:10.1063/1.2354035
15. Koleini, M.; Brandbyge, M. *Beilstein J. Nanotechnol.* **2012,** *3,* 589–596. doi:10.3762/bjnano.3.69
16. Lu, X.; Feng, L.; Akasaka, T.; Nagase, S. *Chem. Soc. Rev.* **2012,** *41,* 7723–7760. doi:10.1039/c2cs35214a
17. Saffarzadeh, A.; Kirczenow, G. *Appl. Phys. Lett.* **2013,** *102,* 173101. doi:10.1063/1.4803471
18. Stróżecka, A.; Muthukumar, K.; Dybek, A.; Dennis, T. J.; Larsson, J. A.; Mysliveček, J.; Voigtländer, B. *Appl. Phys. Lett.* **2016,** *95,* 133118. doi:10.1063/1.3236529
19. Guo, S.; Fogarty, D. P.; Nagel, P. M.; Kandel, S. A. *J. Phys. Chem. B* **2004,** *108,* 14074–14081. doi:10.1021/jp048481m
20. Kaneko, S.; Wang, L.; Luo, G.; Lu, J.; Nagase, S.; Sato, S.; Yamada, M.; Slanina, Z.; Akasaka, T.; Kiguchi, M. *Phys. Rev. B* **2012,** *86,* 155406. doi:10.1103/PhysRevB.86.155406
21. Cheng, Z.-L.; Skouta, R.; Vazquez, H.; Widawsky, J. R.; Schneebeli, S.; Chen, W.; Hybertsen, M. S.; Breslow, R.; Venkataraman, L. *Nat. Nanotechnol.* **2011,** *6,* 353–357. doi:10.1038/nnano.2011.66
22. Chen, W.; Widawsky, J. R.; Vázquez, H.; Schneebeli, S. T.; Hybertsen, M. S.; Breslow, R.; Venkataraman, L. *J. Am. Chem. Soc.* **2011,** *133,* 17160–17163. doi:10.1021/ja208020j
23. Gatchell, M.; Zettergren, H. *J. Phys. B: At., Mol. Opt. Phys.* **2016,** *49,* 162001. doi:10.1088/0953-4075/49/16/162001
24. Hu, Y. H.; Ruckenstein, E. *J. Chem. Phys.* **2003,** *119,* 10073. doi:10.1063/1.1617971
25. Lui, L. V.; Tian, W. Q.; Wang, Y. A. *Int. J. Quantum Chem.* **2009,** *109,* 3441. doi:10.1002/qua.22298
26. Altman, E. I.; Colton, R. J. *Surf. Sci.* **1992,** *279,* 49–67. doi:10.1016/0039-6028(92)90741-N
27. Altman, E. I.; Colton, R. J. *Phys. Rev. B* **1993,** *48,* 18244–18249. doi:10.1103/PhysRevB.48.18244
28. Altman, E. I.; Colton, R. J. *Surf. Sci.* **1993,** *295,* 13–33. doi:10.1016/0039-6028(93)90181-I
29. Paßens, M.; Waser, R.; Karthäuser, S. *Beilstein J. Nanotechnol.* **2015,** *6,* 1421–1431. doi:10.3762/bjnano.6.147
30. Zhang, X.; Yin, F.; Palmer, R. E.; Guo, Q. *Surf. Sci.* **2008,** *602,* 885–892. doi:10.1016/j.susc.2007.12.036
31. Gardener, J. A.; Briggs, G. A. D.; Castell, M. R. *Phys. Rev. B* **2009,** *80,* 235434. doi:10.1103/PhysRevB.80.235434
32. Lehtinen, O.; Kotakoski, J.; Krasheninnikov, A. V.; Tolvanen, A.; Nordlund, K.; Keinonen, J. *Phys. Rev. B* **2010,** *81,* 153401. doi:10.1103/PhysRevB.81.153401
33. Krasheninnikov, A. V.; Banhart, F. *Nat. Mater.* **2007,** *6,* 723. doi:10.1038/nmat1996
34. López-Polín, G.; Gómez-Navarro, C.; Parente, V.; Guinea, F.; Katsnelson, M. I.; Pérez-Murano, F.; Gómez-Herrero, J. *Nat. Phys.* **2015,** *11,* 26–31. doi:10.1038/nphys3183
35. Wang, H.; Zeng, C.; Wang, B.; Hou, J. G.; Li, Q.; Yang, J. *Phys. Rev. B* **2001,** *63,* 085417. doi:10.1103/PhysRevB.63.085417
36. Schull, G.; Berndt, R. *Phys. Rev. Lett.* **2007,** *99,* 226105. doi:10.1103/PhysRevLett.99.226105
37. Shin, H.; Schwarze, A.; Diehl, R. D.; Pussi, K.; Colombier, A.; Gaudry, É.; Ledieu, J.; McGuirk, G. M.; Serkovic Loli, L. N.; Fournée, V.; Wang, L. L.; Schull, G.; Berndt, R. *Phys. Rev. B* **2014,** *89,* 245428. doi:10.1103/PhysRevB.89.245428
38. Barth, J. V.; Brune, H.; Ertl, G.; Behm, R. J. *Phys. Rev. B* **1990,** *42,* 9307. doi:10.1103/PhysRevB.42.9307
39. Maksymovych, P.; Sorescu, D. C.; Dougherty, D.; Yates, J. T., Jr. *J. Phys. Chem. B* **2005,** *109,* 22463. doi:10.1021/jp058154u
40. Hedberg, K.; Hedberg, L.; Bethune, D. S.; Brown, C. A.; Dorn, H. C.; Johnson, R. D.; De Vries, M. *Science* **1991,** *254,* 410. doi:10.1126/science.254.5030.410
41. Leclercq, F.; Damay, P.; Foukani, M.; Chieux, P.; Bellissent-Funel, M. C.; Rassat, A.; Fabre, C. *Phys. Rev. B* **1993,** *48,* 2748. doi:10.1103/PhysRevB.48.2748
42. Hanke, F.; Björk, J. *Phys. Rev. B* **2013,** *87,* 235422. doi:10.1103/PhysRevB.87.235422
43. Hamada, I.; Tsukada, M. *Phys. Rev. B* **2011,** *83,* 245437. doi:10.1103/PhysRevB.83.245437
44. Lu, X.; Grobis, M.; Khoo, K. H.; Louie, S. G.; Crommie, M. F. *Phys. Rev. B* **2004,** *70,* 115418. doi:10.1103/PhysRevB.70.115418
45. Schull, G.; Néel, N.; Becker, M.; Kröger, J.; Berndt, R. *New J. Phys.* **2008,** *10,* 065012. doi:10.1088/1367-2630/10/6/065012
46. Wang, L.-L.; Cheng, H.-P. *Phys. Rev. B* **2004,** *69,* 165417. doi:10.1103/PhysRevB.69.165417
47. Soler, J. M.; Artacho, E.; Gale, J. D.; García, A.; Junquera, J.; Ordejón, P.; Sánchez-Portal, D. *J. Phys.: Condens. Matter* **2002,** *14,* 274. doi:10.1088/0953-8984/14/11/302
48. Perdew, J. P.; Burke, K.; Ernzerhof, M. *Phys. Rev. Lett.* **1996,** *77,* 3865–3868. doi:10.1103/PhysRevLett.77.3865
49. van Duijneveldt, F. B.; van Duijneveldt-van de Rijdt, J. G. C. M.; van Lenthe, J. H. *Chem. Rev.* **1994,** *94,* 1873–1885. doi:10.1021/cr00031a007

License and Terms

BEILSTEIN JOURNAL OF NANOTECHNOLOGY

Ultrasmall magnetic field-effect and sign reversal in transistors based on donor/acceptor systems

Thomas Reichert[1] and Tobat P. I. Saragi[*1,2]

Full Research Paper

Open Access

Address:
[1]Macromolecular Chemistry and Molecular Materials, Department of Mathematics and Science, Center for Interdisciplinary Nanostructure Science and Technology (CINSaT), University of Kassel, Heinrich-Plett-Straße 40, 34132 Kassel, Germany and [2]Accenture GmbH, Kaistraße 20, 40221 Düsseldorf, Germany

Email:
Tobat P. I. Saragi[*] - tobat.saragi@gmx.de

* Corresponding author

Keywords:
donor/acceptor system; organic magnetoresistance; organic transistors; sign reversal; ultrasmall magnetic field-effects

Beilstein J. Nanotechnol. **2017,** *8,* 1104–1114.
doi:10.3762/bjnano.8.112

Received: 31 January 2017
Accepted: 04 May 2017
Published: 19 May 2017

This article is part of the Thematic Series "Towards molecular spintronics".

Guest Editor: G. Salvan

Abstract

We present magnetoresistive organic field-effect transistors featuring ultrasmall magnetic field-effects as well as a sign reversal. The employed material systems are coevaporated thin films with different compositions consisting of the electron donor 2,2',7,7'-tetrakis-(*N*,*N*-di-*p*-methylphenylamino)-9,9'-spirobifluorene (Spiro-TTB) and the electron acceptor 1,4,5,8,9,12-hexaazatriphenylene hexacarbonitrile (HAT-CN). Intermolecular charge transfer between Spiro-TTB and HAT-CN results in a high intrinsic charge carrier density in the coevaporated films. This enhances the probability of bipolaron formation, which is the process responsible for magnetoresistance effects in our system. Thereby even ultrasmall magnetic fields as low as 0.7 mT can influence the resistance of the charge transport channel. Moreover, the magnetoresistance is drastically influenced by the drain voltage, resulting in a sign reversal. An average B_0 value of ≈2.1 mT is obtained for all mixing compositions, indicating that only one specific quasiparticle is responsible for the magnetoresistance effects. All magnetoresistance effects can be thoroughly clarified within the framework of the bipolaron model.

Introduction

In recent years, the development of organic π-conjugated materials have perfectly meet the requirements for low-cost and flexible electronic devices and optoelectronic applications such as displays and lighting, which are already commercially available. To push organic electronics to the next level, the scientific community is shifting its activities towards the study of spin transport and spin phenomena in organic materials. Generally, three different topics are in the focus of this emerging

research field, namely organic spin-valves [1-6], organic magnetoresistance [7-12] and spin-related effects in hybrid devices [13-15].

Research on organic spintronics have mostly used a diode as device structure (two-terminal device). In contrast, our tool in organic spintronics are field-effect transistors (three-terminal device), which gain new insight into spin transport phenomena in organic π-conjugated materials. In field-effect transistors, the sign of charge carriers is defined by the gate voltage, and the mobility and charge type can be determined independently [16]. The possibility of injecting holes or electrons or both into the conduction channel allows us to address the transport regime individually, depending on the applied drain and gate voltages. One interesting material system for transistors is the charge-transfer complex molecule, which this system has already shown magnetoresistive effects in organic diodes [17]. In a previous study we presented the first magnetoresistive effects in transistor structures based on a coevaporated (50:50) thin film materials system consisting of 2,2',7,7'-tetrakis-(*N*,*N*-di-*p*-methylphenylamino)-9,9'-spirobifluorene (Spiro-TTB) as donor and 1,4,5,8,9,12-hexaazatriphenylene hexacarbonitrile (HAT-CN) as acceptor [18]. While transistors based on the pure individual compounds are not influenced by external magnetic fields, their coevaporation allows the fabrication of highly magnetosensitive devices. With these findings, we were the first to establish donor–acceptor interactions as one powerful way to create magnetosensitive transistors but we could not yet cover all experimental aspects of this materials system.

In this paper, we will describe several important themes not featured in our previous paper. Further experimental investigations including different mixing compositions reveal a voltage-induced sign reversal and allow the first in-depth study of ultra-small magnetic-field effects in transistor structures. In particular, the influence of the drain and the gate voltage will be described. We also present magnetoresistive effects at ultrasmall fields as low as 0.7 mT. Figure 1 shows the applied experimental scheme, the corresponding experimental parameters and the chemical structures of the active materials. The details of the experiments can be found in the experimental section of this paper.

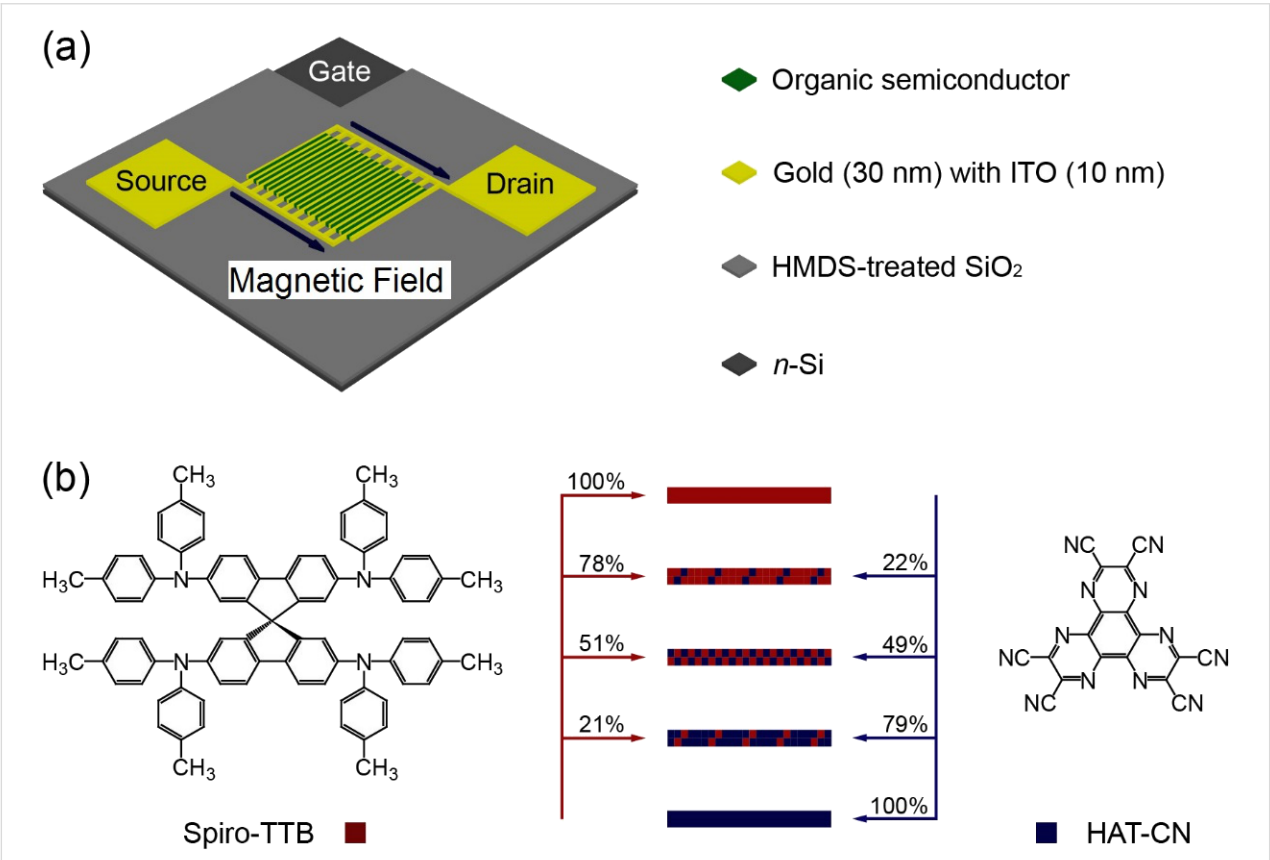

Figure 1: (a) Device layout of a bottom-contact organic field-effect transistor, showing *n*-Si as gate electrode, HMDS-treated SiO_2 as gate dielectric, gold with ITO as source and drain electrodes and organic semiconductor. (b) The chemical structures of Spiro-TTB and HAT-CN, including mixing compositions of 78:22, 51:49 and 21:79 for Spiro-TTB/HAT-CN, respectively. For a better overview, the organic semiconductor thin film is only depicted in the region of the transistor channel.

Results and Discussion

Coevaporating Spiro-TTB and HAT-CN results in mixed thin-film systems containing similar surface-morphologies as the corresponding "single" films suggesting an insignificant influence of the morphology on the magnetoresistive behaviour (see Supporting Information File 1, Figure S1). Instead, the magnetoresistance dependence on the source- and drain voltages as shown in Figure 2 for different mixing ratios. All compositions behave qualitatively equal for *p*-channel as well as for *n*-channel conditions. Thereby the gate voltage V_g does not significantly influence the magnetoresistance, but it strongly depends on the drain voltage V_d. These trends consolidate the conclusions drawn from the electrical characterization, showing a relatively gate-independent transport behaviour [18]. Due to the charge transfer between the HOMO of Spiro-TTB (E_{HOMO} = −4.9 eV) and the LUMO of HAT-CN (E_{LUMO} = −5.1 eV), the intrinsically available number of holes and electrons is so large that the gate-induced charge carrier accumula-

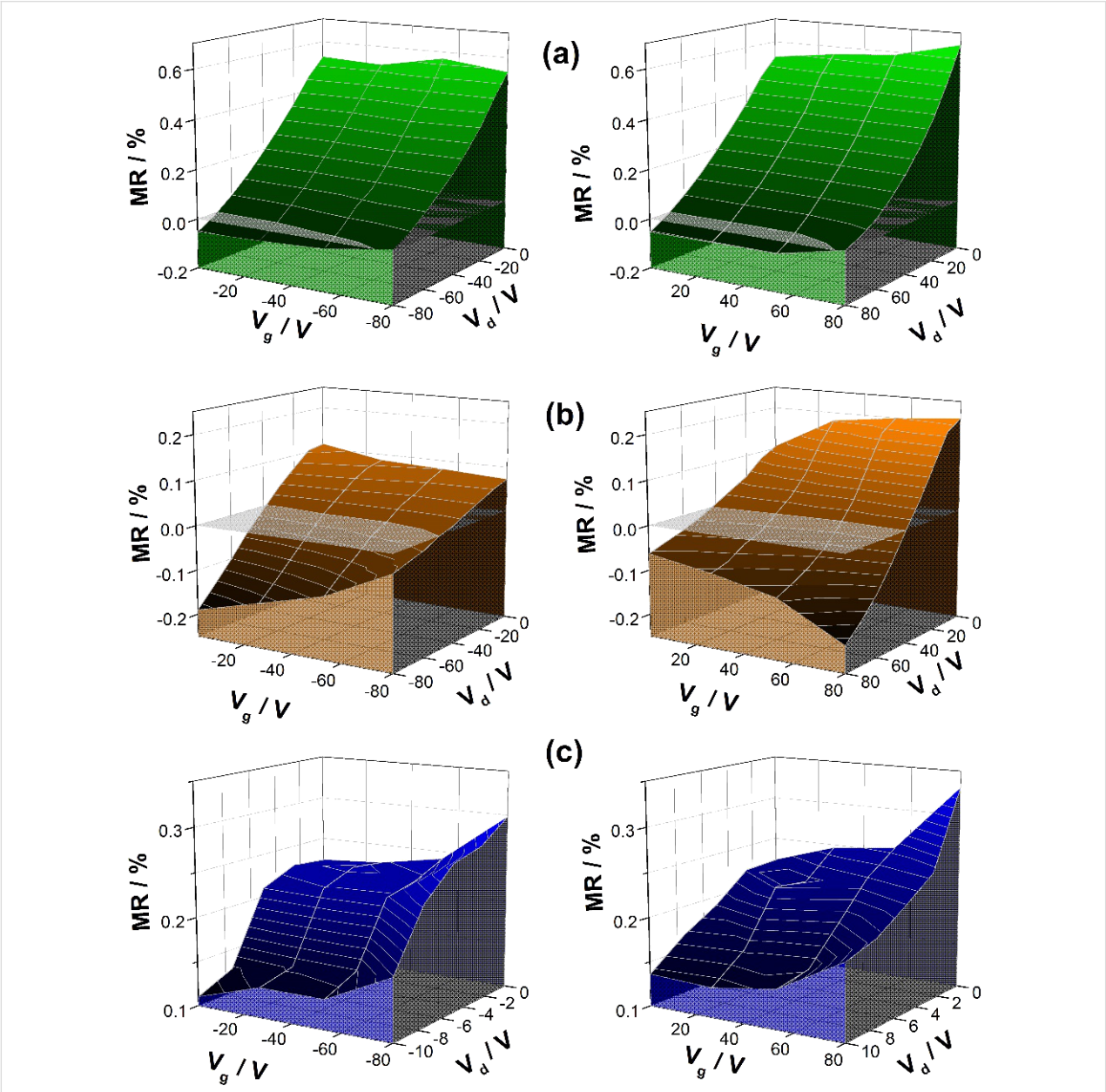

Figure 2: Voltage dependence (V_d and V_g) of the magnetoresistance for compositions of (a) 51:49, (b) 78:22 and (c) 21:79. On the left side, *p*-channel conditions are shown, while *n*-channel conditions are depicted on the right side. In order to allow a continuous 3D representation of the explored magnetoresistance landscape, the Renka–Cline fit was used to interpolate between all experimental data points. The underlying experimental data is displayed in Supporting Information File 1, Figure S2 [19]. The inserted grey-shaded plane serves to illustrate the voltage-induced sign reversal. All measurements were carried out for B = 60 mT.

tion does not has a significant influence on the drain current I_d [18]. Therefore, V_d does not only dominate the charge transport but also the magnetotransport behaviour. For small V_d and for devices containing mixing ratios of 51:49 and 78:22 there is a positive magnetoresistance, which decreases with an increase of $|V_d|$ until reaching a sign reversal, as displayed in Figure 2a and 2b. Indications of the voltage-induced sign reversal can also be found in the data of 21:79 composition, as shown in Figure 2c. Unfortunately, it could not be detected experimentally because V_d values higher than 10 V result in current values above the upper limit of our measurement setup. However, the data also shows a reduction of the positive magnetoresistance with increasing of $|V_d|$. This implies that the sign of magnetoresistance can be changed electrically in all Spiro-TTB/HAT-CN mixing ratios.

We define V_d^{SC} as the drain voltage at which the magnetoresistance sign-change takes place. In order to estimate V_d^{SC} the MR(V_d)-curves at different values of V_g were fitted with a simple exponential function. The resulting values of V_d^{SC} are summarized in Figure 3 as a function of V_g for the different mixing ratios. The sign reversal takes place at 74 V for a mixing ratio of 51:49. The V_d^{SC} values for the mixing ratios of 78:22 and 21:79 are significantly lower with values of 41 V and 24 V, respectively. Based on these results we can conclude that the MR landscape as well as the sign of the magnetoresistance can be electrically controlled in transistor structures based on Spiro-TTB/HAT-CN films. Furthermore, the corresponding V_d^{SC} values of the voltage-induced sign reversal can be significantly influenced by the composition of the donor/acceptor system.

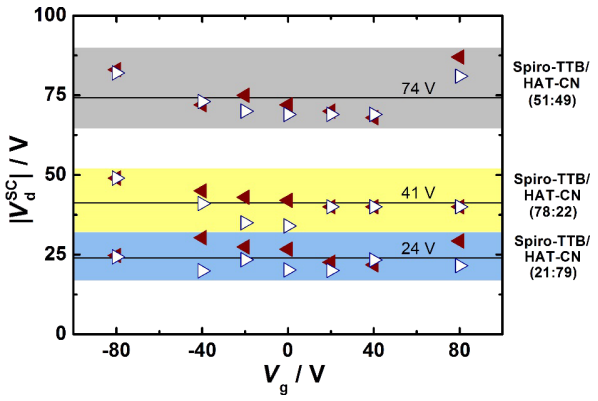

Figure 3: The drain voltage V_d^{SC}, at which the sign reversal takes place, is plotted for different V_g for all mixing ratios. All points belonging to one mixing ratio are highlighted in a separate colour. Red triangles denote the measurements with positive V_d, while white triangles represent negative V_d. The solid black lines represent the average V_d^{SC} values for each mixing ratio.

For a detailed analysis of the MR curves, separate measurement series were performed for small fields (2 mT < B < 85 mT) and ultrasmall fields (0.5 mT < B < 5 mT). First, a typical MR line shape curve for magnetic fields between 2 and 85 mT is displayed in Figure 4. It becomes clear that the non-Lorentzian line shape fits our data better than the Lorentzian line shape. This holds true for all Spiro-TTB/HAT-CN compositions (See also Table S1, S2 and S3 in Supporting Information File 1). Figure 5 shows the MR line shapes for all mixing ratios obtained at different V_d. Increasing V_d results in a reduction of the positive magnetoresistance in all mixing ratios and a

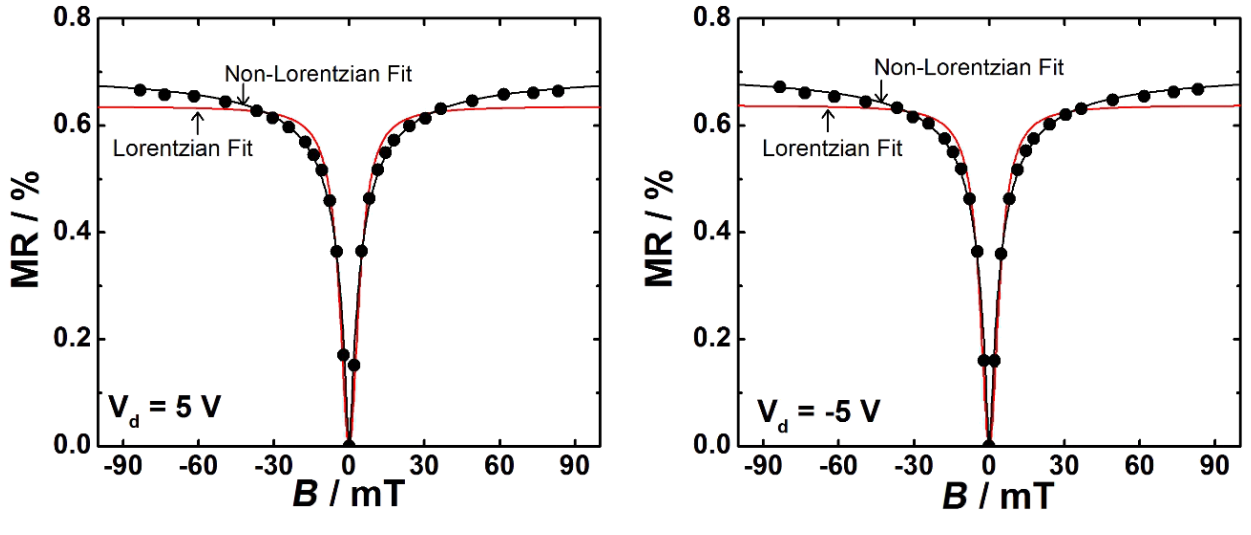

Figure 4: Representative MR line shape curves are shown at V_d = −5 V and +5 V. Black and red lines indicate fits with a Lorentzian (Supporting Information File 1, Equation S1) and a non-Lorentzian function (Supporting Information File 1, Equation S2), respectively. Hereby, devices with a mixing ratio of 51:49 were used. The applied magnetic fields are higher than 2 mT and V_g was zero for all measurements.

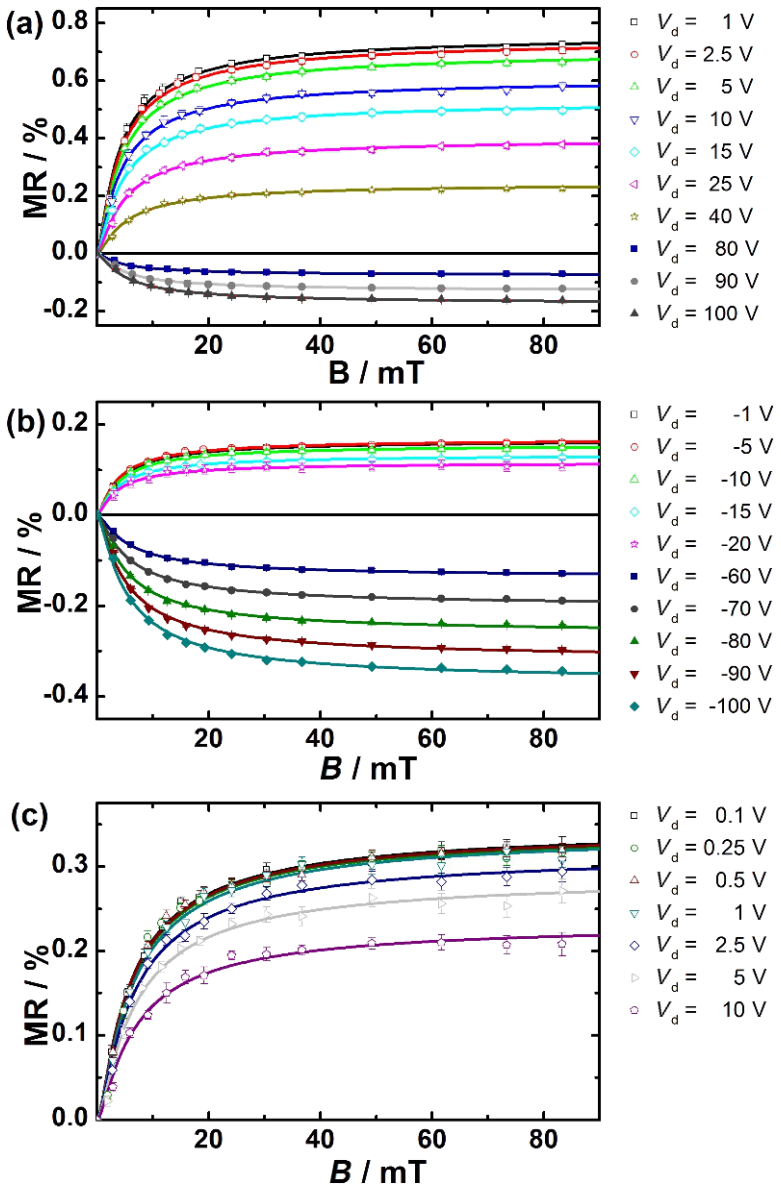

Figure 5: The dependence of the MR line shape curves on the drain voltage V_d is shown for a mixing ratio of (a) 51:49, (b) 78:22 and (c) 21:79. All measurements were performed at V_g fixed at zero voltage.

clear magnetoresistance sign-change can be tailored for mixing ratios of 51:49 and 78:22.

Derived from the fitting results presented in Figure 5 we obtained B_0 values for all measurements as displayed in Figure 6. The values of B_0 for all compositions are quite similar in magnitude and relatively independent of the applied voltage. Thus, the average B_0 value is estimated to be 2.11 ± 0.06 mT, which can be regarded as representative value for all coevaporated Spiro-TTB/HAT-CN compositions. The fit parameter B_0 is often correlated with the strength of the molecular hyperfine fields that affect the magnetosensitive quasiparticles [7,11,20,21]. Furthermore, it depends on the microscopic details of the underlying model [22]. The voltage and composition independence of B_0 suggests that one specific quasiparticle type can explain the entire magnetoresistive behaviour. Therefore, both the positive and the negative magnetoresistance should derive from one specific elementary process and the sign reversal should not be based on different components.

Furthermore, our experimental data shows a significant and reproducible influence of ultrasmall magnetic fields on I_d for

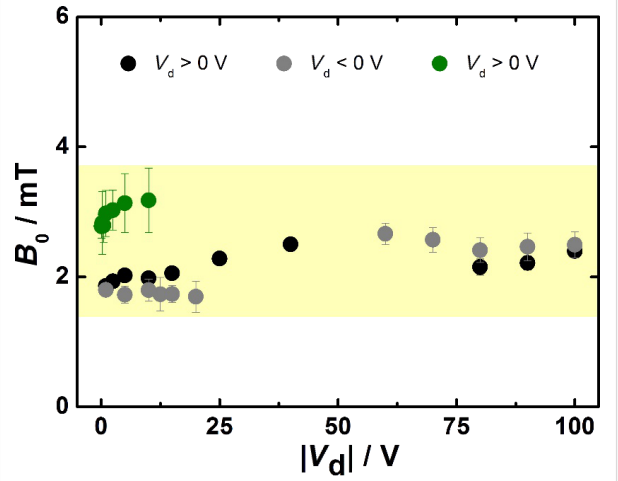

Figure 6: Voltage dependence of the line shape width B_0. The values of B_0 were obtained from fitting the data with the non-Lorentzian fit function.

B < 5 mT including an additional magnetic field induced MR sign-change (Figure 7). At a magnetic field of ≈1 mT, the effect of ultrasmall fields is reversed, resulting in a different MR-sign for B < 1 mT, than for B > 1 mT is obtained. So far, experimental evidence for this phenomenon, which is known as the ultrasmall magnetic field effect (USMFE), has only been provided by two research groups in organic diodes [19,23-26]. Here, we are able to verify it for the first time in organic transistors.

Up to now, USMF effects have been discussed controversially in the scientific community. For example, they have been explained based on the energetic crossover (and thus the increase of the spin mixture) of spin sublevels of correlated polaron pairs, coupled to nuclear spins [20,24,26]. Alternatively, the competition between the exciton or bipolaron formation and spin mixing serves as an explanation for USMF effects [22,27-29]. Both explanatory approaches have in common that they are applicable to neutral and charged spin pairs and the quasi-particles can be bipolarons, excitons or electron hole pairs. USMFE could be detected in both unipolar and bipolar diodes and they represent a fundamental component of the MR line shape [24-26]. Herby, simple non-Lorentzian and Lorentzian functions are not suitable to fit MR line shapes including the more complex USMF effects. Instead, a theory developed by Bobbert and co-workers has been used to fit USMFE according to the following equation [22]:

$$\mathrm{MR}_{\mathrm{USMFE}} = \mathrm{MR}_{\infty} \cdot D(B) \cdot \left[1 - F(B)\right] \qquad (1)$$

MR_{∞} is the maximum magnetoresistance, which can be achieved in the "slow hopping regime" at infinitely high magnetic-field strength. $D(B)$ is a dephasing factor to account for the average differences in the precession frequency of interacting polaron spins. $F(B)$ is the form factor, allowing reproducing both, the non-Lorentzian and Lorentzian line shapes. This factor includes model specific components responsible for line shape broadening, which does not derive from the strength of the hyperfine fields. In the following, $\mathrm{MR}_{\mathrm{USMFE}}(B)$ is used to illustrate the MR line shape together with the USMF effects.

USMFE could be detected in transistor structures with different mixing ratios of Spiro-TTB/HAT-CN and are presented as a

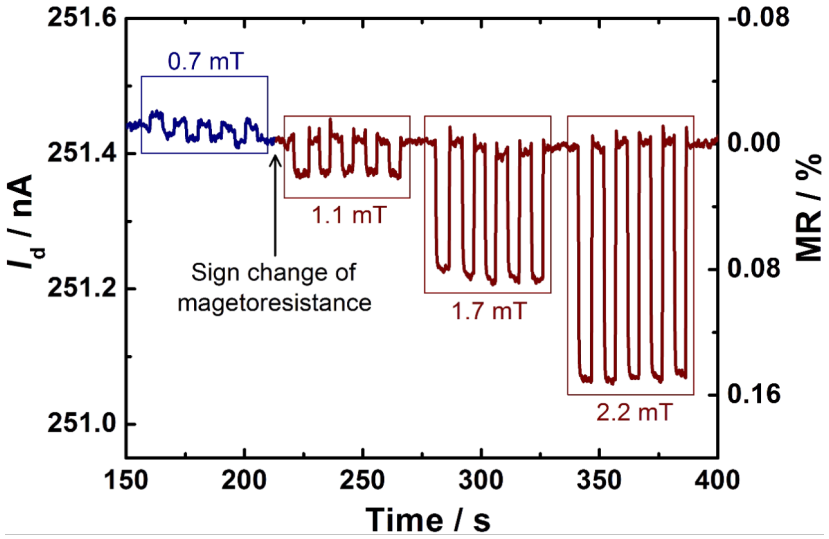

Figure 7: Experimental raw data covering ultrasmall magnetic-field effects including a MR sign-reversal. For B = 0.7 mT the I_d is increased (highlighted in blue) while I_d decreases for larger magnetic fields (highlighted in red). The experiment was carried out for zero V_g = 0, V_d = −2.5 V and a mixing ratio of 51:49.

function of V_d. The corresponding results, including the fits based on the function MR_{USMFE} (Equation 1), are displayed in Figure 8. They show that a MR sign-change takes place in all measurements at a magnetic field strength of ≈1 mT. For low to moderate V_d the sign of the MR changes from negative (B < 1 mT) to positive (B > 1 mT). This behavior is reversed for higher V_d, where MR is changing from positive (B < 1 mT) to negative (B > 1 mT). Our results are quite similar as obtained for π-conjugated polymers [20,23,26]. The USMFE in coevaporated Spiro-TTB/HAT-CN systems is sensitive to the voltage conditions and V_d can control the sign of MR. This dependence on V_d is analogous to the effects at moderate magnetic field

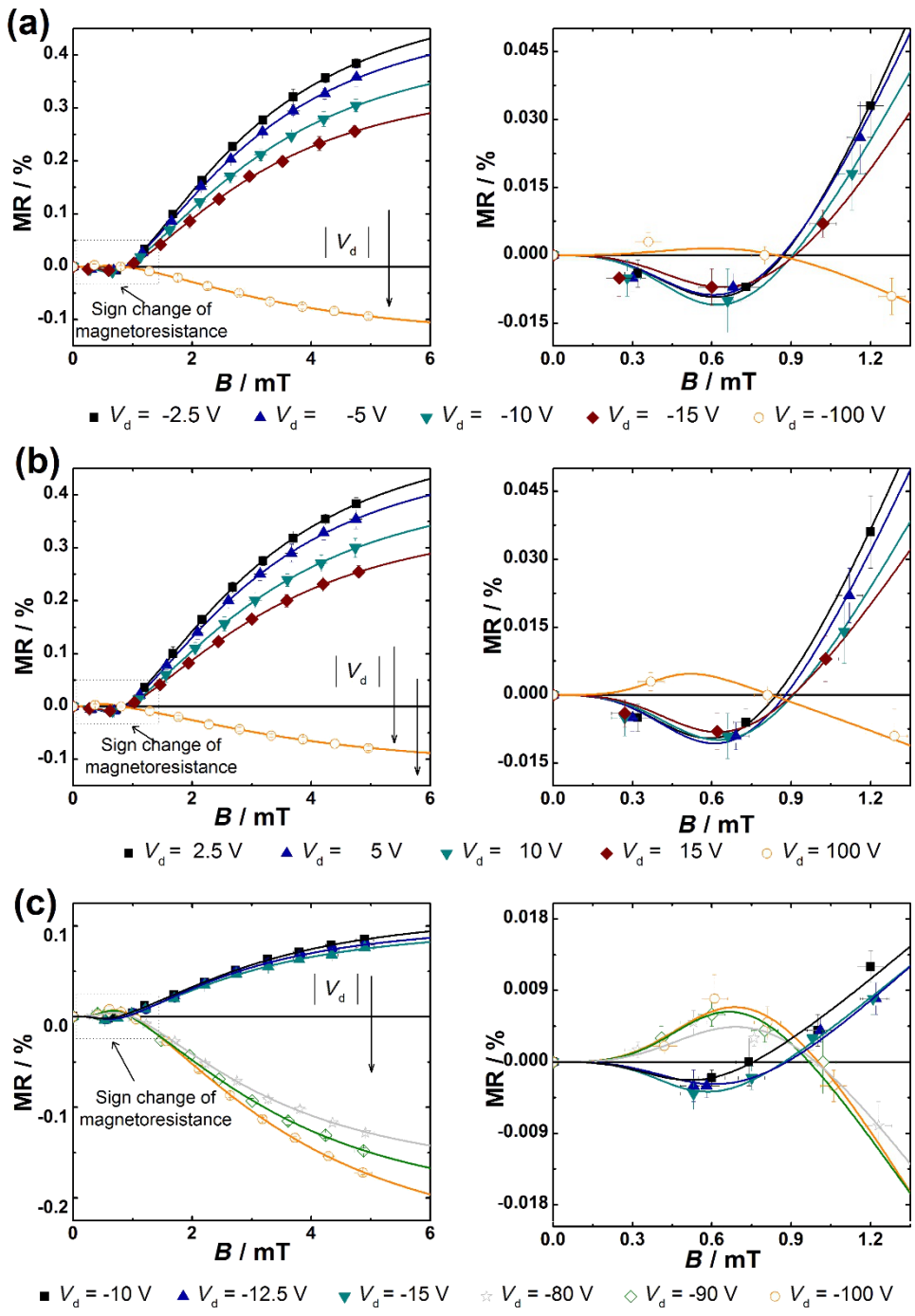

Figure 8: Ultrasmall magnetic field effects obtained for different compositions of Spiro-TTB/HAT-CN systems with a mixing ratio of (a) and (b) 51:49 and (c) 78:22 [19]. The measurements were performed at different values of V_d while keeping V_g constant at zero voltage. The solid lines are the fitting curves according to Equation 1.

strengths (5 mT < B < 85 mT) and the USMFE is subject to the same trends (see Figure 2 and Figure 5).

Now we combine the experimental data obtained from small fields (2 mT < B < 85 mT) and ultrasmall fields (0.5 mT < B < 5 mT). The fit function of MR_{USMFE} (Equation 1) is used to illustrate the curve shape over the complete measuring range (0.5 mT < B < 85 mT). The combined measurement results are shown in Figure 9 together with the fits based on MR_{USMFE} [19]. We have shown that both the non-Lorentzian line shape for small magnetic field strengths as well as the magnetic field induced MR sign change at ultrasmall magnetic field strengths are successfully fitted for all measured V_d. The saturation behaviour of the line shape and USMFE can be described simultaneously and the fit function MR_{USMFE} proves to be suitable for the complete MR values. The results of the separate measurement series are thus integrated into a uniform functional context.

Our results show for the first time ultrasmall magnetic-field effects in organic transistors. Under moderate drain voltage conditions; there is a positive magnetoresistance, which changes its sign at large drain voltages. Independent of the mixing ratio as well as the applied drain or source voltages, similar non-Lorentzian like MR line shapes and an average B_0 value of ≈2.1 mT are observed. The individual line shape was recently used as the most important criterion for the identification of the underlying magnetosensitive process [25,30]. Since all curves result in similar B_0-values, one can conclude that the magnetoresistance effects in Spiro-TTB/HAT-CN compositions depend on one specific quasiparticle species and the corresponding model should be capable to explain both positive and negative magnetoresistance. The low B_0 value of ≈2.1 mT is a typical characteristic for low-fields effects based on spin mixing due to the molecular hyperfine fields [22,25,30]. In principle, low-fields effects can be achieved with the electron–hole pair, exciton–polaron interaction and the bipolaron model [25,30,31]. In the absence of specific assumptions, only the unmodified bipolaron model leads to positive magnetoresistance. In addition, other low-field concepts appear to be less likely to explain all magnetoresistance effects in coevaporated Spiro-TTB/HAT-CN systems, alternative explanations cannot be excluded. In

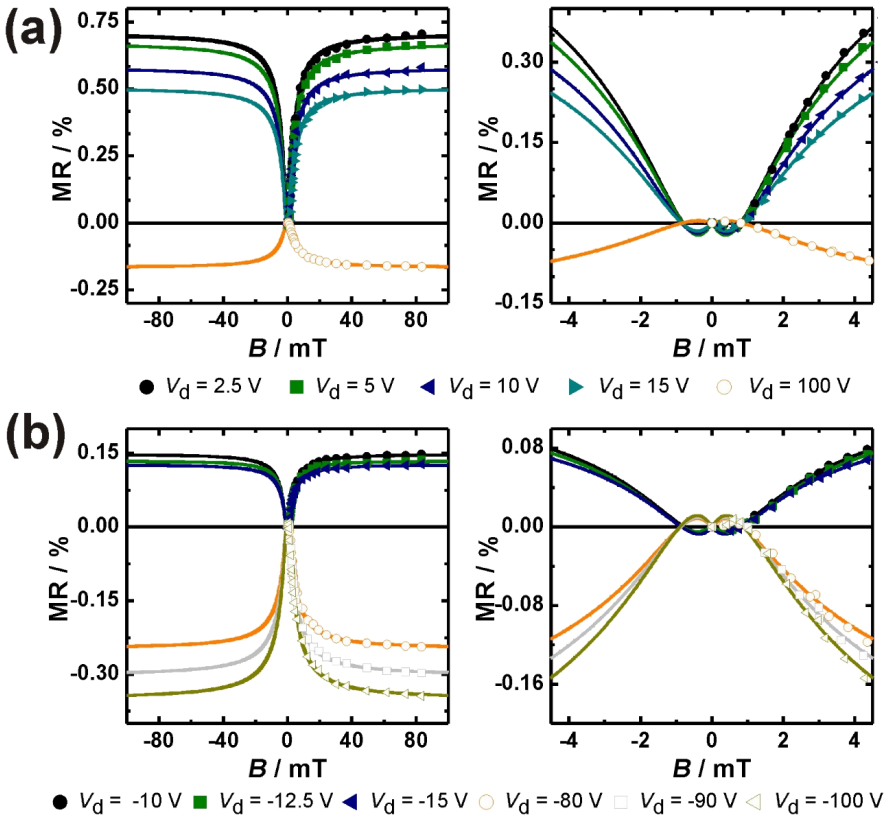

Figure 9: Magnetic-field effects in transistors based on different composition of Spiro-TTB and HAT-CN with a mixed ratio of (a) 51:49 and (b) 78:22 measured at different values of V_d are shown. The high quality of fit in the saturation regime can be seen in the left side. The right side gives evidence of sign reversal of magnetoresistance and the ultrasmall magnetic field effect. The solid lines are fitting curves according to Equation 1. All measurements were carried out at zero gate voltage.

particular magnetic-field sensitive intermolecular radical pair states [18] as well as a magnetic-field dependent electron transfer between donor–acceptor units may also play a role [32]. However, our experimental findings can be satisfactorily elucidated within the framework of the bipolaron model.

Bipolarons can be stabilized by the presence of counter charges [33-35]. Furthermore, the coulomb repulsive interaction occurring in the formation of bipolarons species can be compensated by a correspondingly high energetic disorder of the thin films [11,22,36-38]. Doping of amorphous organic films results in a broadening of the density of states and, thus, is increasing the energetic disorder [39,40]. Therefore, the high density of intrinsic charges in Spiro-TTB/HAT-CN compositions as well as the broadened density of states leads to an increased probability for the formation of bipolaronic species. According to the bipolaron model, two equally charged polarons can only simultaneously occupy a molecular transport site if their spin states are antiparallel [11,37]. For parallel polaron spins, bipolaron formation is energetically forbidden. Thus, the formation of bipolarons depends on the relative orientation of the precursor polaron spins and the process is magnetosensitive. The singlet and triplet states of the precursor polarons pairs are energetically degenerated in the absence of external magnetic fields and are mixed by the statistically distributed hyperfine fields. In magnetic fields larger than the hyperfine fields, the Zeeman splitting decreases the energetic degeneracy and the spin mixture is reduced [11,37]. Since the spin mixture enhances the generation of (singlet) bipolarons, the magnetic field decreases the probability of bipolaron formation. Typically, more free charge carriers are blocked. This results in a decrease in mobility and we obtain positive magnetoresistance. On the other hand, if a large number of bipolarons is present, the effect of the magnetic field is reversed [11,22]. At a certain number of bipolarons no sufficient number of free charge carriers is available and the charge transport is hindered. In this scenario, the magnetic field induced reduction of the spin mixture and thus, the reduced bipolaron formation-probability leads to a release of charge carriers, resulting in an increase of the current. Finally, negative magnetoresistance is obtained. In the context of the bipolaron model, the magnetoresistive behaviour of Spiro-TTB/HAT-CN compositions can be discussed as follows: The doping process between Spiro-TTB and HAT-CN in thin films generates intrinsic counter charges and increases the energetic disorder, which favours the formation of bipolarons. The formation process is spin-sensitive and the number of bipolarons is reduced for an increasing external magnetic field. At low drain voltage, a moderate number of bipolaron species is present and positive magnetoresistance is obtained. For larger V_d values, the current density increases and, thus, the probability of individual polarons to meet each other increases as well. Hence, more bipolarons are formed at high drain voltages and negative magnetoresistance gets predominant. Since positive and negative magnetoresistance are derived from the same quasiparticle species, whose magnetosensitivity is based on the spin mixture by hyperfine fields, ultrasmall magnetic-field effects are observed. The USMFE can also be described within the context of the bipolaron model. In unipolar diodes, the effect can be attributed to the change in singlet-triplet mixing near the energetic crossover of spin sublevels of bipolaronic species coupled to nuclear spins [23,25]. Alternatively, the competition between the bipolaron formation and the spin mixing is used to explain USMFE [27,29]. Both concepts propose an initial increase of spin mixing at ultrasmall magnetic fields. For stronger magnetic fields, the reduction of the spin mixing due to the Zeeman decoupling of the singlet and triplet levels dominates leading to the MR sign-change typical for USMFE. The polarity of the MR sign-change is controlled by the drain voltage, which can be explained with the previously discussed arguments.

Conclusion

Magnetoresistance in organic transistors has been proven for the first time without additional illumination by employing a mixed system of Spiro-TTB/HAT-CN. Intermolecular charge transfer between both molecules results in high intrinsic charge carrier density in the mixed films, which is sensitive to magnetic fields. The current flow can also be efficiently modulated with ultrasmall magnetic fields. A magnetic field-induced MR sign change occurs at $B \approx 1$ mT (USMFE). The magneto-resistive behavior is sensitive to the voltage conditions and the MR sign can be reversed by the drain voltage. The magnetoresistance effects can be successfully described within the framework of the bipolaron model, whereby the formation of the magnetosensitive bipolaronic species is made possible by the presence of (counter) charges present in the Spiro-TTB/HAT-CN mixed system. The ionizing donor–acceptor interaction can thus be regarded as a promising concept for the generation of highly conductive, magnetosensitive transport layers. Hence, organic transistors appear to represent an upcoming platform for studying spin-dependent processes in molecular semiconductors thereby leading the way towards efficient, multifunctional organic spin-devices.

Experimental

Bottom-contact field-effect transistor substrates were purchased from Fraunhofer IPMS (Dresden, Germany) with channel lengths (L) between 2.5 and 20 μm and channel width (W) of 10 mm. The isolation layer consists of 230 ± 10 nm thick SiO_2 and the source and drain electrodes are 30 nm Au with 10 nm ITO as adhesion layer. For all experiments transistors were used with $L = 2.5$ μm and $W = 10$ mm which are measured in a glove box (O_2, $H_2O < 0.1$ ppm) at room temperature. Spiro-

TTB and HAT-CN were synthesized and purified in our laboratory. Prior to the deposition of Spiro-TTB and HAT-CN, the predefined substrates were cleaned with acetone, 2-propanol and deionized water, followed by oxygen-plasma treatment and exposure to hexamethyldisilazane to replace the natural hydroxyl end group of SiO_2 with an apolar methoxy group. Finally, Spiro-TTB and HAT-CN were deposited by thermal evaporation at a base pressure of 1×10^{-7} Torr ($T_{substrate}$ = 298 K) with a thickness of 40 nm. For mixed system, the composition was controlled by using different evaporation rates for Spiro-TTB and HAT-CN, respectively. The mixing ratios (mass ratios) between Spiro-TTB and HAT-CN are 21:79, 51:49 and 78:22, respectively. The evaporation rates were monitored by two independent oscillating quartz-sensors. The uncertainty of our deposition process is ±2.5%. From the vacuum chamber, the samples were directly transferred to a glove box (O_2, H_2O < 0.1 ppm) and placed in a homebuilt sample holder. This sample holder was placed between the poles of an (unshielded) electromagnet with the magnetic field being perpendicular to the direction of the current flow in OFETs. The magnetic field was varied between −85 mT and +85 mT. Due to the (unshielded) earth magnetic field, reminiscence effects of the electromagnet and the uncertainty of our magnetic-field sensor, the uncertainty of the stated magnetic-field strength is ±80 μT. Current–voltage measurements were performed by using a Keithley 4200 semiconductor characterization system equipped with preamplifiers for improving low-current measurements. All measurements were performed at room temperature (≈298 K).

Supporting Information

Supporting Information File 1

The dependency of magnetoresistance on the drain and gate voltage for Spiro-TTB/HAT-CN for different mixing ratios and resulting fit parameters.
[http://www.beilstein-journals.org/bjnano/content/supplementary/2190-4286-8-112-S1.pdf]

Acknowledgements

We are gratefully acknowledged Prof. J. Salbeck for his long-standing support in this work. We also thank Dr. Manfred Kussler for synthesizing and purifying HAT-CN.

References

1. Xiong, Z. H.; Wu, D.; Vardeny, Z. V.; Shi, J. *Nature* **2004,** *427,* 821–824. doi:10.1038/nature02325
2. Wang, F. J.; Yang, C. G.; Vardeny, Z. V.; Li, X. G. *Phys. Rev. B* **2007,** *75,* 245324. doi:10.1103/PhysRevB.75.245324
3. Nguyen, T. D.; Ehrenfreund, E.; Vardeny, Z. V. *Science* **2012,** *337,* 204–209. doi:10.1126/science.1223444
4. Dediu, V.; Murgia, M.; Matacotta, F. C.; Taliani, C.; Barbanera, S. *Solid State Commun.* **2002,** *122,* 181–184. doi:10.1016/S0038-1098(02)00090-X
5. Prezioso, M.; Riminucci, A.; Bergenti, I.; Graziosi, P.; Brunel, D.; Dediu, V. A. *Adv. Mater.* **2011,** *23,* 1371–1375. doi:10.1002/adma.201003974
6. Gobbi, M.; Golmar, F.; Llopis, R.; Casanova, F.; Hueso, L. E. *Adv. Mater.* **2011,** *23,* 1609–1613. doi:10.1002/adma.201004672
7. Mermer, O.; Veeraraghavan, G.; Francis, T. L.; Sheng, Y.; Nguyen, D. T.; Wohlgenannt, M.; Köhler, A.; Al-Suti, M. K.; Khan, M. S. *Phys. Rev. B* **2005,** *72,* 205202. doi:10.1103/PhysRevB.72.205202
8. Kalinowski, J.; Cocchi, M.; Virgili, D.; Di Marco, P.; Fattori, V. *Chem. Phys. Lett.* **2003,** *380,* 710–715. doi:10.1016/j.cplett.2003.09.086
9. Prigodin, V. N.; Bergeson, J. D.; Lincoln, D. M.; Epstein, A. J. *Synth. Met.* **2006,** *156,* 757–761. doi:10.1016/j.synthmet.2006.04.010
10. Nguyen, T. D.; Sheng, Y.; Rybicki, J.; Wohlgenannt, M. *Phys. Rev. B* **2008,** *77,* 235209. doi:10.1103/PhysRevB.77.235209
11. Bobbert, P. A.; Nguyen, T. D.; van Oost, F. W. A.; Koopmans, B.; Wohlgenannt, M. *Phys. Rev. Lett.* **2007,** *99,* 216801. doi:10.1103/PhysRevLett.99.216801
12. Shakya, P.; Desai, P.; Kreouzis, T.; Gillin, W. P. *J. Appl. Phys.* **2008,** *103,* 043706. doi:10.1063/1.2885097
13. Wang, F.; Macià, F.; Wohlgenannt, M.; Kent, A. D.; Flatté, M. E. *Phys. Rev. X* **2012,** *2,* 021013. doi:10.1103/PhysRevX.2.021013
14. Harmon, N. J.; Macià, F.; Wang, F.; Wohlgenannt, M.; Kent, A. D.; Flatté, M. E. *Phys. Rev. B* **2013,** *87,* 121203. doi:10.1103/PhysRevB.87.121203
15. Cox, M.; Kersten, S. P.; Veerhoek, J. M.; Bobbert, P.; Koopmans, B. *Phys. Rev. B* **2015,** *91,* 165205. doi:10.1103/PhysRevB.91.165205
16. Reichert, T.; Saragi, T. P. I. *Appl. Phys. Lett.* **2011,** *98,* 063307. doi:10.1063/1.3554388
17. Lee, T.-H.; Li, J.-H.; Huang, W.-S.; Hu, B.; Huang, J. C. A.; Guo, T.-F.; Wen, T.-C. *Appl. Phys. Lett.* **2011,** *99,* 073307. doi:10.1063/1.3627170
18. Reichert, T.; Saragi, T. P. I.; Salbeck, J. *RSC Adv.* **2012,** *2,* 7388–7390. doi:10.1039/c2ra20901b
19. Reichert, T. Organische Magnetooptoelektronik: Magnetowiderstand in Organischen Feldeffekt-Transistoren. Ph.D. Thesis, Universität Kassel, Germany, 2014.
20. Nguyen, T. D.; Hukic-Markosian, G.; Wang, F.; Wojcik, L.; Li, X.-G.; Ehrenfreund, E.; Vardeny, Z. V. *Nat. Mater.* **2010,** *9,* 345–352. doi:10.1038/nmat2633
21. Giro, R.; Rosselli, F. P.; dos Santos Carvalho, R.; Capaz, R. B.; Cremona, M.; Achete, C. A. *Phys. Rev. B* **2013,** *87,* 125204. doi:10.1103/PhysRevB.87.125204
22. Wagemans, W.; Janssen, P.; Schellekens, A. J.; Bloom, F. L.; Bobbert, P. A.; Koopmans, B. *SPIN* **2011,** *1,* 93–108. doi:10.1142/S2010324711000082
23. Nguyen, T. D.; Ehrenfreund, E.; Vardeny, Z. V. *Org. Electron.* **2013,** *14,* 1852–1855. doi:10.1016/j.orgel.2013.04.031
24. Nguyen, T. D.; Gautam, B. R.; Ehrenfreund, E.; Vardeny, Z. V. *Phys. Rev. Lett.* **2010,** *105,* 166804. doi:10.1103/PhysRevLett.105.166804
25. Janssen, P.; Cox, M.; Wouters, S. H. W.; Kemerink, M.; Wienk, M. M.; Koopmans, B. *Nat. Commun.* **2013,** *4,* 2286. doi:10.1038/ncomms3286
26. Nguyen, T. D.; Gautam, B. R.; Ehrenfreund, E.; Vardeny, Z. V. *Synth. Met.* **2011,** *161,* 604–607. doi:10.1016/j.synthmet.2010.11.051

27. Schellekens, A. J.; Wagemans, W.; Kersten, S. P.; Bobbert, P. A.; Koopmans, B. *Phys. Rev. B* **2011,** *84,* 075204. doi:10.1103/PhysRevB.84.075204
28. Kersten, S. P.; Schellekens, A. J.; Koopmans, B.; Bobbert, P. A. *Phys. Rev. Lett.* **2011,** *106,* 197402. doi:10.1103/PhysRevLett.106.197402
29. Danon, J.; Wang, X.; Manchon, A. *Phys. Rev. Lett.* **2013,** *111,* 066802. doi:10.1103/PhysRevLett.111.066802
30. van Reenen, S.; Kersten, S. P.; Wouters, S. H. W.; Cox, M.; Janssen, P.; Koopmans, B.; Bobbert, P. A.; Kemerink, M. *Phys. Rev. B* **2013,** *88,* 125203. doi:10.1103/PhysRevB.88.125203
31. Janssen, P. Spins in organic semiconductors. Ph.D. Thesis, Eindhoven University of Technology, The Netherlands, 2013.
32. Kersten, S. P.; Meskers, S. C. J.; Bobbert, P. A. *Phys. Rev. B* **2012,** *86,* 045210. doi:10.1103/PhysRevB.86.045210
33. Crispin, A.; Crispin, X.; Fahlman, M.; dos Santos, D. A.; Cornil, J.; Johansson, N.; Bauer, J.; Weissörtel, F.; Salbeck, J.; Brédas, J. L.; Salaneck, W. R. *J. Chem. Phys.* **2002,** *116,* 8159–8167. doi:10.1063/1.1465408
34. Ito, A.; Tanaka, K.; Yamabe, T. *J. Phys.: Condens. Matter* **1996,** *8,* 771–779. doi:10.1088/0953-8984/8/7/004
35. Brazovskii, S.; Kirova, N.; Yu, Z. G.; Bishop, A. R.; Saxena, A. *Opt. Mater.* **1998,** *9,* 502–506. doi:10.1016/S0925-3467(97)00121-3
36. Wagemans, W.; Koopmans, B. *Phys. Status Solidi B* **2011,** *248,* 1029–1041. doi:10.1002/pssb.201046383
37. Wagemans, W.; Bloom, F. L.; Bobbert, P. A.; Wohlgenannt, M.; Koopmans, B. *J. Appl. Phys.* **2008,** *103,* 07F303. doi:10.1063/1.2828706
38. Bobbert, P. A.; Nguyen, T. D.; Wagemans, W.; van Oost, F. W. A.; Koopmans, B.; Wohlgenannt, M. *Synth. Met.* **2010,** *160,* 223–229. doi:10.1016/j.synthmet.2009.06.002
39. Arkhipov, V. I.; Heremans, P.; Emelianova, E. V.; Bässler, H. *Phys. Rev. B* **2005,** *71,* 045214. doi:10.1103/PhysRevB.71.045214
40. Tal, O.; Rosenwaks, Y.; Preezant, Y.; Tessler, N.; Chan, C. K.; Kahn, A. *Phys. Rev. Lett.* **2005,** *95,* 256405. doi:10.1103/PhysRevLett.95.256405

License and Terms

BEILSTEIN JOURNAL OF NANOTECHNOLOGY

Adsorption characteristics of $Er_3N@C_{80}$ on W(110) and Au(111) studied via scanning tunneling microscopy and spectroscopy

Sebastian Schimmel[1], Zhixiang Sun[1], Danny Baumann[1], Denis Krylov[1], Nataliya Samoylova[1], Alexey Popov[1], Bernd Büchner[1,2,3] and Christian Hess[*1,3]

Full Research Paper

Open Access

Address:
[1]Leibniz-Institute for Solid State and Materials Research, IFW-Dresden, Helmholtzstrasse 20, 01069 Dresden, Germany, [2]Institut für Festkörperphysik, TU Dresden, 01069 Dresden, Germany and [3]Center for Transport and Devices, TU Dresden, 01069 Dresden, Germany

Email:
Christian Hess[*] - C.Hess@ifw-dresden.de

* Corresponding author

Keywords:
adsorption; Au(111); $Er_3N@C_{80}$; scanning tunnelling microscopy; scanning tunnelling spectroscopy; W(110)

Beilstein J. Nanotechnol. **2017,** *8,* 1127–1134.
doi:10.3762/bjnano.8.114

Received: 31 January 2017
Accepted: 03 May 2017
Published: 23 May 2017

This article is part of the Thematic Series "Towards molecular spintronics".

Guest Editor: G. Salvan

Abstract

We performed a study on the fundamental adsorption characteristics of $Er_3N@C_{80}$ deposited on W(110) and Au(111) via room temperature scanning tunneling microscopy and spectroscopy. Adsorbed on W(110), a comparatively strong bond to the endohedral fullerenes inhibited the formation of ordered monolayer islands. In contrast, the Au(111)-surface provides a sufficiently high mobility for the molecules to arrange in monolayer islands after annealing. Interestingly, the fullerenes modify the herringbone reconstruction indicating that the molecule–substrate interaction is of considerable extent. Investigations concerning the electronic structure of $Er_3N@C_{80}$/Au(111) reveals spatial variations dependent on the termination of the Au(111) at the interface.

Introduction

Fullerenes provide the feasibility of tunable physical properties by their capacity to encapsulate atoms or clusters inside the carbon cage [1,2]. Thus since their discovery in 1985 they excite great attention of the scientific community. Sustained efforts on the synthesis of endohedral fullerenes led to the trimetallic nitride template (TNT) process and consequently to the creation of the class of trimetallic nitride endohedral fullerenes in 1999, which can be produced in a sufficiently high yield for experimental studies and possible applications [3]. These molecules $A_{3-n}B_nN@C_k$ (n = 0–3; A, B = rare earth metal or transition metals of the IVth subgroup; k = 68–96) are composed of a carbon cage which encapsulates a triangular cluster consisting of 3 rare-earth or transition metal atoms and a nitrogen atom at its center [4]. Dependent on the cluster composition and due to the intercalation inside a protecting carbon cage, intriguing properties emerge. For instance, single molecular magnetism

was observed for $DySc_2N@C_{80}$ [5] and conductance switching by tunneling current induced cluster rotations between chiral conformations was demonstrated for $Sc_3N@C_{80}$ [6]. Furthermore, the magneto-optically active endohedral fullerene $Er_3N@C_{80}$ permits a direct non-cage-mediated optical interaction with the incarcerated Er^{3+} ion in near-infrared that might make its use as optical manipulable fullerene-qubit possible [7-9]. Due to the versatile characteristics, the trimetallic nitride endohedral fullerenes are considered as promising candidates for applications in the fields of molecular electronics, molecular spintronics and quantum information processing. The implementation of these ambitious applications requires the knowledge about the molecules' behavior in interaction with possible electrode surfaces. One aspect regards the formation of one respectively two dimensional and addressable arrays. Another important issue concerns the elucidation of the system's electronic structure and adsorption site dependent effects on it.

In order to examine the adsorption characteristics and the electronic structure of $Er_3N@C_{80}$ in consideration of adsorbate–substrate interaction, we performed scanning tunneling microscopy (STM) and scanning tunneling spectroscopy (STS) investigations on sub-monolayer covered W(110) and Au(111) single crystal substrates. Beside their potential application as electrode materials, the choice of these established standard substrate for STM/STS investigations provides the advantages of comparability to results of earlier measurements and well-known fast cleaning treatments.

Experimental

$Er_3N@C_{80}$ was purchased from SES Research. For STM measurements, the samples was purified by high-pressure liquid chromatography (HPLC) with Buckyprep-M column and toluene as a solvent, washed with acetone and hexane, and then transferred to the crucible of the Knudsen cell by drop-casting from toluene.

To achieve the reproducible preparation of sub-monolayer $Er_3N@C_{80}$-coverage on substrates with the demanded cleanliness for systematically STM/STS investigations, the molecules were deposited via organic molecular beam epitaxy under ultra-high vacuum (UHV) conditions ($p < 10^{-9}$ mbar) and subsequently analyzed in situ in a variable temperature STM.

To provide contamination free substrate surfaces, cleaning treatments were applied to the used single crystals, prior to the measurement. According to the proceeding suggested by Bode et al. [10], the W(110)-surface was cleaned by repeated cycles of annealing ($T \approx 1500$ K) at increased oxygen pressure and subsequent e-beam flashing ($T \approx 2300$ K). This process was conducted 4 times in which the oxygen raised chamber pressure was stepwise reduced from $p \approx 5 \times 10^{-7}$ mbar down to $p \approx 2 \times 10^{-8}$ mbar. Thus, the W(110)-surface possesses clean terraces of monoatomic height and without its conventionally carbon-induced reconstruction. The preparation of the Au(111)-surface was done by Ar-ion sputtering with an ion-energy of 1 keV. By posterior annealing ($T \approx 823$ K; $t \approx 60$–120 min) extended terraces with monoatomic step edges could be obtained. By this standard procedure, as is typical for a clean Au(111) surface, the herring bone reconstruction occurred. The success of these prior treatments was checked by STM before depositing the molecules.

After that the thermally stable endohedral fullerenes $Er_3N@C_{80}$ were evaporated from a home-built and carefully degassed evaporator for $t \approx 4$ min at a temperature of about $T \approx 800$ K on the single crystal substrates. By this procedure, samples with a coverage of about 16% could be prepared reproducibly. In order to induce the formation of monolayer height molecule islands on the surfaces, the substrates were heated ($T = 620$–670 K) during and after the deposition, to increase the molecule mobility [11,12]. This annealing treatment was applied to all samples presented in this study.

The measurement data was acquired at room temperature and under UHV conditions. The topographic images were produced in constant-current mode, with the bias voltage applied to the tip. The generated images were processed using WSxM [13]. The spatially resolved spectroscopy information was taken by $I(U)$ measurements at open feedback loop at every pixel of the corresponding image. In order to obtain $\mathrm{d}I/\mathrm{d}U(U)$ data a posterior numerical derivation using the analysis software WSxM [13] was performed. For the measurements, mechanically cut Pt–Ir-tips have been used.

Results and Discussion

Following the previously mentioned treatments for depositing $Er_3N@C_{80}$, on clean W(110) sub-monolayer-coverage could be obtained as verified by Figure 1. On the representatively chosen area, single molecules and monoatomic steps of W(110) are simultaneously visible. The step edges appear as straight boarders of areas with almost constant color (the terraces) in the background of the image (Figure 1). On the terraces round bright structures are visible corresponding to the spherical shaped endohedral fullerenes. The image shows randomly distributed molecules on the W(110)-surface. Within our investigations, no preferred accumulation to favored adsorption positions like step edges have been observed. Individual molecules remain immobilized on the terraces and even attempts to induce self-assembling by surface diffusion via annealing ($T = 670$ K) were not successful. This means, the formation of monolayer islands is inhibited for this system. Apparently, the

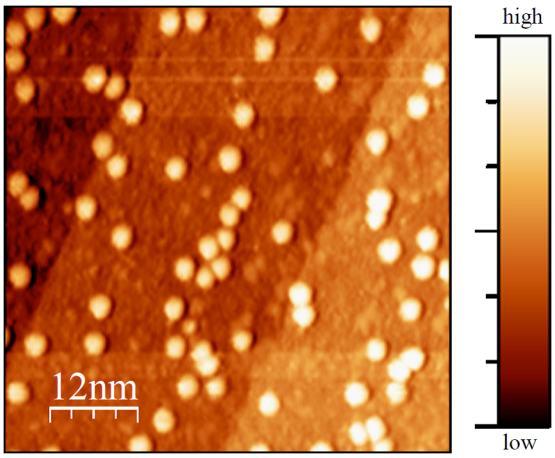

Figure 1: Topographic image (U = 2 V; I = 0.5 nA) of $Er_3N@C_{80}$ on W(110). The molecules appear as bright round structures on the straight monoatomic steps of W(110). The fullerenes are randomly distributed on the surface. The residual roughness visible in the image most probably emerges from multiple imaging of the molecules due to the imperfection of the tip. The scale bar colors are also representative for all following images.

fullerene–W(110) bond is relatively strong. This is surprising in view of the well-known donation of six electrons from the incarcerated cluster to the cage [4], which causes a weaker adsorbate–substrate interaction [11] in comparison to empty fullerenes. The effects of higher annealing temperatures were not examined.

In contrast to the adsorption characteristics of $Er_3N@C_{80}$ on W(110), the molecules exhibit a sufficiently high mobility on the Au(111)-surface. In this case annealing initiated surface diffusion of the fullerenes on the terraces and along the lower level of step edges. Thus, they could form 1D single molecule lines at step edges (Figure 2a). These molecular lines seem to play an important role as initial nucleus for the 2D-growth of $Er_3N@C_{80}$ islands (Figure 2a,b), since at all observed instances, the 2D-islands are connected to step edges (not shown).

Note that under our preparation conditions fully saturated step edges were no precondition for the island growth to occur. Rarely, islands and inordinate aggregations on terraces were found where most likely local impurities served as nucleation points. The spatial extent of the monolayers reached sizes of several 100 × 100 nm^2. The STM image of Figure 2b taken at the edge of an $Er_3N@C_{80}$-island illustrates that the molecules are organized in a hcp structure with a nearest neighbor distance of 1.15 ± 0.01 nm, consistent with earlier findings [11,12].

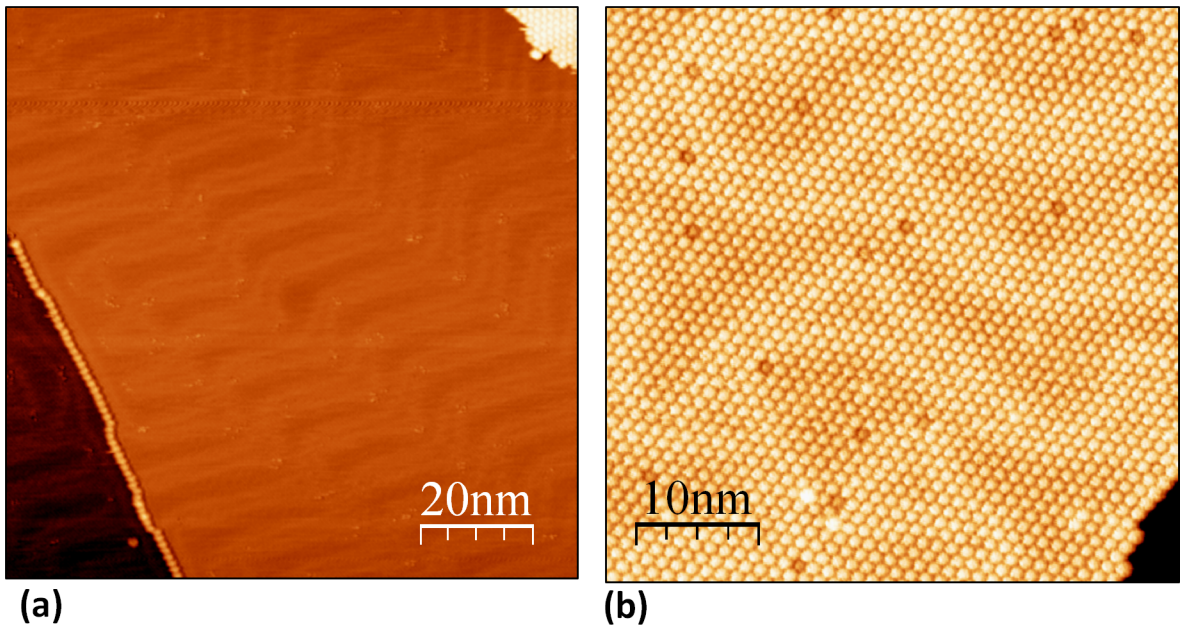

Figure 2: Topographic images (U = 1.5 V; I = 0.2 nA) of $Er_3N@C_{80}$ on Au(111). Figure (a) shows a one-dimensional chain of the endohedral fullerenes at the monoatomic step edge of the reconstructed Au(111) surface. Due to the presence of the molecules the reconstruction lines are distorted and prevented to pass the molecule line at the step edge. The molecules are positioned at fcc terminated adsorption sites indicated by the discommensuration line course. At the upper right corner the 2D-monolayer is visible. A fullerene monolayer on Au(111) is shown in Figure (b). The molecules arrange in a hcp-structure with a nearest neighbor distance on about 1.15 ± 0.01 nm. Several fullerenes of the monolayer appear darker respectively brighter in the image. This effect, caused by the fullerene monolayer induced restructuring of the Au(111) interface, could be assigned to an anomalous electronic structure resulting from the proposed formation of nanopits at the Au(111) interface that consequently lead to a changed number of Au-atoms interacting with the affected molecules [12,14]. Note that the presence of impurities cannot be excluded.

The orientation of the monolayers was examined by comparing them with the herringbone reconstruction visible at bare Au(111) surface regions (Figure 2a and Figure 3a,b). The typical double line pattern results from a 4.34% uniaxial compression along the closed packed <1$\bar{1}$0>-direction and runs perpendicular to that [15]. With respect to the non-reconstructed Au(111)-(1 × 1) surface, the orientation of the molecular adlayers closed-packed-direction coincides with Au(111)-<1$\bar{1}$0> (Figure 3a), whereby the monolayers can be described as (4 × 4) superstructure [11,12]. Our data reveal a new alignment in addition to this known in-phase orientation of $Er_3N@C_{80}$-monolayer on Au(111). In this case, the monolayer was found to be rotated to form an incommensurate (4 × 4)*R*30° phase (Figure 3b) with respect to the bulk fcc termination. Independent of monolayer orientation, the spacing between the fullerenes is the same value. This finding is reminiscent of results by Altman and Colton [16,17]. They performed detailed studies regarding the adsorption behavior of C_{60} on Au(111). There, even though the diameter of C_{60} is smaller than that of $Er_3N@C_{80}$, similar orientations of the monolayer were observed. Since the monolayer orientation of C_{60} is determined by the orientation of the step edge [16], a similar reason for the two observed phases of $Er_3N@C_{80}$-monolayers is likely. Thus, an adsorption to a step edge that is orientated along the [110]-direction would lead to an in phase monolayer.

Another interesting observation concerns the Au(111) surface reconstruction at the interface regions. As is evident from Figure 2a,b and Figure 3a,b, the reconstruction is modified by the interaction of the molecules with the bare Au(111)-surface. Beside the assembled fullerenes the herringbone reconstruction is visible at the bare Au(111) sections (Figure 2a and Figure 3a,b) as well as at the interface region (Figure 2a,b and Figure 3a,b). Due to the presence of the molecules, the herringbones are apparently disturbed and lose the straight long range zigzag course. This is the case for both, the one-dimensional molecular lines at the step edges as well as for the two-dimensional molecular layers. At the step edges (Figure 2a) the herring bones apparently cannot pass the single fullerene line. This is in contrast to the usual case of a clean Au(111) surface step edge where the reconstruction lines continue over the step edge [18]. Since the molecules are preferably located at the herringbone reconstruction's fcc termination in our data, this termination appears energetically favorable for the adsorption.

In the 2D-case, beneath the $Er_3N@C_{80}$ covered areas the herringbone reconstruction is modified (Figure 3a,b) as well. This interfacial reconstruction reveals as a superimposed double stripe pattern on the monolayers. In contrast to the reconstruction of clean Au(111), the line pairs frequently coalesce to form rounded triangular structures (Figure 3a) and rather exhibit a

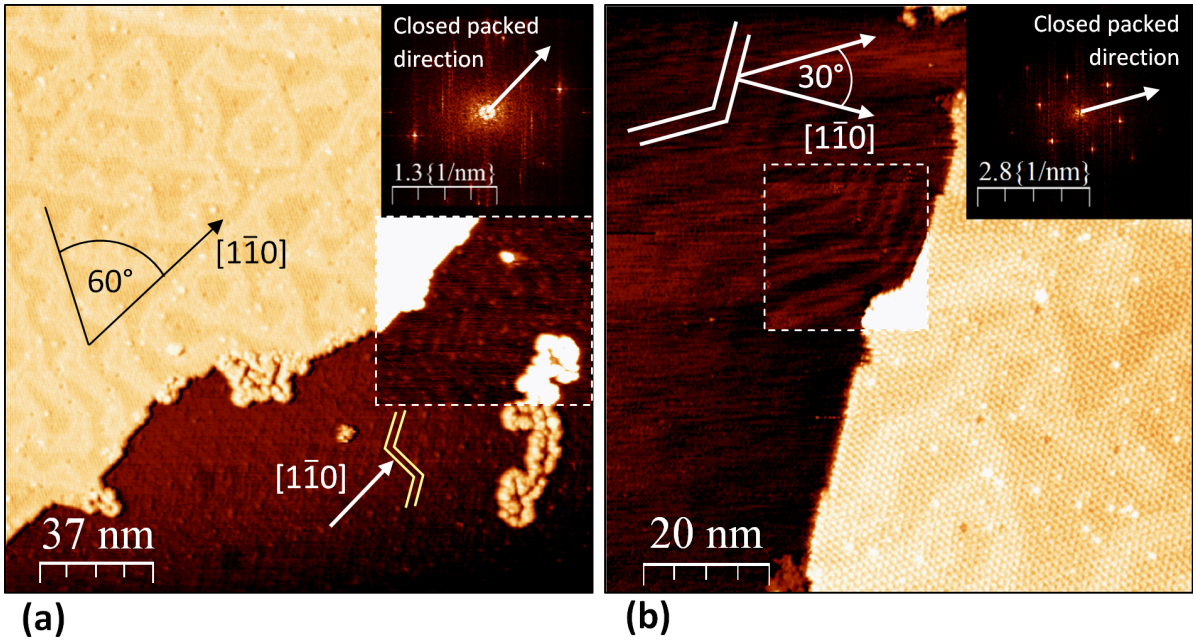

Figure 3: The $Er_3N@C_{80}$-monolayer orientations on Au(111) and the new interfacial reconstruction are depicted on these constant-current-images (U = 1.5 V; I = 0.2 nA). In Figure (a) the monolayer with in-phase orientation can be seen at the left upper half of the image. The arrows on the real-space image visualize the [1$\bar{1}$0]-direction determined by the highlighted herringbone reconstruction (changed-contrast-inset and yellow double-line). The closed packed direction of the fullerenes is shown by an arrow inside the FFT-image (upper right corner) and corresponds to the Au(111)-[1$\bar{1}$0]-direction. The double line pattern of the interfacial reconstruction is visible on the monolayer. The pattern is dominated by ubiquitous 60°-angles. Figure (b) shows the out-of-phase oriented $Er_3N@C_{80}$-monolayer (right half) on Au(111). The closed packed direction of the molecules reveals a 30°-angle to the [1$\bar{1}$0]-direction as described by the arrows inside the FFT-image (upper right corner) and the real space topography.

less sharply defined course than for the clean Au(111)-surface. Figure 3a and b show that the reconstruction-lines between the covered and bare Au(111) areas are not linked to each other. Corresponding to the threefold symmetry of the Au(111) surface, 3 equivalent directions dominate the discommensuration line propagation, which can be concluded by ubiquitous 60° angles, as illustrated in Figure 3a. Thus, the elongation of the line pairs concerns the $<1\bar{1}0>$-directions, the remaining compression of the Au-interface is indicated to point along $<1\bar{1}\bar{2}>$. As compared to the spacing of 6.3 nm [15] between the line-pairs in the pristine surface, an increased and variable spacing (9.5–16 nm) was observed. These characteristics could be attributed to a decompression in the first atomic layer of Au(111) at the interface regions, which is likely induced by a rearrangement of Au-atoms in order to reduce interfacial energy. It seems plausible that reducing the mismatch between the monolayer and the Au(111) plays a crucial role for the latter, thereby enhancing the tendency of the $Er_3N@C_{80}$-adlayer to grow quasi-epitaxially on the Au(111)-surface. According to our data, the decrease of compression rather enlarged the distance between the line pairs than between the lines of the pairs. A favored adsorption on fcc sites is therefore suggested.

The observed interfacial reconstruction line pattern exhibits a lack of long range periodicity and uniformity as assumed for a thermodynamically most favored arrangement. This could be assigned to a frozen structure resulting from too short annealing times which implies that the rearrangement of the interfacial Au-atoms is most probably a thermally assisted and time-dependent process. While effects of longer annealing times and different temperatures were not further elaborated within this study, our conjecture is corroborated by pertinent results for C_{60}-fullerenes on Au(111) [14,17,19-21].

The above results show that the monolayer growth and the minimization of the interface energy lead to a clear change of the reconstruction of the Au(111) surface. Considering the fact that the surface reconstruction of the pristine Au(111) is driven by a remarkable energy gain on 20 meV per Au-atom [22], and that van der Waals bond molecular layers on Au(111) typically leave the herringbone reconstruction unchanged [23] our observation of a modification of the reconstruction implies a molecular substrate interaction stronger than typical van der Waals interaction. A certain degree of hybridization of the molecules and Au(111) surface electronic structure is therefore conjectured. In order to investigate this further, we performed scanning tunneling spectroscopy (STS) on the $Er_3N@C_{80}$-monolayer on Au(111).

The obtained spectroscopic results, presented in Figure 4, exhibit two dominant peaks related to the HOMO- and LUMO-derived states (HDS and LDS) (Figure 4b). In between the mo-

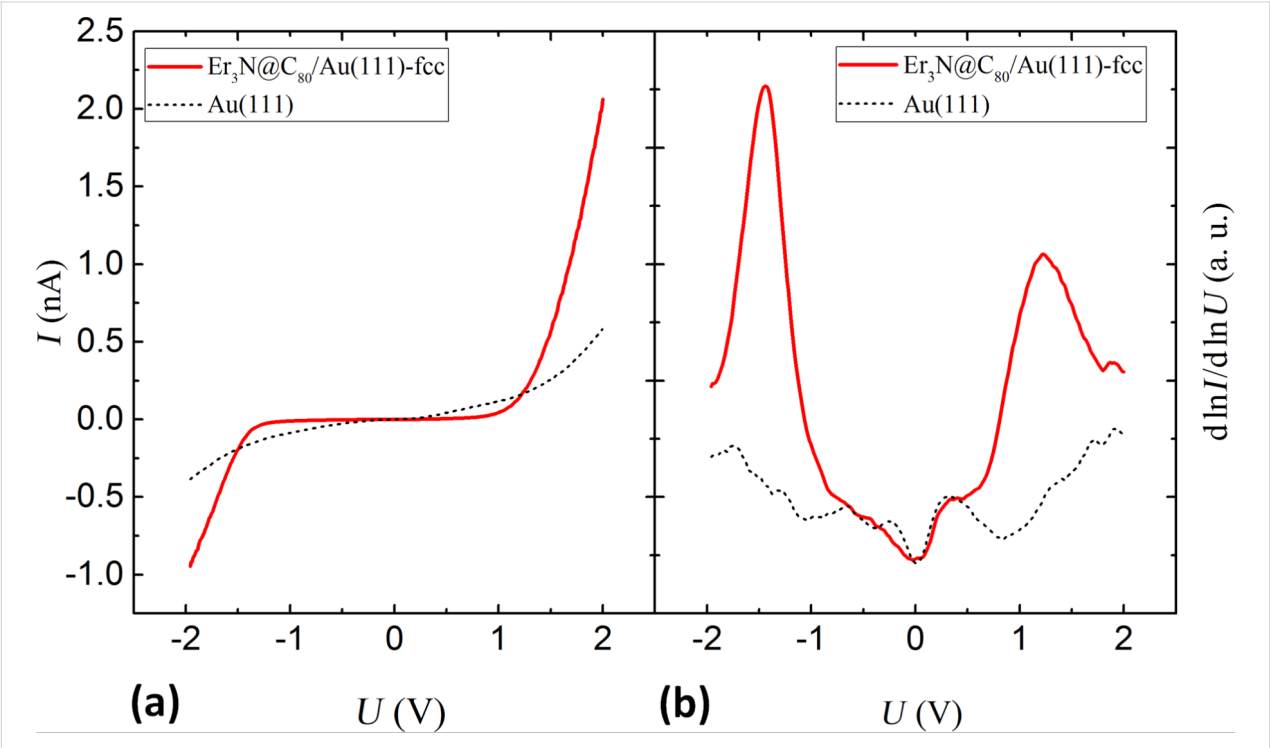

Figure 4: The *I*/*U*-spectrum (a) and the normalized dln*I*/dln*U*-spectrum (b) of $Er_3N@C_{80}$/Au(111). The voltage is considered as applied to the sample. The Au(111) surface state is not visible in the spectrum.

lecular orbital derived states the tunneling current is suppressed (Figure 4a) and the HDS-LDS energy gap was determined to be of about 2.6 eV wide (peak to peak). The peaks are well defined and energetically located at a distinct distance to E_F. This implies that even if a significant hybridization of molecular and substrate states occurs, the effective transfer of electrons remains relatively subtle. Nevertheless, the broadening of the peaks (≈1 eV) clearly exceeds the room temperature energy broadening (≈0.1 eV). Typical energies of intramolecular vibrations are also in the order of ≤0.2 eV.

It remains unclear, to what extent the additional broadening is due to a distribution of HOMO/LUMO multiplets or due to hybridization effects.

In order to investigate this further, we performed spectroscopy dI/dU-mapping of the $Er_3N@C_{80}$-monolayers. Figure 5a shows the topographic data of the investigated area: the $Er_3N@C_{80}$-monolayer (bright half), the slightly visible interfacial reconstruction and the bare Au(111)-surface (dark half) can be seen. Interestingly, as illustrated in Figure 5b and c, spatial variations of the electronic structure occurred. The corresponding differential conductance maps (Figure 5b,c) respectively chosen at bias voltages of 0.826 V and −1.181 V reveal a bright-dark pattern on the monolayer coinciding with the interfacial reconstruction. Regions where the Au(111)-interface is considered to be of fcc termination appear darker in Figure 5b whereas the hcp adsorption sites are imaged brighter. Figure 5c shows the equivalent result with an inversed contrast. Since the fullerenes are located at distinguishable absorption sites, the observed contrast implies a spatially varying hybridization. This conclusion is supported by the comparison of the averaged spectra taken at the distinguished fcc and hcp areas (Figure 5d). Apparently, differences in the Au(111)-interface termination induce a 0.1 eV shift of the

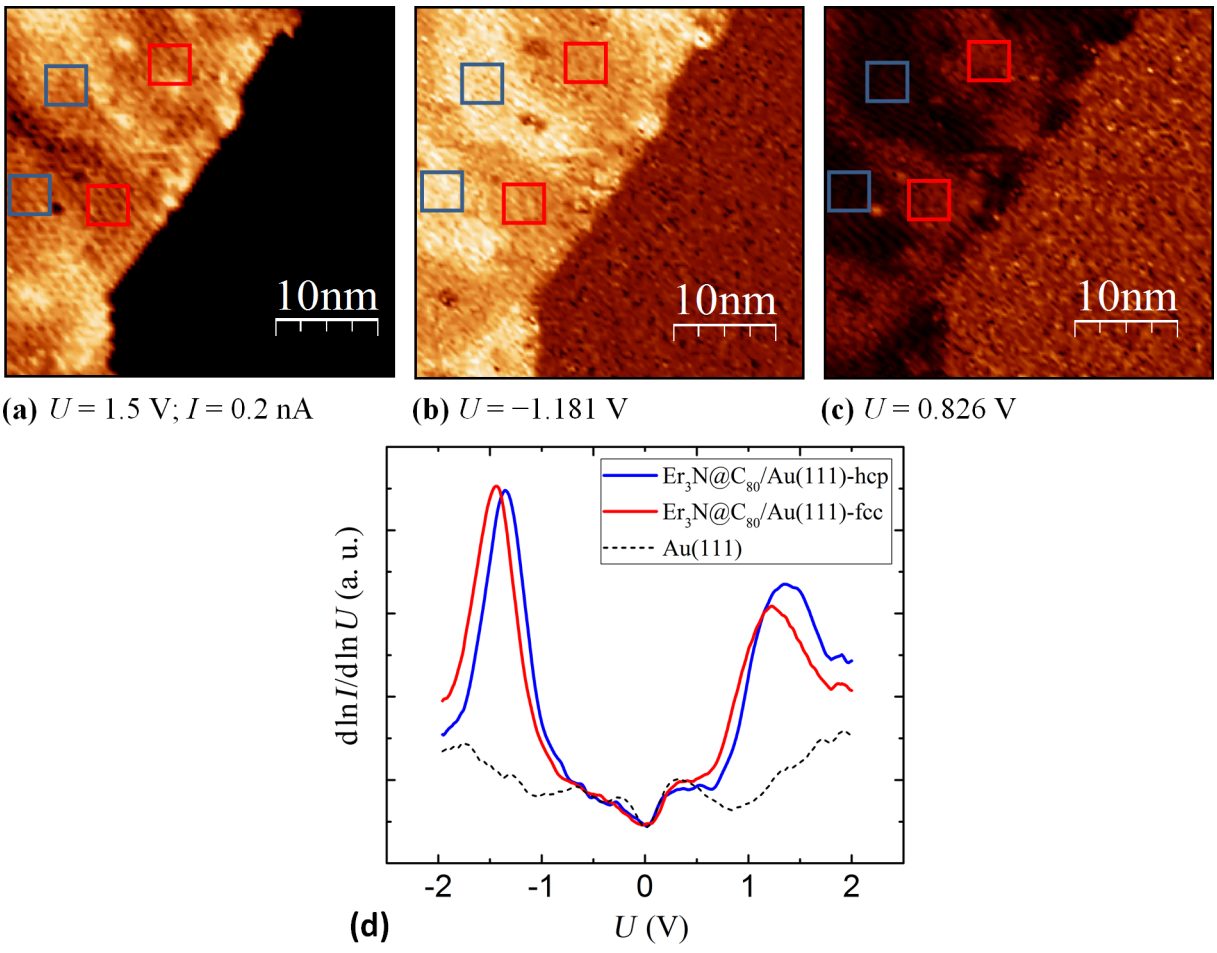

Figure 5: The left half of the constant-current-image (U = 1.5 V; I = 0.2 nA) (a) shows an $Er_3N@C_{80}$-monolayer and the pristine Au(111)-surface (right half). The corresponding dI/dU-maps at the voltages (considered as applied to the sample) of U = −1.181 V (b) and U = 0.826 V (c), reveal a bright dark pattern at the interface region accordingly to the interfacial reconstruction which is slightly visible in (a). The comparison of the dln$I$/dln$U$-spectra (d) (sample bias) taken at the highlighted (red respectively blue squares) areas in (a), (b) and (c), illustrate the spatial difference of the electronic structure.

peaks relatively to each other. The features in the spectrum corresponding to the fcc regions (red) are positioned at lower energies relatively to E_F than those of the hcp related spectrum (blue). The rigid downward shift of the molecular derived states at the fcc adsorption sites could be assigned to a more pronounced pillow effect [24-26]. The influence of the interface dipole which appears stronger in the fcc regions led to a further reduction of the Au(111)-work-function accompanied by a reduction of the electron injection barrier. Furthermore, fcc-spectrums LUMO derived peak obviously exhibit a more pronounced broadening. Thus, a stronger adsorbate-substrate-interaction of the fullerenes on the fcc adsorption sites is suggested, leading to a higher degree of hybridization. This proposal could be consistent with a weaker bond of the Au-electrons in the fcc regions than that in hcp regions [27,28].

There is evidence that due to adsorption at fcc sites the $Er_3N@C_{80}$/Au(111) systems energy gain is the highest in comparison to the other possibilities. This interpretation is also consistent with the observed enlargement of fcc terminated region. Nevertheless, the energy gained by rearranging the interface Au-atoms in fcc termination is not high enough to entirely lift the reconstruction, i.e., the molecule-induced effect is competing with the energy gained by the typical contraction of the first atomic layer of the Au(111) surface (E = 20 meV/Au-atom [22]). It is conceivable that the observed $Er_3N@C_{80}$-monolayer on Au(111) did not reach its global energetically minimum and a change of the interfacial reconstruction pattern could occur in time.

Conclusion

In the presented STM/STS-study, the respectively observed adsorption behavior of $Er_3N@C_{80}$ on W(110) and Au(111) is found to differ significantly from each other. On W(110) the endohedral fullerenes exhibits a surprisingly strong bond to the surface which inhibits monolayer formation via annealing in the analyzed temperature range ($T_{max} \approx 670$ K). On the contrary to W(110), monolayer height molecule islands of hcp structure were formed on Au(111). Those monolayers possess two distinguishable orientations on the Au(111)-surface. Beside the known in-phase (4 × 4) superstructure an out-of-phase alignment (4 × 4)R30° has been observed. A change of the Au(111)-reconstruction initiated by the presence of the fullerenes indicates a energetically favored adsorption on fcc terminated Au(111) interface sites. The obtained STS data reveals a HDS-LDS-gap of about 2.6 eV and spatial differences in the energetic location of the peaks as well as of the LDS-peaks broadening on the monolayer. These results are consistent to our STM data, since the pattern of the found variations correlates with the modified reconstruction pattern and the spectra taken at adsorption sites of Au(111)-fcc termination are affected by means of an enhanced broadening of the LDS-peak and a shift of 0.1 eV towards lower energies. The obtained adsorption properties on Au(111) are namely the sufficiently high mobility to form island, the ability to modify the herringbone reconstruction and the hybridization of the molecular electronic states most probably accompanied with charge transfer. Therefore the bonding character is conjectured to exceed the strength of van der Waals interaction.

Acknowledgements

This work has been supported by the Deutsche Forschungsgemeinschaft through the Research Unit 1154 (Grant HE3439/10). Furthermore, this project has received funding from the European Research Council (ERC) under the European Union's Horizon 2020 research and innovation programme (grant agreement No 647276 – MARS – ERC-2014-CoG and grant agreement No 648295 – GraM3 – ERC-2014-CoG).

References

1. Kroto, H. R.; Heath, J. R.; O'Brien, S. C.; Curl, R. F.; Smalley, R. E. *Nature* **1985,** *318,* 162–163. doi:10.1038/318162a0
2. Heath, J. R.; O'Brien, S. C.; Zhang, Q.; Liu, Y.; Curl, R. F.; Tittel, F. K.; Smalley, R. E. *J. Am. Chem. Soc.* **1985,** *107,* 7779–7780. doi:10.1021/ja00311a102
3. Stevenson, S.; Rice, G.; Glass, T.; Harich, K.; Cromer, F.; Jordan, M. R.; Craft, J.; Hadju, E.; Bible, R.; Olmstead, M. M.; Maitra, K.; Fisher, A. J.; Balch, A. L.; Dorn, H. C. *Nature* **1999,** *401,* 55–57. doi:10.1038/43415
4. Popov, A. A.; Yang, S.; Dunsh, L. *Chem. Rev.* **2013,** *113,* 5989–6113. doi:10.1021/cr300297r
5. Westerström, R.; Dreiser, J.; Piamonteze, C.; Muntwiler, M.; Weyeneth, S.; Brune, H.; Rusponi, S.; Nolting, F.; Popov, A.; Yang, S.; Dunsch, L.; Greber, T. *J. Am. Chem. Soc.* **2012,** *134,* 9840–9843. doi:10.1021/ja301044p
6. Huang, T.; Zhao, J.; Feng, M.; Popov, A. A.; Yang, S.; Dunsch, L.; Petek, H. *Nano Lett.* **2011,** *11,* 5327–5332. doi:10.1021/nl2028409
7. Benjamin, S. C.; Ardavan, A.; Briggs, G. A. D.; Britz, D. A.; Gunlycke, D.; Jefferson, J.; Jones, M. A. G.; Leigh, D. F.; Lovett, B. W.; Khlobystove, A. N.; Lyon, S. A.; Morton, J. J. L.; Porfyrakis, K.; Sambrook, M. R.; Tyryshkin, A. M. *J. Phys.: Condens. Matter* **2006,** *18,* S867. doi:10.1088/0953-8984/18/21/S12
8. Jones, M. A. G.; Taylor, R. A.; Ardavan, A.; Porfyrakis, K.; Briggs, G. A. D. *Chem. Phys. Lett.* **2006,** *428,* 303–306. doi:10.1016/j.cplett.2006.06.094
9. Jones, M. A. G.; Morton, J. J. L.; Taylor, R. A.; Ardavan, A.; Briggs, G. A. D. *Phys. Status Solidi B* **2006,** *243,* 3037–3041. doi:10.1002/pssb.200669162
10. Bode, M.; Krause, S.; Berbli-Bautista, L.; Heinze, S.; Wiesendanger, R. *Surf. Sci.* **2007,** *601,* 3308–3314. doi:10.1016/j.susc.2007.06.017
11. Leigh, D. F.; Nörenberg, C.; Cattaneo, D.; Owen, J. H. G.; Porfyrakis, K.; Li Bassi, A.; Ardavan, A.; Briggs, G. A. D. *Surf. Sci.* **2007,** *601,* 2750–2755. doi:10.1016/j.susc.2006.12.035
12. Nörenberg, C.; Leigh, D. F.; Cattaneo, D.; Porfyrakis, K.; Li Bassi, A.; Casari, C. S.; Passoni, M.; Owen, J. H. G.; Briggs, G. A. D. *J. Phys.: Conf. Ser.* **2008,** *100,* 052080. doi:10.1088/1742-6596/100/5/052080

13. Horcas, I.; Fernández, R.; Gómez-Rodríguez, J. M.; Colchero, J.; Gómez-Herrero, J.; Baro, A. M. *Rev. Sci. Instrum.* **2007,** *78,* 013705. doi:10.1063/1.2432410
14. Gardener, J. A.; Briggs, G. A. D.; Castell, M. R. *Phys. Rev. B* **2009,** *80,* 235434. doi:10.1103/PhysRevB.80.235434
15. Hanke, F.; Björk, J. *Phys. Rev. B* **2013,** *87,* 235422. doi:10.1103/PhysRevB.87.235422
16. Altman, E. I.; Colton, R. J. *Surf. Sci.* **1993,** *295,* 13–33. doi:10.1016/0039-6028(93)90181-I
17. Altman, E. I.; Colton, R. J. *J. Vac. Sci. Technol., B* **1994,** *12,* 1906. doi:10.1116/1.587667
18. Barth, J. V.; Brune, H.; Ertl, G.; Behm, R. J. *Phys. Rev. B* **1990,** *42,* 9307. doi:10.1103/PhysRevB.42.9307
19. Gimzewski, J. K.; Modesti, S.; Gerber, C.; Schlittler, R. R. *Chem. Phys. Lett.* **1993,** *213,* 401–406. doi:10.1016/0009-2614(93)85153-F
20. Zhang, X.; Yin, F.; Palmer, R. E.; Guo, Q. *Surf. Sci.* **2008,** *602,* 885–892. doi:10.1016/j.susc.2007.12.036
21. Fujita, D.; Yakabe, T.; Nejoh, H.; Sato, T.; Iwatsuki, M. *Surf. Sci.* **1996,** *366,* 93–98. doi:10.1016/0039-6028(96)00786-8
22. Wang, Y.; Hush, N. S.; Reimers, J. R. *Phys. Rev. B* **2007,** *75,* 233416. doi:10.1103/PhysRevB.75.233416
23. Haiss, W.; Lackey, O.; Sass, J. K.; Besocke, K. H. *J. Chem. Phys.* **1991,** *95,* 2193. doi:10.1063/1.460967
24. Ishii, H.; Sugiyama, K.; Ito, E.; Seki, K. *Adv. Mater.* **1999,** *11,* 605–625. doi:10.1002/(SICI)1521-4095(199906)11:8<605::AID-ADMA605>3.0.CO;2-Q
25. Kahn, A.; Koch, N.; Gao, W. *J. Polym. Sci., Part B: Polym. Phys.* **2003,** *41,* 2529–2548. doi:10.1002/polb.10642
26. Crispin, X.; Geskin, V.; Crispin, A.; Cornil, A.; Lazzaroni, R.; Salaneck, W. R.; Brédas, J.-L. *J. Am. Chem. Soc.* **2002,** *124,* 8131–8141. doi:10.1021/ja025673r
27. Bürgi, L.; Brune, H.; Kern, K. *Phys. Rev. Lett.* **2002,** *89,* 176801. doi:10.1103/PhysRevLett.89.176801
28. Chen, W.; Madhavan, V.; Jamneala, T.; Crommie, M. F. *Phys. Rev. Lett.* **1998,** *80,* 1469–1472. doi:10.1103/physrevlett.80.1469

License and Terms

BEILSTEIN JOURNAL OF NANOTECHNOLOGY

Synthesis, spectroscopic characterization and thermogravimetric analysis of two series of substituted (metallo)tetraphenylporphyrins

Rasha K. Al-Shewiki[1], Carola Mende[1], Roy Buschbeck[1], Pablo F. Siles[2,3], Oliver G. Schmidt[2,3], Tobias Rüffer[*1] and Heinrich Lang[1]

Full Research Paper

Open Access

Address:
[1]Inorganic Chemistry, Institute of Chemistry, Faculty of Natural Sciences, TU Chemnitz, 09107 Chemnitz, Germany, [2]Material Systems for Nanoelectronics, TU Chemnitz, 09107 Chemnitz, Germany and [3]Institute for Integrative Nanosciences, IFW Dresden, Helmholtzstrasse 20, 01069 Dresden, Germany

Email:
Tobias Rüffer[*] - tobias.rueffer@chemie.tu-chemnitz.de

* Corresponding author

Keywords:
electrospray ionization mass spectrometry; IR spectroscopy; metalloporphyrin; porphyrin; thermogravimetry; UV–vis spectroscopy

Beilstein J. Nanotechnol. **2017,** *8,* 1191–1204.
doi:10.3762/bjnano.8.121

Received: 24 February 2017
Accepted: 11 May 2017
Published: 02 June 2017

This article is part of the Thematic Series "Towards molecular spintronics".

Guest Editor: G. Salvan

Abstract

Subsequent treatment of $H_2TPP(CO_2H)_4$ (tetra(*p*-carboxylic acid phenyl)porphyrin, **1**) with an excess of oxalyl chloride and HNR_2 afforded $H_2TPP(C(O)NR_2)_4$ (R = Me, **2**; iPr, **3**) with yields exceeding 80%. The porphyrins **2** and **3** could be converted to the corresponding metalloporphyrins $MTPP(C(O)NR_2)_4$ (R = Me/iPr for M = Zn (**2a**, **3a**); Cu (**2b**, **3b**); Ni (**2c**, **3c**); Co (**2d**, **3d**)) by the addition of 3 equiv of anhydrous MCl_2 (M = Zn, Cu, Ni, Co) to dimethylformamide solutions of **2** and **3** at elevated temperatures. Metalloporphyrins **2a**–**d** and **3a**–**d** were obtained in yields exceeding 60% and have been, as well as **2** and **3**, characterized by elemental analysis, electrospray ionization mass spectrometry (ESIMS) and IR and UV–vis spectroscopy. Porphyrins **2**, **2a**–**d** and **3**, **3a**–**d** are not suitable for organic molecular beam deposition (OMBD), which is attributed to their comparatively low thermal stability as determined by thermogravimetric analysis (TG) of selected representatives.

Introduction

Over the last decades metalloporphyrins have been studied in great detail as they exhibit a high chemical and thermal stability, are aromatic and possess distinctive electrochemical and photophysical properties [1-4]. For example, access to the first organic spin valves, which were based on tris(8-hydroxyquinolinato)aluminium (Alq_3) sandwiched between $La_{2/3}Sr_{1/3}MnO_3$ and cobalt electrodes, was reported more than a decade ago [5]. This finding motivated the development of

further novel devices as, for example, spin-OFETs (organic field effect transistors) [4]. The nature of the molecules integrated into spintronic devices ranges from purely diamagnetic molecules to individual single molecule magnets (SMMs) [4]. Among such molecules metalloporphyrins are very promising in terms of diverse applications [4]. Recently, we reported on the deposition of thin films of porphyrins of the type $H_2TPP(OH)_4$ (tetra(*p*-hydroxyphenyl)porphyrin) [6,7] and $MTPP(OMe)_4/H_2TPP(OMe)_4$ (tetra(*p*-methoxyphenyl)porphyrin) (M = Cu [8,9], Ni [9]), cf. Figure 1.

The properties of the metalloporphyrins are governed by the (transition) metal ions and the exocyclic moieties on the individual pyrrole fragments and/or on the meso positions. Comparative studies of the accessibility and characterization of metalloporphyrins are scarcely reported in literature [1-3,10-12], which limits, for example, the possibility to select a certain metalloporphyrin with respect to a desired property by a knowledge-based approach. Along with a preliminary work of us, we noticed that "[…]the electrical analysis and the understanding of the underlying transport mechanism become important for future implementation of porphyrin-based (spintronic) devices.[…]" [8]. It was thus desired to have access to metalloporphyrins of which the central metal ion varies on the one hand, while on the other hand these metalloporphyrins should be sterically more demanding to vary the film morphology compared to our original report [8]. In order to support the idea that different central metals as well as sterically more demanding substituents will vary film morphologies one can, for example, inspect the results of the single-crystal crystallographic characterization even of the compounds displayed in Figure 1. It is instructive to notice, that for $ZnTPP(OMe)_4$ [13] the formation of 2D layers is observed in which symmetry-related molecules with planar porphyrin cores interact with each other by, for example, formation of intermolecular $Zn^{II}\cdots O$ contacts. Further intermolecular interactions refer to those that were described in detail by, for example, Goldberg et al. [14] or by us [15]. In contrast, saddle-shape distorted molecules of $CuTPP(OMe)_4$ are described as interacting via C–H···π and C–H···O bonds to give a 3D supramolecular motif [16]. Furthermore, if one substitutes the terminal methyl substituents of $H_2TPP(OMe)_4$ (Figure 1) by sterically more demanding substituents as reported for $H_2TPP(OR)_4$ (OR = *p*-(*N*-*n*-butylcarbamoyl)methoxyphenyl) [17] one decreases the density to the materials to ρ = 1.036 g/cm^3 compared to ρ = 1.491 g/cm^3 for $ZnTPP(OMe)_4$ [13] or ρ = 1.398 g/cm^3 for $CuTPP(OMe)_4$ [16].

Thus, we report herein on two novel series of (metallo)porphyrins of the type $H_2/MTPP(C(O)N(R)_2)_4$ (R = Me, with $H_2TPP(C(O)NMe_2)_4$ (**2**) and $MTPP(C(O)N(iPr)_2)_4$ (M = Zn (**2a**), Cu (**2b**), Ni (**2c**), Co (**2d**); R = iPr, with $H_2TPP(C(O)N(iPr)_2)_4$ (3) and $MTPP(C(O)N(iPr)_2)_4$ (M = Zn (**3a**), Cu (**3b**), Ni (**3c**), Co (**3d**)). The aim of this report is not only to describe their synthesis and characterization (ESIMS, FTIR, NMR, UV–vis) but also to study to which extend these new (metallo)porphyrins are suitable to be deposited in form of thin films by OMBD. Therefore, the thermal stabilities derived from TG studies of selected representatives of **2**/**2a**–**d** and **3**/**3a**–**d** in comparison with that of $H_2TPP(OH)_4$ [6,7] will be discussed together with the results of OMBD studies.

Results and Discussion

Synthesis

Porphyrins **2** and **3** were synthesized as shown in Scheme 1 according to a procedure reported by Gradl et al. [18]. Literature-known $H_2TPP(CO_2H)_4$ (**1**) was treated first with an excess of oxalyl chloride in dichloromethane in the presence of dimethylformamide. As we used a larger amount of dimethylformamide as indicated in [18], the yields of **2** and **3** could be increased significantly. This is attributed to the solubility of **1** in dimethylformamide. The addition of a large excess of the mild chlorinating agent oxalyl chloride converted **1** to $H_2TPP(C(O)Cl)_4$

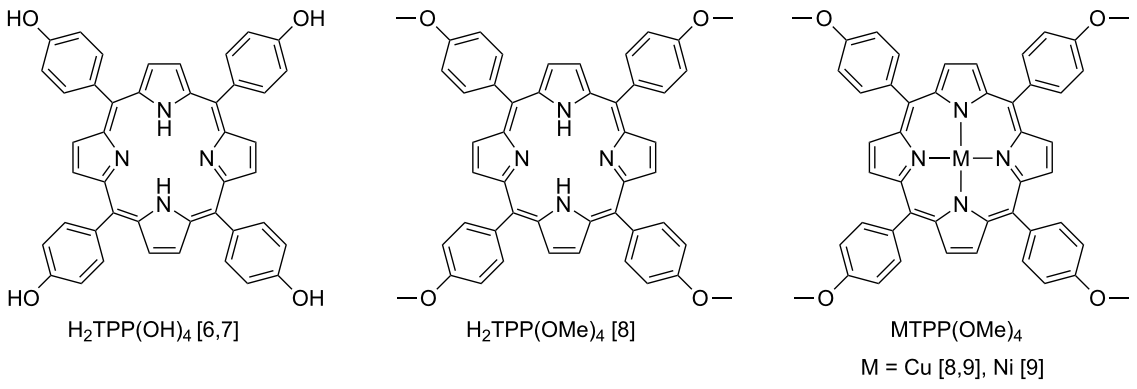

Figure 1: Chemical structures of porphyrins and metalloporphyrins successfully deposited by organic molecular beam deposition.

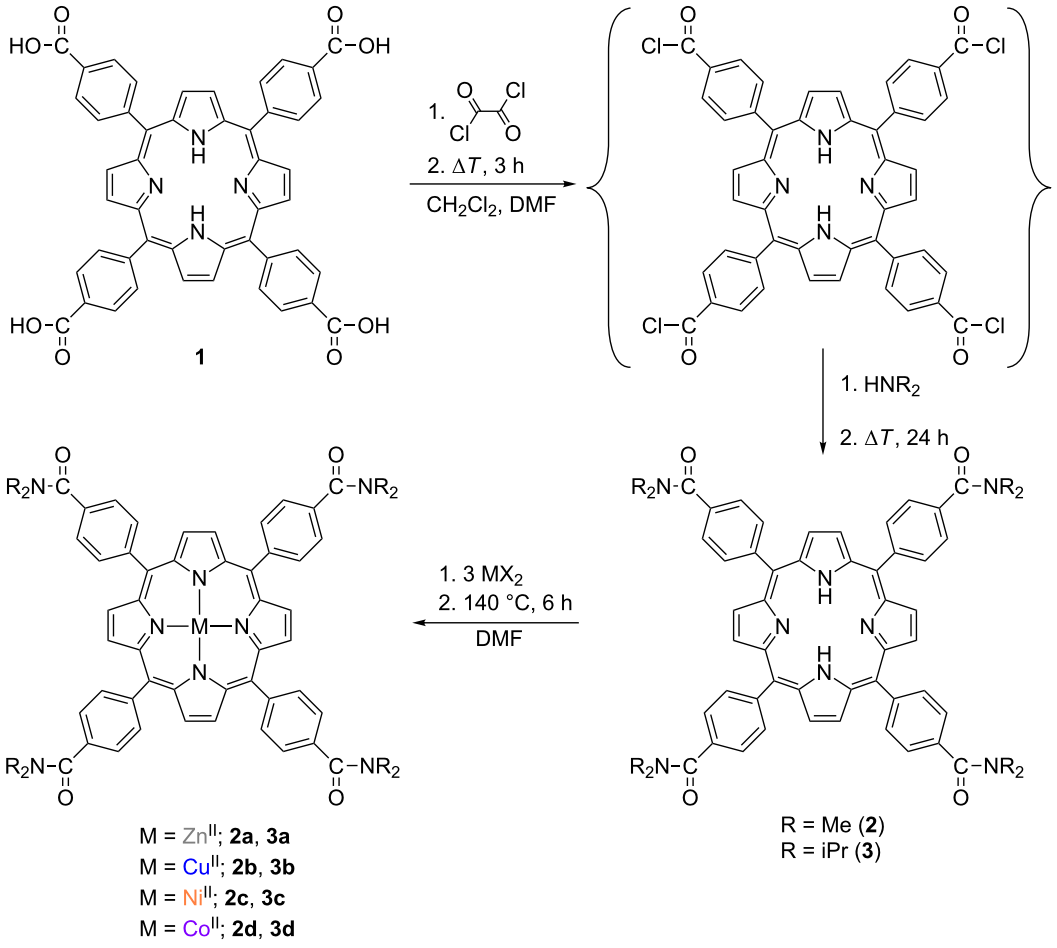

Scheme 1: Synthetic methodology to prepare (metallo)porphyrins **2, 2a–d** and **3, 3a–d**.

(Scheme 1) which further reacted with the secondary amines $HNMe_2$ and $HN(iPr)_2$ to give **2** ($H_2TPP(C(O)NMe_2)_4$) and **3** ($H_2TPP(C(O)N(iPr)_2)_4$). The molar excess of oxalyl chloride compared to **1** should be above 25:1, as otherwise **1** cannot be fully converted to $H_2TPP(C(O)Cl)_4$. However, the use of thionyl chloride to convert **1** to $H_2TPP(C(O)Cl)_4$ is accompanied by chlorination of the β-pyrrolic positions. After formation of $H_2TPP(C(O)Cl)_4$ all volatiles must be removed in vacuum in order to avoid, for example, unwanted reactions upon the addition of $HNMe_2$ and $HN(iPr)_2$. Appropriate work-up, gave **2** and **3** in yields exceeding 80% without any column-chromatographic purification (cf. Experimental section).

The metalation reactions performed in this study correspond to the well-known "dimethylformamide method" (M^{II} = Zn, Cu, Ni, Co), cf. Scheme 1 and [19]. In agreement with details reported for the dimethylformamide method, "[…]best results have been obtained with anhydrous metal chlorides[…]" [19], although the reaction temperatures should be kept at 140 °C. According to [19], complete metalation needs the subsequent addition of an excess of the metal chlorides. Hence, we decided to use initially an excess of the metal chlorides. The metalloporphyrins **2a–d** and **3a–d** (Scheme 1) have been obtained in yields exceeding 60%. No purification by column chromatography was required although in case of **2d**, **3a** and **3d** the metalloporphyrins were re-precipitated for purification purposes (cf. Experimental section).

The purity of **2, 2a–d** and **3, 3a–d** was determined by CHN elemental analysis (EA), although this method has limits. For example, it is difficult to recognize by EA the presence of traces of impurities below ca. 0.5%. Furthermore, the measurement conditions of an EA may influence results as recently demonstrated for a series of octachlorometallophthalocyanines of the type $MPcCl_8$ (M^{II} = Cu, Ni, Co, Fe, Mn) [20]. However, for the herein reported porphyrins **2** and **3** and their corresponding metalloporphyrins **2a–d** and **3a–d** the CHN contents deviate by at most ±0.5%. Since **2**/**3** and **2a–d**/**3a–d** are well soluble in sol-

vents such as CH_2Cl_2, $CHCl_3$, MeCN, DMSO, DMF it is possible to follow certain "criteria of purity" established by White, Bachmann and Burnham [21]. Thus, analytical amounts of these (metallo)porphyrins were chromatographed by thin layer chromatography (TLC) on alumina by using $CHCl_3$/n-hexane mixtures (ratio 1:1, v/v) as eluent, showing that they were formed in high purity.

Furthermore, ^{1}H NMR studies allowed us to monitor the progress of the metalation reactions of **2** and **3**, even for the paramagnetic metalloporphyrins **2b**,**d** and **3b**,**d**. For example, the complete metalations of the free-base porphyrins **2** and **3** are indicated by the disappearance of their N–*H* ^{1}H NMR resonances.

Electrospray ionization mass spectrometry

High-resolution mass spectrometry (HRMS) studies enable one to verify the successful formation of **2**/**3** and of **2a–d**/**3a–d**. The ESIMS measurements in positive-ionization mode were performed under identical conditions, including the use of MeCN/CH_2Cl_2 solutions of the respective (metallo)porphyrin. The ESIMS spectra and the respective isotopic patterns of the ion peaks in form of $[M]^+$, $[M + H]^+$, $[M + Na]^+$ or $[M + K]^+$ agree to the calculated ones (cf. the ESIMS spectra in Supporting Information File 1). In agreement with Buchler [19] and Budzikiewicz [22] the mass spectrometric measurements served well to identify the type of the incorporated transition metal since the ion peaks of $[M]^+$ and/or $[M + H]^+$ are the ones with the highest intensity. The observation of $[M + Na]^+$ as well as $[M + K]^+$ ions and of cations of low *m*/*z* values, for example $[393]^+$ (observed in the ESIMS spectra of **2c**,**d** and **3c**,**d**), is due to contaminants that typically appear in such measurements as described in the literature [23,24]. For **2b**,**c**, **3** and **3a–c** double charged ion peaks are visible, clearly identifiable by an isotopic peak distance of $m/z = 0.5$. This is a common occurrence in ESI measurements when a higher concentration of the analyte is present [23].

IR studies

Severe difficulties were noticed when measuring KBr pellets of **2**/**3** and **2a–d**/**3a–d**, as described by Alben [25]. These difficiculties are due to, for example, the optical inhomogeneity of the pellets. In order to avoid them, and as suggested by Alben [25], all (metallo)poprhyrins were intensively grinded to a fine flour before further grinding with KBr was done. It must be emphasized that due to the recommended intense and thus time-consuming grinding of the pure (polycrystalline) materials the IR spectra reveal the presence of water, likely due to the hygroscopic nature of the compounds and/or of KBr. In Figure 2 (**2**, **2a–d**) and Figure 3 (**3**, **3a–d**) the spectral region between 500 and 1800 cm^{-1} is displayed. Shaded areas within individual IR spectra displayed in Figure 2 and Figure 3 belong to related absorptions and are numbered. The wavenumbers of these absorptions are summarized in Table 1 for **2**/**2a–d** and **3**/**3a–d**. Full IR spectra (KBr) of **2**/**3** and of **2a–d**/**3a–d** are given in Supporting Information File 1. Furthermore, Supporting Information File 1 shows the IR spectra of **2**/**3** and of **2a–d**/**3a–d** as obtained by FTIR measurements with a Nicolet iS10 spectrometer (ATR attachment, ZnSe crystal) for comparison.

For the porphyrins **2** and **3** three different N–H vibrations at 3310–3326 cm^{-1}, 975–990 cm^{-1} and 675–700 cm^{-1} are expected according to [25]. The one observed at 3317 cm^{-1} for both **2** and **3** (Supporting Information File 1) fits well into the expected range. The vibrations no. 5 and no. 13 for **2** (966 and 732 cm^{-1}) and **3** (968 and 737 cm^{-1}), cf. Figure 2 and Figure 3 and Table 1, are attributed to the other two N–H vibrations. They deviate to some extend from the expected ranges, see above, but the corresponding metalloporphyrins do not show related vibrations (Figure 2 and Figure 3).

The spectral range from 3000 to 2800 cm^{-1} is governed by ν_{as}(C–H) and ν_s(C–H) absorptions of the aliphatic substituents R of the $-C(O)NR_2$ groups of both **2**/**2a–d** and **3**/**3a–d** (Supporting Information File 1). According to [26], CH_3 groups can be identified by one ν_{as}(C–H) absorption at ca. 2950 cm^{-1} and up to two ν_s(C–H) absorptions at lower spatial frequencies of ca. 2800 cm^{-1}. The number of CH_3 groups is eight for **2**/**2a–d**, that of **3**/**3a–d** is 16. This difference is nicely reflected in the intensities and shapes of the ν_{as}(C–H) and ν_s(C–H) absorptions. Among **2**/**2a–d** only for **2a** and **2c** all three possible absorptions could be observed, while further members exhibit only one ν_s(C–H) and the ν_{as}(C–H) vibration (Supporting Information File 1). For **3**/**3a–d** the ν_{as}(C–H) vibration is always the most intensive one at 2970 ± 1 cm^{-1}, followed by a less intensive first ν_s(C–H) absorption (2932 ± 1 cm^{-1}) and a third even less intensive ν_s(C–H) band (2874 ± 4 cm^{-1}). Due to these different spectral features it is possible to differentiate between a type **2**/**2a–d** or **3**/**3a–d** (metallo)porphyrin.

For the porphyrin cores and the aromatic C_6H_4 moieties, respectively, ν(C⋯H) and ν(C=H) vibrations are expected above 3000 cm^{-1}. However, these vibrations as well as combinations of γ(C⋯H) vibrations between 2000 and 1600 cm^{-1}, could not be identified unambiguously or were too weak. Likely, this is due to the substitution of the aromatic C_6H_4 rings, decreasing the intensities of these vibrations [26].

The presence of CH_3 groups in a compound is indicated in the IR spectra in general by one δ_{as}(C–H) (ca. 1465 cm^{-1}) vibration and at least one δ_s(C–H) (ca. 1380 cm^{-1}) vibration [26]. Furthermore, a single δ_s(C–H) absorption verifies that the CH_3

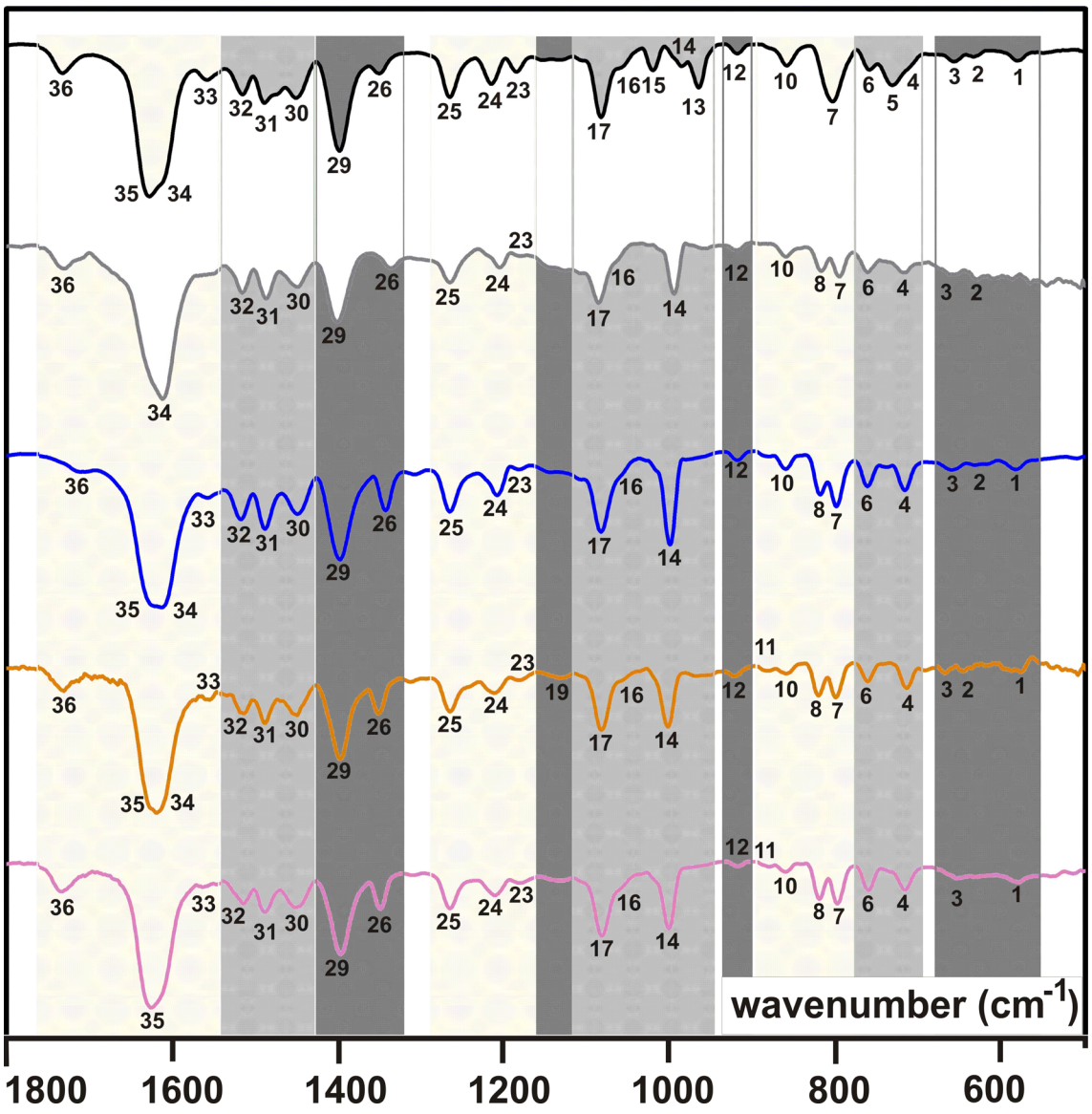

Figure 2: IR spectra (KBr) in the range of 500–1800 cm^{-1} for $H_2TPP(CONMe_2)_4$ (**2**, top) and $MTPP(CONMe_2)_4$ (M^{II} = Zn, **2a** (gray); Cu, **2b** (blue); Ni, **2c** (orange); Co, **2d** (purple)).

group belongs to an aliphatic chain that is not branched, or that the Me group is terminal as in the $–NMe_2$ entities of **2/2a–d**. For branched alkyl chains the δ_s(C–H) vibration splits into two [26]. Thus, the absorptions no. 30 and no. 26 of **2/2a–d** (1450 ± 2 cm^{-1} and 1344 ± 7 cm^{-1}) are attributed to the δ_{as}(C–H) and δ_s(C–H) vibrations of the terminal CH_3 groups (Figure 2 and Table 1). Due to a larger number of CH_3 groups in **3/3a–d** compared to **2/2a–d** the ν_{as}(C–H), ν_s(C–H), δ_{as}(C–H) and δ_s(C–H) absorptions of **3/3a–d** are more intensive compared to **2/2a–d**. For example, the absorption no. 30 of **3/3a–d** (δ_{as}(C–H), 1442 ± 2 cm^{-1}) is significantly more intensive compared to **2/2a–d** (Figure 2, Figure 3 and Table 1). As expected, for **3/3a–d** two δ_s(C–H) vibrations are observed, see no. 28 (1379 ± 1 cm^{-1}) and no. 27 (1371 ± 1 cm^{-1}) in Figure 3 and Table 1. The presence of iPr groups in **3/3a–d** was recognized further by their skeletal vibrations at 1158 ± 3 cm^{-1} (no. 23), shouldered at 1136 ± 2 cm^{-1} (no. 22) [21], while for **2/2a–d** only a weak absorption at 1183 ± 3 cm^{-1}, denoted as no. 23, is observed.

For para-substituted C_6H_4 aromatic units one γ(C⋯H) absorption between 800 and 860 cm^{-1} is expected [27], which is one of absorptions no. 7, 8 or 10 of **2/2a–d** and **3/3a–d,** (Figure 2, Figure 3 and Table 1). A more precise assignment is not possible, because C⋯H vibrations of the β-pyrrolic hydrogens are expected to lead to absorptions at 772–805 cm^{-1} [27].

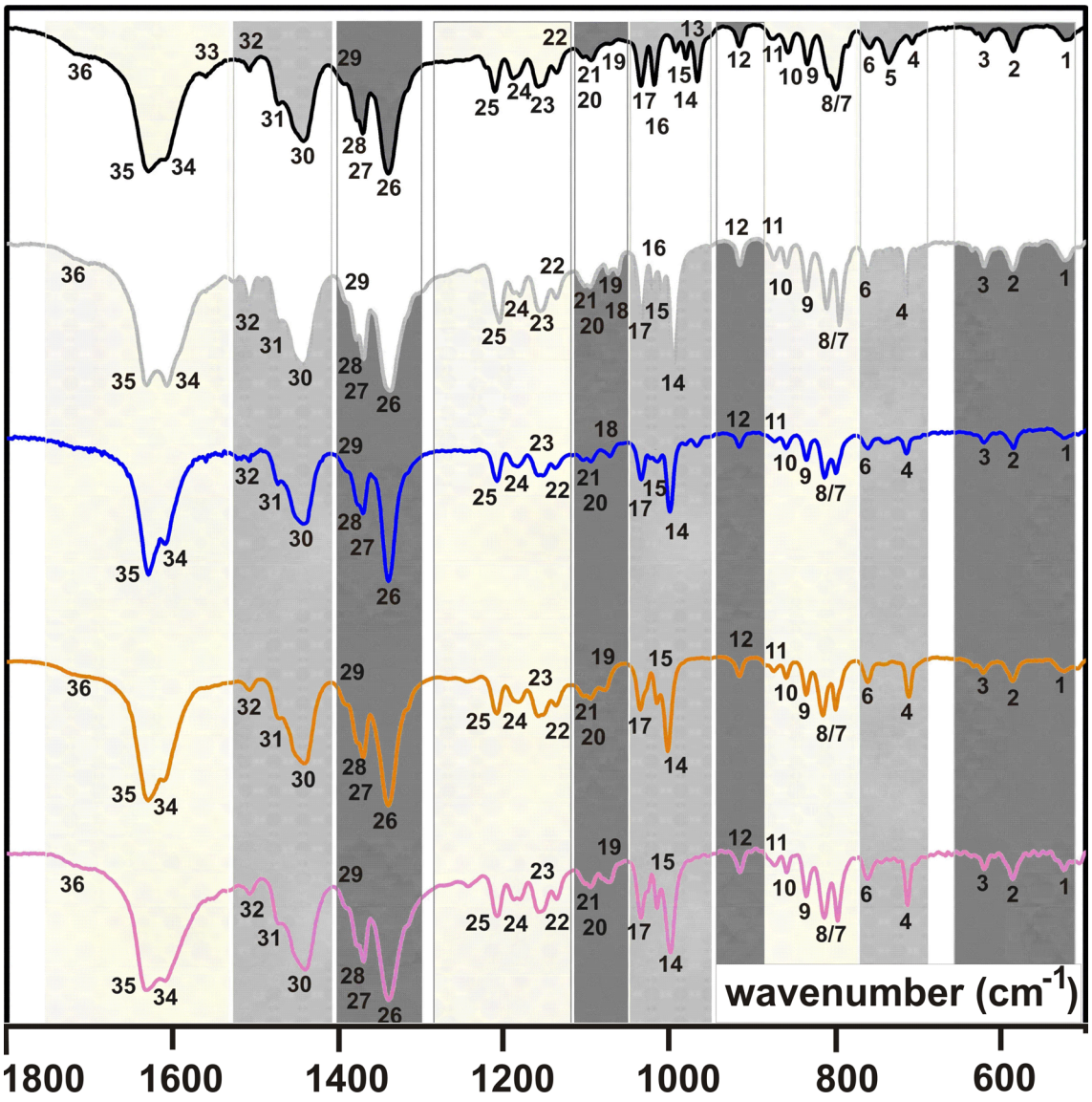

Figure 3: IR spectra (KBr) in the range of 500–1800 cm^{-1} for $H_2TPP(CON(iPr)_2)_4$ (**3**, top) and $MTPP(CON(iPr)_2)_4$ (M^{II} = Zn, **3a** (gray); Cu, **3b** (blue); Ni, **3c** (orange); Co, **3d** (purple)).

Further β-pyrrolic C⋯H vibrations are expected at 1045–1065 cm^{-1} [13], and thus no. 17 of **2/2a–d** and **3/3a–d** can be assigned to them (Figure 2, Figure 3 and Table 1).

The two strongest absorptions of **2/2a–d** and **3/3a–d** are due to ν(C⋯C) vibration of the aromatic moieties and ν(C=O) vibrations of the terminal $–C(O)NR_2$ groups [27]. The ν(C⋯C) vibrations are expected at ca. 1600 cm^{-1}, while the more intense ν(C=O) are observed between 1650 and 1690 cm^{-1} [27]. This allows for an assignment of no. 35 and no. 34 (Figure 2, Figure 3 and Table 1) to the former and the latter type of vibration, respectively. However, **2/2a–d** always exhibit one broad absorption band at ca. 1620 cm^{-1}, which hinders a more precise assignment. For **3/3a-d** this situation is different and these two absorption bands occur well resolved. Most likely, that difference can be attributed to the different substitution of the terminal $–C(O)NR_2$ groups.

UV–vis studies

The UV–vis absorption spectra of **2/2a–d** and **3/3a–d** were recorded in $CHCl_3$ solution in the spectral range of 230–700 nm. In order to avoid possible impact of the concentrations on λ_{abs} and ε, which was reported for (metallo)phthalocyanines [28], we performed concentration-dependent UV–vis measurements. According to [28] the nature (cofacial, face-to-face, tilted) and degree (dimer, oligomer, polymer) of mutual interactions

Table 1: Wavenumbers of numbered IR vibrations of **2**/**2a–d** and **3**/**3a–d** in the range from 500–1800 cm^{-1}.[a]

no.	H_2		Zn		Cu		Ni		Co	
	2	**3**	**2a**	**3a**	**2b**	**3b**	**2c**	**3c**	**2d**	**3d**
1	582	524	—	524	585	526	588	526	581	528
2	632	587	630	587	634	588	647	588	632	587
3	658	622	659	622	668	622	668	623	656	623
4	711	709	718	716	719	715	715	712	718	715
5	732	737	—	—	—	—	—	—	—	—
6	760	760	762	762	761	762	762	762	761	762
7	804	800	796	797	800	798	800	801	798	800
8	—	810	818	812	819	815	822	816	820	815
9	—	835	—	836	—	836	—	837	—	836
10	860	859	860	860	861	860	860	860	861	861
11	—	878	—	875	—	875	883	876	882	875
12	920	917	919	917	918	917	921	917	919	917
13	966	968	—	—	—	—	—	—	—	—
14	987	982	996	996	1000	1000	1003	1003	1002	1001
15	1021	994	—	1011	—	1016	—	1016	—	1017
16	1059	1019	1063	1021	1059	—	1055	—	1057	—
17	1084	1036	1086	1034	1083	1035	1083	1037	1082	1036
18	—	—	—	1063	—	1072	—	—	—	—
19	—	1073	—	1076	—	—	1030	1078	1134	1072
20	—	1096	—	1097	—	1095	—	1096	—	1096
21	—	1106	—	1105	—	1105	—	1106	—	1106
22	—	1137	—	1138	—	1138	—	1137	—	1138
23	1186	1160	1180	1156	1182	1158	1180	1161	1180	1160
24	1216	1190	1205	1181	1206	1190	1211	1183	1211	1186
25	1266	1212	1264	1206	1266	1209	1265	1209	1265	1209
26	1351	1340	1337	1339	1345	1340	1351	1340	1349	1339
27	—	1370	—	1370	—	1371	—	1370	—	1370
28	—	1378	—	1378	—	1378	—	1379	—	1379
29	1399	1395	1400	1390	1398	1391	1397	1393	1397	1392
30	1451	1442	1448	1443	1450	1441	1450	1441	1451	1440
31	1489	1473	1487	1472	1489	1472	1489	1472	1488	1473
32	1516	1508	1515	1507	1518	1506	1514	1507	1514	1508
33	1558	1561	—	—	1560	—	1556	—	1560	—
34	1609	1609	1612	1607	1608	1608	1619	1610	—	1609
35	1628	1630	—	1632	1622	1632	1626	1630	1625	1629
36	1732	1701	1730	1700	1711	—	1730	1710	1733	1699

[a]cf. Figure 2 and Figure 3.

between (metallo)phthalocyanine molecules might modify their optical absorption spectra [28]. However, the UV–vis studies of **2**/**2a–d** and **3**/**3a–d** with varying concentrations revealed marginal impact on λ_{abs} (max. ±1 nm) and ε (max. ±4%), see Supporting Information File 1. Larger deviations of ε are attributed to random errors due to, for example, uncertainties in diluting the sample solutions. The UV–vis spectra of **2**/**2a–d** and **3**/**3a–d** displaying the absorption spectral range from 280–700 nm are shown in Figure 4. For better comparison we select the spectrum of an individual (metallo)porphyrin in which the maximum of the absorption is closest to 1.5 (Supporting Information File 1). Inserts in Figure 4 correspond to the enlarged spectral range of 480–700 nm. Optical absorptions are numbered in relation to the wavelength, λ_{abs} and log ε values are summarized in Table 2.

Generally, absorption spectra of free-base porphyrins consist of characteristic absorption bands: The more intense Soret band (or *B* band) arising from $a_{1u}(\pi)\rightarrow e_g^*(\pi)$ transitions and two *Q* bands ($Q_x(0,0)$ and $Q_y(0,0)$ from $a_{2u}(\pi)\rightarrow e_g^*(\pi)$ transitions

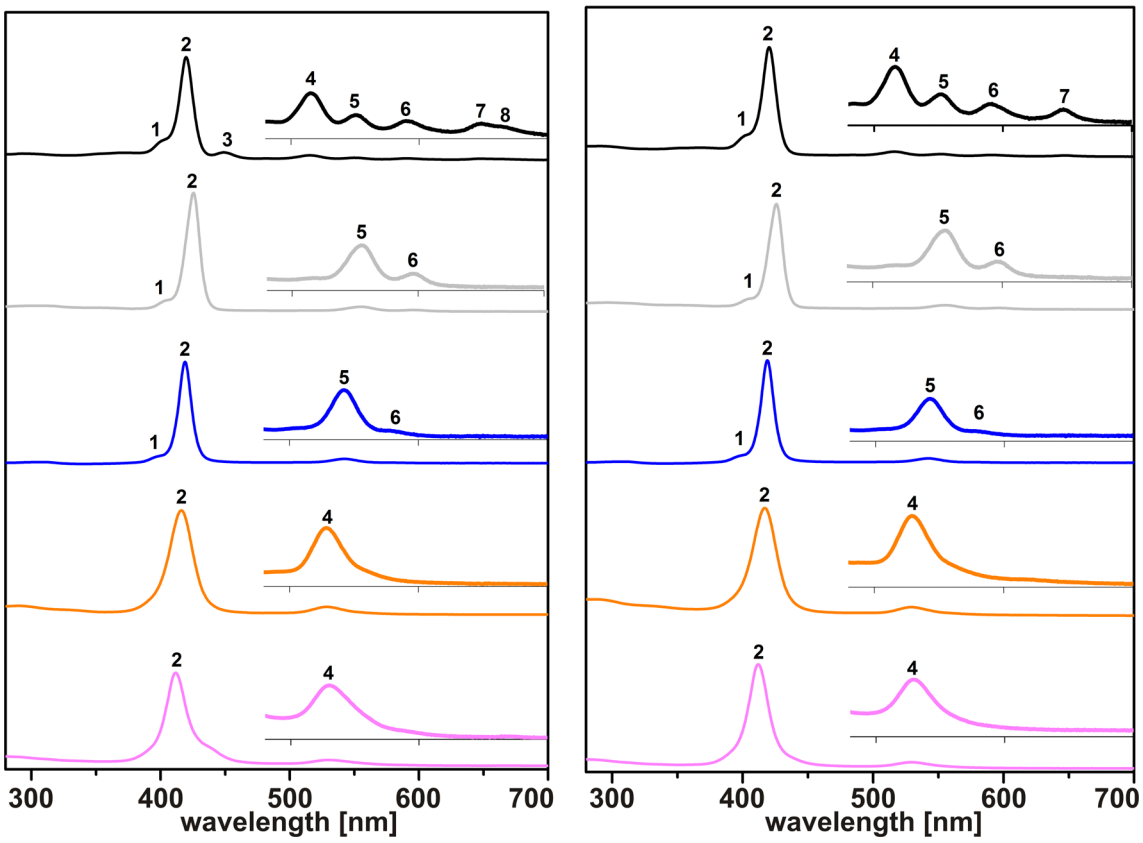

Figure 4: Left: UV–vis spectra ($CHCl_3$, 280–700 nm) of $H_2TPP(C(O)NMe_2)_4$ (**2**) and $MTPP(C(O)NMe_2)_4$ (M^{II} = Zn, **2a** (gray); Cu, **2b** (blue); Ni, **2c** (orange); Co, **2d** (purple)). Right: UV–vis spectra ($CHCl_3$, 280–700 nm) of $H_2TPP(C(O)N(iPr)_2)_4$ (**3**) and $MTPP(C(O)N(iPr)_2)_4$ (M^{II} = Zn, **3a** (gray); Cu, **3b** (blue); Ni, **3c** (orange); Co, **3d** (purple)).

Table 2: Wavelengths of UV–vis absorption bands of **2**/**2a–d** and **3**/**3a–d** in the range of 280–700 nm.[a]

compound	absorption band no.							
	1	2	3	4	5	6	7	8
	λ_{abs} (log ε)							
2	401 (4.95)	420 (5.64)	449 (4.74)	516 (4.35)	551 (4.08)	591 (3.96)	647 (3.93)	666 (3.93)
3	400 (4.80)	421 (5.49)	—	517 (4.17)	552 (3.91)	590 (3.74)	648 (3.58)	—
2a	403 (4.55)	426 (5.55)	—	—	555 (4.19)	596 (3.73)	—	—
3a	404 (4.33)	426 (5.29)	—	—	556 (3.93)	597 (3.53)	—	—
2b	396 (4.44)	419 (5.65)	—	—	542 (4.28)	578 (3.39)	—	—
3b	397 (4.58)	419 (5.74)	—	—	542 (4.37)	579 (3.43)	—	—
2c	—	416 (5.30)	—	528 (4.17)	—	—	—	—
3c	—	417 (5.32)	—	530 (4.23)	—	—	—	—
2d	—	412 (5.24)	442 (4.44)	530 (4.03)	—	—	—	—
3d	—	412 (5.47)	—	529 (4.25)	—	—	—	—

[a]cf. Figure 4

[29,30]. According to Goutermann the *B*(0,0) band appears between 380 and 420 nm ($\varepsilon > 10^5$ $M^{-1}\cdot cm^{-1}$) and is accompanied in case of well-resolved spectra by a blue-shifted (ca. 1250 cm^{-1}) *B*(1,0) band [29,30]. *Q*-band absorptions occur in the spectral region between 500 and 700 nm ($\varepsilon > 10^4$ $M^{-1}\cdot cm^{-1}$) [29,30]. The $Q_x(0,0)$ and $Q_y(0,0)$ bands of D_{2h}-symmetric porphyrins, separated by ca. 3000 cm^{-1}, might be observed inclusive a vibronic overtone absorption of each *Q* band, denoted as $Q_x(1,0)$ and $Q_y(1,0)$ [29,30]. For metalloporphyrins adapting D_{4h}-type symmetry, the four *Q* bands are observed to collapse into two *Q* bands, in some cases into only one [19,29]. The accompanying "[…]Soret band may remain in the usual range or shifted to higher or lower frequency.[…]", according to Buchler [19]. Furthermore, (metallo)porphyrins may show a weak *N* (ca. 325 nm) and *M* band (ca. 215 nm), often with an even weaker *L* band [29].

As expected, for **2** and **3** the intensive *B*(0,0) band appears at ca. 420 nm (no. 2 in Figure 4, Table 2) and is followed by four significantly weaker *Q* bands at ca. 516, 551, 591 and 647 nm (no. 4–7 in Figure 4, Table 2). The separation between absorption no. 4 and no. 6 as well as between no. 5 and no. 7 amounts to, respectively, 2394 cm^{-1} as well as 2684 cm^{-1} for **3**, in good agreement with the expected difference between the $Q_x(0,0)$ and $Q_y(0,0)$ band of free-base porphyrins (see below). The blue-shifted shoulder of the *B*(0,0) band at 401/400 nm (no. 1 in Figure 4, Table 2) corresponds to the *B*(1,0) band of **2** and **3**, confirmed by blue-shifts of 1128 and1247 cm^{-1} (see above). As described earlier, and due to symmetry reasons, for Zn^{II}- and Cu^{II}-containing **2a**/**3a** and **2b**/**3b**, two *Q* bands are observed, while Ni^{II}- and Co^{II}-containing **2c**/**3c** and **2d**/**3d** possess only one *Q* band (Figure 4). The difference in numbers of the *Q* bands could be caused by a higher molecular symmetry of **2c**/**3c** or **2d**/**3d** compared to **2a**/**3a** and **2b**/**3b**, but is most likely attributable to weak perturbations by the central metal according to Goutermann [29]. A comparison of the λ_{abs} values of both the *B*(0,0) and the *Q* band(s) along **2**/**2a**–**d** and **3**/**3a**–**d** reveals a red-shift along the series $Co^{II} < Ni^{II} < Cu^{II} < Zn^{II}$ (Figure 4 and Table 2). This observation is in agreement with observations summarized by Buchler [19] and Goutermann [29]. The same tendency has been observed more recently [11] and no significant differences of λ_{abs} values have been noticed [12], although the UV–vis spectra were recorded in both cases in $CHCl_3$.

Thermogravimetric studies

Part of our motivation to synthesize **2**/**2a**–**d** and **3**/**3a**–**d** originates from a number of cooperations with our partners in the DFG-supported research unit "Towards Molecular Spintronics" [6-9]. For example, (metallo)porphyrins were synthesized and deposited by OMBD for different kinds of physical thin-film studies [6-9]. In one of these contributions thin films of $CuTPP(OMe)_4$ (Figure 1) were investigated by current-sensing atomic force microscopy [8]. It was concluded that for the investigation of films with different morphologies and transport properties further (metallo)porphyrins should be studied, as outlined in the Introduction section [6-9].

However, we were not able to deposit thin films of **3**, **3b** and **3d** nor of **2**, **2c** and **2d** by means of OMBD. In more detail: OMBD parameters were initially chosen as reported in [8]. Thus, at 2×10^{-7} mbar a deposition rate of 5 Å/min was adjusted. In all investigated cases, deposition rates were not stable and constantly decreased over time. In order to maintain a stable deposition rate, the deposition temperatures were constantly increased from 300 to 350 °C in a Knudsen cell. After keeping the materials for ca. 20 min at these high temperatures, it was observed that the deposition rates dropped significantly. From this point onwards, it was not possible to perform any (further) deposition of the materials. In case of **3b** and **3d** the remaining material in the Knudsen cell was subjected to IR measurements (Supporting Information File 1) in comparison with measurements of the starting materials, showing that both metalloporphyrins decomposed during the OMBD studies.

In order to shine more light into the temperature stability we carried out TG studies for **3**, **3b**, **3d**, **2**, **2c** and **2d**. The TG traces are shown in Figure 5 together with the one of $H_2TPP(OH)_4$. In our earlier studies [6,7], $H_2TPP(OH)_4$ could be deposited successfully by applying OMBD parameters analogous the those described above. A comparison especially of the onset temperatures of the decomposition processes reveals that $H_2TPP(OH)_4$ is obviously significantly more thermally stable than the here reported (metallo)porphyrins. Because of this, OMBD of **2**/**2a**–**d** and **3**/**3a**–**d** is not possible and we are recently fabricating thin layers of these compounds by spin-coating [31].

Conclusion

Two series of metalloporphyrins $MTPP(C(O)NR_2)_4$ (M = Co^{II}, Ni^{II}, Cu^{II}, Zn^{II}) derived out of their free-base species $H_2TPP(C(O)NR_2)_4$ (R = Me (**2**/**2a**–**d**), iPr (**3**/**3a**–**d**)) were synthesized and characterized by NMR, IR and UV–vis spectroscopy as well as by ESI mass-spectrometry. The comparison of the obtained analytical results revealed only minor differences in vibrational and optical spectra, both with respect to the varied transition metal ions as well as the terminal organic substituent R. That provides potentially useful insight into the material properties of these porphyrins. It was anticipated that the variation of the central transition metal ions along **2a**–**d** and **3a**–**d** modify to the local transport characteristics of OMBD-deposited thin films of these compounds. In addition, in order to modify thin-film morphologies of successfully OMBD-

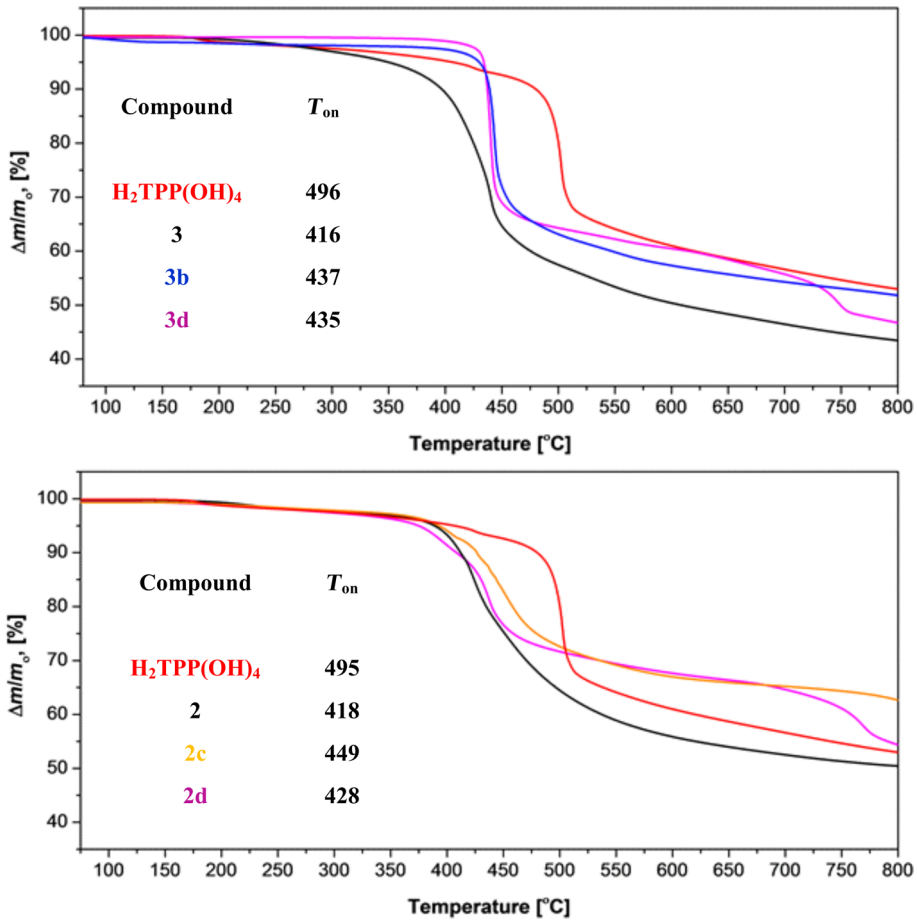

Figure 5: Top: TG traces of **3**, **3b** and **3d** in comparison with $H_2TPP(OH)_4$. Bottom: TG traces of **2**, **2c** and **2d** in comparison with $H_2TPP(OH)_4$.

deposited $CuTPP(OMe)_4$ **2/2a–d** and **3/3a–d** were equipped with sterically more bulky terminal organic groups. Unfortunately, all trials to deposit members of **2/2a–d** and **3/3a–d** by OMBD failed, which is attributed to a significantly lower thermal stability compared to $CuTPP(OMe)_4$ [8]. Most likely, the decreased thermal stability of **2/2a–d** and **3/3a–d** can be attributed to fragmentations of the terminal $–C(O)NR_2$ functionalities during heating. Thus, this study shows that the thermal stability of (metallo)porphyrins is subjected to certain limits, and the application of other thin-film depositions techniques is required for **2/2a–d** and **3/3a–d**.

Experimental

General conditions

All chemicals were purchased from commercial sources and were used as received, unless stated otherwise. All reactions were carried out under argon atmosphere using standard Schlenk techniques and vacuum-line manipulations unless stated otherwise. All solvents were distilled prior to use and were purified/dried according to standard procedures [32].

Starting materials

5,10,15,20-Tetra(4-carboxyphenyl)porphyrin ($H_2TPP(COOH)_4$, **1**) was synthesized according to [33] and $MCl_2{\cdot}nH_2O$ salts (M = Zn^{II}, Cu^{II}, Ni^{II}, Co^{II}) were dried according to [34].

Instruments

NMR spectra were recorded at ambient temperature with a Bruker Avance III 500 Ultra Shield Spectrometer (^1H at 500.300 MHz and $^{13}C\{^1H\}$ at 125.813 MHz) in the Fourier transform mode. Chemical shifts are reported in δ (ppm) versus $SiMe_4$ with the solvent as the reference signal $CDCl_3$: ^1H NMR, δ = 7.26; and $^{13}C\{^1H\}$ NMR, δ = 77.16. FTIR spectra were recorded in the range of 400–4000 cm^{-1} with a Perkin-Elmer 1000 FTIR spectrometer as KBr pellets and in the range of 650–4000 cm^{-1} with a Thermo Scientific Smart iTR, Nicolet iS10. (The two absorptions at ca. 2360 cm^{-1}, which appear different in intensity from spectra to spectra, are due to CO_2.) C, H, N elemental analyses were performed using a Thermo FlashAE 1112 series analyzer. High-resolution mass spectra were recorded with a Bruker micrOTOF QII equipped with an

Apollo II ESI source. UV–vis absorption spectra were recorded with a Spectronic GENESYS 6 UV–visible spectrophotometer (Thermo Electron Corporation) between 200–800 nm. TG experiments were performed using a Mettler Toledo TGA/DSC1 1600 system with an MX1 balance.

Synthesis of **2**

To a suspension of **1** (1.00 g, 1.26 mmol) in dichloromethane (140 mL) dimethylformamide (1 mL, 12.9 mmol) was added. This reaction mixture was cooled to 0 °C and oxalyl chloride (3.20 mL, 37.31 mmol) was added dropwise (within 20 min) under continuous stirring. The mixture was stirred at 0 °C for further 30 min followed by refluxing for 3 h. After all volatiles were removed under reduced pressure the obtained crude product was dissolved in dichloromethane (30 mL) and a mixture of dimethylamine (2 M in tetrahydrofuran, 16 mL, 32 mmol) and triethylamine (1 mL, 7.17 mmol) was added dropwise at ambient temperature. The reaction mixture was stirred at this temperature for another 3 h, followed by refluxing for 24 h. Afterward, all volatiles were removed under reduced pressure and hot distilled water (100 mL) was added to the crude product with continuous stirring for 30 min. The purple precipitate formed was filtered off, washed with hot distilled water (5 × 20 mL) and dried at 110 °C in an oven. Yield: 0.91 g (80% based on **1**). Anal. calcd for $C_{56}H_{50}N_8O_4$ (899.05): C, 74.81; H, 5.61; N, 12.46; found: C, 74.3; H, 5.7; N, 12.2; ^{1}H NMR ($CDCl_3$) δ −2.80 (s, 2H, $H^{a,a'}$), 3.32 (s, 24H, $H^{1,2}$), 7.84 (d, 8H, $H^{6,6'}$), 8.26 (d, 8H, $H^{5,5'}$), 8.87 (s, 8H, $H^{10,10'}$); $^{13}C\{^1H\}$ NMR ($CDCl_3$) δ 35.80 (C^1), 40.15 (C^2), 119.62 (C^8), 125.80 ($C^{6,6'}$), 134.57 (C^7), 135.93 ($C^{5,5'}$), 143.46 (C^4), 171.80 (C^3); HRMS (ESI-TOF, positive mode, MeCN/CH_2Cl_2): *m/z* 899.4058 [**2** + H]$^+$, 937.3515 [**2** + K]$^+$; calcd for $C_{56}H_{51}N_8O_4$/$C_{56}H_{50}KN_8O_4$ ([**2** + H]/[**2** + K]) = 899.4028/937.3587; IR (KBr, cm^{-1}) ν: 3317 (w, N–H); 2929/2897/2866 (m/w/w, C–H); 1629/1609 (s/w, C=O); UV–vis ($CHCl_3$) λ_{abs} [nm] (log ε): 401 (5.24), 420 (5.95), 449 (4.83), 516 (4.64), 551 (4.36), 591 (3.24), 647 (4.17), 666 (4.07); Supporting Information File 1 gives the IR, ^{1}H NMR, $^{13}C\{^1H\}$ NMR, UV–vis and ESIMS spectra of **2**.

Comments: According to Jones and Wilkins [35] for the –NMe_2 groups two ^{13}C NMR chemical shifts are observed. According to Manke et al. [36] the ^{13}C NMR resonances of the pyrrole carbon atoms $C^{9,9'}$ and $C^{10,10'}$ are not observable.

Synthesis of **3**

To a suspension of **1** (1.00 g, 1.26 mmol) in dichloromethane (140 mL), dimethylformamide (1 mL, 12.9 mmol) was added. This reaction mixture was cooled to 0 °C and oxalyl chloride (3.20 mL, 37.31 mmol) was added dropwise (within 20 min) under continuous stirring. The mixture was stirred at 0 °C for further 30 min followed by refluxing for 3 h. After all volatiles were removed under reduced pressure the obtained crude product was dissolved in dichloromethane (30 mL), and a mixture of diisopropylamine (11.52 g, 0.114 mol, 16 mL) and triethylamine (1 mL, 7.17 mmol) was added dropwise at ambient temperature. The reaction mixture was refluxed for 24 h. After cooling to ambient temperature, all volatiles were removed under reduced pressure, and hot distilled water (100 mL) was added to the crude product under continuous stirring for 30 min. The purple precipitate formed was filtered off, washed with hot distilled water (5 × 20 mL) and dried at 110 °C. Yield: 1.21 g (85% based on **1**). Anal. calcd for $C_{72}H_{82}N_8O_4$ (1123.47): C, 76.97; H, 7.36; N, 9.97; found: C, 76.8; H, 7.2; N 9.9. ^{1}H NMR ($CDCl_3$) δ −2.78 (s, 2H, $H^{a,a'}$), 1.43/1.66 (s(broad)/s(broad), 24H/24H, $H^{1,1',2,2'}$), 3.71/4.31 (s(broad)/s(broad), 4H/4H, $H^{3,3'}$), 7.74 (d, 8H, $H^{7,7'}$), 8.24 (d, 8H, $H^{6,6'}$), 8.90 (s, 8H, $H^{11,11'}$); $^{13}C\{^1H\}$ NMR ($CDCl_3$) δ 21.24 ($C^{1,1',2,2'}$), 119.8 (C^9), 124.6 ($C^{7,7'}$), 134.8 (C^8), 138.6 ($C^{6,6'}$), 142.8 (C^5), 171.3 (C^4); HRMS (ESI-TOF, positive mode, MeCN/CH_2Cl_2): *m/z* 1123.6520 [**3** + H]$^+$, 1145.6319 [**3** + Na]$^+$; calcd for $C_{72}H_{83}N_8O_4$/$C_{72}H_{82}NaN_8O_4$ ([3 + H]/[**3** + Na]) = 1123.6532/1145.6351; IR (KBr, cm^{-1}) ν: 3317 (w, N–H); 2969/2932/2874 (m/w/w, C–H); 1630/1608 (s, C=O); UV–vis ($CHCl_3$) λ_{abs} [nm] (log ε): 400 (4.80), 420 (5.49), 482 (3.74), 517 (4.17), 552 (3.91), 591 (3.74), 648 (3.58). Supporting Information File 1 gives the IR, ^{1}H NMR, $^{13}C\{^1H\}$ NMR, UV–vis and ESIMS spectra of **3**.

Comments: The ^{1}H NMR resonances of the $N(iPr)_2$ groups are all broadened. The hydrogen atoms $H^{1,1',2,2'}$ are regarded to correspond to the two broad singlets at 1.39 and 1.69 ppm. The hydrogen atoms $H^{3,3'}$ are regarded to correspond to the two singlets at 3.71 and 4.31 ppm. Both assignments could, however, not be verified by additional 2D NMR experiments (^{1}H,^{1}H-COSY, ^{1}H,^{13}C-HSQCETGP and HMBCGP) because of too broad NMR resonances and/or the comparatively poor solubility. According to Jones and Wilkins [35] for the –NMe_2 groups two ^{13}C NMR chemical shifts are observed. According to Manke et al. [36] the ^{13}C NMR resonances of the pyrrole carbon atoms $C^{9,9'}$ and $C^{10,10'}$ are not observable.

General procedure for the synthesis of **2a–d** and **3a–d**

Unless stated otherwise, the following procedure was used: To a solution of **2** (0.200 g, 0.222 mmol) for **2a**–**d**, or **3** (0.200 g, 0.178 mmol) for **3a**–**d** in dimethylformamide (25 mL), a solution of the MCl_2 salt (3 equiv) in dimethylformamide (5 mL) was added dropwise (within 5 min) at ambient temperature. The reaction temperature was raised to 140 °C for 6 h. After cooling the reaction mixture to ambient temperature, chloroform (50 mL) was added and the combined organic

phases were washed with water (3 × 40 mL) and brine (3 × 40 mL) to remove the excess of the MCl_2 salt. The organic phase was dried over magnesium sulfate, and all volatiles were removed in vacuo to afford solids of the corresponding metalloporphyrins, which were dried additionally in vacuo for 12 h. Afterward, the corresponding solids were dissolved in $CHCl_3$ and precipitated with *n*-hexane. That procedure is referred to in the following as "re-precipitation".

Data for **2a**

2 (0.200 g, 0.222 mmol), $ZnCl_2$ (0.0909 g, 0.667 mmol). Yield: 0.156 g (73% based on **2**); purple solid. Anal. calcd for $C_{56}H_{48}N_8O_4Zn$ (962.44): C, 69.88; H, 5.03; N, 11.64; found: C, 69.5; H, 5.0; N, 11.5; ^{1}H NMR ($CDCl_3$) δ 3.16/3.26 (s/s, 12H/12H, $H^{1,2}$), 7.68 (d, 8H, $H^{6,6'}$), 8.23 (d, 8H, $H^{5,5'}$), 8.93 (s, 8H, $H^{10,10'}$); HRMS (ESI-TOF, positive mode, MeCN/CH_2Cl_2): *m*/*z* 960.3058/961.3149 [**2a**]$^+$/[**2a** + H]$^+$, 983.2908 [**2a** + Na]$^+$, 999.2716 [**2a** + K]$^+$; calcd for $C_{56}H_{48}N_8O_4Zn$/$C_{56}H_{49}N_8O_4Zn$, $C_{56}H_{48}NaN_8O_4Zn$, $C_{56}H_{48}KN_8O_4Zn$ ([**2a**]/[**2a** + H], [**2a** + Na], [**2a** + K] = 960.3058/961.3163, 983.2982, 999.2722; IR (KBr, cm^{-1}) ν: 2929 (w, C–H); 1612 (s, C=O); UV–vis ($CHCl_3$) λ_{abs} [nm] (log ε): 403 (4.55), 426 (5.55), 555 (4.19), 596 (3.73). Supporting Information File 1 gives the IR, ^{1}H NMR, UV–vis and ESIMS spectra of **2a**.

Comments: No re-precipitation needed. Due to the poor solubility of **2a** a ^{13}C NMR spectrum could not be recorded. The ESIMS spectra of **2a** reveals as basis peak 988.3599. The origin of this peak remains unclear and may likely correspond to a fragmentation/recombination process under ESIMS measurement conditions.

Data for **2b**

2 (0.200 g, 0.222 mmol), $CuCl_2$ (0.0897 g, 0.667 mmol). Yield: 0.130 g (61% based on **2**); wine red solid. Anal. calcd for $C_{56}H_{48}CuN_8O_4$ (960.58): C, 70.02; H, 5.04; N, 11.76; found: C, 69.9; H, 5.0; N, 11.6; HRMS (ESI-TOF, positive mode, MeCN/CH_2Cl_2): *m*/*z* 960.3254 [**2b**]$^+$; calcd for $C_{56}H_{48}CuN_8O_4$ [**2b**] 960.3128; IR (KBr, cm^{-1}) ν: 2928/2932 (w/w, C–H); 1622 (C=O); UV–vis ($CHCl_3$) λ_{abs} [nm] (log ε): 396 (4.44), 419 (5.65), 543 (4.28), 578 (3.39). Supporting Information File 1 gives the IR, UV–vis and ESIMS spectra of **2b**.

Comments: No re-precipitation needed.

Data for **2c**

2 (0.200 g, 0.222 mmol), $NiCl_2$ (0.0865 g, 0.667 mmol). Yield: 0.149 g (70% based on **2**); brown solid. Anal. calcd for $C_{56}H_{48}N_8NiO_4$ (955.72): C, 70.38; H, 5.06; N, 11.72; found: C, 70.1; H, 5.0; N, 11.6; ^{1}H NMR ($CDCl_3$) δ 3.27 (s, 24H, $H^{1,2}$), 7.76 (d, 8H, $H^{6,6'}$), 8.05 (d, 8H, $H^{5,5'}$), 8.76 (s, 8H, $H^{10,10'}$); ^{13}C{^{1}H} NMR ($CDCl_3$) δ 24.41 (C^1), 33.87 (C^2), 118.47 (C^8), 125.96 ($C^{6,6'}$), 132.46 ($C^{10,10'}$), 133.73 (C^7), 135.96 ($C^{5,5'}$), 142.20 ($C^{9,9'}$), 142.67 (C^4), 171.69 (C^3); HRMS (ESI-TOF, positive mode, MeCN/CH_2Cl_2): *m*/*z* 955.3153 [**2c** + H]$^+$; calcd for $C_{56}H_{49}N_8NiO_4$ [**2c** + H] = 955.3225; IR (KBr, cm^{-1}) ν: 2924/2854 (w/w, C–H); 1626 (s, C=O); UV–vis ($CHCl_3$) λ_{abs} [nm] (log ε): 416 (5.30), 528 (4.17). Supporting Information File 1 gives the IR, ^{1}H NMR, ^{13}C{^{1}H} NMR, UV–vis and ESIMS spectra of **2c**.

Comments: No re-precipitation needed. Due to a better solubility of **2c** as compared to **2a**, ^{13}C NMR spectra could be recorded. In contrast to comments made for **2**, all chemically different carbon atoms were observable, although for the –NMe_2 groups of **2c** two ^{13}C NMR resonances were observed as reported for **2**.

Data for **2d**

2 (0.200 g, 0.222 mmol), $CoCl_2$ (0.0867 g, 0.667 mmol). Yield: 0.155 g (73%, based on **2**); wine red solid. Anal. calcd for $C_{56}H_{48}CoN_8O_4$ (955.96): C, 70.36; H, 5.05; N, 11.72; found: C, 70.1; H, 5.0;N, 11.7; HRMS (ESI-TOF, positive mode, MeCN/CH_2Cl_2): *m*/*z* 955.3125 [**2d**]$^+$; calcd for $C_{56}H_{48}N_8CoO_4$ [**2d**] = 955.3125; IR (KBr, cm^{-1}) ν: 2927/2852 (w/w, C–H); 1625 (s, C=O); UV–vis ($CHCl_3$) λ_{abs} [nm] (log ε): 412 (5.24), 442 (4.44), 530 (4.03). Supporting Information File 1 gives the IR, UV–vis and ESIMS spectra of **2d**.

Comments: Re-precipitation needed.

Data for **3a**

3 (0.200 g, 0.178 mmol), $ZnCl_2$ (0.0728 g, 0.534 mmol). Yield: 0.192 g (91% based on **3**); purple solid. Anal. calcd for $C_{72}H_{80}N_8O_4Zn$ (1186.87): C, 72.86; H, 6.79; N, 9.44, found: C, 72.1; H, 6.6; N, 9.23; ^{1}HNMR ($CDCl_3$) δ 1.45/1.59 (s(broad)/s(broad), 24H/24H, $H^{1,1',2,2'}$), 3.68/4.31 (s(broad)/s(broad), 4H/4H, $H^{3,3'}$), 7.65 (d, 8H, $H^{7,7'}$), 8.22 (d, 8H, $H^{6,6'}$), 8.98 (s, 8H, $H^{11,11'}$); ^{13}C{^{1}H} NMR ($CDCl_3$) δ 20.85 ($C^{1,1',2,2'}$), 120.46 (C^9), 124.11 ($C^{7,7'}$), 132.08 ($C^{11,11'}$), 134.48 (C^8), 137.85 ($C^{6,6'}$), 143.34 (C^5), 150.08 ($C^{10,10'}$), 171.08 (C^4); HRMS (ESI-TOF, positive mode, MeCN/CH_2Cl_2): *m*/*z* 1185.5632 [**3a** + H]$^+$, 1207.5471 [**3a** + Na]$^+$; calcd for $C_{72}H_{81}ZnN_8O_4$/$C_{72}H_{80}NaZnN_8O_4$ ([**3a** + **H**]/[**3a** + Na]) = 1185.5667/1207.5486; IR (KBr, cm^{-1}) ν: 2969/2928/2869 (m/w/w, C–H); 1632 (s, C=O); UV–vis ($CHCl_3$) λ_{abs} [nm] (log ε): 404 (4.33), 426 (5.29), 556 (3.93), 597 (3.53). Supporting Information File 1 gives the IR, ^{1}H NMR, ^{13}C{^{1}H} NMR, UV–vis and ESIMS spectra of **3a**.

Comments: Re-precipitation needed. Because **3a** is better soluble than **2a**, ^{13}C NMR spectra could be recorded. In con-

trast to comments made for **3**, all chemically different carbon atoms beside $C^{3,3'}$ (belonging to the $-N(iPr)_2$ groups) were observable. On the other hand, as discussed for **3** broad singlets in the ^1H NMR spectra are regarded to correspond to the hydrogen atoms $H^{1,1',2,2',3,3'}$.

Data for **3b**

3 (0.200 g, 0.178 mmol), $CuCl_2$ (0.0718, 0.534 mmol). Yield: 0.124 g (59% based on **3**); wine red solid. Anal. calcd for $C_{72}H_{80}CuN_8O_4$(1185.0): C, 72.98; H, 6.80; N, 9.46; found: C, 72.5; H, 6.7;N, 9.4; HRMS (ESI-TOF, positive mode, MeCN/CH_2Cl_2): *m*/*z* 1184.5665 [**3b**]$^+$; calcd for $C_{72}H_{80}CuN_8O_4$ [**3b**] = 1184.5671; IR (KBr, cm^{-1}) ν: 2966/2928/2869 (m/w/w, C–H); 1632 (s, C=O); UV–vis ($CHCl_3$) λ_{abs} [nm] (log ε): 397 (4.58), 419 (5.72), 542 (4.36), 579 (3.46). Supporting Information File 1 gives the IR, UV–vis and ESIMS spectra of **3b**.

Comments: No re-precipitation needed.

Data for **3c**

3 (0.200 g, 0.178 mmol), $NiCl_2$ (0.0692 g, 0.534 mmol). Yield: 0.126 g (60%, based on **3**); brown solid. Anal. calcd for $C_{72}H_{80}N_8NiO_4$(1180.15): C, 73.28; H, 6.83; N, 9.49; found: C, 72.9; H, 6.8; N, 9.4; ^1H NMR ($CDCl_3$) δ 1.40/1.62 (s(broad)/s(broad), 24H/24H, $H^{1,1',2,2'}$), 3.70/4.23 (s(broad)/s(broad), 4H/4H, $H^{3,3'}$), 7.66 (d, 8H, $H^{7,7'}$), 8.03 (d, 8H, $H^{6,6'}$), 8.79 (s, 8H, $H^{11,11'}$); $^{13}C\{^1H\}$ NMR ($CDCl_3$) δ 21.00 ($C^{1,1',2,2'}$), 118.55 (C^9), 124.65 ($C^{7,7'}$), 132.46 ($C^{11,11'}$), 133.96 (C^8), 138.57 ($C^{6,6'}$), 141.34 (C^5), 142.76 ($C^{10,10'}$), 171.07 (C^4); HRMS (ESI-TOF, positive mode, MeCN/CH_2Cl_2): *m*/*z* 1179.5713 [**3c** + H]$^+$, 1201.5520 [**3c** + Na]$^+$; calcd for $C_{72}H_{81}NiN_8O_4$/$C_{72}H_{80}NaNiN_8O_4$ ([**3c** + H]/[**3c** + Na]) = 1179.5729/1201.5548; IR (KBr, cm^{-1}) ν: 2969/2928/2875 (w/w/w, C–H); 1630 (s, C=O); UV–vis ($CHCl_3$) λ_{abs} [nm] (log ε): 417 (5.32), 530 (4.23). Supporting Information File 1 gives the IR, ^1H NMR, $^{13}C\{^1H\}$ NMR, UV–vis and ESIMS spectra of **3c**.

Comments: No re-precipitation needed. As discussed for **3a** (above), analogous observations were made for **3c**.

Data for **3d**

3 (0.200 g, 0.178 mmol), $CoCl_2$ (0.0693 g, 0.534 mmol). Yield: 0.164 g (78%, based on **3**); wine red solid. Anal. calcd for $C_{72}H_{80}CoN_8O_4$ (1180.39): C, 73.26; H, 6.83; N, 9.49; found: C, 72.8; H, 6.7; N, 9.3; HRMS (ESI-TOF, positive mode, MeCN/CH_2Cl_2): *m*/*z* 1179.5561 [**3d**]$^+$; calcd for $C_{72}H_{80}CuN_8O_4$ [**3d**] = 1179.5629; IR (KBr, cm^{-1}) ν: 2963/2931/2869 (m/w/w, C–H); 1629 (s, C=O); UV–vis ($CHCl_3$) λ_{abs} [nm] (log ε): 412 (5.47), 529 (4.25). Supporting Information File 1 gives the IR, UV–vis and ESIMS spectra of **3d**.

Comments: Re-precipitation needed.

Supporting Information

Supporting Information File 1 features ^1H and $^{13}C\{^1H\}$ NMR spectra of **2**, **2a**, **2c**, **3**, **3a** and **3c**, ESIMS, UV–vis and IR spectra (ATR-IR and KBr) of **2**, **2a**–**2d**, **3** and **3a**–**3d**, and IR spectra of **3b** and **3d** before and after OMBD together with optical photographs of the materials.

Supporting Information File 1

Additional experimental data.
[http://www.beilstein-journals.org/bjnano/content/supplementary/2190-4286-8-121-S1.pdf]

Acknowledgements

This work has been supported by the Deutsche Forschungsgemeinschaft through project FOR 1154 “Towards Molecular Spintronics”. We thank Janine Freytag, Brigitte Kempe and Dipl.-Chem. Natalia Rüffer for EA, ESIMS and TG measurements.

References

1. Dolphin, D. *The Porphyrins;* Academic Press: New York, NY, USA, 1978.
2. Kadish, K. M.; Smith, K. M.; Guiard, R. *The Porphyrins Handbook;* Academic Press (Elsevier Science): Amsterdam, Netherlands, 2000.
3. Vicente, M. G. H.; Smith, K. M. *Curr. Org. Synth.* **2014,** *11,* 3–28. doi:10.2174/15701794113106660083
4. Birnbaum, T.; Hahn, T.; Martin, C.; Kortus, J.; Fronk, M.; Lungwitz, F.; Zahn, D. R. T.; Salvan, G. *J. Phys.: Condens. Matter* **2014,** *26,* 104201. doi:10.1088/0953-8984/26/10/104201
5. Wang, F. J.; Yang, C. G.; Vardeny, Z. V. *Phys. Rev. B* **2007,** *75,* 245324. doi:10.1103/PhysRevB.75.245324
6. Smykalla, L.; Shukrynau, P.; Mende, C.; Rüffer, T.; Lang, H.; Hietschold, M. *Surf. Sci.* **2014,** *628,* 92–97. doi:10.1016/j.susc.2014.05.015
7. Smykalla, L.; Shukrynau, P.; Mende, C.; Rüffer, T.; Lang, H.; Hietschold, M. *Surf. Sci.* **2014,** *628,* 132–140. doi:10.1016/j.susc.2014.06.001
8. Siles, P. F.; Bufon, C. C. B.; Grimm, D.; Jalil, A. R.; Mende, C.; Lungwitz, F.; Salvan, G.; Zahn, D. R. T.; Lang, H.; Schmidt, O. G. *Org. Electron.* **2014,** *15,* 1432–1439. doi:10.1016/j.orgel.2014.04.004
9. Lungwitz, F.; Mende, C.; Fronk, M.; Haidu, F.; Lang, H.; Salvan, G.; Zahn, D. R. T. *Thin Solid Films* **2014,** *571,* 377–383. doi:10.1016/j.tsf.2014.03.055
10. Granados-Oliveros, G.; Páez-Mozo, E. A.; Ortega, F. M.; Piccinato, M. T.; Silva, F. N.; Guedes, C. L. B.; Di Mauro, E.; da Costa, M. F.; Ota, A. T. *J. Mol. Catal. A: Chem.* **2011,** *339,* 79–85. doi:10.1016/j.molcata.2011.02.015
11. Wang, C.; Yang, G.-M.; Li, J.; Mele, G.; Słota, G.; Broda, M. A.; Duan, M.-Y.; Vasapollo, G.; Zhang, X.; Zhang, F.-X. *Dyes Pigm.* **2009,** *80,* 321–328. doi:10.1016/j.dyepig.2008.08.008

12. Zheng, W.; Shan, N.; Yu, L.; Wang, X. *Dyes Pigm.* **2008,** *77,* 153–157. doi:10.1016/j.dyepig.2007.04.007
13. McGill, S.; Nesterov, V. N.; Gould, S. L. *Acta Crystallogr., Sect. E* **2013,** *69,* m471. doi:10.1107/S1600536813019338
14. Goldberg, I.; Krupitsky, H.; Stein, Z.; Hsiou, Y.; Strouse, C. E. *Supramol. Chem.* **1994,** *4,* 203–221. doi:10.1080/10610279408029473
15. Isthaiwi, Z.; Rüffer, T.; Klaib, S.; Buschbeck, R.; Walfort, B.; Lang, H. *Dalton Trans.* **2014,** *43,* 7868–7888. doi:10.1039/C3DT53535E
16. Chen, W.; El-Khouly, M. E.; Fukuzumi, S. *Inorg. Chem.* **2011,** *50,* 671–678. doi:10.1021/ic102208y
17. Shirakawa, M.; Kawano, S. I.; Fujita, N.; Sada, K.; Shinkai, S. *J. Org. Chem.* **2003,** *68,* 5037–5044. doi:10.1021/jo0341822
18. Gradl, S. N.; Felix, J. P.; Isacoff, E. Y.; Garcia, M. L.; Trauner, D. *J. Am. Chem. Soc.* **2003,** *125,* 12668–12669. doi:10.1021/ja036155z
19. Buchler, J. W. Synthesis and Properties of Metalloporphyrins. In *The Porphyrins;* Dolphin, D., Ed.; Academic Press: New York, NY, USA, 1978; Vol. 1, pp 389–483. doi:10.1016/B978-0-12-220101-1.50017-2
20. Rüffer, T.; Nurpeisova, D.; Jakupova, Z.; Tashenov, A.; Uhlig, N.; Khalladi, A.; Mertens, L.; Gonser, A.; Mehring, M.; Lang, H. *Z. Naturforsch., B* **2017,** submitted.
21. White, W. I.; Bachmann, R. C.; Burnham, B. F. Chromatography of porphyrins and metalloporphyrins. In *The Porphyrins;* Dolphin, D., Ed.; Academic Press: New York, USA, 1978; Vol. I, pp 553–580. doi:10.1016/b978-0-12-220101-1.50019-6
22. Budzikiewicz, H. Mass spectra of porphyrins and related compounds. In *The Porphyrins;* Dolphin, D., Ed.; Academic Press: New York, NY, USA, 1978; Vol. 3, pp 395–461. doi:10.1016/B978-0-12-220103-5.50016-7
23. Cole, R. B. *Electrospray ionization mass spectrometry: fundamentals, instrumentation, and applications;* John Wiley & Sons, Inc.: New York, NY, USA, 1997.
24. Keller, B. O.; Sui, J.; Young, A. B.; Whittal, R. M. *Anal. Chim. Acta* **2008,** *627,* 71–81. doi:10.1016/j.aca.2008.04.043
25. Alben, J. O. Infrared Spectroscopy of Porphyrins. In *The Porphyrins;* Dolphin, D., Ed.; Academic Press: New York, NY, USA, 1978; Vol. 3, pp 323–345. doi:10.1016/B978-0-12-220103-5.50014-3
26. Steger, E.; Adler, B.; Brunn, J.; Doerffel, K.; Höbold, W.; Mehlhorn, A.; Müller, E.; Treibmann, D. *Lehrwerkreihe Chemie: Strukturaufklärung-Spektroskopie und Röntgenbeugung, Arbeitsbuch;* VEB Deutscher Verlag für Grundstoffindustrie: Leipzig, GDR, 1973.
27. Becker, H. G. O.; Domschke, G.; Fanghänel, E.; Fischer, M.; Gewald, K.; Mayer, R.; Pavel, D.; Schmidt, H.; Schwetlick, K.; Berger, W.; Faust, J.; Gentz, F.; Gluch, R.; Müller, K.; Schollberg, K.; Seiler, E.; Zeppenfeld, G.; Fabian, J.; Frach, K.; Lohs, K.; Kläsz, V. *Organikum;* Deutscher Verlag der Wissenschaften: Berlin, GDR, 1976.
28. McKeown, N. B. *Phthalocyanine Materials Synthesis, Structure and Function;* Cambridge University Press: UK, 1998; pp 88–93.
29. Gouterman, M. Optical Spectra and Electronic Structure of Porphyrins and Related Rings. In *The Porphyrins;* Dolphin, D., Ed.; Academic Press: New York, NY, USA, 1978; Vol. 3, pp 2–24. doi:10.1016/B978-0-12-220103-5.50008-8
30. Gouterman, M. *J. Mol. Spectrosc.* **1961,** *6,* 138–163. doi:10.1016/0022-2852(61)90236-3
31. Abdulmalic, M. A.; Fronk, M.; Bräuer, B.; Zahn, D. R. T.; Salvan, G.; Meva, F. E.; Rüffer, T. *J. Magn. Magn. Mater.* **2016,** *419,* 17–28. doi:10.1016/j.jmmm.2016.06.002
32. Perin, D. D.; Armarego, W. L. F. *Purification of Laboratory Chemicals,* 3rd ed.; Pergamon: New York, NY, USA, 1988.
33. Adler, A. D.; Longo, F. R.; Finarelli, J. D.; Goldmacher, J.; Assour, J.; Korsakoff, L. A. *J. Org. Chem.* **1967,** *32,* 476. doi:10.1021/jo01288a053
34. Freeman, J. H.; Smith, M. L. *J. Inorg. Nucl. Chem.* **1958,** *7,* 224–227. doi:10.1016/0022-1902(58)80073-1
35. Jones, R. G.; Wilkins, J. M. *Org. Magn. Reson.* **1978,** *11,* 20–26. doi:10.1002/mrc.1270110106
36. Manke, A.-M.; Geisel, K.; Fetzer, A.; Kurz, P. *Phys. Chem. Chem. Phys.* **2014,** *16,* 12029–12042. doi:10.1039/c3cp55023k

License and Terms

BEILSTEIN JOURNAL OF NANOTECHNOLOGY

Charge transport in organic nanocrystal diodes based on rolled-up robust nanomembrane contacts

Vineeth Kumar Bandari[1,2], Lakshmi Varadharajan[1,2], Longqian Xu[1,2], Abdur Rehman Jalil[1,2], Mirunalini Devarajulu[1,2], Pablo F. Siles[*1,2], Feng Zhu[*1,2] and Oliver G. Schmidt[1,2]

Letter

Open Access

Address:
[1]Material Systems for Nanoelectronics, TU Chemnitz, Reichenhainer Str. 70, 09107 Chemnitz, Germany and [2]Institute for Integrative Nanosciences, IFW Dresden, Helmholtz Str. 20, 01069 Dresden, Germany

Email:
Pablo F. Siles[*] - p.r.siles@ifw-dresden.de; Feng Zhu[*] - f.zhu@ifw-dresden.de

* Corresponding author

Keywords:
charge transport; nanomembrane; organic diode; organic nanocrystal; rolled-up nanotechnology

Beilstein J. Nanotechnol. **2017,** *8,* 1277–1282.
doi:10.3762/bjnano.8.129

Received: 31 January 2017
Accepted: 29 May 2017
Published: 19 June 2017

This article is part of the Thematic Series "Towards molecular spintronics".

Guest Editor: G. Salvan

Abstract

The investigation of charge transport in organic nanocrystals is essential to understand nanoscale physical properties of organic systems and the development of novel organic nanodevices. In this work, we fabricate organic nanocrystal diodes contacted by rolled-up robust nanomembranes. The organic nanocrystals consist of vanadyl phthalocyanine and copper hexadecafluorophthalocyanine heterojunctions. The temperature dependent charge transport through organic nanocrystals was investigated to reveal the transport properties of ohmic and space-charge-limited current under different conditions, for instance, temperature and bias.

Introduction

Organic semiconductors have been widely applied in developing optoelectronic devices including light-emitting diodes, transistors, sensors [1-3]. Because the large variety of physical properties can be conveniently tuned by manipulating the molecular structure, a clever design of the nanoscale device geometry opens up further intriguing options for novel applications in the fields of optoelectronics and spintronics [4-6]. Organic nanocrystals have drawn much attention in the community because high quality material can be efficiently generated by controlling the nanoscale physical growth and/or chemical synthesis process [7-10]. The deposition of organic conjugated molecules is usually realized by thermal evaporation in vacuum. The molecules have van der Waals interaction with an inert substrate which makes them weakly bonded to the substrate [11]. As a result, by controlling the molecules deposition parameters, such as deposition rate and the substrate temperature, it is possible to obtain either amorphous smooth and continuous organic thin films with thicknesses down to a few monolayers or inhomogeneous organic nanocrystals such as organic nanopillars and nanopyramids [11-13].

However, the fabrication of organic nanodevices based on nanostructures is a persistent challenge due to difficulties in creating non-destructive contacts [14-16]. Although there have been remarkable advances in the methods for vertically contacting a variety of organic thin films, one of the main challenges to perform such fabrication still lies in the preparation of reliable vertical junctions [16]. Mainly due to the inhomogeneous distribution of nanostructures on the substrate surface, the metallic atoms can inter-diffuse and produce unwanted short-circuit junctions during the contact formation [14]. Thus, the fabrication of a reliable robust top contact is expected to solve this tedious problem. Part of the authors of this report have developed a novel 'rolled-up nanotechnology' to tackle this challenge [17-19]. By this method, strained nanomembranes are released from a substrate surface and the elastic relaxation of the built-in strain gradient triggers a self-rolling process of the nanomembranes. The strained nanomembranes roll-up into full microtubes and finally land on top of the organic nanostructures, e.g., self-assembled monolayers and organic nanopyramids [17,19]. Compared to other 'soft' contact methods developed recently, including chemical binding [20,21], indirect evaporation [22,23], 'ready-made' approaches [24,25], and robust mechanical contacts [26-29], the rolled-up nanotechnology provides the precise positioned electrodes and high fabrication yield of array devices, and does not require the chemical modification of functional organic layers. Furthermore, the candidate materials for rolled-up nanomembranes are metals, ferromagnetic layers, oxides, and complex materials, of which the various properties of thin solid films, e.g., work function and magnetic properties, can be utilized to develop novel functional organic devices [30,31]. In our previous report, organic nanocrystal diodes have been successfully developed, in which rolled-up nanomembranes provide robust contacts to fully unleash the advantages of organic nanocrystals for sensing gas molecules [19]. Apart from the demonstration of functional nanodevices, the investigation and understanding of charge transport mechanisms across the organic nanostructure is a key topic nowadays for developing and optimizing novel nanostructured devices [8,9,32,33].

In this work, we fabricate organic nanocrystal diodes sandwiched between flat metal electrode and rolled-up nanomembrane electrode contacts. The nanocrystals consist of vanadyl phthalocyanine (VOPc) and copper hexadecafluorophthalocyanine (F_{16}CuPc) heterojunctions. The temperature dependent current–voltage behaviors were investigated to unveil the charge transport properties of the nanocrystals. As most of the well-studied charge transport systems are based on planar or vertical bulky organic thin-film devices [34], the conduction mechanism in this report will provide a helpful insight into the charge transport in nanoscale systems.

Results and Discussion

The fabrication protocol of the organic nanocrystal diodes is the same as in our previous reports [19]. The fabrication yield of the devices contacted by rolled-up electrodes on the single chip can achieve more than 95% owing to the reliable parallel nanofabrication when the whole process is carefully performed. To study the charge transport properties of the crystalline heterojunction nanopyramids, three kinds of organic nanopyramids were grown on well-defined bottom Au finger electrodes (Au mesa), i.e., pure VOPc (10 nm), F_{16}CuPc (1 nm)/VOPc (9 nm) and F_{16}CuPc (1 nm)/VOPc (8 nm)/F_{16}CuPc (1 nm). The thicknesses are the nominal values detected by the thickness monitor. However, the deposited molecules form inhomogeneous nanopyramids during growth. The heights of the nanopyramids range between 50–100 nm, as observed from atomic force microscopy (AFM) measurements. Figure 1 shows the device configuration and molecular structures. After formation of organic nanopyramids, the rolled-up Au tube electrodes land on top and form reliable contacts. The geometric contacting area between organic and finger electrodes is estimated by considering the circumference of the tube electrode and the width of the mesa electrode, which is on average about 8 μm^2. An uncertainty concerning the effective electrical contact to the tube electrode remains, because the total number of current pathways across the crystalline nanopyramids is experimentally difficult to determine. The morphology properties of organic layer will determine the effective contact area to a great extent. For instance, a smooth organic layer or self-assembly monolayer has larger contact area when the tube lands on top, while nanopyramid geometry restricts the contact area only within the limited peaks' surface which can touch the tube. Due to geometry deviation of single nanopyramid structure, it is quite challenging to precisely predict how the single tube surface contacts with nanopyramids and calculate the contact area. As a compromise, in this report the transport properties will be deducted based on the electrical current through device, instead of the intrinsic conductivity of single organic nanostructures.

To study the charge transport properties of the crystalline nanopyramids, an electrical characterization is performed by measuring the current–voltage (*I–V*) characteristics. As shown in Figure 2a, the strong charge transfer (CT) between VOPc and F_{16}CuPc causes the heterojunction nanopyramids with double F_{16}CuPc buffer layers to experience much-improved charge injection/transport under the positive bias, and a smaller open voltage compared to the devices consisting of pure VOPc and single F_{16}CuPc buffer layer. As introduced in our previous report [19], the Schottky barrier due to the poor electric contact between the organic material and the electrodes will restrain the charge transport in the diodes consisting of pure VOPc or organic nanostructure with single F_{16}CuPc buffer layer. In this

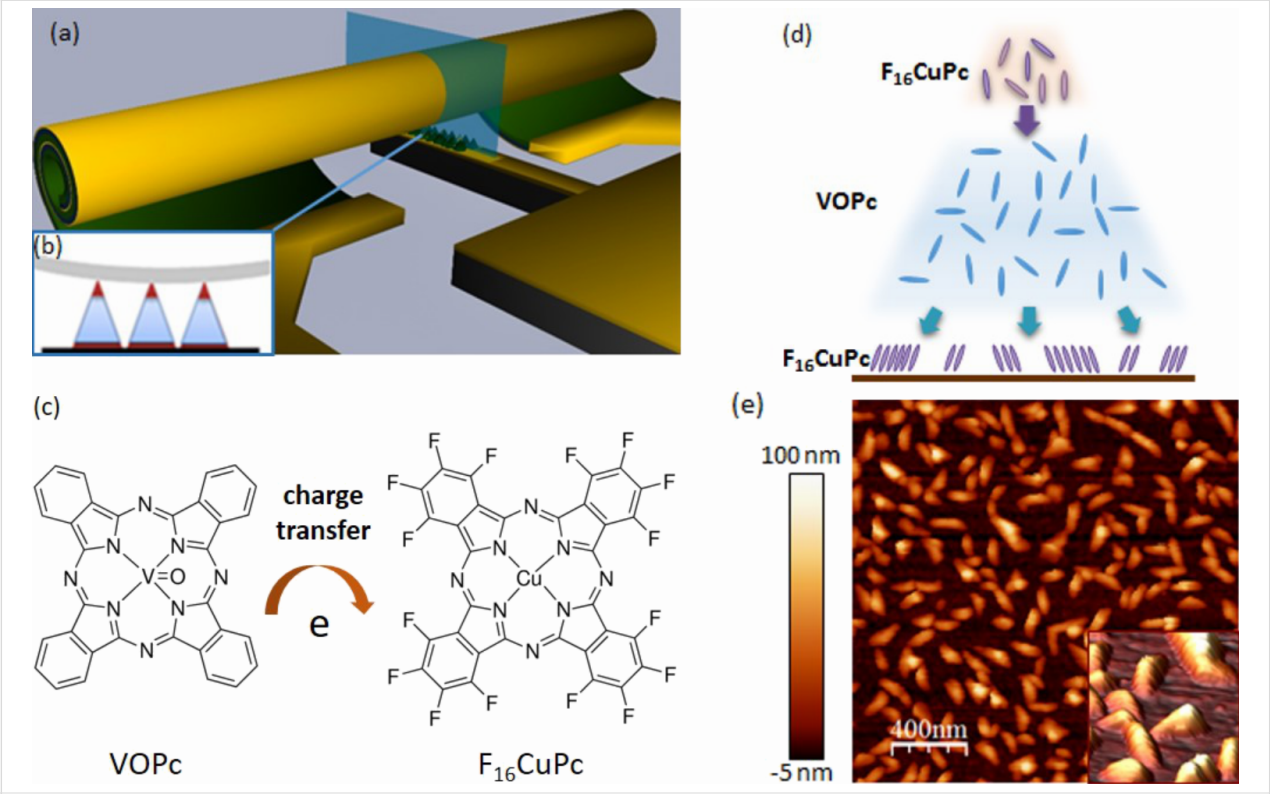

Figure 1: (a) Schematic picture of organic nanocrystal diode with rolled-up contact electrode. (b) Schematic picture of the vertical junction with the nanopyramid sandwiched between the Au mesa electrode and Au tube electrode. (c) Molecular structures of VOPC and F_{16}CuPc. (d) Illustration of the F_{16}CuPc/VOPc/F_{16}CuPc nanopyramid. (e) AFM topography image of the F_{16}CuPc/VOPc/F_{16}CuPc nanostructures.

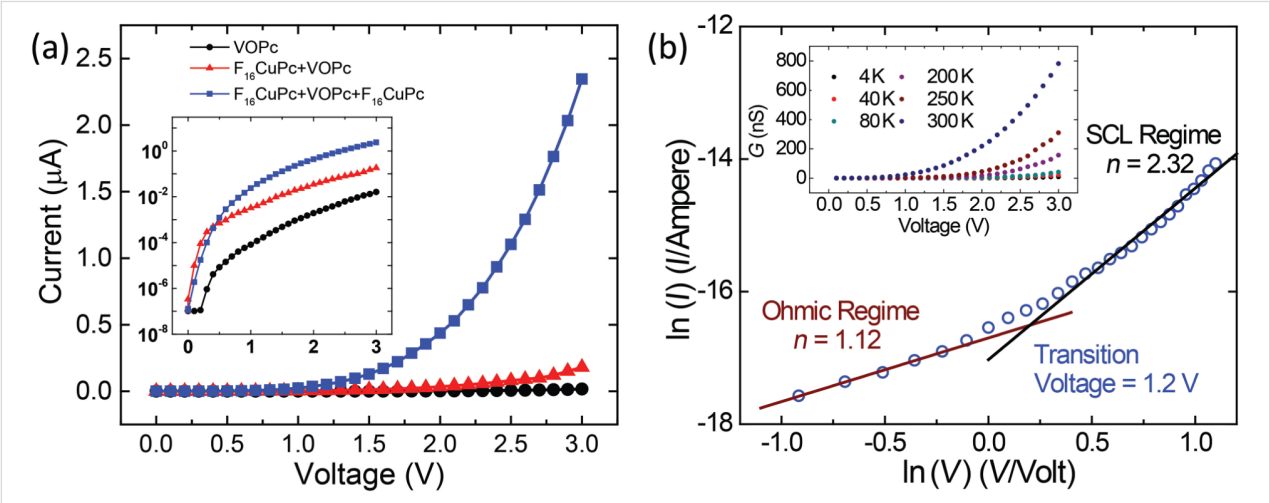

Figure 2: (a) *I*–*V* characteristics of three kinds of nanopyramid structures: pure VOPc (black), F_{16}CuPc/VOPc (red) and F_{16}CuPc/VOPc/F_{16}CuPc (blue), (b) ln(*I*)–ln(*V*) plot showing the transition of transport regimes from ohmic to SCL.

report, we will focus on the investigation of charge transport in the F_{16}CuPc/VOPc/F_{16}CuPc organic nanopyramid diode by applying a forward bias to the tube electrode.

With the F_{16}CuPc buffer layers the electrical contacts between the organic nanopyramids and the tube electrode are ohmic at room temperature. A typical plot of the natural logarithm of the current versus natural logarithm of the voltage (ln(*I*)–ln(*V*)) is shown in Figure 2b, which allows us to determine two transport regimes. The curve has a slope of $n = 1.12$ for low bias and a slope of $n = 2.32$ for a high bias. The transition voltage is about 1.2 V. According to the Mott–Gurney Law the transport can be

regarded as ohmic in the low bias regime and space-charge-limited (SCL) in the high bias regime [35], which agrees with our previous report [19,36].

To assess the transport process of the vertical nanopyramid device based on the Au mesa electrode/F_{16}CuPc/VOPc/F_{16}CuPc/Au tube electrode, *I*–*V* measurements at different temperatures were performed, as shown in Figure 3a. Similar to the current–voltage characteristics at room temperature, the current under forward bias remains dominant also at lower temperatures. By plotting the temperature dependent current behavior (ln(*I*)–1000/*T*) under different bias we obtain two distinct regions with different slopes the change-over of which occur at around 125 K, as shown in Figure 3b. The curves for $T > 125$ K (left part) show more pronounced temperature dependence, which indicates that thermal activation plays an important role during the transport [37]. Both the left and right regions of Figure 3b are well-described by the classical Arrhenius relation.

$$I_0 = A_1 SV \cdot \exp\frac{-E_a}{k_B T} \quad (1)$$

where E_a is the activation energy, k_B the Boltzmann's constant, A_1 the pre-exponential factor, and S the estimated contact area.

The occurrence of two thermally activated regions can be explained as the following: for lower temperature, the CT effect between VOPc and F_{16}CuPc becomes weak and the contact between the organic material and the electrodes lose their ohmic contact properties. Thus, the current is mainly governed by the Schottky barrier. For higher temperature and higher bias, the current depends on the charge transport ability which is limited by the hopping mobility. For higher temperature and lower bias, the ohmic current is dominated by the temperature dependent carrier density which is provided by the CT between VOPc and F_{16}CuPc. In the left part of the curves which are subject to higher activation energy, the activation energy E_a is plotted for each bias voltage.

As shown in Figure 3c, the E_a as a function of applied voltage V can provide more direct information about the thermal activated transport progress above 125 K. The plotted region can be divided into three regimes. Region A under low bias corresponds to the ohmic conduction region. The amount of current is mainly determined by the density of carriers. With low electric field, the injected mobile carriers are much lower than the carriers generated from CT effect between VOPc and F_{16}CuPc, therefore, the current is mainly due to the movement of CT mobile carriers, of which the density is subject to thermal activation. The activation energy E_a is almost constant with decreasing voltage, and calculated to be about 0.41 eV for the voltages below 0.7 V, which is regarded as the CT energy between VOPc and F_{16}CuPc. Region C under high bias conditions corresponds to the complete SCL region. As discussed above, the amount of current is mainly determined by the

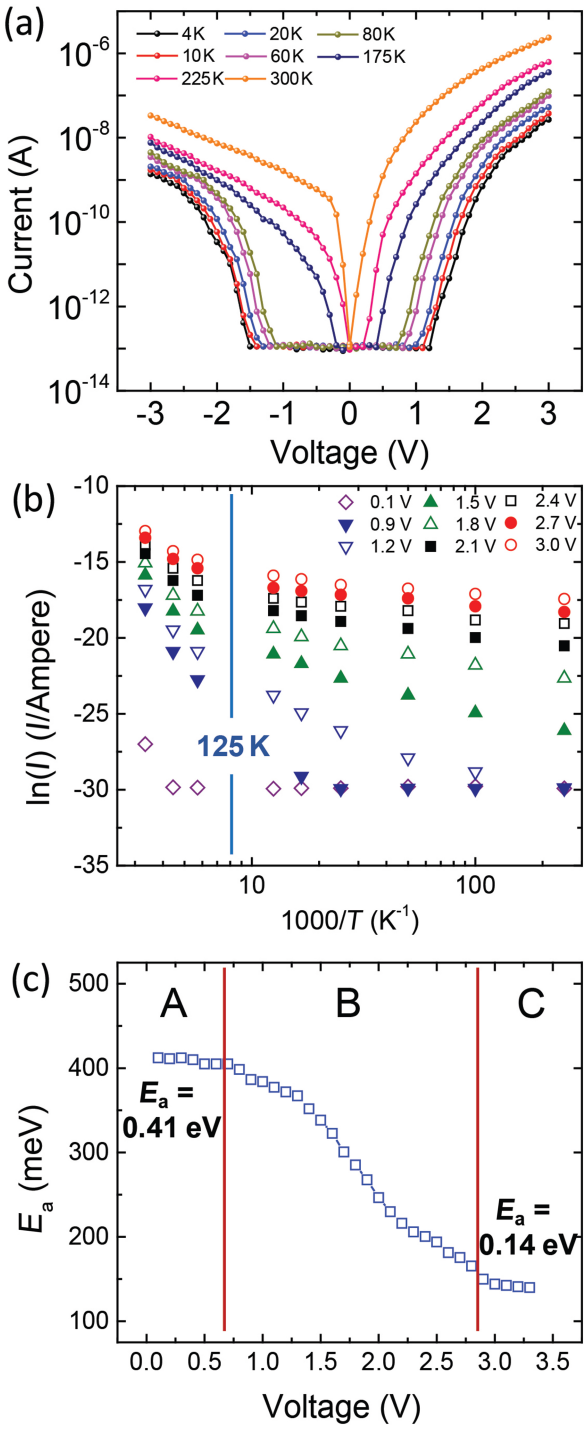

Figure 3: (a) Current–voltage characteristics of Au/F_{16}CuPc/VOPc/F_{16}CuPc/Au diode as a function of temperature. (b) Current–temperature characteristics at different voltages. (c) Applied voltage dependence of thermal activation energy.

hopping mobility as the amount of injected carriers are much higher than the carriers generated from CT. The activation energy E_a is almost constant with increasing voltage, and calculated to be about 0.14 eV for the voltages above 2.8 V, which is regarded as the activation energy for the carrier hopping transport [34,35,38]. Region B is the transition region between ohmic and SCL current. Here, the activation energy decreases due to the increase of the charge carrier injection with increasing bias, while the hopping motion in nanocrystals gradually dominates the charge transport. This corresponds to the *I–V* trace in Figure 2b, which shows a smooth transition from ohmic to SCL. As shown in the upper inset of Figure 2b, the voltage dependence of the conductance (G) demonstrates that with increasing bias the conductance increases non-linearly and with decreasing temperature the conductance decreases correspondingly. It is worthy to compare here with the diodes consisting of self-assembly monolayer contacted with rolled-up tube electrodes, which is previously reported by some of the authors of this contribution [17]. The transport in such diode is subject to tunneling and field emission mechanisms due to the ultra-thin smooth film, while in the present report the thermal activated transport via bulk nanostructures dominates the transport progress.

Conclusion

In summary, in this work we investigated the charge transport in F_{16}CuPc/VOPc/F_{16}CuPc organic nanocrystal diodes, which are contacted by robust metallic rolled-up nanomembranes. The temperature dependent measurement results demonstrate in the temperature region above 125 K carrier injection, and the hopping mechanism dominates the transport through the organic nanocrystals. These conclusions prove that with the assistance of the charge transfer effect, the soft yet robust contacts generated from rolled-up nanotechnology provide an efficient route for fabricating reliable organic nanocrystal electronic and spintronic devices.

Acknowledgements

The authors acknowledge Paul Plocica and Eric Pankenin for their technical support. This research was financially supported by the Deutsche Forschungsgemeinschaft DFG Research Unit 1154 “Towards Molecular Spintronics” and Europäischen Sozialfonds (ESF).

References

1. Reineke, S.; Lindner, F.; Schwartz, G.; Seidler, N.; Walzer, K.; Lüssem, B.; Leo, K. *Nature* **2009,** *459,* 234–238. doi:10.1038/nature08003
2. McCarthy, M. A.; Liu, B.; Donoghue, E. P.; Kravchenko, I.; Kim, D. Y.; So, F.; Rinzler, A. G. *Science* **2011,** *332,* 570–573. doi:10.1126/science.1203052
3. Di, C.-a.; Zhang, F.; Zhu, D. *Adv. Mater.* **2013,** *25,* 313–330. doi:10.1002/adma.201201502
4. Sirringhaus, H.; Tessler, N.; Friend, R. H. *Science* **1998,** *280,* 1741–1744. doi:10.1126/science.280.5370.1741
5. Forrest, S. R.; Thompson, M. E. *Chem. Rev.* **2007,** *107,* 923–925. doi:10.1021/cr0501590
6. Dediu, V. A.; Hueso, L. E.; Bergenti, I.; Taliani, C. *Nat. Mater.* **2009,** *8,* 707–716. doi:10.1038/nmat2510
7. Vilan, A.; Shanzer, A.; Cahen, D. *Nature* **2000,** *404,* 166–168. doi:10.1038/35004539
8. Song, H.; Reed, M. A.; Lee, T. *Adv. Mater.* **2011,** *23,* 1583–1608. doi:10.1002/adma.201004291
9. Ratner, M. *Nat. Nanotechnol.* **2013,** *8,* 378–381. doi:10.1038/nnano.2013.110
10. Ortmann, F.; Radke, K. S.; Günther, A.; Kasemann, D.; Leo, K.; Cuniberti, G. *Adv. Funct. Mater.* **2015,** *25,* 1933–1954. doi:10.1002/adfm.201402334
11. Yang, J.; Yan, D.; Jones, T. S. *Chem. Rev.* **2015,** *115,* 5570–5603. doi:10.1021/acs.chemrev.5b00142
12. Forrest, S. R. *Chem. Rev.* **1997,** *97,* 1793–1896. doi:10.1021/cr941014o
13. Wang, W.; Chi, L. *Acc. Chem. Res.* **2012,** *45,* 1646–1656. doi:10.1021/ar200299w
14. Haick, H.; Cahen, D. *Acc. Chem. Res.* **2008,** *41,* 359–366. doi:10.1021/ar700099n
15. Metzger, R. M. *Chem. Rev.* **2015,** *115,* 5056–5115. doi:10.1021/cr500459d
16. Xiang, D.; Wang, X.; Jia, C.; Lee, T.; Guo, X. *Chem. Rev.* **2016,** *116,* 4318–4440. doi:10.1021/acs.chemrev.5b00680
17. Bof Bufon, C. C.; Arias Espinoza, J. D.; Thurmer, D. J.; Bauer, M.; Deneke, C.; Zschieschang, U.; Klauk, H.; Schmidt, O. G. *Nano Lett.* **2011,** *11,* 3727–3733. doi:10.1021/nl201773d
18. Bof Bufon, C. C.; Vervacke, C.; Thurmer, D. J.; Fronk, M.; Salvan, G.; Lindner, S.; Knupfer, M.; Zahn, D. R. T.; Schmidt, O. G. *J. Phys. Chem. C* **2014,** *118,* 7272–7279. doi:10.1021/jp409617r
19. Jalil, A. R.; Chang, H.; Bandari, V. K.; Robaschik, P.; Zhang, J.; Siles, P. F.; Li, G.; Bürger, D.; Grimm, D.; Liu, X.; Salvan, G.; Zahn, D. R. T.; Zhu, F.; Wang, H.; Yan, D.; Schmidt, O. G. *Adv. Mater.* **2016,** *28,* 2971–2977. doi:10.1002/adma.201506293
20. Loo, Y.-L.; Lang, D. V.; Rogers, J. A.; Hsu, J. W. P. *Nano Lett.* **2003,** *3,* 913–917. doi:10.1021/nl034207c
21. Akkerman, H. B.; Blom, P. W. M.; de Leeuw, D. M.; de Boer, B. *Nature* **2006,** *441,* 69–72. doi:10.1038/nature04699
22. Haick, H.; Niitsoo, O.; Ghabboun, J.; Cahen, D. *J. Phys. Chem. C* **2007,** *111,* 2318–2329. doi:10.1021/jp065357p
23. Bonifas, A. P.; McCreery, R. L. *Nat. Nanotechnol.* **2010,** *5,* 612–617. doi:10.1038/nnano.2010.115
24. Magnussen, O. M.; Ocko, B. M.; Deutsch, M.; Regan, M. J.; Pershan, P. S.; Abernathy, D.; Grübel, G.; Legrand, J.-F. *Nature* **1996,** *384,* 250–252. doi:10.1038/384250a0
25. Selzer, Y.; Salomon, A.; Cahen, D. *J. Am. Chem. Soc.* **2002,** *124,* 2886–2887. doi:10.1021/ja0177511
26. Reed, M. A.; Zhou, C.; Muller, C. J.; Burgin, T. P.; Tour, J. M. *Science* **1997,** *278,* 252–254. doi:10.1126/science.278.5336.252
27. Zhou, C.; Deshpande, M. R.; Reed, M. A.; Jones, L., II; Tour, J. M. *Appl. Phys. Lett.* **1997,** *71,* 611–613. doi:10.1063/1.120195
28. Kushmerick, J. G.; Naciri, J.; Yang, J. C.; Shashidhar, R. *Nano Lett.* **2003,** *3,* 897–900. doi:10.1021/nl034201n
29. Xiang, D.; Jeong, H.; Lee, T.; Mayer, D. *Adv. Mater.* **2013,** *25,* 4845–4867. doi:10.1002/adma.201301589

30. Mei, Y.; Solovev, A. A.; Sanchez, S.; Schmidt, O. G. *Chem. Soc. Rev.* **2011,** *40,* 2109–2119. doi:10.1039/c0cs00078g
31. Streubel, R.; Lee, J.; Makarov, D.; Im, M.-Y.; Karnaushenko, D.; Han, L.; Schäfer, R.; Fischer, P.; Kim, S.-K.; Schmidt, O. G. *Adv. Mater.* **2014,** *26,* 316–323. doi:10.1002/adma.201303003
32. de Silva, A. P.; Uchiyama, S. *Nat. Nanotechnol.* **2007,** *2,* 399–410. doi:10.1038/nnano.2007.188
33. Lörtscher, E. *Nat. Nanotechnol.* **2013,** *8,* 381–384. doi:10.1038/nnano.2013.105
34. Coropceanu, V.; Cornil, J.; da Silva Filho, D. A.; Olivier, Y.; Silbey, R.; Brédas, J.-L. *Chem. Rev.* **2007,** *107,* 926–952. doi:10.1021/cr050140x
35. Kao, K. C.; Hwang, W. *Electrical Transport in Solids: With particular reference to organic semiconductors;* Pergamon: New York, 1981.
36. Zhu, F.; Yang, J.; Song, D.; Li, C.; Yan, D. *Appl. Phys. Lett.* **2009,** *94,* 143305. doi:10.1063/1.3118581
37. Selzer, Y.; Cabassi, M. A.; Mayer, T. S.; Allara, D. L. *J. Am. Chem. Soc.* **2004,** *126,* 4052–4053. doi:10.1021/ja039015y
38. Craciun, N. I.; Wildeman, J.; Blom, P. W. M. *Phys. Rev. Lett.* **2008,** *100,* 056601. doi:10.1103/PhysRevLett.100.056601

License and Terms

BEILSTEIN JOURNAL OF NANOTECHNOLOGY

Synthesis of $[Fe(L_{eq})(L_{ax})]_n$ coordination polymer nanoparticles using blockcopolymer micelles

Christoph Göbel[1], Ottokar Klimm[1], Florian Puchtler[2], Sabine Rosenfeldt[3], Stephan Förster[3] and Birgit Weber[*1]

Full Research Paper

Open Access

Address:
[1]Inorganic Chemistry II, University of Bayreuth, Universitätsstr. 30, 95440 Bayreuth, Germany, [2]Inorganic Chemistry I, University of Bayreuth, Universitätsstr. 30, 95440 Bayreuth, Germany and [3]Physical Chemistry I and Bavarian Polymer Institute, University of Bayreuth, Universitätsstr. 30, 95440 Bayreuth, Germany

Email:
Birgit Weber* - weber@uni-bayreuth.de

* Corresponding author

Keywords:
block copolymer; composite; nanoparticles; self-assembly; spin crossover

Beilstein J. Nanotechnol. **2017,** *8,* 1318–1327.
doi:10.3762/bjnano.8.133

Received: 01 February 2017
Accepted: 24 May 2017
Published: 26 June 2017

This article is part of the Thematic Series "Towards molecular spintronics".

Guest Editor: G. Salvan

Abstract

Spin-crossover compounds are a class of materials that can change their spin state from high spin (HS) to low spin (LS) by external stimuli such as light, pressure or temperature. Applications demand compounds with defined properties concerning the size and switchability that are maintained when the compound is integrated into composite materials. Here, we report the synthesis of $[Fe(L_{eq})(L_{ax})]_n$ coordination polymer (CP) nanoparticles using self-assembled polystyrene-*block*-poly(4-vinylpyridine) (PS-*b*-P4VP) block copolymer (BCP) micelles as template. Variation of the solvent (THF and toluene) and the rigidity of the axial ligand L_{ax} (L_{ax} = 1,2-di(pyridin-4-yl)ethane) (bpea), *trans*-1,2-di(pyridin-4-yl)ethene (bpee), and 1,2-di(pyridin-4-yl)ethyne) (bpey); L_{eq} = 1,2-phenylenebis(iminomethylidyne)-bis(2,4-pentanedionato)(2−)) allowed the determination of the preconditions for the selective formation of nanoparticles. A low solubility of the CP in the used solvent and a high stability of the Fe–L bond with regard to ligand exchange are necessary for the formation of composite nanoparticles where the BCP micelle is filled with the CP, as in the case of the $[FeL_{eq}(bpey)]_n$@BCP. Otherwise, in the case of more flexible ligands or ligands that lead to high spin complexes, the formation of microcrystals next to the CP–BCP nanoparticles is observed above a certain concentration of $[Fe(L_{eq})(L_{ax})]_n$. The core of the nanoparticles is about 45 nm in diameter due to the templating effect of the BCP micelle, independent of the used iron complex and $[Fe(L_{eq})(L_{ax})]_n$ concentration. The spin-crossover properties of the composite material are similar to those of the bulk for $FeL_{eq}(bpea)]_n$@BCP while pronounced differences are observed in the case of $[FeL_{eq}(bpey)]_n$@BCP nanoparticles.

Introduction

Nanomaterials and especially nanocomposites of coordination polymers (CPs) and (porous) coordination networks are of great interest in current research because of their various applications as sensors, data-storage devices, catalysts or contrast agents [1-5]. For these applications the formation of stable, uniform and monodisperse particles with defined properties is necessary. Synthetic procedures for nanoparticles with size control (gold [6,7], metal oxides [8,9]) and/or shape control (gold and silver [10]) are already well known. The reduction of metal salts is very common for noble metals [11], while (fast) precipitation or inverse-micelle technique are often used for metal oxides (mostly magnetite) [12]. For coordination polymers (CP) or networks a limited amount of methods are applicable because of the very demanding reaction conditions and/or incompatible reactants. Recently we demonstrated that the use of block copolymers (BCPs) is a highly promising and easy approach for the size control of CPs [13]. BCPs form micellar structures through self-assembly in specific solvents and can therefore be used as nanoreactors [14-16]. Using this approach, a very controlled miniaturisation of coordination polymers or networks can be envisioned, provided it is easily transferable to other systems. In this work we will analyse which preconditions need to be fulfilled for a successful synthesis of uniform CP–BCP nanoparticles.

Coordination polymers with spin crossover (SCO) properties are well known in the literature [4,5,17,18], but their miniaturisation into precisely defined nanomaterials with SCO properties comparable to those of the bulk material is still in its infancy [19-23]. SCO materials can be switched by external stimuli such as temperature, pressure or light between a high spin (HS) and a low spin (LS) state [5,18]. Switching between these two states alters physical properties such as magnetism, structure or colour, which make these materials interesting for sensors [2,24-26], display devices [27-29] or as functional contrast agents [30-34]. The SCO properties deeply depend on the precise control of size and crystallinity of the nanocomposite. Most commonly the inverse-micelle technique is used for the preparation of nanoparticles [35-39]. However, the spin-crossover properties of the bulk are often lost upon miniaturisation and only few examples preserving the hysteresis (bistability) in a nanostructured system are known [21,40-43]. This is most likely due to a loss of the crystallinity of the particles. Especially SCO complexes are highly sensitive to small changes in the crystal packing and thus excellently suited to investigate the impact of nanostructuration of the material. In our recent work [13] we used the block copolymer polystyrene-*b*-poly(4-vinylpyridine) (PS-*b*-P4VP) to prepare spherical nanoparticles of the 1D spin-crossover coordination polymer $[FeL_{eq}(bipy)]_n$. We were able control the crystallinity of the $[FeL_{eq}(bipy)]_n$ core through successive addition of starting material and by variation of the reaction time and temperature. Having a high crystallinity of the core, the SCO properties were closer to those of the bulk material (thermal hysteresis loop).

We herein report the synthesis of three further coordination polymer block copolymer nanocomposites (CP–BCP) using the same synthesis strategy. This allows us to investigate the influence of the coordination polymer on the formation and the SCO activity of the final nanocompound. The CPs differ in the axial ligands (L_{ax}), namely 1,2-di(pyridin-4-yl)ethane (bpea), *trans*-1,2-di(pyridin-4-yl)ethene (bpee) and 1,2-di(pyridin-4-yl)ethyne

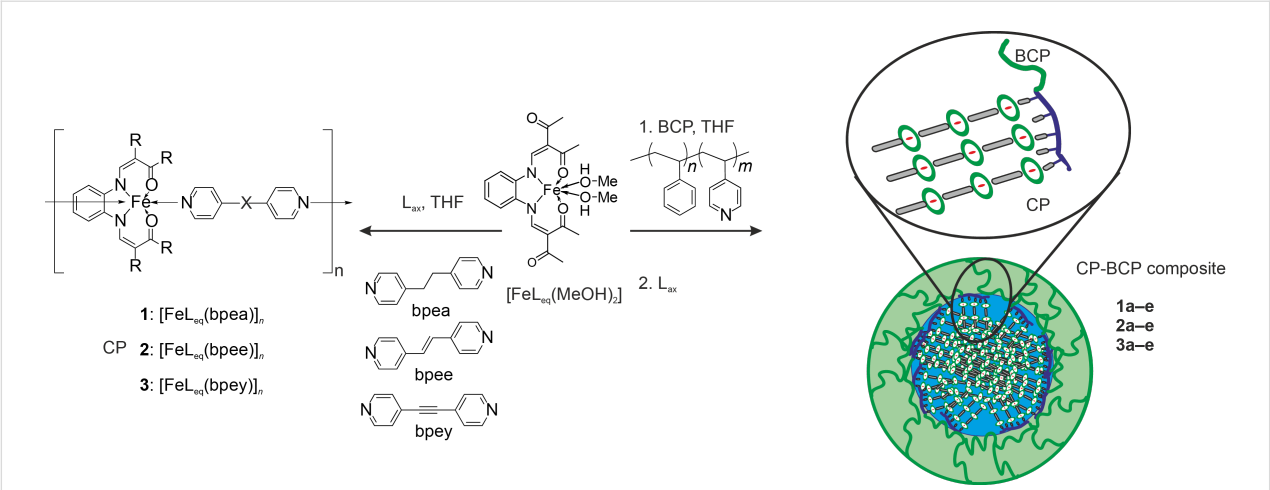

Scheme 1: Synthesis of the three different coordination polymers $[FeL_{eq}(bpea)]_n$ (**1**), $[FeL_{eq}(bpee)]_n$ (**2**) and $[FeL_{eq}(bpey)]_n$ (**3**) and the respective coordination polymer–block copolymer composites (CP–BCP) $[FeL_{eq}(bpea)]_n$@BCP (**1a–e**), $[FeL_{eq}(bpee)]_n$@BCP (**2a–e**) and $[FeL_{eq}(bpey)]_n$@BCP (**3a–e**).

(bpey) (Scheme 1). The ligands were chosen because of their different flexibility. From the synthesis of the bulk complexes it is known, that an increasing flexibility of the ligand leads to an increase in solubility of the obtained CP [44,45]. This way we can investigate the impact of the solubility of the CP on the selective formation of nanoparticles in the BCP micelle cores. In Scheme 1, the general approach and the abbreviations used for the different samples are given.

Results and Discussion

Bulk complexes

The magnetic properties of SCO coordination polymers often depend on solvent molecules included in the crystal packing [46-49]. To allow a comparison between bulk material and nanoparticles and to study the influence of nanostructuring on magnetism, the bulk complexes were synthesised in THF and their magnetic properties were investigated. $[FeL_{eq}(bpea)]_n$ and $[FeL_{eq}(bpee)]_n$ were already synthesised in methanol [44,50], the coordination polymer $[FeL_{eq}(bpey)]_n$ is described here for the first time. The coordination polymers **1**, **2** and **3** were synthesised by dissolving the iron(II) complex $[FeL_{eq}(MeOH)_2]$ and the respective axial ligand in THF. The solution was refluxed for 1 h. After cooling down overnight, the fine crystalline precipitate was filtered off and dried in vacuo to yield brown or dark violet powders. The crystals were too small for single-crystal X-ray structure analysis. In Figure 1, the magnetic properties of $[FeL_{eq}(bpea)]_n$ (**1**) and $[FeL_{eq}(bpey)]_n$ (**3**) as plot of the $\chi_M T$ product (χ_M = magnetic susceptibility, T = temperature) as a function of the temperature is given. Sample **1** is paramagnetic at RT with a $\chi_M T$ value of 3.25 $cm^3 \cdot K \cdot mol^{-1}$, typical for iron(II) in the HS state [51]. Upon cooling the $\chi_M T$ value remains constant down to 140 K where an abrupt, incomplete spin crossover occurs. In the first step, the $\chi_M T$ value descends to 1.78 $cm^3 \cdot K \cdot mol^{-1}$ at 120 K corresponding to about 50% of the iron centres in the HS state. Further cooling reveals a second, gradual and incomplete step with a $\chi_M T$ value of 0.93 $cm^3 \cdot K \cdot mol^{-1}$ at 50 K; about one third of the iron centres remains in the HS state. Upon heating, a 3 K wide hysteresis is observed in the region of the first step with $T_{1/2}\uparrow$ = 127 K and $T_{1/2}\downarrow$ = 130 K. In the temperature range between 75 and 100 K first a decrease and then an increase of the $\chi_M T$ product upon heating is observed. This is due to a kinetic trapping effect, often observed in this temperature region when the thermal spin transition temperature ($T_{1/2}$) and the transition temperature for the thermally trapped exited spin state (T_{TIESST}) are in close proximity [44,52-54]. In such a case the completeness of the spin crossover, in this case the second step, strongly depends on the scan rate used for the magnetic measurements. For the measurements presented in Figure 1, the settle mode was used, which corresponds to an approximate scan rate of 0.3 $K \cdot min^{-1}$. This allows the system to equilibrate at each temperature step

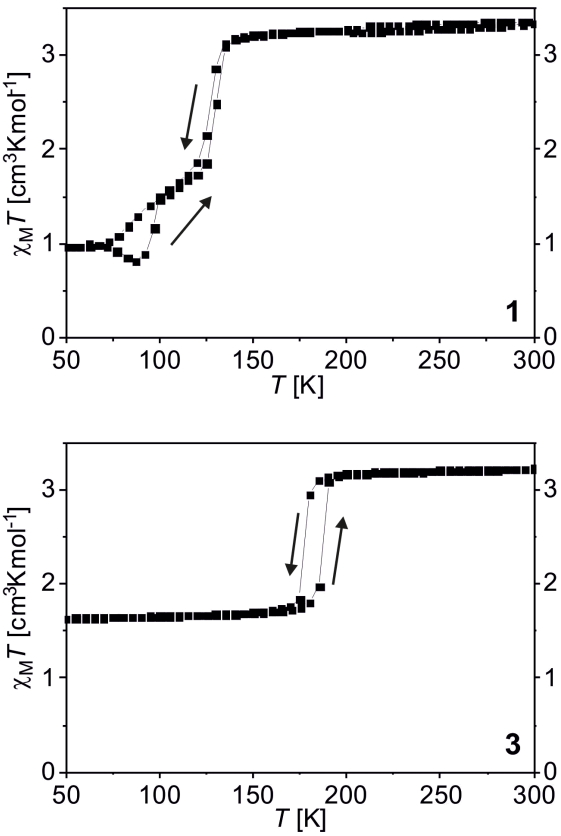

Figure 1: Magnetic susceptibility data for the coordination polymers $[FeL_{eq}(bpea)]_n$ (**1**) and $[FeL_{eq}(bpey)]_n$ (**3**), which undergo spin crossover.

where a measurement point is taken and kinetic effects can be considered to be almost irrelevant. Despite the very slow measurements, upon cooling a part of the iron centres remain trapped in the HS state. Upon slow heating they equilibrate to the LS state as long as the temperature is below the thermal spin transition temperature, which leads to the observed decrease of the $\chi_M T$ product upon heating. An even slower scan rate would lead to a more complete spin transition and the disappearance of the decrease of the $\chi_M T$ product upon heating while a higher scan leads to the complete disappearance of the second step. The two-step behaviour is similar to the one observed for $\{[FeL_{eq}bpea)]\cdot 0.25MeOH\}_n$, where the temperatures differ slightly and the second step is complete [44]. The differences due to the impact of the different solvents are also reflected in the powder diffraction patterns (Supporting Information File 1, Figure S1) in which some of the reflexes are shifted compared to the sample prepared in methanol. Sample **2** ($[FeL_{eq}(bpee)]_n$) is paramagnetic at room temperature with a $\chi_M T$ value of 3.20 $cm^3 \cdot K \cdot mol^{-1}$ (Supporting Information File 1, Figure S2). Upon cooling the sample remains in the HS state over the whole temperature range, as already reported for the complex synthesised from methanol [50]. Sample **3** ($[FeL_{eq}(bpey)]$) is

paramagnetic at room temperature with a $\chi_M T$ value of 3.23 $cm^3 \cdot K \cdot mol^{-1}$, typical for iron(II) complexes in the HS state (bottom of Figure 1). Upon cooling the $\chi_M T$ value remains almost constant down to 190 K ($\chi_M T$ value: 3.14 $cm^3 \cdot K \cdot mol^{-1}$), where an abrupt and incomplete spin transition occurs with about 50% of the iron centres involved. The $\chi_M T$ value drops to 1.73 $cm^3 \cdot K \cdot mol^{-1}$ at 165 K and no further changes are observed down to 50 K ($\chi_M T$ value: 1.63 $cm^3 \cdot K \cdot mol^{-1}$). Upon heating up to 300 K an abrupt spin transition takes place revealing a hysteresis with a width of 10 K and $T_{1/2}\downarrow$ = 177 K and $T_{1/2}\uparrow$ = 187 K. For the sake of completeness, the complex was also synthesised from methanol yielding the same spin-crossover properties, in good agreement with the absence of solvent molecules in the crystal packing. Mössbauer spectra were collected for all three samples to verify the HS state at room temperature. The spectra (Supporting Information File 1, Figure S3) reveal one quadrupole split doublet in each case with parameters for the quadrupole splitting ΔE_Q and an isomer shift δ (Supporting Information File 1, Table S1) in the range expected for iron(II) HS complexes of this ligand type [55]. The steps and the incomplete spin crossover observed in the magnetic measurements could be due to inequivalent iron centres [56,57]. The Mössbauer spectra do not support this as no line broadening (FWHM Γ in Supporting Information File 1, Table S1) is observed and the doublet is very symmetric in each case. Thus the steps observed in the transition curve are due to the packing of the CP in the crystal and will strongly depend on the crystallinity of the material.

Synthesis of the nanocomposite

For the CP–BCP composites $[FeL_{eq}(bpea)]_n$@BCP (**1a**–**e**), $[FeL_{eq}(bpee)]_n$@BCP (**2a**–**e**) and $[FeL_{eq}(bpey)]_n$@BCP (**3a**–**e**), the starting iron(II) complex $[FeL_{eq}(MeOH)_2]$ and the block copolymer were dissolved in THF and refluxed for 2 h. After cooling down to room temperature, the respective bridging ligand was added and the mixture was refluxed again for 1 h. Depending on the number of additions of starting material, either the solvent is removed by cold distillation (1 cycle, samples **1a**, **2a**, **3a**) or a further cycle of addition of $[FeL_{eq}(MeOH)_2]$ and axial ligand (simultaneously for all further cycles) followed by reflux for 1 h was performed prior to solvent removal (samples **1b**–**e**, **2b**–**e**, **3b**–**e** for 2 to 5 cycles). The resulting solids were dried in vacuo. IR spectroscopy was used to follow the formation of the coordination polymer in the BCP matrix. The corresponding spectra are given in Supporting Information File 1, Figure S4. The increasing relative intensity of the C=O stretching vibration of $[FeL_{eq}]$ clearly indicates the formation of the coordination polymer in the matrix. Elemental analysis also confirms the increasing concentration of the coordination polymer in the BCP micelle with an increasing nitrogen content.

Room-temperature Mössbauer spectra were collected of $[FeL_{eq}(bpea)]_n$@BCP after four and after five cycles (**1d** and **1e**) and of $[FeL_{eq}(bpey)]_n$@BCP after four and five cycles (**3d** and **3e**) to get a deeper insight into the sample composition. Due to the long measurement time of the very diluted (low iron content) and soft (low Lamb–Mössbauer factor) composite materials, only the more crystalline samples with a high CP amount (**d** and **e**) showing spin crossover were characterised. The corresponding spectra are given in Figure 3 (**1d** and **3e**) and in Supporting Information File 1, Figure S5. The Mössbauer parameters are summarised in Supporting Information File 1, Table S2. For the composite materials, different iron species are possible due to the coordination of the starting complex $[Fe(L_{eq})]$ to the vinylpyridine parts of the equatorial ligand, which can be distinguished using Mössbauer spectroscopy. Sample **1d** shows two different doublets which correspond to an iron(II) HS and iron(II) LS species (75% and 25%). The LS species derives from two P4VP units coordinated to the iron centre as already shown [13,58], with the formula $[Fe(L_{eq})(VP)_2]$ (VP = vinyl pyridine) The HS species corresponds to the desired $[Fe(L_{eq})(bpea)]$ unit. For sample **1e** again two doublets are observed with a similar HS/LS ratio (Supporting Information File 1 ,Table S2). The sample **3d** also shows two different iron species of which one corresponds to an iron(II) in the HS state and the other one to an iron(II) in the LS state. However, the HS/LS ratio changes to 83%:17%. For sample **3e** only one doublet is observed that can be assigned to an iron(II) HS species. It concludes that in the case of $[FeL_{eq}(bpey)]_n$@BCP the HS fraction increases with higher cycles since more or longer coordination polymer is formed in the BCP micelle, in agreement with previous observations for $[FeL_{eq}(bipy)]_n$@BCP[13,58]. In the case of $[FeL_{eq}(bpea)]_n$@BCP a different behaviour is observed that is indicative for differences in the sample composition.

Characterisation of the nanocomposite

Particle sizes of the nanocomposites were determined by dynamic light scattering (DLS) in solution, transmission electron microscopy (TEM) and powder X-ray diffraction (PXRD) in the solid. The hydrodynamic diameter of the polymeric micelles loaded with the CP measured by DLS is constant within the error of the measurement throughout all measured samples with sizes around 150 nm (Supporting Information File 1, Figure S6). This is in agreement with the results reported previously for similar composite nanoparticles with 4,4′-bipyridine as bridging axial ligand [13]. In Figure 2, a TEM picture and the size distribution obtained from TEM and DLS of **3e** ($[FeL_{eq}(bpey)]_n$@BCP, five cycles) is given as typical representative of all samples. A detailed characterisation of all samples with TEM is given in Supporting Information File 1, Table S3. The TEM picture of **3e** in Figure 2a clearly reveals the for-

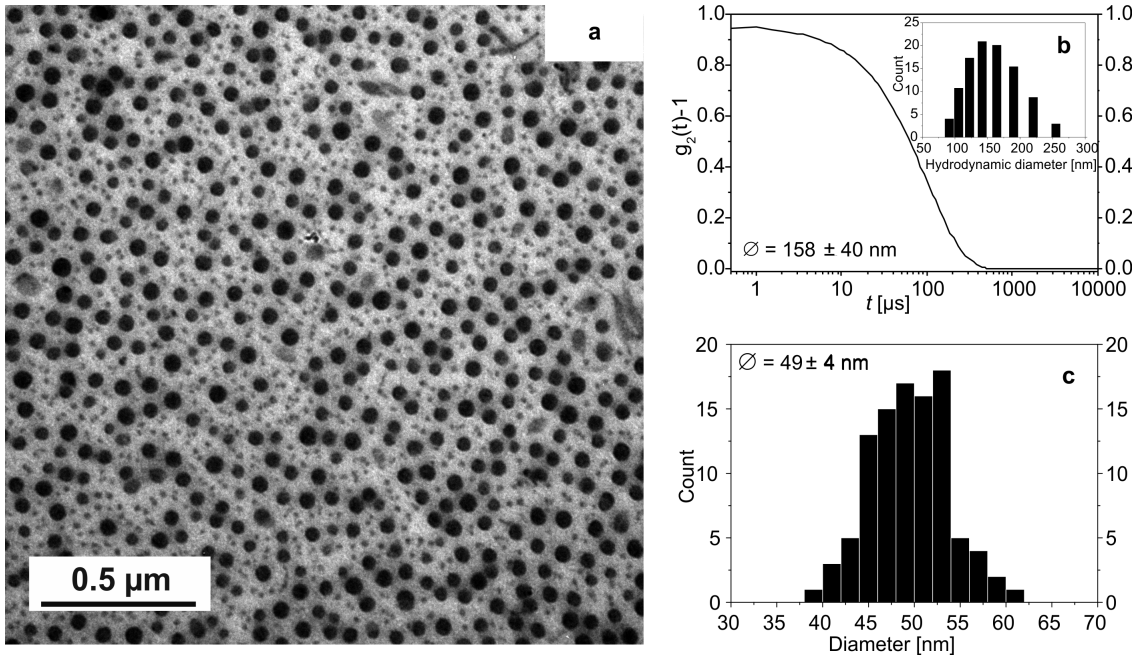

Figure 2: Characterisation of CP–BCP composite micelles. a) TEM picture of **3e** ($[FeL_{eq}(bpey)]_n$@BCP, five cycles) illustrating the core–shell nature of the particles. b) Autocorrelation function from dynamic light scattering of **3e** in THF (43 wt %) with size histogram. c) Size histogram of the core from the TEM picture given in panel a).

mation of spherical nanoparticles with a core–shell nature. The differences in contrast of the iron-containing CP and the BCP prove that the CP nanoparticles are solely formed in the core of the nanocomposite.

The particle core diameter is significantly smaller than the hydrodynamic radius because of the polymeric nature of the BCP (solvent-swollen). Within the error of the measurement, the NP core size is in the same order of magnitude for all samples with an average size of 45 nm (Table 1), demonstrating the excellent size control by the micelles themselves. The NP core size is independent of the number of cycles and independent of the used coordination polymer clearly demonstrating the high potential of the templating effect of BCP micelles (cage effect). This in in very good agreement with our first observation on the similar system with 4,4′-biypridine as bridging ligand. It can be explained with the assumption, that the nanocomposite is very amorphous at the beginning with a low density in the core. With increasing coordination polymer concentration the crystallinity of the core and therefore its density increases, while the size does not change significantly [13].

In order to investigate, whether the flexibility of the used bridging ligand has an impact on regioselectivity of the nanoparticle core formation, the samples were carefully analysed for the observation of microcrystals as function of the increasing CP concentration (number of cycles, e.g., $[FeL_{eq}(bpea)]_n$@BCP = **1a**–**e** for one to five cycles of addition of starting material) in the composite material. The results are summarised in Table 1.

The first microcrystals (3–6 µm) were observed for bpee as bridging ligand after four cycles of addition of starting material (**2d**), while for the more flexible bpea the first microcrystals are observed only after five cycles (**1e**, 1.5–2.0 µm). In the case of

Table 1: Investigation of the core size [nm] and crystallinity of the CP-BCP composite obtained from TEM. "MC" denotes the observation of microcrystals.

L_{ax}	cycles				
	1 (**a**)	2 (**b**)	3 (**c**)	4 (**d**)	5 (**e**)
bpea (1a–e)	42 ± 5	46 ± 4	49 ± 4	46 ± 4	49 ± 4/MC
bpee (2a–e)	40 ± 4	46 ± 5	42 ± 4	48 ± 4/MC	47 ± 4/MC
bpey (3a–e)	48 ± 5	46 ± 4	49 ± 6	49 ± 4	49 ± 4
bipy [13]	52 ± 8	57 ± 8	62 ± 13	44 ± 6	49 ± 5

the more rigid bpey, no microcrystals are observed. This cannot solely be explained with the rigid nature of the ligand, which increases in the order bpea < bpee < bpey. One possibility to explain the observed order is to consider the stability of the complexes with regard to M–L ligand exchange with excess axial ligands and/or solvent molecules. For octahedral complexes, a weak ligand field splitting leads to the occupation of antibonding orbitals (HS complexes) and by this supports ligand exchange. A fast ligand exchange will increase the probability of the formation of microcrystals outside the BCP micelle. In this case the templating effect of the BCP micelles does not work. In agreement with this consideration, the pure HS complex $[FeL_{eq}(bpee)]_n$ with the weakest ligand field splitting is the first one where microcrystals are observed, while for the spin-crossover complexes $[FeL_{eq}(bpea)]_n$, $[FeL_{eq}(bpey)]_n$ and the previously investigated $[FeL_{eq}(bipy)]_n$ the expected order with regard to the rigid nature of the ligand is observed. With increasing solubility of the complex (increasing flexibility of the ligand) in the solvent used for the synthesis of the nanomaterial, the probability for the formation of microcrystals outside the BCP micelles increases. In agreement with this, it was not possible to synthesise nanoparticles of the coordination polymer $[FeL_{eq}(bppa)]_n$ [44], when bppa = 1,3-di(pyridin-4-yl)propane, a very flexible ligand (high solubility), is used. Syntheses were also performed in toluene to investigate the influence of the solvent on the nanoparticle synthesis. It should be pointed out that previous investigations showed that the complexes have a higher solubility in toluene compared to tetrahydrofuran. In agreement with this, first microcrystals were observed already after two cycles for all ligands. In Supporting Information File 1, Figure S7, a TEM picture of $[FeL_{eq}(bpea)]_n$@BCP after two cycles synthesised in toluene is given as typical representative. Thus the higher solubility of the coordination polymers in toluene favours the formation of microcrystals outside of the block copolymer micelle and reduces the regioselectivity.

The influence of the CP concentration on the crystallinity of the CP–BCP nanocomposite core was investigated using PXRD. In Supporting Information File 1, Figure S8, the PXRD patterns of the composite materials are compared with those of the bulk materials **1**–**3**. In all cases, the crystallinity of the particles increases with higher CP concentration, which is indicated by sharper reflexes. It should be pointed out, that in the case of the samples **3a**–**e** even after five cycles some of the prominent reflexes observed for the bulk material are missing. Either the crystallinity of the obtained NPs is still very low or a different packing compared to the bulk material is obtained.

In Figure 3 (**1d** and **3e**) and Supporting Information File 1, Figure S9 (**1d,e**, **2d,e** and **3d,e**) the $\chi_M T$-versus-T plots of the composite materials after four and five cycles are given. Previous investigations showed, that amorphous nanoparticles

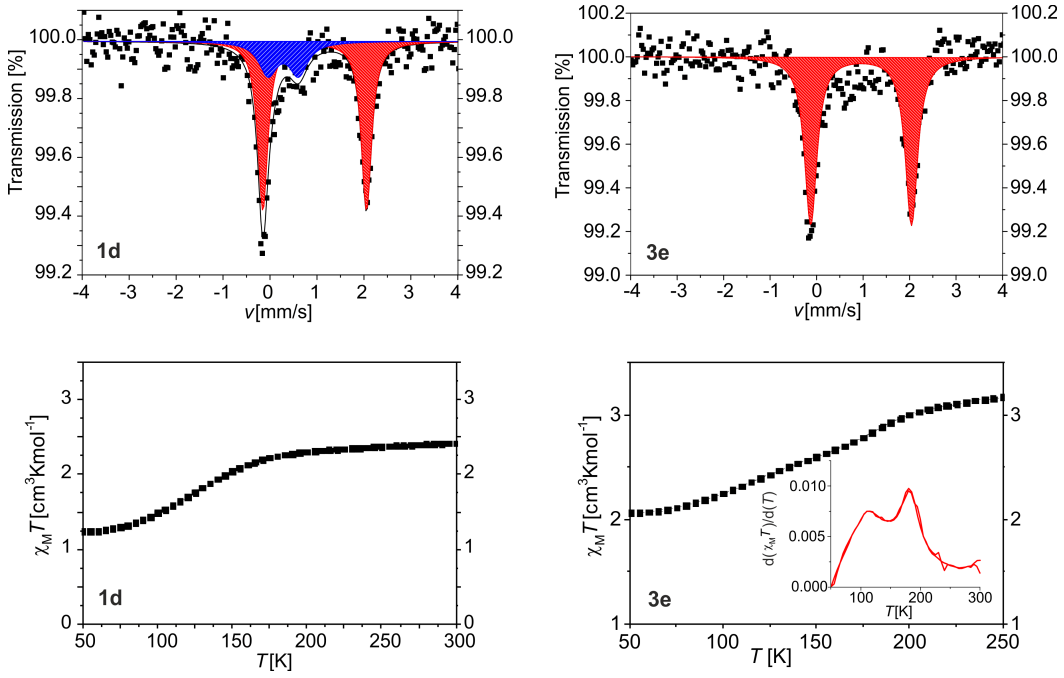

Figure 3: Characterisation of the magnetic properties of **1d** and **3e** Top: Mössbauer spectra of **1d** (left) and **3e** (right). Bottom: Magnetic susceptibility data displayed as $\chi_M T$ vs T of **1d** (left) and **3e** (right). In the case of **3e** in the inset the first derivative of the $\chi_M T$ vs T plot is given to illustrate the steps in the transition curve more clearly.

of [FeL_{eq}(bipy)] (1–3 cycles) showed gradual and incomplete spin crossover very different to that of the bulk material [13]. Additionally, the samples **a**–**c** are magnetically very diluted and the change in the spin state of the few SCO-active iron centres is difficult to be reliably detected. An increasing crystallinity of the nanoparticles did change the spin crossover behaviour towards that of the bulk complexes. Consequently, magnetic measurements were done for the samples **d** and **e** after four and five cycles of addition of complex in the temperature range between 50 and 300 K in the cooling and heating mode. In the case of **1d**, a gradual spin transition is observed with about 30% of the iron centres involved and $T_{1/2}$ = 122 K, close to the first step of the bulk material. In contrast, sample **1e** (containing microcrystals) shows a less gradual but still incomplete spin crossover with a small hysteresis of 5 K. The $\chi_M T$ value is 3.25 $cm^3 \cdot K \cdot mol^{-1}$ at room temperature and decreases to 1.03 $cm^3 \cdot K \cdot mol^{-1}$ at 50 K with $T_{1/2}\downarrow$ of 109 K and $T_{1/2}\uparrow$ of 114 K. Interestingly, the step in the transition curve that is present in the bulk material is not observed for sample **1e**. **3d** shows a very gradual spin crossover in the temperature range between 100 and 225 K with about 30% of the iron centres involved. This is very different to the abrupt spin transition with hysteresis of the bulk material. For sample **3e**, also a very gradual spin crossover is observed upon cooling. Two steps can be distinguished around 175 K and 110 K (see first derivative in Figure 2c). While the first step is in a similar range as the one observed for the bulk material, the second step has no relation to the spin-crossover properties of the bulk material. This is in good agreement with the results from the PXRD measurements, where pronounced differences between the diffraction pattern of the bulk CP and the nanocomposite are observed. Apparently, a different crystalline polymorph is obtained. The $\chi_M T$ value is 2.07 $cm^3 \cdot K \cdot mol^{-1}$ at 50 K indicating that 65% of the iron centres are still in the HS state.

Conclusion

This work focused on the transfer of the concept for the formation of nanoparticles of coordination polymers in a block copolymer matrix. The central goal was to demonstrate that this concept of block copolymers as microreactors is not restricted to one specific coordination polymer and can easily be applied to other systems. Therefore, three coordination polymers have been chosen to be incorporated inside the block copolymer as nanoparticles. In our previous work [13] we did show that longer reaction times, higher reaction temperatures and higher amounts of CP in the BCP micelles (number of cycles) improve the crystallinity of the CP nanoparticle core while the cores size is almost constant. The improved crystallinity did change the SCO properties from gradual to abrupt with hysteresis. Here we show that the coordination polymer does not have an influence on the size of the CP–BCP composite and that the final size arises mainly from the BCP. In agreement with our previous observations, the NP size does not change significantly with increasing CP concentration in the BCP micelle. However, the formation of stable nanoparticles critically depends on the coordination polymer and the solvent used for the synthesis. The investigations reveal an interplay between two different effects: (1) The rigidity and stacking features of the bridging ligand influences the solubility of the CP and a low solubility is favourable for the selective formation of crystalline nanoparticles in the BCP micelle. (2) Weak-field ligands lead to HS complexes where anti-bonding orbitals are occupied. This supports ligand exchange and prevents the templating effect of the BCP micelle. We found that the CP–BCP composites with the most rigid ligand ([FeL_{eq}(bpey)]$_n$@BCP, **3a**–**e**) form the most stable crystalline nanoparticles that are spin-crossover active. For the HS complexes [FeL_{eq}(bpee)]$_n$@BCP, (**2a**–**e**), first microcrystals are observed after four cycles and for [FeL_{eq}(bpea)]$_n$@BCP, (**1a**–**e**) with the most flexible ligand microcrystals are observed after five cycles in THF. The differences observed for the SCO properties and the PXRD data of the bulk material **3** and the composite material **3e** are one further example for the influence of micelle formation on the crystallisation of a material [59].

Experimental

All syntheses were performed under inert conditions using argon 5.0 (purity ≥ 99.999%) and Schlenk technique. The synthesis of all samples was repeated at least twice. Polystyrene-*b*-poly(4-vinylpyridine) (PS-P4VP, purum, $M_W \approx 150.000$) was synthesised as described before [15]. 1,2-di(pyridin-4-yl)ethane) (bpea) and trans-1,2-di(pyridin-4-yl)ethene (bpee) were obtained from Sigma-Aldrich and used as received. Tetrahydrofurane (THF) p.a. and toluene were obtained from Sigma-Aldrich and degassed with argon for at least 30 min. [$FeL_{eq}(MeOH)_2$] was synthesized as described before [60]. The ligand bpey was synthesised according to the literature [61].

Synthesis

The same synthesis procedures were used for all samples independent of the used L_{ax}. Therefore, the general procedures are given for [FeL_{eq}(bpea)]$_n$ (**1**) and the composite materials [FeL_{eq}(bpea)]$_n$@BCP (**1a**–**e**), and the specific values for [FeL_{eq}(bpee)]$_n$ (**2**)/[FeL_{eq}(bpey)]$_n$ (**3**) and the composite materials [FeL_{eq}(bpee)]$_n$@BCP (**2a**–**e**)/[FeL_{eq}(bpey)]$_n$@BCP (**3a**–**e**) are given in brackets. The synthesis of the composite materials in toluene was done using the same procedures and amounts as described for THF. Due to the observation of microcrystals at a very early stage, the products were not characterized further.

1 (**2**/**3**): 200 mg (0.45 mmol) [$FeL_{eq}(MeOH)_2$] and 206 mg (204 mg/202 mg) (1.125 mmol, 2.5 equiv) bpea (bpee/bpey)

were dissolved in 20 mL THF in a 50 mL flask. The solution was refluxed for 1 h. After cool-down to room temperature, the solution was let for crystallisation overnight. The solid was filtered, washed with THF once and dried in vacuo to yield a brown (dark violet) powder. Elemental analysis, Anal. calcd for $C_{30}H_{30}N_4O_4Fe$ (**1**): C, 63.61; H, 5.34; N, 9.89; found: C, 62.91; H, 5.19; N, 9.22; (Anal. calcd for $C_{30}H_{28}N_4O_4Fe$ (**2**): C, 63.84; H, 5.00; N, 9.93; found: C, 63.15; H, 6.05; N, 9.18/Anal. calcd for $C_{30}H_{26}N_4O_4Fe$ (**3**): C, 64.07; H, 4.66; N, 9.96; found: C, 63.63; H, 4.77; N, 9.25).

1a, one cycle (**2a**/**3a**): 50 mg (0.33 µmol) PS-*b*-P4VP and 6.7 mg (15 µmol) [$FeL_{eq}(MeOH)_2$] were dissolved in 20 mL THF in a 50 mL flask. The solution was refluxed for 2 h. After, 6.9 mg (6.8 mg/6.8 mg) (37.5 µmol, 2.5 equiv) bpea (bpee/bpey) was added and refluxed again for 1 h. The solution was cooled down to room temperature and the solvent was removed via cold distillation to yield a brown, polymer-like solid. Elemental analysis, found: C, 64.96; H, 7.44; N, 2.82; (C, 71.23; H, 7.24; N, 3.10/C, 59.99; H, 7.46; N, 2.48).

1b, two cycles (**2b**/**3b**): The synthesis for one cycle was repeated. Prior to solvent removal, 6.7 mg (15 µmol) [$FeL_{eq}(MeOH)_2$] and 6.9 mg (6.8 mg/6.8 mg) (37.5 µmol, 2.5 equiv) bpea (bpee/bpey) were added for a new cycle and refluxed for another hour. The solvent was removed via cold distillation to yield a dark brown, polymer-like solid. Elemental analysis, found: C, 61.98; H, 7.35; N, 3.38; (C, 59.75; H, 7.43; N, 3.37/C, 57.18; H, 7.42; N, 3.05).

1c, three cycles (**2c**/**3c**): The synthesis for two cycles was repeated and one more cycle was carried out. 6.7 mg (15 µmol) [$FeL_{eq}(MeOH)_2$] and 6.9 mg (6.8 mg/6.8 mg) (37.5 µmol, 2.5 equiv) bpea (bpee/bpey) were added and refluxed for another hour before the solvent was removed via cold distillation to yield a dark brown, polymer-like solid. Elemental analysis, found: C, 69.43; H, 7.30; N, 5.00 (C, 63.08; H, 7.21; N, 3.71/C, 70.94; H, 6.67; N, 4.88).

1d, four cycles (**2d**/**3d**): The synthesis for three cycles was repeated and one more cycle was run. 6.7 mg (15 µmol) [$FeL_{eq}(MeOH)_2$] and 6.9 mg (6.8 mg/6.8 mg) (37.5 µmol, 2.5 equiv) bpea (bpee/bpey) were added and refluxed for another hour before the solvent was removed via cold distillation to yield a dark brown, polymer-like solid. Elemental analysis, found: C, 68.18; H, 6.55; N, 5.64 (C, 71.09; H, 6.79; N, 5.90/C, 68.04; H, 6.18; N, 5.48).

1e, five cycles (**2e**/**3e**): The synthesis for four cycles was repeated and one more cycle was run. 6.7 mg (15 µmol) [$FeL_{eq}(MeOH)_2$] and 6.9 mg (6.8 mg/6.8 mg) (37.5 µmol, 2.5 equiv) bpea (bpee/bpey) were added and refluxed for another hour before the solvent was removed via cold distillation to yield a dark brown, polymer-like solid. Elemental analysis, found: C, 68.09; H, 6.97; N, 5.86; (C, 68.12; H, 6.63; N, 6.09/C, 65.92; H, 6.04; N, 5.70).

The colour of the samples became darker with increasing cycles due to the higher amount of iron inside the samples. The increasing nitrogen content in the elemental analysis from **a**–**e** also confirms the increasing amount of coordination polymer in the samples.

Characterisation methods

Transmission electron microscopy: Transmission electron microscopy was carried out at a Zeiss CEM902 electron microscope (Zeiss, Oberkochen, Germany). Samples were dispersed in toluene applying vortex. The solution was dropped on a copper grid (mesh 200, Science Services, Munich). Electron acceleration voltage was set to 80 kV. Micrographs were taken with a MegaView III/iTEM image acquiring and processing system from Olympus Soft Imaging Systems (OSIS, Münster, Germany) and an Orius 830 SC200W/DigitalMicrograph system from Gatan (Munich, Germany). Particles size measurements were done with "ImageJ" image processing software by Wayne Rasband (National Institutes of Health, USA).

Elemental analysis: Carbon, nitrogen and hydrogen content was measured using a Vario EL III with acetanilide as standard. The samples were placed in tin boats and measured at least twice. The average of the measurements was used.

Infrared spectroscopy measurements: Transmission infrared spectra were collected using a Perkin Elmer Spectrum 100 FTIR (ATR). The samples were measured directly as solids.

Magnetic measurements: Magnetic susceptibility measurements were performed with a Quantum Design MPMS-XL-5 SQUID magnetometer. Field strength of 3 T was applied and a temperature range of 50–300 K was used to determine the temperature dependency of the magnetism and the spin-crossover behaviour. Settle mode was used in all measurements with a cooling and heating rate of 5 K/min. The samples were prepared in gelatine capsules placed in a plastic straw. The measured values were corrected for the diamagnetism of the sample holder, the polymer matrix (measured values) and the ligand (tabulated Pascal constants).

Dynamic light scattering: The samples were measured using a Malvern Instruments Zetasizer Nano ZS90 in glass cuvettes from Carl Roth GmbH + Co. KG at 25 °C. One measurement consisted of three consecutive runs.

Mössbauer spectroscopy: ^{57}Fe Mössbauer spectra were recorded in transmission geometry under constant acceleration using a conventional Mössbauer spectrometer with a 50 mCi ^{57}Co(Rh) source. The samples were sealed in the sample holder in an argon atmosphere. The spectra were fitted using Recoil 1.05 Mössbauer Analysis Software [62]. The isomer shift values are given with respect to α-Fe as reference at room temperature. At present, only measurements at room temperature are possible with the instrumental setup.

Powder X-ray diffraction: Powder X-ray diffraction data for all samples were collected at a STOE StadiP X-Ray diffractometer in transmission geometry in a 2θ range of 5–30°. Samples **1**, **2** and **3** were placed in capillaries and composite samples **1a**–**3e** were placed on flat surfaces. Cu Kα_1 radiation was used for the measurement and the radiation was detected with a Mythen 1K detector.

Supporting Information

In the Supporting Information the characterization of the bulk complexes (PXRD, magnetism, Mössbauer spectra and Mössbauer parameter), the full characterization of the composite materials **1a**–**e, 2a**–**e** and **3a**–**e** (IR spectra, DLS, PXRD, Mössbauer spectra and Mössbauer parameters of **1d**, **1e**, **3d** and **3e**, TEM pictures and magnetic measurements of **1d**, **1e**, **2d**, **2e**, **3d** and **3e**) and a TEM picture of the composite material synthesised from toluene are given.

Supporting Information File 1

Additional experimental data.
[http://www.beilstein-journals.org/bjnano/content/supplementary/2190-4286-8-133-S1.pdf]

Acknowledgements

Financial support of the University of Bayreuth and the SFB 840 (TP A10 and B10) is gratefully acknowledged. O.K. was supported by the BayNAT program of the UBT. We thank Juliane Kary for her contribution to the synthesis of the CP and CP–BCP composites.

References

1. Sindoro, M.; Yanai, N.; Jee, A.-Y.; Granick, S. *Acc. Chem. Res.* **2014,** *47,* 459–469. doi:10.1021/ar400151n
2. Coronado, E.; Giménez-Marqués, M.; Mínguez Espallargas, G.; Rey, F.; Vitórica-Yrezábal, I. J. *J. Am. Chem. Soc.* **2013,** *135,* 15986–15989. doi:10.1021/ja407135k
3. Zhao-Yang Li, O. S.; Yao, Z.-S.; Kang, S.; Kanegawa, S. Multifunctional Materials Combining Spin-Crossover with Conductivity and Magnetic Ordering. In *Spin-Crossover Materials;* Halcrow, M. A., Ed.; John Wiley & Sons Ltd: Chichester, United Kingdom, 2013; pp 303–319.
4. Gaspar, A. B.; Weber, B. Spin Crossover Phenomenon in Coordination Compounds. In *Molecular Magnetic Materials;* Sieklucka, B.; Pinkowicz, D., Eds.; Wiley-VCH Verlag GmbH & Co. KGaA: Weinheim, Germany, 2017; pp 231–252. doi:10.1002/9783527694228.ch9
5. Halcrow, M. A., Ed. *Spin-Crossover Materials: Properties and Applications;* John Wiley & Sons Ltd: Chichester, United Kingdom, 2013. doi:10.1002/9781118519301
6. Turkevich, J.; Stevenson, P. C.; Hillier, J. *Discuss. Faraday Soc.* **1951,** *11,* 55. doi:10.1039/DF9511100055
7. Frens, G. *Nature* **1973,** *241,* 20–22. doi:10.1038/physci241020a0
8. Sun, S.; Zeng, H. *J. Am. Chem. Soc.* **2002,** *124,* 8204–8205. doi:10.1021/ja026501x
9. Lu, A.-H.; Salabas, E. L.; Schüth, F. *Angew. Chem., Int. Ed.* **2007,** *46,* 1222–1244. doi:10.1002/anie.200602866
10. Sun, Y.; Xia, Y. *Science* **2002,** *298,* 2176–2179. doi:10.1126/science.1077229
11. Brust, M.; Fink, J.; Bethell, D.; Schiffrin, D. J.; Kiely, C. *J. Chem. Soc., Chem. Commun.* **1995,** 1655. doi:10.1039/C39950001655
12. Gupta, A. K.; Gupta, M. *Biomaterials* **2005,** *26,* 3995–4021. doi:10.1016/j.biomaterials.2004.10.012
13. Klimm, O.; Göbel, C.; Rosenfeldt, S.; Puchtler, F.; Miyajima, N.; Marquardt, K.; Drechsler, M.; Breu, J.; Förster, S.; Weber, B. *Nanoscale* **2016,** *8,* 19058–19065. doi:10.1039/C6NR06330F
14. Förster, S.; Zisenis, M.; Wenz, E.; Antonietti, M. *J. Chem. Phys.* **1996,** *104,* 9956. doi:10.1063/1.471723
15. Förster, S.; Antonietti, M. *Adv. Mater.* **1998,** *10,* 195–217. doi:10.1002/(SICI)1521-4095(199802)10:3<195::AID-ADMA195>3.0.CO;2-V
16. Fan, Z.; Chen, X.; Köhn Serrano, M.; Schmalz, H.; Rosenfeldt, S.; Förster, S.; Agarwal, S.; Greiner, A. *Angew. Chem., Int. Ed.* **2015,** *54,* 14539–14544. doi:10.1002/anie.201506415
17. Carmen Muñoz, M.; Antonio Real, J. Polymeric Spin-Crossover Materials. In *Spin-Crossover Materials;* Halcrow, M. A., Ed.; John Wiley & Sons Ltd.: Chichester, United Kingdom, 2013; pp 121–146. doi:10.1002/9781118519301.ch4
18. Gütlich, P.; Gaspar, A. B.; Garcia, Y. *Beilstein J. Org. Chem.* **2013,** *9,* 342–391. doi:10.3762/bjoc.9.39
19. Martinho, P. N.; Rajnak, C.; Ruben, M. Nanoparticles, Thin Films and Surface Patterns from Spin-Crossover Materials and Electrical Spin State Control. In *Spin-Crossover Materials: Properties and Applications;* Halcrow, M. A., Ed.; John Wiley & Sons Ltd: Chichester, United Kingdom, 2013; pp 375–404. doi:10.1002/9781118519301.ch14
20. Herrera, J. M.; Titos-Padilla, S.; Pope, S. J. A.; Berlanga, I.; Zamora, F.; Delgado, J. J.; Kamenev, K. V.; Wang, X.; Prescimone, A.; Brechin, E. K.; Colacio, E. *J. Mater. Chem. C* **2015,** *3,* 7819–7829. doi:10.1039/c5tc00685f
21. Giménez-Marqués, M.; García-Sanz de Larrea, M. L.; Coronado, E. *J. Mater. Chem. C* **2015,** *3,* 7946–7953. doi:10.1039/c5tc01093d
22. Roubeau, O. *Chem. – Eur. J.* **2012,** *18,* 15230–15244. doi:10.1002/chem.201201647
23. Luo, Y.-H.; Liu, Q.-L.; Yang, L.-J.; Sun, Y.; Wang, J.-W.; You, C.-Q.; Sun, B.-W. *J. Mater. Chem. C* **2016,** *4,* 8061–8069. doi:10.1039/c6tc02796b

24. Coronado, E.; Mínguez Espallargas, G. *Chem. Soc. Rev.* **2013,** *42,* 1525. doi:10.1039/c2cs35278h
25. Ohba, M.; Yoneda, K.; Agustí, G.; Muñoz, M. C.; Gaspar, A. B.; Real, J. A.; Yamasaki, M.; Ando, H.; Nakao, Y.; Sakaki, S.; Kitagawa, S. *Angew. Chem., Int. Ed.* **2009,** *48,* 4767–4771. doi:10.1002/anie.200806039
26. Linares, J.; Codjovi, E.; Garcia, Y. *Sensors* **2012,** *12,* 4479–4492. doi:10.3390/s120404479
27. Létard, J.-F.; Guionneau, P.; Goux-Capes, L. Towards Spin Crossover Applications. In *Spin Crossover in Transition Metal Compounds I-III;* Gütlich, P.; Goodwin, H., Eds.; Topics in Current Chemistry, Vol. 233–235; Springer: Berlin, Germany, 2004; pp 221–249. doi:10.1007/b95429
28. Kahn, O.; Jay Martinez, C. *Science* **1998,** *279,* 44–48. doi:10.1126/science.279.5347.44
29. Kahn, O.; Jay, C.; Krober, J.; Claude, R.; Groliere, F. Spin-transition chemical compounds, and devices comprising read-, memory-, and erase-units, active medium which contains at least one of those compounds. Eur. Pat. EP0666561, Aug 9, 1995.
30. Muller, R. N.; Vander Elst, L.; Laurent, S. *J. Am. Chem. Soc.* **2003,** *125,* 8405–8407. doi:10.1021/ja0349599
31. Venkataramani, S.; Jana, U.; Dommaschk, M.; Sönnichsen, F. D.; Tuczek, F.; Herges, R. *Science* **2011,** *331,* 445–448. doi:10.1126/science.1201180
32. Dommaschk, M.; Peters, M.; Gutzeit, F.; Schütt, C.; Näther, C.; Sönnichsen, F. D.; Tiwari, S.; Riedel, C.; Boretius, S.; Herges, R. *J. Am. Chem. Soc.* **2015,** *137,* 7552–7555. doi:10.1021/jacs.5b00929
33. Hasserodt, J.; Kolanowski, J. L.; Touti, F. *Angew. Chem., Int. Ed.* **2014,** *53,* 60–73. doi:10.1002/anie.201305662
34. Nowak, R.; Prasetyanto, E. A.; de Cola, L.; Bojer, B.; Siegel, R.; Senker, J.; Rössler, E.; Weber, B. *Chem. Commun.* **2017,** *53,* 971–974. doi:10.1039/C6CC08618G
35. Volatron, F.; Catala, L.; Rivière, E.; Gloter, A.; Stéphan, O.; Mallah, T. *Inorg. Chem.* **2008,** *47,* 6584–6586. doi:10.1021/ic800803w
36. Forestier, T.; Mornet, S.; Daro, N.; Nishihara, T.; Mouri, S.-i.; Tanaka, K.; Fouché, O.; Freysz, E.; Létard, J.-F. *Chem. Commun.* **2008,** 4327–4329. doi:10.1039/B806347H
37. Boldog, I.; Gaspar, A. B.; Martínez, V.; Pardo-Ibañez, P.; Ksenofontov, V.; Bhattacharjee, A.; Gütlich, P.; Real, J. A. *Angew. Chem., Int. Ed.* **2008,** *47,* 6433–6437. doi:10.1002/anie.200801673
38. Forestier, T.; Kaiba, A.; Pechev, S.; Denux, D.; Guionneau, P.; Etrillard, C.; Daro, N.; Freysz, E.; Létard, J.-F. *Chem. – Eur. J.* **2009,** *15,* 6122–6130. doi:10.1002/chem.200900297
39. Martínez, V.; Boldog, I.; Gaspar, A. B.; Ksenofontov, V.; Bhattacharjee, A.; Gütlich, P.; Real, J. A. *Chem. Mater.* **2010,** *22,* 4271–4281. doi:10.1021/cm101022u
40. Larionova, J.; Salmon, L.; Guari, Y.; Tokarev, A.; Molvinger, K.; Molnár, G.; Bousseksou, A. *Angew. Chem., Int. Ed.* **2008,** *47,* 8236–8240. doi:10.1002/anie.200802906
41. Cobo, S.; Molnár, G.; Real, J. A.; Bousseksou, A. *Angew. Chem., Int. Ed.* **2006,** *45,* 5786–5789. doi:10.1002/anie.200601885
42. Molnár, G.; Cobo, S.; Real, J. A.; Carcenac, F.; Daran, E.; Vieu, C.; Bousseksou, A. *Adv. Mater.* **2007,** *19,* 2163–2167. doi:10.1002/adma.200700448
43. Bartual-Murgui, C.; Natividad, E.; Roubeau, O. *J. Mater. Chem. C* **2015,** *3,* 7916–7924. doi:10.1039/c5tc01174d
44. Bauer, W.; Scherer, W.; Altmannshofer, S.; Weber, B. *Eur. J. Inorg. Chem.* **2011,** 2803–2818. doi:10.1002/ejic.201001363
45. Baldé, C.; Bauer, W.; Kaps, E.; Neville, S.; Desplanches, C.; Chastanet, G.; Weber, B.; Létard, J. F. *Eur. J. Inorg. Chem.* **2013,** 2744–2750. doi:10.1002/ejic.201201422
46. Šalitroš, I.; Fuhr, O.; Ruben, M. *Materials* **2016,** *9,* 585. doi:10.3390/ma9070585
47. Dankhoff, K.; Lochenie, C.; Puchtler, F.; Weber, B. *Eur. J. Inorg. Chem.* **2016,** *2016,* 2136–2143. doi:10.1002/ejic.201501175
48. Lochenie, C.; Bauer, W.; Railliet, A. P.; Schlamp, S.; Garcia, Y.; Weber, B. *Inorg. Chem.* **2014,** *53,* 11563–11572. doi:10.1021/ic501624b
49. Nowak, R.; Bauer, W.; Ossiander, T.; Weber, B. *Eur. J. Inorg. Chem.* **2013,** 975–983. doi:10.1002/ejic.201201051
50. Weber, B. *Coord. Chem. Rev.* **2009,** *253,* 2432–2449. doi:10.1016/j.ccr.2008.10.002
51. Weber, B. *Koordinationschemie. Grundlagen und aktuelle Trends;* Springer Spektrum: Berlin, Germany, 2014.
52. Brooker, S. *Chem. Soc. Rev.* **2015,** *44,* 2880–2892. doi:10.1039/c4cs00376d
53. Schönfeld, S.; Lochenie, C.; Thoma, P.; Weber, B. *CrystEngComm* **2015,** *17,* 5389–5395. doi:10.1039/C5CE00800J
54. Money, V. A.; Carbonera, C.; Elhaïk, J.; Halcrow, M. A.; Howard, J. A. K.; Létard, J.-F. *Chem. – Eur. J.* **2007,** *13,* 5503–5514. doi:10.1002/chem.200601312
55. Bauer, W.; Pfaffeneder, T.; Achterhold, K.; Weber, B. *Eur. J. Inorg. Chem.* **2011,** 3183–3192. doi:10.1002/ejic.201100224
56. Weber, B.; Kaps, E. *Heteroat. Chem.* **2005,** *16,* 391–397. doi:10.1002/hc.20108
57. Weber, B.; Carbonera, C.; Desplances, C.; Létard, J.-F. *Eur. J. Inorg. Chem.* **2008,** *2008,* 1589–1598. doi:10.1002/ejic.200701216
58. Göbel, C.; Palamarciuc, T.; Lochenie, C.; Weber, B. *Chem. – Asian J.* **2014,** *9,* 2232–2238. doi:10.1002/asia.201402144
59. Xu, L.; Jiang, L.; Drechsler, M.; Sun, Y.; Liu, Z.; Huang, J.; Tang, B. Z.; Li, Z.; Stuart, M. A. C.; Yan, Y. *J. Am. Chem. Soc.* **2014,** *136,* 1942–1947. doi:10.1021/ja410443n
60. Weber, B.; Jäger, E.-G. *Eur. J. Inorg. Chem.* **2009,** *2009,* 465–477. doi:10.1002/ejic.200800891
61. Tanner, M.; Ludi, A. *Chimia* **1980,** *34,* 23–24.
62. *Recoil, mössbauer spectral analysis software for windows,* Version 1.0; Department of Physics, University of Ottawa: Ottawa, Canada, 1998.

License and Terms

BEILSTEIN JOURNAL OF NANOTECHNOLOGY

Deposition of exchange-coupled dinickel complexes on gold substrates utilizing ambidentate mercapto-carboxylato ligands

Martin Börner[1], Laura Blömer[1], Marcus Kischel[1], Peter Richter[2], Georgeta Salvan[2], Dietrich R. T. Zahn[2], Pablo F. Siles[3,4], Maria E. N. Fuentes[4], Carlos C. B. Bufon[4], Daniel Grimm[4], Oliver G. Schmidt[4], Daniel Breite[5], Bernd Abel[5] and Berthold Kersting[*1]

Full Research Paper

Open Access

Address:
[1]Institut für Anorganische Chemie, Universität Leipzig, Johannisallee 29, 04103 Leipzig, Germany, [2]Semiconductor Physics, Chemnitz University of Technology, D-09107 Chemnitz, Germany, [3]Material Systems for Nanoelectronics, Chemnitz University of Technology, Reichenhainer Str. 70, 09107 Chemnitz, Germany, [4]Institute for Integrative Nanosciences, IFW Dresden, Helmholtz Str. 20, 01069 Dresden, Germany, and [5]Leibniz-Institute of Surface Modification (IOM), Permoser Str. 15, D-04318 Leipzig, Germany

Email:
Berthold Kersting[*] - b.kersting@uni-leipzig.de

* Corresponding author

Keywords:
ambidentate ligands; chemisorption; gold surfaces; macrocyclic complexes; mercapto-alkanecarboxylic acid

Beilstein J. Nanotechnol. **2017,** *8,* 1375–1387.
doi:10.3762/bjnano.8.139

Received: 03 April 2017
Accepted: 07 June 2017
Published: 05 July 2017

This article is part of the Thematic Series "Towards molecular spintronics" and is dedicated to Prof. Dr. Dr. Evamarie Hey-Hawkins on the occasion of her 60th birthday.

Associate Editor: J. J. Schneider

Abstract

The chemisorption of magnetically bistable transition metal complexes on planar surfaces has recently attracted increased scientific interest due to its potential application in various fields, including molecular spintronics. In this work, the synthesis of mixed-ligand complexes of the type $[Ni^{II}_2L(L')](ClO_4)$, where L represents a 24-membered macrocyclic hexaazadithiophenolate ligand and L' is a ω-mercapto-carboxylato ligand (L' = $HS(CH_2)_5CO_2^-$ (**6**), $HS(CH_2)_{10}CO_2^-$ (**7**), or $HS(C_6H_4)_2CO_2^-$ (**8**)), and their ability to adsorb on gold surfaces is reported. Besides elemental analysis, IR spectroscopy, electrospray ionization mass spectrometry (ESIMS), UV–vis spectroscopy, and X-ray crystallography (for **6** and **7**), the compounds were also studied by temperature-dependent magnetic susceptibility measurements (for **7** and **8**) and (broken symmetry) density functional theory (DFT) calculations. An $S = 2$ ground state is demonstrated by temperature-dependent susceptibility and magnetization measurements, achieved by ferromagnetic coupling between the spins of the Ni(II) ions in **7** ($J = +22.3$ cm^{-1}) and **8** ($J = +20.8$ cm^{-1}; $H = -2JS_1S_2$). The reactivity of complexes **6**–**8** is reminiscent of that of pure thiolato ligands, which readily chemisorb on Au surfaces as verified by contact angle, atomic force microscopy (AFM) and spectroscopic ellipsometry measurements. The large $[Ni_2L]$ tail groups, however, prevent the packing and self-assembly of the hydrocarbon chains. The smaller film thickness of **7** is attributed to the specific coordination mode of the coligand. Results of preliminary transport measurements utilizing rolled-up devices are also reported.

Introduction

The deposition of switchable transition metal complexes on Au surfaces is a topical research area [1-4] due to the many potential applications such as storage of information at the molecular level [5-7] and in the area of molecular spintronice [8-11]. For a review concerning the organization of electronically bistable molecule or molecular switches on surfaces see [4]. The deposition of single molecule magnets (SMMs) has received increased attention [12-14] and several strategies have been designed to deposit these materials as rows [15], thin films [16-19], or multilayers [20-26]. However, the limited thermal and kinetic stability of most SMMs prevents their thermal evaporation [27] and has initiated the search for milder, solution-based methods for surface functionalization. Of these, the formation of self-assembled monolayers of SMMs appears to be an attractive and suitable method [28-36].

Our work involves the deposition of exchange-coupled complexes of the type $[M^{II}_2L(\mu\text{-}L')](ClO_4)$, where L represents a hexaazadithiophenolate macrocycle (Scheme 1), L' an ambidentate coligand, and M is a paramagnetic transition metal ion, usually Mn^{II}, Fe^{II}, Co^{II}, or Ni^{II} [37].

The ambidentate phosphane-carboxylato [38] and thiol-carboxylato coligands H_2L^2 and H_1L^3 (Figure 1) were found to bind selectively via their carboxylate function to form the carboxylato-bridged complexes $[Ni_2L(HL^2)](ClO_4)$ (**2**) and $[Ni_2L(L^3)](ClO_4)$ (**3**) [39,40] such that an exposed thiol or phosphane group is available for further functionalization. Indeed, **2** dimerizes via a disulphide bond upon oxidation in air to generate a tetranuclear $[\{Ni_2L\}_2(O_2CC_6H_4S)_2]^{2+}$ complex, while "auration" of **2** and **3** with Au^I sources leads to the trinu-

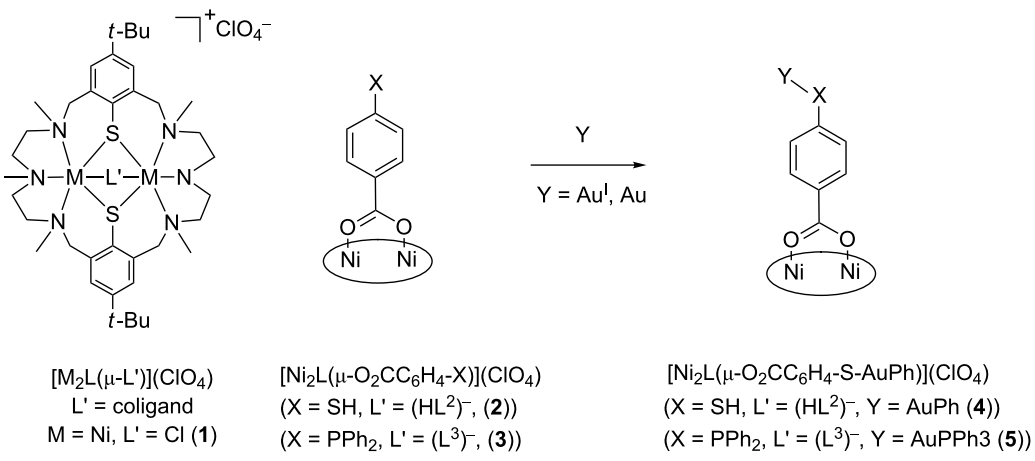

Scheme 1: Structure of the dinuclear complexes $[M_2L(\mu\text{-}L')](ClO_4)$ and representation of the structure of complexes **2**–**5** bearing ambidentate coligands $(HL^2)^-$ and $(L^3)^-$ (the doubly deprotonated macrocycle H_2L is shown as an ellipse for clarity).

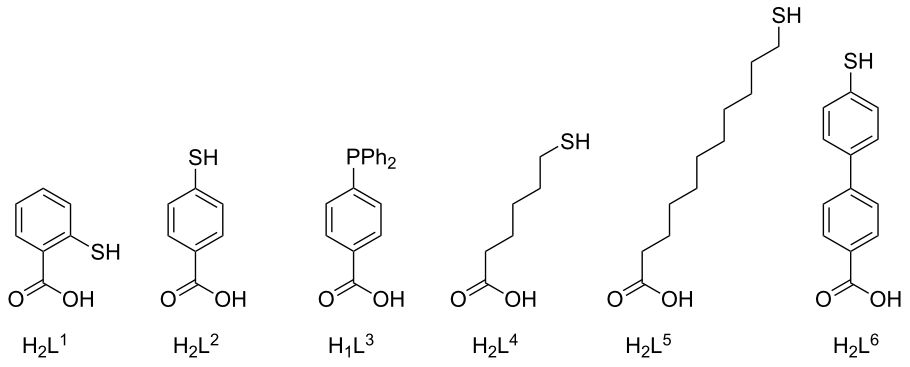

Figure 1: Ambidentate ligands with soft (–SH, $–PPh_2$) and hard ($–CO_2H$) donor functions.

clear $Ni^{II}_2Au^{I}$ species **4** and **5**. Moreover, complexes **2** and **3** interact also with Au surfaces via Au–S and Au–P bonds without complex disintegration as established by contact angle, spectroscopic ellipsometry, atomic force microscopy (AFM), X-ray photoelectron spectroscopy (XPS) and scanning tunneling microscopy (STM) measurements [41].

The present study is an extension of this work and focuses on the synthesis, characterization and deposition of dinuclear $[Ni_2L(L')](ClO_4)$ complexes **6**–**8** bearing the ambidentate coligands H_2L^4–H_2L^6 (Figure 1, Scheme 2). The crystal structure, reactivity features, and magnetic properties of compounds **6**–**8** are presented along with the results stemming from characterization of the surface assemblies by contact angle measurements, spectroscopic ellipsometry, AFM and transport measurements. To our knowledge, polynuclear macrocyclic complexes have not been anchored to gold via ambidentate mercaptobenzoate ligands. However, polynuclear Mn_{12} complexes have been fixed to gold via perfluorinated mercaptobenzoate linkers [42].

Results and Discussion

Synthesis and characterization of complexes

The investigated compounds and their labels are collected in Scheme 2. The compounds were prepared in analogy to the synthesis of $[Ni_2L(HL^2)](ClO_4)$ (**2**) [39]. Thus, treatment of $[Ni_2L(\mu\text{-}Cl)](ClO_4)$ (**1**) [43,44] with a slight excess of the triethylammonium salt of the corresponding mercapto-carboxylate anion (prepared in situ from the free acid and NEt_3) in methanol at ambient temperature resulted in pale-green solutions. Upon addition of an excess of $LiClO_4$ green, air-sensitive compounds of composition $[Ni_2L(L')](ClO_4)$ (where L' = $(HL^4)^-$ (**6**), $(HL^5)^-$ (**7**), and $(HL^6)^-$ (**8**)) could be obtained in good yields (56–60%). Compounds **6**–**8** are soluble in polar aprotic solvents (e.g., acetone, acetonitrile, or dichloromethane), but are only sparingly soluble in alcohols and insoluble in H_2O. The products gave satisfactory elemental analyses and the electrospray ionization mass spectrometry (ESIMS) spectra with base peaks for the individual $[Ni_2L(L')]^+$ cations (Table 1) were consistent with the formulation as mixed ligand $[Ni_2L(L')](ClO_4)$ complexes.

It has already been demonstrated that the $[Ni_2L]^{2+}$ dication has a higher affinity for carboxylate ions than for thiophenolate groups, and that the former, when attached to $[Ni_2L]^{2+}$, invariably act as a $\mu_{1,3}$-bridge [45,46]. The UV–vis spectra of **6**–**8** recorded in MeCN solution provided convincing evidence that the present mercapto-carboxylate ligands are also coordinated in this fashion. Similar to **2** and **3**, **6**–**8** exhibit two electronic absorption bands at wavelengths of ≈650 nm and 1120 nm, typical for an octahedral NiN_3S_2O carboxylate chromophore (assigned as $\nu_2(^3A_{2g}\rightarrow{}^3T_{2g})$ and $\nu_1(^3A_{2g}\rightarrow{}^3T_{1g})$, respectively, in pure O_h symmetry). Infrared spectroscopy (IR) is also a powerful method to examine carboxylate coordination modes [47,48]. As can be seen (Table 1), the present complexes reveal two strong bands, one around 1596–1581 cm^{-1} and the other between 1407 and 1423 cm^{-1}, as in other carboxylato-bridged complexes supported by H_2L [45]. These are assigned to the asymmetric and symmetric RCO_2^- stretching frequencies. Weak bands at ≈2550 cm^{-1} ν(SH) typical for a RSH group are also present.

Description of the crystal structure of **6** and **7**

Attempts to grow single crystals of **6**–**8** met with little success. Only preliminary X-ray crystallographic data for the complexes **6** and **7** can be presented. Although the quality of the structure determination is low and insufficient for publication, these data can surely validate the atom connectivity of the $[Ni_2L(L')]^+$ complex and the binding mode of the coligands. Figure 2 shows ORTEP and van der Waals representations of the structure of

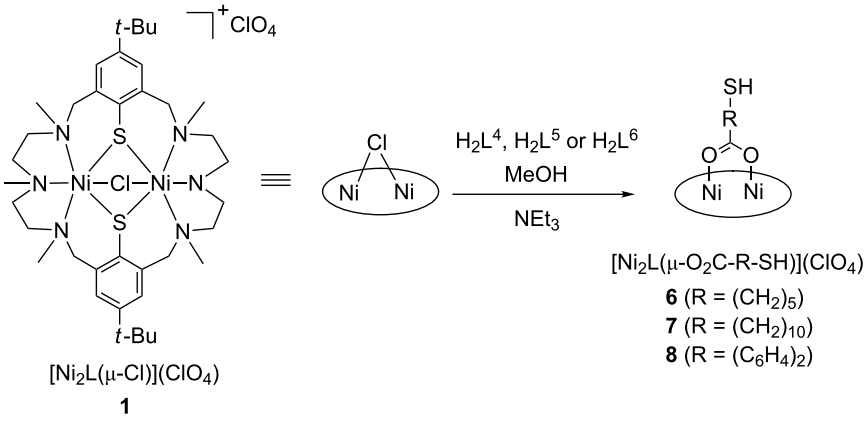

Scheme 2: Synthesis of the complexes **6**–**8** (the doubly deprotonated macrocycle H_2L is represented as an ellipse for clarity).

Table 1: Selected UV–vis spectroscopy, IR spectroscopy, and ESIMS data and their assignments for compounds **6**–**8**. The data for the reference compounds (**1**–**5**, **9**–**11**) have been included for comparison.

Compound	UV–vis ν_1, ν_2 [nm]	IR ν_{as}, $\nu_s(RCO_2)$, ν(SH) [cm^{-1}]	ESI [M^+] *m*/*z*	Ref.
1 $[Ni_2L(Cl)](ClO_4)$	658, 1002	–, –, –	n.d.[a]	[43]
2 $[Ni_2L(HL^2)](ClO_4)$	652, 1125	1599, 1408, 2550	937.2	[39]
3 $[Ni_2L(HL^3)](ClO_4)$	650, 1122	1550, 1408, –	1089.4	[40]
4 $[Ni_2L(L^2)Au(PPh_3)](ClO_4)$	653, 1129	1587, 1403, –	1397.4	[39]
5 $[Ni_2L(L^3)Au(Ph)](BPh_4)$	651, 1119	1552, 1437, –	1363.3	[39]
6 $[Ni_2L(HL^4)](ClO_4)$	649, 1129	1596, 1407, 2547	932.39	this work
7 $[Ni_2L(HL^5)](ClO_4)$	650, 1133	1581, 1423, 2547	1002.5	this work
8 $[Ni_2L(HL^6)](ClO_4)$	650, 1118	1596, 1408, 2548	1013.37	this work
9 $[Ni_2L(O_2CPh)](ClO_4)$	651, 1123	1569, 1407, –	n.d.[a]	[45]
10 $[Ni_2L(O_2CCH_3)](ClO_4)$	650, 1131	1588, 1428, –	n.d.[a]	[45]
11 $[Ni_2L(SPh)](ClO_4)$	667, 1141	–, –, –	n.d.[a]	[46]

[a]n.d. = not determined.

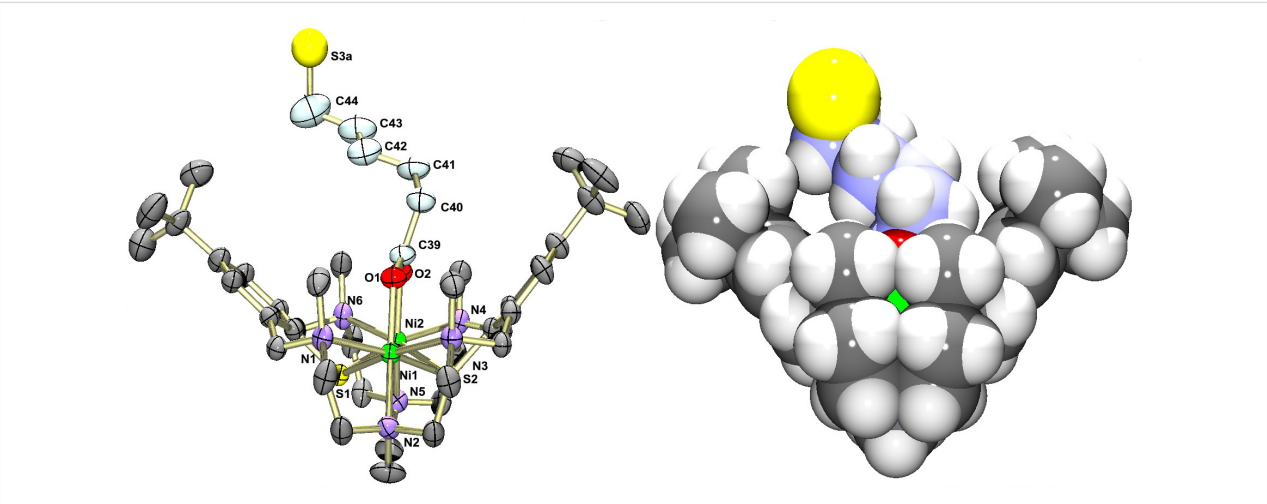

Figure 2: ORTEP (left) and van der Waals representations (right) of the molecular structure of the $[Ni_2L(O_2C(CH_2)_5SH)]^+$ cation in crystals of **6**. The accessibility of the thiol head group (atom labeled S3a) is obvious from this view.

the $[Ni_2L(HL^4)]^+$ cation in **6**, with the mercaptohexanoate unit bridging the two Ni(II) ions in a symmetrical fashion as expected from the spectroscopic data. The $[Ni_2L]^{2+}$ fragment adopts a cleft-like structure as observed in other carboxylato-bridged complexes supported by L [45]. In contrast to other ω-mercapto-alkanethiols, which adopt an extended zig-zag conformation, the coligand is twisted about the C40–C41 bond ("gauche" conformation) most likely due to steric constraints exerted by the surrounding NMe groups. We have observed similar effects in an azido-bridged complex, where the surrounding alkyl groups dictate the coordination mode of the azido ligand [49].

Figure 3 provides a ball and stick and a van der Waals representation of the molecular structure of the $[Ni_2L(O_2C(CH_2)_{10}SH)]^+$ cation in **7**. The coligand is again coordinated via its carboxylate function, and the $[Ni_2L]^{2+}$ fragment is isostructural with that in **6**. Twisting of the coligand is also encountered in this case (about the C40–C41 (β) and C41–C42 (γ) bonds). As in **6**, the undecanoate moiety protrudes laterally out of the binding pocket of the $[Ni_2L]^{2+}$ fragment. Thus, in all the cases that we have examined so far, coordination of the carboxylato group is strongly preferred over binding through the RSH tail group both in solution as well as in the solid state and there is no ambiguity concerning the regiochemistry of the complexation.

Magnetic properties of **6** and **7**

The magnetic properties of a series of dinuclear $[Ni_2L(L')]^+$ complexes with various bridging ligands have been reviewed [37]. All $[Ni_2L(\mu\text{-carboxylato})]^+$ complexes are characterized

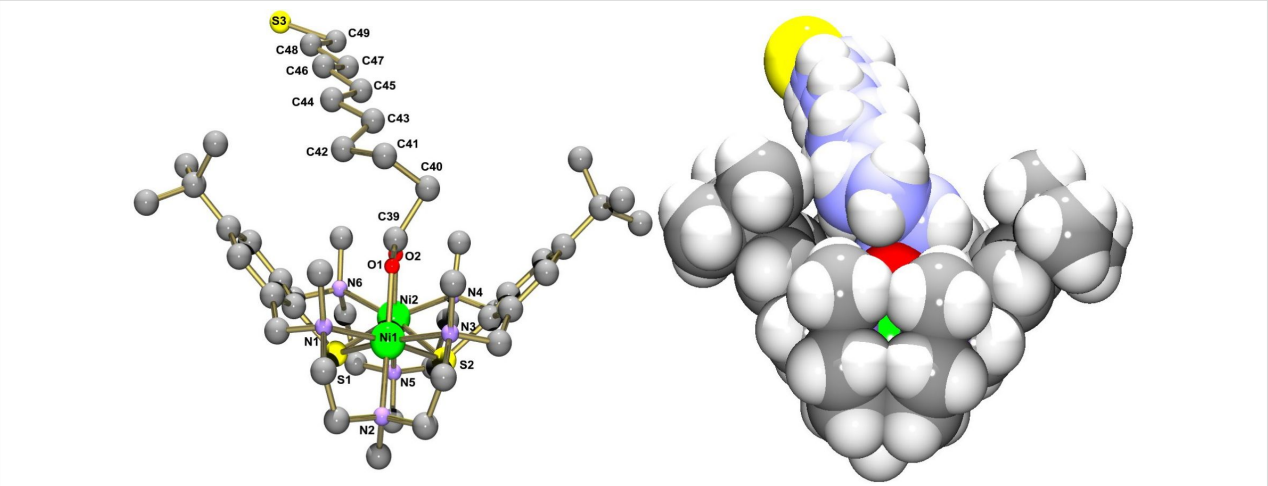

Figure 3: Ball and stick (left) and van der Waals representations (right) of the molecular structure of the $[Ni_2L(O_2C(CH_2)_{10}SH)]^+$ cation in crystals of **7**.

by an $S = 2$ ground state that is attained by a net ferromagnetic exchange interaction with J values ranging from approximately +15 to +25 cm^{-1} ($H = -2JS_1S_2$) [50].

To gain insight into the magnetic properties of the present complexes, variable-temperature magnetic susceptibility data were measured for **7** and **8** between 2 and 330 K in applied external magnetic fields of B = 0.1, 0.5, and 1.0 T. Figure 4 shows the susceptibility data (per dinuclear complex) in the form of μ_{eff} versus T plots at 1 T. Both complexes behave similarly. Thus, for complex **7**, the effective magnetic moment per dinuclear complex at 300 K increases from 4.78·μ_B (**8**: 4.80 μ_B) at 300 K to a maximum value of 5.36 μ_B at 23 K (**8**: 5.27 μ_B). On lowering the temperature further the magnetic moment decreases to 4.60 μ_B (or 4.34 μ_B) at 2 K. This behavior suggests that the electron spins on the two Ni(II) ($S = 1$) ions are coupled by an intramolecular ferromagnetic exchange interaction. This would lead to an $S_t = 2$ ground state, in agreement with other carboxylato-bridged compounds supported by L. The decrease in $\chi_M T$ below 20 K can be attributed to zero-field splitting of Ni(II) [51].

The magnetic moment data were analyzed in order to determine the magnetic parameters. The appropriate spin-Hamiltonian (Equation 1) [52] should include additional terms to account for single-ion zero-field splitting for each Ni^{2+} ion. J is

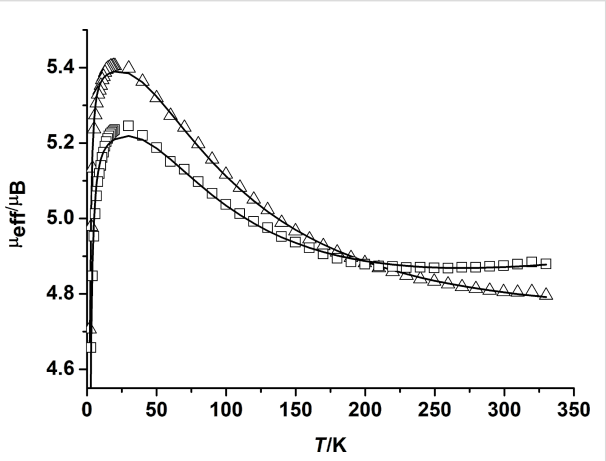

Figure 4: Temperature dependence of the effective magnetic moment μ_{eff} (per dinuclear complex) for **7** (open triangles) and **8** (open squares). The solid lines represent the best fits to Equation 2.

the exchange coupling constant, D_i, E_i/D_i, and g_i are the local axial and rhombic zero-field splitting parameters and g-values (isotropic average) [53]. It is well-known that temperature-dependent magnetic susceptibility measurements do not allow a concise determination of the magnitude and sign of D [54]. As a consequence, the data for **7** and **8** were analyzed with the approximation in Equation 2 [55]. The D and g values were kept identical for the two nickel atoms.

$$H = -2JS_1S_2 + \sum_{i=1}^{2} D_i \left[S_{z,i}^2 - \frac{1}{3} S_i(S_i+1) + \frac{E_i}{D_i}(S_{x,i}^2 - S_{y,i}^2) \right] + g_i \mu_B B_\tau \hat{S}_{i,\tau} \quad (1)$$

$$H = -2JS_1S_2 + \sum_{i=1}^{2} D_i (S_{z,i}^2 - \frac{1}{3} S_i(S_i+1)) + g_i \mu_B B_\tau \hat{S}_{i,\tau} (\tau = x, y, z) \quad (2)$$

By taking into account the zero-field splitting and temperature-independent paramagnetism (TIP), reasonable fits of the experimental data were possible, yielding $J = +23$ cm^{-1} ($g = 2.20$, $D = 2.59$ cm^{-1}) for **7** and $J = +25$ cm^{-1} ($g = 2.25$, $D = 3.21$ cm^{-1}) for **8**. The inclusion of the *D*-parameter improved the low-temperature fits significantly, but as stated above, these values by no means represent accurate values [56,57]. The *D*-values obtained from temperature-dependent magnetic susceptibility measurements should be taken as indicative rather than definitive because these measurements are not the most appropriate for the determination of *D*-values. It should also be noted that HFEPR experiments for carboxylato-bridged $[Ni_2L(O_2CR)]^+$ complexes revealed a negative axial magnetic anisotropy parameter ($D < 0$) with *D*-values of approximately −0.04 cm^{-1}, indicative of an easy magnetic anisotropy axis. However, the magnetic anisotropy barrier is too small to allow for sufficient retention of magnetization at finite temperature. The value of *J*, on the other hand, does not significantly depend on *D*. Thus, *J* is unambiguous and provides a correct value for the magnetic coupling in **7** and **8**. The experimental *J*-values agree also reasonably well with those obtained by broken symmetry density functional calculations for exchange interactions ($J = +26$ cm^{-1} for **7**; $J = +27$ cm^{-1} for **8**).

In order to evaluate the coupling through the thiophenolato and carboxylato bridges within the $N_3Ni(\mu\text{-}SR)_2(\mu_{1,3}\text{-}O_2CR)NiN_3$ core, we utilized a breakdown approach in which the carboxylate group was virtually removed to obtain the hypothetical $[Ni_2(L)]^{2+}$ dication, which was subjected to broken symmetry DFT density functional theory calculations. The details of these investigations will be published elsewhere. This method has previously been shown to be a powerful tool to unravel the contribution of the azido and thiolato-bridges for the complex $[Ni_2L^{Me2H4}(\mu\text{-}N_3)]ClO_4$ [49], where L^{Me2H4} represents a 28-membered variant of the macrocycle L. The results imply that a moderate "ferromagnetic" contribution of ≈30 cm^{-1} through the $\mu_{1,1}$-bridging thiophenolato groups of the supporting macrocycle is counterbalanced by a weak antiferromagnetic interaction ($J \approx -5$ cm^{-1}) through the carboxylato-bridges (J_{O2CR}), to produce a net ferromagnetic exchange interaction of $J \approx 25$ cm^{-1}. A magneto-structural correlation has recently been reported for related dinuclear nickel complexes of the type $[Ni_2L^{Me2H4}(\mu\text{-}L')]^+$, where L' = F^-, Cl^-, Br^-, OH^-, and N_3^-) [58]. The *J*-values were found to depend primarily on the bridging Ni–S–Ni and Ni–L'–Ni angles. The findings made for the carboxylato-bridged compounds are in good agreement with the reported trend.

Chemisorption of complexes **6–8** on gold surfaces

In view of the results obtained with the complexes **2** and **3**, the deposition of the nickel complexes **6**–**8** on flat gold surfaces was examined. The deposition experiments were carried out in solution according to a protocol developed for the preparation of self-assembled thiol monolayers [59] as the complexes cannot be deposited via the gas phase. They decompose without melting. Thus, clean gold-coated Si wafers were immersed in a 1×10^{-3} M solution of the respective complex in MeCN or CH_2Cl_2 for 24 h followed by washing with EtOH and drying under N_2 flow. The modified Au(111) surfaces were examined by contact angle measurements, AFM topography analysis, and spectroscopic ellipsometry. Table 2 lists the results. The data for **2** and **3** and other compounds have been included for comparison.

Table 2: Water contact angles, AFM roughness, and optical thickness obtained for Au(111) surfaces modified with various dinickel(II) complexes.

Compound	Contact angle [°][a,b]	Roughness (rms) [Å][b,c]	Optical film thickness [Å]	Ref.
bare gold	75.8 (1.5)	6 (1)	–	[39]
2 $[Ni_2L(L^2)](ClO_4)$	71.4 (2.1) 75.9 (2.1)[d] 76.0 (2.0)[e]	17 (5) 16 (2) n.d.[f]	16 (7) n.d.[f] n.d.[f]	[39], this work
3 $[Ni_2L(L^3)](ClO_4)$	71.5 (1.6) 76.7 (1.9)[d] 76.5 (2.1)[e]	17 (5) n.d.[f] n.d.[f]	15 (8) n.d.[f] n.d.[f]	[40]
6 $[Ni_2L(L^4)](ClO_4)$	n.d.	n.d.	n.d.	–
7 $[Ni_2L(L^5)](ClO_4)$	70.8 (1.0)	13 (4)	20 (7)	this work
8 $[Ni_2L(L^6)](ClO_4)$	69.6 (3.3)	19 (4)	24 (7)	this work
9 $[Ni_2L(O_2CPh)](ClO_4)$	75.9 (2.0)	6 (1)	n.d.[f]	[40]
10 $[Ni_2L(O_2CMe)](ClO_4)$	75.8 (1.5)	6 (1)	n.d.[f]	[40]

[a]The values represent the average of five 4 µL drops of distilled, deionized water. The "bare" gold surfaces were identically treated to the modified surfaces except with omission of any adsorbate in the solvent. [b]Standard deviations are given in parentheses. [c]Root mean squared (rms) surface roughness determined by AFM. [d]Tetraphenylborate salt. [e]After metathesis with $NaBPH_4$. [f]n.d. = not determined.

Static contact angle measurements, atomic force microscopy and optical thickness

The chemisorption of the perchlorate salts **7** and **8** leads to smaller contact angles (70.8° and 69.6°) than that of bare gold, and the values compare well with those reported previously for **2** and **3** (Table 2). The contact angles are relatively high, particularly considering the ionic nature of the layers, and this may relate to the fact that the charges are well-shielded by the apolar groups of the supporting macrocycle. The contact angles for **2**, **3**, **7**, and **8** should otherwise be compared with those of reference compounds **9** and **10**, which lack end groups for surface fixation (and which are apparently not chemisorbed on the gold surfaces), as suggested by contact angles close to that of the bare gold.

The topography of the gold surfaces was further investigated by AFM microscopy. Figure 5 shows the topography of a sample of $[Ni_2L(HL^5)](ClO_4)$ (**7**) on Au, which is representative. The topographic analysis of the bare gold and of complexes **2** and **8** are supplied in Supporting Information File 1. The presence of adsorbed complexes is indicated by the larger rms roughnesses of the samples (**7**: 13 Å, **8**: 19 Å) relative to that of the bare gold (6 Å). Similar rms roughnesses were previously found for **2** (17 Å) and **3** (17 Å), and the values match quite well with the estimated diameter of 12 Å of the globular-shaped $[Ni_2L(L')]^+$ cation (neglecting the ClO_4^- ion). We attribute the smaller rms roughness of **7** (13 Å) (relative to that of **8** (19 Å)) to be a consequence of the specific coordination mode of the coligand (see Figure 6).

For complexes **7** and **8** the film thickness was also investigated by spectroscopic ellipsometry. The ellipsometry data were fitted with the aid of the appropriate Cauchy model [60,61] as done for **2** and **3**. Others authors use A = 1.50, which in the case of the present monolayers would only make a thickness difference of about 0.1 nm. Reasonable fits were produced resulting in av-

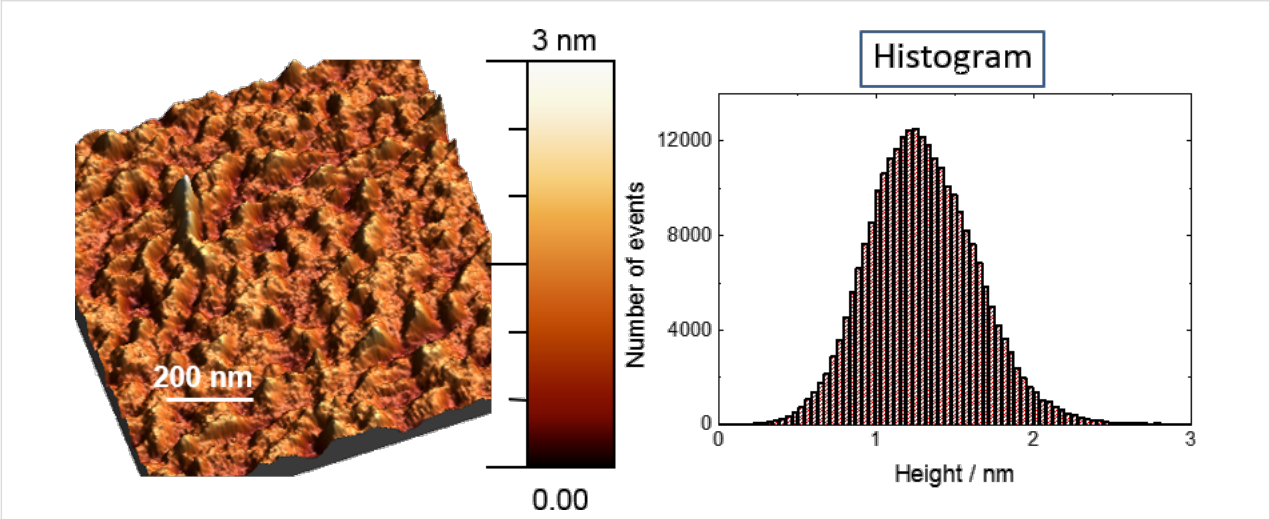

Figure 5: AFM topography characteristics considering a 1 × 1 μm^2 area, after deposition of $[Ni_2L(HL^5)](ClO_4)$ (**7**) on gold with an rms roughness of 13 Å.

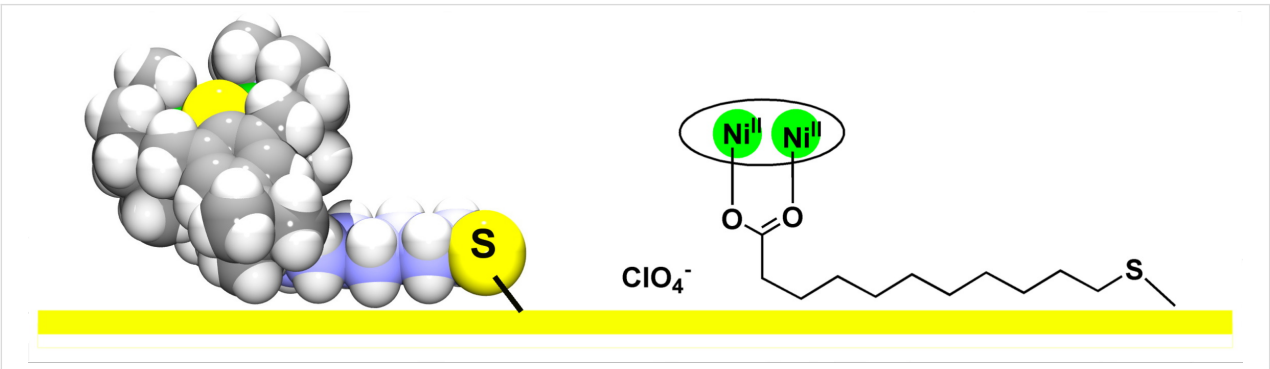

Figure 6: Proposed binding mode of complex **7** to gold (left: van der Waals representation of the $[Ni_2L(L^5)]^+$ cation; right: representation with a Lewis formula. The macrocycle is shown as an ellipse encircling the two Ni^{2+} ions for clarity.

erage thicknesses of 20 ± 7 Å for **7** and 24 ± 8 Å for **8**, which agree reasonably well with those determined by AFM. The thickness for **7** is again found to be smaller than that of **8**, indicative of an effect of the length of coligand on the thickness of the layer. Overall, the contact angle, AFM and ellipsometric data support the assumption that all complexes form monolayers rather than multilayer films, with the cationic $[Ni_2L(L')]^+$ molecules covalently bound to the Au surface.

Surface binding model

On the basis of the crystal structure of complex **7** and the AFM and ellipsometry measurements above, one can propose a specific orientation on the gold surface, as sketched in Figure 6. Note that the coligands in the complexes **2**, **3**, and **8** are more or less buried in the binding pocket of the $[Ni_2L]^{2+}$ fragment, and so the film thicknesses are determined largely by the dimensions of the $[Ni_2L]^{2+}$ dication alone. In case of complex **7**, however, approximately half of the coligand protrudes out of the pocket, and a coplanar orientation of this part of the coligand to the Au surface is likely. The smaller film thickness of **7** would be consistent with this in view of the proposed absorption model. Also, in the absence of packing and self-assembly of hydrocarbon chains, a coplanar binding of alkane thiol to gold is possible [62]. It is likely that van der Waals interactions exist between the Au surface and the alkyl (methylene and methyl) groups of the supporting ligands.

Transport measurements

In orienting experiments, the deposition of complex **2** on gold was further investigated by transport measurements using an approach based on self-rolled-up nanomembranes [63,64]. Standard two point measurements at room temperature were carried out for the electrical characterization of the heterojunctions (Supporting Information File 1). The data analysis provides a characteristic transition voltage (V_T) of 0.50 ± 0.05 V, a value which, albeit rather indicative than definitive, is in good agreement with the value of ≈0.6 V reported for monolayers of conjugated thiols on gold (≈0.6 V) [65]. According to these data, layers of paramagnetic complexes of **2** on gold behave as ultrathin insulating tunnel barriers, comparable to the self-assembled alkanethiol monolayers reported in previous work.

Conclusion

In conclusion, three new mixed ligand complexes bearing ω-mercapto-carboxylato ligands were designed with the aim of facilitating the chemisorption of large magnetic bi-metallic complexes on gold surfaces by self-assembling of monolayers. The synthesis of $[Ni_2L(O_2C(CH_2)_5SH)](ClO_4)$ (**6**), $[Ni_2L(O_2C(CH_2)_{10}SH)](ClO_4)$ (**7**), and $[Ni_2L(O_2C(C_6H_4)_2SH)](ClO_4)$ (**8**) was successfully realized. The coligands act invariably in a bridging mode as established by IR and UV–vis spectroscopy, ESIMS, and X-ray crystallography (for **6** and **7**). The structures of the complexes bearing ω-thiolalkane-carboxylates (H_2L^4, H_2L^5) are distinguished from the aromatic variants (H_2L^2, H_2L^6) by a bent conformation of the alkyl chain (alkyl chain perpendicular to the O_2CC–C bond), such that the surface active thiol groups protrude laterally out of the cleft-like binding pocket of the $[Ni_2L]^{2+}$ fragments. The reactivity of complexes **6**–**8** is reminiscent of that of pure thiolato ligands. All are readily chemisorbed on Au surfaces as ascertained by contact angle measurements, AFM, spectroscopic ellipsometry and preliminary transport measurements (for **2**). The results may suggest that the length of the coligand affects the thickness of the corresponding films.

Experimental

Synthesis of compounds

All manipulations were carried out using standard Schlenk techniques and vacuum-line manipulations under a protective atmosphere of nitrogen unless otherwise stated. Compound **1** was prepared according to the published procedure [43]. All other compounds were purchased from commercial sources unless otherwise specified. The solvents were distilled prior to use and were deaerated according to standard procedures [66]. The IR spectra were recorded as KBr disks using a Bruker Tensor 27 FTIR spectrophotometer. UV–vis spectra were recorded on a Jasco V-670 UV/vis/near-IR spectrophotometer. Elemental analyses were carried out on a Vario EL elemental analyzer. NMR spectra were recorded on a Bruker AVANCE DPX-200 spectrometer at 300 K. ^1H and ^{13}C chemical shifts refer to solvent signals. ESIMS spectra were recorded on a Bruker Daltronics ESQUIRE3000 PLUS spectrometer. Temperature-dependent magnetic susceptibility measurements on powdered solid samples were carried out using a MPMS 7XL SQUID magnetometer (Quantum Design) over a temperature range 2–330 K at an applied magnetic field of 0.1, 0.5, and 1.0 Tesla. The observed susceptibility data were corrected for underlying diamagnetism.

Safety note! Perchlorate salts of transition metal complexes are hazardous and may explode. Only small quantities should be prepared and great care should be taken.

Synthesis of H_2L^6, step 1, 4-methylphenylboronic acid

Magnesium turnings (1.70 g, 70.2 mmol) were placed in a nitrogen-flushed three-neck vessel equipped with a dropping funnel and a reflux condenser. 40 mL of THF and a small grain of iodine were added to the vessel. A solution of 4-bromotoluene (7.19 mL, 10.0 g, 58.46 mmol) in 20 mL of THF was added drop wise to the solution to keep the solvent refluxing. The reaction mixture was kept under reflux for another 8 h. The

resulting suspension was cooled to −80 °C and a solution of $B(OMe)_3$ (7.3 mL, 6.80 g, 65.84 mmol) in 20 mL of THF was added drop wise. After complete addition, the mixture was allowed to warm up to room temperature. 35 mL of concentrated aqueous HCl (10%) were added for hydrolysis of unreacted $B(OMe)_3$. The aqueous phase was separated and extracted with ether (4 × 15 mL). The organic phase was washed with brine, dried over $MgSO_4$ and evaporated to dryness. The residue was recrystallized from an ethanol/water (1:1) solvent system to give 4-methylphenylboronic acid as colorless needles (2.94 g, 21.63 mmol, 37%). ^{1}H NMR (400 MHz, $CDCl_3$) δ 2.42 (s, 3H, CH_3), 7.29 (d, ^3J = 7.5 Hz, 2H, ArH), 8.13 (d, ^3J = 7.5 Hz, 2H, ArH). This material was used without further purification in the next step.

Synthesis of H_2L^6, step 2, 4-carboxyphenylboronic acid

To a solution of $KMnO_4$ (5.71 g, 36.13 mmol) and Bu_4NBr (0.17 g, 0.53 mmol) in water (175 mL) a solution of 4-methylphenylboronic acid in 10% aqueous NaOH (20 mL) was added. The reaction mixture was stirred at 60 °C for 5 h. EtOH (8 mL) was added and the suspension was stirred for an additional 10 min to destroy the remaining $KMnO_4$. The mixture was filtered and reduced to 1/2 of its original volume. The pH was adjusted to 1–2 using 2 M aqueous HCl. The resulting white precipitate was collected and dried in vacuo to give 4-boronobenzoic acid as a white powder (2.07 g, 12.47 mmol, 35%). ^{1}H NMR (300 MHz, acetone-d_6) δ 7.96–8.03 (m, 4H, ArH). This material was used without further purification in the next step.

Synthesis of H_2L^6, step 3,4'-(methylthio)-[1,1'-biphenyl]-4-carboxylic acid

4-Boronobenzoic acid (3.00 g, 18.08 mmol), 4-bromothioanisole (4.41 g, 21.70 mmol), $Pd(OAc)_2$ (20.2 mg, 0.09 mmol) and K_2CO_3 (8.75 g, 63.28 mmol) were suspended in a PEG 400/H_2O 1:1 solvent system (110 mL). The reaction mixture was stirred for 6 days at 60–65 °C, cooled down to room temperature and filtered. The filter cake was extracted repeatedly with diethyl ether. The ether phase was removed under reduced pressure and the pH of the remaining aqueous solution adjusted to 1 using 2 M aqueous HCl. The precipitate was filtered, washed with a small amount of dichloromethane to give the crude material, which was redissolved in acetone and filtered. Evaporation of the solvent gave 4'-(methylthio)-[1,1'-biphenyl]-4-carboxylic acid as a white solid (1.15 g, 4.71 mmol, 26% based on 4-boronobenzoic acid). ^{1}H NMR (300 MHz, DMSO-d_6) δ 2.53 (s, 3H, CH_3), 7.38 (d, ^3J = 9 Hz, 2H, ArH), 7.71 (d, ^3J = 9 Hz, 2H, ArH), 7.71 (d, ^3J = 9 Hz, 2H, ArH). This material was used without further purification in the next step.

Synthesis of H_2L^6, step 4,4'-mercapto-[1,1'-biphenyl]-4-carboxylic acid

4'-(Methylthio)-[1,1'-biphenyl]-4-carboxylic acid (428 mg, 1.75 mmol) and $NaSCH_3$ were dissolved in degassed *N*-methyl-2-pyrrolidone (40 mL) and stirred at 110 °C for 72 h. The solvent was removed in vacuo, the resulting residue was suspended in degassed 20% aqueous HCl (50 mL) and the mixture was stirred at room temperature for 30 min and at 40 °C for an additional 45 min. The solid was filtered off, washed with water (3 × 75 mL) and dried under vacuum. Yield: 387 mg (1.68 mmol, 96%), white air-sensitive powder. This material was used without further purification in the next step. ^{1}H NMR (300 MHz, DMF-d_7) δ 4.00 (s, 1H, SH), 7.40–8.10 (m, 8H, 8 ArH); ^{13}C NMR (75 MHz, DMF-d_7) δ 127.02 (*C*-COOH), 128.28 (*C*-HS), 130.46 (C1'), 162,24, 162,63, 162,83 (C4), 163,03, 167,64 (COOH); ESI$^+$-MS (MeCN) *m*/*z*: 231,05 [M + H]$^+$; IR (KBr pellet) $\tilde{\nu}$: 2985 (m), 2850 (m), 2671 (m), 2550 (m, ν(SH)), 1684 (s, ν(RCO_2)), 1607(s, ν(RCO_2)), 1575 (m), 1521 (w), 1483 (m), 1425 (s), 1396 (m), 1297 (s), 1283 (s), 1199 (w), 1179 (w), 1130 (w), 1106 (m), 1017 (w), 1004 (w), 942 (w), 865 (w), 824 (s), 771 (s), 753 (w), 697 (w), 679 (w), 556 (w), 542 (w), 482 (w) cm^{-1}

Preparation of $[Ni_2L(\mu\text{-}O_2C(CH_2)_5SH)]ClO_4$ (**6**)

This compound was prepared from **1** and 6-mercaptohexanoic acid by the procedure detailed for **2**. Yield: 191.1 mg (0.186 mmol, 56%). Recrystallization from a MeOH/EtOH 1:1 solvent system provided the title compound as a green microcrystalline solid, which was washed with EtOH and ether and dried in vacuum. Yield: 191.1 mg (0.186 mmol, 56%). ESI$^+$-MS (MeCN) *m*/*z*: 932.39 [M$^+$]; IR (KBr pellet) $\tilde{\nu}$: 2962 (s), 2902 (s), 2868 (s), 2808 (m), 2547 (w, ν(SH)), 1717 (w), 1596 (s, $\nu_{as}(RCO_2)$), 1565 (m), 1546 (w), 1461 (s), 1407 (s, $\nu_s(RCO_2)$), 1363 (m), 1309 (w), 1292 (w), 1264 (w), 1233 (w), 1152 (m), 1096 (s), 1060 (s), 1039 (s), 846 (m), 824 (s), 752 (s), 623 (s) cm^{-1}; UV–vis (CH_3CN) λ_{max}/nm (ε/M^{-1} cm^{-1}): 209 (40040), 270 (15840), 304 (14100), 327 (11900), 372 (2150), 451 (140), 649 (26), 1129 (63); anal. calcd for $C_{44}H_{75}ClN_6Ni_2O_6S_3$ (1033.14): C, 51.15; H, 7.32; N, 8.13; found: C, 50.78; H, 7.26; N, 8.05. This compound was additionally characterized by X-ray crystallography.

Preparation of $[Ni_2L(\mu\text{-}O_2C(CH_2)_{10}SH)]ClO_4$ (**7**)

A solution of **1** (200 mg, 0.217 mmol), 11-mercaptoundecanoic acid (62 mg, 0.285 mmol), and NEt_3 (28 mg, 40 µL, 0.282 mmol) was stirred at room temperature for 8 h. A solution of $LiClO_4{\cdot}3H_2O$ (348 mg, 2.17 mmol) in degassed EtOH (15 mL) was added. The solution was reduced to about 10 mL. The resulting pale-green precipitate was filtered off, washed with EtOH and ether and dried in vacuum. Recrystallization from a MeOH/EtOH 1:1 solvent system provided the title com-

pound as a green, microcrystalline solid, which was washed with EtOH and ether and dried in vacuum. Yield: 158 mg (0.143 mmol, 66%). ESI^+-MS (MeCN) *m/z*: 1002.5 [M^+]; IR (KBr pellet) $\tilde{\nu}$: 3600–3300 (m), 2962 (s), 2902 (s), 2868 (s), 2808 (m), 2547 (w, ν(SH)), 1717 (w), 1581 (s, $\nu_{as}(RCO_2)$), 1565 (m), 1546 (w), 1461 (s), 1423 (s, $\nu_s(RCO_2)$), 1363 (m), 1309 (w), 1292 (w), 1264 (w), 1233 (w), 1152 (m), 1096 (s), 1060 (s), 1039 (s), 846 (m), 824 (s), 752 (s), 623 (s) cm^{-1}; UV–vis (CH_3CN) λ_{max}/nm (ε/M^{-1} cm^{-1}): 202 (91450), 279 (28200), 331 (14140), 373 (2200), 453 (142), 650 (30), 1133 (64) nm; anal. calcd for $C_{51}H_{73}ClN_6Ni_2O_6S_3{\cdot}3H_2O$ (1115.20 + 54.03): C, 52.39; H, 6.81; N, 7.19; found: C, 52.77; H, 6.51; N, 7.23.

Preparation of $[Ni_2L(\mu\text{-}O_2C(C_6H_4)_2SH)]ClO_4$ (**8**)

The dinuclear nickel complex **1** (307 mg, 0.333 mmol) and 4'-mercapto-[1,1'-biphenyl]-4-carboxylic acid (76.6 mg, 0.333 mmol) were dissolved in a nitrogen-purged MeOH/CH_2Cl_2 (1:1) solvent mixture (50 mL). NEt_3 (34 mg, 46 µL, 0.333 mmol) was added and the resulting green solution was stirred at room temperature for 8 hours. A solution of $LiClO_4{\cdot}3H_2O$ (534.2 mg, 3.33 mmol) in degassed EtOH (20 mL) was added. The solution was reduced to about 10 mL. The resulting pale-green precipitate was filtered off, washed with EtOH and ether and dried in vacuum. Recrystallization from a EtOH/MeCN 1:1 solvent system provided the title compound as a green, microcrystalline solid, which was washed with EtOH and ether and dried in vacuum. Yield: 219.1 mg (0.196 mmol, 59%). ESI^+-MS (MeCN) *m/z*: 1013.37 [M^+]; IR (KBr pellet) $\tilde{\nu}$: 3600–3300 (m), 2962 (s), 2902 (s), 2868 (s), 2808 (m), 2548 (w, ν(SH)), 1717 (w), 1596 (s, $\nu_{as}(RCO_2)$), 1565 (m), 1546 (w), 1461 (s), 1408 (s, $\nu_s(RCO_2)$), 1363 (m), 1309 (w), 1292 (w), 1264 (w), 1233 (w), 1152 (m), 1096 (s), 1060 (s), 1039 (s), 846 (m), 824 (s), 752 (s), 623 (s) cm^{-1}; UV–vis (CH_3CN) λ_{max}/nm (ε/M^{-1} cm^{-1}): 202 (91450), 279 (28200), 331 (14140), 373 (2200), 453 (142), 650 (30), 1118 (64); anal. calcd. for $C_{51}H_{73}ClN_6Ni_2O_6S_3{\cdot}3H_2O$ (1115.20 + 54.03): C, 52.39; H, 6.81; N, 7.19, found: C, 52.77; H, 6.51; N, 7.23.

X-ray crystallography

Crystals of **6** and **7** were grown by slow evaporation of a mixed acetonitrile/ethanol solvent system and subjected to diffraction experiments on a STOE-IPDS-2T-diffractometer. Graphite-monochromated Mo Kα radiation (λ = 0.71073 Å) was used throughout. The data were processed with X-AREA and corrected for absorption using STOE X-Red32 [67]. The structures were solved by direct methods (SHELXS-2013) [68] and refined by full-matrix least-squares on F^2. However, the quality of the refinement for the two compounds was very low. The ClO_4^- anions and solvate molecules could not be located, and so the structures can only serve to validate the atom connectivity of the complex cations.

Crystal data for $[Ni_2L(O_2C(CH_2)_5SH)](ClO_4)$ (**6**)

$C_{44}H_{75}ClN_6Ni_2O_6S_3$, M_r = 1033.14 g/mol, triclinic, space group $P\bar{1}$, *a* = 13.6528(9) Å, *b* = 13.9237(9) Å, *c* = 16.2949(10) Å, α = 69.323(5), β = 74.211(5)°, γ = 86.429(5)°, *V* = 2786.8(3) $Å^3$, *Z* = 2, ρ_{calcd} = 1.113 g/cm^3, *T* = 180 K, μ(Mo Kα) = 0.823 mm^{-1} (λ = 0.71073 Å), 23125 reflections measured, 10911 unique, 8853 with $I > 2\sigma(I)$. Final R1 = 0.0784, wR2 = 0.2512 ($I > 2\sigma(I)$). The ClO_4^- anion could not be located. The structure contains large (solvent accessible voids) of ≈750 $Å^3$ attributed to MeCN or EtOH solvate molecules. Only the structure of the complex cation could be identified.

Crystal data for $[Ni_2L(O_2C(CH_2)_{10}SH)](ClO_4)$ (**7**)

$C_{49}H_{85}ClN_6Ni_2O_6S_3$, M_r = 1103.27 g/mol, monoclinic, space group $P2_1/n$, *a* = 21.689(4) Å, *b* = 13.593(3) Å, *c* = 21.698(4) Å, β = 104.20(3)°, *V* = 6201(3) $Å^3$, *Z* = 4, ρ_{calcd} = 1.182 g/cm^3, *T* = 180 K, μ(Mo Kα) = 0.80 mm^{-1} (λ = 0.71073 Å), 34319 reflections measured, 11365 unique, 4520 with $I > 2\sigma(I)$. Final R1 = 0.1247, wR2 = 0.3743 ($I > 2\sigma(I)$). The ClO_4^- anion could not be located. The structure contains large (solvent accessible voids) of ≈1000 $Å^3$ attributed to MeCN or EtOH solvate molecules. Only the structure of the complex cation could be identified.

Computational details

DFT calculations were carried out utilizing density functional theory (DFT). Perdew, Burke and Ernzerhof's PBE0 hybrid functional [69,70] and Ahlrich's triple-zeta valence basis set (TZV(P)) [71] were used. Calculations were performed with the ORCA [72,73] program package (revision 3.0.3) as previously described [59]. The coordinates were taken from the crystal structures and were fixed during the calculations.

Contact angle measurements

Surface hydrophobicity was examined by performing water contact angle measurements with a DSA II (Krüss, Hamburg, Germany) contact angle analyzer. The contact angle measurements were collected using a 4 µL drop size of deionized, distilled water. At least 5 contact angles per five different locations were averaged.

Atomic force microscopy

An Agilent 5600LS AFM system was used to collect topography data under Ar and ambient conditions in order to keep the integrity of the organic system. Measurements were performed in tapping mode in order to minimize the contact between the AFM probe and the sample surface and avoid damage or modi-

fication of the topographic characteristics. Special ultrasharp (4–10 nm tip radius) Olympus cantilevers were employed, allowing high sensitivity measurements. Data shown in the respective Figures correspond to a 1 × 1 μm^2 area, although a mapping of the topographic characteristics was performed on different points of the samples in order to verify the uniformity of the organic system over the Au substrate.

Ellipsometry

Spectroscopic ellipsometric measurements were conducted on a J. A. Woollam Co., Inc. M-2000 T-Solar ellipsometer operating with a xenon lamp. Ellipsometry scans were recorded under ambient conditions in a spectral range from 0.7 eV to 5 eV at light incidence angles of 65°, 70°, and 75°. The samples were immediately measured after preparation. Gold substrates were cleaned, immersed in a 1×10^{-3} M solution of the complexes in CH_2Cl_2 for at least 12 h, rinsed with absolute ethanol and dried in a stream of ultrahigh purity nitrogen. The modelling environments CompleteEASE and WVASE32 (both J. A. Woollam Co., Inc.) were used for data evaluation. The dielectric function of a pristine gold substrate, measured and modelled in agreement with database values, was taken as a reference substrate layer for all measurements. For each molecular complex, ellipsometry spectra were recorded for at least nine different locations on the sample surface. In a parameter-coupled fitting procedure, the organic film thickness values were determined using a Cauchy dispersion model that is commonly applied for the refractive index of monolayers described as transparent media. Error bars represent the standard deviation from the mean thickness value within one sample series. The scatter observed in the data was typically ±0.6 nm, arising most likely from a film roughness of the gold substrates of about 0.6 nm (measured by AFM).

Transport measurements

Devices used for transport measurements were fabricated on silicon substrates employing standard photolithographic processes combined with thermal deposition. The top electrode was prepared by rolling a metallic nanomembrane over a monolayer of chemisorbed molecules of **2** previously synthesized on a thin gold film deposited onto a silicon pillar (for details, see Supporting Information File 1).

Supporting Information

Supporting Information File 1

Additional AFM topography images, detailed description of transport measurements.
[http://www.beilstein-journals.org/bjnano/content/supplementary/2190-4286-8-139-S1.pdf]

Acknowledgements

The authors thank the Deutsche Forschungsgemeinschaft for funding through the research group DFG-FOR 1154 ("Towards molecular spintronics") and the University of Leipzig for general support. We thank Prof. Dr. H. Krautscheid for providing facilities for X-ray crystallographic measurements and L. J. Endter for her assistance in the synthesis of the organic compounds.

References

1. Cornia, A.; Mannini, M.; Sainctavit, P.; Sessoli, R. *Chem. Soc. Rev.* **2011,** *40,* 3076–3091. doi:10.1039/c0cs00187b
2. Gómez-Segura, J.; Veciana, J.; Ruiz-Molina, D. *Chem. Commun.* **2007,** 3699–3707. doi:10.1039/b616352a
3. Cavallini, M.; Facchini, M.; Albonetti, C.; Biscarini, F. *Phys. Chem. Chem. Phys.* **2008,** *10,* 784–793. doi:10.1039/B711677B
4. Szaciłowski, K. *Chem. Rev.* **2008,** *108,* 3481–3548. doi:10.1021/cr068403q
5. Urdampilleta, M.; Klyatskaya, S.; Cleuziou, J.-P.; Ruben, M.; Wernsdorfer, W. *Nat. Mater.* **2011,** *10,* 502–506. doi:10.1038/nmat3050
6. Gatteschi, D.; Sessoli, R.; Villain, J. *Molecular Nanomagnets;* Oxford University Press: Oxford, UK, 2006. doi:10.1093/acprof:oso/9780198567530.001.0001
7. Troiani, F.; Affronte, M. *Chem. Soc. Rev.* **2011,** *40,* 3119–3129. doi:10.1039/c0cs00158a
8. Rocha, A. R.; Garcia-Suárez, V. M.; Bailey, S. W.; Lambert, C. J.; Ferrer, J.; Sanvito, S. *Nat. Mater.* **2005,** *4,* 335–339. doi:10.1038/nmat1349
9. Bogani, L.; Wernsdorfer, W. *Nat. Mater.* **2008,** *7,* 179–186. doi:10.1038/nmat2133
10. Meded, V.; Bagrets, A.; Fink, K.; Chandrasekar, R.; Ruben, M.; Evers, F.; Bernand-Mantel, A.; Seldenthuis, J. S.; Beukman, A.; van der Zant, H. S. J. *Phys. Rev. B* **2011,** *83,* 245415. doi:10.1103/PhysRevB.83.245415
11. Komeda, T.; Isshiki, H.; Liu, J.; Zhang, Y.-F.; Lorente, N.; Katoh, K.; Breedlove, B. K.; Yamashita, M. *Nat. Commun.* **2011,** *2,* 217. doi:10.1038/ncomms1210
12. Clemente-León, M.; Soyer, H.; Coronado, E.; Mingotaud, C.; Gómez-Garcia, C. J.; Delhaès, P. *Angew. Chem., Int. Ed.* **1998,** *37,* 2842–2845. doi:10.1002/(SICI)1521-3773(19981102)37:20<2842::AID-ANIE2842>3.0.CO;2-B
13. Cornia, A.; Fabretti, A. C.; Pacchioni, M.; Zobbi, L.; Bonacchi, D.; Caneschi, A.; Gatteschi, D.; Biagi, R.; Del Pennino, U.; De Renzi, V.; Gurevich, L.; van der Zant, H. S. J. *Angew. Chem.* **2003,** *115,* 1683–1686. doi:10.1002/ange.200350981
Angew. Chem., Int. Ed. **2003,** *42,* 1645–1648. doi:10.1002/anie.200350981
14. Mannini, M.; Pineider, F.; Sainctavit, P.; Danieli, C.; Otero, E.; Sciancalepore, C.; Talarico, A. M.; Arrio, M.-A.; Cornia, A.; Gatteschi, D.; Sessoli, R. *Nat. Mater.* **2009,** *8,* 194–197. doi:10.1038/nmat2374
15. Alam, M. S.; Stocker, M.; Gieb, K.; Müller, P.; Haryono, M.; Student, K.; Grohmann, A. *Angew. Chem.* **2010,** *122,* 1178–1182. doi:10.1002/ange.200905062
Angew. Chem., Int. Ed. **2010,** *49,* 1159-1163. doi:10.1002/anie.200905062

16. Hieringer, W.; Flechtner, K.; Kretschmann, A.; Seufert, K.; Auwärter, W.; Barth, J. V.; Görling, A.; Steinrück, H.-P.; Gottfried, J. M. *J. Am. Chem. Soc.* **2011,** *133,* 6206–6222. doi:10.1021/ja1093502
17. Choi, T.; Bedwani, S.; Rochefort, A.; Chen, C.-Y.; Epstein, A. J.; Gupta, J. A. *Nano Lett.* **2010,** *10,* 4175–4180. doi:10.1021/nl1024563
18. Gopakumar, T. G.; Matino, F.; Naggert, H.; Bannwarth, A.; Tuczek, F.; Berndt, R. *Angew. Chem.* **2012,** *124,* 6367–6371. doi:10.1002/ange.201201203
Angew. Chem., Int. Ed. **2012,** *51,* 6262–6266. doi:10.1002/anie.201201203
19. Gambardella, P.; Stepanow, S.; Dmitriev, A.; Honolka, J.; de Groot, F. M. F.; Lingenfelder, M.; Gupta, S. S.; Sarma, D. D.; Bencok, P.; Stanescu, S.; Clair, S.; Pons, S.; Lin, N.; Seitsonen, A. P.; Brune, H.; Barth, J. V.; Kern, K. *Nat. Mater.* **2009,** *8,* 189–193. doi:10.1038/nmat2376
20. Soyer, H.; Mingotaud, C.; Boillot, M.-L.; Delhaes, P. *Thin Solids Films* **1998,** *327–329,* 435–438. doi:10.1016/S0040-6090(98)00680-4
21. Gaspar, A. B.; Seredyuk, M.; Gütlich, P. *Coord. Chem. Rev.* **2009,** *253,* 2399–2413. doi:10.1016/j.ccr.2008.11.016
22. Agustí, G.; Cobo, S.; Gaspar, A. B.; Molnár, G.; Moussa, N. O.; Szilágyi, P. Á.; Pálfi, V.; Vieu, C.; Muñoz, M. C.; Real, J. A.; Bousseksou, A. *Chem. Mater.* **2008,** *20,* 6721–6732. doi:10.1021/cm8019878
23. Boldog, I.; Gaspar, A. B.; Martínez, V.; Pardo-Ibañez, P.; Ksenofontov, V.; Bhattacharjee, A.; Gütlich, P.; Real, J. A. *Angew. Chem.* **2008,** *120,* 6533–6537. doi:10.1002/ange.200801673
Angew. Chem., Int. Ed. **2008,** *47,* 6433–6437. doi:10.1002/anie.200801673
24. Volatron, F.; Catala, L.; Riviére, E.; Gloter, A.; Stéphan, O.; Mallah, T. *Inorg. Chem.* **2008,** *47,* 6584–6586. doi:10.1021/ic800803w
25. Rajadurai, C.; Schramm, F.; Brink, S.; Fuhr, O.; Ghafari, M.; Kruk, R.; Ruben, M. *Inorg. Chem.* **2006,** *45,* 10019–10021. doi:10.1021/ic0612350
26. Bodenthin, Y.; Pietsch, U.; Möhwald, H.; Kurth, D. G. *J. Am. Chem. Soc.* **2005,** *127,* 3110–3114. doi:10.1021/ja0447210
27. Margheriti, L.; Mannini, M.; Sorace, L.; Gorini, L.; Gatteschi, D.; Caneschi, A.; Chiappe, D.; Moroni, R.; Buatier de Mongeot, F.; Cornia, A.; Piras, F. M.; Magnani, A.; Sessoli, R. *Small* **2009,** *5,* 1460–1466. doi:10.1002/smll.200801594
28. Love, J. C.; Estroff, L. A.; Kriebel, J. K.; Nuzzo, R. G.; Whitesides, G. M. *Chem. Rev.* **2005,** *105,* 1103–1170. doi:10.1021/cr0300789
29. Ulman, A. *Chem. Rev.* **1996,** *96,* 1533–1554. doi:10.1021/cr9502357
30. Ulman, A. *Acc. Chem. Res.* **2001,** *34,* 855–863. doi:10.1021/ar0001564
31. Naitabdi, A.; Bucher, J.-P.; Gerbier, P.; Rabu, P.; Drillon, M. *Adv. Mater.* **2005,** *17,* 1612–1616. doi:10.1002/adma.200401623
32. Steckel, J. S.; Persky, N. S.; Martinez, C. R.; Barnes, C. L.; Fry, E. A.; Kulkarni, J.; Burgess, J. D.; Pacheco, R. B.; Stoll, S. L. *Nano Lett.* **2004,** *4,* 399–402. doi:10.1021/nl0343553
33. Coronado, E.; Forment-Aliaga, A.; Romero, F. M.; Corradini, V.; Biagi, R.; De Renzi, V.; Gambardella, A.; Del Pennino, U. *Inorg. Chem.* **2005,** *44,* 7693–7695. doi:10.1021/ic0508021
34. Zobbi, L.; Mannini, M.; Pacchioni, M.; Chastanet, G.; Bonacchi, D.; Zanardi, C.; Biagi, R.; Del Pennino, U.; Gatteschi, D.; Cornia, A.; Sessoli, R. *Chem. Commun.* **2005,** 1640–1642. doi:10.1039/b418072k
35. Mannini, M.; Pineider, F.; Danieli, C.; Totti, F.; Sorace, L.; Sainctavit, P.; Arrio, M.-A.; Otero, E.; Joly, L.; Cezar, J. C.; Cornia, A.; Sessoli, R. *Nature* **2010,** *468,* 417–421. doi:10.1038/nature09478
36. Pacchioni, M.; Cornia, A.; Fabretti, A. C.; Zobbi, L.; Bonacchi, D.; Caneschi, A.; Chastanet, G.; Gatteschi, D.; Sessoli, R. *Chem. Commun.* **2004,** 2604–2605. doi:10.1039/b411320a
37. Lozan, V.; Loose, C.; Kortus, J.; Kersting, B. *Coord. Chem. Rev.* **2009,** *253,* 2244–2260. doi:10.1016/j.ccr.2008.08.016
38. Reis, A.; Dehe, D.; Farsadpour, S.; Munstein, I.; Sun, Y.; Thiel, W. R. *New J. Chem.* **2011,** *35,* 2488–2495. doi:10.1039/c1nj20448c
39. Lach, J.; Jeremies, A.; Breite, D.; Abel, B.; Mahns, B.; Knupfer, M.; Matulis, V.; Ivashkevich, O. A.; Kersting, B. *Inorg. Chem.* **2014,** *53,* 10825–10834. doi:10.1021/ic500683f
40. Golecki, M.; Lach, J.; Jeremies, A.; Lungwitz, F.; Fronk, M.; Salvan, G.; Zahn, D. R. T.; Park, J.; Krupskaya, Y.; Kataev, V.; Klingeler, R.; Büchner, B.; Mahns, B.; Knupfer, M.; Siles, P. F.; Grimm, D.; Schmidt, O. G.; Reis, A.; Thiel, W. R.; Breite, D.; Abel, B.; Kersting, B. *Chem. – Eur. J.* **2013,** *19,* 7787–7801. doi:10.1002/chem.201300496
41. Salazar, C.; Lach, J.; Rückerl, F.; Baumann, D.; Schimmel, S.; Knupfer, M.; Kersting, B.; Büchner, B.; Hess, C. *Langmuir* **2016,** *32,* 4464–4471. doi:10.1021/acs.langmuir.6b00772
42. Voss, S.; Burgert, M.; Fonin, M.; Groth, U.; Rüdiger, U. *Dalton Trans.* **2008,** 499–505. doi:10.1039/B712371J
43. Kersting, B.; Steinfeld, G. *Chem. Commun.* **2001,** 1376–1377. doi:10.1039/b103050g
44. Klingele, M. H.; Steinfeld, G.; Kersting, B. *Z. Naturforsch., B: J. Chem. Sci.* **2001,** *56,* 901–907. doi:10.1515/znb-2001-0907
45. Lehmann, U.; Klingele, J.; Lozan, V.; Steinfeld, G.; Klingele, M. H.; Käss, S.; Rodenstein, A.; Kersting, B. *Inorg. Chem.* **2010,** *49,* 11018–11029. doi:10.1021/ic101574a
46. Lozan, V.; Kersting, B. *Inorg. Chem.* **2008,** *47,* 5386–5393. doi:10.1021/ic8003432
47. Nakamoto, K. *Infrared and Raman Spectra of Inorganic and Coordination Compounds,* 5th ed.; Wiley: New York, 1997.
48. Deacon, G. B.; Philipp, R. J. *Coord. Chem. Rev.* **1980,** *33,* 227–250. doi:10.1016/S0010-8545(00)80455-5
49. Jeremies, A.; Gruschinski, S.; Meyer, M.; Matulis, V.; Ivashkevich, O. A.; Kobalz, K.; Kersting, B. *Inorg. Chem.* **2016,** *55,* 1843–1853. doi:10.1021/acs.inorgchem.5b02743
50. Lach, J.; Jeremies, A.; Lozan, V.; Loose, C.; Hahn, T.; Kortus, J.; Kersting, B. *Inorg. Chem.* **2012,** *51,* 12380–12388. doi:10.1021/ic301710b
51. Ginsberg, A. P.; Martin, R. L.; Brookes, R. W.; Sherwood, R. C. *Inorg. Chem.* **1972,** *11,* 2884–2889. doi:10.1021/ic50118a006
52. O'Connor, C. J. *Prog. Inorg. Chem.* **1982,** *29,* 203–283. doi:10.1002/9780470166307.ch4
53. Kahn, O. *Molecular magnetism;* Wiley-VCH: Weinheim, 1993.
54. Herchel, R.; Boča, R.; Krzystek, J.; Ozarowski, A.; Durán, M.; van Slageren, J. *J. Am. Chem. Soc.* **2007,** *129,* 10306–10307. doi:10.1021/ja0725807
55. Azuah, R. T.; Kneller, L. R.; Qiu, Y.; Tregenna-Piggott, P. L. W.; Brown, C. M.; Copley, J. R. D.; Dimeo, R. M. *J. Res. Natl. Inst. Stand. Technol.* **2009,** *114,* 341–358. doi:10.6028/jres.114.025
56. Krupskaya, Y.; Alfonsov, A.; Parameswaran, A.; Kataev, V.; Klingeler, R.; Steinfeld, G.; Beyer, N.; Gressenbuch, M.; Kersting, B.; Büchner, B. *ChemPhysChem* **2010,** *11,* 1961–1970. doi:10.1002/cphc.200900935
57. Meyer, A.; Gleizes, A.; Girerd, J.-J.; Verdaguer, M.; Kahn, O. *Inorg. Chem.* **1982,** *21,* 1729–1739. doi:10.1021/ic00135a006

58. Jeremies, A.; Lehmann, U.; Gruschinski, S.; Matulis, V.; Ivashkevich, O. A.; Jäschke, A.; Kersting, B. *J. Organomet. Chem.* **2016,** *821,* 171–181. doi:10.1016/j.jorganchem.2016.04.003
59. Ulman, A. *An Introduction to Ultrathin Organic Films from Langmuir–Blodgett to Self-assembly;* Academic Press: New York, 1991.
60. Singh, J., Ed. *Optical Properties of Condensed Matter and Applications;* John Wiley & Sons: Chichester, 2006.
61. Allara, D. L.; Nuzzo, R. G. *Langmuir* **1985,** *1,* 45–52. doi:10.1021/la00061a007
62. Poirier, G. E.; Pylant, E. D. *Science* **1996,** *272,* 1145–1148. doi:10.1126/science.272.5265.1145
63. Bufon, C. C. B.; Arias Espinoza, J. D.; Thurmer, D. J.; Bauer, M.; Deneke, C.; Zschieschang, U.; Klauk, H.; Schmidt, O. G. *Nano Lett.* **2011,** *11,* 3727–3733. doi:10.1021/nl201773d
64. Bufon, C. C. B.; Vervacke, C.; Thurmer, D. J.; Fronk, M.; Salvan, G.; Lindner, S.; Knupfer, M.; Zahn, D. R. T.; Schmidt, O. G. *J. Phys. Chem. C* **2014,** *118,* 7272–7279. doi:10.1021/jp409617r
65. Beebe, J. M.; Kim, B.; Gadzuk, J. W.; Frisbie, C. D.; Kushmerick, J. G. *Phys. Rev. Lett.* **2006,** *97,* 026801. doi:10.1103/PhysRevLett.97.026801
66. Armarego, W. L. F. *Purification of Laboratory Chemicals,* 3rd ed.; Pergamon Press: New York, 1988.
67. X-Area; STOE & Cie GmbH: Darmstadt, Germany, 2006.
68. Sheldrick, G. M. *Acta Crystallogr., Sect. A: Found. Crystallogr.* **2008,** *64,* 112–122. doi:10.1107/S0108767307043930
69. Perdew, J. P.; Burke, K.; Errnzerhof, M. *Phys. Rev. Lett.* **1997,** *78,* 1396. doi:10.1103/PhysRevLett.78.1396
70. Adamo, C.; Barone, V. *J. Chem. Phys.* **1999,** *110,* 6158–6169. doi:10.1063/1.478522
71. Schäfer, A.; Horn, H.; Ahlrichs, R. *J. Chem. Phys.* **1992,** *97,* 2571–2577. doi:10.1063/1.463096
72. Neese, F. *J. Chem. Phys.* **2003,** *119,* 9428–9444. doi:10.1063/1.1615956
73. Neese, F. *Int. J. Quantum Chem.* **2001,** *83,* 104–114. doi:10.1002/qua.1202

License and Terms

BEILSTEIN JOURNAL OF NANOTECHNOLOGY

Spin-chemistry concepts for spintronics scientists

Konstantin L. Ivanov[1,2], Alexander Wagenpfahl[3], Carsten Deibel[3] and Jörg Matysik[*4]

Review

Open Access

Address:
[1]International Tomography Center, Siberian Branch of Russian Academy of Science, Institutskaya 3a, Novosibirsk, 630090 Russia, [2]Novosibirsk State University, Institutskaya 3a, Novosibirsk, 630090 Russia, [3]Institut für Physik, Technische Universität Chemnitz, 09126 Chemnitz, Germany and [4]Universität Leipzig, Institut für Analytische Chemie, Linnéstr. 3, D-04103 Leipzig, Germany

Email:
Jörg Matysik* - joerg.matysik@uni-leipzig.de

* Corresponding author

Keywords:
CIDEP; magnetic field effects; photo-CIDNP; radical pairs; triplet states

Beilstein J. Nanotechnol. **2017,** *8,* 1427–1445.
doi:10.3762/bjnano.8.143

Received: 03 March 2017
Accepted: 13 June 2017
Published: 11 July 2017

This article is part of the Thematic Series "Towards molecular spintronics".

Guest Editor: G. Salvan

Abstract

Spin chemistry and spintronics developed independently and with different terminology. Until now, the interaction between the two fields has been very limited. In this review, we compile the two “languages” in an effort to enhance communication. We expect that knowledge of spin chemistry will accelerate progress in spintronics.

Review

Introduction

In general, chemical reactions are discussed in terms of thermodynamics: reaction enthalpy, reaction entropy and free energy. It is also recognized that steric and charge effects can lead to kinetic control of the reaction dynamics by introduction of activation energies. In some cases, chemical reactions are controlled by diffusional transport of highly reactive particles, for example, free radicals, to the reaction zone. This view on chemistry is sufficient for processes which are spin conserving, that is, the spin multiplicity is not changed during the entire process. If during the course of reaction the spin multiplicity is changed, spin rules apply and magnetic field effects (MFE), magnetic isotope effects (MIE), as well as electron and nuclear spin polarizations might occur. This is the field of spin chemistry [1-3].

The field of spin chemistry emerged with the discovery of anomalous electron paramagnetic resonance (EPR) intensities in CH_4 gas under irradiation by Fessenden and Schuler in 1963 [4]. Soon later, Bargon and Fischer observed anomalous nuclear magnetic resonance (NMR) intensities upon thermal radical-pair formation [5]. Such anomalous intensity patterns are nowadays interpreted in terms of transient non-Boltzmann magnetization and called chemically induced dynamic electron polarization (CIDEP) and chemically induced dynamic nuclear polarization (photo-CIDNP). The theoretical description by Kaptein and Oosterhoff [6] as well as by Closs [7] in 1969 established spin chemistry as a new field, which was initially mainly run by physical organic chemists as well as EPR and NMR

spectroscopists. The discovery of CIDEP and CIDNP was followed by reports of MFE [8,9] on chemical reactions and MIE [10,11]. All these effects originate from the spin-conserving nature of most chemical reactions and from singlet–triplet interconversion in radical pairs, which is sensitive to external magnetic fields and local hyperfine fields of magnetic nuclei. Although experiments have been done in gas phase (see Sections IV.A and V.A of [2] and the references therein) and in solid state (e.g., in photosynthetic reaction centers [12-14] and in organic solids [15,16]), spin chemistry mostly deals with small organic molecules in the solution state. The radical-pair formation is now-a-days often initiated photochemically either by electron transfer or by bond breaking, although thermal bond breaks also cause radical pairs. With the introduction of the concept of the "spin-correlated radical pair" (SCRP) [17-20], spin chemistry appeared to be a "completed field", in the notation of Heisenberg's closed theory (abgeschlossene Theorie in German). The techniques of spin chemistry, such as CIDNP, CIDEP, magnetically affected reaction yield (MARY) and reaction yield detected magnetic resonance (RYDMR) allow one to detect elusive paramagnetic species, such as radicals, radical pairs and triplet states, and to obtain their EPR parameters.

This review is dedicated to scientists of the field of spintronics as an introduction into the older field of spin chemistry. It seems to be economically reasonable to learn spin chemistry language and concepts to prevent reinvention of previous knowledge. We will first review the languages that developed mostly independently in both fields. By providing a dictionary, we can short-cut the introduction into the world of spin chemistry for scientists from the spintronics area. However, while spintronics focuses on spin transport, spin chemistry deals with spin effects during chemical reactions. Since this paper contains many acronyms, we additionally summarize them all in a separate section at the end.

The language of spin chemistry

The following two tables compare the terminology of spin chemistry and spintronics for states (Table 1) and processes (Table 2). Obviously, two different "languages" have developed in parallel without having had much influence on each other, except probably by EPR spectroscopists. To ease communication between different scientific communities (and to avoid the situation that important concepts are lost in translation) we present Table 1 and Table 2 as a simple "translator" between the two languages.

Obviously the states are named very differently (Table 1), even the two Zeeman states of a radical are often labeled differently. Molecules with an unpaired electron are called radicals ($R^{\bullet}$). Two radicals on the same molecule form a biradical ($R^{\bullet}$–$R^{\bullet}$). In this case, normally the two radicals are at the two ends of a long molecule. If the two radicals are on the same molecule and close together, they need to be in different orbitals, mostly one is in the highest occupied and the other in the lowest unoccupied molecular orbital. In this case, a molecular triplet state can occur ($^3R^{\bullet\bullet}$). A pair of two radicals on two different molecules is called a radical pair ($R^{\bullet} + R^{\bullet}$). This pair is often formed by the same chemical process, for example a bond break or a photochemically induced electron transfer: in this situation it is formed in a particular spin state, either the singlet or the triplet state. Such a radical pair is termed a spin-correlated radical pair (SCRP). In liquids, where radicals can diffuse, radical pairs are usually classified as geminate pairs (G-pairs), that is, pairs of radicals born in the same chemical event, or radical pairs formed upon encounters of free radicals in the solvent bulk (F-pairs).

For the more complex processes (Table 2), sometimes the same terminology is used. Interestingly, both spin phenomena and processes are not only termed differently but also interpreted differently: A spin chemist will discuss a radical pair mainly in

Table 1: Comparison of terminology and states in spin chemistry and spintronics.

State	Spin chemistry Intermediate, transient	Spintronics Topological excitation, defect
$R^{\bullet}$	spin states "α" and "β"	spin states "up" and "down"
$R^{\bullet}$	(mobile) radical	soliton
$R^{-}/R^{\bullet-}$	anion/radical anion	negatively charged polaron
$R^{+}/R^{\bullet+}$	cation/radical cation	positively charged polaron
R* (local)	electronic excitation	electronic excitation, exciton–bipolaron formation
R* (in crystal)	electronic excitation	exciton
$R^{\bullet+}$–$R^{\bullet-}$	radical pair, SCRP	radical pair, bipolaron, polaron pair, charge-transfer exciton, (bound) electron–hole pair, geminate pair
$^3R^{\bullet\bullet}$	molecular triplet state	triplet polaron pair, triplet exciton
$R^{\bullet}$–$R^{\bullet}$	biradical	soliton–antisoliton pair

Table 2: Comparison of terminology and processes in spin chemistry and spintronics.

Process	Spin chemistry Spin dynamics	Spintronics Soliton and polaron dynamics
$2R \rightarrow R^{\bullet+}–R^{\bullet-}$	charge separation, radical-pair formation, electron transfer	charge transfer, charge transfer exciton formation
$^1(R^{\bullet+}–R^{\bullet-}) \leftrightarrow {}^3(R^{\bullet+}–R^{\bullet-})$	singlet–triplet interconversion	intersystem crossing[a], singlet–triplet interconversion
$^1(R^{\bullet+}–R^{\bullet-}) \leftrightarrow {}^3(R^{\bullet+}–R^{\bullet-})$	phase coherence, quantum beats	phase coherence, quantum beats
$^1(R^{\bullet+}–R^{\bullet-}) \leftrightarrow {}^3(R^{\bullet+}–R^{\bullet-})$	dephasing, T_2 relaxation	dephasing, T_2 relaxation
$^1(R + R)^* \rightarrow (^3P + {}^3P)$	singlet fission	singlet fission
$^3R + {}^3R \rightarrow R + R$	triplet–triplet annihilation	triplet–triplet annihilation
$R^{\bullet} + R^{\bullet} \rightarrow R–R$, $R^{\bullet+}–R^{\bullet-} \rightarrow R\text{-}R$	recombination reaction	soliton–antisoliton annihilation, charge-carrier recombination, geminate recombination
$R^{\bullet+}–R^{\bullet-} \rightarrow R^{\bullet+} + R^{\bullet-}$	escape reaction	spin diffusion
$\mathbf{R_1} + R_2 \rightarrow R_1 + \mathbf{R_2}$	spin diffusion	polarization transfer

[a]In photochemistry, the term inter-system crossing (ISC) is only defined for an intra-molecular process (according the recommendations of the IUPAC for terms used in photochemistry). Therefore, in spin chemistry, the change of spin multiplicity, which occurs in an inter-molecular process, is termed singlet–triplet interconversion. We would recommend using this term also in spintronics.

terms of its spin evolution driven by internal interactions but will tend to ignore interactions with the environment. A spin physicist, however, will often focus on electric polarization effects on the surrounding and might skip the magnetic forces between the two centers. One should note, however, that chemists are aware of the importance of electric polarization in chemical processes; a prominent example of theoretical understanding of electric polarization effects is given in the famous Marcus theory [21] of electron transfer. Spin–orbit coupling is not a very prominent issue in spin chemistry of radical pairs because of the absence of heavy atoms in most (but not all) of the molecules, for which spin-chemical effects have been studied. Spin–orbit coupling is of importance for the triplet mechanism in spin chemistry and also for triplet state ONP and OEP; these cases are also briefly discussed later. One should also note that the difference, Δg, in g-factors of radicals, which is of great importance for spin chemistry, is also due to perturbation terms in the spin Hamiltonian coming from spin−orbit coupling. For spin physicists, however, it might be crucial since it can occur at defects, determining how fast a triplet return to the ground state. On the other hand, spin physicists have often neglected hyperfine coupling (HFC) interactions, which are a central issue in spin chemistry. Furthermore, similar (or even identical) methods are termed differently.

Finally, Table 3 compares the terminology used in existing methods. One can readily see that some methods exist in both fields. It is obvious that both fields will profit from a fruitful exchange of ideas and concepts. In such a situation, a better communication between scientists of the two fields is desirable not only for having a unified terminology, but mostly to avoid possible rediscoveries of the same methods. Using some examples, we will show that scientists from both fields can learn from each other. The CIDNP method, despite its utility for studying short-lived radicals, has yet no analogue in spintronics.

Molecular systems

Open-shell compounds, such as radicals, radical pairs and triplet states are at the heart of spin chemistry. Radicals are frequent intermediates of many light-induced processes in chemistry. Furthermore, some stable radicals are known that are not transient short-lived species but rather long-lived molecules with an unpaired electron. Radical pairs can be generated in various media by bond cleavage of a photo-excited molecule or by electron transfer from an excited electron donor to an acceptor (or by electron transfer to an excited electron acceptor from a donor). Such radical pairs inherit the spin state of their precursor. Likewise, biradicals can be formed by photo-induced intramolecular electron transfer or by bond cleavage in a cyclic mol-

Table 3: Comparison of terminology and techniques for spin chemistry and spintronics.

Technique	Spin chemistry Reaction yield, reaction rate	Spintronics Conductivity or resistance
MFE detection	MARY, MFE	OMAR
Effect of resonance fields	RYDMR	EDMR, ODMR
Electron spin polarization	CIDEP, CIDEP in SCRPs	EPR of hyperpolarized charge transfer complex
Nuclear spin polarization	CIDNP	no analog

ecule. Since the ground state of most molecules is the singlet state, triplet states are usually only transient species, which are formed upon light excitation with subsequent intersystem crossing producing the triplet state.

For similar reasons magnetic and spin effects are of importance for physicists working in the spintronics field. The corresponding devices allow the manipulation or detection of spins [22,23]. The most prominent type of organic spintronics device is the spin valve, in which a thin organic semiconductor layer is sandwiched between two ferromagnetic electrodes [24]. A spin-polarized current is injected from one of these electrodes and transported through the semiconductor. Another type also implements spin current, but without charge current, in the structure ferromagnetic metal/organic semiconductor/nonmagnetic metal, in which the first interface induces spin pumping [25]. Other devices do not rely on spin manipulation by ferromagnetic layers, but on the intrinsic properties of the organic semiconductor to show, for instance, organic magnetoresistance [26]. These devices also allow spin detection by electrical means. Organic light emitting diodes also rely on spin manipulation of radical pairs created from injected charge carriers in order to increase their electroluminescence quantum efficiency. Another molecular system in which spins play a major role are organic solar cells (OSCs) [27,28]. We chose this to serve as example as it closely resembles the functional principles of systems found in spin chemistry. While OSCs have significant potential to become an inexpensive, large area and flexible photovoltaic technology at lower cost than conventional technologies, we will focus here on the spin processes from absorption to the generation of free charge carriers. The study of spins in organic semiconductors has a long-standing history, but their role in the fundamental processes in OSC has only very recently been highlighted in key publications [29-31]. Also, exploiting the unique properties of electronic spin interactions, the development of novel routes to enhance both the power conversion efficiency and lifespan of solar cells should be possible.

State-of-the-art OSCs consist of the combination of two organic semiconductors, (electron) donor and (electron) acceptor, as the photoactive layer. These two materials are combined either as a blend (the resulting architecture is called bulk heterojunction solar cell) or as two adjacent layers, yielding a planar heterojunction solar cell. The key processes for photovoltaic energy conversion in these types of OSCs are shown in Figure 1. Ideally, singlet excitons in either donor or acceptor material are generated upon light absorption (a), here shown as $S_0 \rightarrow S_1$ transition. For sake of simplicity we just consider the absorption taking place in the donor: the singlet exciton can diffuse towards the heterojunction, where an ultrafast electron transfer (et) to the acceptor occurs on the femtosecond time scale with almost unity yield. One reason is that this process is much faster than the intersystem crossing within, for example, the donor from S_1 to the triplet state T_1. The resulting polaron pair, the negative polaron on the acceptor molecules with the positive polaron remaining on the donor molecules, is called the charge transfer state (CTS) or charge transfer complex. They have been reported to show the emission–absorption signatures in transient EPR as expected for SCRP [32]. The free charge carrier photogeneration in OSCs is mainly determined by the properties of the CTS. The dominant fraction of the CTS thermalizes [33] and only a small fraction might remain "hot" before dissociation [34,35] (d and d*, respectively) into free electrons and holes (charge separated state (CSS)). These separated charge carriers can be extracted to yield the photocurrent. The role of the spin in several loss mechanisms [30,36,37], which reduce the power conversion efficiency, is only partly understood. For instance, if the delocalization of charge carriers in the CTS is

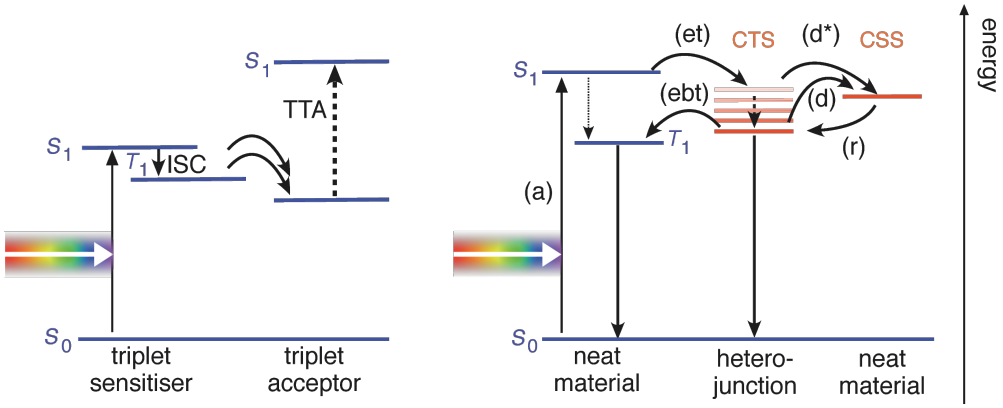

Figure 1: Spin dependent processes in organic solar cells. (Right) The steps from light absorption (a) towards generation of free charge carriers (d), potentially supported by (Left) triplet–triplet annihilation (TTA), are described in the text. Only the lowest excited states of each kind are shown for clarity.

limited, for example, by energetic disorder, CTS dissociation will be uncompetitive compared to geminate recombination, leading to a lower photogeneration yield. The CTS can be in singlet and triplet configuration, although (due to the weak interaction within the polaron pair) energetically close. Therefore, the interconversion from singlet to triplet within the CTS might be comparatively fast. The detailed role of the spin in the geminate recombination (in competition with the charge photogeneration) is still unresolved. In principle, while the CTS singlet can recombine to the ground state, a spin flip (interconversion) to the CTS triplet can occur, which makes an electron back transfer (labeled as ebt in Figure 1) into an intramolecular triplet state of either donor or acceptor possible. The loss in photocurrent due to the electron back transfer is not known quantitatively. It can be minimized by increasing the donor LUMO–acceptor LUMO gap [31], which shifts the CTS below the neat materials' triplet energies, but this tuning of the energy levels limits the achievable open circuit voltage. Up to now, it is unclear what the spin statistics of the interfacial CTS recombination are and how they are influenced by morphology and energetic or spatial disorder [38].

Two optimization strategies for improving the power conversion efficiency based on spin processes are singlet fission and triplet–triplet annihilation (TTA). Singlet fission is the spin allowed conversion of one spin singlet exciton to two spin triplet excitons, which can occur with high yield in some organic semiconductors [39]. It can therefore be seen as down conversion and so-called multiexciton generation. An enhanced power conversion efficiency is then foreseen, with the premise that fission of these high-energy singlet excitations into two independent triplets is quantitative, and that the resulting triplets subsequently dissociate into pairs of free charge carriers. The singlet fission process is also known to spin chemists; furthermore, it is known that this process is magnetic field-dependent [40,41]. Another approach for harvesting low energy photons is TTA [42] (see Figure 1). A singlet exciton is photogenerated in the triplet sensitizer molecule and converted to a triplet by intersystem crossing (ISC). When two of such triplet excitons are transferred to the triplet acceptor, they can undergo TTA to generate a higher energy singlet exciton. The latter can be harvested by the solar cell concept as described above. This concept allows, therefore, internal up-conversion of incident photons, thus extending the absorption range of the photovoltaic system to the little exploited near-infrared regime of the solar spectrum.

Spin dynamics in radical pairs

Radical pairs, or to be more precise, SCRPs, allow for magnetic-field-dependent chemistry. The radical pair mechanism (RPM) is seen as the key mechanism for magnetic field effects on chemical reactivity. One should note that RPM is not the only mechanism, since, for example, the d-type triplet mechanism and triplet–radical mechanism (discussed below) also lead to magnetic field effects in chemistry. The RPM attributes MFEs to (i) spin-selective recombination of radical pairs and (ii) to singlet–triplet interconversion, which is, in turn, sensitive to magnetic fields. Sometimes organic chemistry textbooks state that the recombination reaction of the two radicals ($R_1^{\bullet} + R_2^{\bullet} \rightarrow R_1–R_2$) typically occurs without any activation barrier. That statement, however, is only true if the radical pair ($R_1^{\bullet} + R_2^{\bullet}$) forms a singlet state, that is, the electronic spin wavefunction is antisymmetric. If the spin wavefunction is symmetric (i.e., the radical pair is in a triplet state), then the recombination is usually forbidden. Generally, the total spin of reactants should be the same as that of the reaction products:

$$\sum_{i,\,\text{reactant}} \hat{S}_i = \sum_{k,\,\text{product}} \hat{S}_k$$

meaning that the singlet radical pair can only recombine to a product in the singlet state (here the summation is taken over each i-th reactant and k-th reaction product). Likewise, the triplet radical pair can only recombine to a product in the triplet spin state. In most cases, the two rates are considerably different with the singlet-state recombination usually being more efficient (although cases of more efficient triplet-state recombination are also known [43] and even should not be treated as exceptional). Spin rules strictly apply and impose a rigorous kinetic control over thermodynamics. Hence, only singlet-state radical pairs recombine, while triplet-state radical pairs do not recombine, even when this would be energetically very favorable, and will follow an alternative reaction pathway.

Two radicals forming a radical pair can exist in four possible spin states. Namely, these states are a single singlet state $(\alpha\beta - \beta\alpha)/\sqrt{2}$, also called S (or, sometimes, S_0) state, and three triplet states: $\alpha\alpha$, $\beta\beta$ as well as $(\alpha\beta + \beta\alpha)/\sqrt{2}$. The three triplet states are also called T_+, T_- and T_0, respectively. Therefore, in three of four cases, a recombination of radicals, although thermodynamically favorable, is spin-forbidden. In this case, radicals would move apart or react with neighboring molecules to form more stable radicals. The latter reaction is spin-allowed because the total spin state is not changed.

When a radical pair is formed in a particular spin state (singlet or triplet) its fate is different: in the former case, fast recombination occurs, whereas in the latter case, the radical pair decays through a different pathway. Because of this, the radical pair reactivity strongly depends on the rate of singlet–triplet intercon-

version. The strongest effects of such interconversion on the recombination yield are expected in the situation where the radical pair is born in a nonreactive state. Thus, recombination can *only* occur after the interconversion takes place. In turn, the interconversion rate depends on the magnetic fields, which are external fields (static or oscillating) and the local fields of magnetic nuclei of radicals. Below we explain the origin of such a dependence and discuss its consequences. These consequences are the magnetic and spin phenomena in chemistry.

In order to describe the spin dynamics of radical pairs on the quantitative level, the Stochastic Liouville equation for its spin density matrix, $\hat{\rho}$, is commonly used [44,45]. This equation takes into account the coherent spin evolution (driven by the radical pairs Hamiltonian, $\hat{H}$), spin relaxation and chemical reactions. Additionally, one can take into account the relative motion, which is described by a corresponding operator $\hat{L}$, for instance, for diffusing radicals $\hat{L} = D\Delta_r$ with the reflecting boundary condition at closest approach (here D is the relative diffusion coefficient, Δ_r is the Laplace operator where r is the distance between the radicals. The equation for the density matrix takes the following form:

$$\frac{\mathrm{d}\hat{\rho}(\mathbf{r},t)}{\mathrm{d}t} = \hat{L}\hat{\rho}(\mathbf{r},t) - \frac{i}{\hbar}\left[\hat{H},\hat{\rho}(\mathbf{r},t)\right] - \hat{\hat{R}}\hat{\rho}(\mathbf{r},t) - \hat{\hat{K}}\hat{\rho}(\mathbf{r},t)$$

where the portion of the equation in square brackets is the commutator, $\hat{\hat{R}}$ is the relaxation super-operator and the $\hat{\hat{K}}$ super-operator stands for spin selective recombination. Here, for simplicity, we do not discuss relaxation effects. When the radical pair selectively recombines from the singlet state, $\hat{\hat{K}}$ acts on the density matrix in the following way:

$$\hat{\hat{K}}\hat{\rho}(\mathbf{r},t) = \frac{w_S(\mathbf{r})}{2}\left\{\hat{P}_S,\hat{\rho}(\mathbf{r},t)\right\},$$

Where $w_S(\mathbf{r})$ is the position-dependent recombination rate, $\hat{P}_S$ is the projection operator for the S_0 state and the portion of the equation in brackets stands for the anti-commutator. For a static radical pair the position-dependent rate $w_S(\mathbf{r})$ can be replaced simply by a constant rate k_S. Such a form of the reaction operator corresponds to the decay of the singlet-state population at a rate k_S, whereas the phase elements, singlet–triplet coherences, decay at $k_S/2$ [46,47] Recently, possible corrections to such a form of the operator were discussed [48] differing in the decay of the coherences, which is faster than $k_S/2$ in some models. The time-dependent rate of the product is given by the following quantity:

$$R(t) = k_S\rho_{SS}(t) = k_S\mathrm{Tr}\left\{\hat{P}_S\hat{\rho}(t)\right\}$$

or, when the reactivity is position-dependent, by the integral over spatial coordinates:

$$R(t) = \int\mathrm{d}\mathbf{r}\, w_S(\mathbf{r})\rho_{SS}(\mathbf{r},t) = \int\mathrm{d}\mathbf{r}\, w_S(\mathbf{r})\mathrm{Tr}\left\{\hat{P}_S\hat{\rho}(\mathbf{r},t)\right\}.$$

To calculate the steady-state reaction yield, one should perform integration over time from 0 to ∞. The reaction yield, Y, is obtained by integration of $R(t)$ from zero to infinity:

$$Y(B_0) = \int_0^\infty R(t)\mathrm{d}t.$$

In this formula we stress that the yield is a function of the field strength, B_0. The reaction operator presented here and the method of calculating $R(t)$ is valid for singlet-state recombination and weak spin–orbit coupling.

The Hamiltonian of the radical pair typically takes into account the Zeeman interactions of spins with the external field $\mathbf{B}_0$ (hereafter, the static field directed parallel to the z-axis), HFC and electronic exchange interaction. For simplicity, we consider only the case of isotropic liquids. In this situation the Hamiltonian takes the form (here written in the angular frequency units):

$$\begin{aligned}\hat{H}(\mathbf{r}) = {} & \omega_{1e}\hat{S}_{1z} + \omega_{2e}\hat{S}_{2z} \\ & + \sum_j a_j^{(1)}\left(\hat{\mathbf{S}}_1\cdot\hat{\mathbf{I}}_j^{(1)}\right) + \sum_k a_k^{(2)}\left(\hat{\mathbf{S}}_2\cdot\hat{\mathbf{I}}_k^{(2)}\right) \\ & - 2J_{\mathrm{ex}}(\mathbf{r})\left\{\left(\hat{\mathbf{S}}_1\cdot\hat{\mathbf{S}}_2\right) + \frac{1}{2}\right\}.\end{aligned}$$

Here $\omega_{ie} = g_i\mu_B B_0$ are the electronic Zeeman interactions with g_1 and g_2 being the electronic g-factors (μ_B is the Bohr magneton), $\hat{\mathbf{S}}_1$ and $\hat{\mathbf{S}}_2$ are the electron spin operators. We assume that each radical has a set of magnetic nuclei with spins $\hat{\mathbf{I}}_j^{(1)}$ and $\hat{\mathbf{I}}_k^{(2)}$ (the superscript denotes the radical, to which the nuclei belong) and HFC constants $a_j^{(1)}$ and $a_k^{(2)}$. Finally, $J_{\mathrm{ex}}(\mathbf{r})$ is the position-dependent exchange coupling (also giving rise to the r-dependence of the Hamiltonian). In the presence of a transverse microwave (MW) field, which is commonly used to affect the spin evolution of radical pairs or to detect its CIDEP spectrum, one should add the corresponding terms to the Hamiltonian. Such terms are generally time-dependent but typically vanish in the MW-rotating frame of reference. The nuclear Zeeman interaction is omitted in the expression for the Hamiltonian because in liquids it is usually irrelevant. The reason is that at low fields this interaction is way too small to affect the spin dynamics, whereas at high fields, the nuclear Zeeman

interaction simply changes the splitting between the eigenstates of the Hamiltonian corresponding to the nuclear states α and β and does not affect spin mixing. In solids, however, such states are mixed by the anisotropic parts of the HFCs, which thus become relevant as well as the electron–electron dipolar coupling. In liquids anisotropic interactions are averaged out by molecular motion.

To simplify the description, it is common to present the spin state of SCRPs using a vector model (Figure 2) [1,2,18,19]. The arrows shown on the cones are not static but considered to precess with their Larmor frequency around the central axis. In this diagram, all four states are distinguished by different quantum numbers. In the singlet state, the total spin is zero. In fact, both arrows point into opposite directions and their magnetism is cancelled, i.e., a singlet state is not magnetic and does not interact with external magnetic fields. The situation is different for the three triplet states. Here, the magnetism does not disappear, and a triplet state is able to interact with external magnetic fields. While for the singlet state and the $T_0 = (\alpha\beta + \beta\alpha)/\sqrt{2}$ triplet, the energies are not affected by external magnetic fields, the αα triplet gets destabilized while the ββ triplet becomes stabilized. Hence, the transition energies of a triplet are affected by external magnetic fields (Figure 3). For radical pairs, the transition between $T_+ = \alpha\alpha$ and $T_- = \beta\beta$ is considered to be a double-quantum transition and is forbidden by optical means as well as in magnetic resonance. Such triplet states do not only occur in radical pairs but also by ISC at a single molecule mostly having one free electron in the HOMO and the second one in the LUMO.

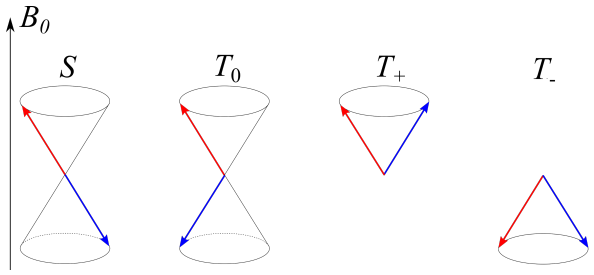

Figure 2: Vector model of the spin states of a radical pair. Here the red and blue arrows show the spin vectors of the two radicals; at high B_0 field, each spin precesses on a cone about the z-axis, here $z \| B_0$. The singlet state is the state with anti-parallel spins. In the T_+ and T_- state there is positive and negative net polarization of the two spins on the direction of the B_0 field axis, respectively. In the T_0 state there is no *net* z-magnetization, but the total spin is non-zero.

The vector model also assumes that the electron spins precess about their effective magnetic fields, which are given by the superposition of the external fields and the local fields [49,50]. The scheme allows one to understand in a simple way how

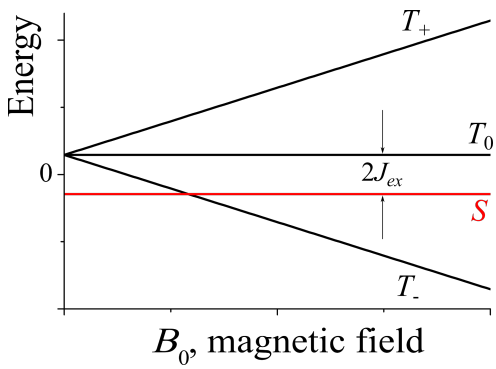

Figure 3: Schematic representation of the energy levels of a radical pair. The spacing between the S and T_0 levels is equal to $2J_{ex}$. In radical pairs, typically, the singlet state is lower in energy at $B_0 = 0$, although the opposite situation can also be met. The splitting between the triplet levels linearly increases with the magnetic field due to the Zeeman effect.

interconversion in radical pairs is occurring. The S–T_0 conversion proceeds due to different precession frequencies of the two electrons: when one electron spin precesses about the z-axis faster than the other one, the radical pair oscillates between the S state and the T_0 state. If one of the spins rotates about the x-axis (or y-axis), transitions between S and $T_\pm$ triplet states occurs. We will use this description to give a simple explanation of magnetic and spin phenomena in radical pairs. Of course, such a simplistic treatment is not always applicable, in particular, for quantitative assessment of magnetic phenomena in chemistry. The reason, for instance, is that depicting the singlet state by two anti-parallel arrows is an over-simplification, which does not take into account the rules of quantum mechanics. Nonetheless, the vector model provides a reasonable qualitative view on the spin dynamics.

MFE, MIE, MARY

As far as MFEs are concerned, their origin can be explained in simple terms using the vector model [1,2,18,19]. To do so, we compare the situations of high external fields and low fields, as compared to the electron–nuclear HFC interaction. HFCs induce local magnetic fields in the x,y,z-directions in space, which can "rotate" the electron spins about the x-, y-, and z-axes, as shown in Figure 4. At low fields, due to HFC, all rotations are possible. Hence, all three interconversion pathways, $S \leftrightarrow T_-$, $S \leftrightarrow T_0$ and $S \leftrightarrow T_+$ are operative. At high fields, however, the $S \leftrightarrow T_\pm$ transitions become energy forbidden because a small HFC cannot flip the electron spins. So, only the $S \leftrightarrow T_0$ conversion pathway is left, which is driven by the secular part of HFC and by the difference, $\Delta g = (g_1 - g_2)$ in the g-factors of the radicals. Consequently, the interconversion efficiency drops: in this simple model, roughly by a factor of three. In real cases, a quantum mechanical treatment should be used to calculate the

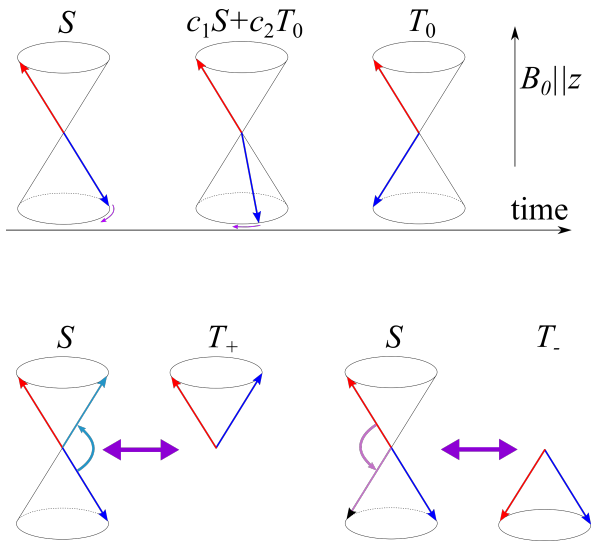

Figure 4: Schematic representation of singlet−triplet transitions in a radical pair. Top: S−T_0 transitions occur due to the difference in the precession frequency of the two radicals. Consequently, a radical pair starting from the singlet state transforms to a superposition of the S and T_0 states, then to T_0 and back. The difference in the precession frequencies can be caused by secular HFCs and by $\Delta g \neq 0$. Bottom: Flips of the spins, e.g., due to local HFC fields or due to external MW-fields, can lead to mixing between the S state and $T_\pm$ states. The B_0 field is parallel to the z-axis.

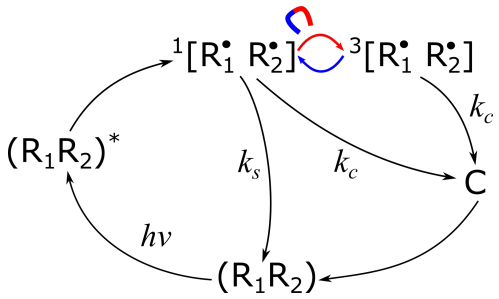

Figure 5: Formation of MFEs upon recombination of SCRPs. In this example the (R_1R_2) molecule goes to the singlet excited state $(R_1R_2)^*$; subsequently, the SCRP $[R_1^\bullet R_2^\bullet]$ is formed in the singlet state. The singlet-state SCRP can recombine to the ground state or go to the triplet state by interconversion: this stage is magneto-sensitive as symbolically indicated. Both singlet and triplet SCRP can go to the state C, e.g., SCRP can undergo diffusional separation to form escaped radicals. Typically, the interconversion is slower at higher fields, i.e., formation of (R_1R_2) is more efficient at high fields. For the triplet precursor the MFE is the opposite: formation of (R_1R_2) is less efficient at high fields. The same scheme can be used to explain MIE: the interconversion rate depends on the content of magnetic isotopes in radicals. The interconversion rate is, e.g., higher for ^{13}C enriched radicals. One should note the similarities with Figure 1: $(R_1R_2)^*$ corresponds to (singlet) exciton in neat material; $^1[R_1^\bullet R_2^\bullet]$ and $^3[R_1^\bullet R_2^\bullet]$ correspond to CTS; (R_1R_2) = ground state; C = charge separated state (CSS).

conversion efficiency as a function of the external magnetic field strength. Thus, we obtain that the interconversion efficiency is sensitive to external magnetic fields, giving rise to MFEs on chemical reactions. Such MFEs are well-established and can be found in a number of reactive systems. For further details we recommend reviews on this subject [1-3,51-54].

The formation of MFEs on recombination of SCRPs can be explained using the scheme shown in Figure 5 (the outline of this figure is following that of Figure 1 of [53]). Due to the presence of the magneto-sensitive interconversion stage, the reaction yield becomes sensitive to the magnetic field strength. In this example, when the radical pair is born from a singlet precursor the yield of (R_1R_2) is higher at high magnetic fields. When the initial state of the radical pair is a triplet, the MFE is just the opposite. The size of the MFE also depends on the precursor. Specifically, MFEs are stronger when the magneto-sensitive interconversion is the kinetic bottleneck of the process. In liquids, MFEs can be formed for recombination of G-pairs as well as for F-pairs. The formation of MFEs of G-pairs generated in a particular spin state is the same as described above. For F-pairs formed in a random spin state, the existence of MFEs is, at first glance, puzzling. However, one should bear in mind that the size of MFEs for singlet-born and triplet-born is different. MFEs from such pairs, though opposite in sign, do not compensate each other completely.

For observing MFEs on chemical reactions one can either monitor the concentration of the reaction product in real time at various magnetic fields or perform a steady-state experiment. For observing MFEs in steady-state experiments, it is necessary to have some “branching”, which makes the overall product yield dependent on the interconversion rate, i.e., on the external magnetic field strength. In the absence of such branching, all radical pairs would eventually recombine, leading to cancellation of potential MFEs. In the example given in Figure 5, branching is provided by the reactions, in which C is formed.

MFEs can be obtained not only for recombining radicals but also in other cases where spin interconversion affects the reactivity. Such cases are the quenching of excited triplet states by radicals [55,56] and triplet−triplet annihilation [57-59]. In the former case, the process is usually allowed from the doublet state (producing the molecule in the singlet ground state and not causing any chemical changes of the radical) so that the magneto-sensitive doublet−quartet interconversion comes into play. In the latter case, the total spin of the reactants can be equal to zero (singlet), one (triplet) or two (quintet) with only the singlet reaction channel being reactive. This spin selectivity in combination with the magnetic field-dependent interconversion can give rise to MFEs.

The same scheme can be used to obtain a simple explanation of MIE. MIE in chemical reactions are not due to the difference in mass of isotopes (which is less than 10% for ^{12}C and ^{13}C) but

due to the different spin and gyromagnetic ratio of them. For instance, the ^{12}C carbon isotope is non-magnetic having zero spin, whereas ^{13}C is a magnetic spin-1/2 nucleus. Consequently, in a ^{13}C labelled radical HFC appears, which can drive the interconversion and make it faster. MIEs can be positive or negative depending on the initial state of the radical pair. Typical applications of MIEs are fractioning of isotopes and elucidating the mechanism of chemical reaction: the presence of MIE provides clear evidence that radical pairs are reaction intermediates, and allows one to identify the spin multiplicity of reaction intermediates. For learning more about MIE in chemistry, we advise the reader to go for more specialized reviews [60-62].

In this context it is also important to mention the so-called "cage effect", which is crucial for MFEs in liquids [1-3]. Generally, the spin dynamics of radical pairs needs a certain time to develop. The typical time required for interconversion is on the nanosecond timescale, meaning that the radical pair partners need to stay close to each other for a time period of comparable duration. This becomes possible due to the cage affect: solvent molecules trap radicals and do not let them separate immediately. Importantly, when radicals undergo stochastic motion (diffusion) due to "kicks" from solvent molecules, they collide many times before radical pair separation, i.e., numerous re-encounters of radicals occur. Generally, for radicals separated by a distance r, the probability of at least one re-encounter is equal [63] to R/r. Consequently, the two radicals spend an extended time in the proximity of each other and completely loose correlation with each other after the characteristic time, which is equal [64] to $\tau_D = R^2/D$, see Figure 6. For spherical particles diffusing in three dimensions, R is the closest approach distance equal to the sum of the radical radii.

MFEs can be studied using different techniques. The concentration of radicals, as well as the radical pair recombination yield

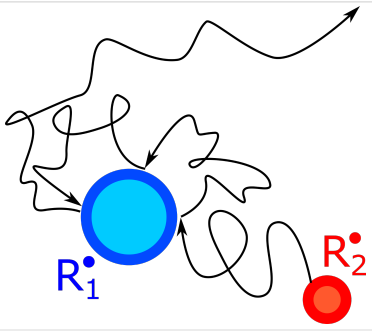

Figure 6: Re-encounters of radicals. In liquids, particles usually move by means of diffusion. In this situation, two radicals, R_1 and R_2, collide a few times before they escape to the solvent bulk and lose correlation with each other (after the characteristic time, which is equal to $\tau_D = R^2/D$).

can be traced by detecting optical absorption, luminescence, photocurrent, etc. These quantities can be monitored either in steady-state experiments or in a time-resolved fashion. Time-resolved measurements can reveal very unusual behavior of the reaction rate of radical pair recombination: this rate has an oscillatory component due to the coherent nature of singlet−triplet mixing [65-67]. The oscillations, often termed "quantum beats", are driven by HFC and Δg. Hence, the frequency of the quantum beats is given by HFCs and, when the magnetic field is sufficiently strong, also by the Δg-term, see Figure 7. Time-resolved MFEs allow one to obtain EPR parameters of radical pairs, which are often too short-lived for detection by conventional EPR methods. Quantum beats are usually observed on the nanosecond timescale; however, when the Δg-term is extraordinarily large, quantum beats occur on the picosecond timescale [68].

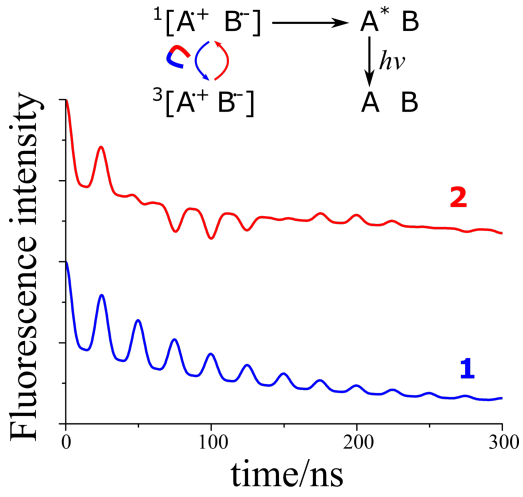

Figure 7: Calculated time-resolved MFE traces as obtained by monitoring recombination fluorescence, resulting from recombination of radical ion pairs in singlet state (such a situation is frequently met upon pulsed radiolysis of non-polar solutions of electron and hole acceptors). Magneto-sensitive interconversion (indicated in the reaction scheme) results in oscillations (quantum beats) of the singlet-state population, which manifest themselves in the fluorescence of A^*. Quantum beats can be due to HFCs (curve 1, HFC-driven quantum beats) and also due to $\Delta g \neq 0$ (curve 2, HFC-driven and Δg-driven quantum beats are superimposed). For convenience of the reader, trace 2 is shifted along the vertical axis (at $t = 0$, the fluorescence intensity is the same in both cases). Here we consider a radical ion pair with equivalent magnetic nuclei with HFC of 20 MHz; for curve 2, the Δg-term is taken equal to 5 MHz. Fluorescence decays due to recombination of the SCRP (additionally, quantum beats decay due to relaxation).

The magnetic field dependence of the reaction yield of a radical pair is often termed a MARY curve. MARY curves typically contain maxima and minima with their positions depending on the EPR parameters of radical pairs, see Figure 8 [69-73]. At zero field, there are two kinds of features observed: a broad feature having a width

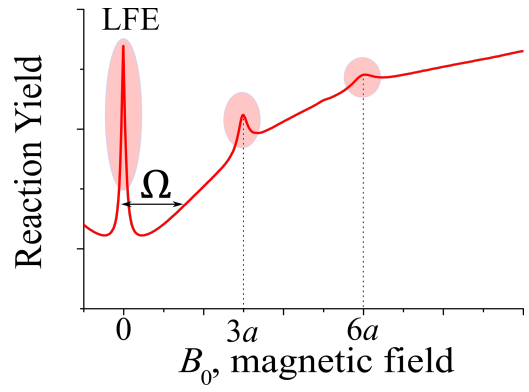

Figure 8: MARY curve, i.e., magnetic field dependence of the reaction yield for a singlet-born radical pair. Here sharp maxima correspond to crossings of the spin energy levels of the radical pair. A crossing at zero field gives rise to the low-field effect (LFE). Additional level crossings are found at specific field strengths (e.g., for radical with 6 equivalent magnetic nuclei these fields are 3*a* and 6*a*). The width, Ω (given by the effective HFC of the radical pair), of the broad MARY line at $B_0 = 0$ is also indicated.

$$\Omega = \sqrt{\frac{2}{3}\sum_k a_k^2 I_k \left(I_k + 1\right)}$$

(summation is performed over all magnetic nuclei of the radical pair having HFC constants a_k and spins I_k) of about the effective HFC in the radical pair and a sharp feature (often termed low-field effect (LFE)). The broad feature is, in fact, a level anti-crossing effect, whereas the sharp feature results from a pure level crossing, which is always present in radical pairs at zero field (originating from the equivalence of all directions in space). As usual, we assume that level crossing corresponds to a situation where two levels, $|K\rangle$ and $|L\rangle$, become degenerate at particular field strength. However, it is known that if there is small perturbation, V_{KL} mixing the two levels, they never cross. Hence, the level crossing turns into a level anti-crossing (often termed avoided crossing); at the level anti-crossing the initial states $|K\rangle$ and $|L\rangle$ become mixed. The width of the LFE feature is given by the inverse decoherence time in the radical pair, which comes from the electronic spin relaxation as well as from chemical reactions, i.e., radical pair recombination and radical pair transformation. Hence, the LFE width can be used to determine rates of fast chemical processes on the nanosecond time scale. Interestingly, in some radical pair systems, additional sharp features at $B_0 \neq 0$ can be found, resulting from additional level crossings. For instance, in radical pairs comprising radicals of hexafluorobenzene (which has six equivalent ^{19}F nuclei), sharp features on top of a smooth background have been found for $B = 0$, $B = 3a$, $B = 6a$; here a is the ^{19}F HFC constant of the hexafluorobenzene radical anion [74,75]. Such findings are in agreement with analytical theory, which can be developed for radicals with a set of equivalent nuclei [76]. Sharp features coming from level crossings (at $B_0 = 0$ as well as at non-zero fields) have been found [70,71,74,75,77] for a number of experimental systems where the SCRP has a set of equivalent nuclei.

Considerable MFEs and additional features in MARY curves can also arise due to other interactions, notably, due to the electron–electron exchange interaction. In the presence of J_{ex} there is an energy gap between the singlet and triplet levels; consequently, the interconversion slows down. Only at a particular field strength, $B = 2|J_{ex}|$, which matches the singlet–triplet energy gap, one of the triplet levels, T_+ or T_-, that tends to cross with the singlet level. At this field, the interconversion becomes efficient due to the transitions between the crossing energy levels; these transitions are operative due to HFCs, which also turn the level crossing into an avoided crossing. Consequently, in the field dependence of the reaction yield a peak or a dip is observed at $B = 2|J_{ex}|$. Additional features can appear at other matching conditions, for instance, when the HFC term matches the Δg-term: upon such a matching the interconversion in a particular nuclear spin ensemble is slowed down.

The MARY and organic magneto-resistance (OMAR) [78] techniques represent essentially the same method, despite having different names. The OMAR effect is observed by monitoring the resistance of an organic material originating from the spin-dependent nature of charge carrier transport and recombination. The mechanism underlying OMAR is the same as for MARY. On the one hand, MARY is a more general term, since MARY is not supposed to be bound to only organic systems (examples of MARY in inorganic systems also exist [77]) and does not imply that resistance is used to monitor reaction yield. In OMAR, effects known for MARY have been reported. For instance, the LFE-type behavior has been found [79-81] in a number of systems used for spintronics applications. On the other hand, OMAR is just one instance of MFE, which has been reported not only for (magneto)resistance, but also electroluminescence and other observables [82].

The exact mechanism leading to MFE, as observed in organic diodes, is still not completely understood. Several relevant processes have been proposed: as mentioned above, they are all similar in relying on spin-selective reactions of particle pairs. The most important underlying mechanism is spin mixing of the particles by hyperfine interaction, which is suppressed by the magnetic field. The particle pairs are bipolarons, electron–hole (polaron) pairs (or charge transfer excitons), but also polarons interacting with triplets, as well as triplet–exciton pairs. The bipolaron model [83] can explain a positive magnetoresistance in energetically disordered systems, such as a conjugated

polymer film. A mobile polaron is able to hop to a site already occupied by a polaron of the same charge type (unipolar OMAR), if the thus-generated bipolaron is in the singlet state, while the triplet formation is unfavorable. The singlet bipolaron enhances current flow, whereas the triplet configuration blocks the current. This so-called spin blocking can be cancelled by the magnetic field. The spin mixing seems to be most pronounced in the slow hopping regime [84], for instance, when deep traps reduce the charge carrier mobility [85]. Oppositely charged polaron pairs [16] (or correlated radical ion pairs) can show a bipolar OMAR, if the charge transport is limited by spin-selective electron–hole recombination [86]. In contrast to the unipolar OMAR (where bipolarons enhance the current flow) here two (oppositely charged) polaron pairs usually reduce the current: either by recombination or generation of a triplet exciton. Accordingly, the resulting OMAR is usually negative [84], although the original model [82] can in principle accommodate also positive changes. The Δ*g*-mechanism described above can show MFE [82], usually of the opposite sign than the OMAR due to suppression of the hyperfine induced spin mixing. Spin–orbit coupling is usually of lesser importance, unless the hyperfine interaction is strongly suppressed (e.g. in C60, which lacks the protons and contains 99% ^{12}C, having zero nuclear spin [87]) or heavy metal atoms are present as part of the molecule or by doping [86,88]. An MFE can also be observed by interactions with excitons: polaron–triplet interactions [89], triplet–triplet annihilation [90], or singlet fission [40].

Generally, the magnetic field is characterized not only by its strength but also by its direction with respect to the molecular axes system. Hence, there is not only the dependence of the reaction yield on the field strength, but also on the molecular orientation [91], for instance due to the anisotropy of the hyperfine interaction. The orientation dependence is of importance in solids, since in liquids molecules usually tumble so fast that anisotropic spin interactions are averaged out and all field directions in space become completely equivalent. However, in solids the reaction yield and the MFE can depend on the direction of the external magnetic field [91-93].

RYDMR

One more important member of the family of spin-chemistry techniques is RYDMR [94-97]. The idea of RYDMR is based on affecting the singlet–triplet interconversion in radical pairs by applying resonant MW-fields, see Figure 9. When such MW-fields enhance or slow down the interconversion, the reaction yield is altered. Of course, MW-fields affect the interconversion only when they are applied resonantly to some of the EPR transitions in the radical pair. Therefore, variation of the MW-frequency (to be more precise, by variation of the external magnetic field, as usually done in EPR) allows one to obtain the EPR spectrum of the radical pair by monitoring the reaction yield. This is the essence of the RYDMR technique, which can be used for two purposes: (i) controlling the reactivity of radical pairs by using spin degrees of freedom and (ii) obtaining EPR parameters of short-lived radicals and radical pairs.

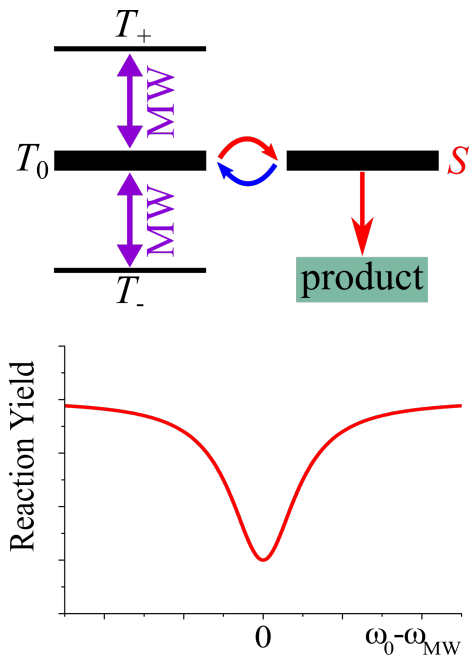

Figure 9: Principle of the RYDMR method. Top: reaction scheme – interconversion mixes the *S* and T_0 of a radical pair, which reacts from the *S* state. Hereafter, in the energy level diagram, the thickness of levels corresponds to the state population. A MW-field can drive the $T_0 \leftrightarrow T_+$ and $T_0 \leftrightarrow T_-$ transitions. Bottom: schematic representation of the RYDMR spectrum – the singlet-state population can be monitored by measuring the reaction yield as a function of the MW-frequency. When the MW-field is applied in resonance with the triplet transitions, $T_0 \leftrightarrow T_+$ and $T_0 \leftrightarrow T_-$ (i.e., the MW frequency is matched to ω_0, which is the precession frequency of the SCRP partners), the populations of the *S* and T_0 states are decreased. The RYDMR signal can be obtained as a dip in the dependence of the reaction yield on the MW-frequency, ω_{MW}. Experiments with MW-pulses with variable lengths and inter-pulse delays can be performed to obtain quantum beats and echo-like signals.

RYDMR spectra can be obtained [95] by monitoring optical absorption, luminescence of the reaction product or photocurrent from radical ions which escape recombination, i.e., RYDMR exists in different versions depending on the observable. Although RYDMR is not as generally applicable as EPR, it has advantages, namely, sensitivity and time resolution. In addition to the possibility of acquiring EPR spectra of radical pairs, one can also perform more complicated experiments. For instance, it is possible to obtain quantum beats in the recombination efficiency, which are indicative of the coherent spin dynamics and can be used for precise measurements of EPR parameters [98,99]. Typically, selective excitation of one of the

radicals results in quantum beats with the nutation frequency ω_1 of the MW-field, whereas non-selective excitation (spin locking) produces "double beats" with the frequency of $2\omega_1$. Somewhat later than in spin chemistry, such effects were also discussed in the spintronics field [100,101]. One more important aspect of using RYDMR is that it allows one to affect the reactivity of radical pairs. This can most easily be done by applying a strong MW-field that drives the EPR transitions of both partners of the radical pair. In this situation, spin locking takes place: the singlet state of the two spins is isolated from the triplet state. Consequently, the interconversion is blocked (if a very strong field is used) or at least suppressed.

The RYDMR equivalent in spintronics is electrically detected magnetic resonance (EDMR) or optically detected magnetic resonance (ODMR) [16,102]. Recently, important results have been obtained in the EDMR field [102]: pulsed EPR experiments have become feasible by combining EPR pulse sequences with sensitive current detection. In such experiments echo-type signals have been obtained. One should note that RYDMR and EPR use different observables; for this reason, one cannot use EPR pulse sequences in RYDMR without a pertinent modification [103]. Specifically, in EPR, spin magnetization is detected, whereas the RYDMR signal is maximal when the radical pair is in the singlet state. However, in such a pair, all magnetization components are zero. Likewise, pure spin magnetization does not give any contribution to the singlet state population because the singlet spin order is essentially a two-spin order.

These problems can be overcome by using a modification of spin echo experiments in EPR [102]. At the instance of time where the spin echo is formed, the refocused magnetization can be converted into two-spin order by applying an additional 90° pulse. The echo is then monitored by changing the instance of time when the last pulse is applied. Such a scheme can be modified further to exploit more advanced EPR methods for RYDMR purposes. For instance, the feasibility of the electron–electron double resonance [104] and electron–nuclear double resonance [105] has been demonstrated.

CIDEP and CIDNP

In this section, we provide a short description of spin "hyperpolarization" generated in chemical processes. Hyperpolarization refers to non-Boltzmann spin polarization which is highly desired by spectroscopists since it enhances the sensitivity of the method. Polarization of electron spins (CIDEP) and nuclear spins (CIDNP) results from spin selectivity of chemical reactions and can be used for sensitive detection of transient radical species. We start our description from CIDEP and introduce the main mechanisms for CIDNP formation.

In SCRPs, singlet and triplet states are not eigenstates but allowed to evolve in a coherent superposition of states. At high fields, in particular, a dynamic interconversion between the S and T_0 states occurs if there is a difference in the precession frequency of the SCRP partners. There are two reasons for having different precession frequencies: (i) both individual radicals have different g-values, i.e., have different "chemical shifts" on their EPR axis, which is due to different chemical environments. In this case, Δg is not equal to 0. (ii) Coupling of an electron spin to magnetic nuclei by HFC interaction will either accelerate or slow down the precession frequency of the electron depending on the direction of the nuclear spin state. As a consequence of the spin mixing, the population becomes evenly distributed between the two spin states, S and T_0.

SCRPs, in contrast to radical pairs with equilibrium populations of the spin states, show a particular intensity pattern in the EPR experiment (Figure 10) [1,3,106,107]. While a thermally relaxed radical pair shows transitions with absorptive (positive) intensity, a SCRP born for example by a bond break from a singlet state would populate initially only the S state, which has 50% αβ and 50% βα characteristics. This population distribution leads to a special pattern showing both emissive (negative) and enhanced absorptive (positive) signal intensities. The spectrum thus consists of two "anti-phase" doublets. Such transient electron spin order is often observed in EPR spectroscopy, cor-

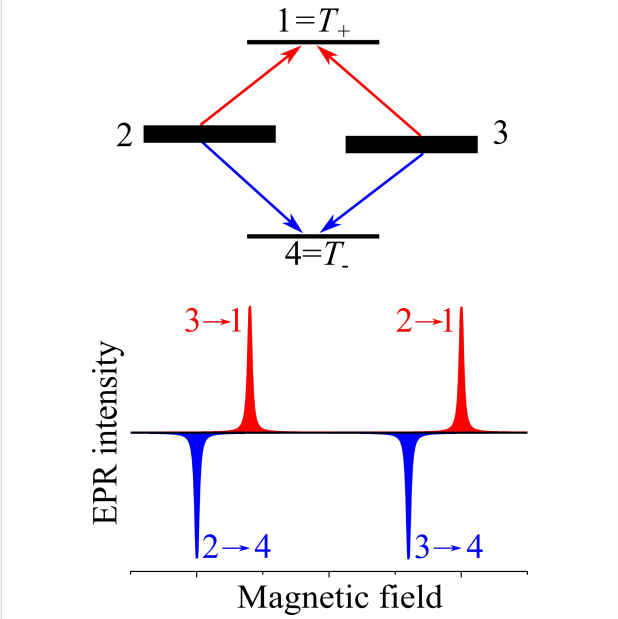

Figure 10: Top: Populations of the electronic spin state of an SCRP – when the radical pair is singlet-born initially, only the two central states, |2〉 and |3〉 have "singlet character" (each of them is a superposition of |S〉 and |T_0〉) and are populated, resulting in two EPR transitions in absorption and two in emission. Positions of the energy levels are not to scale. Bottom: Schematic representation of the corresponding CIDEP spectrum, consisting of two anti-phase doublets.

responding to CIDEP. For observing such CIDEP spectra, it is required that either J_{ex} is non-zero or that a non-averaged electronic dipolar coupling is present, which is often the case in solids.

A more complex situation arises in solids where a distribution of different interactions exists, notably, of *g*-anisotropies and of the electronic dipolar coupling. As a result, the shape of the spectral doublets can change but the antiphase nature of polarization remains [106,107]. The antiphase polarization originates from the spin-selective formation of radical pairs: in this situation no net polarization is expected (because the initial magnetization of the pair of spins is zero). Instead, two-spin order is formed. This spin order results in different phase of EPR lines within each multiplet; for this reason, such CIDEP is sometimes termed "multiplet CIDEP". Detection of spin echo from SCRPs is also possible by EPR methods. It is worth noting that the spin echo is collected 90° out-of-phase [107-109]. This feature of the spin echo formation is markedly different from the spin echo coming from thermally polarized spins, allowing for selective detection of SCRPs. Furthermore, the out-of-phase echo signal is modulated due to the electronic spin–spin coupling, exchange or dipolar. Consequently, a precise determination of this coupling becomes feasible, providing the information about the SCRP structure, notably, about the distance between the radical centers.

In liquids, detection of CIDEP of SCRPs is often impossible because radicals quickly separate. Nevertheless, CIDEP of radicals can be often detected. Such CIDEP usually results in the opposite phase of polarization of the partner radicals avoiding geminate recombination: when the SCRP is singlet-born, no *net* spin polarization can be formed. The formation of such CIDEP can be explained using the fictitious spin representation of CIDEP, as proposed by Adrian [110].

Other CIDEP mechanisms are also known. CIDEP can be generated from molecular triplet states. The corresponding mechanism is termed "triplet mechanism" [1-3], see the Section "Optical nuclear polarization" which follows later in this article. In this situation, the polarization formation is due to the difference in the ISC rates for different triplet substates in non-symmetric molecules. For instance, when a triplet T_1 state is formed from an excited singlet state, S_1, the ISC rate is different for the three triplet sublevels, T_x, T_y, T_z. Consequently, the triplet state is formed in a non-equilibrium spin state and exhibits CIDEP. This mechanism is termed the "p-type" (population-type) triplet mechanism [111,112]. Alternatively, CIDEP can be formed due to the "d-type" (depopulation-type) triplet mechanism [113] when the decay of the triplet state is different for the different sublevels. In contrast to the "p-type" triplet mechanism, "d-type" triplet mechanism can also lead to magnetic field effects on product yield [114-116]. When a radical pair is formed from the polarized triplet state, it inherits the triplet-state CIDEP. Finally, we would like to mention that CIDEP can be due spin-selective processes involving particles with higher spin, e.g., due to the radical–triplet pair mechanism [117,118]. CIDEP effects have already been observed in materials, which are used for OPV: Behrends et al. [32] and Kobori et al. [119] have detected antiphase EPR lines of photo-induced charge transfer complexes, i.e., of SCRPs, whereas Lukina et al. [120] have recently reported a study of the out-of-phase electron spin echo.

Until now, no CIDNP phenomenon has been observed in spintronics [121-124], although the possibility of obtaining such effects has been mentioned [125]: "If nuclear spin resonance is found to have an impact on the spin-dependent electron transport due to the hyperfine interaction, ultimately the opposite process may become possible: storing electronic spin information in the nuclear spin." Despite that we want to describe the basic CIDNP theory, based on the classical RPM [1,3] with the intention to stimulate future NMR research in that field. Figure 11 explains the situation for a radical pair with a single proton ($R_1H + R_2$). Here we schematically show the EPR spectrum of the radical pair assuming that the two partners R_1H and R_2 have slightly different *g*-values. Therefore, the two electrons have also slightly different precession frequencies and oscillate between S and T_0 states. The R_1 signal in the EPR spectrum in Figure 11, however, is split into two components. The origin of this split is due to the HFC of the nearby proton. Also the proton has two nuclear spin states, either α or β. Hence, the interaction with the nucleus induces on the electron frequency a splitting into two lines of similar intensity. The frequency difference between the two lines (given in units of Tesla or Hertz) is the HFC. The term "constant" is used although it is actually a factor. Figure 11 shows a special situation in which the three-spin system $R_1H + R_2$ might operate: The half of Δg is close to the value of the HFC. In this case, half of the population of R_1 has a Larmor frequency close to that of R_2, while the other half is far off that matching frequency. Hence, in one half of the radical pair, the total spin state remains, while it is oscillating in the other half. If a radical pair is born in the triplet T_0 state, half of the population will remain in the triplet state, while the other half soon will undergo interconversion to the singlet state and react. The control over the spin dynamics, therefore, is given by the spin state of the nucleus. This control is also called "spin sorting" and is considered to be the first step – the initial spin-physical step of the RPM.

Radical pairs in their singlet state are allowed to recombine to the recombination products (Figure 7). That reaction is spin-

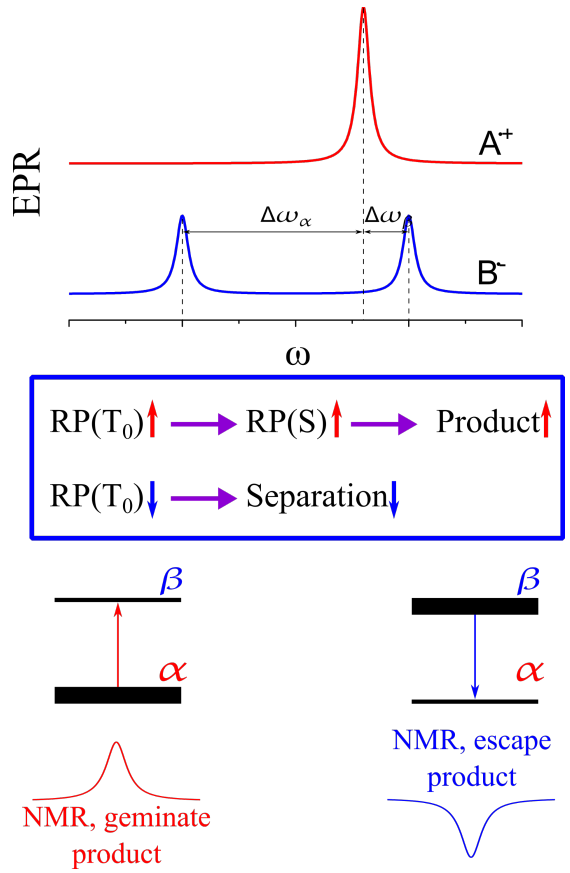

Figure 11: Scheme of CIDNP formation by spin sorting at high magnetic fields. Top: EPR spectra of the two radicals – one radical has a single spin-1/2 nucleus resulting in splitting of the EPR line into two components; the other radical has no nuclei, i.e., a single EPR line. The difference in EPR frequencies, $\Delta\omega_\alpha$ and $\Delta\omega_\beta$, are indicated for the radical pairs with the nucleus in the α-state and β-state, respectively. Since $\Delta\omega_\alpha \neq \Delta\omega_\beta$, the $S - T_0$ interconversion rate is different for the two nuclear spin states. Middle: Kinetic scheme of CIDNP formation – a triplet-born radical pair in the T_0 state rapidly goes to the reactive single state for the α nuclear spin state, resulting in a reaction product enriched in this nuclear spin state. For the β nuclear spin state, radical pairs react less efficiently and undergo separation. Bottom: The geminate reaction product is enriched in the α nuclear spin state giving an NMR line with enhanced absorption, whereas for reaction products of the escaped radicals, the opposite sign of polarization and opposite CIDNP sign is expected.

forbidden for radical pairs in their triplet state. In solution state, the triplet radical pair will diffuse apart and form two independent radicals surrounded by their own solvation shell each. These radicals of the so-called escape reaction might undergo subsequent chemical reactions for example with solvent molecules. If the products of the both reaction pathways are chemically distinguished, i.e., have different chemical shifts, they will appear in an NMR spectrum with opposite sign as either emissive (negative) or enhanced absorptive (positive) signals. The nuclear polarization pattern appearing in NMR shows positive ("enhanced absorptive") and negative ("emissive") signals. Hence, spin sorting can be observed by NMR if the products are different chemical species allowing for the second, the spin-chemical step of the RPM. Therefore, photo-CIDNP NMR spectra transiently show intensity patterns having the same area of positive and negative signal intensities. Photo-CIDNP NMR provides indeed an attractive hyperpolarization technique since it relies simply on the irradiation of the sample by visible light.

The efficiency of photo-CIDNP mechanisms is highly dependent on the strength of the magnetic fields [126-128]. Photo-CIDNP can also appear at low fields comparable to HFCs [126,128,129], at the earth field, as well as under solid-state conditions [130-135]. In confined systems, such as SCRP in micelles or biradicals, CIDNP can also exhibit features caused by the electronic exchange coupling found at $B_0 = 2\langle J_{ex}\rangle$ [136-138]. In solids, CIDNP is strongly affected by non-averaged spin interactions [133,139,140], such as anisotropic HFC and electron–electron dipolar coupling. Generally, the spin dynamics underlying CIDNP in liquids and in solids is considerably different. For these cases, we refer to the literature [123,124,132,141].

Optical nuclear polarization (ONP)

To manipulate chemical reactions by magnetic fields, i.e., to do spin chemistry, transient magnetic species need to occur during the reaction course. Mostly, spin dynamics of SCRPs is used to this end. Another option is to employ molecular triplet states. Depending on symmetry considerations, its three substates T_0, T_+ and T_- might be formed and might decay with individual kinetics, allowing for enrichment of a particular substate (i.e., electron-spin hyperpolarization).

Using highly purified anthracene single crystals under continuous illumination under UV-rich white light, in 1967 Maier et al. [142] observed nuclear hyperpolarization for the first time. The effect could also be detected in doped crystals of similarly fused aromatic compounds. It appeared that the phenomenon has a maximum at rather low fields (around 0.01 T), which is the range of hyperfine fields, and often remains observable at higher magnetic fields. Normally, the samples are illuminated in the stray field of the magnet and can be conveniently transferred into the magnet for the NMR experiment due to the long nuclear T_1. In any case, the sample needs to pass the stray field which will provide at some place the same strength as the hyperfine field.

It is the electron hyperpolarization occurring in the molecular triplet state, called optical electron polarization (OEP), which is converted into optical nuclear polarization (ONP) [143,144]: the illumination with UV or white light initially caused an excited electronic singlet state (Figure 12). Upon ISC, the population is

transferred into the electronic triplet states. In extended molecules, owing to zero-field splitting (ZFS), the three triplet states are not degenerate. Under these conditions, as proven by Wolf et al. [142] as well as Schmidt and van der Waals [145,146] in the late 1960s, the pathways of spin–orbit coupling which enable ISC are strongly spin selective. As a result, often only that triplet state gets populated, matching the symmetry of the preceding excited singlet state. In the same way, the decay to the electronic ground state also depends on spin-selective ISC. Therefore, transient non-equilibrium electron populations can occur, which are observable with EPR spectroscopy.

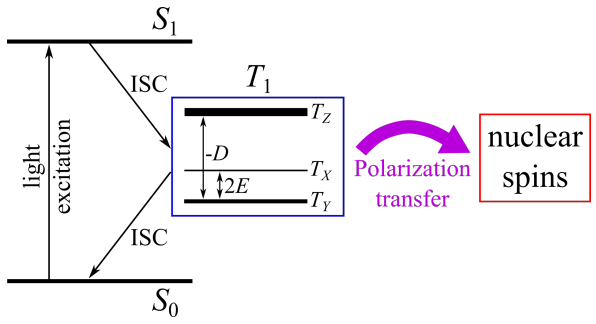

Figure 12: Scheme of triplet-state OEP and ONP formation. In anisotropic molecules, the ISC process $S_1 \rightarrow T_1$ has a different rate for the three triplet states resulting in OEP of the T_1-state; the triplet states, T_x, T_y, and T_z, are indicated as well as the ZFS parameters, D and E. Alternatively, OEP can be formed due to the different T_1 depopulation rates in the ISC process $T_1 \rightarrow S_0$. ONP is formed by spin-polarization transfer from the polarized T_1 state to nuclear spins of the matrix.

In the second step, electron–spin hyperpolarization is converted to nuclear hyperpolarization by static hyperfine interaction. Independently, both Veeman et al. [147] and Stehlik et al. [148-150] demonstrated that the optimum polarization transfer to nuclei occurs upon matching of the hyperfine field with the external stray field. In this case, a hyperfine interaction occurs, leading to a selective mixing of the electronic triplet states, which results in a level anti-crossing without a change of the total magnetic quantum number. In molecular crystals, the kinetics and site of the occurrence of ONP may be controlled by migration of triplet excitations and their trapping. Triplet-state OEP and ONP, despite using a different photo-cycle, can also be generated in negatively charged nitrogen vacancy (NV^-) centers in diamond crystals, which is presently a hot field of research [151-154].

Hence, spin chemistry deals with transient magnetic species as SCRPs and molecular triplet states interacting with the external magnetic field. Their production in chemical reactions often leads to spin-hyperpolarization, which can be observed with NMR and EPR spectroscopy.

Conclusion

Magnetic field sensitive techniques are a well-established field for spin-dependent reactions in chemistry, mainly focusing on molecules in solution phase. More recently, spin-sensitive techniques have also been proposed for investigation of spin dynamics in organic photovoltaics and light emitting diodes. Based on solid films of molecules, a complete independent nomenclature has been developed. This begins with the terminology of spins, “α” and “β” versus "up" and "down" and reaches through the entire field. An adequate exchange of knowledge between both fields is cumbersome and ends far too often at language barriers.

If one is familiar with both fields, it becomes evident that certain spin-sensitive techniques have been reinvented during the last decades. This obviously can be seen as an unpleasant development: Time and money is lost to recreate already available knowledge, existing measurement setups are unused and early stage scientists do not receive their deserved recognition. Therefore, it is wise to be aware of the two fields, spin chemistry and spintronics. Examples of independently developed methods are, e.g., RYDMR for spin chemisty and EDMR for spintronics. Another example is given by CIDEP and certain EPR measurements. However, there are still techniques like CIDNP available which are not yet used in device physics.

Organic spintronics is a wide field, covering devices with spin-polarized injection or light emitting diodes, which also show a magnetic field effect. We consider the relation to spin chemistry from the perspective of organic photovoltaics, as an example with close similarity to spin chemistry, in which the influence of spin dynamics for the working solar cell is still only superficially investigated. Spin chemistry makes clear that singlet–triplet interaction will have an effect. The recombination of anions and cations, i.e., polarons, is a desired effect in light emitting diodes and an undesired one for solar cells. If recombination could be engineered by spin statistics, an increase of the quantum and power conversion efficiency should be the consequence.

Regarding Tables 1–3, it becomes evident that scientists from spin chemistry will have a problem reading literature from spintronics and vice versa. We therefore hope to give an impetus to both communities to exchange their knowledge. If successful, a foreseeable time and money consuming process will be abridged, introducing hitherto unknown techniques as CIDNP to spintronics and the solid state systems to spin chemistry. Considering the current progresses in both fields, this might be the right time to merge them together. The exchange of ideas between the two fields would strongly enhance progress in both research directions.

List of Acronyms

The following is a list of acronyms used throughout this review article: CIDEP = chemically induced dynamic nuclear polarization, CIDNP = chemically induced dynamic electron polarization, CSS = charge separated state, CTS = charge transfer state, EDMR = electrically detected magnetic resonance, EPR/ESR = electron paramagnetic resonance/electron spin resonance, et/ebt = electron transfer/electron back transfer, F-pair/G-pair = free pair/geminate pair, ISC = intersystem crossing, LFE = low-field effect, MARY = magnetically affected reaction yield, MFE = magnetic field effect, MIE = magnetic isotope effect, NMR = nuclear magnetic resonance, NV = nitrogen vacancy, OMAR = organic magnetoresistance, ODMR = optically detected magnetic resonance, OEP = optical electron polarization, ONP = optical nuclear polarization, OSC = organic solar cells, RPM = radical pair mechanism, RYDMR = reaction yield detected magnetic resonance, SCRP = spin-correlated radical pair, TTA = triplet–triplet annihilation, ZFS = zero field splitting.

Acknowledgements

This article is dedicated to Herrn Prof. Dr. Dr. h.c. Lothar Beyer (Universität Leipzig) on the occasion of his 80th birthday. J.M. acknowledges the Deutsche Forschungsgemeinschaft DFG for kind support (MA 4972/2-1, MA 4972/5-1). K.L.I. acknowledges the Russian Science Foundation (grant No. 15-13-20035) and FASO of RF (project No. 0333-2016-0001). C.D. acknowledges support through the European Union's Horizon 2020 research and innovation programme under the Marie Sklodowska Curie grant agreement No. 722651, and thanks the SEPOMO project partners for interesting discussions.

References

1. Salikhov, K. M.; Molin, Y. N.; Sagdeev, R. Z.; Buchachenko, A. L. *Spin polarization and magnetic effects in chemical reactions;* Elsevier: Amsterdam, Netherlands, 1984.
2. Steiner, U. E.; Ulrich, T. *Chem. Rev.* **1989,** *89,* 51. doi:10.1021/cr00091a003
3. Hayashi, H. *Introduction to Dynamic Spin Chemistry: Magnetic Field Effects on Chemical and Biochemical Reactions;* World Scientific Lecture and Course Notes in Chemistry, Vol. 8; World Scientific Publishing Co. Pte. Ltd.: Singapore, 2004. doi:10.1142/5316
4. Fessenden, R. W.; Schuler, R. H. *J. Chem. Phys.* **1963,** *39,* 2147. doi:10.1063/1.1701415
5. Bargon, J.; Fischer, H. *Z. Naturforsch., A: Astrophys., Phys. Phys. Chem.* **1967,** *22,* 1551. doi:10.1515/zna-1967-1015
6. Kaptein, R.; Oosterhoff, J. L. *Chem. Phys. Lett.* **1969,** *4,* 195. doi:10.1016/0009-2614(69)80098-9
7. Closs, G. L. *J. Am. Chem. Soc.* **1969,** *91,* 4552. doi:10.1021/ja01044a043
8. Sagdeev, R. Z.; Molin, Yu. N.; Salikhov, K. M.; Leshina, T. V.; Kamha, M. A.; Shein, S. M. *Org. Magn. Reson.* **1973,** *5,* 603. doi:10.1002/mrc.1270051212
9. Brocklehurst, B.; Dixon, R. S.; Gardy, E. M.; Lopata, V. J.; Quinn, M. J.; Singh, A.; Sargent, F. P. *Chem. Phys. Lett.* **1974,** *28,* 361. doi:10.1016/0009-2614(74)80366-0
10. Buchachenko, A. L.; Galimov, E. M.; Nikiforov, G. A. *Dokl. Akad. Nauk SSSR* **1976,** *228,* 379.
11. Sagdeev, R. Z.; Leshina, T. V.; Kamha, M. A.; Belchenko, O. I.; Molin, Yu. N.; Rezvukhin, A. E. *Chem. Phys. Lett.* **1977,** *48,* 89. doi:10.1016/0009-2614(77)80220-0
12. Hoff, A. J.; Rademaker, H.; van Grondelle, R.; Duysens, L. N. M. *Biochim. Biophys. Acta* **1977,** *460B,* 547. doi:10.1016/0005-2728(77)90094-9
13. Boxer, S. G.; Chidsey, C. E. D.; Roelofs, M. G. *Annu. Rev. Phys. Chem.* **1983,** *34,* 389. doi:10.1146/annurev.pc.34.100183.002133
14. Camacho, I. S.; Matysik, J. Spin transport in photosynthesis. In *The Biophysics of Photosynthesis;* Golbeck, J.; van der Est, A., Eds.; Springer: Berlin, Germany, 2014; pp 141–170.
15. Sokolik, I. A.; Frankevich, E. L. *Phys.-Usp.* **1974,** *16,* 687.
16. Frankevich, E. L.; Lymarev, A. A.; Sokolik, I.; Karasz, F. E.; Blumstengel, S.; Baughman, R. H.; Hörhold, H. H. *Phys. Rev. B* **1992,** *46,* 9320. doi:10.1103/PhysRevB.46.9320
17. Closs, G. L.; Forbes, M. D. E.; Norris, J. R. *J. Phys. Chem.* **1987,** *91,* 3592. doi:10.1021/j100297a026
18. McLauchlan, K. A.; Steiner, U. E. *Mol. Phys.* **1991,** *73,* 241. doi:10.1080/00268979100101181
19. Woodward, J. R. *Prog. React. Kinet. Mech.* **2002,** *27,* 165.
20. Buckley, C. D.; Hunter, D. A.; Hore, P. J.; McLauchlan, K. A. *Chem. Phys. Lett.* **1987,** *135,* 307. doi:10.1016/0009-2614(87)85162-X
21. Marcus, R. A. *Rev. Mod. Phys.* **1993,** *65,* 599. doi:10.1103/RevModPhys.65.599
22. Sun, D.; Ehrenfreund, E.; Vardeny, Z. V. *Chem. Commun.* **2014,** *50,* 1781. doi:10.1039/c3cc47126h
23. Koopmans, B.; Wagemans, W.; Bloom, F. L.; Bobbert, P. A.; Kemerink, M.; Wohlgenannt, M. *Philos. Trans. R. Soc., A* **2011,** *369,* 3602. doi:10.1098/rsta.2011.0172
24. Barraud, C.; Seneor, P.; Mattana, R.; Fusil, S.; Bouzehouane, K.; Deranlot, C.; Graziosi, P.; Hueso, L.; Bergenti, I.; Dediu, V.; Petroff, F.; Fert, A. *Nat. Phys.* **2010,** *6,* 615–620. doi:10.1038/nphys1688
25. Watanabe, S.; Ando, K.; Kang, K.; Mooser, S.; Vaynzof, Y.; Kurebayashi, H.; Saitoh, E.; Sirringhaus, H. *Nat. Phys.* **2014,** *10,* 308–313. doi:10.1038/nphys2901
26. Mermer, Ö.; Veeraraghavan, G.; Francis, T. L.; Sheng, Y.; Nguyen, D. T.; Wohlgenannt, M.; Köhler, A.; Al-Suti, M. K.; Khan, M. S. *Phys. Rev. B* **2005,** *72,* 205202. doi:10.1103/PhysRevB.72.205202
27. Riede, M.; Mueller, T.; Tress, W.; Schueppel, R.; Leo, K. *Nanotechnology* **2008,** *19,* 424001. doi:10.1088/0957-4484/19/42/424001
28. Deibel, C.; Dyakonov, V. *Rep. Prog. Phys.* **2010,** *73,* 096401. doi:10.1088/0034-4885/73/9/096401
29. Liedtke, M.; Sperlich, A.; Kraus, H.; Baumann, A.; Deibel, C.; Wirix, M. J. M.; Loos, J.; Cardona, C. M.; Dyakonov, V. *J. Am. Chem. Soc.* **2011,** *133,* 9088. doi:10.1021/ja2025432
30. Rao, A.; Chow, P. C. Y.; Gelinas, S.; Schlenker, C. W.; Li, C.-Z.; Yip, H.-L.; Jen, A. K.-Y.; Ginger, D. S.; Friend, R. H. *Nature* **2013,** *500,* 435. doi:10.1038/nature12339

31. Chang, W.; Congreve, D. N.; Hontz, E.; Bahlke, M. E.; McMahon, D. P.; Reineke, S.; Wu, T. C.; Bulovic, V.; Van Voorhis, T.; Baldo, M. A. *Nat. Commun.* **2015,** *6,* 6415. doi:10.1038/ncomms7415
32. Behrends, J.; Sperlich, A.; Schnegg, A.; Biskup, T.; Teutloff, C.; Lips, K.; Dyakonov, V.; Bittl, R. *Phys. Rev. B* **2012,** *85,* 125206. doi:10.1103/PhysRevB.85.125206
33. Vandewal, K.; Albrecht, S.; Hoke, E. T.; Graham, K. R.; Widmer, J.; Douglas, J. D.; Schubert, M.; Mateker, W. R.; Bloking, J. T.; Burkhard, G. F.; Sellinger, A.; Fréchet, J. M. J.; Amassian, A.; Riede, M. K.; McGehee, M. D.; Neher, D.; Salleo, A. *Nat. Mater.* **2014,** *13,* 63. doi:10.1038/nmat3807
34. Bakulin, A. A.; Rao, A.; Pavelyev, V. G.; van Loosdrecht, P. H. M.; Pshenichnikov, M. S.; Niedzialek, D.; Cornil, J.; Beljonne, D.; Friend, R. H. *Science* **2012,** *335,* 1340. doi:10.1126/science.1217745
35. Grancini, G.; Maiuri, M.; Fazzi, D.; Petrozza, A.; Egelhaaf, H.-J.; Brida, D.; Cerullo, G.; Lanzani, G. *Nat. Mater.* **2013,** *12,* 29. doi:10.1038/nmat3502
36. Deibel, C.; Strobel, T.; Dyakonov, V. *Adv. Mater.* **2010,** *22,* 4097. doi:10.1002/adma.201000376
37. Zhang, Y.; Basel, T. P.; Gautam, B. R.; Yang, X.; Mascaro, D. J.; Liu, F.; Vardeny, Z. V. *Nat. Commun.* **2012,** *3,* 1043. doi:10.1038/ncomms2057
38. Gehrig, D. W.; Howard, I. A.; Laquai, F. *J. Phys. Chem. C* **2015,** *119,* 13509. doi:10.1021/acs.jpcc.5b03467
39. Xia, J.; Sanders, S. N.; Cheng, W.; Low, J. Z.; Liu, J.; Campos, L. M.; Sun, T. *Adv. Mater.* **2017,** *29,* 1601652. doi:10.1002/adma.201601652
40. Burdett, J. J.; Piland, G. B.; Bardeen, C. J. *Chem. Phys. Lett.* **2013,** *585,* 1. doi:10.1016/j.cplett.2013.08.036
41. Piland, G. B.; Burdett, J. J.; Dillon, R. J.; Bardeen, C. J. *J. Phys. Chem. Lett.* **2014,** *5,* 2312. doi:10.1021/jz500676c
42. Zhao, J.; Ji, S.; Guo, H. *RSC Adv.* **2011,** *1,* 937. doi:10.1039/c1ra00469g
43. Roth, H. D. *J. Photochem. Photobiol., C* **2001,** *2,* 93–116. doi:10.1016/S1389-5567(01)00013-2
44. Pedersen, J. B.; Freed, J. H. *J. Chem. Phys.* **1972,** *57,* 1004. doi:10.1063/1.1678279
45. Pedersen, J. B.; Freed, J. H. *J. Chem. Phys.* **1973,** *58,* 2746. doi:10.1063/1.1679576
46. Haberkorn, R. *Mol. Phys.* **1976,** *32,* 1491. doi:10.1080/00268977600102851
47. Ivanov, K. L.; Petrova, M. V.; Lukzen, N. N.; Maeda, K. *J. Phys. Chem. A* **2010,** *114,* 9447. doi:10.1021/jp1048265
48. Jones, J. A.; Hore, P. J. *Chem. Phys. Lett.* **2010,** *488,* 90. doi:10.1016/j.cplett.2010.01.063
49. Schulten, K.; Wolynes, P. G. *J. Chem. Phys.* **1978,** *68,* 3292. doi:10.1063/1.436135
50. Knapp, E.-W.; Schulten, K. *J. Chem. Phys.* **1979,** *71,* 1878. doi:10.1063/1.438541
51. Brocklehurst, B. *Chem. Soc. Rev.* **2002,** *31,* 301. doi:10.1039/b107250c
52. Rodgers, C. T. *Pure Appl. Chem.* **2009,** *81,* 19. doi:10.1351/PAC-CON-08-10-18
53. Rodgers, C. T.; Hore, P. J. *Proc. Natl. Acad. Sci. U. S. A.* **2009,** *106,* 353. doi:10.1073/pnas.0711968106
54. Hore, P. J.; Mouritsen, H. *Annu. Rev. Biophys.* **2016,** *45,* 299. doi:10.1146/annurev-biophys-032116-094545
55. Ern, V.; Merrifield, R. E. *Phys. Rev. Lett.* **1968,** *21,* 609. doi:10.1103/PhysRevLett.21.609
56. Faulkner, L. R.; Bard, A. J. *J. Am. Chem. Soc.* **1969,** *91,* 6497. doi:10.1021/ja01051a057
57. Faulkner, L. R.; Bard, A. J. *J. Am. Chem. Soc.* **1969,** *91,* 6495. doi:10.1021/ja01051a056
58. Merrifield, R. E. *Acc. Chem. Res.* **1968,** *1,* 129. doi:10.1021/ar50005a001
59. Pope, M.; Geacintov, N. E.; Fogel, F. *Mol. Cryst. Liq. Cryst.* **1969,** *6,* 83–104.
60. Buchachenko, A. L. *Pure Appl. Chem.* **2000,** *72,* 2243–2258. doi:10.1351/pac200072122243
61. Buchachenko, A. L. *J. Phys. Chem. A* **2001,** *105,* 9995. doi:10.1021/jp011261d
62. Turro, N. J. *Proc. Natl. Acad. Sci. U. S. A.* **1983,** *80,* 609. doi:10.1073/pnas.80.2.609
63. Deutsch, J. M. *J. Chem. Phys.* **1972,** *56,* 6076. doi:10.1063/1.1677157
64. Noyes, R. M. *Prog. React. Kinet.* **1961,** *1,* 129.
65. Anisimov, O. A.; Bizyaev, V. L.; Lukzen, N. N.; Grigiryantz, V. M.; Molin, Yu. N. *Chem. Phys. Lett.* **1983,** *101,* 131. doi:10.1016/0009-2614(83)87356-4
66. Molin, Yu. N. *Bull. Korean Chem. Soc.* **1999,** *20,* 7–15.
67. Molin, Yu. N. *Mendeleev Commun.* **2004,** *14,* 85. doi:10.1070/MC2004v014n03ABEH001933
68. Gilch, P.; Pöllinger-Dammer, F.; Musewald, C.; Steiner, U. E.; Michel-Beyerle, M. E. *Science* **1998,** *281,* 982. doi:10.1126/science.281.5379.982
69. Salikhov, K. M. *Chem. Phys.* **1983,** *82,* 145–162. doi:10.1016/0301-0104(83)85353-1
70. Stass, D. V.; Lukzen, N. N.; Tadjikov, B. M.; Molin, Yu. N. *Chem. Phys. Lett.* **1995,** *233,* 444. doi:10.1016/0009-2614(94)01489-I
71. Saik, V. O.; Ostafin, A. E.; Lipsky, S. *J. Chem. Phys.* **1995,** *103,* 7347–7358. doi:10.1063/1.470307
72. Hamilton, C. A.; Hewitt, J. P.; McLauchlan, K. A.; Steiner, U. E. *Mol. Phys.* **1988,** *65,* 423. doi:10.1080/00268978800101141
73. Justinek, M.; Grampp, G.; Landgraf, S.; Hore, P. J.; Lukzen, N. N. *J. Am. Chem. Soc.* **2004,** *126,* 5635. doi:10.1021/ja0394784
74. Tadjikov, B. M.; Stass, D. V.; Usov, O. M.; Molin, Yu. N. *Chem. Phys. Lett.* **1997,** *273,* 25. doi:10.1016/S0009-2614(97)00587-3
75. Stass, D. V.; Tadjikov, B. M.; Molin, Yu. N. *Chem. Phys. Lett.* **1995,** *235,* 511. doi:10.1016/0009-2614(95)00135-Q
76. Sukhenko, S. A.; Purtov, P. A.; Salikhov, K. M. *Sov. J. Chem. Phys.* **1985,** *2,* 29.
77. Sergey, N. V.; Verkhovlyuk, V. N.; Kalneus, E. V.; Korolev, V. V.; Melnikov, A. R.; Burdukov, A. B.; Stass, D. V.; Molin, Yu. N. *Chem. Phys. Lett.* **2012,** *552,* 32. doi:10.1016/j.cplett.2012.08.069
78. Wagemans, W.; Koopmans, B. *Phys. Status Solidi B* **2011,** *248,* 1029. doi:10.1002/pssb.201046383
79. Nguyen, T. D.; Gautam, B. R.; Ehrenfreund, E.; Vardeny, Z. V. *Phys. Rev. Lett.* **2010,** *105,* 166804. doi:10.1103/PhysRevLett.105.166804
80. Nguyen, T. D.; Hukic-Markosian, G.; Wang, H.; Wojcik, L.; Li, X.-G.; Ehrenfreund, E.; Vardeny, Z. V. *Nat. Mater.* **2010,** *9,* 345. doi:10.1038/nmat2633
81. Wagemans, W.; Janssen, P.; Schellekens, A. J.; Bloom, F. L.; Bobbert, P. A.; Koopmans, B. *SPIN* **2011,** *1,* 93. doi:10.1142/S2010324711000082
82. Gautam, B. R.; Nguyen, T. D.; Ehrenfreund, E.; Vardeny, Z. V. *Phys. Rev. B* **2012,** *85,* 205207. doi:10.1103/PhysRevB.85.205207
83. Bobbert, P. A.; Nguyen, T. D.; van Oost, F. W. A.; Koopmans, B.; Wohlgenannt, M. *Phys. Rev. Lett.* **2007,** *99,* 216801. doi:10.1103/PhysRevLett.99.216801

84. Harmon, N. J.; Flatté, M. E. *Phys. Rev. B* **2012,** *85,* 075204. doi:10.1103/PhysRevB.85.075204
85. Rybicki, J.; Lin, R.; Wang, F.; Wohlgenannt, M.; He, C.; Sanders, T.; Suzuki, Y. *Phys. Rev. Lett.* **2012,** *109,* 076603. doi:10.1103/PhysRevLett.109.076603
86. Prigodin, V. N.; Bergeson, J. D.; Lincoln, D. M.; Epstein, A. J. *Synth. Met.* **2006,** *156,* 757–761. doi:10.1016/j.synthmet.2006.04.010
87. Ehrenfreund, E.; Vardeny, Z. V. *Isr. J. Chem.* **2012,** *52,* 552. doi:10.1002/ijch.201100120
88. Rybicki, J.; Nguyen, T. D.; Sheng, Y.; Wohlgenannt, M. *Synth. Met.* **2010,** *160,* 280. doi:10.1016/j.synthmet.2009.09.032
89. Desai, P.; Shakya, P.; Kreouzis, T.; Gillin, W. P.; Morley, N. A.; Gibbs, M. R. J. *Phys. Rev. B* **2007,** *75,* 094423. doi:10.1103/PhysRevB.75.094423
90. Merrifield, R. E. *Pure Appl. Chem.* **1971,** *27,* 481. doi:10.1351/pac197127030481
91. Maeda, K.; Henbest, K. B.; Cintolesi, F.; Kuprov, I.; Rodgers, C. T.; Liddell, P. A.; Gust, D.; Timmel, C. R.; Hore, P. J. *Nature* **2008,** *453,* 387. doi:10.1038/nature06834
92. Ritz, T.; Wiltschko, R.; Hore, P. J.; Rodgers, C. T.; Stapput, K.; Thalau, P.; Timmel, C. R.; Wiltschko, W. *Biophys. J.* **2009,** *96,* 3451. doi:10.1016/j.bpj.2008.11.072
93. Cox, M.; Zhu, F.; Veerhoek, J. M.; Koopmans, B. *Phys. Rev. B* **2014,** *89,* 195204. doi:10.1103/PhysRevB.89.195204
94. Frankevich, E. L.; Pristupa, A. I. *JETP Lett.* **1976,** *24,* 397–400.
95. Murai, H. *J. Photochem. Photobiol., C* **2003,** *3,* 183. doi:10.1016/S1389-5567(02)00038-2
96. Anisimov, O. A.; Grigiryantz, V. M.; Molchanov, V. K.; Molin, Yu. N. *Chem. Phys. Lett.* **1979,** *66,* 265. doi:10.1016/0009-2614(79)85013-7
97. Maeda, K.; Araki, Y.; Kamata, Y.; Enjo, K.; Murai, H.; Azumi, T. *Chem. Phys. Lett.* **1996,** *262,* 110. doi:10.1016/0009-2614(96)01047-0
98. Salikhov, K. M.; Molin, Yu. N. *J. Phys. Chem.* **1993,** *97,* 13259. doi:10.1021/j100152a033
99. Gorelik, V. R.; Maeda, K.; Yashiro, H.; Murai, H. *J. Phys. Chem. A* **2001,** *105,* 8011. doi:10.1021/jp0109628
100. Boehme, C.; Lips, K. *Phys. Rev. B* **2003,** *68,* 245105. doi:10.1103/PhysRevB.68.245105
101. Boehme, C.; Lips, K. *Phys. Rev. Lett.* **2003,** *91,* 246603. doi:10.1103/PhysRevLett.91.246603
102. Schnegg, A.; Behrends, J.; Fehr, M.; Lips, K. *Phys. Chem. Chem. Phys.* **2012,** *14,* 14418. doi:10.1039/c2cp41258f
103. Nasibulov, E. A.; Kulik, L. V.; Kaptein, R.; Ivanov, K. L. *Phys. Chem. Chem. Phys.* **2012,** *14,* 13325. doi:10.1039/c2cp42117h
104. Suckert, M.; Hoehne, F.; Dreher, L.; Kuenzl, M.; Huebl, H.; Stutzmann, M.; Brandt, M. S. *Mol. Phys.* **2013,** *111,* 2690. doi:10.1080/00268976.2013.816796
105. Hoehne, F.; Huebl, H.; Galler, B.; Stutzmann, M.; Brandt, M. S. *Phys. Rev. Lett.* **2010,** *104,* 046402. doi:10.1103/PhysRevLett.104.046402
106. Hoff, A. J. *Q. Rev. Biophys.* **1984,** *17,* 153–282. doi:10.1017/S0033583500005308
107. Bittl, R.; Zech, S. G. *Biochim. Biophys. Acta* **2001,** *1507,* 194. doi:10.1016/S0005-2728(01)00210-9
108. Salikhov, K. M.; Kandrashkin, Yu. E.; Salikhov, A. K. *Appl. Magn. Reson.* **1992,** *3,* 199. doi:10.1007/BF03166790
109. Tang, J.; Thurnauer, M. C.; Norris, J. R. *Chem. Phys. Lett.* **1994,** *219,* 283. doi:10.1016/0009-2614(94)87059-4
110. Adrian, F. J. *Res. Chem. Intermed.* **1991,** *16,* 99. doi:10.1163/156856791X00200
111. Wong, S. K.; Hutchinson, D. A.; Wan, J. K. S. *J. Chem. Phys.* **1973,** *58,* 985. doi:10.1063/1.1679355
112. Atkins, P. W.; Evans, G. T. *Mol. Phys.* **1974,** *27,* 1633. doi:10.1080/00268977400101361
113. Katsuki, A.; Kobori, Y.; Tero-Kubota, S.; Milikisyants, S.; Paul, H.; Steiner, U. E. *Mol. Phys.* **2002,** *100,* 1245. doi:10.1080/00268970110113579
114. Steiner, U. *Ber. Bunsenges. Phys. Chem.* **1981,** *85,* 228–233. doi:10.1002/bbpc.19810850311
115. Milikisyants, S.; Katsuki, A.; Steiner, U.; Paul, H. *Mol. Phys.* **2002,** *100,* 1215. doi:10.1080/00268970110112408
116. Hayashi, H.; Sakaguchi, Y. *J. Photochem. Photobiol., C* **2005,** *6,* 25. doi:10.1016/j.jphotochemrev.2005.01.001
117. Kawai, A.; Obi, K. *J. Phys. Chem.* **1992,** *96,* 52. doi:10.1021/j100180a014
118. Blättler, C.; Jent, F.; Paul, H. *Chem. Phys. Lett.* **1990,** *166,* 375. doi:10.1016/0009-2614(90)85046-F
119. Kobori, Y.; Noji, R.; Tsuganezawa, S. *J. Phys. Chem. C* **2013,** *117,* 1589. doi:10.1021/jp309421s
120. Lukina, E. A.; Popov, A. V.; Uvarov, M. N.; Suturina, E. A.; Reijerse, E. J.; Kulik, L. V. *Phys. Chem. Chem. Phys.* **2016,** *18,* 28585. doi:10.1039/C6CP05389K
121. Hore, P. J.; Broadhurst, R. W. *Prog. Nucl. Magn. Reson. Spectrosc.* **1993,** *25,* 345. doi:10.1016/0079-6565(93)80002-B
122. Mok, K. H.; Hore, P. J. *Methods* **2004,** *34,* 75. doi:10.1016/j.ymeth.2004.03.006
123. Goez, M. *Annu. Rep. NMR Spectrosc.* **2009,** *66,* 77. doi:10.1016/S0066-4103(08)00403-1
124. Goez, M. Elucidating Organic Reaction Mechanisms Using Photo-CIDNP Spectroscopy. In *Hyperpolarization Methods in NMR Spectroscopy;* Kuhn, L. T., Ed.; Topics in Current Chemistry, Vol. 338; Springer: Berlin, Germany, 2013; pp 1–32. doi:10.1007/128_2012_348
125. Lupton, J. M.; McCamey, D. R.; Boehme, C. *ChemPhysChem* **2010,** *11,* 3040. doi:10.1002/cphc.201000186
126. Kaptein, R.; Den Hollander, J. A. *J. Am. Chem. Soc.* **1972,** *94,* 6269. doi:10.1021/ja00773a003
127. Lyon, C. E.; Lopez, J. J.; Cho, B.-M.; Hore, P. J. *Mol. Phys.* **2002,** *100,* 1261. doi:10.1080/00268970110113988
128. Ivanov, K. L.; Lukzen, N. N.; Vieth, H.-M.; Grosse, S.; Yurkovskaya, A. V.; Sagdeev, R. Z. *Mol. Phys.* **2002,** *100,* 1197. doi:10.1080/00268970110111797
129. Tarasov, V. F.; Shkrob, I. A. *J. Magn. Reson., Ser. A* **1994,** *109,* 65. doi:10.1006/jmra.1994.1135
130. Zysmilich, M. G.; McDermott, A. *J. Am. Chem. Soc.* **1994,** *116,* 8362. doi:10.1021/ja00097a052
131. Polenova, T.; McDermott, A. E. *J. Phys. Chem. B* **1999,** *103,* 535. doi:10.1021/jp9822642
132. Bode, B. E.; Thamarath, S. S.; Gupta, K. B. S. S.; Alia, A.; Jeschke, G.; Matysik, J. The Solid-State Photo-CIDNP Effect and Its Analytical Application. In *Hyperpolarization Methods in NMR Spectroscopy;* Kuhn, L. T., Ed.; Topics in Current Chemistry, Vol. 338; Springer: Berlin, Germany, 2013; pp 105–121. doi:10.1007/128_2012_357
133. Jeschke, G.; Matysik, J. *Chem. Phys.* **2003,** *294,* 239. doi:10.1016/S0301-0104(03)00278-7
134. Thamarath, S. S.; Heberle, J.; Hore, P. J.; Kottke, T.; Matysik, J. *J. Am. Chem. Soc.* **2010,** *132,* 15542. doi:10.1021/ja1082969

135. Thamarath, S. S.; Bode, B. E.; Prakash, S.; Gupta, K. B. S. S.; Alia, A.; Jeschke, G.; Matysik, J. *J. Am. Chem. Soc.* **2012,** *134,* 5921. doi:10.1021/ja2117377
136. de Kanter, F. J. J.; den Hollander, J. A.; Huizer, A. H.; Kaptein, R. *Mol. Phys.* **1977,** *34,* 857. doi:10.1080/00268977700102161
137. Closs, G. L.; Doubleday, C. E. *J. Am. Chem. Soc.* **1973,** *95,* 2735. doi:10.1021/ja00789a082
138. Miesel, K.; Yurkovskaya, A. V.; Vieth, H.-M. *Appl. Magn. Reson.* **2004,** *26,* 51–64. doi:10.1007/BF03166562
139. Jeschke, G. *J. Am. Chem. Soc.* **1998,** *120,* 4425. doi:10.1021/ja973744u
140. Sosnovsky, D. V.; Jeschke, G.; Matysik, J.; Vieth, H.-M.; Ivanov, K. L. *J. Chem. Phys.* **2016,** *144,* 144202. doi:10.1063/1.4945341
141. Daviso, E.; Jeschke, G.; Matysik, J. Photochemically Induced Dynamic Nuclear Polarization (Photo-CIDNP) Magic-Angle Spinning NMR. In *Biophysical Techniques in Photosynthesis;* Aartsma, T. J.; Matysik, J., Eds.; Advances in Photosynthesis and Respiration, Vol. 26; Springer: Berlin, Germany, 2008; pp 385–399. doi:10.1007/978-1-4020-8250-4_19
142. Maier, G.; Haeberlen, U.; Wolf, H. C.; Hausser, K. H. *Phys. Lett. A* **1967,** *25,* 384–385. doi:10.1016/0375-9601(67)90712-8
143. Goodson, B. M. *Annu. Rep. NMR Spectrosc.* **2005,** *55,* 299. doi:10.1016/S0066-4103(04)55006-8
144. Colpa, J. P.; Hausser, K. H.; Stehlik, D. *Z. Naturforsch., A: Astrophys., Phys. Phys. Chem.* **1971,** *26,* 1792–1799.
145. Schmidt, J.; van der Waals, J. H. *Chem. Phys. Lett.* **1968,** *2,* 640. doi:10.1016/0009-2614(63)80039-1
146. van der Waals, J. H. *Appl. Magn. Reson.* **2001,** *20,* 545. doi:10.1007/BF03162337
147. Veeman, W. S.; van der Poel, A. L. J.; van der Waals, J. H. *Mol. Phys.* **1975,** *29,* 225. doi:10.1080/00268977500100161
148. Colpa, J. P.; Seiff, F.; Stehlik, D. *Chem. Phys.* **1978,** *33,* 79. doi:10.1016/0301-0104(78)87073-6
149. Colpa, J. P.; Stehlik, D. *Chem. Phys.* **1977,** *21,* 273. doi:10.1016/0301-0104(77)80022-0
150. Stehlik, D. The Mechanism of Optical Nuclear Polarization in Molecular Crystals. In *Excited States;* Lim, E. C., Ed.; Academic Press: New York, NY, U.S.A., 1977; pp 204 ff. doi:10.1016/B978-0-12-227203-5.50009-3
151. Chipaux, M.; Xavier, S.; Tallaire, A.; Achard, J.; Pezzagna, S.; Meijer, J.; Jacques, V.; Roch, J. F.; Debuisschert, T. *Proc. SPIE* **2015,** *9370,* 93701V. doi:10.1117/12.2084082
152. Alvarez, G. A.; Bretschneider, C. O.; Fischer, R.; London, P.; Kanda, H.; Onoda, S.; Isoya, J.; Gershoni, D.; Frydman, L. *Nat. Commun.* **2015,** *6,* 8456. doi:10.1038/ncomms9456
153. Gruber, A.; Dräbenstedt, A.; Tietz, C.; Fleury, L.; Wrachtrup, J.; von Borczyskowski, C. *Science* **1997,** *276,* 2012. doi:10.1126/science.276.5321.2012
154. Doherty, M. W.; Manson, N. B.; Delaney, P.; Jelezko, F.; Wrachtrup, J.; Hollenberg, L. C. L. *Phys. Rep.* **2013,** *528,* 1. doi:10.1016/j.physrep.2013.02.001

License and Terms

BEILSTEIN JOURNAL OF NANOTECHNOLOGY

Formation of ferromagnetic molecular thin films from blends by annealing

Peter Robaschik[1], Ye Ma[1], Salahud Din[1,2] and Sandrine Heutz[*1]

Full Research Paper

Open Access

Address:
[1]Department of Materials and London Centre for Nanotechnology, Imperial College London, Exhibition Rd, London SW7 2AZ, United Kingdom and [2]Kurt J. Lesker Company, Sidney Little Rd, St Leonard's on Sea TN38 9PU, United Kingdom

Email:
Sandrine Heutz[*] - s.heutz@imperial.ac.uk

* Corresponding author

Keywords:
co-deposition; molecular spintronics; organic thin films; phthalocyanines; tetracyanoquinodimethane (TCNQ)

Beilstein J. Nanotechnol. **2017,** *8,* 1469–1475.
doi:10.3762/bjnano.8.146

Received: 15 March 2017
Accepted: 20 June 2017
Published: 14 July 2017

This article is part of the Thematic Series "Towards molecular spintronics".

Guest Editor: G. Salvan

Abstract

We report on a new approach for the fabrication of ferromagnetic molecular thin films. Co-evaporated films of manganese phthalocyanine (MnPc) and tetracyanoquinodimethane (TCNQ) have been produced by organic molecular beam deposition (OMBD) on rigid (glass, silicon) and flexible (Kapton) substrates kept at room temperature. The MnPc:TCNQ films are found to be entirely amorphous due to the size mismatch of the molecules. However, by annealing while covering the samples highly crystalline MnPc films in the β-polymorph can be obtained at 60 °C lower than when starting with pure MnPc films. The resulting films exhibit substantial coercivity (13 mT) at 2 K and a Curie temperature of 11.5 K.

Introduction

Controlling the structure of molecular thin films is of great interest for their application in optoelectronic and spintronic devices [1,2]. One of the key physical properties determining the performance is crystallinity, which significantly influences electron/hole mobility and magnetic coupling [3,4]. We recently reported on an approach to achieve crystalline porphyrazine films, which are amorphous on non-interacting substrates, by depositing the molecules on a 3,4,9,10-perylenetetracarboxylic dianhydride (PTCDA) surface, leading to a transformation from paramagnetic to antiferromagnetic behaviour [5]. Another promising class of molecules are phthalocyanines (Pc) that can be easily incorporated in thin films that exhibit outstanding semiconducting and magnetic properties [6].

Phthalocyanines feature different polymorphs, often defined by the angle formed by the molecule and the stacking axis, φ, which can be controlled via different temperature treatments. For instance, at room temperature, films commonly adopt the α-phase (φ = 65°) and can be transformed to the thermodynamically stable β-phase (φ = 45°) by annealing in vacuum at 330 °C

[7-9]. However, such temperatures are too high for most flexible substrates, and therefore limit one of the main fabrication advantages of molecular materials.

The β-phase is particularly attractive for MnPc, where it leads to ferromagnetism in polycrystalline powders and single crystals [10,11]. Due to the arrangement in molecular columns with a stacking angle of 45° the Mn ion lies directly underneath a nitrogen atom of the nearest-neighbouring MnPc molecule. The magnetic interaction has been attributed to superexchange [11-13], although more recent results highlight that indirect exchange also contributes to the mechanism [14].

Here we develop a strategy to lower the phase-transition temperature of MnPc by 60 °C by blending the MnPc film with TCNQ in the starting films deposited at room temperature. Optical microscopy and X-ray diffraction (XRD) are used to identify the phase transition by investigation of the surface morphology and the structure of the films, while FTIR spectroscopy provides information about the chemical composition and structure of the films. Furthermore superconducting quantum interference device (SQUID) magnetometry measurements reveal the ferromagnetic behaviour of the β-MnPc films, which exhibit remarkable coercivity. The opening of the hysteresis loop is preserved at temperatures up to 10 K, and the Curie temperature as determined by susceptibility measurements is 11.5 K. The combination of new processing methodologies with attractive magnetic properties will have important implications for spintronics.

Results and Discussion

Sample preparation

Blended films comprising MnPc and TCNQ (Figure 1a) have been prepared by organic molecular beam deposition (OMBD). A one-to-one ratio of the desired molecules in the films was obtained with a deposition rate of 0.5 Å/s and a thickness of 100 nm for MnPc. Due to its higher molecular density TCNQ is deposited at a lower rate of 0.22 Å/s leading to a thickness of 44 nm. Hence the total thickness of the blended film amounts to 144 nm.

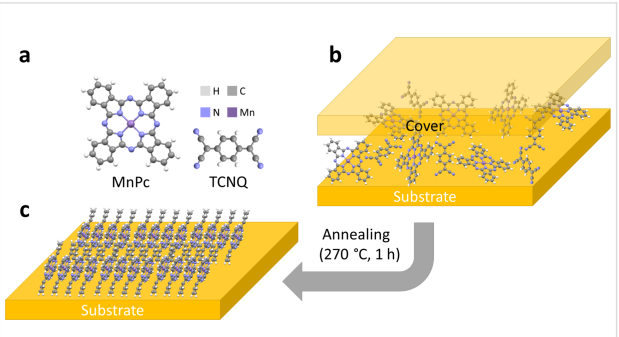

Figure 1: (a) Manganese phthalocyanine (MnPc) and tetracyanoquinodimethane (TCNQ) molecules. (b) Annealing procedure applied to the blended thin films prepared by OMBD. (c) Well-ordered β-MnPc film after annealing.

Figure 1b shows the annealing procedure in which the blended film is covered (see Experimental section) without applying any additional force and put inside a tube furnace. Once the tube is pumped down and flushed with nitrogen at a flow rate of 150 sccm for at least one hour the furnace is set to 270 °C and left dwelling for one hour after the final temperature is reached. During this process the TCNQ molecules can slowly escape the film due to their low sublimation temperature of approximately 100 °C [15].

We compare these films with neat MnPc films, prepared using sublimation of MnPc on substrates at room temperature at a rate of 0.5 Å/s up to a thickness of 100 nm, and subjected to subsequent annealing procedures as for the blends. As will be discussed later we believe that the emerging vacancies in the mixed films generate sufficient free volume around the MnPc molecules for a rearrangement to the thermodynamically stable β-phase (Figure 1c), which normally forms above 300 °C [7,8].

Film morphology, structure and composition

Optical micrographs in Figure 2 reveal the surface morphology of the organic films following different thermal treatments. For comparison the neat MnPc film deposited on glass kept at room temperature (Figure 2a) is shown with a very smooth surface and a grain size that is below the detection limit of the optical microscope. Annealing at 270 °C without a cover for one hour (Figure 2b) does not affect the surface morphology. However, increasing the temperature to 330 °C and covering the films (Figure 2c) leads to the formation of larger crystallites.

Similar results are obtained for the mixed films (Figure 2d–f), although annealing at a temperature of 270 °C already allows the molecules to rearrange into large elongated crystallites. This was observed previously for iron phthalocyanine (FePc) thin films deposited at different substrate temperatures [16]. However, in that case the length of the major axis was found to be 200 nm at a temperature of 260 °C. The crystallites in our MnPc films reach a size of up to 10 µm for their longer axis, which is attractive for high coercivity in magnetism and improved charge transport along the crystallites.

Results from optical microscopy can be refined by X-ray diffraction (XRD). Figure 3a shows the XRD patterns of the as-deposited MnPc:TCNQ film on silicon as well as the films that have been annealed with and without cover. The sample without any heat treatment appears entirely amorphous showing

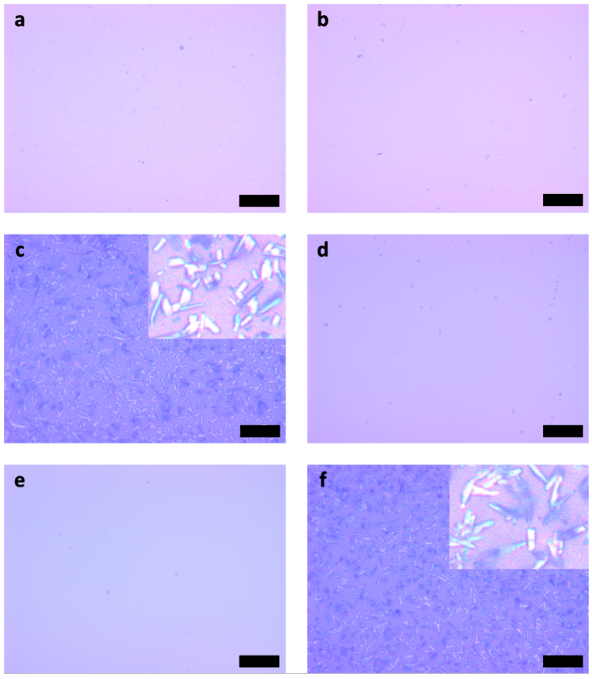

Figure 2: Optical micrographs for molecular thin films grown on glass substrates. (a) α-MnPc film grown at room temperature. (b) MnPc film annealed at 270 °C without cover. (c) β-MnPc film formed by annealing of the α-MnPc sample at 330 °C with cover. (d) MnPc:TCNQ film grown at room temperature. (e) MnPc:TCNQ film annealed at 270 °C without cover. (f) β-MnPc film formed by annealing of a MnPc:TCNQ sample at 270 °C with cover. The scale bars correspond to a length of 20 µm for the images and 5 µm for the insets.

no peaks in a range up to 2θ = 30°, where phthalocyanine fingerprints usually appear [4]. Annealing at a temperature of 270 °C without a cover also leads to a featureless XRD pattern. However, as will be shown by FTIR this is due to the absence of any thin film rather than to its amorphous nature.

The annealed MnPc:TCNQ films that were additionally covered, however, show two high intensity peaks at 2θ = 7.13° and 9.37°, which correspond to the diffraction from the (001) and (20−1) planes of β-MnPc [17,18]. We note that the (20−1) plane is not usually observed in β-MnPc films obtained by annealing of the α-phase and its observation indicates a reduced texture. This is presumably due to the disordered nature of the starting film in this case, in contrast to the case of highly oriented α-phase film. The inset of Figure 3a reveals the sharp nature of both peaks and fits using the Lorentz function result in full width at half maximums (FWHM) of 0.11° and 0.10°, respectively. From the obtained FWHMs we can estimate the grain dimensions, τ, out of the sample plane by using the Scherrer equation [19]:

$$\tau = \frac{K\lambda}{\beta\cos(\theta)}, \qquad (1)$$

where K is the dimensionless shape factor, λ is the wavelength of the X-ray source, β is the FWHM and θ is the Bragg angle. Calculations using $K = 1$ give a grain size of 84 ± 9 nm for the β-MnPc film, which is in line with the equivalent film thickness of MnPc in the blended film prior to annealing.

By comparison a neat 100 nm thick MnPc film annealed at 270 °C for one hour shows only one broad diffraction peak at 2θ = 7.09°, which most likely combines the contributions of the (100) and (001) planes of the α- and β-polymorphs, respective-

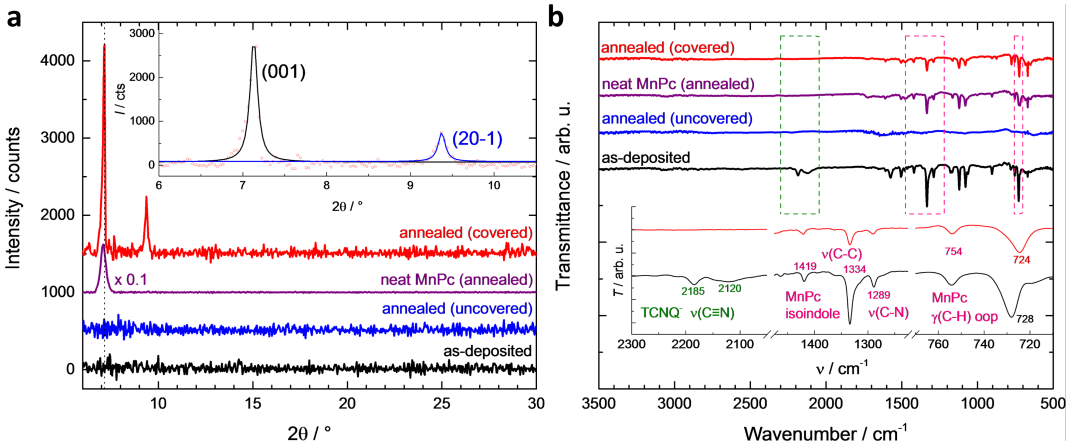

Figure 3: (a) X-ray diffraction patterns. For an as-deposited 144 nm thick MnPc:TCNQ film on silicon (black) no diffraction peaks are observed. Annealing without cover (blue) leads to similar results, whereas the covered film (red) exhibits two diffraction peaks with high intensity. For comparison the XRD pattern of a neat MnPc film (purple) that was annealed at the same temperature is shown. All films were annealed at a temperature of 270 °C. (b) FTIR spectra for the same films deposited on KBr substrates. The green frame highlights the range of 2050–2300 cm^{-1} where the ν(C≡N) stretching peaks for TCNQ appear. The pink frames show the area of the MnPc isoindole vibrations around 1225–1475 cm^{-1} and the γ(C-H) out-of-plane deformation of the MnPc ligand at 710–770 cm^{-1}, respectively. The inset shows specific regions in the mixed films (colour coding as in main graph).

ly [17,20], assuming that MnPc is isostructural with CuPc. This represents an intermediate case with a partial transformation from α- to β-phase as shown earlier for metal-free phthalocyanine thin films where Yim et al. proposed a phase-transition mechanism that involves tilting of the α-phase molecular columns to form the β-phase [9]. Therefore, for the neat MnPc film the thermal energy provided is not sufficient to transform the entire film from α- into β-phase. Due to the combination of both α- and β-phases, the diffraction peak has been fitted to two Lorentz functions centred at 2θ = 7.03° and 7.16° leading to FWHMs of 0.20° and 0.21°, respectively. The values correspond to a grain size of 45 ± 5 nm, which is in agreement with the values of phthalocyanine films previously deposited at room temperature [16,21], correlates with the smooth morphology and is much lower than the value of the β-MnPc films generated from the blended film.

To further investigate the phase transformation we have conducted FTIR spectroscopy measurements (Figure 3b) on the same films deposited on KBr substrates. The ν(C≡N) stretching peaks of TCNQ for the as-deposited blended film can be found at 2185 and 2120 cm^{-1}, respectively. This finding is in contrast to the peak at 2228 cm^{-1} for the neutral TCNQ [22] and suggests charge transfer (CT) from the Mn ion of the phthalocyanines to the TCNQ molecules forming Mn^{3+} and $TCNQ^{-}$. Similar CT was previously observed for MnPc/F_4TCNQ films by Rückerl and collaborators [23]. Both peaks vanish for every annealed sample proving that all TCNQ molecules sublime during the annealing process. The ν(C–C) (1429 and 1334 cm^{-1}) and ν(C–N) (1289 cm^{-1}) vibrations of the MnPc isoindole [24] are preserved for the annealed neat film and the annealed mixed film with cover. However, for the MnPc:TCNQ blended film that was annealed without cover it seems that both phthalocyanine and TCNQ molecules sublime. Furthermore, for the covered sample, one peak of the γ(C–H) out-of-plane deformation of the MnPc ligand shows a shift from 728 to 724 cm^{-1} and can be attributed to phase transformation to the β-phase [25].

We believe that the successful crystallisation of the β-phase MnPc at lower temperatures compared to the α→β phase transition thanks to the blending with sacrificial TCNQ molecules is due to two main factors. Firstly, the presence of TCNQ hinders crystallisation of the MnPc molecules, preventing them from forming strong intermolecular bonds and enabling higher mobility for crystallisation into the thermodynamically stable β-phase. This is substantiated by the observation in FTIR of the sublimation of MnPc molecules, which are not stabilised by the crystal lattice, in the uncovered blend film at 270 °C whereas neat α-phase films remain on the substrate under the same conditions. Secondly, when the blend film is covered, MnPc molecules cannot sublime as readily, but TCNQ molecules can diffuse out of the film due to their small size and lower sublimation temperature, creating vacant space which allows the MnPc molecular columns to arrange into the β-phase.

So the co-deposition of phthalocyanines with small molecules could allow for the formation of highly oriented molecular films at lower process temperatures. This is crucial for later integration into electronic and spintronic devices, especially on flexible substrates.

Magnetic characterisation

As expected from optical microscopy and XRD the β-MnPc film formed by annealing of the MnPc:TCNQ utilising a cover exhibits remarkable magnetic properties. Figure 4 shows magnetic hysteresis loops of a MnPc film on Kapton at different temperatures. A substantial coercivity of 13 mT, which coincides with the 15 mT found for MnPc powder annealed in Ar atmosphere [26], can be detected at 2 K and an opening of the hysteresis is preserved up to a temperature of 10 K. The magnetisation increases rapidly until a field of 100 mT is reached and is not saturated at the maximum field of 7 T. This is in line with earlier reports on β-MnPc powder and single-crystal samples [10,11,27,28]. However, to our knowledge no reports on the coercivity in β-MnPc thin films from OMBD have been made. The magnetic moment at 7 T amounts to 2.1 μ_B per MnPc molecules, which is below the expected value of 3 μ_B for a system with $S = 3/2$. This can be explained by the absence of magnetic saturation at the maximum available field and the reduction of magnetic moment due to crystal field effects [29]. Due to the observation of a reasonable magnetic moment per MnPc we can further confirm that no significant

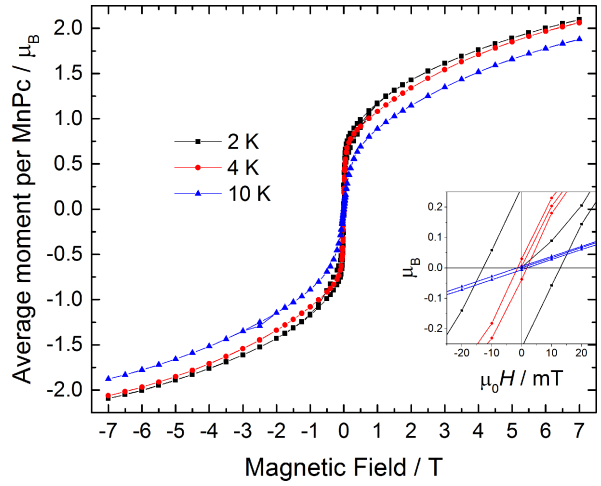

Figure 4: Magnetic hysteresis loops of a MnPc thin film on Kapton obtained from annealing of a MnPc:TCNQ blend. The inset shows that the film exhibits a coercivity of up to 13 mT at 2 K.

amount of phthalocyanine molecules have been sublimed during the annealing process.

For further analysis the temperature dependence of the magnetisation (Figure 5a) has been measured at fields of 20 and 40 mT for both field cooled (FC) and zero-field cooled (ZFC) protocols. The average magnetic moment per MnPc molecule increases rapidly below 20 K and shows a bifurcation in both ZFC measurements at 3 K, whereas a steady increase in the FC data can be observed. This finding coincides with reports on DC and AC susceptibility measurements of pure β-MnPc powder showing a slow relaxation of magnetisation [30,31]. Further studies by Wang and Seehra were able to rule out spin-glass behaviour and found that the zero-field splitting (ZFS) parameter $|D|/k_B$ = 8.3 K is much larger than the coupling constant J/k_B = 2.6 K [32]. According to Moriya, in this case ($|D|/J > 1$) long-range ordering is not possible [33], which leads to the assumption that β-MnPc can be treated as a single-chain magnet.

From the temperature-dependent magnetisation values collected at two different fields the inverse differential susceptibility was determined and is shown in Figure 5b. The data follows a linear behaviour at higher temperatures and can be fitted to the Curie–Weiss law in a temperature range from 20 to 50 K. The Curie temperature is found from the intercept with the *y*-axis at 11.5 K and is slightly higher compared to reported values of 6–10 K for β-MnPc crystals [10,11,28,34].

Conclusion

We report on an approach to fabricate ferromagnetic β-MnPc films by annealing of MnPc:TCNQ blends, which reduces the process temperature by 60 °C compared to the preparation procedure starting from a neat MnPc film. The resulting films form large elongated crystallites with their long axis measuring up to 10 µm. X-ray diffraction studies show that the out-of-plane dimensions of the grains (84 ± 9 nm) are comparable to the target film thickness of 100 nm, which means that no grain boundaries parallel to the substrate plane are expected. Magnetic measurements reveal remarkable ferromagnetic properties with a substantial coercivity of up to 13 mT at 2 K and a Curie temperature of 11.5 K. These findings are significant for a future implementation of magnetic molecular thin films in spintronic devices, especially on flexible substrates that are commonly sensitive to high process temperatures. We anticipate that the methodology for reducing phase-transition temperatures through the blending strategy can be generalised to a wide range of systems, provided the sacrificial molecules used in the blend reduce intermolecular interactions and have a sublimation point below that of the molecule of interest.

Experimental

Organic thin films have been grown using a SPECTROS deposition chamber by Kurt J. Lesker Company with a base pressure of 3×10^{-7} mbar. During the co-deposition in total three quartz crystal microbalances (QCM) were utilised to achieve a one-to-one ratio of the molecules. Two QCMs monitored the deposition rate of each organic source and the combined rate was confirmed by a third QCM next to the substrates.

The annealing procedure was carried out in a furnace (Carbolite HZS-12/900E) fitted with a 150 cm long quartz tube (3 cm outer diameter). For the covered samples the films on glass and silicon substrates were sandwiched between microscope slides, whereas the Kapton samples were covered by another Kapton sheet. The tube was pumped down to 1×10^{-1} mbar followed

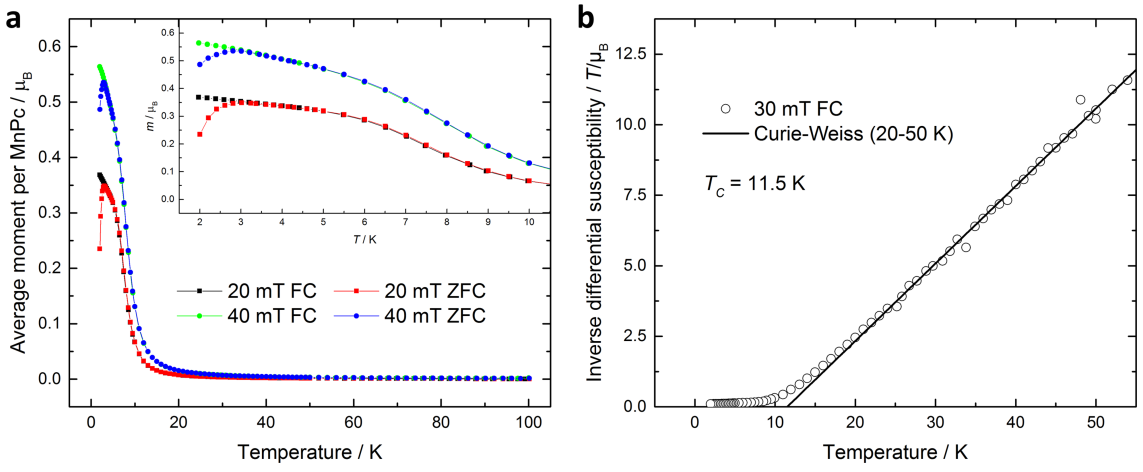

Figure 5: (a) Magnetisation as a function of the temperature at fields of 20 mT and 40 mT using both FC and ZFC protocols. (b) Inverse differential susceptibility calculated from the magnetisation measurements showing a Curie temperature of 11.5 K.

by nitrogen flushing at a flow rate of 150 sccm for at least one hour. After flushing the nitrogen flow was kept at the same rate leading to a pressure of approximately 25 mbar. All three zones of the furnace were set up to 270 °C and once the final temperature was achieved the furnace was left for dwelling for one hour.

The surface morphology was observed with an Olympus BX51 optical microscope using a 100× objective. The crystal structure was studied by using a Panalytical X'Pert PRO MPD X-Ray diffractometer (Ni filtered Cu K_α radiation at 40 kV and 40 mA) operated in the θ–2θ mode. The background was subtracted using the Sonneveld method [35].

The composition of the films was investigated in transmission mode utilising a Nicolet iS10 FTIR spectrometer from Thermo Scientific with an optimised spectral range of 7800–350 cm^{-1} and a resolution of 0.4 cm^{-1}.

The magnetic measurements were conducted with a Quantum Design MPMS-7 SQUID (superconducting quantum interference device) magnetometer. The films were deposited with a stripe shadow mask (4 × 90 mm^2) on flexible Kapton foil and rolled into a tube as reported by Heutz et al. [28]. Therefore the size of the Kapton foil was chosen to be larger than the scanning length of the coils in the SQUID to compensate for any background signals that could occur from the substrate.

Acknowledgements

We thank R. Sweeney and Dr R. Thorogate for help with XRD and SQUID measurements, respectively. We thank the Research Council UK and the Engineering and Physical Sciences Research Council (EPSRC, grants number EP/F039948/1 and EP/F04139X/1) for financial support. P. R. and S. H. thank Kurt J. Lesker Company and Imperial College London for funding.

References

1. Forrest, S. R. *Nature* **2004,** *428,* 911–918. doi:10.1038/nature02498
2. Rocha, A. R.; García-Suárez, V. M.; Bailey, S. W.; Lambert, C. J.; Ferrer, J.; Sanvtio, S. *Nat. Mater.* **2005,** *4,* 335–339. doi:10.1038/nmat1349
3. Bao, Z.; Lovinger, A. J.; Dodabalapur, A. *Appl. Phys. Lett.* **1996,** *69,* 3066–3068. doi:10.1063/1.116841
4. Serri, M.; Wu, W.; Fleet, L. R.; Harrison, N. M.; Hirjibehedin, C. F.; Kay, C. W. M.; Fisher, A. J.; Aeppli, G.; Heutz, S. *Nat. Commun.* **2014,** *5,* 3079. doi:10.1038/ncomms4079
5. Eguchi, K.; Nanjo, C.; Awaga, K.; Tseng, H.-H.; Robaschik, P.; Heutz, S. *Phys. Chem. Chem. Phys.* **2016,** *18,* 17360–17365. doi:10.1039/C6CP01932C
6. Jiang, J., Ed. *Functional Phthalocyanine Molecular Materials;* Structure and Bonding, Vol. 135; Springer: Berlin, Germany, 2010. doi:10.1007/978-3-642-04752-7
7. Bayliss, S. M.; Heutz, S.; Rumbles, G.; Jones, T. S. *Phys. Chem. Chem. Phys.* **1999,** *1,* 3673–3676. doi:10.1039/a904089g
8. Heutz, S.; Bayliss, S. M.; Middleton, R. L.; Rumbles, G.; Jones, T. S. *J. Phys. Chem. B* **2000,** *104,* 7124–7129. doi:10.1021/jp0000836
9. Yim, S.; Heutz, S.; Jones, T. S. *J. Appl. Phys.* **2002,** *91,* 3632–3636. doi:10.1063/1.1446218
10. Miyoshi, H.; Ohya-Nishiguchi, H.; Deguchi, Y. *Bull. Chem. Soc. Jpn.* **1973,** *46,* 2724–2728. doi:10.1246/bcsj.46.2724
11. Mitra, S.; Gregson, A. K.; Hatfield, W. E.; Weller, R. R. *Inorg. Chem.* **1983,** *22,* 1729–1732. doi:10.1021/ic00154a007
12. Barraclough, C. G.; Martin, R. L.; Mitra, S.; Sherwood, R. C. *J. Chem. Phys.* **1970,** *53,* 1638–1642. doi:10.1063/1.1674236
13. Yamada, H.; Shiamda, T.; Koma, A. *J. Chem. Phys.* **1998,** *108,* 10256–10261. doi:10.1063/1.476486
14. Wu, W.; Kerridge, A.; Harker, A. H.; Fisher, A. J. *Phys. Rev. B* **2008,** *77,* 184403. doi:10.1103/PhysRevB.77.184403
15. Tseng, H.-H.; Serri, M.; Harrison, N. M.; Heutz, S. *J. Mater. Chem. C* **2015,** *3,* 8694–8699. doi:10.1039/C5TC01778E
16. Gentry, K. P.; Gredig, T.; Schuller, I. K. *Phys. Rev. B* **2009,** *80,* 174118. doi:10.1103/PhysRevB.80.174118
17. Brown, C. J. *J. Chem. Soc. A* **1968,** 2488–2493. doi:10.1039/J19680002488
18. Figgs, B. N.; Mason, R.; Williams, G. A. *Acta Crystallogr., Sect. B* **1980,** *36,* 2963–2970. doi:10.1107/S056774088001062X
19. Scherrer, P. *Nachr. Ges. Wiss. Goettingen, Math.-Phys. Kl.* **1918,** *2,* 98–100.
20. Hoshino, A.; Takenaka, Y.; Miyaji, H. *Acta Crystallogr., Sect. B* **2003,** *B59,* 393–403. doi:10.1107/S010876810300942X
21. Robaschik, P.; Siles, P. F.; Bülz, D.; Richter, P.; Monecke, M.; Fronk, M.; Klyatskaya, S.; Grimm, D.; Schmidt, O. G.; Ruben, M.; Zahn, D. R. T.; Salvan, G. *Beilstein J. Nanotechnol.* **2014,** *5,* 2070–2078. doi:10.3762/bjnano.5.215
22. Khatkale, M. S.; Devlin, J. P. *J. Chem. Phys.* **1979,** *70,* 1851–1859. doi:10.1063/1.437662
23. Rückerl, F.; Mahns, B.; Dodbiba, E.; Nikolis, V.; Herzig, M.; Büchner, B.; Knupfer, M.; Hahn, T.; Kortus, J. *J. Chem. Phys.* **2016,** *145,* 114702. doi:10.1063/1.4962578
24. Seoudi, R.; El-Bahy, G. S.; El Sayed, Z. A. *J. Mol. Struct.* **2005,** *753,* 119–126. doi:10.1016/j.molstruc.2005.06.003
25. Kendall, D. N. *Anal. Chem.* **1953,** *25,* 382–389. doi:10.1021/ac60075a002
26. Nath, A.; Kopelev, N.; Tyagi, S. D.; Chechersky, V.; Wie, Y. *Mater. Lett.* **1993,** *16,* 39–44. doi:10.1016/0167-577X(93)90180-6
27. Awaga, K.; Maruyama, Y. *Phys. Rev. B* **1991,** *44,* 2589–2594. doi:10.1103/PhysRevB.44.2589
28. Heutz, S.; Mitra, C.; Wu, W.; Fisher, A. J.; Kerridge, A.; Stoneham, M.; Harker, T. H.; Gardener, J.; Tseng, H.-H.; Jones, T. S.; Renner, C.; Aeppli, G. *Adv. Mater.* **2007,** *19,* 3618–3622. doi:10.1002/adma.200701458
29. Barraclough, C. G.; Gregson, A. K.; Mitra, S. *J. Chem. Phys.* **1974,** *60,* 962–968. doi:10.1063/1.1681174
30. Taguchi, Y.; Miyake, T.; Margadonna, S.; Kato, K.; Prassides, K.; Iwasa, Y. *J. Am. Chem. Soc.* **2006,** *128,* 3313–3323. doi:10.1021/ja0582657
31. Taguchi, Y.; Miyake, T.; Margadonna, S.; Kato, K.; Prassides, K.; Iwasa, Y. *J. Magn. Magn. Mater.* **2007,** *310,* 1229–1230. doi:10.1016/j.jmmm.2006.10.733
32. Wang, Z.; Seehra, M. S. *J. Phys.: Condens. Matter* **2016,** *28,* 136002. doi:10.1088/0953-8984/28/13/136002
33. Moriya, T. *Phys. Rev.* **1960,** *117,* 635. doi:10.1103/PhysRev.117.635

34. Lever, A. B. P. *J. Chem. Soc.* **1965,** 1821–1829. doi:10.1039/jr9650001821
35. Sonneveld, E. J.; Visser, J. W. *J. Appl. Crystallogr.* **1975,** *8,* 1–7. doi:10.1107/S0021889875009417

License and Terms

BEILSTEIN JOURNAL OF NANOTECHNOLOGY

Light-induced magnetoresistance in solution-processed planar hybrid devices measured under ambient conditions

Sreetama Banerjee[*1,2], Daniel Bülz[1], Danny Reuter[2,3], Karla Hiller[2], Dietrich R. T. Zahn[1] and Georgeta Salvan[*1]

Letter

Open Access

Address:
[1]Semiconductor Physics, Technische Universität Chemnitz, Germany, [2]Center for Microtechnologies, Technische Universität Chemnitz, Germany and [3]Fraunhofer ENAS, Chemnitz, Germany

Email:
Sreetama Banerjee[*] - sreetama.banerjee@physik.tu-chemnitz.de;
Georgeta Salvan[*] - salvan@physik.tu-chemnitz.de

* Corresponding author

Keywords:
HED-TIEs; hybrid electronic devices; organic field-effect transistors (OFETs); organic magnetoresistance; planar hybrid devices; TIPS-pentacene

Beilstein J. Nanotechnol. **2017,** *8,* 1502–1507.
doi:10.3762/bjnano.8.150

Received: 28 March 2017
Accepted: 19 June 2017
Published: 21 July 2017

This article is part of the Thematic Series "Towards molecular spintronics".

Associate Editor: P. Leiderer

Abstract

We report light-induced negative organic magnetoresistance (OMAR) measured in ambient atmosphere in solution-processed 6,13-bis(triisopropylsilylethynyl)pentacene (TIPS-pentacene) planar hybrid devices with two different device architectures. Hybrid electronic devices with trench-isolated electrodes (HED-TIE) having a channel length of ca. 100 nm fabricated in this work and, for comparison, commercially available pre-structured organic field-effect transistor (OFET) substrates with a channel length of 20 µm were used. The magnitude of the photocurrent as well as the magnetoresistance was found to be higher for the HED-TIE devices because of the much smaller channel length of these devices compared to the OFETs. We attribute the observed light-induced negative magnetoresistance in TIPS-pentacene to the presence of electron–hole pairs under illumination as the magnetoresistive effect scales with the photocurrent. The magnetoresistance effect was found to diminish over time under ambient conditions compared to a freshly prepared sample. We propose that the much faster degradation of the magnetoresistance effect as compared to the photocurrent was due to the incorporation of water molecules in the TIPS-pentacene film.

Findings

The field of molecular spintronics has received lot of research interest in the last years because of the possibility of designing nano-scalable molecule-based multi-functional devices [1]. Among the various reports on spin transport and/or magnetoresistive measurements in molecule-based devices, those regarding organic magnetoresistance (OMAR) are particularly interesting, because this effect can be observed at room temperature and in low magnetic fields of several milliteslas [2].

Several organic semiconductors consisting of small molecules such as aluminium-tris(8-hydroxyquinoline) (Alq_3) [3,4], pentacene [5], α-sexithiophene [6] or even conjugated poly-

mers such as poly(*N*-vinyl carbazole) and poly (*p*-phenylene vinylene) [6,7] derivatives have been found to exhibit an OMAR effect as an intrinsic material property without any spin injection from ferromagnetic materials. Even though OMAR has been extensively investigated over the last few years, most of the studies on OMAR have been carried out mainly on vertical devices, in which the active organic layer is sandwiched between two conductive metal layers [3,4,8]. Saragi et al. carried out studies on the magnetic field effect on three terminal bottom-contact organic field-effect transistors (OFET) and showed the existence of light-induced magnetoresistance in pentacene and its derivative 6,13-bis(triisopropylsilylethynyl)pentacene (TIPS-pentacene) molecules [5,9] deposited by thermal evaporation in vacuum. The influence of gate voltage on the magnetoresistance was also thoroughly investigated in these two reports.

In fact, most of the studies on OMAR in small molecules reported so far deal with thermally evaporated molecules and were carried out in a controlled atmosphere such as nitrogen-purged glove boxes or a cryostat to prevent the degradation of the devices in ambient atmosphere [3,5,9].

Here we demonstrate that light-induced magnetoresistance can be observed at room temperature even in ambient atmosphere. TIPS-pentacene is an ideal candidate for this proof of concept, as it is a solution-processable molecule that exhibits high carrier mobility and air-stability [10,11]. Moreover, the existence of light-induced magnetoresistance in TIPS-pentacene was already shown for thermally evaporated films by Saragi et al. [9].

In order to investigate the influence of the electrode distance on the OMAR magnitude and on the timeline of the OMAR response to the switching of magnetic field, we used two planar device geometries: i) commercially available micro-structured bottom-contact OFET substrates as used in [5] to compare the results obtained from solution processed devices with the previously reported results for evaporated TIPS-pentacene and ii) submicrometre-structured substrates for hybrid electronic devices with trench isolated electrodes (HED-TIE) designed and developed in this work.

Negative magnetoresistance (positive magnetoconductance) was observed for both types of devices similar to the observations in [9]. Magnetoresistance is defined as the change in resistivity of a material/device due to application of an external magnetic field. Magnetoconductance (MC) is the change in conductivity of a material/device upon application of an external magnetic field. The magnetoresistance effect, however, was found to degrade over time significantly faster than the photocurrent. We suggest that this degradation is due to incorporation of water molecules from the ambient atmosphere into the TIPS-pentacene.

The OFET substrates were purchased from Fraunhofer IPMS (Dresden, Germany) with channel lengths varying between 2.5 µm and 20 µm and a channel width of 10 mm. The gate oxide SiO_2 is 270 ± 10 nm thick and the source and drain electrodes are made of 30 nm Au with a 10 nm ITO adhesion layer. It should be noted that the gate electrode was kept at ground voltage for the magnetoresistance measurements and the devices were used as two-terminal devices for making the results comparable with the HED-TIE devices. For the HED-TIE devices, submicrometre trenches were patterned using conventional UV lithography and partially refilled with a thermally grown SiO_2 layer of 130 nm. The cavity-like trench (see Figure 1b for a sketch) electrically isolates the electrodes. The process flow for the preparation of the HED-TIEs is similar to

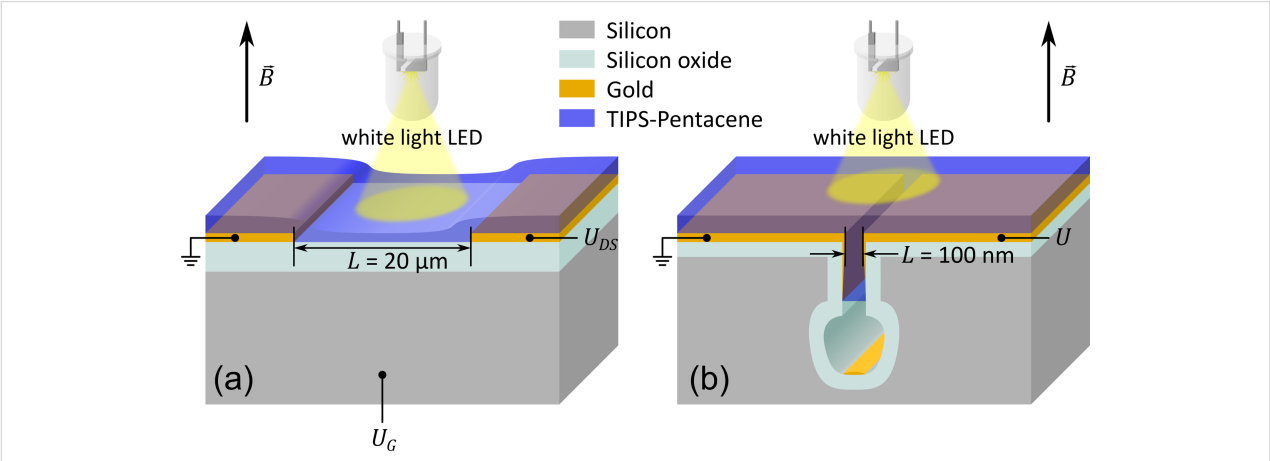

Figure 1: Schematic diagram of the experimental setup: (a) Commercial bottom-contact OFET substrates; (b) planar device structure with trench-isolated electrodes (HED-TIE).

that described in [12]. 30 nm Au was deposited as the electrode layer with a 10 nm Cr as the adhesion layer (please refer to Supporting Information File 1 for further details of HED-TIE structures). TIPS-pentacene powder with a purity of 99.9% was purchased from Ossila. The solution was prepared in a mixture of toluene/tetralin (2:1) with a concentration of 8 mg/mL. Prior to drop-coating, the fabricated structures with gold electrodes were cleaned using acetone, ethanol and deionized water respectively. 5 µL of solution was used to drop-coat the OFET substrates of 0.8 cm × 0.8 cm area and 3 µL solution was used to drop-coat the HED-TIE devices for a 1 cm × 1 cm area. TIPS-pentacene solution coats the gold surface much better than the SiO_2 surface and hence to eventually have similar coverage at the device-channel area, different amounts of solution were used for OFET and HED-TIE devices. The drop-coating of the substrates was performed at 65 °C on a hot plate and the samples were kept at 65 °C for 30 min after drop-coating, to initiate crystallization of the TIPS-pentacene film and to ensure evaporation of the solvents from the film. Unless otherwise mentioned, the electrical characterisation including the photo-switching, *I*–*V* characteristics and magnetoresistance measurements was performed immediately after the sample preparation. The total measurement time was about 1 h.

The schematic diagram of the experimental set-up is shown in Figure 1. The entire sample surface was illuminated with a white light emitting diode (LED), with an emission ranging from 400 to 700 nm for the measurements of the photocurrent and of the magnetoresistance. The measurements were performed at room temperature (ca. 25 °C) and the ambient humidity was maintained at (20 ± 5)%.

The electrical measurements were conducted using a Keithley 2636A SYSTEM source-meter unit in the auto-range mode. The magnetic field was applied perpendicular to the electrical transport channel and to the substrate plane, using an electromagnet. It should be mentioned, though, that previous reports showed OMAR to be independent of the sign and direction of the applied magnetic field [13].

Figure 2a and Figure 2b show the percentage of photocurrent with respect to the dark current, when the white light LED was switched on and off for OFET and HED-TIE devices, respectively. The percentage of the change in current was found to be more representative when comparing two device architectures with significantly different volume of the active organic channel. The photocurrent of the HED-TIE devices is a factor of two higher and the photo-switching occurs to be faster in the HED-TIE devices, due to the smaller electrode gap.

Figure 2c and Figure 2d show the magnetoconductance response of the same devices. Here, the device current over time was measured by switching on and off a constant applied magnetic field while the illumination was kept on throughout the

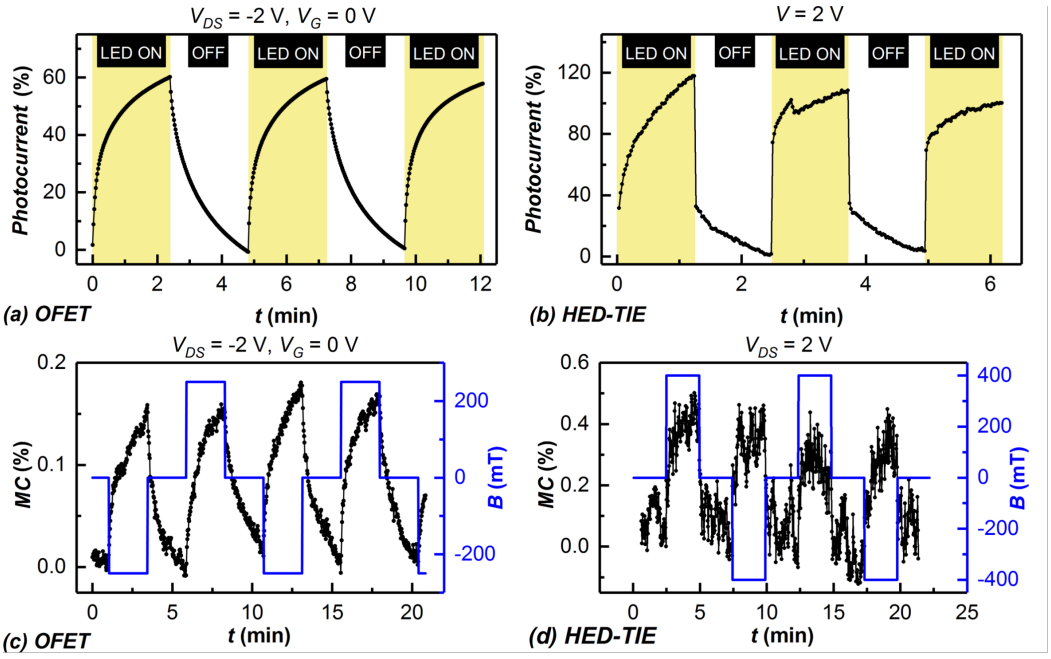

Figure 2: Light-switching behaviour of TIPS-pentacene-based (a) organic field-effect transistor (OFET) and (b) hybrid electronic device with trench-isolated electrodes (HED-TIE). Light-induced magnetoresistance in TIPS-pentacene obtained from both types of planar devices: (c) OFET and (d) HED-TIE device.

measurements. Both OFETs and the HED-TIE devices were found to exhibit positive magnetoconductance (negative magnetoresistance) as previously reported for evaporated TIPS-pentacene [9]. The magnitude of OMAR is independent of the sign of the applied magnetic field, as expected.

For the switching of both light and magnetic field, the HED-TIE devices were found to respond faster whereas the OFETs exhibit a slower carrier relaxation. This can be attributed to higher electric fields and shorter charge-carrier transit times in the shorter channels of the HED-TIEs (ca. 100 nm) compared to that of OFETs (20 µm). Also the magnitude of switching in the HED-TIE device for both light and magnetic field was found to be twice as much as OFET, similar to the photocurrent.

It should be mentioned here that the TIPS-pentacene OFETs fabricated by thermal evaporation in [9] showed a fast switching response, similar to our HED-TIEs. This is most probably due to the significantly smaller volume of the OFET channel (78 nm film thickness in [9], compared to ca. 500 nm film thickness in our drop-coated OFETs at the same channel length), because the mobility values determined for our solution-processed OFETs are in the range from 10^{-2} to 1 $cm^2 \cdot V^{-1} \cdot s^{-1}$, which is higher than the mobility values reported for thermally evaporated TIPS-pentacene ($6 \cdot 10^{-3}$ to 1 $cm^2 \cdot V^{-1} \cdot s^{-1}$) [9].

As no magnetoresistance was observed in the absence of illumination and hence of a photocurrent, the observed effect in the solution-deposited TIPS-pentacene OFETs and HED-TIEs is supposedly based on the presence of spin-carrying polarons related to electrons and holes created by photoexcitation. These weakly interacting polarons are labelled as "electron–hole (e–h) pairs" and are considered to contribute to OMAR because of their flexible spin configuration (singlet or triplet). The same mechanism was proposed to be responsible for the OMAR observed in thermally evaporated TIPS-pentacene OFETs in [9], which is an indication that the processing methods of the TIPS-pentacene do not influence the intrinsic mechanism of the OMAR in this organic semiconducting material. In the e–h model, the recombination into electrically neutral excitons and the dissociation of the weakly bound e–h pairs into charge carriers available for the electrical transport is influenced by an applied magnetic field, in favour of the latter effect [9,14]. An applied magnetic field will thus trigger an increase in the conductance of the device [9,14]. It should be noted that although the applied constant magnetic field was different for our OFETs and HED-TIEs, this should not have an influence on the magnitude of the OMAR effect. It was shown in [5] for pentacene that the magnitude of OMAR almost reaches a saturation at about 80 mT and a similar saturation field was also reported for other materials such as Alq_3 [3].

The observed magnetoresistance effect was found to diminish approximately after two days of sample preparation in case of the HED-TIE devices kept under ambient conditions, while the photocurrent decreased from 120% to only 65%. The photoresponse time, however, was increased compared to the freshly prepared sample (shown in Figure 3b). The magnetoresistive effect and the photocurrent in the OFETs were also found to decrease in magnitude, but the magnetoresistance did not disappear completely in the same time interval considered for the HED-TIEs. This could be due to the TIPS-pentacene layer being thicker for the OFETs, which confers a higher stability over time. The degradation of the devices in ambient atmosphere can be attributed to the penetration of oxygen and/or water molecules in the TIPS-pentacene film, additionally accelerated by white light illumination. Vollmer et al. showed [15], by investigating the occupied electronic states using ultraviolet photoemission spectroscopy, that the diffusion of molecular

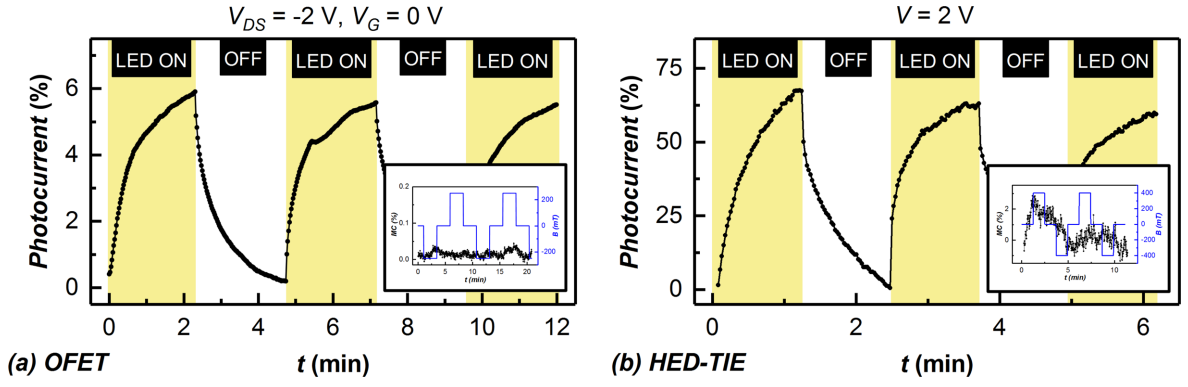

Figure 3: (a) Light switching of an OFET prepared by drop-coating of TIPS-pentacene diluted in water. The inset shows absence of the magnetoresistance in such an OFET. (b) Degraded light-switching behaviour of a TIPS-pentacene HED-TIE after two days of exposure to ambient atmosphere. The inset shows the response to applied magnetic field.

oxygen and water from the ambient into pentacene layers is reversible when the air exposure takes place in the dark or under visible light. The exposure to ambient under UV illumination leads to a reaction, most probably with singlet oxygen and/or ozone [15]. As the magnetoresistance measurements are performed in presence of white light with a spectrum ranging from 400 to 700 nm, we believe that different parts of the wavelength spectra can have different contributions to the device degradation. It was also shown by Jurchescu et al. [16] that pentacene single crystals behave differently when the electrical conductivity is measured in ambient or dry air, with and without illumination. It should be mentioned here that previously we found the decrease in photoluminescence caused by the diffusion of oxygen/water in TIPS-pentacene films in the HED-TIE devices to be reversible [12] and that the recovery is much faster under nitrogen purging and single-wavelength illumination.

To verify the role of the diffusion of water molecules into the TIPS-pentacene film in the deterioration of the magnetoresistance, an OFET was prepared by drop-coating a substrate with the same TIPS-pentacene solution as used for the preparation of the devices discussed before (cf. Figure 2) but now diluted (1:1) in deionized water. As shown in Figure 3a, the magnitude of the photocurrent of the freshly prepared device was found to be only 6% (compared to 60% for the device prepared with a water-free solution, see Figure 2a) whereas the magnetoresistance disappeared completely in this case. The output characteristics of such a device showed (please refer to Supporting Information File 1) a drastic change in the line shape compared to the TIPS-pentacene transistor prepared from water-free solution.

This experiment shows that TIPS-pentacene, despite of its solution processability in non-polar solvents, exhibits a degradation in electrical properties upon water incorporation in the films. We assume that the water molecules in the film shift the energy level of the singlet and triplet states of the e–h pairs and thereby change the probability of intermixing between these two states. In a changed energy landscape of the excited electronic states, the effect of the magnetic field on the singlet/triplet intermixing could become negligible, explaining the dramatic reduction in magnetoresistance.

To summarize, we demonstrated the presence of light-induced negative magnetoresistance in freshly prepared solution-processed TIPS-pentacene planar devices of two different architectures, measured under ambient atmosphere. The HED-TIE devices with smaller electrode gap yielded a higher photocurrent, a higher magnetoresistance and a lower switching time. Although TIPS-pentacene is supposed to be stable in air, the influence of ambient atmosphere was found to cause diminishing of the magnetoresistance of the fabricated devices within a period of two days after sample preparation. We assume this is due to incorporation of water molecule in the TIPS-pentacene film when it is exposed to ambient. To support this hypothesis, we showed the absence of magnetoresistance in OFETs prepared with TIPS-pentacene solution diluted in deionized water accompanied by a reduction, but not disappearance of the photocurrent. We propose that the usage of a suitable capping layer could protect the organic film and thus increase the lifetime of such devices, if used as magnetoresistive sensors working under ambient atmosphere.

Supporting Information

Supporting Information describes the fabrication of HED-TIE devices and the electrical output characteristics for both HED-TIE and OFET devices.

Supporting Information File 1

Additional epxerimental data.
[http://www.beilstein-journals.org/bjnano/content/supplementary/2190-4286-8-150-S1.pdf]

Acknowledgements

The authors would like to thank the staff of the Centre for Microtechnologies and Fraunhofer ENAS for their assistance in the fabrication process of the devices with trench isolated electrodes. This work was funded by the Deutsche Forschungsgemeinschaft within the Research Unit DFG FOR 1154 “Towards Molecular Spintronics”.

References

1. Dediu, V. A.; Hueso, L. E.; Bergenti, I.; Taliani, C. *Nat. Mater.* **2009,** *8,* 707–716. doi:10.1038/nmat2510
2. Wohlgenannt, M. *Phys. Status Solidi RRL* **2012,** *6,* 229–242. doi:10.1002/pssr.201206129
3. Mermer, Ö.; Veeraraghavan, G.; Francis, T. L.; Wohlgenannt, M. *Solid State Commun.* **2005,** *134,* 631–636. doi:10.1016/j.ssc.2005.02.044
4. Zhang, S.; Rolfe, N. J.; Desai, P.; Shakya, P.; Drew, A. J.; Kreouzis, T.; Gillin, W. P. *Phys. Rev. B* **2012,** *86,* 75206. doi:10.1103/PhysRevB.86.075206
5. Reichert, T.; Saragi, T. P. I. *Appl. Phys. Lett.* **2011,** *98,* 063307. doi:10.1063/1.3554388
6. Martin, J. L.; Bergeson, J. D.; Prigodin, V. N.; Epstein, A. J. *Synth. Met.* **2010,** *160,* 291–296. doi:10.1016/j.synthmet.2010.01.009
7. Hu, B.; Wu, Y. *Nat. Mater.* **2007,** *6,* 985–991. doi:10.1038/nmat2034
8. Francis, T. L.; Mermer, Ö.; Veeraraghavan, G.; Wohlgenannt, M. *New J. Phys.* **2004,** *6,* 185. doi:10.1088/1367-2630/6/1/185
9. Reichert, T.; Saragi, T. P. I. *Org. Electron.* **2012,** *13,* 377–383. doi:10.1016/j.orgel.2011.11.026

10. Murtaza, G.; Ahmad, I.; Chen, H.; Wu, J. *Synth. Met.* **2014,** *194,* 146–152. doi:10.1016/j.synthmet.2014.04.034
11. Feng, L.; Tang, W.; Zhao, J.; Yang, R.; Hu, W.; Li, Q.; Wang, R.; Guo, X. *Sci. Rep.* **2016,** *6,* 20671. doi:10.1038/srep20671
12. Banerjee, S.; Bülz, D.; Solonenko, D.; Reuter, D.; Deibel, C.; Hiller, K.; Zahn, D. R. T.; Salvan, G. *Nanotechnology* **2017,** *28,* 195303. doi:10.1088/1361-6528/aa6713
13. Mermer, Ö.; Veeraraghavan, G.; Francis, T. L.; Sheng, Y.; Nguyen, D. T.; Wohlgenannt, M.; Köhler, A.; Al-Suti, M. K.; Khan, M. S. *Phys. Rev. B* **2005,** *72,* 205202. doi:10.1103/PhysRevB.72.205202
14. Wagemans, W.; Koopmans, B. *Phys. Status Solidi B* **2011,** *248,* 1029–1041. doi:10.1002/pssb.201046383
15. Vollmer, A.; Jurchescu, O. D.; Arfaoui, I.; Salzmann, I.; Palstra, T. T. M.; Rudolf, P.; Niemax, J.; Pflaum, J.; Rabe, J. P.; Koch, N. *Eur. Phys. J. E* **2005,** *17,* 339–343. doi:10.1140/epje/i2005-10012-0
16. Jurchescu, O. D.; Baas, J.; Palstra, T. T. M. *Appl. Phys. Lett.* **2005,** *87,* 052102. doi:10.1063/1.2001130

License and Terms

BEILSTEIN JOURNAL OF NANOTECHNOLOGY

Charge transfer from and to manganese phthalocyanine: bulk materials and interfaces

Florian Rückerl[1], Daniel Waas[1], Bernd Büchner[1], Martin Knupfer*[1], Dietrich R. T. Zahn[2], Francisc Haidu[2], Torsten Hahn[3] and Jens Kortus[3]

Review

Open Access

Address:
[1]IFW Dresden, Helmholtzstr. 20, D-01069 Dresden, Germany, [2]Semiconductor Physics, Chemnitz University of Technology, D-09107 Chemnitz, Germany and [3]Institute of Theoretical Physics, TU Bergakademie Freiberg, Leipziger Str. 23, D-09596 Freiberg, Germany

Email:
Martin Knupfer* - m.knupfer@ifw-dresden.de

* Corresponding author

Keywords:
charge transfer; electronic properties; manganese phthalocyanine

Beilstein J. Nanotechnol. **2017,** *8,* 1601–1615.
doi:10.3762/bjnano.8.160

Received: 03 March 2017
Accepted: 13 June 2017
Published: 04 August 2017

This article is part of the Thematic Series "Towards molecular spintronics".

Guest Editor: G. Salvan

Abstract

Manganese phthalocyanine (MnPc) is a member of the family of transition-metal phthalocyanines, which combines interesting electronic behavior in the fields of organic and molecular electronics with local magnetic moments. MnPc is characterized by hybrid states between the Mn 3d orbitals and the π orbitals of the ligand very close to the Fermi level. This causes particular physical properties, different from those of the other phthalocyanines, such as a rather small ionization potential, a small band gap and a large electron affinity. These can be exploited to prepare particular compounds and interfaces with appropriate partners, which are characterized by a charge transfer from or to MnPc. We summarize recent spectroscopic and theoretical results that have been achieved in this regard.

Review

Introduction

The family of metal-centered phthalocyanines has been considered for future technological applications because of their favorable electronic and optical properties and their advantageous chemical stability [1-8]. Phthalocyanine molecules can harbor a number of metal ions, in particular transition-metal ions such as cobalt, iron or manganese. A special characteristic of transition-metal centered phthalocyanines is, that transition-metal ions often are characterized by a magnetic moment, and therefore such phthalocyanines also show very interesting magnetic behavior [9]. They have even been discussed in terms of molecular magnets including their discussion in future applications in the field of molecular spintronics [10-12].

Among these transition-metal phthalocyanines, manganese phthalocyanine (MnPc) is one of the most interesting molecules due to its particular electronic and magnetic properties in the bulk [13-16]. A schematic representation of the molecule structure is depicted in Figure 1 below. For instance, MnPc is characterized by an unusual $S = 3/2$ spin state of the central Mn(II) ion. The spin of MnPc is a consequence of three unpaired 3d electrons in the Mn 3d levels, which also lie close to the chemical potential. In essence, the electronic properties (partly) reflect the behavior of these 3d electrons, and MnPc plays a special role in the group of the transition-metal phthalocyanines. The energy gap between the occupied and unoccupied molecular orbitals of MnPc is the smallest among all transition-metal phthalocyanines [17-21], its ionization potential also is the smallest within this class of material [17,18,22], while the electron affinity is larger than those of the others [17,18]. Furthermore, the exciton binding energy related to the lowest electronic singlet excitation is somewhat larger compared to, e.g., CuPc [18-20,23]. In Table 1 we summarize these values in comparison to CuPc, the most prominent and most extensively investigated transition-metal phthalocyanine to date.

Table 1: Summary of characteristic electronic parameters for MnPc determined for thin films in comparison to those for CuPc. In detail, we compare the ionization potential (IP), the electron affinity (EA), the energy gap as seen in optical studies (E_g^{opt}), the transport energy gap (E_g^{tr}), and the exciton binding energy (E_B^{exc}) of the lowest singlet excitation (see text for references). All values are given in eV.

	IP	EA	E_g^{opt}	E_g^{tr}	E_B^{exc}
MnPc	4.5	3.3	0.5	1.2	0.7
CuPc	5.0	2.7	1.8	2.3	0.5

These exceptional properties of MnPc render it possible that this molecule can undergo charge-transfer reactions of either kind, i.e., it can be oxidized or reduced by suitable reaction partners. This can be utilized to synthesize new compounds with potentially interesting properties. In this contribution we present a summary of recent results in regard of charge transfer compounds, or interfaces characterized by charge transfer, which all are based on MnPc.

Materials and methodology

This article covers charge-transfer reactions of manganese phthalocyanine with the alkali metal potassium as well as with further organic molecules. The latter are characterized by a rather large electron affinity to enable charge transfer from MnPc to these structures. In Figure 1 we show the structure of all molecules discussed below. These are MnPc, its phthalocyanine relative F_{16}CoPc (both purchased from Sigma-Aldrich), F_4TCNQ (2,3,5,6-tetrafluoro-7,7,8,8-tetracyanoquinodimethane, TCI Europe) and F_6TCNNQ (1,3,4,5,7,8-hexafluorotetracyanonaphthoquinodimethane, Novaled AG). F_4TCNQ is quite well known for its high electron affinity [24], and it is also known to form many charge-transfer crystals with appropriate partners [25,26]. Further, it has also been used as dopant material for organic electronic devices [27-29]. More recently, F_6TCNNQ has been introduced into organic devices with advantages such as an even higher electron affinity and a larger molecular mass, which prevents diffusion of the molecule in organic devices [30]. F_{16}CoPc has been applied recently in a few cases only, in order to induce charge transfer across interfaces to other insulating (or semiconducting) materials [31-33]. The electron affinities of the three acceptor molecules are 4.5 eV (F_{16}CoPc [34]), 5.2 eV (F_4TCNQ [35]) and 5.6 eV (F_6TCNNQ [36]).

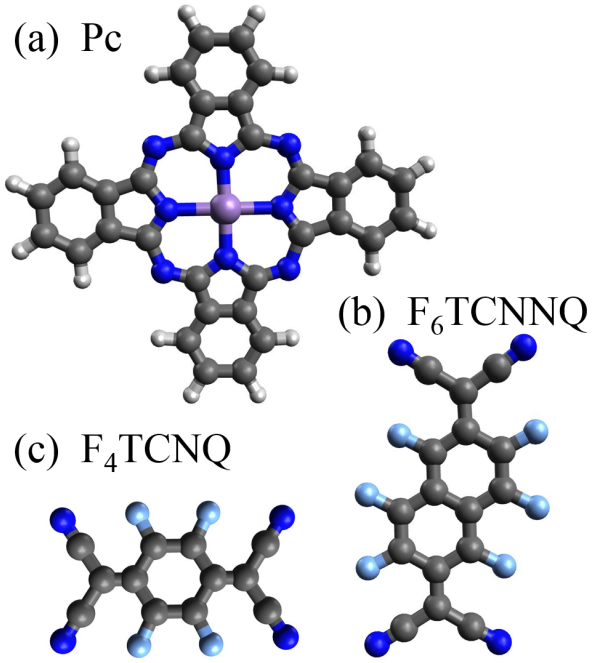

Figure 1: Molecular structure of (a) transition metal phthalocyanines, (b) 1,3,4,5,7,8-hexafluorotetracyanonaphthoquinodimethane (F_6TCNNQ), and (c) 2,3,5,6-tetrafluoro-7,7,8,8-tetracyanoquinodimethane (F_4TCNQ). The transition-metal center in the phthalocyanine molecule can vary; in this work Mn and Co are relevant. Moreover, phthalocyanines can be modified by the substitution of hydrogen with fluorine atoms as in F_{16}CoPc. Different atoms are shown with different colors (C: black, N: blue, H: white, F: light blue, and Mn/Co: purple).

The results presented in this contribution were achieved by either solid-state spectroscopy methods or density functional based calculations. The experimental methods comprise photoelectron (or photoemission) spectroscopy (PES), inverse photoemission spectroscopy (IPES), electron energy-loss spectroscopy (EELS), spectroscopic ellipsometry and X-ray absorption

spectroscopy (XAS). Here, we only briefly mention the kind of information that is provided by these methods, and we refer the reader to comprehensive literature for detailed information.

PES [37-39] is based on the photoelectric effect and provides insight into the valence-band electronic density of states as well as the binding energy and line shape of core levels, which give information about the composition of the sample and the chemical state (e.g., valency) of the atoms or ions. In IPES [19,40-42], the unoccupied density of states is probed. EELS [43-45] can also be called inelastic electron scattering and measures the electronic excitations either in the valence-band region, or from core levels into unoccupied states, whereas momentum-dependent studies are possible [43,45,46]. The EELS cross section is proportional to $\mathrm{Im}(-1/\varepsilon)$ (ε is the dielectric function). In this way, one can investigate valence-band excitations (cf. optical methods) and the element-projected unoccupied density of states. Also, access to orbital selective occupations and the magnetic moment of open shells is accessible. Spectroscopic ellipsometry [47-49] measures the change in the light polarization after reflection on a sample surface. This information allows for the determination of the real and the imaginary part of the dielectric function. XAS [42,50] is equivalent to EELS in the core-level region, and polarization-dependent studies have often been carried out to study the molecular orientation on substrates. In addition to our experiments we performed calculations within the density functional theory (DFT) framework. We used a recent version of the NRLMOL all-electron DFT code [51,52], which uses large Gaussian-orbital basis sets for the representation of the electronic wavefunctions [53]. Unless noted otherwise we used the PBE functional [54] within the general gradient approximation (GGA) was used for all calculations. We semi-empirically included dispersion correction according to the Grimme DFT-D3 method [55] in all of our calculations.

K_xMnPc: formation of stable phases with MnPc anions

The formation of compounds with composition K_xMnPc was achieved by evaporation of potassium from so-called K dispensers (SAES Getters, S.P.A, Italy) onto MnPc thin films under ultra-high vacuum conditions. These then were thoroughly characterized by the spectroscopic methods in order to obtain a comprehensive picture. We start the presentation of our spectroscopic data with the development of the electronic excitation spectra of MnPc as a function of potassium doping. These were determined using EELS and spectroscopic ellipsometry. In Figure 2 we show the corresponding results.

The EELS measurements were carried out at a momentum transfer of 0.1 $\mathrm{Å}^{-1}$ which represents the so-called optical limit,

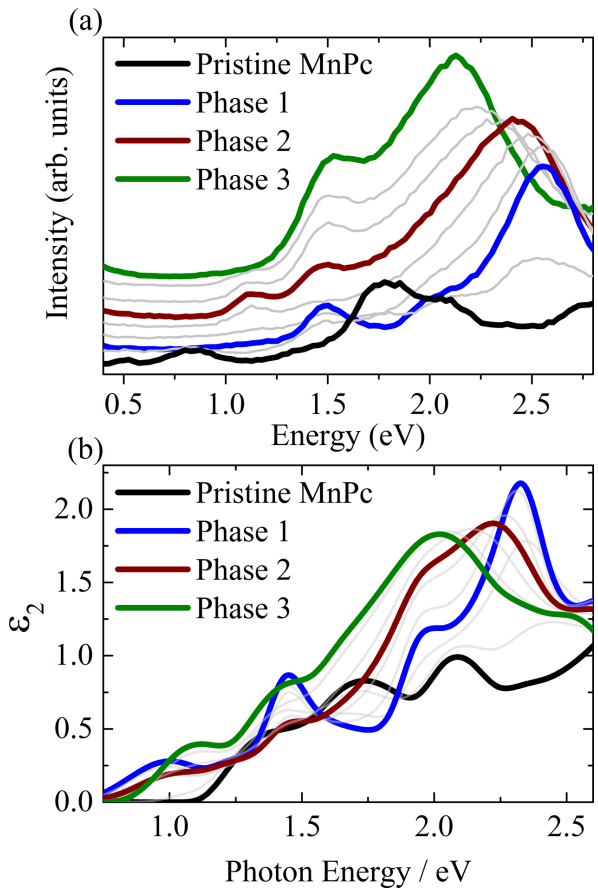

Figure 2: Evolution of the electronic-excitation spectra of MnPc upon potassium doping as determined using electron energy-loss spectroscopy (panel (a)) and spectroscopic ellipsometry (panel (b)). Panel (a) shows the so-called loss function, $\mathrm{Im}(-1/\varepsilon)$ [56], while panel (b) shows the imaginary part of the dielectric function, ε_2 [49]. The potassium concentration increases from MnPc over phase 1 to phase 2 and 3. Thicker lines depict the spectra for particular doped phases as described in the text.

i.e., the data are equivalent to those from corresponding optical studies [43]. Note that the ellipsometry results in Figure 2b start at higher energies due to instrumental limitations. The spectrum of pristine MnPc is characterized by several spectral features at about 0.5, 0.8, 1.4, 1.8, and 2.1 eV [23], which are clearly seen in Figure 2a. Around 2 eV, the excitations are usually ascribed to the Q band common to many phthalocyanines [57-59]. They are due to transitions from the highest occupied molecular orbital (HOMO) to the lowest unoccupied molecular orbital (LUMO) [58]. The observed fine structure was attributed to a combination of Davydov splitting, the admixture of charge-transfer excitations as well as vibronic satellites [60-68]. The appearance of further excitations at lower energies for MnPc is still not fully understood. Certainly, they are connected to the contribution of Mn 3d states to the molecular orbitals close to the chemical potential, a complete picture, however, is elusive [23,69-73].

The addition of potassium induces particular changes in regard of the electronic excitations. The two lowest-lying features (at about 0.5 and 0.8 eV, see panel (a)) disappear, also the intensity in the Q band region is drastically reduced. Instead, spectral structures show up at 1.5 eV and about 2.6 eV up to a particular doping level (called phase 1 in Figure 2). Further potassium doping results in the appearance of an excitation at about 1.1 eV, while the structure at about 2.6 eV shows a downshift in energy. The intensity of the excitation at 1.1 eV as seen in panel (a) reaches a maximum at a second distinct doping level (phase 2), thereafter it starts to vanish again. In contrast, the excitation at 1.5 eV is steadily growing in intensity and the highest-lying excitation continues to downshift until a third composition is reached (phase 3).

A detailed analysis of these data together with those from electron diffraction [56] revealed the existence of particular K_xMnPc compositions (phases 1, 2, and 3). This, in general, parallels the behavior of other transition-metal phthalocyanines upon potassium doping, where also particular stable phases were reported [74-76]. We emphasize that this conclusion is nicely supported by the fact that all EELS spectra at doping levels between these three phases can be modeled by a corresponding superposition of the spectra of the phases in the direct neighborhood [56]. The exact composition of these phases was finally determined by an analysis of the respective C 1s and K 2p core-level excitations. These data are depicted in Figure 3.

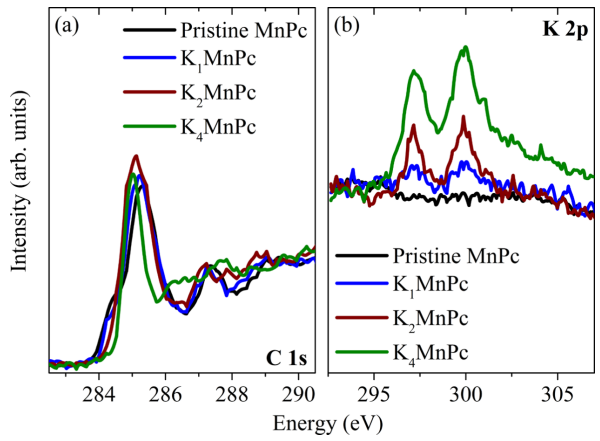

Figure 3: C 1s (panel (a)) and K 2p (panel (b)) excitation edges of MnPc and the three potassium-doped phases (adapted from [56]). The relative intensities of these two edges were used to analyze the composition of the doped phases.

In this Figure, excitation from the C 1s core level in unoccupied π-derived states start at about 285 eV, those into σ-derived carbon states at about 292 eV, while K 2p to K 3d excitations are seen at 297.1 and 298.8 eV [50,77]. The spectral evolution in Figure 3 clearly signals the increasing K content in our samples. The analysis of the relative spectral weights allowed for the determination of the exact composition of the three potassium-doped MnPc phases: K_1MnPc, K_2MnPc, and K_4MnPc [56]. Thus, the spectra highlighted in Figure 2 above represent the electronic excitation spectra of these three phases. In addition, the spectral shape of the C 1s excitation data change in a characteristic manner as a function of doping, in particular right at the excitation onset.

In the case of undoped MnPc, the excitation edge starts with a low-energy shoulder around 284.5 eV before the first maximum at 285.3 eV is reached. Also for other transition-metal phthalocyanines such a C 1s excitation edge is observed [78-80]. This two-peak structure has its origin in the fact that the phthalocyanine ring consists of carbon atoms with different chemical environments, namely those with nitrogen as neighbors and those without. This is clearly seen in corresponding C 1s core-level photoemission data [74,81,82], in which the binding energy for the two carbon species is different. Considering the C 1s excitations as seen in Figure 3a, the excitations from these two carbon sites into the lowest unoccupied orbital give rise to a two-peak structure. Upon doping, there are two changes that impact the C 1s excitations. First, the unoccupied levels are filled with the doping-induced electrons. Second, the carbon binding energies change, as revealed by photoemission data, which show a broadening and the appearance of significantly less structured C 1s core level features in the doped compounds [74,79,80]. As a consequence, the low-energy shoulder in the C 1s excitations is lost and only a single low-energy feature is seen for higher doping levels. Again, this parallels the observations for other doped phthalocyanines [78-80]. There is, however, an important difference to the evolution of the C 1s excitation edges of FePc, CoPc and CuPc upon potassium doping. For these three materials the low-energy shoulder virtually disappeared at a doping level of about one K atom per molecule [78,79,83]. In the case of MnPc here (see Figure 3), this state is reached not until the composition K_2MnPc is reached. This nicely corroborates that the lowest-lying unoccupied MnPc orbital that is filled by electrons, has predominantly Mn 3d character [22,72,84], whereas for the other phthalocyanines a ligand π^* state is filled right from the beginning.

The results shown above already indicate that all of the potassium-doped MnPc phases are characterized by an energy gap. This observation is in full agreement with the results of photoelectron spectroscopy studies and inverse photoelectron studies of K-doped MnPc [49] as discussed in the following. The samples for these investigations again were prepared by potassium addition to MnPc thin films in ultra-high vacuum. The doping level of the films was determined by analyzing the relative in-

tensities of the core level photoemission from the C 1s and the K 2p core levels [49]. In Figure 4 we summarize the results of PES and IPES data that could be obtained for compositions close to the K_xMnPc phases that were discussed above.

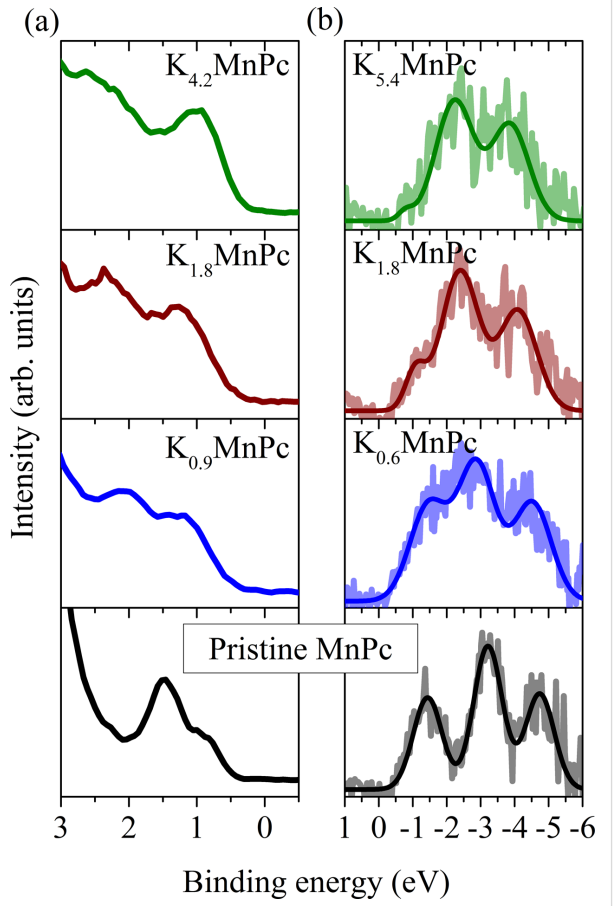

Figure 4: Panel (a): valence band photoelectron spectroscopy results for undoped and three potassium-doped MnPc films, which represent the occupied density of states. The doping levels were determined using PES from C 1s and K 2p core levels [49]. Panel (b) depicts data from inverse photoelectron spectroscopy, i.e., the unoccupied density of states.

We start the discussion with the spectra for undoped MnPc. The PES data in Figure 4a show the well-known two maxima close to the chemical potential (0 eV binding energy) [18,22]. They arise from emission from the highest occupied molecular orbital (HOMO) at about 1.5 eV binding energy, and from the so-called SOMO (singly occupied molecular orbital) at about 0.7 eV. Going to $K_{0.9}$MnPc, there is an energy shift to higher binding energies, which is due to a shift of the Fermi level towards the unoccupied levels. Furthermore, the feature at lowest binding energy grows in intensity, which reflects the filling of the SOMO with one more electron. Adding more potassium ($K_{1.8}$MnPc) results in a further shift of the maxima to somewhat higher energies, while the spectral onset moves slightly downward. This downshift is related to the filling of the former LUMO with electrons, i.e., a new occupied state appears in the photoemission data. Further doping to $K_{4.2}$MnPc causes an intensity increase at low binding energy, which results from further filling of the former LUMO.

Figure 4b presents information on the unoccupied electronic states as measured using IPES [49]. For undoped MnPc the spectrum represents the first three unoccupied levels, the LUMO (lowest unoccupied molecular orbital), the LUMO+1, and the LUMO+2. We note that the IPES data do not reveal the unoccupied part of the SOMO (see above), which is attributed to the limited energy resolution of the data. The formation of K_xMnPc phases results in an intensity decrease of the feature representing the LUMO due to electron addition into this orbital, in agreement to the discussion above. Importantly, independent of the potassium concentration both PES and IPES data, in agreement with the EELS data above demonstrate a clear energy gap, i.e., none of the K_xMnPc phases is metallic. This, in general, resembles the situation in many molecular crystals doped with alkali metals, where it was observed that the doping did not result in a metallic ground state although metallicity would be expected on the basis of band-structure calculations since half-filled bands are present. Molecular crystals usually have energy bands with small band widths, which is a direct consequence of the rather small interaction between the molecules in the material. Furthermore, the bandwidth often is similar to the Coulomb repulsion of two charge carriers on one molecule. Thus, molecular crystals also are correlated materials, where the electronic correlations often are strong enough to induce an insulating Mott–Hubbard ground state [85-94].

MnPc cations in an organic salt: MnPc/F_4TCNQ

In the following we present information on the electronic properties of a purely organic salt in which MnPc is oxidized. In order to obtain such a compound we have prepared mixed films consisting of MnPc and the particularly strong electron acceptor F_4TCNQ. It is well known that high-quality organic charge transfer crystals with F_4TCNQ as electron acceptor can be grown [95-103]. Phthalocyanine-based compounds, however, have not been reported yet. We prepared the mixed films by evaporating F_4TCNQ on top of a MnPc film and taking advantage of the diffusion of F_4TCNQ into the MnPc film, or by simultaneously evaporating both materials [104]. Subsequently, we have applied an in situ distillation procedure, which was already applied in previous experiments to achieve stoichiometric molecular salts [105-108]. After the initial preparation step, the films were heated up to 340 K for about half an hour, where an evaporation of surplus F_4TCNQ could be seen even with bare eye [104]. Also, this procedure resulted in the forma-

tion of MnPc/F_4TCNQ films with a well-defined composition and with well-defined spectral response, which signalled the homogeneity of the films. The composition was analyzed using the relative intensities of photoemission core-level features [104], and in all cases we obtained a stoichiometric ratio of 1:1.

We have analyzed the electronic properties of the new organic charge-transfer compound MnPc/F_4TCNQ using photoemission and electron energy-loss spectroscopy as well as density functional theory based calculations. In Figure 5 we show the PES results in the valence band region.

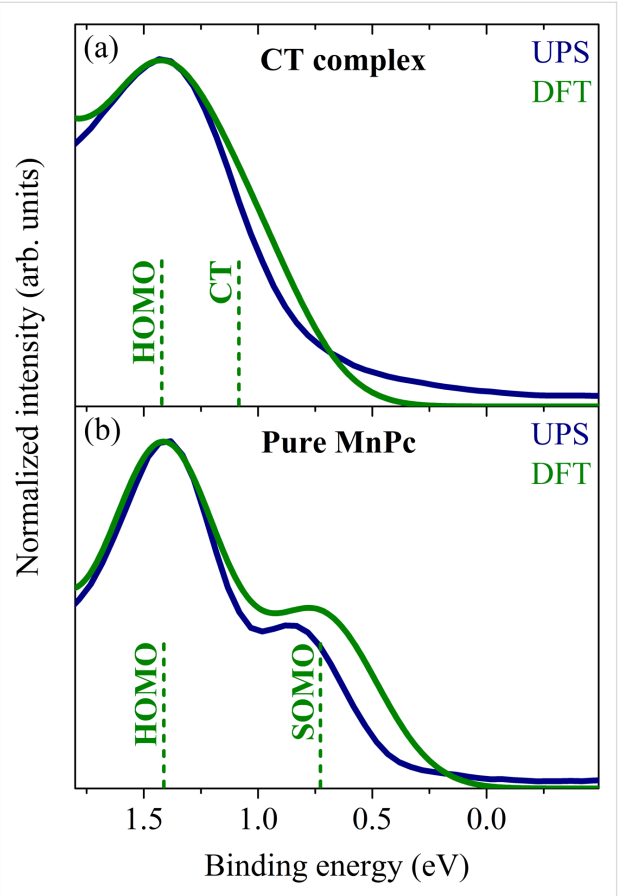

Figure 5: Comparison of valence band photoelectron spectroscopy (UPS) data to those from density functional based calculations (DFT) for pure MnPc (lower panel) and the charge-transfer compound MnPc/F_4TCNQ (upper panel). The vertical bars denote the energy position of the molecular orbitals as determined by the calculations. For pure MnPc the two-peak structure arises from the singly occupied molecular orbital (SOMO) and the highest occupied molecular orbital (HOMO). The formation of the charge-transfer (CT) compound leads to a disappearance of the SOMO. Instead, a CT hybrid state shows up, closer in energy to the HOMO (see also [104]).

These data clearly illustrate a substantial variation going from pure MnPc to the charge-transfer compound. For pure MnPc our data demonstrate the well-known two peak structure at lowest binding energy (see also the previous chapter). The formation of the MnPc/F_4TCNQ compound is accompanied by the disappearance of the feature at lowest binding energy (here called SOMO = singly occupied molecular orbital). This indicates that electrons are removed from MnPc, i.e., the phthalocyanine molecule is oxidized. Since the leading orbital in pure MnPc (SOMO) is a hybrid state of Mn 3d and ligand π orbitals with a large Mn 3d contribution [22,84,109], this oxidation is also clearly seen in core-level photoemission from MnPc 2p core level states as depicted in Figure 6.

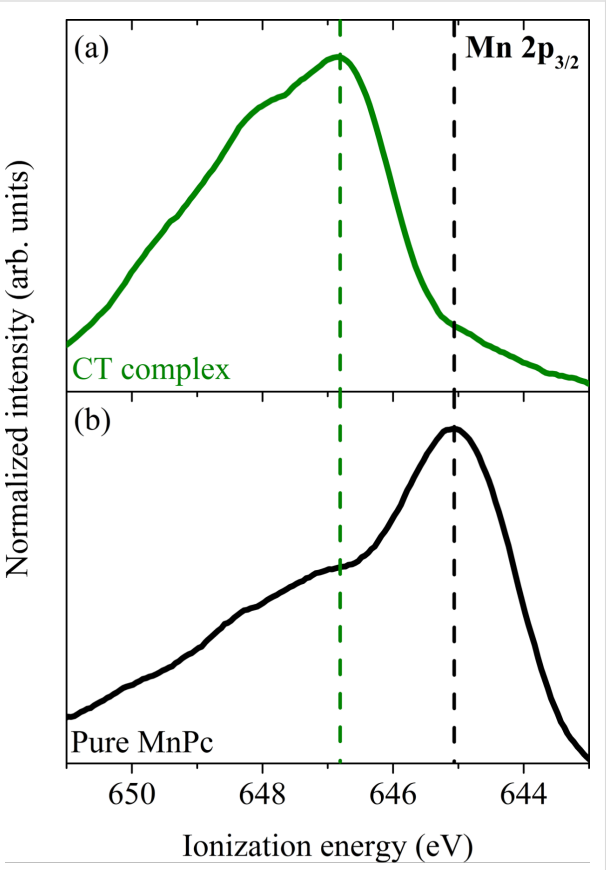

Figure 6: Core-level photoelectron spectroscopy data in the energy region of the Mn $2p_{3/2}$ core level (adapted from [104]). Note that the energy is referenced to the vacuum level in this case, since two different compounds with different Fermi-level positions are compared. Panel (a) shows the core-level emission of the MnPc/F_4TCNQ charge-transfer compound, while panel (b) shows that of pure MnPc. Clearly, the formation of MnPc/F_4TCNQ results in an energy shift of about 1.8 eV to higher ionization energy.

This figure presents the comparison of the Mn $2p_{3/2}$ core-level emission spectrum from a pure MnPc film and from the charge-transfer compound MnPc/F_4TCNQ. The overall spectral shape is controlled by an underlying multiplet structure [110,111] and is not discussed here further. For MnPc/F_4TCNQ the Mn 2p core level is significantly shifted to a higher ionization energy by about 1.8 eV, which results from the oxidation of the central Mn atom in MnPc. Shifts of the Mn 2p photoemission core-

level features to higher energies were also observed going from MnO to, e.g., Mn_3O_4 [112], where also the number of Mn 3d electrons is reduced. Thus, the core-level data corroborate our conclusion above.

The charge-transfer reaction between MnPc and F_4TCNQ was also studied on the basis of dimer calculations. These calculations indicate the formation of a hybrid state between the highest occupied orbital of MnPc (here called SOMO for singly occupied molecular orbital) and the LUMO of F_4TCNQ, see Figure 7. The energy position of this hybrid state is lower than that of the SOMO of MnPc. In addition, the calculations demonstrate a charge transfer between the molecules of about 0.6 electrons per dimer. The experimental results indicate an even larger charge transfer, which most likely is related to the localization error inherent to all DFT semi-local exchange correlation functionals [113]. Nevertheless, the calculations provide a reasonable understanding of the occupied electronic states of MnPc/F_4TCNQ as demonstrated in Figure 5. Both the disappearance of the spectral feature at lowest binding energy of MnPc as well as the broadening of the structures is well reproduced. The calculations also indicate that the hybrid state is too close to the MnPc HOMO to be resolved spectroscopically.

The formation of the charge-transfer complex MnPc/F_4TCNQ also results in corresponding changes of the electronic excitation spectra in comparison to those from pure MnPc or F_4TCNQ. This is illustrated in Figure 8, where the corresponding data from EELS are depicted. The measured spectrum of pure F_4TCNQ is characterized by a rather large energy gap and an excitation onset at about 2.7 eV that is followed by a broad structure around 3.3 eV [114,115]. The rather complex excitation spectrum of MnPc was already discussed above. The formation of the charge-transfer compound MnPc/F_4TCNQ gives rise to clearly different electronic excitations. The lowest excitation feature as seen for pure MnPc at about 0.5 eV cannot be seen any more. This can be associated to the removal of an electron from the leading orbital of MnPc as discussed above. The excitation spectrum of MnPc/F_4TCNQ consists of rather sharp

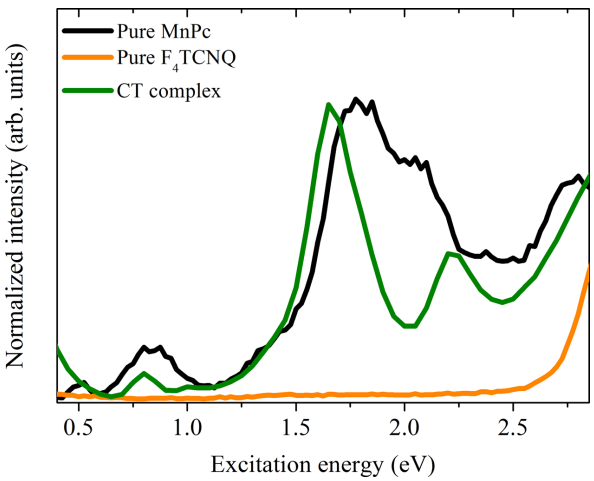

Figure 8: Comparison of the electronic excitation spectra of MnPc, F_4TCNQ and the charge-transfer compound MnPc/F_4TCNQ (adapted from [104]).

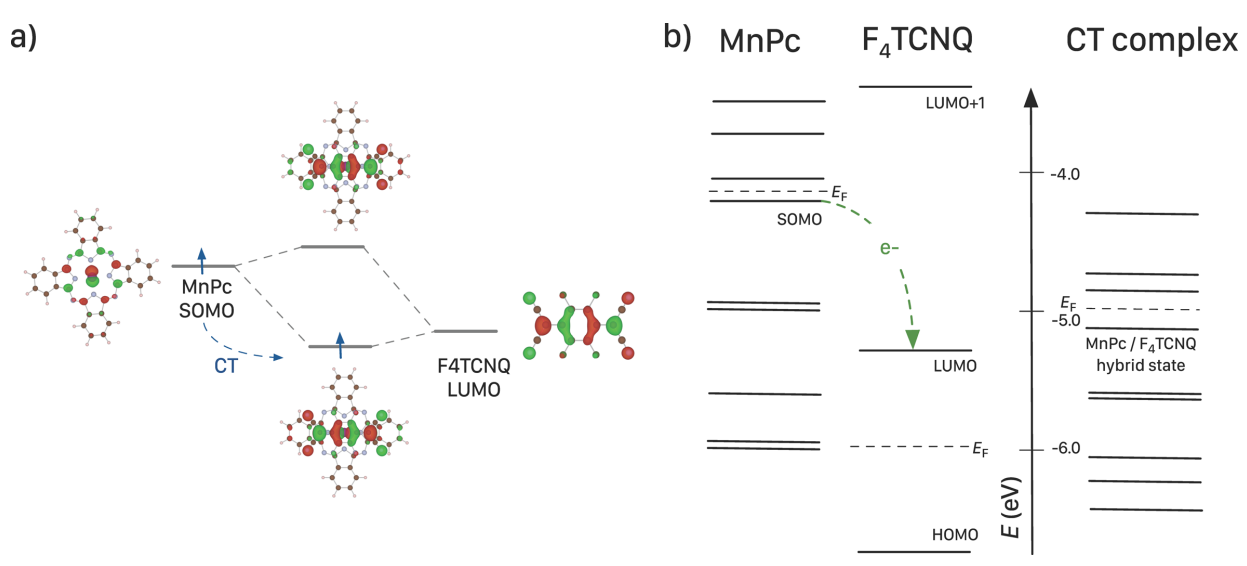

Figure 7: Results of the DFT calculations for the MnPc/F_4TCNQ dimer model systems: a) The SOMO of MnPc and the LUMO of F_4TCNQ hybridize and charge is transferred into the newly formed bonding hybrid state. b) Comparison of the eigenvalues of the Kohn–Sham orbitals as obtained from the calculations for a single MnPc molecule, a single F_4TCNQ molecule and the dimer model compound (for more information see [104]).

excitation maxima at around 0.8 eV, 1.65 eV and 2.2 eV. A detailed quantitative description of these excitations has not been achieved yet [104]. In general, our data show that the MnPc/F_4TCNQ compound has an energy gap of about 0.6 eV represented by the spectral onset in the excitation data. In particular, the lowest energy (gap) excitation is ascribed to the excitation within the two-level system, which originates from the charge-transfer reaction and the related hybrid-state formation as discussed above.

Thus, the oxidation of MnPc molecules upon the formation of the new charge transfer salt MnPc/F_4TCNQ is clearly seen in our spectroscopic data and supporting calculations. Together with the results on potassium-doped MnPc as presented in the previous chapter, this nicely demonstrates the variability of MnPc in charge-transfer compounds, where it can be either reduced or oxidized. We conclude the discussion of the MnPc-based charge-transfer compounds with a comparison of the electronic excitation spectra of MnPc, oxidized $MnPc^+$ and reduced $MnPc^-$ as measured for the MnPc/F_4TCNQ and K_1MnPc compounds. We argue that for both compounds the low-energy excitations predominantly stem from MnPc-derived orbitals. In the case of K_1MnPc this is quite clear since potassium ions do not contribute in the relevant energy region. For MnPc/F_4TCNQ the situation is more complex. Based on a purely ionic picture, also excitations from the negatively charged F_4TCNQ should show up. In solution, an excitation for F_4TCNQ^- radicals at about 1.65 eV was reported [116]. Keeping this in mind, we present a comparison of our electronic excitation data obtained using EELS for MnPc, K_1MnPc ($MnPc^-$), and MnPc/F_4TCNQ ($MnPc^+$) in Figure 9. In addition, we also included the energies of optical absorption studies for oxidized and reduced MnPc in solution [117,118]. Taking into account a broadening upon transition from single molecules in solution to the solid state as well as energy shifts due to different polarization screening, there is very good agreement between our data and those in solution from the literature. This nicely corroborates the interpretation of our results in terms of MnPc salts and the related electronic properties.

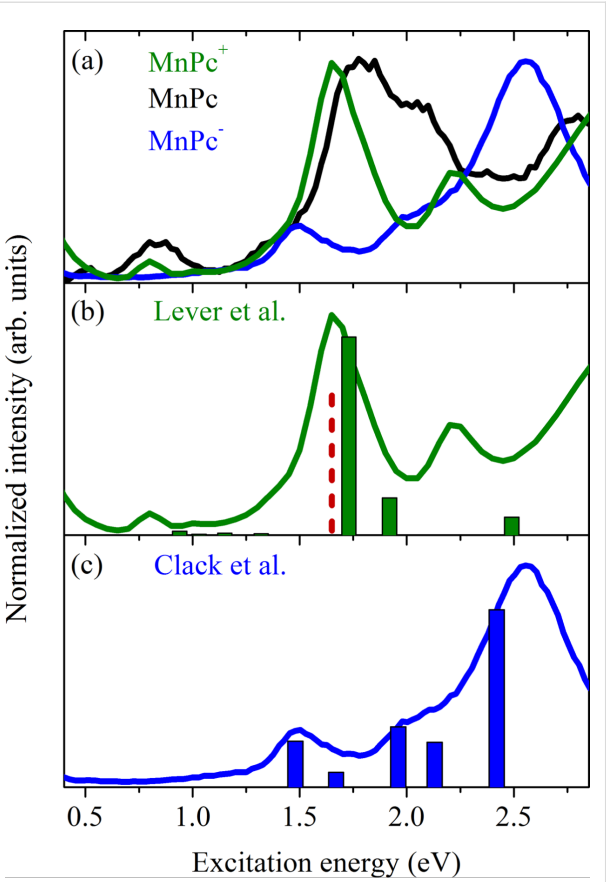

Figure 9: (a) Comparison of the electronic excitation spectra of MnPc, K_1MnPc and MnPc/F_4TCNQ as measured using EELS. In the lower two panels, we compare these data to the optical absorption energies (denoted by vertical bars) as observed for (b) $MnPc^+$ [117] and (c) $MnPc^-$ [118] in solution. In panel (b) we additionally show the optical absorption energy of F_4TCNQ^- radicals in solution (dashed line) [116].

MnPc/F_6TCNNQ: charge transfer at an interface

The organic heterojunction MnPc/F_6TCNNQ represents an example, where MnPc is involved in a charge transfer across an interface. In consideration of the results of the previous chapter, it is reasonable to expect charge transfer between MnPc and F_6TCNNQ, since F_6TCNNQ is an even stronger electron acceptor compared to F_4TCNQ. Moreover, it is larger and heavier, which prevents it from diffusion in or into organic films. Thus, it will form well-defined interfaces, i.e., also the charge-transfer reaction is confined to the interface region.

In general, charge transfer from insulators or semiconductors on one side of the interface to those on the other side can have dramatic effects and result in interfacial electronic properties that differ substantially from those of the individual materials [32,119-124]. For instance, particular interfaces between two initially semiconducting organic materials were shown to become even metallic [32,120].

First photoemission studies of the MnPc/F_6TCNNQ interface indeed suggest that there is substantial charge transfer, which might also lead to interesting physics at these interfaces. In Figure 10 we show the results of the measurements of the Mn $2p_{3/2}$ core-level emission during the formation of the MnPc/F_6TCNNQ interface. Here, F_6TCNNQ was deposited stepwise onto a 10 nm thick MnPc film. Due to the rather small electron escape depth (a few angstroms only [39]) the Mn $2p_{3/2}$ core-level data increasingly stem from regions very close to the interface with increasing F_6TCNNQ top layer thickness. The

data in Figure 10 demonstrate a clear change in line shape and energy position of the the Mn $2p_{3/2}$ core-level feature, which is analogous to the changes seen above for MnPc/F_4TCNQ. Thus, these data evidence that there is charge transfer at the MnPc/F_6TCNNQ interface and that the Mn central atom in MnPc again is oxidized.

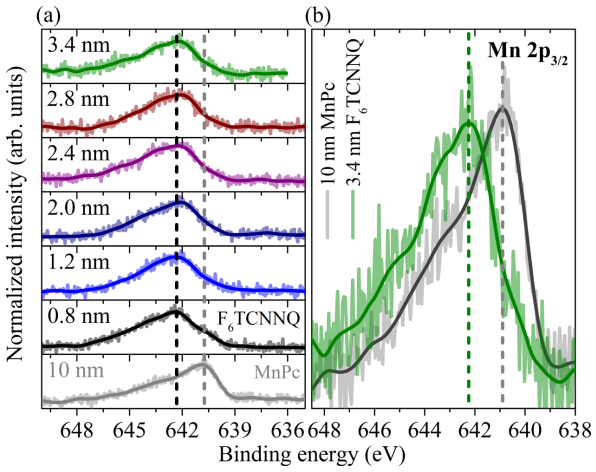

Figure 10: Core-level photoelectron spectroscopy data in the energy region of the Mn $2p_{3/2}$ core level for the MnPc/F_6TCNNQ interface. Panel (a) shows the data as a function of F_6TCNNQ thickness on top of MnPc (as indicated), while panel (b) compares the Mn $2p_{3/2}$ features for pure MnPc and with a 3.4 nm top layer of F_6TCNNQ. There is a clear energy shift of 1.5 eV to higher binding energy.

Furthermore, also the valence band data clearly indicate this charge transfer. Figure 11 illustrates the evolution of the high binding energy cutoff (a) and the energy region close to the Fermi energy (b). The data in panel (a) show the evolution of the work function of the layer system as a function of increasing F_6TCNNQ layer thickness. With the exception of the thinnest F_6TCNNQ layer on top of MnPc, the well-pronounced and sharp cutoff spectra affirm the formation of well-defined organic layers. In the case of 0.2 nm F_6TCNNQ, a step is visible in the region of the secondary cutoff, which most likely is due to a coverage of less than a monolayer F_6TCNNQ on MnPc, which results in surface/interface regions with and without the charge-transfer reaction. Figure 11b depicts the data close to the Fermi level for a selection of F_6TCNNQ overlayer thicknesses. Again, for pure MnPc the spectrum is characterized by a two peak feature as described above. The features at lowest binding energy (about 0.7 eV) vanishes when F_6TCNNQ is added, which signals the oxidation of MnPc in analogy to the previous section. The second feature, initially at about 1.4 eV, first broadens, then becomes somewhat sharper again and shifts to 1.2 eV. We attribute this feature to the emission from the now filled, formerly lowest unoccupied molecular orbital of F_6TCNNQ, which is occupied at the interface as a result of the charge transfer. Consequently, our data provide evidence for a considerable charge transfer at the MnPc/F_6TCNNQ interface, and further investigations are necessary to provide more insight into the physics as, e.g., whether there is electrical conduction along the interface.

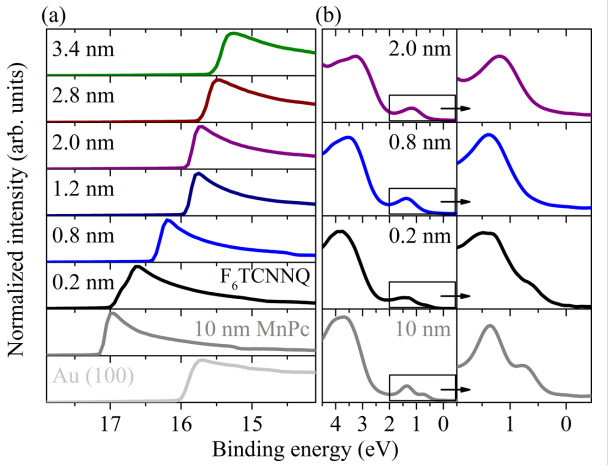

Figure 11: Valence-band photoemission data from the MnPc/F_6TCNNQ interface as a function of the F_6TCNNQ top-layer thickness. Panel (a) shows the evolution of the secondary electron cutoff, which represents the changes of the work function. Panel (b) focusses on the energy region close to the Fermi level.

A charge and spin transfer interface: MnPc/F_{16}CoPc

A further example in which a charge transfer across an interface results in new physical properties at this interface is provided by bringing together MnPc and F_{16}CoPc. Highly ordered interfaces of this kind were realized by depositing one of the two phthalocyanines on a gold(100) single crystal, which resulted in well-oriented thin films [125-127]. Subsequently, the partner phthalocyanine was deposited on top, which finally gave rise to well-ordered heterojunctions as revealed by polarization dependent X-ray absorption spectroscopy (XAS) studies [127].

In Figure 12 we present corresponding N 1s absorption spectra for pure MnPc and two different film thicknesses of an F_{16}CoPc overlayer, deposited on a gold single crystal. Different light polarizations with respect to the film surface normal were achieved by variation of the angle between the incident light and the surface normal (see angles in Figure 12). For phthalocyanines it is well known that $1s\rightarrow\sigma^*$ and $1s\rightarrow\pi^*$ excitations take place for a light polarization vector perpendicular and parallel to the molecular planes, respectively. Moreover, previous studies [128,129] have demonstrated that the relatively sharp N 1s excitation features around 398 eV are due to transitions from the N 1s core level into the unoccupied π^* orbitals

with N 2p orbital contributions, which are oriented perpendicular to the molecular plane. The higher energy structures above 405 eV are related to N 1s→σ* transitions.

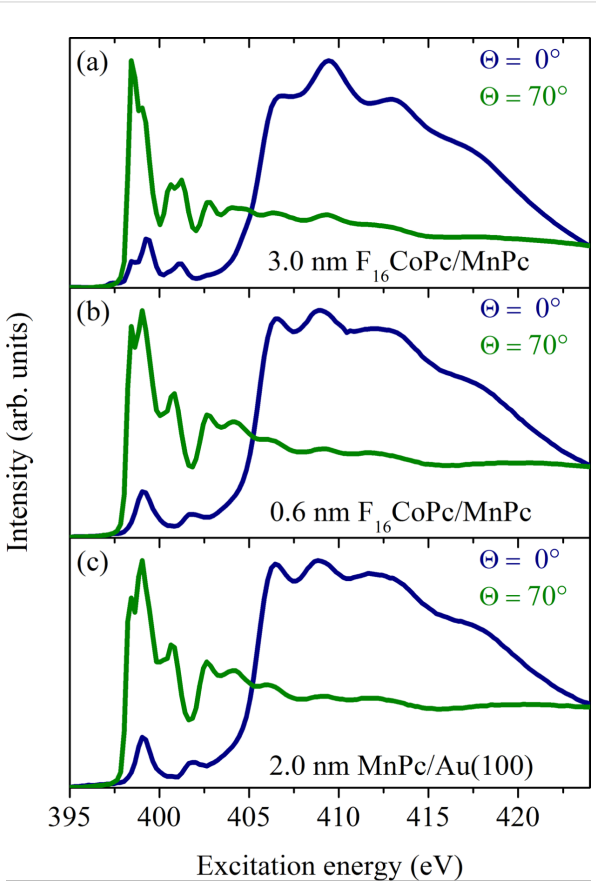

Figure 12: N 1s excitation spectra as obtained using X-ray absorption spectroscopy (adapted from [127]). Corresponding data for (c) a 2.0 nm thick MnPc film on Au(100), (b) an additional 0.6 nm thick F_{16}CoPc overlayer on MnPc, and (a) a relatively thick F_{16}CoPc overlayer (3 nm) are depicted. The spectra were recorded with two different angles of beam incidence. Θ denotes the angle between the surface normal and the direction of the incident beam. The incoming radiation is linearly polarized.

The data shown in Figure 12 reveal a very strong polarization dependence for the absorption edges of pure MnPc. The observed intensity variations show that the respective phthalocyanine molecules are arranged parallel to the substrate surface with a very high degree of orientation. The mean deviation from exactly parallel lying molecules is only about 5% [127]. This very high degree of order is also kept across the MnPc/F_{16}CoPc interface, as can be seen from Figure 12. In other words, the two phthalocyanines form an interface where they lie face to face. This high degree of order also allowed us to study the anisotropy of the excitations into Co-derived 3d levels in F_{16}CoPc close and far from the interface to MnPc. The corresponding data at the Co 2p absorption edges again show a very clear anisotropy when taken with different polarization directions of the incident synchrotron radiation, as depicted in Figure 13.

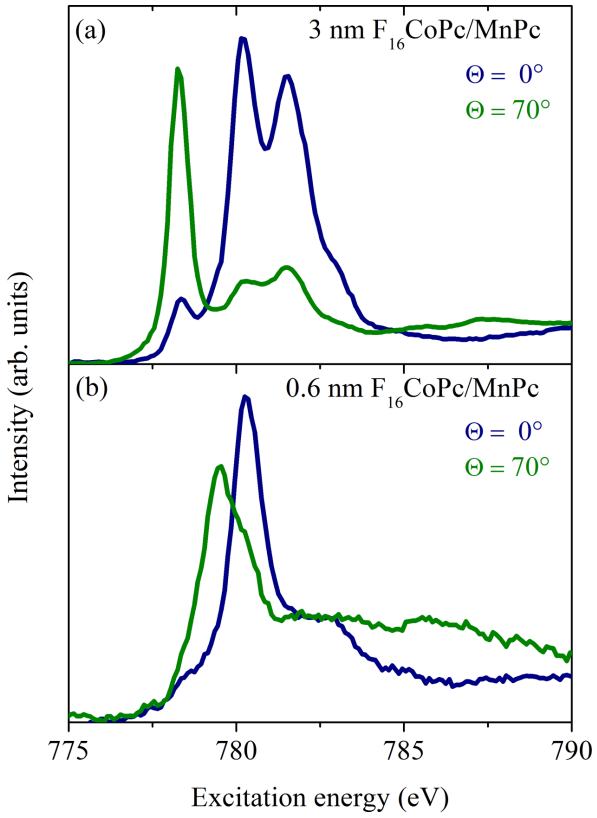

Figure 13: Polarization dependent X-ray absorption data at the Co L_3 edge for a (a) 3 nm and (b) 0.6 nm F_{16}CoPc overlayer on MnPc (adapted from [127]). Again, the incident beam direction is given by the angle Θ (see Figure 12 above).

The data for a 3 nm thick F_{16}CoPc film on top of MnPc are very similar to the corresponding absorption spectra of pure CoPc on gold [130]. This indicates that fluorination of CoPc has little impact on the electronic 3d states of the central Co atom. The lowest lying absorption feature, which is maximal for a light polarization perpendicular to the F_{16}CoPc molecules, can be assigned to transitions from the Co 2p into unoccupied $3d_{z^2}$ states. The higher lying features stem from a multiplet structure related to the excitations into the Co $3d_{x^2-y^2}$ orbital [130].

For thin F_{16}CoPc films deposited onto MnPc we observe considerably different spectra. Features that are characteristic for pure F_{16}CoPc disappear while new structures show up around 780 eV, which are still anisotropic. This provides clear evidence that there is a reaction between F_{16}CoPc and MnPc at the corresponding interface, which affects the cobalt states of F_{16}CoPc. This conclusion is supported by equivalent investiga-

tions of CoPc monolayers on gold and silver surfaces, where similar changes in the absorption spectra were observed and where a charge transfer between the cobalt 3d states and the underlying metallic substrate occurs [131,132]. Moreover, also the Mn $L_{2,3}$ absorption edge is subject to substantial changes for MnPc molecules in contact to F_{16}CoPc in comparison to pure MnPc [127]. This provides clear evidence that the charge transfer at the MnPc/F_{16}CoPc interface again results in charge removal from Mn 3d orbitals in MnPc.

A charge-transfer reaction at the MnPc/F_{16}CoPc interface is also seen in photoelectron spectroscopy studies [31]. Looking at the Co $2p_{3/2}$ core-level data of this interface, there is a significant change in line shape and binding energy as a function of the F_{16}CoPc layer thickness. These data are shown in Figure 14.

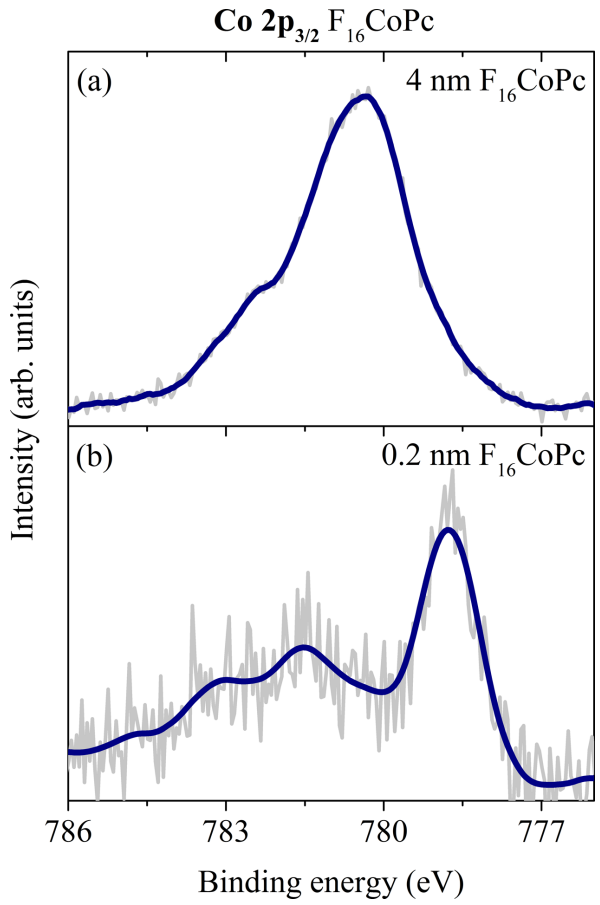

Figure 14: Co $2p_{3/2}$ core-level photoemission spectra of a (a) thick and (b) thin F_{16}CoPc layer on top of MnPc. The appearance of a structure of low binding energy for the thin F_{16}CoPc layer clearly indicates a reduction of the Co center in this molecule (adapted from [31]).

The data for the thin F_{16}CoPc layer are rather similar to what has been reported so far for cobalt porphyrines and phthalocyanines deposited on various metals. In these cases, a relatively strong interaction of the Co center of the molecules and the metal surface takes place [133-137]. The result of this interaction usually is rationalized in terms of a reduction of the metal center to Co(I). Consequently, there is clear evidence that at the MnPc/F_{16}CoPc interface the Co center of F_{16}CoPc is also reduced as a result of a charge transfer across this interface. Also, a corresponding shift of the Mn 2p core-level feature to a higher binding energy is observed [31] (cf. Figure 6). The charge transfer arises from the formation of hybrid states between the transition-metal centers of the two phthalocyanines, with a concomitant oxidation of Mn-derived states of MnPc, similar to the charge transfer as discussed in previous sections. This situation is nicely supported by model calculations of a MnPc/F_{16}CoPc dimer [31,138]. The calculations demonstrate that the states of the two phthalocyanines combine to form new bonding and anti-bonding states. The Mn $3d_{xz}$ and the Co $3d_{z2}$ states hybridize and form a two-level system as illustrated qualitatively in Figure 15.

The occupation of the lower of these hybrid states also is related to the observed charge transfer. Intriguingly, as a result of our calculations the MnPc/F_{16}CoPc dimer is characterized by a net spin of $S = 2$. Thus, the charge transfer is connected to a transfer/change of spin, which justifies to call the corresponding interface a spin-transfer interface with potential applications in the area of spintronics.

Finally, we note that also a bulk material consisting of MnPc/F_{16}CoPc dimers could be prepared via the co-evaporation of these two materials. Spectroscopic studies of the resulting films confirmed the formation of MnPc/F_{16}CoPc charge-transfer dimers in analogy to the related interface as discussed above [139]. The electronic excitation spectrum of these co-evaporated MnPc/F_{16}CoPc films is characterized by a new feature at low energies (about 0.6 eV). Our density functional theory based calculations of the excitation spectrum reveal that this low-energy signal is due to transitions between the states of the dimer related two level system (see Figure 15).

Conclusion

The compilation of our results on bulk compounds and interfaces based on manganese phthalocyanines and partners, where the phthalocyanine is either reduced or oxidized demonstrates the variability of MnPc in the formation of novel, potentially interesting systems. Moreover, apart from interesting electronic properties that are associated with the charge transfer in either case, the spin/magnetic state of MnPc must also be changed since Mn 3d orbitals participate in the charge transfer. Future studies will certainly unravel more details and intriguing features in these respects.

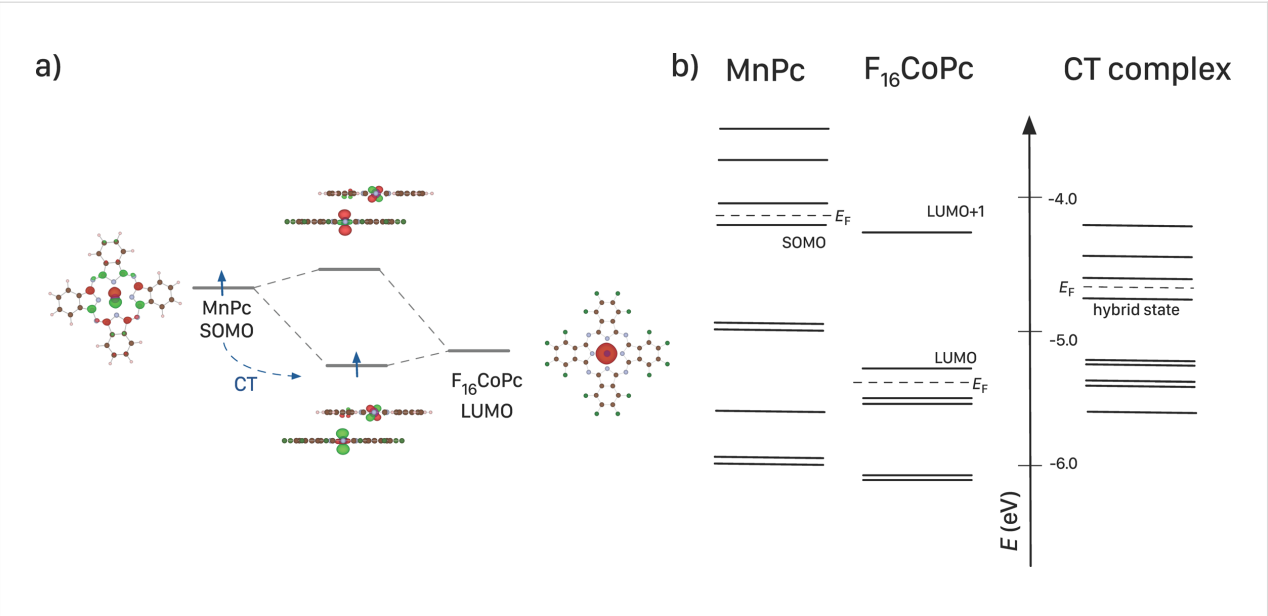

Figure 15: Results of the DFT calculations for the MnPc/F_{16}CoPc model systems: a) The hybrid state is formed by the Mn $3d_{xz}$ and the Co $3d_{z^2}$ states. b) Comparison of the eigenvalues of the Kohn–Sham orbitals as obtained from the calculations for a single MnPc molecule, a single F_{16}CoPc molecule and the dimer model (complex).

Acknowledgements

We are grateful to R. Hübel, S. Leger and M. Naumann for technical assistance. Financial support by the Deutsche Forschungsgemeinschaft within the Forschergruppe FOR 1154 (KN393/14, KO1924/5, ZA146/23), as well as in projects KN393/25, and HA5070/3 is gratefully acknowledged.

References

1. Gregory, P. *J. Porphyrins Phthalocyanines* **2000,** *4,* 432–437. doi:10.1002/(SICI)1099-1409(200006/07)4:4<432::AID-JPP254>3.0.CO;2-N
2. Singh, T. B.; Sariciftci, N. S. *Annu. Rev. Mater. Res.* **2006,** *36,* 199–230. doi:10.1146/annurev.matsci.36.022805.094757
3. Rand, B. P.; Genoe, J.; Heremans, P.; Poortmans, J. *Prog. Photovoltaics* **2007,** *15,* 659–676. doi:10.1002/pip.788
4. Li, Y.; Chen, S.; Liu, Q.; Wang, L.; Someya, T.; Ma, J.; Wang, X.; Hu, Z. *J. Phys. Chem. C* **2012,** *116,* 4287–4292. doi:10.1021/jp210547j
5. Lin, Y.; Li, Y.; Zhan, X. *Chem. Soc. Rev.* **2012,** *41,* 4245–4272. doi:10.1039/c2cs15313k
6. Baeg, K.-J.; Binda, M.; Natali, D.; Caironi, M.; Noh, Y.-Y. *Adv. Mater.* **2013,** *25,* 4267–4295. doi:10.1002/adma.201204979
7. Melville, O. A.; Lessard, B. H.; Bender, T. P. *ACS Appl. Mater. Interfaces* **2015,** *7,* 13105–13118. doi:10.1021/acsami.5b01718
8. Gsänger, M.; Bialas, D.; Huang, L.; Stolte, M.; Würthner, F. *Adv. Mater.* **2016,** *28,* 3615–3645. doi:10.1002/adma.201505440
9. van den Brink, J.; Morpurgo, A. F. *Nature* **2007,** *450,* 177–178. doi:10.1038/450177a
10. Lach, S.; Altenhof, A.; Tarafder, K.; Schmitt, F.; Ali, M. E.; Vogel, M.; Sauther, J.; Oppeneer, P. M.; Ziegler, C. *Adv. Funct. Mater.* **2012,** *22,* 989–997. doi:10.1002/adfm.201102297
11. Djeghloul, F.; Ibrahim, F.; Cantoni, M.; Bowen, M.; Joly, L.; Boukari, S.; Ohresser, P.; Bertran, F.; Le Fèvre, P.; Thakur, P.; Scheurer, F.; Miyamachi, T.; Mattana, R.; Seneor, P.; Jaafar, A.; Rinaldi, C.; Javaid, S.; Arabski, J.; Kappler, J. P.; Wulfhekel, W.; Brookes, N. B.; Bertacco, R.; Taleb-Ibrahimi, A.; Alouani, M.; Beaurepaire, E.; Weber, W. *Sci. Rep.* **2013,** *3,* 1272. doi:10.1038/srep01272
12. Barraud, C.; Bouzehouane, K.; Deranlot, C.; Kim, D. J.; Rakshit, R.; Shi, S.; Arabski, J.; Bowen, M.; Beaurepaire, E.; Boukari, S.; Petroff, F.; Seneor, P.; Mattana, R. *Dalton Trans.* **2016,** *45,* 16694–16699. doi:10.1039/C6DT02467J
13. Barraclough, C. G.; Martin, R. L.; Mitra, S.; Sherwood, R. C. *J. Chem. Phys.* **1970,** *53,* 1638–1642. doi:10.1063/1.1674236
14. Mitra, S.; Gregson, A.; Hatfield, W. E.; Weller, R. R. *Inorg. Chem.* **1983,** *22,* 1729–1732. doi:10.1021/ic00154a007
15. Heutz, S.; Mitra, C.; Wu, W.; Fisher, A.; Kerridge, A.; Stoneham, M.; Harker, A.; Gardener, J.; Tseng, H.-H.; Jones, T.; Renner, C.; Aeppli, G. *Adv. Mater.* **2007,** *19,* 3618–3622. doi:10.1002/adma.200701458
16. Taguchi, Y.; Miyake, T.; Margadonna, S.; Kato, K.; Prassides, K.; Iwasa, Y. *J. Am. Chem. Soc.* **2006,** *128,* 3313–3323. doi:10.1021/ja0582657
17. Mazur, U.; Hipps, K. *J. Phys. Chem. B* **1999,** *103,* 9721–9727. doi:10.1021/jp9923419
18. Haidu, F.; Fechner, A.; Salvan, G.; Gordan, O. D.; Fronk, M.; Lehmann, D.; Mahns, B.; Knupfer, M.; Zahn, D. R. T. *AIP Adv.* **2013,** *3,* 062124. doi:10.1063/1.4812230
19. Zahn, D. R. T.; Gavrila, G. N.; Gorgoi, M. *Chem. Phys.* **2006,** *325,* 99–112. doi:10.1016/j.chemphys.2006.02.003
20. Hill, I. G.; Kahn, A.; Soos, Z. G.; Pascal, R. A., Jr. *Chem. Phys. Lett.* **2000,** *327,* 181–188. doi:10.1016/S0009-2614(00)00882-4
21. Brumboiu, I. E.; Totani, R.; de Simone, M.; Coreno, M.; Grazioli, C.; Lozzi, L.; Herper, H. C.; Sanyal, B.; Eriksson, O.; Puglia, C.; Brena, B. *J. Phys. Chem. A* **2014,** *118,* 927–932. doi:10.1021/jp4100747

22. Grobosch, M.; Mahns, B.; Loose, C.; Friedrich, R.; Schmidt, C.; Kortus, J.; Knupfer, M. *Chem. Phys. Lett.* **2011,** *505,* 122–125. doi:10.1016/j.cplett.2011.02.039
23. Kraus, R.; Grobosch, M.; Knupfer, M. *Chem. Phys. Lett.* **2009,** *469,* 121–124. doi:10.1016/j.cplett.2008.12.090
24. Rangger, G. M.; Hofmann, O. T.; Romaner, L.; Heimel, G.; Bröker, B.; Blum, R.-P.; Johnson, R. L.; Koch, N.; Zojer, E. *Phys. Rev. B* **2009,** *79,* 165306. doi:10.1103/PhysRevB.79.165306
25. Toyota, N.; Müller, J.; Lang, M. *Low-dimensional molecular metals;* Springer Science & Business Media, 2007. doi:10.1007/978-3-540-49576-5
26. Ouahab, L.; Yagubskii, E. *Organic conductors, superconductors and magnets: from synthesis to molecular electronics;* Springer Science & Business Media, 2004. doi:10.1007/978-94-007-1027-6
27. Walzer, K.; Maennig, B.; Pfeiffer, M.; Leo, K. *Chem. Rev.* **2007,** *107,* 1233–1271. doi:10.1021/cr050156n
28. Aziz, E. F.; Vollmer, A.; Eisebitt, S.; Eberhardt, W.; Pingel, P.; Neher, D.; Koch, N. *Adv. Mater.* **2007,** *19,* 3257–3260. doi:10.1002/adma.200700926
29. Lüssem, B.; Riede, M.; Leo, K. *Phys. Status Solidi A* **2013,** *210,* 9–43. doi:10.1002/pssa.201228310
30. Lüssem, B.; Tietze, M. L.; Kleemann, H.; Hoßbach, C.; Bartha, J. W.; Zakhidov, A.; Leo, K. *Nat. Commun.* **2013,** *4,* 2775. doi:10.1038/ncomms3775
31. Lindner, S.; Knupfer, M.; Friedrich, R.; Hahn, T.; Kortus, J. *Phys. Rev. Lett.* **2012,** *109,* 027601. doi:10.1103/PhysRevLett.109.027601
32. Krupskaya, Y.; Rückerl, F.; Knupfer, M.; Morpurgo, A. F. *Adv. Mater. Interfaces* **2016,** *3,* 1500863. doi:10.1002/admi.201500863
33. Rückerl, F.; Waas, D.; Büchner, B.; Knupfer, M. *J. Electron Spectrosc. Relat. Phenom.* **2017,** *215,* 1–7. doi:10.1016/j.elspec.2016.11.013
34. Toader, M.; Gopakumar, T. G.; Shukrynau, P.; Hietschold, M. *J. Phys. Chem. C* **2010,** *114,* 21548–21554. doi:10.1021/jp1078295
35. Pinto, H.; Jones, R.; Goss, J. P.; Briddon, P. R. *J. Phys.: Condens. Matter* **2009,** *21,* 402001. doi:10.1088/0953-8984/21/40/402001
36. Méndez, H.; Heimel, G.; Winkler, S.; Frisch, J.; Opitz, A.; Sauer, K.; Wegner, B.; Oehzelt, M.; Röthel, C.; Duhm, S.; Többens, D.; Koch, N.; Salzmann, I. *Nat. Commun.* **2015,** *6,* 8560. doi:10.1038/ncomms9560
37. Cardona, M.; Ley, L. *Photoemission in Solids I: General Principles;* Springer, 1978. doi:10.1007/3-540-08685-4
38. Ley, L.; Cardona, M. *Photoemission in Solids II: Case Studies;* Springer, 1979. doi:10.1007/3-540-09202-1
39. Hüfner, S. *Photoelectron spectroscopy: principles and applications;* Springer Science & Business Media, 2013.
40. Smith, N. V. *Rep. Prog. Phys.* **1988,** *51,* 1227. doi:10.1088/0034-4885/51/9/003
41. Himpsel, F.; Fauster, T. *J. Vac. Sci. Technol., A* **1984,** *2,* 815–821. doi:10.1116/1.572514
42. Fuggle, J. C.; Inglesfield, J. E. Introduction. *Unoccupied Electronic States;* Springer, 1992; pp 1–23. doi:10.1007/3540541624_11
43. Fink, J. *Adv. Electron. Electron Phys.* **1989,** *75,* 121–232. doi:10.1016/S0065-2539(08)60947-6
44. Fink, J. Transmission electron energy-loss spectroscopy. *Unoccupied Electronic States;* Springer, 1992; pp 203–241. doi:10.1007/3540541624_17
45. Roth, F.; König, A.; Fink, J.; Büchner, B.; Knupfer, M. *J. Electron Spectrosc. Relat. Phenom.* **2014,** *195,* 85–95. doi:10.1016/j.elspec.2014.05.007
46. Knupfer, M.; Pichler, T.; Golden, M. S.; Fink, J.; Murgia, M.; Michel, R. H.; Zamboni, R.; Taliani, C. *Phys. Rev. Lett.* **1999,** *83,* 1443–1446. doi:10.1103/PhysRevLett.83.1443
47. Tompkins, H. G.; Irene, E. A. *Handbook of Ellipsometry;* William Andrew: New York, 2005. doi:10.1016/B978-081551499-2.50002-2
48. Fujiwara, H. *Spectroscopic Ellipsometry;* Wiley: Chechester, 2007. doi:10.1002/9780470060193
49. Haidu, F. Tailoring the Electronic and Optical Properties of Molecular Thin Films by Reducing and Oxidising Agents. Ph.D. Thesis, Technische Universität Chemnitz, Germany, 2014.
50. Stöhr, J. *NEXAFS Spectroscopy;* Springer, 1992. doi:10.1007/978-3-662-02853-7
51. Pederson, M. R.; Jackson, K. A. *Phys. Rev. B* **1990,** *41,* 7453–7461. doi:10.1103/PhysRevB.41.7453
52. Pederson, M. R.; Porezag, D. V.; Kortus, J.; Patton, D. C. *Phys. Status Solidi B* **2000,** *217,* 197–218. doi:10.1002/(SICI)1521-3951(200001)217:1<197::AID-PSSB197>3.0.CO;2-B
53. Porezag, D.; Pederson, M. R. *Phys. Rev. A* **1999,** *60,* 2840–2847. doi:10.1103/PhysRevA.60.2840
54. Perdew, J. P.; Burke, K.; Ernzerhof, M. *Phys. Rev. Lett.* **1996,** *77,* 3865–3868. doi:10.1103/PhysRevLett.77.3865
55. Grimme, S.; Antony, J.; Ehrlich, S.; Krieg, H. *J. Chem. Phys.* **2010,** *132,* 154104. doi:10.1063/1.3382344
56. Mahns, B.; Roth, F.; Grobosch, M.; Zahn, D. R. T.; Knupfer, M. *J. Chem. Phys.* **2011,** *134,* 194504. doi:10.1063/1.3591347
57. Eastwood, D.; Edwards, L.; Gouterman, M.; Steinfeld, J. *J. Mol. Spectrosc.* **1966,** *20,* 381–390. doi:10.1016/0022-2852(66)90009-9
58. Leznoff, C. C.; Lever, A. B. P., Eds. *Phthalocyanines: Properties and Applications;* VCH Publishers: New York, NY, USA, 1993.
59. Dini, D.; Hanack, M. *J. Porphyrins Phthalocyanines* **2004,** *8,* 915–933. doi:10.1142/S1088424604000301
60. Lucia, E. A.; Verderame, F. D. *J. Chem. Phys.* **1968,** *48,* 2674–2681. doi:10.1063/1.1669501
61. Hernandez, J. P.; Choi, S.-i. *J. Chem. Phys.* **1969,** *50,* 1524–1532. doi:10.1063/1.1671237
62. Hollebone, B. R.; Stillman, M. J. *Chem. Phys. Lett.* **1974,** *29,* 284–286. doi:10.1016/0009-2614(74)85032-3
63. Saito, T.; Sisk, W.; Kobayashi, T.; Suzuki, S.; Iwayanagi, T. *J. Phys. Chem.* **1993,** *97,* 8026–8031. doi:10.1021/j100132a036
64. Umeda, M.; Mohamedi, M.; Itoh, T.; Uchida, I. *J. Appl. Phys.* **2001,** *90,* 3984–3987. doi:10.1063/1.1403674
65. Auerhammer, J. M.; Knupfer, M.; Peisert, H.; Fink, J. *Surf. Sci.* **2002,** *506,* 333–338. doi:10.1016/S0039-6028(02)01517-0
66. Knupfer, M.; Schwieger, T.; Peisert, H.; Fink, J. *Phys. Rev. B* **2004,** *69,* 165210. doi:10.1103/PhysRevB.69.165210
67. Maslov, V. G. *Opt. Spectrosc.* **2006,** *101,* 853–861. doi:10.1134/S0030400X0612006X
68. Bondarev, I. V.; Popescu, A.; Younts, R. A.; Hoffman, B.; McAfee, T.; Dougherty, D. B.; Gundogdu, K.; Ade, H. W. *Appl. Phys. Lett.* **2016,** *109,* 213302. doi:10.1063/1.4968821
69. Fielding, P. E.; MacKay, A. G. *Aust. J. Chem.* **1975,** *28,* 1445–1454. doi:10.1071/CH9751445
70. Williamson, B. E.; VanCott, T. C.; Boyle, M. E.; Misener, G. C.; Stillman, M. J.; Schatz, P. N. *J. Am. Chem. Soc.* **1992,** *114,* 2412–2419. doi:10.1021/ja00033a016

71. Nyokong, T. *Struct. Bonding* **2010,** *135,* 45–87. doi:10.1007/978-3-642-04752-7_2
72. Stradi, D.; Díaz, C.; Martín, F.; Alcamí, M. *Theor. Chem. Acc.* **2011,** *128,* 497–503. doi:10.1007/s00214-010-0852-1
73. Friedrich, R.; Hahn, T.; Kortus, J.; Fronk, M.; Haidu, F.; Salvan, G.; Zahn, D. R. T.; Schlesinger, M.; Mehring, M.; Roth, F.; Mahns, B.; Knupfer, M. *J. Chem. Phys.* **2012,** *136,* 064704. doi:10.1063/1.3683253
74. Giovanelli, L.; Vilmercati, P.; Castellarin-Cudia, C.; Themlin, J.-M.; Porte, L.; Goldoni, A. *J. Chem. Phys.* **2007,** *126,* 044709. doi:10.1063/1.2432115
75. Flatz, K.; Grobosch, M.; Knupfer, M. *J. Chem. Phys.* **2007,** *126,* 214702. doi:10.1063/1.2741539
76. Roth, F.; König, A.; Kraus, R.; Knupfer, M. *J. Chem. Phys.* **2008,** *128,* 194711. doi:10.1063/1.2920179
77. de Groot, F. M. F.; Fuggle, J. C.; Thole, B. T.; Sawatzky, G. A. *Phys. Rev. B* **1990,** *41,* 928–937. doi:10.1103/PhysRevB.41.928
78. Molodtsova, O. V.; Knupfer, M.; Aristov, V. Yu.; Vyalikh, D. V.; Zhilin, V. M.; Ossipyan, Yu. A. *J. Appl. Phys.* **2008,** *103,* 053711. doi:10.1063/1.2874001
79. Aristov, V. Yu.; Molodtsova, O. V.; Maslyuk, V. V.; Vyalikh, D. V.; Bredow, T.; Mertig, I.; Preobrajenski, A. B.; Knupfer, M. *Org. Electron.* **2010,** *11,* 1461–1468. doi:10.1016/j.orgel.2010.04.028
80. Nilson, K.; Åhlund, J.; Shariati, M.-N.; Schiessling, J.; Palmgren, P.; Brena, B.; Göthelid, E.; Hennies, F.; Huismans, Y.; Evangelista, F.; Rudolf, P.; Göthelid, M.; Mårtensson, N.; Puglia, C. *J. Chem. Phys.* **2012,** *137,* 044708. doi:10.1063/1.4738755
81. Peisert, H.; Knupfer, M.; Fink, J. *Surf. Sci.* **2002,** *515,* 491–498. doi:10.1016/S0039-6028(02)01967-2
82. Grobosch, M.; Schmidt, C.; Kraus, R.; Knupfer, M. *Org. Electron.* **2010,** *11,* 1483–1488. doi:10.1016/j.orgel.2010.06.006
83. Aristov, V. Yu.; Molodtsova, O. V.; Knupfer, M. *Org. Electron.* **2011,** *12,* 372–375. doi:10.1016/j.orgel.2010.12.003
84. Marom, N.; Kronik, L. *Appl. Phys. A* **2009,** *95,* 165–172. doi:10.1007/s00339-008-5005-1
85. Giovannetti, G.; Brocks, G.; van den Brink, J. *Phys. Rev. B* **2008,** *77,* 035133. doi:10.1103/PhysRevB.77.035133
86. Wu, X.; Xu, C.; Wang, K.; Xiao, X. *J. Phys. Chem. C* **2016,** *120,* 15446–15452. doi:10.1021/acs.jpcc.6b03686
87. Phan, Q. T. N.; Heguri, S.; Tamura, H.; Nakano, T.; Nozue, Y.; Tanigaki, K. *Phys. Rev. B* **2016,** *93,* 075130. doi:10.1103/PhysRevB.93.075130
88. Ruff, A.; Sing, M.; Claessen, R.; Lee, H.; Tomić, M.; Jeschke, H. O.; Valentí, R. *Phys. Rev. Lett.* **2013,** *110,* 216403. doi:10.1103/PhysRevLett.110.216403
89. Caputo, M.; Di Santo, G.; Parisse, P.; Petaccia, L.; Floreano, L.; Verdini, A.; Panighel, M.; Struzzi, C.; Taleatu, B.; Lal, C.; Goldoni, A. *J. Phys. Chem. C* **2012,** *116,* 19902–19908. doi:10.1021/jp306640z
90. Mahns, B.; Roth, F.; Knupfer, M. *J. Chem. Phys.* **2012,** *136,* 134503. doi:10.1063/1.3699188
91. Knupfer, M.; Peisert, H.; Schwieger, T. *Phys. Rev. B* **2001,** *65,* 033204. doi:10.1103/PhysRevB.65.033204
92. Brühwiler, P. A.; Maxwell, A. J.; Nilsson, A.; Mårtensson, N.; Gunnarsson, O. *Phys. Rev. B* **1993,** *48,* 18296–18299. doi:10.1103/PhysRevB.48.18296
93. Knupfer, M.; Poirier, D. M.; Weaver, J. H. *Phys. Rev. B* **1994,** *49,* 2281–2284. doi:10.1103/PhysRevB.49.2281
94. Lof, R. W.; van Veenendaal, M. A.; Koopmans, B.; Jonkman, H. T.; Sawatzky, G. A. *Phys. Rev. Lett.* **1992,** *68,* 3924–3927. doi:10.1103/PhysRevLett.68.3924
95. Hotta, S.; Kobayashi, H. *Synth. Met.* **1994,** *66,* 117–122. doi:10.1016/0379-6779(94)90087-6
96. Sato, A.; Okada, M.; Saito, K.; Sorai, M. *Acta Crystallogr., Sect. C* **2001,** *57,* 564–565. doi:10.1107/S0108270100019454
97. Zhu, L.; Yi, Y.; Li, Y.; Kim, E.-G.; Coropceanu, V.; Brédas, J.-L. *J. Am. Chem. Soc.* **2012,** *134,* 2340–2347. doi:10.1021/ja210284s
98. Mahns, B.; Kataeva, O.; Islamov, D.; Hampel, S.; Steckel, F.; Hess, C.; Knupfer, M.; Büchner, B.; Himcinschi, C.; Hahn, T.; Renger, R.; Kortus, J. *Cryst. Growth Des.* **2014,** *14,* 1338–1346. doi:10.1021/cg401841n
99. Yoshida, Y.; Kumagai, Y.; Mizuno, M.; Isomura, K.; Nakamura, Y.; Kishida, H.; Saito, G. *Cryst. Growth Des.* **2015,** *15,* 5513–5518. doi:10.1021/acs.cgd.5b01138
100. Kataeva, O.; Khrizanforov, M.; Budnikova, Y.; Islamov, D.; Burganov, T.; Vandyukov, A.; Lyssenko, K.; Mahns, B.; Nohr, M.; Hampel, S.; Knupfer, M. *Cryst. Growth Des.* **2015,** *16,* 331–338. doi:10.1021/acs.cgd.5b01301
101. Chernenkaya, A.; Morherr, A.; Backes, S.; Popp, W.; Witt, S.; Kozina, X.; Nepijko, S. A.; Bolte, M.; Medjanik, K.; Öhrwall, G.; Krellner, C.; Baumgarten, M.; Elmers, H. J.; Schönhense, G.; Jeschke, H. O.; Valent, R. *J. Chem. Phys.* **2016,** *145,* 034702. doi:10.1063/1.4958659
102. Morherr, A.; Witt, S.; Chernenkaya, A.; Bäcker, J.-P.; Schönhense, G.; Bolte, M.; Krellner, C. *Phys. B (Amsterdam, Neth.)* **2016,** *496,* 98–105. doi:10.1016/j.physb.2016.05.023
103. Hu, P.; Du, K.; Wei, F.; Jiang, H.; Kloc, C. *Cryst. Growth Des.* **2016,** *16,* 3019–3027. doi:10.1021/acs.cgd.5b01675
104. Rückerl, F.; Mahns, B.; Dodbiba, E.; Nikolis, V.; Herzig, M.; Büchner, B.; Knupfer, M.; Hahn, T.; Kortus, J. *J. Chem. Phys.* **2016,** *145,* 114702. doi:10.1063/1.4962578
105. Poirier, D. M. *Appl. Phys. Lett.* **1994,** *64,* 1356–1358. doi:10.1063/1.111933
106. Knupfer, M.; Poirier, D. M.; Weaver, J. H. *Phys. Rev. B* **1994,** *49,* 8464–8474. doi:10.1103/PhysRevB.49.8464
107. Poirier, D. M.; Olson, C. G.; Weaver, J. H. *Phys. Rev. B* **1995,** *52,* R11662–R11664. doi:10.1103/PhysRevB.52.R11662
108. Poirier, D. M.; Ownes, D. W.; Weaver, J. H. *Phys. Rev. B* **1995,** *51,* 1830–1843. doi:10.1103/PhysRevB.51.1830
109. Andjelković, L.; Stepanović, S.; Vlahović, F.; Zlatar, M.; Gruden, M. *Phys. Chem. Chem. Phys.* **2016,** *18,* 29122–29130. doi:10.1039/C6CP03859J
110. Nesbitt, H. W.; Banerjee, D. *Am. Mineral.* **1998,** *83,* 305–315. doi:10.2138/am-1998-3-414
111. Kroll, T.; Kraus, R.; Schönfelder, R.; Aristov, V. Yu.; Molodtsova, O.; Hoffmann, P.; Knupfer, M. *J. Chem. Phys.* **2012,** *137,* 054306. doi:10.1063/1.4738754
112. Oku, M.; Hirokawa, K.; Ikeda, S. *J. Electron Spectrosc. Relat. Phenom.* **1975,** *7,* 465–473. doi:10.1016/0368-2048(75)85010-9
113. Mori-Sánchez, P.; Cohen, A. J.; Yang, W. *Phys. Rev. Lett.* **2008,** *100,* 146401. doi:10.1103/PhysRevLett.100.146401
114. Dixon, D. A.; Calabrese, J. C.; Miller, J. S. *J. Phys. Chem.* **1989,** *93,* 2284–2291. doi:10.1021/j100343a019
115. Müller, E.; Mahns, B.; Büchner, B.; Knupfer, M. *J. Chem. Phys.* **2015,** *142,* 184702. doi:10.1063/1.4919881
116. Le, T. H.; Lu, J.; Bond, A. M.; Martin, L. L. *Inorg. Chim. Acta* **2013,** *395,* 252–254. doi:10.1016/j.ica.2012.10.019
117. Lever, A. B. P.; Pickens, S. R.; Minor, P. C.; Licoccia, S.; Ramaswamy, B. S.; Magnell, K. *J. Am. Chem. Soc.* **1981,** *103,* 6800–6806. doi:10.1021/ja00413a003

118. Clack, D. W.; Yandle, J. R. *Inorg. Chem.* **1972,** *11,* 1738–1742. doi:10.1021/ic50114a003
119. Wang, J.; Wang, H.; Yan, X.; Huang, H.; Yan, D. *Appl. Phys. Lett.* **2005,** *87,* 093507. doi:10.1063/1.2037204
120. Alves, H.; Molinari, A. S.; Xie, H.; Morpurgo, A. F. *Nat. Mater.* **2008,** *7,* 574–580. doi:10.1038/nmat2205
121. Nakano, M.; Alves, H.; Molinari, A. S.; Ono, S.; Minder, N.; Morpurgo, A. F. *Appl. Phys. Lett.* **2010,** *96,* 232102. doi:10.1063/1.3449558
122. Lezama, I. G.; Nakano, M.; Minder, N. A.; Chen, Z.; Di Girolamo, F. V.; Facchetti, A.; Morpurgo, A. F. *Nat. Mater.* **2012,** *11,* 788–794. doi:10.1038/nmat3383
123. Alves, H.; Pinto, R. M.; Maçôas, E. S. *Nat. Commun.* **2013,** *4,* 1842. doi:10.1038/ncomms2890
124. Krupskaya, Y.; Lezama, I. G.; Morpurgo, A. F. *Adv. Funct. Mater.* **2016,** *26,* 2334–2340. doi:10.1002/adfm.201502082
125. Molodtsova, O. V.; Knupfer, M.; Ossipyan, Yu. A.; Aristov, V. Yu. *J. Appl. Phys.* **2008,** *104,* 083704. doi:10.1063/1.3000105
126. Petraki, F.; Peisert, H.; Hoffmann, P.; Uihlein, J.; Knupfer, M.; Chassé, T. *J. Phys. Chem. C* **2012,** *116,* 5121–5127. doi:10.1021/jp211445n
127. Lindner, S.; Mahns, B.; Treske, U.; Vilkov, O.; Haidu, F.; Fronk, M.; Zahn, D. R. T.; Knupfer, M. *J. Chem. Phys.* **2014,** *141,* 094706. doi:10.1063/1.4894757
128. Åhlund, J.; Nilson, K.; Schiessling, J.; Kjeldgaard, L.; Berner, S.; Mårtensson, N.; Puglia, C.; Brena, B.; Nyberg, M.; Luo, Y. *J. Chem. Phys.* **2006,** *125,* 034709. doi:10.1063/1.2212404
129. Shariati, M.-N.; Lüder, J.; Bidermane, I.; Ahmadi, S.; Göthelid, E.; Palmgren, P.; Sanyal, B.; Eriksson, O.; Piancastelli, M. N.; Brena, B.; Puglia, C. *J. Phys. Chem. C* **2013,** *117,* 7018–7025. doi:10.1021/jp307626n
130. Kroll, T.; Aristov, V. Yu.; Molodtsova, O. V.; Ossipyan, Yu. A.; Vyalikh, D. V.; Büchner, B.; Knupfer, M. *J. Phys. Chem. A* **2009,** *113,* 8917–8922. doi:10.1021/jp903001v
131. Petraki, F.; Peisert, H.; Biswas, I.; Aygül, U.; Latteyer, F.; Vollmer, A.; Chassé, T. *J. Phys. Chem. Lett.* **2010,** *1,* 3380–3384. doi:10.1021/jz101395s
132. Petraki, F.; Peisert, H.; Latteyer, F.; Aygül, U.; Vollmer, A.; Chassé, T. *J. Phys. Chem. C* **2011,** *115,* 21334–21340. doi:10.1021/jp207568q
133. Bai, Y.; Buchner, F.; Kellner, I.; Schmid, M.; Vollnhals, F.; Steinrück, H.-P.; Marbach, H.; Gottfried, J. M. *New J. Phys.* **2009,** *11,* 125004. doi:10.1088/1367-2630/11/12/125004
134. Petraki, F.; Peisert, H.; Biswas, I.; Chassé, T. *J. Phys. Chem. C* **2010,** *114,* 17638–17643. doi:10.1021/jp104141s
135. Lindner, S.; Treske, U.; Grobosch, M.; Knupfer, M. *Appl. Phys. A* **2011,** *105,* 921–925. doi:10.1007/s00339-011-6648-x
136. Lindner, S.; Treske, U.; Knupfer, M. *Appl. Surf. Sci.* **2013,** *267,* 62–65. doi:10.1016/j.apsusc.2012.06.104
137. Gottfried, J. M. *Surf. Sci. Rep.* **2015,** *70,* 259–379. doi:10.1016/j.surfrep.2015.04.001
138. Friedrich, R.; Lindner, S.; Hahn, T.; Loose, C.; Liebing, S.; Knupfer, M.; Kortus, J. *Phys. Rev. B* **2013,** *87,* 115423. doi:10.1103/PhysRevB.87.115423
139. Lindner, S.; Mahns, B.; König, A.; Roth, F.; Knupfer, M.; Friedrich, R.; Hahn, T.; Kortus, J. *J. Chem. Phys.* **2013,** *138,* 024707. doi:10.1063/1.4774060

License and Terms

BEILSTEIN JOURNAL OF NANOTECHNOLOGY

(Metallo)porphyrins for potential materials science applications

Lars Smykalla[1], Carola Mende[2], Michael Fronk[3], Pablo F. Siles[4,5], Michael Hietschold[1], Georgeta Salvan[3], Dietrich R. T. Zahn[3], Oliver G. Schmidt[4,5], Tobias Rüffer[*2] and Heinrich Lang[*2]

Review

Open Access

Address:
[1]Solid Surfaces Analysis Group, Institute of Physics, Faculty of Natural Sciences, TU Chemnitz, D-09107 Chemnitz, Germany, [2]Inorganic Chemistry, Institute of Chemistry, Faculty of Natural Sciences, TU Chemnitz, D-09107 Chemnitz, Germany, [3]Semiconductor Physics, Institute of Physics, Faculty of Natural Sciences, TU Chemnitz, D-09107 Chemnitz, Germany, [4]Material Systems for Nanoelectronics, TU Chemnitz, D-09107 Chemnitz, Germany and [5]Institute for Integrative Nanosciences, IFW Dresden, Helmholtzstrasse 20, 01069 Dresden, Germany

Email:
Tobias Rüffer* - tobias.rueffer@chemie.tu-chemnitz.de;
Heinrich Lang* - heinrich.lang@chemie.tu-chemnitz.de

* Corresponding author

Keywords:
atomic force microscopy; magneto-optical Kerr effect spectroscopy; scanning tunnelling microscopy and spectroscopy; self-assembly; surface-confined 2D polymerization; transport properties

Beilstein J. Nanotechnol. **2017,** *8,* 1786–1800.
doi:10.3762/bjnano.8.180

Received: 28 February 2017
Accepted: 16 July 2017
Published: 29 August 2017

This article is part of the Thematic Series "Towards molecular spintronics".

Associate Editor: J. J. Schneider

Abstract

The bottom-up approach to replace existing devices by molecular-based systems is a subject that attracts permanently increasing interest. Molecular-based devices offer not only to miniaturize the device further, but also to benefit from advanced functionalities of deposited molecules. Furthermore, the molecules itself can be tailored to allow via their self-assembly the potential fabrication of devices with an application potential, which is still unforeseeable at this time. Herein, we review efforts to use discrete (metallo)porphyrins for the formation of (sub)monolayers by surface-confined polymerization, of monolayers formed by supramolecular recognition and of thin films formed by sublimation techniques. Selected physical properties of these systems are reported as well. The application potential of those ensembles of (metallo)porphyrins in materials science is discussed.

Review

Introduction

Macrocyclic compounds occurring in nature play an essential role in biological and chemical processes, whereby porphyrins and their corresponding metal species rank among the most frequently occurring and important representatives [1-3]. In addition, there is a plethora of synthetic possibilities to functionalize (metallo)porphyrins in order to better match their physical

properties to requirements of the envisaged application [1-3]. Because of the general high chemical and thermal stability, thin films of (metallo)porphyrins can be obtained by using organic molecular beam deposition (OMBD) techniques, which enable a better potential to build molecular spintronic devices [4-9].

A crucial step and thus, a prerequisite for the reliable implementation of (metallo)porphyrin-based thin films in a device, is the understanding of the electrical response and local transport properties [10]. However, thorough investigations of the latter properties, also in dependence of the thin film morphology, are still missing. Since magneto-optical effects are used in various optoelectronic devices [11], the optical characterization of thin films of (metallo)porphyrins by means of spectroscopic magneto-optical Kerr effect (MOKE) measurements would be very interesting.

Moreover, as MOKE measurements allow one to address magnetic properties with both high sensitivity and high spatial resolution, magneto-optical techniques in the visible or X-ray photon energy range have been supposed to be important for the integration of single-molecule magnets into spintronic or quantum computing devices [12]. For the design of such devices the knowledge of the photon energy at which the MOKE is largest in magnitude is of crucial importance.

The number of reports on spectroscopic MOKE investigations are very limited, while magneto-optical studies of porphyrinoids [13] conducted by magnetic circular dichroism (MCD) are numerous and have been already comprehensively reviewed [14]. As the commonly applied MCD spectroscopy requires the compounds to be solubilized or deposited on transparent substrates, spectroscopic MOKE measurements are not limited by such prerequisites. To the best of our knowledge there are, besides our own contributions, no reports available on spectroscopic MOKE measurements of either multimetallic complexes [15] or porphyrinoids [16-19], although MOKE magnetometric investigations have been already reported for multimetallic complexes [20,21].

For potential applications it is necessary that thin films and/or (sub)monolayers of (metallo)porphyrins can be fabricated with a high degree of reproducibility. One possibility to achieve controlled ordering on surfaces (beyond lithography [22,23]) is to functionalize the (metallo)porphyrins with terminal groups that allow their self-assembly on surfaces. Self-assemblies, giving rise to well-defined long-range ordered lateral structures, are frequently reported [24-28]. For example, in case that (metallo)porphyrins were functionalized with terminal hydroxyl groups they self-assemble on surfaces through the formation of hydrogen bonds [29-33]. This promising approach has, however, the disadvantage that the 2D networks lack stability as their mutual interactions are noncovalent and thus weak in nature. It would be thus fascinating to create covalently bonded ensembles on surfaces, or, even more challenging, to induce a 2D surface polymerization. Despite the difficulties to control covalent bond formation on surface, a small number of such studies already exist [34-39], including the first example of a 2D surface polymerization of porphyrins [40-42]. In the latter case, the porphyrins were functionalized with halides, preferably –Br or –I, to enable surface-confined C,C cross-coupling reactions on metallic substrates based on, for example, the Ullman coupling reaction [40-42].

Here, we report on the multifaceted use of appropriate (metallo)porphyrins (Scheme 1) to form (dendritic) thin films, (sub)monolayers and nano-ribbons and describe subsequently performed physical studies of those ensembles. We like to emphasize that the molecular interface formed of mostly (metallo)phthalocyanines as the organic part and different inorganic materials has been the explored with respect to its application potential in a comprehensive recent review [43].

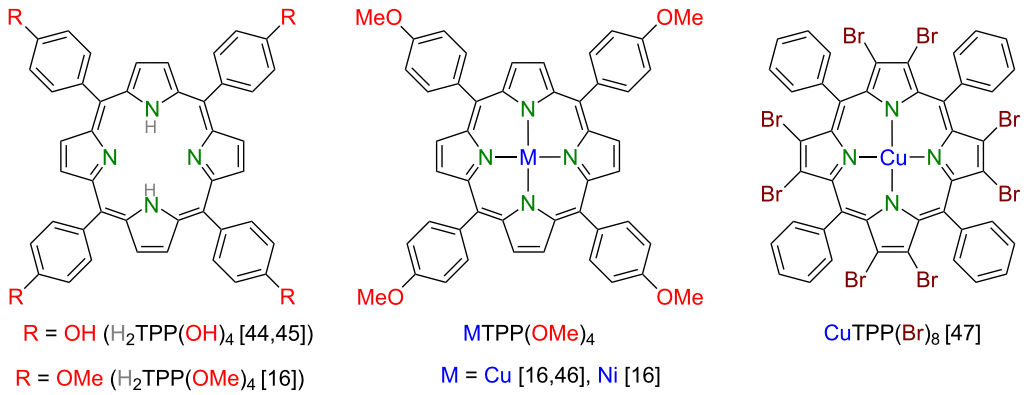

R = OH (H_2TPP(OH)$_4$ [44,45])

R = OMe (H_2TPP(OMe)$_4$ [16])

MTPP(OMe)$_4$

M = Cu [16,46], Ni [16]

CuTPP(Br)$_8$ [47]

Scheme 1: Chemical structures of (metallo)porphyrins under review here.

Results

Local electrical transport characteristics and morphology characteristics of nanostructured CuTPP(OMe)$_4$ on Ni substrates [46]**:** Tailored (metallo)porphyrins present a rich potential for device integration. From the point of view of synthesis, well-developed methodologies allow for the preparation of a variety of functionalized porphyrins. This is essential in order to produce, for example, macromolecules for particular applications by precisely tailoring adequate substituents [48,49]. Besides the high potential as building blocks for molecular spintronic devices [4,6,8,50], (metallo)porphyrins open new venues for the preparation of functional nano-architectures [51-56] that offer novel alternatives for device approaches such as sensors or organic field-effect transistors (OFETs) [57]. The compatibility of (metallo)porphyrin compounds with deposition techniques of organic molecules presents a great potential for the implementation and scaling down of porphyrins into current device fabrication processes, where thin films are required. Therefore, the understanding of the electrical transport properties of (metallo)porphyrin compounds (down to the nanoscale) is a crucial step for a reliable implementation in devices [10]. When performed at the nanoscale level, for example via spectroscopic techniques such as conductive atomic force microscopy, the easy correlation between morphology and electrical properties delivers valuable insights that contribute to elucidate possible microscopic mechanisms that determine the electrical performance of organic devices. Here, dominant transport mechanisms or local defect-driven conductive domains can be revealed.

For the latter reason we aimed to investigate the local transport characteristics of films of CuTPP(OMe)$_4$. Three thin films of CuTPP(OMe)$_4$ with thicknesses of 35, 82, and 117 nm (Figure 1) were deposited by OMBD (pressure 2×10^{-7} mbar, deposition rate 5 Å/min, temperature 325 °C) on a 30 nm thick nickel bottom electrode on top of a Si(100)/SiO_2 wafer (Figure 2). Here, Ni substrates were selected for the growth of CuTPP(OMe)$_4$ in order to investigate a system that may possess valuable possibilities for future device applications, in which the implementation of ferromagnetic substrates would enable interesting physical phenomena such as spintronic capabilities. On the other hand, the possibility of choosing different thicknesses of CuTPP(OMe)$_4$ allows for a quantitative investigation of the transport properties in order to identify dominant transport mechanism of the organic material. A shadow mask during deposition was employed to avoid additional photolithography processing. This shadow mask also allows for the formation of thin molecular dendrites and even single dendrites on the Ni surface (Figure 2). The growth conditions of the dendrites were investigated in detail, as indicated in Figure 1 and Figure 2. For example, height and length of the dendrites increase in dependence of the film thicknesses (Figure 1). We could show that by adequate optimization of parameters of the thin film formation the fabrication of filamentary nanostructures with predefined dimensions seems possible. Related structural aggregates were hitherto obtained through solution processing only [58]. The disadvantages of this wet-chemistry deposition technique are the possible contamination and/or substrate oxidation [11,15,59]. The dendrites could be particularly suitable to match certain device requirements. For example, after proper manipulation and lithography procedures single molecular nanowires or dendrites might be realized. This certainly opens possibilities for application in materials science, for example, the integration into molecular-based devices. In order to investigate this in more detail, we performed current-sensing atomic force microcopy (cs-AFM) studies of thin films of CuTPP(OMe)$_4$ deposited an Ni substrates.

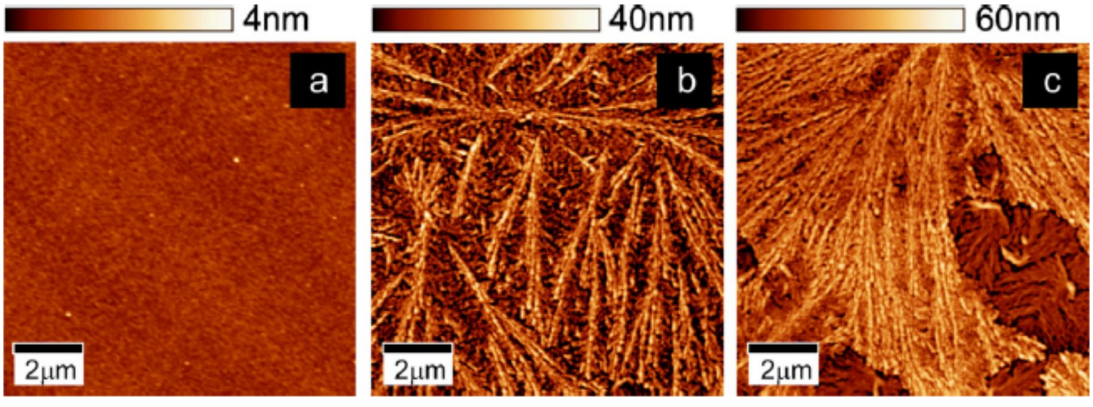

Figure 1: Surface topography determined by AFM as a function of thickness. Cu-TMPP (= CuTPP(OMe)$_4$) (a) 35 nm, (b) 82 nm, and (c) 117 nm thick. Organic films are deposited on a 30 nm thick Ni substrate. Once the organic aggregation is initialized, the sample surface of Cu-TMPP films evolves from an aleatory filamentary distribution (b) to a layered filamentary organization (c). Reproduced with permission from [46], copyright 2014 Elsevier.

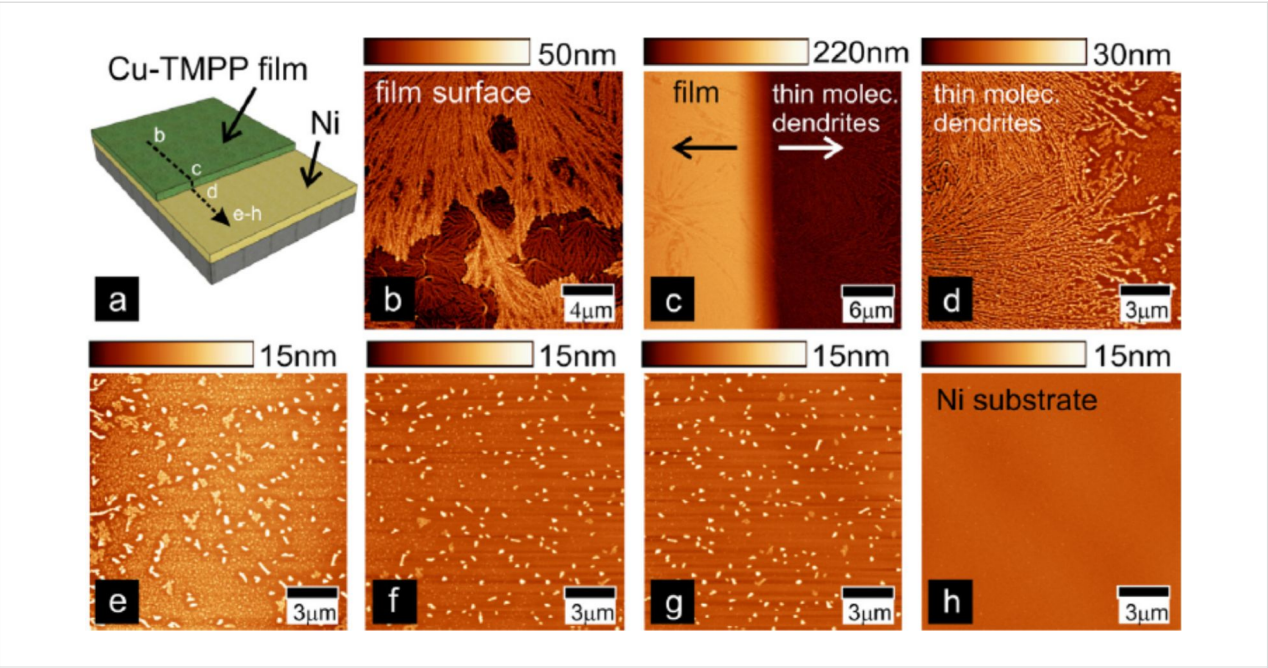

Figure 2: Formation of molecular dendrites in a 117 nm thick Cu-TMPP (= $CuTPP(OMe)_4$) sample at different regions along the surface. (a) Diagram of the sample structure. AFM topography characteristics: (b) on top of the organic film, (c) at the edge, and (d–h) at different areas moving away from the edge. As the molecular dendrites disappear, the bottom Ni substrate (0.4 nm rms) becomes visible (h). Reproduced with permission from [46], copyright 2014 Elsevier.

The electrical characteristics of the $CuTPP(OMe)_4$ thin film with 82 nm thickness determined via a cs-AFM study is shown in Figure 3. As the thin film topography and conductivity were acquired simultaneously the correlation of both features is straightforward. The electrical response of the different organic films appears to be reversible, which suggests that the structural integrity of the molecules is preserved after the electrical measurements [46]. Despite of this, due to the molecular aggregation and dendrite-layered organization of the films, which may induce interface defects, a local inhomogeneity of the electrical transport was detected. The distribution of conducting sites on the organic surface and a transport regime were identified. The transport exhibited a transition from an ohmic (linear) to an exponential conductive regime. The utilization of different thicknesses of $CuTPP(OMe)_4$ provided a proper calibration between the amount of material that is evaporated and the actual dimensions of the organic filaments. This offers valuable information in order to obtain single organic filaments that could eventually play a role as organic nanowires (Figure 2d). cs-AFM studies showed to be suitable to obtain quantitative measures of local transport properties in relation to topographical features and this approach could be applied to other kind of molecular systems, e.g., (metallo)porphyrins with different metal centers. This leads to the control and tuning of the electrical properties, where the interaction and coupling of the metal centers, the molecule and the substrate would play an important role on the transport properties of (metallo)porphyrin-based devices. We concluded that such studies would allow one to find suitable (metallo)porphyrins to explore interesting fields such as spintronic applications by coupling for example ferromagnetic substrates with suitable porphyrin structures. Consequently, we started to synthesize two new series of (metallo)porphyrins for related studies in which the metal centers and the terminal groups were varied [60]. Unfortunately, all of these (metallo)porphyrins were not suited for OMDB as they all thermally decomposed before sublimation (see below).

Optical and magneto-optical characterization of thin films of $H_2TPP(OMe)_4$, $NiTPP(OMe)_4$ and $CuTPP(OMe)_4$ [16]**:** Thin films of the porphyrins under review were deposited by OMBD (pressure ca. 1×10^{-4} Pa, deposition rates of 5–10 Å/min). For the deposition of $NiTPP(OMe)_4$ and $CuTPP(OMe)_4$ sublimation temperatures of 300–310 °C were required, whereas $H_2TPP(OMe)_4$ already sublimated with a stable deposition rate at 295 °C [16]. This might be attributable to the lower molecular weight of $H_2TPP(OMe)_4$ or, more likely, to a different kind of intermolecular interactions. It is this specific finding which prompted us to replace the terminal $-N(iPr)_2$ by $-NMe_2$ groups as described in [60]. However, the lower molecular weight and the potentially different intermolecular interactions did not enable the deposition of the $-NMe_2$-terminated (metallo)porphyrins. As substrates Si(111) wafers covered with a native oxide layer (2 nm) and silicon pieces covered with 100 nm thick Au layers were applied.

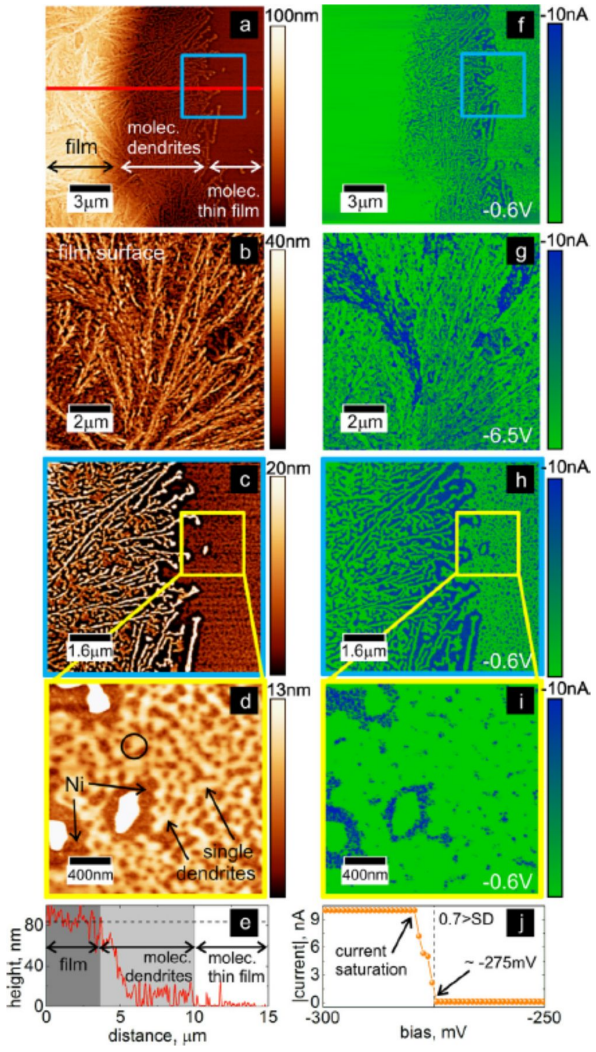

Figure 3: Transport in Cu-TMPP (= CuTPP(OMe)$_4$) films and dendrites, (a–d) AFM topography characteristics. The darker areas correspond to the Ni substrate below the molecular dendrite structures (brighter features), (f–i) cs-AFM current maps for the same areas indicated in a–d, (e) height–distance profile as indicated by the solid red line in (a), showing the organic film, thin molecular dendrites film, and single dendrites regions. The dotted line indicates the average height of the organic film, (j) local *I*–*V* characteristics for a single dendrite (3–4 nm height) as indicated with a black circle in (d), the *I*–*V* data represent an average of five consecutive cycles. The highest standard deviation (SD) for data points corresponds to 0.7. (For interpretation of the references to color in this figure caption, the reader is referred to the web version of this article.) Reproduced with permission from [46], copyright 2014 Elsevier.

mined from VASE in the spectral range of the first absorption band (see Figure 4 for the in plane-and out-of-plane extinction coefficient) allowed for the determination if the molecular tilt angle α, that is, the angle of the deposition molecules with respect to the substrate.

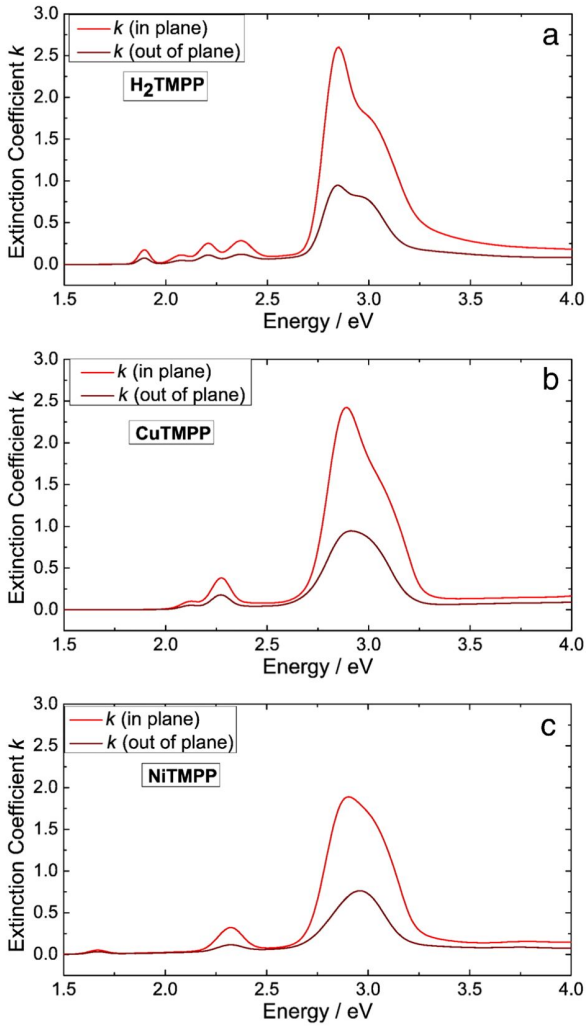

Figure 4: Extinction coefficient *k* for a) H_2TMPP, b) CuTMPP and c) NiTMPP. The uniaxial anisotropic model results in different intensities in- and out-of-plane. Reproduced with permission from [16], copyright 2014 Elsevier. Notice: H_2TMPP, CuTMPP and NiTMPP refer to H_2TPP(OMe)$_4$, NiTPP(OMe)$_4$ and CuTPP(OMe)$_4$, respectively, as displayed in Scheme 1.

Variable angle spectroscopic ellipsometry (VASE) was used to determine the absorption spectra of the as-obtained thin films. The extinction coefficients of the thin films display the typical features expected for (metallo)porphyrins, including expected differences in the number of absorption bands due to symmetry considerations regarding free-base H_2TPP(OMe)$_4$ compared to metalated NiTPP(OMe)$_4$ and CuTPP(OMe)$_4$ [16,17]. Additionally, the optical anisotropy of the extinction coefficient determined from VASE in the spectral range of the first absorption band (see Figure 4 for the in plane-and out-of-plane extinction coefficient) allowed for the determination if the molecular tilt angle α, that is, the angle of the deposition molecules with respect to the substrate.

As the interaction of the (metallo)porphyrins with metallic surfaces is stronger than that with semiconductor surfaces, the angle α of all three different types of compounds was expected to be smaller on Au compared to Si substrates. However, the opposite observation was made. For each investigated compound the angle α on Si is ca. 3° smaller than that on Au substrates. This is attributed to roughness effects. VASE measurements are thus excellently suited to determine the orientation of

(metallo)porphyrins in thin films with respect to the substrate surface. Furthermore, the substrate smoothness was shown to have an impact on the orientation of the (metallo)porphyrins with respect to the substrate surface. Different values of α might be one influencing factor determining the performances of porphyrin-based devices. The molecule–substrate interaction dictates the orientation of the first molecular layer. The orientation of this first layer strongly influences the orientation of the next layers. The templating effect of the first layer can extend up to tens of nanometers in phthalocyanine layers [61].

In subsequent aging studies and in combination with near edge X-ray absorption fine structure (NEXAFS) spectroscopy we could show that the values of α apparently increase by 4–7° on both substrates over a period of nine months. A long-term study showed that also the optical spectra of $H_2TPP(OMe)_4$ change after ageing in air. Not only the ratio of in-plane to out-of-plane extinction coefficient changes with time, but also the roughness of the samples stored in air increases more rapidly leading to an increase of the nominal film thickness (both determined from the ellipsometry data). This could be explained considering that oxygen or moisture from the atmosphere diffuses into the $H_2TPP(OMe)_4$ film progressively, with a slight saturation tendency after 20 days. Increasing roughness might also be a sign of crystallization induced by oxygen or moisture [62]. The origin of these changes might be attributed to (re)crystallization processes. Nevertheless, this study confirmed that long-stime stability studies of any devices based on (metallo)porphyrins are required.

MOKE spectra were successfully acquired both on the diamagnetic ($H_2TPP(OMe)_4$) and paramagnetic ($NiTPP(OMe)_4$ and $CuTPP(OMe)_4$) molecular films on silicon substrates. Based on numerical calculations using an optical model described in [18], which was developed by us and applied successfully for porphyrinoid-based thin films [17,18], it was possible to determine the energetic dispersion of the magneto-optical Voigt constant, which is independent of the film thickness (Figure 5).

Despite its energy dispersion, the complex magneto-optical constant Q is commonly described in literature as the Voigt constant because its material specificity. If known, the Voigt constant can be used to predict the magneto-optical response of a sample both in reflection (MOKE geometry) and transmission (Faraday geometry) measurements. The ellipticity of the transmitted light is labelled as magnetic circular dichroism (MCD). For solutions or transparent samples MCD spectroscopy is often carried out in combination with UV–vis spectroscopy to characterize the electronic properties of molecules, including porphyrinoids. For a better comparison with the existing literature about the magneto-optical response of porphyrinoids we

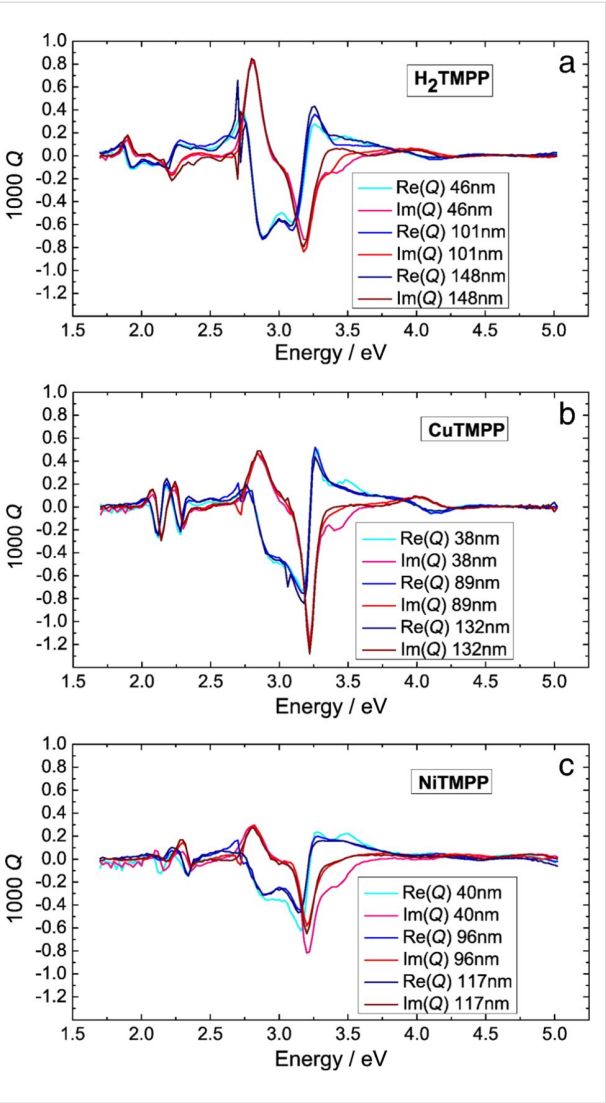

Figure 5: Energy dispersion of the magneto-optical Voigt constant Q for a) H_2TMPP, b) CuTMPP and c) NiTMPP. For reasons of clarity, Q was multiplied by 10^3 and normalized to a magnetic field of 1 T. Reproduced with permission from [16], copyright 2014 Elsevier. Notice: H_2TMPP, CuTMPP and NiTMPP refer to $H_2TPP(OMe)_4$, $NiTPP(OMe)_4$ and $CuTPP(OMe)_4$, respectively, as displayed in Scheme 1.

calculated from the Voigt constant the MCD spectra of the investigated molecules. The predicted spectra are shown in Figure 6 (continuous lines) along with the corresponding fitted curves (line plus symbol).

The fine structure of the MCD spectra can be used to extract information about the degeneracy of electronic states, in addition to what is easily readable in the UV–vis spectra [14]. The reason for the fine structure of the MCD spectra and hence for the higher sensitivity to the electronic properties lies in the Zeeman splitting of degenerate electronic levels induced by an external magnetic field. In addition to the energetic position of the spectral features, their line shape observed in the MCD

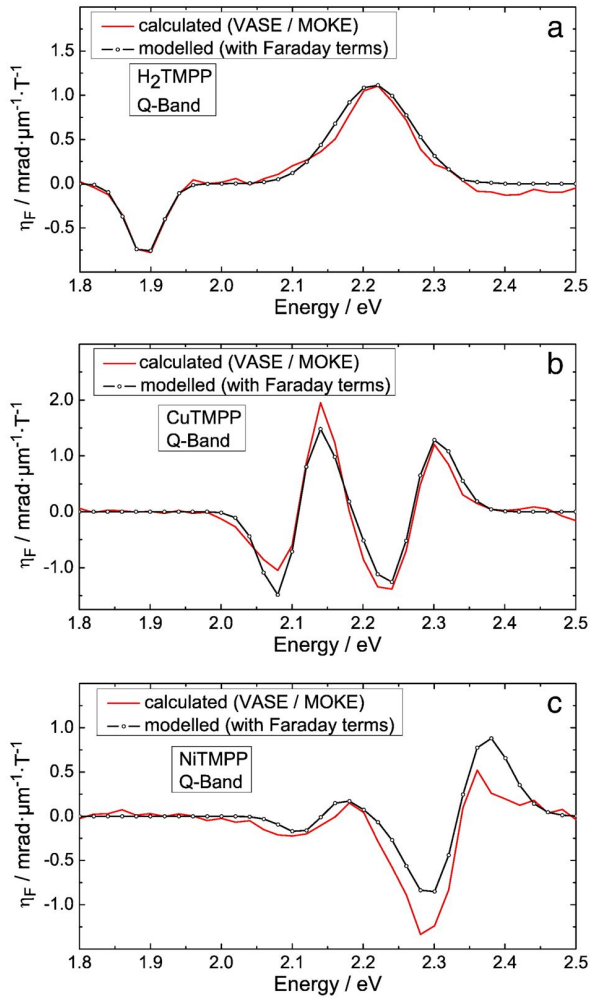

Figure 6: MCD (η_F) spectra in the Q-band region for a) H_2TMPP, b) CuTMPP and c) NiTMPP and the modelling with Faraday terms. Reproduced with permission from [16], copyright 2014 Elsevier. Notice: Here mentioned H_2TMPP, CuTMPP and NiTMPP refer to H_2TPP(OMe)$_4$, NiTPP(OMe)$_4$ and CuTPP(OMe)$_4$, repectively, as displayed in Scheme 1.

spectra is important for the interpretation of the spectra. The typical line shapes observed in various MCD spectra can be classified as the Faraday A-, B- and C-terms [14].

In the following, we will focus our discussion on the spectral range of the Q band. In the case of H_2TPP(OMe)$_4$ the MCD spectrum in Figure 6a shows only one B-term pair. The energies of the two features of opposite sign correspond to the first and third absorption peak of the UV–vis absorption spectrum. According to [14] the observation of a B-term pair is an indication that no degenerate energy states are involved in optical transitions probed. In this case, the fine structure of the band can rather be explained as a consequence of a coupling between vibrational and electronic states, i.e., vibronic coupling [63]. Compared to the MCD spectra of H_2PP (without methoxy groups), the line shape is similar but the amplitude of the bands is reduced, indicating that the methoxy groups thus do not suppress the vibronic coupling. For modelling the Q band of NiTPP(OMe)$_4$ and CuTPP(OMe)$_4$ in the MCD spectra, we employed two A-terms with energy positions corresponding to the observed features in the absorption spectra. This indicates that the LUMO of these molecules generating the Q band is a formerly degenerated state undergoing Zeeman splitting in the magnetic field.

With respect to the spectroscopic ellipsometry and magneto-optical Kerr effect spectroscopy characterization of thin films of (metallo)porphyrin derivatives on opaque substrates, a few key features should be emphasized: The combination of this methods provides access to the intrinsic optical and magneto-optical constants of the (metallo)porphyrins and thereby to the nature of the optically induced electronic transitions. Furthermore, VASE can give an insight into structure and morphology of the films in terms of film thickness, surface roughness, as well as average orientation of the (metallo)porphyrin molecules in the films.

Interplay of hydrogen bonding and molecule–substrate interaction in self-assembled adlayers of H_2TPP(OH)$_4$ on Au(111) and Ag(110) [44]**:** To optimize the transport properties of potential electronic or spintronic devices it is necessary that the thin molecular films show a reproducible and stable arrangement with a high degree of long-range order. One way to improve the self-assembly is to use hydrogen bonding between, e.g., peripheral hydroxyl groups of the porphyrin molecules instead of the previously discussed molecules with OMe groups [30-32]. However for monolayer thin films, the substrate also plays a deciding role in the self-assembly, which will be reviewed in this section.

Thin films of the free-base porphyrin H_2TPP(OH)$_4$ were deposited by OMBD (pressure approximately 1×10^{-8} mbar, temperature around 350 °C) on Au(111) and Ag(110). The thin films were characterized by scanning tunneling microscopy (STM) experiments with a variable-temperature STM device. For further measurement details see [44].

On Au(111), and directly after initial adsorption, the formation of self-assembled small islands composed of several molecules of H_2TPP(OH)$_4$ became visible (Figure 7a,b). At a coverage of around 0.8 of a monolayer the individual islands appear rotated to each other by 120°, induced by the C_3 surface symmetry of the Au(111) surface (Figure 7a,b). Upon annealing to around 150 °C highly ordered and large domains were observed, as shown in Figure 7c.

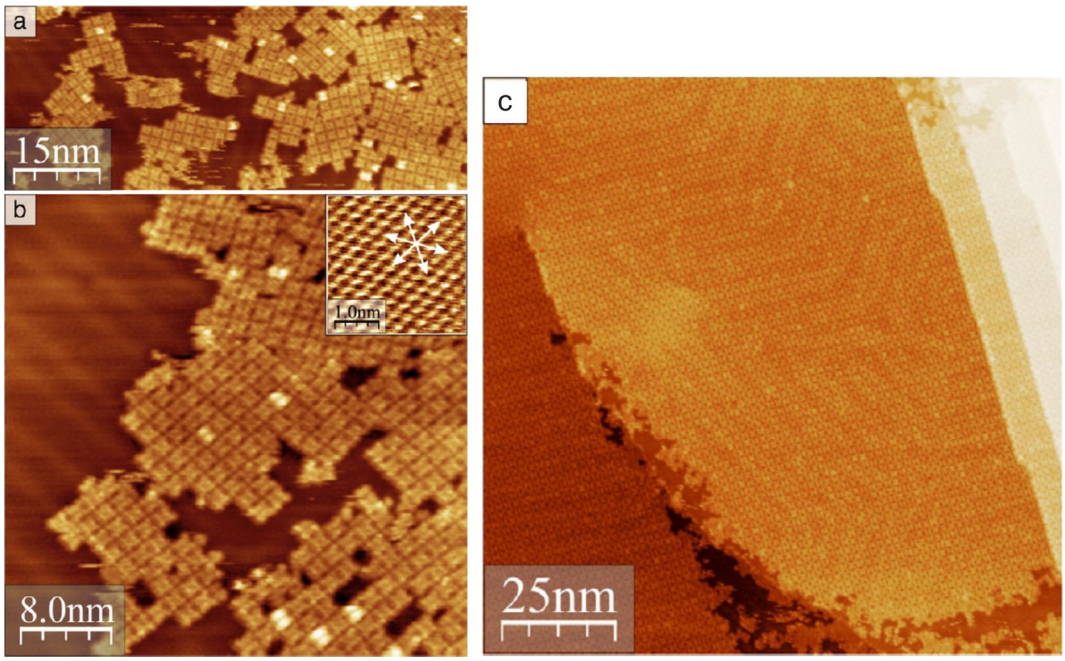

Figure 7: Results of STM measurements: (a,b) Formation of small islands at submonolayer coverage. Molecules on top of the first layer appear brighter (U = −1 V, I = 100 pA). Inset in (b): atomically resolved Au lattice (U = −0.5 V, I = 500 pA). Arrows are along the direction of the unit-cell vectors of the Au(111) substrate. (c) Large ordered domain of H_2THPP (= H_2TPP(OH)$_4$) on Au(111) after annealing at ca. 150 °C (U = −1.5 V). Reproduced with permission from [44], copyright 2014 Elsevier.

O–H···O hydrogen bonds responsible for the formation of the well-ordered domains are shown exemplarily in Figure 8c. A tip-induced azimuthal 90° rotation of individual H_2TPP(OH)$_4$ molecules was observed, as revealed by two successive measurements and proven by the rotation of a defective molecule indicated with a circle in Figure 8d. A further remarkable feature of the adlayers on Au(111) was noticed: While measuring at lower absolute bias voltages (in-gap, see below) an identical appearance of the deposited molecules was found, whereas at higher absolute bias voltages two different appearances were noticed. The origin of this observation is discussed below, see [45].

In additional OMBD experiments, H_2TPP(OH)$_4$ was deposited on Ag(110). In contrast to observations made for the deposition on Au(111), see above, on Ag(110) and immediately after deposition of a submonolayer coverage only isolated molecules of H_2TPP(OH)$_4$ were observed [44]. This observation led to the

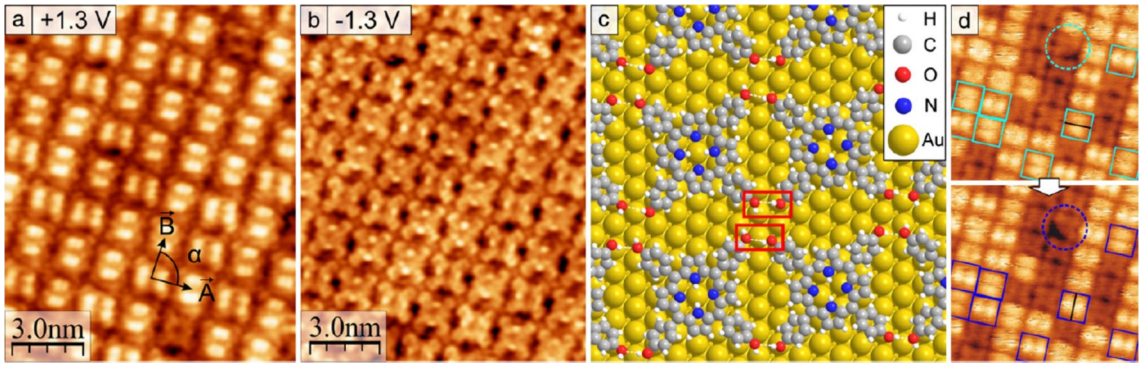

Figure 8: Highly resolved filled (a) and empty molecular states (b) STM image of the square structure of H_2THPP (= H_2TPP(OH)$_4$) on Au(111). (c) Model for the arrangement of H_2THPP (= H_2TPP(OH)$_4$) molecules in this structure. Pair-wise hydrogen bonding is marked with red rectangles. The reconstruction of Au(111) is not included in the model of the epitaxy. (d) Molecules which are rotated by 90° in the subsequently measured image (bottom) are marked by squares. A rotated molecule with one missing phenyl group is indicated by a dotted circle (11 nm × 10.5 nm, U = +1.2 V, sample annealed to ≈150 °C). Reproduced with permission from [44], copyright 2014 Elsevier.

conclusion that $H_2TPP(OH)_4$ has a lower diffusion activity on Ag(110) as compared to Au(111). Annealing at around 150 °C increased the mobility of the adsorbed molecules and resulted in the formation of small islands composed of nine or twelve molecules of $H_2TPP(OH)_4$ (Figure 9a). Subsequent heating to around 200 °C had the molecules rearrange into molecular chains along [1 $\bar{1}$0] near step edges of Ag(110) (Figure 9c), striped islands and differently ordered areas as shown in Figure 7a,b. For further details about the self-assembled ensembles of $H_2TPP(OH)_4$ on Ag(110), including illustrations of the hydrogen bonds that are responsible for interaction of the molecules with each other and accompanying density functional theory calculations, we refer to [44].

This work led to the conclusion that $H_2TPP(OH)_4$) forms a nearly complete monolayer on Au(111) and that this single-crystalline metallic surface does not have major influence on the self-assembly. In contrast, on the highly anisotropic Ag(110) surface the observed self-assembled structures of $H_2TPP(OH)_4$) can be related to the number of hydrogen bonds and the occupation of favorable adsorption positions. Moreover, molecule–substrate interactions are more pronounced on Ag(110) compared to Au(111).

Manipulation of the electronic structure of $H_2TPP(OH)_4$ on Au(111) [45]**:** Molecules with two possible states, e.g., of conductivity, can be used as single-molecule switches. This functionality could be applied in nano-scaled molecular-based memory devices or logic gates [64], However, one must be able to switch reversibly and controllably between the two stable states. An interconversion between different electronic or magnetic properties can be obtained, e.g., by inducing conformational or configurational changes in a molecular system [65], or by binding or releasing small molecules or atoms [66,67].

As described above and in [44], an identical in-gap appearance but two different appearances of the deposited $H_2TPP(OH)_4$ molecules at a higher bias voltage was observed. In order to further investigate this phenomenon, $H_2TPP(OH)_4$ was deposited again by OMBD on Au(111) and subsequently annealed at 150 °C for one hour to achieve uniform coverage [44,45]. The voltage dependence of the appearance of the molecules in STM was investigated and it was realized that bias voltages of larger than 0.7 V were required in order to clearly observe $H_2TPP(OH)_4$ in two different states, denoted as 1 and 2. Scanning tunneling spectroscopy measurements enabled us to determine the HOMO–LUMO gap of 1 to be 2.0 ± 0.1 and of 2 to be 2.5 ± 0.1 eV. If the STM is measured inside the HOMO–LUMO gaps, geometry effects dominate and all molecules in the ordered layer look quite identical. This changed when bias voltages higher than 1.5 V were applied and also a sudden conversion between 1 and 2 was observed. It is possible to control the interconversion between 1 and 2 by the STM tip. A typical case is shown in Figure 10a–e, where the tip is positioned over a molecule and the only the bias voltage is modified. The interconversion events are reversible and are attributed to hydrogen transfer from $H_2TPP(OH)_4$ to the tip and back (Figure 10f). We demonstrated that it is possible to induce the formation of state 2 spatially (Figure 10a–e) and electronically (above 2 V) well resolved for individual molecules by

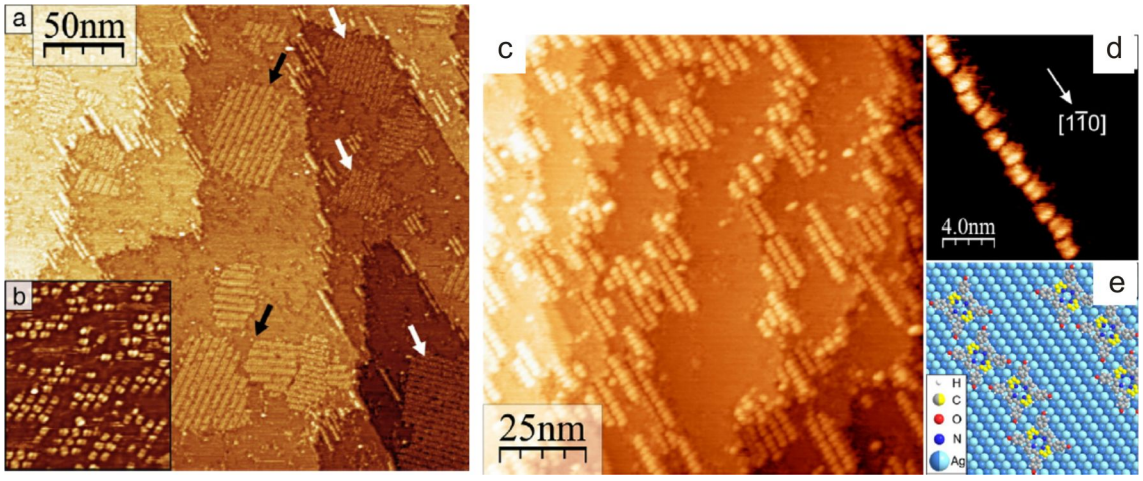

Figure 9: (a) Large scale STM image of submonolayer coverage showing molecular chains and ordered islands of H_2THPP (= $H_2TPP(OH)_4$) on Ag(110) after annealing at about 200 °C (black/white arrows for the different 2D structures, U = +1.0 V). (b) Aggregation into small molecular islands after the first annealing at ca. 150 °C (23.1 nm × 26.2 nm, U = +1.4 V). (c) Molecular chains along [1 $\bar{1}$0] near step edges of Ag(110) (U = +0.7 V). (d) Magnification of a chain. H_2THPP molecules are slightly displaced in a zigzag manner (U = +1.6V). (e) Model of epitaxy of the molecules in chains on Ag(110). Carbon atoms in the pyrrole rings bent away from the surface colored in yellow, Ag atom in first layer in bright blue, in second layer dark blue. Reproduced with permission from [44], copyright 2014 Elsevier.

using voltages between 1.5 and 2 V while higher voltages also switch neighboring molecules. In addition, states 1 and 2 are part of a large and highly ordered self-assembled array and it is possible to read-out the conductance at a specified position, and thus state 1 or 2, in a non-manipulative manner. Furthermore, it is possible to reverse positions of 1 and 2. Due to these unique features it seems possible to apply them for the construction of a nano-scale memory device.

Surface-confined 2D polymerization of $CuTPP(Br)_8$ on Au(111) [47]**:** Covalent linking of organic molecules directly on the surface would allow for the engineering of manifold extended 2D materials with novel transport properties. One major approach for surface-confined polymerization is the halogen-based Ullmann coupling reaction [42]. Thereby, the topography and also electronic properties of the covalent organic framework are determined by especially the halogen substitution

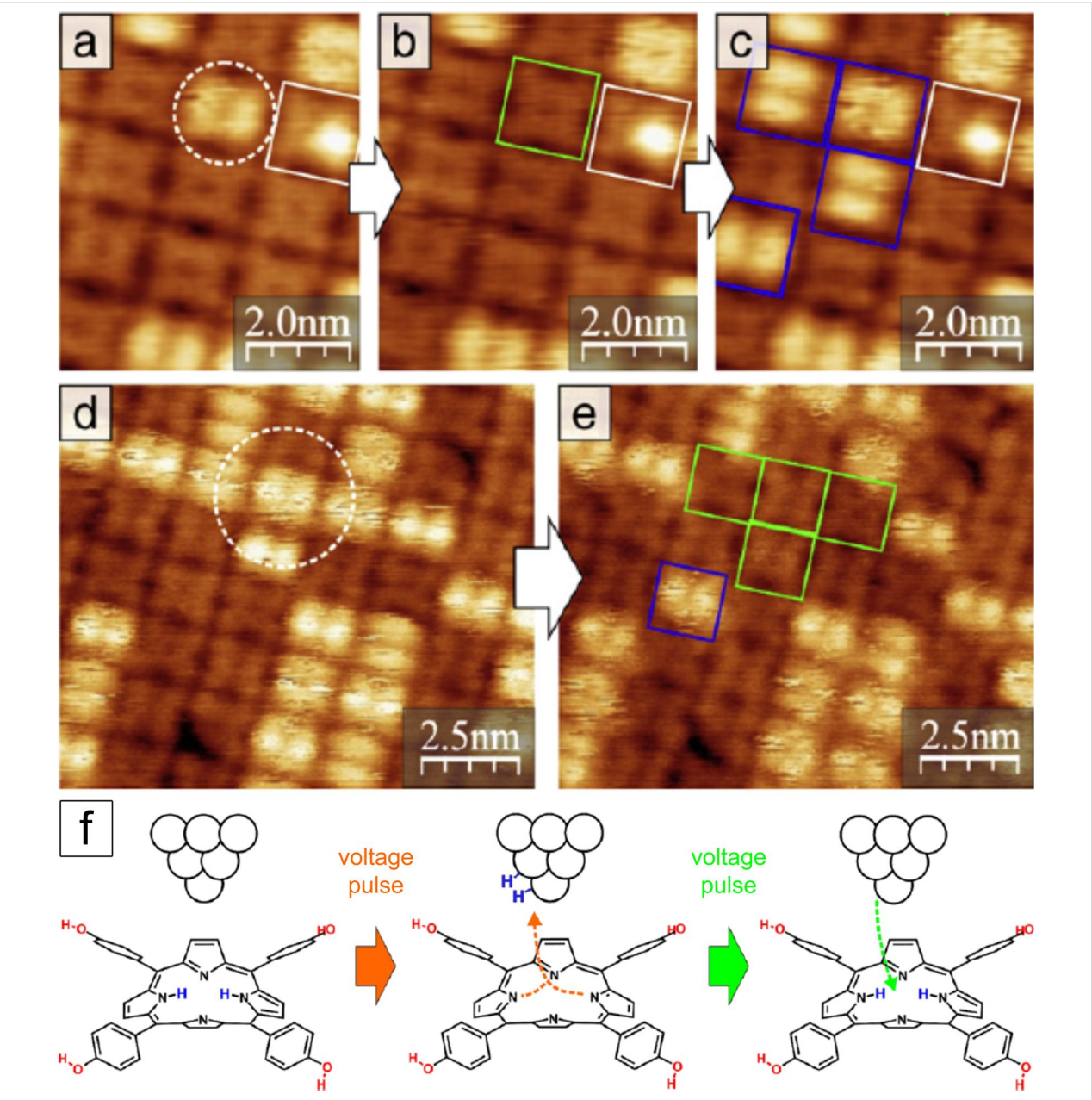

Figure 10: (a–e) Manipulation of the electronic structure by applying a voltage pulse with the STM tip at the position marked with a white circle. Converted molecules are marked with green (1→2) or blue (2→1) rectangles. (a–c) 1→2→1 conversion with 2 V pulses for 3 s (feedback switched on) at the same position before each frame. A molecule with only one protrusion (white rectangle) is used to mark the position in the scanned area. (d,e): Changing of neighboring molecules in both directions during the same pulse of 2.5 V for 3 s imaging parameter: +1.2 V, 100 pA. (f) Scheme of the proposed transfer of 2H from H_2TPP (= $H_2TPP(OH)_4$) to the tip apex and from the tip back to the dehydrogenated molecule by voltage pulses (1→2→1). Reproduced with permission from [45], copyright 2014 Elsevier.

pattern of the monomer. Notably, probably the first example of halogen-based, two-dimensionally covalent self-assembly on a surface was demonstrated by Grill and co-workers [40], where they showed that dimers, oligomer chains and small 2D covalent networks could be formed from porphyrin molecules with different numbers of bromine substitutions. The properties of the substrate surface have a strong influence in this kind of on-surface polymerization reaction. A high reactivity and also high energy barriers for diffusion can result in immediate C,C coupling after dehalogenation of the monomers. So far most 2D polymers that were reported are diffusion-limited and therefore have a small domain sizes, a high density of defects, or the networks are even undesiredly crumpled and without long-range order [68-70]. To solve this problem a coupling-limited polymerization [39,41], in which the radical molecules can diffuse and arrange before they couple irreversibly with each other, is needed. One example of this is summarized in the following. OMBD at around 350 °C was used to deposit approximately one monolayer of CuTPP(Br)$_8$ on a Au(111) wafer kept at room temperature. X-ray photoelectron spectroscopy (XPS) measurements indicated that after initial deposition not all CuTPP(Br)$_8$ molecules remained intact (Figure 11, left column). Likely, some molecules partially debrominate during OMBD in the crucible or when arriving with high thermal energy on the Au(111) surface. Sample annealing at only 130 °C reduced the number of intact CuTPP(Br)$_8$ molecules on a Au(111) further, at 200 °C only surface-adsorbed Br atoms or Br_2 molecules were observed and at 300 °C all bromine species desorbed (Figure 11, left column).

STM measurements were carried out in order to determine surface structures of deposited CuTPP(Br)$_8$ on a Au(111) surface. After deposition of about one monolayer only small periodically structured arrangements were observed. Annealing significantly enlarged the size of ordered areas, which is attributed to a remarkable surface mobility [71] of the adsorbed molecules at increased temperature. At a temperature of 200 °C most of the surface was covered with ordered areas, although some disordered regions were noticed (Figure 11a–c). As depicted in Figure 11c the imaged molecules correspond to radical CuTPP,

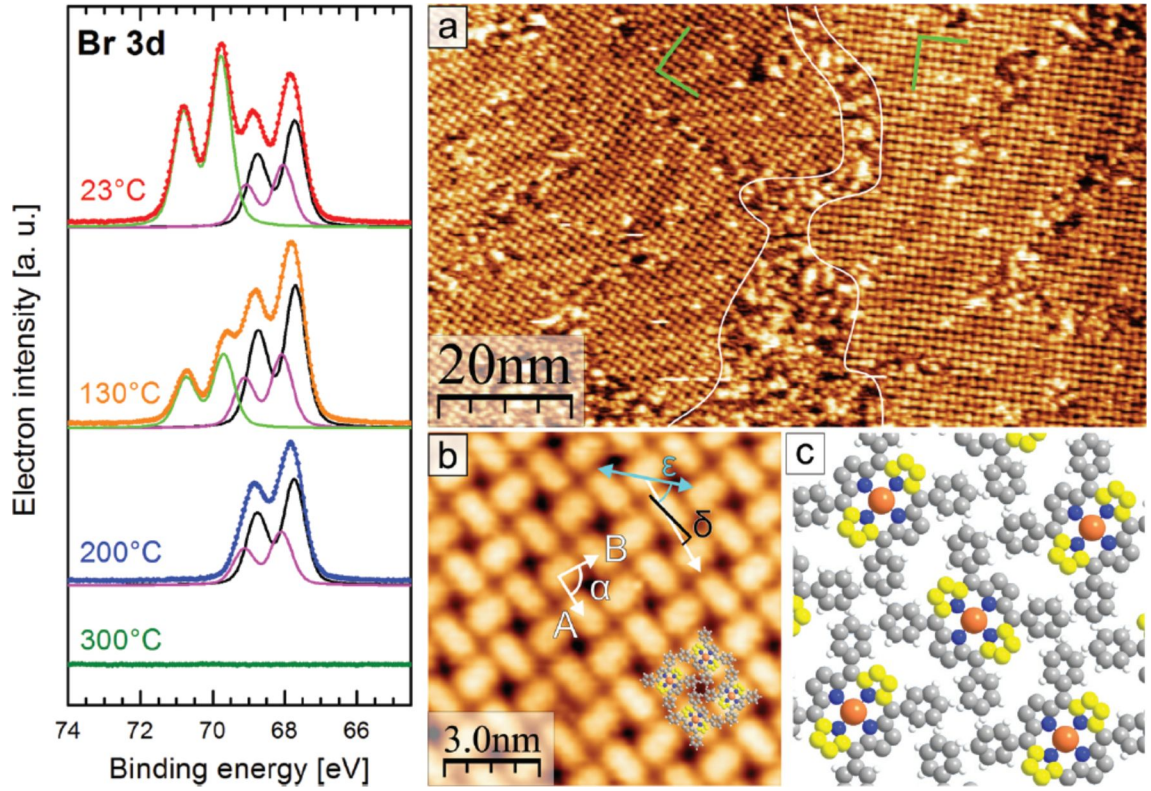

Figure 11: Left: Evolution of the XPS spectra of Br 3d for a molecular monolayer of CuTPP(Br)$_8$ on Au(111) as a function of the indicated annealing temperature. In the Br 3d spectra, the background has been subtracted. Right: (a) STM image after deposition of ca. 1 ML of CuTPP(Br)$_8$ and annealing at max. 200 °C. Two periodically ordered rotational domains and disordered areas in between are shown. The herring-bone reconstruction of the underlying Au(111) is visible through the large ordered areas (U = −0.7 V). (b) Magnification of the adlayer structure of CuTPP(Br)$_8$ on Au(111) with elongated appearance of molecules at U = −1 V. The cyan arrow indicates the direction of one unit cell vector of the Au(111) surface lattice. (c) Model of the molecular arrangement; protruding C atoms of the saddle deformation are colored yellow. Adapted from [47] with permission from The Royal Society of Chemistry.

as XPS measurements demonstrated for that temperature the presence of surface-bound Br/Br_2 only. Interestingly, these surface-stabilized radicals of CuTPP are seemingly long-term stable. The result obtained after heating this sample to 350 °C for one hour is displayed in Figure 11. It resulted in the formation of nano-ribbons (Figure 12) and is accompanied by a coverage reduction of about 25%. Likely, the coverage reduction is due to partial desorption and reassembling, although it remains speculative at the present time to what extent. The STM picture of one nano-ribbon is shown exemplarily in Figure 12. Obviously, several hundred CuTPP species are self-assembled into an at least 75 × 45 nm large ribbon, representing a covalently bonded network of CuTPP. These astonishingly large dimensions of the nano-ribbons might be attributed to several reasons. For example, the surface polymerization could be shown to proceed stepwise, that is, all bromine species were fully cleaved-off before the Ullmann-type C,C-coupling reactions between neighbored porphyrin stages were initiated [42]. Furthermore, the surface-mobility of adsorbed CuTPP$(Br)_8$ and CuTPP species is obviously sufficiently high to allow for reassembling. To the best of our knowledge such a relatively large-scale 2D on-surface polymerization of porphyrin molecules has been observed here for the first time. As illustrated in Figure 12, the nano-ribbon comprises several coupling defects as typically observed for covalent networks. Four different types of such defects have been thoroughly discussed by us together with possibilities to avoid or to cure them.

Conclusion

We have described our investigation of thin films of (metallo)porphyrins deposited by OMBD with particular emphasis on their structural, morphological, (magneto-)optical and electronic properties. We showed a few recipes for functionalization of (metallo)porphyrins on how to assemble individual molecules further into large non-covalently and covalently bonded ensembles. The potential for applications of the results reviewed here ranges from dendrites as nanowires for electronic/spintronic device integration via self-assembled non-covalently locked 2D layers for nano-scaled memory devices to spintronic devices with laterally conductive and magnetic 2D nano-ribbons.

Of course, this is a typical status report that reflects the present state of knowledge acquired. However, the local transport techniques implemented here for the (metallo)porphyrin thin films represent a formidable approach in order to downscale and unveil electrical characteristics, which would certainly drive device performance. For the future the synthesized (metallo)porphyrins and methods used and applied have to be combined even further, whereby especially the combination of structural and (local) spectroscopic investigations is highly promising. For example, we regard the 2D nano-ribbons made of CuTPP$(Br)_8$ molecules as a good starting point to investigate how to functionalize the porphyrins further with different (transition) metal atoms or functional groups to tailor structures and physical properties. The electronic, electrical and local magnetic properties of new 2D nano-ribbons will be investigated by, for example, cs-AFM or in situ four-probe STM. It is both challenging and motivating to investigate how to separate the 2D nano-ribbons from surfaces and to build multilayer devices from them. Thus, the results presented here gave plenty of stimuli to continue our joint efforts [60,72].

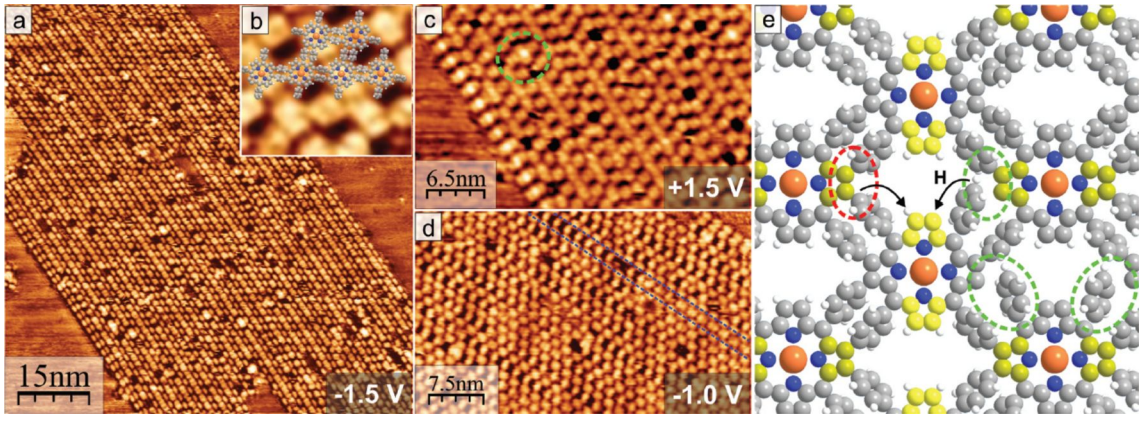

Figure 12: Results of STM measurements: (a) Novel structure of the alternating molecular rows formed after annealing at 350 °C (U = −1.5 V). (b) Overlay of molecular model on the structure (U = +1.5 V, 6.5 nm × 6.5 nm). (c) Image of the occupied molecular orbitals at the left side of the ordered structure shown in (a). The green circle marks a lattice defect. (d) Defect along molecular rows (marked blue) from the incomplete C,C-coupling between neighboring molecules. (e) Model of the arrangement with covalent bonds between the debrominated molecules (red circle). Incomplete polymerization is marked by the green circle. Dissociated hydrogen atoms from the phenyl groups could diffuse and bond to the still unsaturated carbon atoms (arrows). Upwards directed C atoms in the pyrrole units of the porphyrin saddle shape are colored in bright and dark yellow to indicate slightly different angles as explained in the text. Adapted from [47] with permission from The Royal Society of Chemistry.

Finally, we would like to express our hope that the multifaceted fabrication and investigation methods of ensembles of (metallo)porphyrins, as different as they might appear, may stimulate joint approaches of material scientists to further explore their application potential.

Acknowledgements

This work was supported by the Deutsche Forschungsgemeinschaft through the Focused Research Unit FOR 1154 "Towards Molecular Spintronics". We express our gratitude to numerous co-workers and partners, whose contribution is acknowledged in the author list of the original works reviewed in this article. The Graphical Abstract of this publication at the website of the "Beilstein Journal of Nanotechnology" contains copyrighted material that is reproduced with permission from [45,46], copyright 2014 Elsevier.

References

1. Dolphin, D. *The Porphyrins;* Academic Press: New York, NY, USA, 1978.
2. Kadish, K. M.; Smith, K. M.; Guiard, R. *The Porphyrins Handbook;* Academic Press: Amsterdam, Netherlands, 2000.
3. Vicente, M. G. H.; Smith, K. M. *Curr. Org. Synth.* **2014,** *11,* 3–28. doi:10.2174/15701794113106660083
4. Scheybal, A.; Ramsvik, T.; Bertschinger, R.; Putero, M.; Nolting, F.; Jung, T. A. *Chem. Phys. Lett.* **2005,** *411,* 214–220. doi:10.1016/j.cplett.2005.06.017
5. Long, M.-Q.; Chen, K.-Q.; Wang, L.; Qing, W.; Zou, B. S.; Shuai, Z. *Appl. Phys. Lett.* **2008,** *92,* 243303. doi:10.1063/1.2924364
6. Oppeneer, P. M.; Panchmatia, P. M.; Sanyal, B.; Eriksson, O.; Ali, Md. E. *Prog. Surf. Sci.* **2009,** *84,* 18–29. doi:10.1016/j.progsurf.2008.12.001
7. Bernien, M.; Miguel, J.; Weis, C.; Ali, Md. E.; Kurde, J.; Krumme, B.; Panchmatia, P. M.; Sanyal, B.; Piantek, M.; Srivastava, P.; Baberschke, K.; Oppeneer, P. M.; Eriksson, O.; Kuch, W.; Wende, H. *Phys. Rev. Lett.* **2009,** *102,* 047202. doi:10.1103/PhysRevLett.102.047202
8. Wäckerlin, C.; Chylarecka, D.; Kleibert, A.; Müller, K.; Iacovita, C.; Nolting, F.; Jung, T. A.; Ballav, N. *Nat. Commun.* **2010,** *1,* 61. doi:10.1038/ncomms1057
9. Cho, W. J.; Cho, Y.; Min, S. K.; Kim, W. Y.; Kim, K. S. *J. Am. Chem. Soc.* **2011,** *133,* 9364–9369. doi:10.1021/ja111565w
10. Barraud, C.; Seneor, P.; Mattana, R.; Fusil, S.; Bouzehouane, K.; Deranlot, C.; Graziosi, P.; Hueso, L.; Bergenti, I.; Dediu, V.; Petroff, F.; Fert, A. *Nat. Phys.* **2010,** *6,* 615–620. doi:10.1038/nphys1688
11. Sugano, S.; Kojima, N. *Magneto-Optics;* Springer: Berlin, Germany, 2000. doi:10.1007/978-3-662-04143-7
12. Baker, M. L.; Blundell, S. J.; Domingo, N.; Hill, S. Spectroscopy Methods for Molecular Nanomagnets. In *Molecular nanomagnets and related phenomena;* Gao, S., Ed.; Structure and Bonding, Vol. 164; Springer: Berlin, Heidelberg, Germany, 2015; pp 231–291. doi:10.1007/430_2014_155
13. In the context of MOKE and MCD measurements "porphyrinoids" refers to molecules possessing a porphyrin skeleton. This includes (metallo)phthalocyanines, bacteriochlorins and others.
14. Mack, J.; Stillman, M. J.; Kobayashi, N. *Coord. Chem. Rev.* **2007,** *251,* 429–453. doi:10.1016/j.ccr.2006.05.011
15. Abdulmalic, M. A.; Fronk, M.; Bräuer, B.; Zahn, D. R. T.; Salvan, G.; Meva, F. E.; Rüffer, T. *J. Magn. Magn. Mater.* **2016,** *419,* 17–28. doi:10.1016/j.jmmm.2016.06.002
16. Lungwitz, F.; Mende, C.; Fronk, M.; Haidu, F.; Lang, H.; Salvan, G.; Zahn, D. R. T. *Thin Solid Films* **2014,** *571,* 377–383. doi:10.1016/j.tsf.2014.03.055
17. Birnbaum, T.; Hahn, T.; Martin, C.; Kortus, J.; Fronk, M.; Lungwitz, F.; Zahn, D. R. T.; Salvan, G. *J. Phys.: Condens. Matter* **2014,** *26,* 104201. doi:10.1088/0953-8984/26/10/104201
18. Fronk, M.; Bräuer, B.; Kortus, J.; Schmidt, O. G.; Zahn, D. R. T.; Salvan, G. *Phys. Rev. B* **2009,** *79,* 235305. doi:10.1103/PhysRevB.79.235305
19. Fronk, M.; Schubert, C.; Haidu, F.; Scarlat, C.; Dörr, K.; Albrecht, M.; Zahn, D. R. T.; Salvan, G. *IEEE Trans. Magn.* **2012,** *48,* 2777–2780. doi:10.1109/TMAG.2012.2203109
20. Coronado, E.; Makarewicz, M.; Prieto-Ruiz, J. P.; Prima-García, H.; Romero, F. M. *Adv. Mater.* **2011,** *23,* 4323–4326. doi:10.1002/adma.201101513
21. Coronado, E.; Fitta, M.; Prieto-Ruiz, J. P.; Prima-Garcia, H.; Romero, F. M.; Cros, A. *J. Mater. Chem. C* **2013,** *1,* 6981–6988. doi:10.1039/c3tc31316f
22. Ito, T.; Okazaki, S. *Nature* **2000,** *406,* 1027–1031. doi:10.1038/35023233
23. Joachim, C.; Gimzewski, J. K.; Aviram, A. *Nature* **2000,** *408,* 541–548. doi:10.1038/35046000
24. Yoshimoto, S.; Tada, A.; Suto, K.; Narita, R.; Itaya, K. *Langmuir* **2003,** *19,* 672–677. doi:10.1021/la026449i
25. Auwärter, W.; Weber-Bargioni, A.; Riemann, A.; Schiffrin, A.; Gröning, O.; Fasel, R.; Barth, J. V. *J. Chem. Phys.* **2006,** *124,* 194708. doi:10.1063/1.2194541
26. Auwärter, W.; Seufert, K.; Klappenberger, F.; Reichert, J.; Weber-Bargioni, A.; Verdini, A.; Cvetko, D.; Dell'Angela, M.; Floreano, L.; Cossaro, A.; Bavdek, G.; Morgante, A.; Seitsonen, A. P.; Barth, J. V. *Phys. Rev. B* **2010,** *81,* 245403. doi:10.1103/PhysRevB.81.245403
27. Rojas, G.; Chen, X.; Bravo, C.; Kim, J.-H.; Kim, J.-S.; Xiao, J.; Dowben, P. A.; Gao, Y.; Zeng, X. C.; Choe, W.; Enders, A. *J. Phys. Chem. C* **2010,** *114,* 9408–9415. doi:10.1021/jp1012957
28. Beggan, J. P.; Krasnikov, S. A.; Sergeeva, N. N.; Senge, M. O.; Cafolla, A. A. *Nanotechnology* **2012,** *23,* 235606. doi:10.1088/0957-4484/23/23/235606
29. Bhyrappa, P.; Wilson, S. R.; Suslick, K. S. *J. Am. Chem. Soc.* **1997,** *119,* 8492–8502. doi:10.1021/ja971093w
30. Lei, S. B.; Wang, C.; Yin, S. X.; Wang, H. N.; Xi, F.; Liu, H. W.; Xu, B.; Wan, L. J.; Bai, C. L. *J. Phys. Chem. B* **2001,** *105,* 10838–10841. doi:10.1021/jp0105701
31. Hill, J. P.; Wakayama, Y.; Akada, M.; Ariga, K. *J. Phys. Chem. C* **2007,** *111,* 16174–16180. doi:10.1021/jp0745945
32. Lu, G.; Zhang, X.; Cai, X.; Jiang, J. *J. Mater. Chem.* **2009,** *19,* 2417–2424. doi:10.1039/b820127g
33. Garcia-Lekue, A.; González-Moreno, R.; Garcia-Gil, S.; Pickup, D. F.; Floreano, L.; Verdini, A.; Cossaro, A.; Martín-Gago, J. A.; Arnau, A.; Rogero, C. *J. Phys. Chem. C* **2012,** *116,* 15378–15384. doi:10.1021/jp302784r
34. Zwaneveld, N. A. A.; Pawlak, R.; Abel, M.; Catalin, D.; Gigmes, D.; Bertin, D.; Porte, L. *J. Am. Chem. Soc.* **2008,** *130,* 6678–6679. doi:10.1021/ja800906f

35. Gourdon, A. *Angew. Chem., Int. Ed.* **2008,** *47,* 6950–6953. doi:10.1002/anie.200802229
36. Sakamoto, J.; van Heijst, J.; Lukin, O.; Schlüter, A. D. *Angew. Chem., Int. Ed.* **2009,** *48,* 1030–1069. doi:10.1002/anie.200801863
37. Franc, G.; Gourdon, A. *Phys. Chem. Chem. Phys.* **2011,** *13,* 14283–14292. doi:10.1039/c1cp20700h
38. El Garah, M.; MacLeod, J. M.; Rosei, F. *Surf. Sci.* **2013,** *613,* 6–14. doi:10.1016/j.susc.2013.03.015
39. Björk, J.; Hanke, F. *Chem. – Eur. J.* **2014,** *20,* 928–934. doi:10.1002/chem.201303559
40. Grill, L.; Dyer, M.; Lafferentz, L.; Persson, M.; Peters, M. V.; Hecht, S. *Nat. Nanotechnol.* **2007,** *2,* 687–691. doi:10.1038/nnano.2007.346
41. Lafferentz, L.; Eberhardt, V.; Dri, C.; Africh, C.; Comelli, G.; Esch, F.; Hecht, S.; Grill, L. *Nat. Chem.* **2012,** *4,* 215–220. doi:10.1038/nchem.1242
42. Ullmann, F.; Bielecki, J. *Ber. Dtsch. Chem. Ges.* **1901,** *34,* 2174–2185. doi:10.1002/cber.190103402141
43. Cinchetti, M.; Dediu, V. A.; Hueso, L. E. *Nat. Mater.* **2017,** *16,* 507–515. doi:10.1038/nmat4902
44. Smykalla, L.; Shukrynau, P.; Mende, C.; Rüffer, T.; Lang, H.; Hietschold, M. *Surf. Sci.* **2014,** *628,* 132–140. doi:10.1016/j.susc.2014.06.001
45. Smykalla, L.; Shukrynau, P.; Mende, C.; Rüffer, T.; Lang, H.; Hietschold, M. *Surf. Sci.* **2014,** *628,* 92–97. doi:10.1016/j.susc.2014.05.015
46. Siles, P. F.; Bufon, C. C. B.; Grimm, D.; Jalil, A. R.; Mende, C.; Lungwitz, F.; Salvan, G.; Zahn, D. R. T.; Lang, H.; Schmidt, O. G. *Org. Electron.* **2014,** *15,* 1432–1439. doi:10.1016/j.orgel.2014.04.004
47. Smykalla, L.; Shukrynau, P.; Korb, M.; Lang, H.; Hietschold, M. *Nanoscale* **2015,** *7,* 4234–4241. doi:10.1039/C4NR06371F
48. Monti, D.; Nardis, S.; Stefanelli, M.; Paolesse, R.; Di Natale, C.; D'Amico, A. *J. Sens.* **2009,** *2009,* 856053. doi:10.1155/2009/856053
49. Horn, S.; Dahms, K.; Senge, M. O. *J. Porphyrins Phthalocyanines* **2008,** *12,* 1053–1077. doi:10.1142/S108842460800042X
50. Bernien, M.; Miguel, J.; Weis, C.; Ali, M. E.; Kurde, J.; Krumme, B.; Panchmatia, P. M.; Sanyal, B.; Piantek, M.; Srivastava, P.; Baberschke, K.; Oppeneer, P. M.; Eriksson, O.; Kuch, W.; Wende, H. *Phys. Rev. Lett.* **2009,** *102,* 047202. doi:10.1103/PhysRevLett.102.047202
51. Gong, X.; Milic, T.; Xu, C.; Batteas, J. D.; Drain, C. M. *J. Am. Chem. Soc.* **2002,** *124,* 14290–14291. doi:10.1021/ja027405z
52. Wang, Z.; Li, Z.; Medforth, C. J.; Shelnutt, J. A. *J. Am. Chem. Soc.* **2007,** *129,* 2440–2441. doi:10.1021/ja068250o
53. Schwab, A. D.; Smith, D. E.; Rich, C. S.; Young, E. R.; Smith, W. F.; de Paula, J. C. *J. Phys. Chem. B* **2003,** *107,* 11339–11345. doi:10.1021/jp035569b
54. Schwab, A. D.; Smith, D. E.; Bond-Watts, B.; Johnston, D. E.; Hone, J.; Johnson, A. T.; de Paula, J. C.; Smith, W. F. *Nano Lett.* **2004,** *4,* 1261–1265. doi:10.1021/nl049421v
55. Lee, S. J.; Hupp, J. T.; Nguyen, S. T. *J. Am. Chem. Soc.* **2008,** *130,* 9632–9633. doi:10.1021/ja801733t
56. Wang, Z.; Medforth, C. J.; Shelnutt, J. A. *J. Am. Chem. Soc.* **2004,** *126,* 15954–15955. doi:10.1021/ja045068j
57. Hoang, M. H.; Kim, Y.; Kim, S.-J.; Choi, D. H.; Lee, S. J. *Chem. – Eur. J.* **2011,** *17,* 7772–7776. doi:10.1002/chem.201100599
58. Rotomskis, R.; Augulis, R.; Snitka, V.; Valiokas, R.; Liedberg, B. *J. Phys. Chem. B* **2004,** *108,* 2833–2838. doi:10.1021/jp036128v
59. Cornia, A.; Mannini, M. Single-Molecule Magnets on Surfaces. In *Molecular nanomagnets and related phenomena;* Gao, S., Ed.; Structure and Bonding, Vol. 164; Springer: Berlin, Heidelberg, Germany, 2015; pp 293–330. doi:10.1007/430_2014_150
60. Al-Shewiki, R. K.; Mende, C.; Buschbeck, R.; Siles, P. F.; Schmidt, O. G.; Rüffer, T.; Lang, H. *Beilstein J. Nanotechnol.* **2017,** *8,* 1191–1204. doi:10.3762/bjnano.8.121
61. Robaschik, P.; Fronk, M.; Toader, M.; Klyatskaya, S.; Ganss, F.; Siles, P. F.; Schmidt, O. G.; Albrecht, M.; Hietschold, M.; Ruben, M.; Zahn, D. R. T.; Salvan, G. *J. Mater. Chem. C* **2015,** *3,* 8039–8049. doi:10.1039/C5TC01520K
62. Lungwitz, Frank, private communication.
63. Keegan, J. D.; Bunnenberg, E.; Djerassi, C. *Spectrosc. Lett.* **1983,** *16,* 275–286. doi:10.1080/00387018308062345
64. Green, J. E.; Choi, J. W.; Boukai, A.; Bunimovich, Y.; Johnston-Halperin, E.; DeIonno, E.; Luo, Y.; Sheriff, B. A.; Xu, K.; Shin, Y. S.; Tseng, H.-R.; Stoddart, J. F.; Heath, J. R. *Nature* **2007,** *445,* 414–417. doi:10.1038/nature05462
65. Morgenstern, K. *Prog. Surf. Sci.* **2011,** *86,* 115–161. doi:10.1016/j.progsurf.2011.05.002
66. Liu, L.; Yang, K.; Jiang, Y.; Song, B.; Xiao, W.; Li, L.; Zhou, H.; Wang, Y.; Du, S.; Ouyang, M.; Hofer, W. A.; Neto, A. H. C.; Gao, H.-J. *Sci. Rep.* **2013,** *3,* 1210. doi:10.1038/srep01210
67. Katano, S.; Kim, Y.; Hori, M.; Trenary, M.; Kawai, M. *Science* **2007,** *316,* 1883–1886. doi:10.1126/science.1141410
68. Bieri, M.; Nguyen, M.-T.; Gröning, O.; Cai, J.; Treier, M.; Aït-Mansour, K.; Ruffieux, P.; Pignedoli, C. A.; Passerone, D.; Kastler, M.; Müllen, K.; Fasel, R. *J. Am. Chem. Soc.* **2010,** *132,* 16669–16676. doi:10.1021/ja107947z
69. Gutzler, R.; Cardenas, L.; Lipton-Duffin, J.; Garah, M. E.; Dinca, L. E.; Szakacs, C. E.; Fu, C.; Gallagher, M.; Vondrácek, M.; Rybachuk, M.; Perepichka, D. F.; Rosei, F. *Nanoscale* **2014,** *6,* 2660–2668. doi:10.1039/C3NR05710K
70. Eichhorn, J.; Strunskus, T.; Rastgoo-Lahrood, A.; Samanta, D.; Schmittel, M.; Lackinger, M. *Chem. Commun.* **2014,** *50,* 7680–7682. doi:10.1039/C4CC02757D
71. Buchner, F.; Xiao, J.; Zillner, E.; Chen, M.; Röckert, M.; Ditze, S.; Stark, M.; Steinrück, H.-P.; Gottfried, J. M.; Marbach, H. *J. Phys. Chem. C* **2011,** *115,* 24172–24177. doi:10.1021/jp206675u
72. Richter, P.; Plassmeyer, P. N.; Harzdorf, J.; Rüffer, T.; Lang, H.; Kalbacova, J.; Jöhrmann, N.; Schulze, S.; Hietschold, M.; Arekapudi, S. S. P. K.; Albrecht, M.; Zahn, D. R. T.; Page, C. J.; Salvan, G. *Chem. Mater.* **2016,** *28,* 4917–4927. doi:10.1021/acs.chemmater.6b01001

BEILSTEIN JOURNAL OF NANOTECHNOLOGY

Spin-dependent transport and functional design in organic ferromagnetic devices

Guichao Hu*[1,2], Shijie Xie[3], Chuankui Wang[1] and Carsten Timm[2]

Review

Open Access

Address:
[1]School of Physics and Electronics, Shandong Normal University, Jinan 250014, China, [2]Institute of Theoretical Physics, Technische Universität Dresden, 01062 Dresden, Germany and [3]School of Physics, Shandong University, Jinan 250100, China

Email:
Guichao Hu* - hgc@sdnu.edu.cn

* Corresponding author

Keywords:
magnetoresistance; organic ferromagnet; spin-current rectification; spin filtering; transport

Beilstein J. Nanotechnol. **2017,** *8,* 1919–1931.
doi:10.3762/bjnano.8.192

Received: 30 January 2017
Accepted: 18 August 2017
Published: 13 September 2017

This article is part of the Thematic Series "Towards molecular spintronics".

Guest Editor: G. Salvan

Abstract

Organic ferromagnets are intriguing materials in that they combine ferromagnetic and organic properties. Although challenges in their synthesis still remain, the development of organic spintronics has triggered strong interest in high-performance organic ferromagnetic devices. This review first introduces our theory for spin-dependent electron transport through organic ferromagnetic devices, which combines an extended Su–Schrieffer–Heeger model with the Green's function method. The effects of the intrinsic interactions in the organic ferromagnets, including strong electron–lattice interaction and spin–spin correlation between π-electrons and radicals, are highlighted. Several interesting functional designs of organic ferromagnetic devices are discussed, specifically the concepts of a spin filter, multi-state magnetoresistance, and spin-current rectification. The mechanism of each phenomenon is explained by transmission and orbital analysis. These works show that organic ferromagnets are promising components for spintronic devices that deserve to be designed and examined in future experiments.

Introduction

In recent years, organic spintronics has attracted more and more interest [1-3] in order to develop cheap and flexible devices employing the electronic spin degree of freedom. Organic spintronics has several merits compared with inorganic materials. The spin–orbit and hyperfine interactions in organic materials are usually weak [4], which induces a long spin relaxation time and makes organic materials ideal for spin-polarized transport applications. Organic molecules may form a soft interface with metals and ferromagnets via chemical adsorption. The interfacial orbital hybridization may modify the organic interfacial spin polarization (SP), which has triggered the new concept of "organic spinterface" [5]. Recent experimental studies have demonstrated the reproduction of conventional spintronic devices using organic counterparts, e.g., magnetoresi-

tive devices [6-8]. On the other hand, the search for novel functional organic materials remains of high interest for theorists and experimentalists.

Organic ferromagnets (OFs), which combine ferromagnetic and organic properties, are particularly promising for the design of organic spintronic devices. OFs are mainly synthesized artificially, such as by doping transition-metal ions into organic materials or using spin radicals [9-13]. The latter method may generate pure OFs. For example, poly((1,4-bis(2,2,6,6-tetramethyl-4-hydroxy-4-piperidyl-1-oxyl)butadiyne) (poly-BIPO) is a representative of π-conjugated pure OFs with quasi-one-dimensional structure, which can be synthesized from polyacetylene by replacing every other H atom by a spin radical. The radicals are usually heterocycles containing an unpaired electron. The spins of the radicals are coupled to the spins of π-electrons in the main carbon chain. Theoretical studies have found that the radical spins are ferromagnetically ordered in the ground state [14,15]. The magnetic properties of poly-BIPO have been measured experimentally, including high Curie temperature (150–190 °C) [9], magnetic hysteresis with residual magnetization (0.025–0.05 emu/g), and coercive force (295–470 Oe) [10], which are promising for spintronic applications. Although the chemical instability of the radicals still remains a challenge, remarkable progress has recently been made, where several classes of stable spin radicals have been obtained [9,10,16].

In the past decades, the research on OFs has focused on the synthesis, measurement, and characterization of the magnetic properties of the isolated molecules. Recently, the progress in organic and molecular spintronics has motivated us to explore the spin-dependent transport properties of OFs and the possibility to design organic ferromagnetic devices. A related field involves single molecular magnets (SMMs). Extensive experimental and theoretical studies have demonstrated the realization of functional devices based on SMMs, such as molecular switches and negative differential resistance [17-24]. Electronic transport in organic magnets has also been studied. Yoo et al. [25] have experimentally demonstrated the magnetic response of V[TCNE]$_x$-based devices (TCNE stands for tetracyanoethylene) by connecting the organic magnet to gold electrodes. Li et al. [26] have investigated the magnetoresistance effect in organic magnetic devices with one ferromagnetic and one nonmagnetic electrode. Wang et al. [27,28] have performed theoretical studies of electron transport in OFs and have proposed spin–charge separation and spin filtering.

π-Conjugated OFs with spin radicals are ideal materials for device design since the π-orbitals are available for electron transport. The pursuit of novel effects based on the intrinsic properties of the OFs is one of our aims. Prior to that, the role of the following interactions needs to be clarified: First, the coupling between the spins of conducting π-electrons and the radical spins is the origin of the magnetism. How does it affect the spin-dependent transport? Second, the electron–lattice (e–l) interaction is strong in organic materials, which leads to dimerization in the ground state and opens a Peierls gap in the molecular energy band [29]. What is the role of the e–l interaction for the spin-dependent electron transport? Third, in the presence of the above two interactions, how do the molecular π-orbitals respond to an external bias? What is its manifestation in the current?

In the remainder of the paper, we introduce our theory for the electron transport through OF devices, which combines the extended Su–Schrieffer–Heeger (SSH) model [30] and the Green's function method. The two interactions mentioned above are included. Then, we review results on electron transport and functional design of organic ferromagnetic devices, which are based on this theory. We focus on three concepts that are interesting for spintronics, namely spin filtering [31], multistate magnetoresistance [32], and spin–current rectification [33].

Review

SSH model combined with the Green's function method

Generally, an OF device may be constructed by sandwiching the OF molecule between two electrodes, as shown in Figure 1. The two semi-infinite one-dimensional electrodes may be ferromagnetic or nonmagnetic metals. The central OF, such as poly-BIPO, consists of the main carbon chain and spin radicals attached to the odd sites. The OF can be described by an extended SSH model [30] combined with a Kondo term, which captures both the strong e–l interaction and the spin correlation between π-electrons and spin radicals. The Hamiltonian is written as [14,15]

$$\begin{aligned} H_{\mathrm{OF}} = & -\sum_{i,\sigma}\left[\left(t_0-\alpha y_i\right)\left(c^{\dagger}_{i+1,\sigma}c_{i,\sigma}+\mathrm{H.c.}\right)\right]+\frac{K}{2}\sum_i y_i^2 \\ & +U\sum_i c^{\dagger}_{i,\uparrow}c_{i,\uparrow}c^{\dagger}_{i,\downarrow}c_{i,\downarrow}+W\sum_{i,\sigma,\sigma'}c^{\dagger}_{i,\sigma}c_{i,\sigma}c^{\dagger}_{i+1,\sigma'}c_{i+1,\sigma'} \\ & +J\sum_i \delta_{i,\mathrm{odd}}\,\mathbf{S}_i\cdot\mathbf{s}_i. \end{aligned} \quad (1)$$

The first two terms are the expression of the SSH model [30] for an organic molecular chain. The former one is the hopping term of π-electrons along the main chain, where the hopping integral is modulated by the possible lattice distortion. t_0 is the nearest-neighbor hopping integral in a uniform chain. α denotes

the e–l coupling constant. y_i corresponds to the lattice distortion $y_i \equiv u_{i+1} - u_i$, where u_i is the displacement of the carbon atom at site i. $c^{\dagger}_{i,\sigma}(c_{i,\sigma})$ is the creation (annihilation) operator of an electron at site i with spin σ. The second term is the classical elastic energy of the lattice atoms in the main chain, where K is the elastic coefficient. The third and forth terms are the electron–electron interactions between π-electrons, where U and W are the on-site and nearest-neighbor interaction strengths, respectively. The last term is the spin coupling between the π-electron spins $d^{\dagger}_{i,\sigma}(d_{i,\sigma})$ and the radical spins $\mathbf{S}_i$, with strength $J > 0$. This term contains $\delta_{i,\text{odd}} = 1$ ($\delta_{i,\text{odd}} = 0$) for i odd (even), which ensures that the spin coupling only occurs for the odd sites.

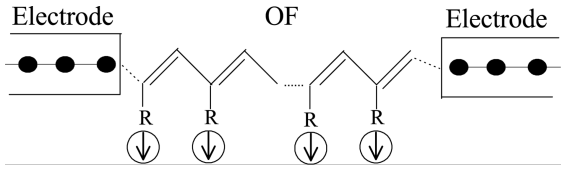

Figure 1: Schematic of an organic ferromagnetic device.

Since we focus on the effects of the interactions in the organic ferromagnet on transport, we model the electrodes by simple one-dimensional chains described by a single-band tight-binding model with a spin-splitting term [34],

$$H_{\text{F}} = \sum_{i,\sigma}\left[\varepsilon_f d^{\dagger}_{i,\sigma}d_{i,\sigma} - t_f\left(d^{\dagger}_{i+1,\sigma}d_{i,\sigma} + \text{H.c.}\right)\right] - \sum_i J_f\left(d^{\dagger}_{i,\uparrow}d_{i,\uparrow} - d^{\dagger}_{i,\downarrow}d_{i,\downarrow}\right). \tag{2}$$

Here, $\mathbf{s}_i = \sum_{\sigma\sigma'} c^{\dagger}_{i,\sigma}\left(\sigma_{\sigma\sigma'}/2\right)c_{i,\sigma'}$ denotes the creation (annihilation) operator of an electron in the metal at site i with spin σ. ε_f is the on-site energy of a metallic atom and t_f the nearest-neighbor hopping integral. J_f is a Stoner-type exchange field, which is set to zero for a nonmagnetic metal. The coupling between the electrode and the OF is described by a transfer integral t_{mf}. Since our focus is on effects coming from the bulk of the OF chain, we here assume spin-independent coupling between the OF and the electrodes.

When a bias voltage V is applied, a spatially varying electric potential is generated along the molecule, which modifies both the electronic and the lattice structure. If the bias is not too large, a linear treatment is justified [35,36], where we assume that a uniform electric field $E = V/[a(N-1)]$ along the molecule is induced. Here, N is the total number of carbon atoms in the main chain and a is the lattice constant. Hence, the Hamiltonian involving the electric potential is

$$H_{\text{E}} = -\sum_{i,\sigma} eE\left[\left(i - \frac{N+1}{2}\right)a + u_i\right]c^{\dagger}_{i,\sigma}c_{i,\sigma} + \sum_i eE\left[\left(i - \frac{N+1}{2}\right)a + u_i\right]. \tag{3}$$

Here, e is the electronic charge of an electron. The first term is the electric potential of the π-electrons, and the second term is the potential of the ion cores.

Before calculating the transport properties, one needs to obtain the stationary structure of the OF under bias. Using the mean-field approximation to treat the electron–electron and spin–spin interactions, the eigenenergies $\varepsilon_{\mu,\sigma}$ and the eigenstates $|\psi_{\mu,\sigma}\rangle$ with (real) eigenfunctions $\psi_{\mu,\sigma,i}$ can be calculated in Wannier space by solving the Schrödinger equation

$$\begin{aligned}\varepsilon_{\mu,\sigma}\psi_{\mu,\sigma,i} &= \sum_j H^{\text{MF}}_{\sigma,ij}\psi_{\mu,\sigma,j}\\ &\equiv -\left(1-\delta_{i,N}\right)t_i\psi_{\mu,\sigma,i+1} - \left(1-\delta_{i,1}\right)t_{i-1}\psi_{\mu,\sigma,i-1}\\ &\quad + V_i\psi_{\mu,\sigma,i} + U\overline{n}_{i,-\sigma}\psi_{\mu,\sigma,i}\\ &\quad + W\left(1-\delta_{i,1}\right)\overline{n}_{i-1}\psi_{\mu,\sigma,i}\\ &\quad + W\left(1-\delta_{i,N}\right)\overline{n}_{i+1}\psi_{\mu,\sigma,i}\\ &\quad + J\delta_{i,\text{odd}}\left\langle S^z_i\right\rangle\frac{\sigma}{2}\psi_{\mu,\sigma,i}.\end{aligned} \tag{4}$$

Here, we set $t_i = t_0 - \alpha y_i$ and

$$V_i = |e|E\left[\left(i - \frac{N+1}{2}\right)a + u_i\right].$$

$H^{\text{MF}}_{\sigma,ij}$ is the matrix element of the mean-field Hamiltonian for the π-electrons with spin σ. The spin quantum number σ assumes the numerical values ↑ ≡ 1 and ↓ ≡ −1. $\overline{n}_{i,\sigma} = \sum_{\mu,\text{occ.}}|\psi_{\mu,\sigma,i}|^2$ is the average occupation number of π-electrons at site i with spin σ. The sum is over all occupied states. $\overline{n}_i = \overline{n}_{i,\sigma} + \overline{n}_{i,-\sigma}$ is the total occupation number at site i. $\langle S^z_i\rangle$ is the average value of the radical spin, assumed to be in the z-direction. The lattice distortion y_i in Equation 4 is determined by minimizing the total energy, $\partial E(\{u_i\})/\partial\{u_i\} = 0$, which leads to the equation

$$y_i = -\frac{2\alpha}{K}\sum_{\mu,\sigma,\text{occ.}}\psi_{\mu,\sigma,i}\psi_{\mu,\sigma,i+1} - \frac{|e|E}{K}\overline{n}_i + \lambda, \tag{5}$$

where the Lagrange multiplier λ guarantees that the length of the molecular chain remains unchanged, i.e., $\sum_i y_i = 0$. A fixed-end boundary condition is adopted since the two ends of

the molecular chain are attached to the electrodes. Equation 4 and Equation 5 are solved self-consistently [14].

In the regime of coherent transport, the current with spin σ through the device can be calculated from the Landauer-Büttiker formula [37]

$$I_\sigma(V)=\frac{e}{h}\int_{-\infty}^{\infty}T_{\sigma\sigma}(E,V)\left[f\left(E,\mu_L\right)-f\left(E,\mu_R\right)\right]\mathrm{d}E. \quad (6)$$

Here, $T_{\sigma\sigma}(E,V)=\mathrm{Tr}[\Gamma_L G_{\sigma\sigma}(E,V)\Gamma_R G^{\dagger}_{\sigma\sigma}(E,V)]$ is the spin-dependent transmission coefficient determined from the retarded single-particle Green's function $G_{\sigma\sigma}(E,V)$ for the central OF [38]. $\Gamma_{L/R}$ denotes the broadening matrix and $f(E,\mu_{L/R})$ is the Fermi distribution function of the left (L) or right (R) electrode with electrochemical potential $\mu_{L/R} = E_F \pm eV/2$ and Fermi energy E_F.

For the numerical calculations we use parameter values appropriate for poly-BIPO [14,31,39]: t_0 = 2.5 eV, α = 4.1 eV/Å, K = 21.0 eV/Å^2, and $\langle S_i^z\rangle = -1/2$. We introduce dimensionless interaction strengths $j = J/t_0$, $u = U/t_0$, and $w = W/t_0$. The parameters for the electrodes vary according to the material adopted. For details on the parameters, see the related works [31-33].

Spin filtering in metal/OF/metal devices

A spin filter is meant to generate a strongly spin-polarized current from an unpolarized current source and is a crucial element for spintronics. Using a magnetic interlayer in a sandwich structure is a valid method that has been reported in inorganic devices, such as Ag/EuSe/Al and Ag/EuS/Al [40,41]. To obtain a current with strong SP in those devices, a strong magnetic field is usually necessary to generate either spin-selective barriers or spin splitting of the resonant level. Interlayers made of OFs deserve to be explored for the possibility to realize an intrinsic organic spin filter. Here, we review progress in this direction made by some of us [31].

We have constructed the OF device by sandwiching the OF molecule between two identical nonmagnetic electrodes [31]. The spin-resolved and the total current calculated using the theory discussed in the previous section are shown in Figure 2a. The SP $P = (I_\uparrow - I_\downarrow)/(I_\uparrow + I_\downarrow)$ of the current is given in Figure 2b. We have found a step-like current–voltage curve with a threshold voltage, which is common in nanojunctions. The spin-up and spin-down currents differ both in threshold voltage and magnitude. This leads to a non-monotonic dependence of the SP on bias, as shown in Figure 2b. In particular, nearly complete SP is obtained in the bias range of [0.7, 1.0] V, which means that strong spin filtering is realized in this bias range. The second peak of the SP appears at about 1.8 V but the SP is reduced to about 40%.

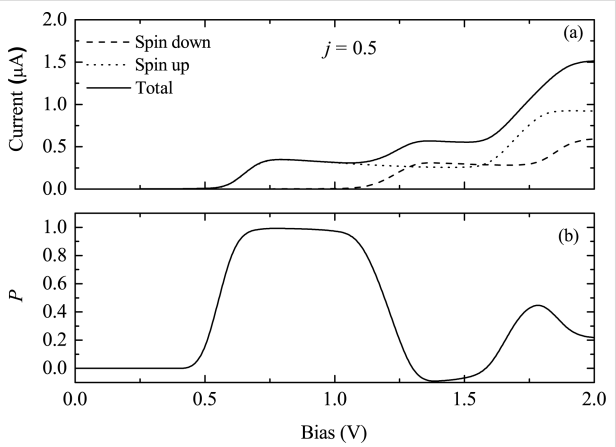

Figure 2: (a) Current–voltage characteristics for a OF device with N = 20 carbon sites. (b) Spin polarization of the current as a function of bias. Reproduced with permission from [31], copyright 2007 American Physical Society.

In order to understand the spin filtering effect, we have calculated the spin-resolved density of states (DOS) of π-orbitals from the Green's function with $\mathrm{DOS}_\sigma(E,V) = -(1/\pi)\mathrm{Im}[G_{\sigma\sigma}(E,V)]$. The result for 0.8 V is shown in Figure 3. Evidently, the DOS is spin-split due to the coupling with radical spins. An energy gap of about 1.0 eV appears between the spin-down highest occupied molecular orbital (HOMO) and the spin-up lowest occupied molecular orbital (LUMO). For a bias of 0.8 V, only the spin-up LUMO falls into the bias window and contributes to the current. Therefore, the current is nearly fully spin polarized. When the bias in-

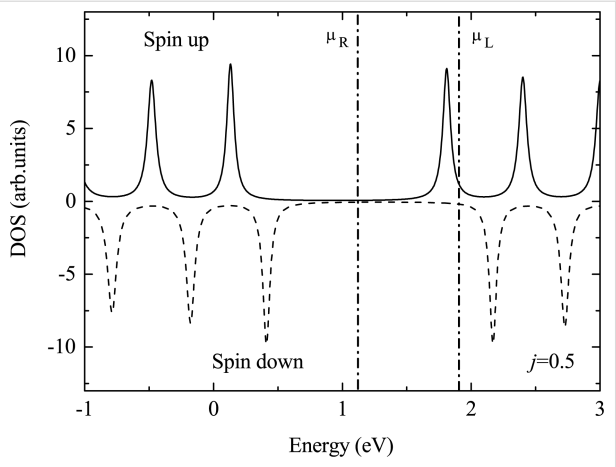

Figure 3: Density of states of the OF device at a bias of 0.8 V. Here, the Fermi energy of the electrodes is taken to be E_F = 1.5 eV, which for a bias voltage of V = 0.8 V leads to the indicated chemical potentials $\mu_{L,R} = E_F \pm 0.4$ eV. Reproduced with permission from [31], copyright 2007 American Physical Society.

creases, additional spin-up and spin-down orbitals will enter the bias window alternately, which results in the oscillation of the SP. Full spin filtering will not be reached again since the current includes contributions from electrons with different spins.

The effects of the spin–spin and e–l interactions on the SP need to be clarified. The dependence of the SP on the spin–spin correlation parameter j is shown in Figure 4a, where the bias is fixed to 0.8 V. It is found that the SP increases rapidly, and then reaches the maximum value of nearly 100% at about $j = 0.25$. The intrinsic mechanism can be understood as follows: Without spin coupling, the molecular π-orbitals are spin-degenerate and the SP of the current is zero. In the case of nonzero j, a spin splitting of the π-orbitals occurs, where the spin-up orbitals are lowered in energy and the spin-down orbitals are raised. This spin splitting reduces the number of spin-down states in the conducting bias window, while it increases the number of spin-up states. As a result, the SP is increased. When the spin-down states are completely pushed out of the bias window, a nearly complete SP is achieved. Note that due to the existence of a large Peierls gap arising from the e–l interaction, the bias window continues to contain only spin-up states when j is increased further so that the SP will remain close to 100%. This means that the strong e–l interaction is crucial for spin filtering.

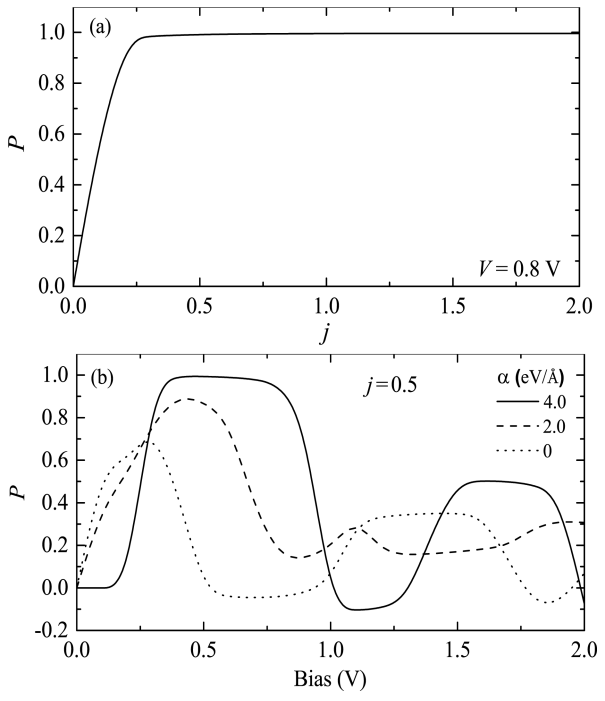

Figure 4: (a) Spin polarization of the current as a function of the spin coupling strength j for a bias of 0.8 V. (b) Bias-dependent spin polarization of the current for three different values of the electron–lattice coupling strength α. Reproduced with permission from [31], copyright 2007 American Physical Society.

To elucidate the role of e–l interaction, we show, in Figure 4b, the SP of the current for three different strengths α of the e–l interaction at $j = 0.5$. $\alpha = 0$ corresponds to a rigid chain without dimerization. In the case of a vanishing ($\alpha = 0$) or weak ($\alpha = 2.0$) e–l interaction, the SP occurs as soon as the bias is applied. However, for a strong e–l interaction ($\alpha = 4.0$), a threshold voltage of about 0.2 V appears. Moreover, the maximum SP and the plateau width at the maximum SP increase with the e–l interaction. The reason is explained in the following: The spin coupling j induces a spin splitting of the π-orbitals, while the e–l interaction generates a Peierls gap separately for the orbitals with different spins. With the present parameters, the Peierls gaps for different spins are not symmetric to the Fermi level of the electrode. The numbers of spin-up and spin-down orbitals falling into the bias window are different, which is adjusted by the e–l interaction. This is the reason why the SP depends on the e–l interaction. It is noted that a nearly complete SP is obtained only for strong e–l interaction. In our calculation, there is a Peierls gap of about 1.65 eV. When the bias is increased to 0.3 V, only one spin-up orbital falls into the bias window, whereas the spin-down DOS is very small due to the Peierls gap. This leads to nearly complete SP. In the case of zero or weak e–l interaction, both spin-up and spin-down orbitals are close to the Fermi energy and contribute to the current, which is thus not fully spin polarized. An analogous phenomenon has been reported in a double-bend structure of a quantum wire, where an antiresonance gap is generated by weak lateral magnetic modulations, which leads to a large SP of the current [42]. Wang [27] also proposed a spin filtering effect in the same material coupled to a quantum wire, which is assumed to be manipulated by a gate voltage. We note that although a different model without e–l interaction was adopted in his work, a Hubbard gap still appears in the molecular band to separate the spin-up and spin-down energy levels.

The spin filtering effect in OF devices was also reported in other theoretical works. For the SSH model and using a Green's function method, Sadaghi et al. [43] have investigated the spin-dependent transport through an OF chain with an odd number of sites, where a soliton in the main chain preexists. They found that spin filtering takes place when the spins of the soliton and the radicals point in opposite directions. Sun [44] has discussed the SP of the current through OF devices in the presence of ferromagnetic leads. A large SP is obtained in a specific bias region, which is enhanced by the polarization ratio of the magnetic electrode, and suppressed by the on-site Coulomb repulsion. Even in a long OF polymer chain, a spin filtering effect was obtained in the regime of polaron transport. Wang et al. [45] have found that a polaron moving under an electric field may be trapped near the spin radicals unless the field is stronger than a critical value. The magnitude of the critical field depends

on the spin of the polaron, which implies a spin-filtering effect of the polaron transport.

Multi-state magnetoresistance in ferromagnet/OF/ferromagnet junctions

Further control over an OF device can be gained by employing ferromagnetic electrodes. Ferromagnetic junctions are the basic building blocks for spin valves to realize the magnetoresistance (MR) effect, which is important in spintronics for magnetic storage. By manipulating the relative magnetic magnetization of the two electrodes with a magnetic field, e.g., parallel or antiparallel, the resistance of the device can be switched between low-resistance and high-resistance states. The utilization of organic molecules as the interlayer has been studied in many experiments, motivated by the long spin relaxation time [4]. Examples are the giant magnetoresistance (GMR) and the room-temperature tunneling magnetoresistance (TMR) in LSMO/Alq_3/Co junctions [6-8].

The MR in the ferromagnet/OF/ferromagnet junction Co/poly-BIPO/Co has been studied theoretically in the work [32], which we here review. The DOS of the isolated Co electrode and the OF are shown in Figure 5a and Figure 5b, respectively. The DOS of Co is consistent with one fully occupied majority-spin band and one half-filled minority-spin band [46]. Because all three components of the device are ferromagnetic, there exist four fundamentally distinct collinear alignments of the magnetizations. We fix the radical spins of the OF in the z-direction, while the magnetization of each ferromagnet may be parallel or antiparallel to the z-direction. The four configurations are labeled as C1 (↑↑↑), C2 (↓↑↓), C3 (↑↑↓), and C4 (↓↑↑) and are illustrated in Figure 5c.

The current–voltage characteristics for the four magnetization configurations are shown in Figure 6. It is found that the threshold voltage and the maximum magnitude of the current

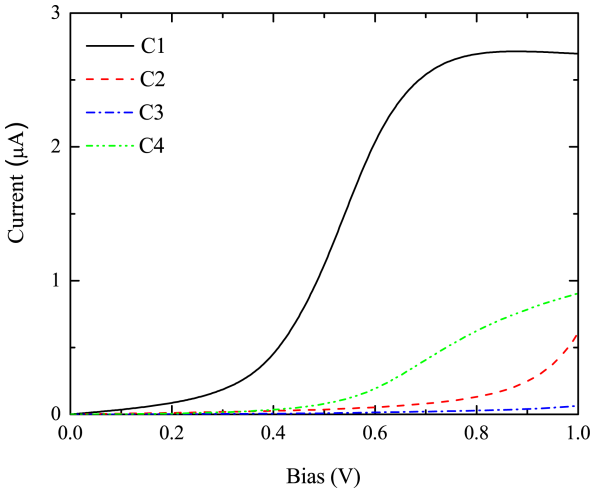

Figure 6: Current–voltage characteristics of a Co/OF/Co junction for the four magnetization configurations C1, C2, C3, and C4 shown in Figure 5c. Reproduced with permission from [32], copyright 2014 AIP Publishing.

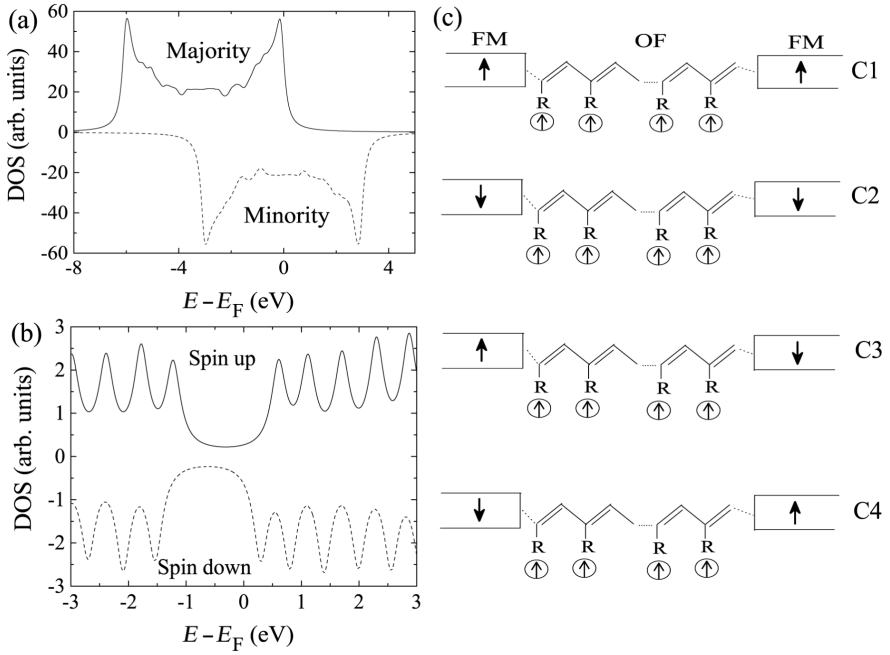

Figure 5: Density of states of (a) Co and (b) the OF poly-BIPO. The molecular length is 20 sites. (c) Schematic of the magnetization configurations C1, C2, C3, and C4 in the ferromagnet/OF/ferromagnet device. Reproduced with permission from [32], copyright 2014 AIP Publishing.

strongly depend on the magnetization configuration. Configuration C1 conducts first, with the smallest threshold voltage of about 0.3V. The maximum current of about 2.7 μA is reached when the bias exceeds 0.8 V. Larger threshold voltages of about 0.9 V and 0.6 V, respectively, is observed for C2 and C4. The current at 1.0 V is 0.5 μA for C2 and 0.9 μA for C4. On the other hand, the current for C3 is strongly suppressed within the calculated bias region. The different transport properties indicate that a multi-state MR effect can be realized by controlling the magnetization orientations of the electrodes and the central OF. One can quantify the bias-dependent multi-state MR as $\mathrm{MR}_i(V) = [R_{\mathrm{C}i}(V) - R_{\mathrm{C1}}(V)]/R_{\mathrm{C}i}(V)$. Threshold voltage, maximum current, and multi-state MR for each case are summarized in Table 1. Obviously, four values of MR are realized with the change of the magnetization configuration. A maximum MR of 98% is obtained at a bias of 1.0 V.

Table 1: Threshold voltage (V_{th}), maximum current for bias voltage in [0,1] V (I_{max}), and multi-state magnetoresistance (MR) at a bias voltage of 1 V for the different magnetization configurations. Reproduced with permission from [32], copyright 2014 AIP Publishing.

configuration	V_{th} (V)	I_{max} (μA)	MR_i (V = 1.0 V)
C1 (↑↑↑)	0.3	2.7	0
C2 (↓↑↓)	0.9	0.5	82%
C3 (↑↑↓)	>1.0	0.06	98%
C4 (↓↑↑)	0.6	0.9	66%

The mechanism of the multi-state MR can be understood as follows: In the present device, electrons tunnel between the Co electrodes through the OF interlayer. In the two-current model [47], and according to the band structure of Co, the electron tunneling in C1 (C2) happens between the two half-filled spin-down (spin-up) Co bands. The situation is different in C3 (C4), where the tunneling takes place from the completely filled spin-up (spin-down) band of the left electrode to the half-filled spin-up (spin-down) bands of the right electrode. This difference is the origin of TMR in conventional spin valves. If the central layer is nonmagnetic, the resistance for C1 should be same as the one for C2, and analogously for C3 and C4. Thus two-state MR, for parallel and antiparallel alignments, will be obtained. However, in the presence of the OF, the π-orbitals in the OF are spin-split. In particular, spin filtering occurs near the Fermi energy, as discussed in the previous section on spin filtering. So, the spin-dependent tunneling for parallel and antiparallel configurations will suffer a further spin selection in the OF, which will induce a splitting of the resistance depending on the spin of the transported electrons. There is a pronounced difference between the currents for configurations C3 and C4, the magnetization configurations of which are mirror images of one another. The main origin of this asymmetry is that in the right (drain) electrode the spin-down band is completely occupied for C3 so that spin-down electrons cannot tunnel into it; spin-down electrons carry most of the current, as shown below. On the other hand, for C4 the spin-down band in the drain electrode is half filled. The additional asymmetry due to the spin radicals

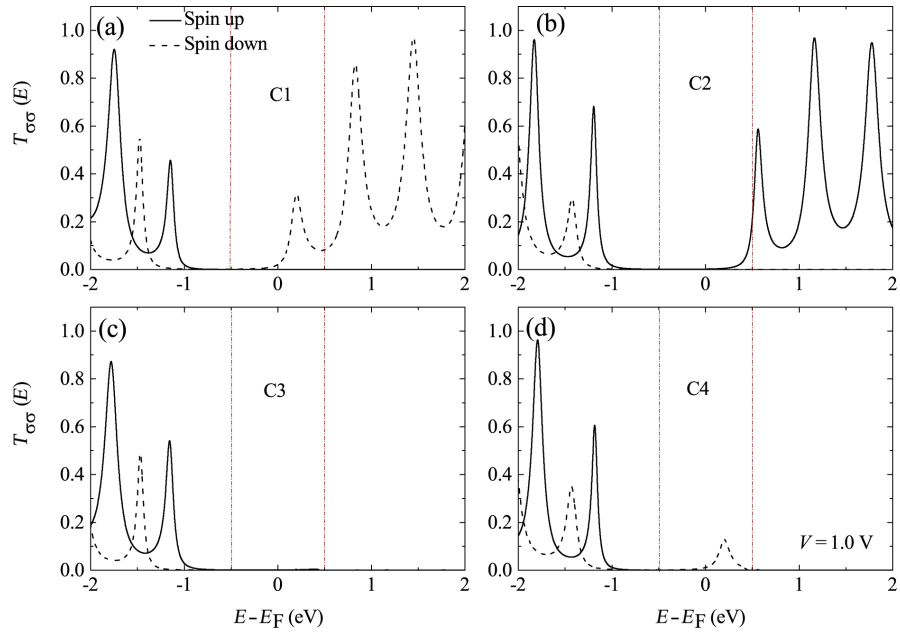

Figure 7: Spin-dependent transmission $T_{\sigma\sigma}(E)$ as a function of energy close to the Fermi energy for the four magnetization configurations. Panels (a–d) correspond to configurations C1–C4, respectively. The bias voltage is V = 1.0 V. Reproduced with permission from [32], copyright 2014 AIP Publishing.

being attached only to odd sites, while the length of the OF is even (N = 20), does not play a large role.

The above analysis may be verified by a calculation of the transmission spectrum. Figure 7 shows the spin-dependent transmission of the four configurations at 1.0 V. For C1 and C4, an efficient transmission peak contributed by the spin-down electrons is found in the bias window, which leads to the higher current shown in Figure 6. However, for C2 and C3, there is no transmission peak in the bias window, and thus a low current is obtained. This is because for the present parameters, the molecular orbital of the OF closest to the Fermi energy is the spin-down LUMO, as shown in Figure 5b. Therefore, only spin-down electrons can tunnel at low bias for C1 and C4. Note that for C2 the tail of the transmission peak from the higher-energy spin-up LUMO enters the bias window, which contributes to the small current seen in Figure 6.

Other designs of four-state resistive devices have also been reported, where a ferroelectric barrier was introduced between two ferromagnets [48-50]. In these designs, both a magnetic field and an electric field are necessary to manipulate both the relative magnetization orientation of the electrodes and the polarization of the barrier. We note that the OF multi-state MR device presented here can be manipulated by only one magnetic field that controls the relative magnetizations. For this, it is useful to employ two ferromagnets with different coercive fields, such as LSMO (30 Oe) and Co (150 Oe) [6]. Then, the different magnetization configurations can be realized by tuning the strength of the magnetic field.

The exploration of OFs in MR devices is still in its infancy except for several pioneering experimental works. For example, Yoo et al. [25] and Li et al. [26] have sandwiched the organic magnet V[TCNE]$_x$ between two Au electrodes or Fe and Al electrodes and demonstrated a room-temperature MR. Organic magnets have also been utilized as spin injectors in organic spin valves. Yoo et al. [51] have constructed V[TCNE]$_x$/rubrene/LSMO junctions and have observed a MR of about 2.5%. Even all-organic spin valves employing organic magnets as both the spin injector and detector have been designed [52], but only a small negative MR of about 0.04% has been observed. However, based on these proofs of principle and the discussed theoretical progress, the utilization of OFs in MR devices looks promising.

Spin-current rectification in asymmetric magnetic co-oligomer devices

The aforementioned studies of spin-dependent transport through OF devices are limited to uniform OF molecular chains. In this section, we discuss the electron transport through an asymmetric OF chain, e.g., a magnetic/nonmagnetic co-oligomer, where a spin-current rectification phenomenon can occur. Rectification of the charge current (CC) refers to an asymmetric current–voltage curve under reversal of the bias voltage. Molecular rectification has been proposed and investigated in the past decades, where the spatial asymmetry of the device, either at the molecule/electrode interfaces or in the central molecule, is necessary [36,53-57]. Spin-current rectification describes an asymmetric spin current (SC) upon reversal of the bias, which is more complex than a CC rectification. One may define the CC as $I_c = I_\uparrow + I_\downarrow$ and the SC as $I_s = (\hbar / 2e)(I_\uparrow - I_\downarrow)$. Hence, a SC contains two characteristics: the amplitude of the current and its SP. As a result, the asymmetry of the SC upon bias reversal can have two origins: The first is that the amplitude of the current is not symmetric, while the SP remains unchanged. This is analogous to CC rectification. We call this effect parallel SC rectification. The second is that the SP is reversed upon bias reversal, which we call antiparallel SC rectification. In the following, we review results [33] that demonstrate that both types of SC rectification may be realized in suitably designed OF devices.

The OF spin diode consists of a magnetic co-oligomer coupled to two nonmagnetic electrodes [33]. The central magnetic co-oligomer is composed of a left OF molecule and a right nonmagnetic one, such as poly-BIPO and polyacetylene, respectively. The magnetic co-oligomer may be described by the Hamiltonian H_{OF} in Equation 1, with the modification that the coupling to radical spins only exists for the odd sites of the left half chain. For simplicity, the electron–electron interaction has been neglected. Results for the CC and SC through the device for the Fermi level in the middle of molecular gap, i.e., $E_F = 0$, are shown in Figure 8. In the considered bias region of [−1.0 V,+1.0 V], the CC is symmetric upon bias reversal. The

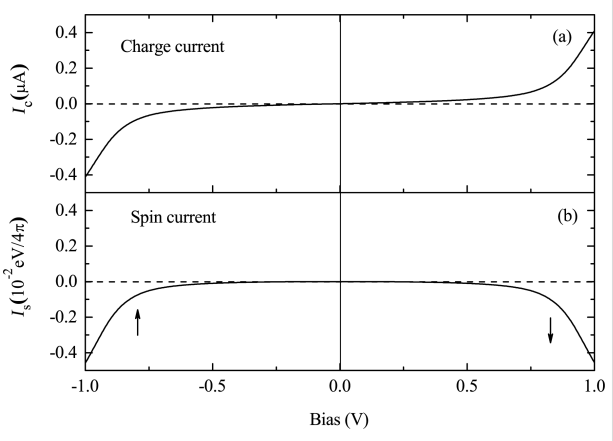

Figure 8: Bias-dependent (a) CC and (b) SC through an asymmetric OF device with N = 20 and E_F = 0. The arrows in (b) indicate the SP of the current. Reproduced with permission from [33], copyright 2008 AIP Publishing.

CC begins to increase quickly when the bias approaches ±0.8 V. The magnitude of the current reaches 0.4 μA at ±1.0 V. Rectification of the CC is not observed. However, for the SC, the SP is reversed, although the amplitude of the SC is symmetric. According to the definition of the SC, the current is spin-down polarized for positive bias, whereas it is spin-up polarized for negative bias. This is the antiparallel rectification of the SC defined above.

The mechanism of the antiparallel rectification can be explored by investigating the spin-dependent transmission under various biases. In Figure 9, the spin-resolved transmission spectra at 0 V and ±1.0 V are shown. At 0 V, there are two transmission peaks with equal distance from the Fermi energy, which result from the spin-up LUMO and the spin-down HOMO. Applying a positive bias of 1.0 V, the transmission peak of the spin-down HOMO is shifted closer to the Fermi energy and enters the bias window, which contributes a spin-down polarized current. Conversely, when a negative bias of −1.0 V is applied, only the spin-up LUMO peak is in the bias window. One can show that the spin-down LUMO and the spin-up HOMO evolve symmetrically with the bias. As a result, the magnitude of the current is symmetric upon bias reversal but the SP is reversed.

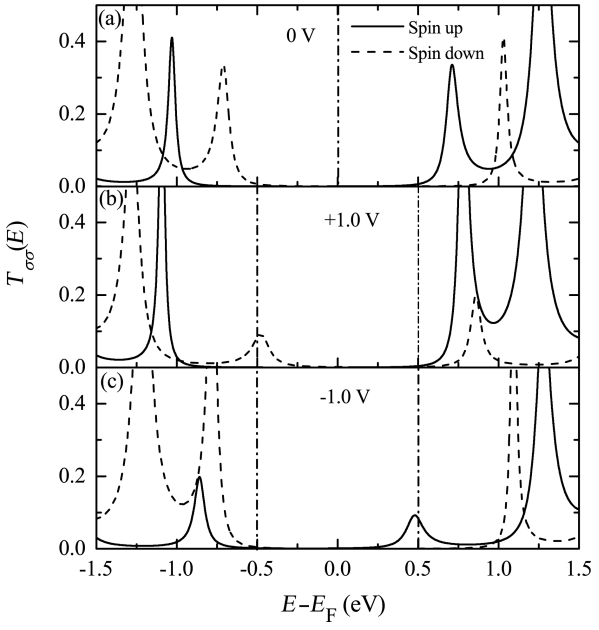

Figure 9: Spin-dependent transmission near the Fermi energy for $N = 20$ and $E_F = 0$ at the bias voltages (a) 0 V, (b) +1.0 V, and (c) −1.0 V. Reproduced with permission from [33], copyright 2008 AIP Publishing.

The relative position of the electrode Fermi level with respect to the molecular energy gap is important for the rectification behavior. If the Fermi level does not lie in the middle of the molecular energy gap, the symmetry of the current contributions from the two nearest peaks is broken. Results for an electrode Fermi level of $E_F = 0.3$ eV are shown in Figure 10. Both the CC and SC are rectified with a similar shape of their current–voltage curves. A larger current is obtained for positive bias, where the rectification ratio, defined as $RR(V) = -I_c(V)/I_c(-V)$ for CC and $SRR(V) = -I_c(V)/I_c(-V)$ for SC, reaches about 22 at 0.8 V for both CC and SC. The rectification of SC is of the type of parallel rectification, where only the amplitude of the current is asymmetric and the SP remains unchanged upon bias reversal. The underlying mechanism can be understood from the bias-dependent transmission spectrum, which is shown in Figure 11. In

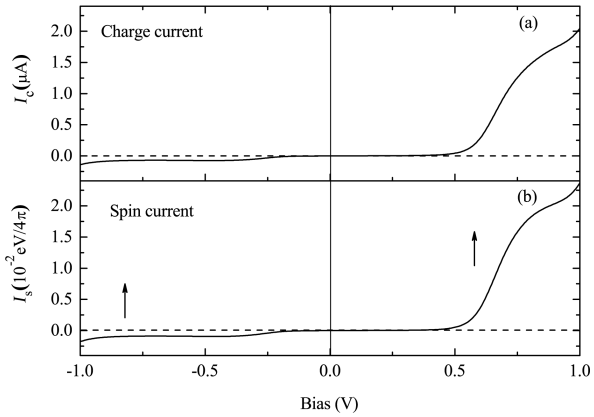

Figure 10: Bias-dependent (a) CC and (b) SC for $N = 32$ and $E_F = 0.3$ eV. The arrows in panel (b) indicate the SP of the current. Reproduced with permission from [33], copyright 2008 AIP Publishing.

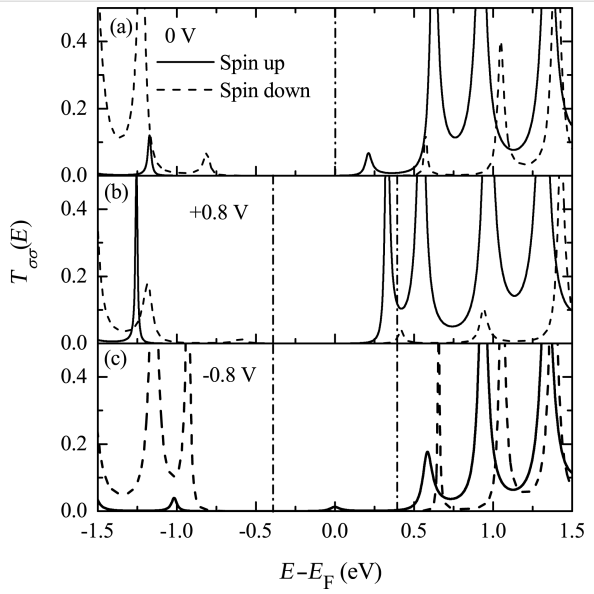

Figure 11: Spin-dependent transmission near the Fermi energy for $N = 32$ and $E_F = 0.3$ eV at the bias voltages (a) 0 V, (b) +0.8 V, and (c) −0.8 V. Reproduced with permission from [33], copyright 2008 AIP Publishing.

this case, the transmission peak from the spin-up LUMO is mainly responsible for the current under either positive or negative bias. However, the height of the peak is strongly enhanced at positive bias compared to negative bias, leading to a larger spin-up polarized current at positive bias.

In principle, the asymmetric transport properties of the OF spin diode originates from the asymmetric response of the molecular eigenstates to a bias voltage. Figure 12 shows the bias-dependent molecular eigenlevels and the electronic localization of the two orbitals closest to the Fermi energy, i.e., the spin-up LUMO and the spin-down HOMO. The localization of an eigenstate is defined as $\xi_{\mu,\sigma}(V)=\sum_i|\psi_{\mu,\sigma,i}(V)|^4$ [58], where $\psi_{\mu,\sigma,i}(V)$ is the wave function of the molecular eigenstate μ with spin σ at site i, for a bias voltage V. A larger ξ means a more strongly localized orbital. Figure 12a demonstrates an asymmetric shift of the molecular eigenlevels under positive and negative biases, especially for the orbitals near the Fermi energy. The shift is opposite for the spin-up LUMO and the spin-down HOMO. This shift of the molecular eigenlevels corresponds to the asymmetric shift of transmission peaks shown in Figure 9 and Figure 11. The electronic localization for the spin-up LUMO and the spin-down HOMO is also asymmetric upon bias reversal. For example, the spin-up LUMO tends to be delocalized at positive bias, whereas it becomes more localized at negative bias. A more delocalized orbital will lead to a larger transmission coefficient, which is the reason for the rectification shown in Figure 11.

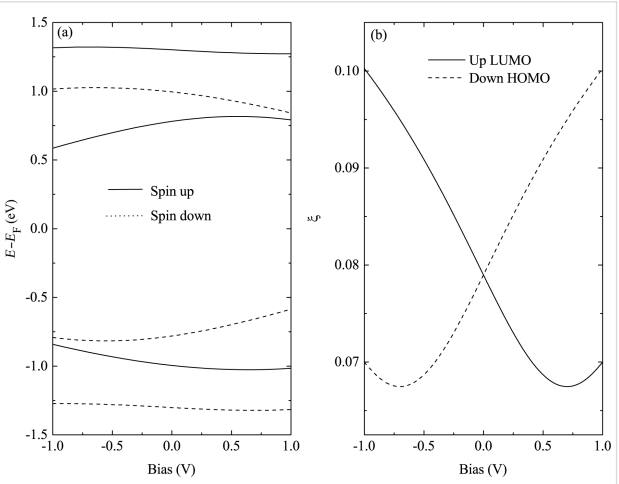

Figure 12: Bias-dependent (a) molecular eigenlevels and (b) electronic localization of the spin-up LUMO and the spin-down HOMO. Reproduced with permission from [59], copyright 2016 Elsevier.

It should be pointed out that the bias-induced evolution of molecular eigenstates is opposite for the spin-up LUMO and the spin-down HOMO, including the energy shift and the change of electronic localization. If the dominant orbital for the transport is changed, e.g., by using a gate voltage, an interesting phenomenon, namely an inversion of the rectification, may happen. This has been discussed in detail in [59]. Note that the concept of SC rectification reviewed here is based on spin-polarized charge transport. This phenomenon has also been reported in a molecular junction with one ferromagnetic and one nonmagnetic electrode [60]. A distinct scheme of rectification compared to our picture has been proposed recently, which leads to a pure SC, that is, a flow of angular momentum without accompanying CC. This type of SC rectification may be generated by spin pumping techniques [61] or via the spin-Seebeck effect [62].

The above proposed prototype of a molecular spin diode has been supported by ab initio calculations. Zhu et al. [63] have studied a biradical (5-bromo-2,4-dimethoxy-1,3-phenylene)-bis(*N*-*tert*-butylnitroxide) molecule connected to two gold electrodes. The molecule is magnetic and spatially asymmetric. The authors have found CC and SC rectification through the device. A high rectification ratio exceeding 100 is reported. Experimental tests of the theoretical predictions are highly desirable.

Conclusion

In this contribution, theoretical results on spin-dependent electron transport through OFs have been reviewed, focusing on our designs of several OF spintronic devices. They are based on a combination of the extended SSH model and the Green's function method, including the intrinsic interactions in OFs, i.e., the e–l interaction and the coupling between the spins of π-electrons and radicals. Using the pure OF poly-BIPO as an example, we have discussed the realization of three important concepts for spintronics with OFs: spin filtering, magnetoresistance, and spin-current rectification.

Spin filtering can be realized with metal/OF/metal sandwich structures [31]. An oscillating SP of the current as a function of the bias voltage in predicted for such devices. An extremely large SP is achieved in a certain bias region, which shows that a strong spin-filtering effect is realized. By examining the DOS, it was found that the spin splitting of π-orbitals induced by the coupling between the spins of π-electrons in the main chain and the residual spins of radicals is responsible for the SP, while the large Peierls energy gap induced by the strong e–l interaction is crucial for the nearly complete SP.

Then, a magnetoresistive device based on coupling the OF to two ferromagnetic electrodes [32] has been reviewed. Considering the possible orientations of the magnetization in each component, four distinct magnetic configurations of the device were proposed and the transport in each case were investigated.

By calculating the current–voltage characteristics, it was found that the current depends strongly on this configuration and a four-state magnetoresistance was predicted. The intrinsic mechanism was revealed by the transmission analysis, where the spin-resolved electron tunneling between the two ferromagnets suffers a further spin selection by the OF. Using two ferromagnets with different coercive fields as the electrodes should allow one to manipulate a multi-state magnetoresistance device by a magnetic field.

Finally, the additional functionality of spin-current rectification can be implemented by replacing the OF by an asymmetric magnetic co-oligomer, for example consisting of poly-BIPO and polyacetylene [33]. It was found that two types of SC rectification may be realized in such spin diodes by adjusting the position of the Fermi energy of the electrodes relative to the molecular energy levels. For parallel SC rectification, only the amplitude of the SC is asymmetric under reversal of the bias, while the SP remains unchanged. This effect is accompanied by a CC rectification. The other type is antiparallel SC rectification, where only the SP of the current is reversed under reversal of the bias. The origin of the SC rectification can be traced back to the bias-induced asymmetric response of molecular eigenstates, which involves both an asymmetric shift of eigenlevels and an asymmetric localization of orbitals.

We should mention that the reviewed works are limited to the regime of coherent transport in nanoscale devices. A comprehensive study beyond coherent transport is required for the future. Especially for large-scale devices composed of long OF polymer chains, polaronic transport is possible, which is very common in organic materials. One of our works not discussed in detail here exhibits a distinctive property of polarons in OFs caused by the spin radicals, namely spin-charge disparity [64]: The charge and spin distributions of a polaron are shifted with respect to each other. This is expected to lead to novel effects for polaron transport in OFs, which will be investigated with a nonadiabatic dynamics method in the future. Furthermore, the coupling between π-electron and radical spins has so far been treated in a mean-field approximation, which neglects the dynamics of the radical spins. Spin and also charge transport is expected to be affected by the dynamics, which requires a quantum-mechanical description since the radicals typically carry spins $S = 1/2$. Another aspect worth studying is the role of disorder, which is generically important in one-dimensional systems [65]. Finally, a simple spin-independent interfacial coupling between the OFs and the electrodes is considered here. In actual devices, orbital hybridization may happen between the interacting atoms, which will modify the spin states of both the molecules and the metal atoms close to the interface. Ab initio tools will be useful in determining the details. In spite of this, we hope that the works discussed in this contribution deepen our understanding of the electron transport through OFs, and increase the interest in the design of organic spintronic devices with OFs.

Acknowledgements

Support from the Natural Science Foundation of China (Nos. 11374195, 11674197), the Natural Science Foundation of Shandong Province China (No. ZR2014AM017), the Taishan Scholar Project of Shandong Province, the Excellent Young Scholars Research Fund of Shandong Normal University, the Excellence Initiative of the German Federal and State Governments, and the Deutsche Forschungsgemeinschaft through Research Unit FOR 1154 “Towards Molecular Spintronics” are gratefully acknowledged.

References

1. Naber, W. J. M.; Faez, S.; van der Wiel, W. G. *J. Phys. D: Appl. Phys.* **2007,** *40,* R205. doi:10.1088/0022-3727/40/12/R01
2. Dediu, V. A.; Hueso, L. E.; Bergenti, I.; Taliani, C. *Nat. Mater.* **2009,** *8,* 707. doi:10.1038/nmat2510
3. Sugawara, T.; Matsushita, M. M. *J. Mater. Chem.* **2009,** *19,* 1738. doi:10.1039/b818851n
4. Pramanik, S.; Stefanita, C.-G.; Patibandla, S.; Bandyopadhyay, S.; Garre, K.; Harth, N.; Cahay, M. *Nat. Nanotechnol.* **2007,** *2,* 216. doi:10.1038/nnano.2007.64
5. Sanvito, S. *Nat. Phys.* **2010,** *6,* 562. doi:10.1038/nphys1714
6. Xiong, Z. H.; Wu, D.; Vardeny, Z. V.; Shi, J. *Nature* **2004,** *427,* 821. doi:10.1038/nature02325
7. Santos, T. S.; Lee, J. S.; Migdal, P.; Lekshmi, I. C.; Satpati, B.; Moodera, J. S. *Phys. Rev. Lett.* **2007,** *98,* 016601. doi:10.1103/PhysRevLett.98.016601
8. Sanvito, S. *Chem. Soc. Rev.* **2011,** *40,* 3336. doi:10.1039/c1cs15047b
9. Korshak, Yu. V.; Medvedeva, T. V.; Ovchinnikov, A. A.; Spector, V. N. *Nature* **1987,** *326,* 370. doi:10.1038/326370a0
10. Cao, Y.; Wang, P.; Hu, Z.; Li, S.; Zhang, L.; Zhao, J. *Synth. Met.* **1988,** *27,* 625. doi:10.1016/0379-6779(88)90209-3
11. Iwamura, H.; Sugawara, T.; Itoh, K.; Takui, T. *Mol. Cryst. Liq. Cryst.* **1985,** *125,* 251. doi:10.1080/00268948508080104
12. Katulevskii, Yu. A.; Magrupov, M. A.; Muminov, A. A. *Phys. Status Solidi A* **1991,** *127,* 223. doi:10.1002/pssa.2211270125
13. Sugano, T.; Blundell, S. J.; Lancaster, T.; Pratt, F. L.; Mori, H. *Phys. Rev. B* **2010,** *82,* 180401. doi:10.1103/PhysRevB.82.180401
14. Fang, Z.; Liu, Z. L.; Yao, K. L. *Phys. Rev. B* **1994,** *49,* 3916. doi:10.1103/PhysRevB.49.3916
15. Fang, Z.; Liu, Z. L.; Yao, K. L.; Li, Z. G. *Phys. Rev. B* **1995,** *51,* 1304. doi:10.1103/PhysRevB.51.1304
16. Alberola, A.; Pilkington, M. *Curr. Org. Synth.* **2009,** *6,* 66. doi:10.2174/157017909787314894
17. Park, J.; Pasupathy, A. N.; Goldsmith, J. I.; Chang, C.; Yaish, Y.; Petta, J. R.; Rinkoski, M.; Sethna, J. P.; Abruña, H. D.; McEuen, P. L.; Ralph, D. C. *Nature* **2002,** *417,* 722. doi:10.1038/nature00791
18. Liang, W.; Shores, M. P.; Bockrath, M.; Long, J. R.; Park, H. *Nature* **2002,** *417,* 725. doi:10.1038/nature00790

19. Heersche, H. B.; de Groot, Z.; Folk, J. A.; van der Zant, H. S. J.; Romeike, C.; Wegewijs, M. R.; Zobbi, L.; Barreca, D.; Tondello, E.; Cornia, A. *Phys. Rev. Lett.* **2006,** *96,* 206801. doi:10.1103/PhysRevLett.96.206801
20. Timm, C.; Elste, F. *Phys. Rev. B* **2006,** *73,* 235304. doi:10.1103/PhysRevB.73.235304
21. Elste, F.; Timm, C. *Phys. Rev. B* **2006,** *73,* 235305. doi:10.1103/PhysRevB.73.235305
22. Toader, M.; Hietschold, M. *J. Phys. Chem. C* **2011,** *115,* 3099. doi:10.1021/jp111478v
23. Toader, M.; Knupfer, M.; Zahn, D. R. T.; Hietschold, M. *J. Am. Chem. Soc.* **2011,** *133,* 5538. doi:10.1021/ja200168a
24. Timm, C.; Di Ventra, M. *Phys. Rev. B* **2012,** *86,* 104427. doi:10.1103/PhysRevB.86.104427
25. Yoo, J.-W.; Edelstein, R. S.; Lincoln, D. M.; Raju, N. P.; Xia, C.; Pokhodnya, K. I.; Miller, J. S.; Epstein, A. J. *Phys. Rev. Lett.* **2006,** *97,* 247205. doi:10.1103/PhysRevLett.97.247205
26. Li, B.; Zhou, M.; Lu, Y.; Kao, C.-Y.; Yoo, J.-W.; Prigodin, V. N.; Epstein, A. J. *Org. Electron.* **2012,** *13,* 1261. doi:10.1016/j.orgel.2012.03.038
27. Wang, W. Z. *Phys. Rev. B* **2006,** *73,* 235325. doi:10.1103/PhysRevB.73.235325
28. Wang, W. Z. *Phys. Rev. B* **2007,** *75,* 085303. doi:10.1103/PhysRevB.75.085303
29. Su, W. P.; Schrieffer, J. R.; Heeger, A. R. *Phys. Rev. Lett.* **1979,** *42,* 1698. doi:10.1103/PhysRevLett.42.1698
30. Su, W. P.; Schrieffer, J. R.; Heeger, A. R. *Phys. Rev. B* **1980,** *22,* 2099. doi:10.1103/PhysRevB.22.2099
31. Hu, G.; Guo, Y.; Wei, J.; Xie, S. *Phys. Rev. B* **2007,** *75,* 165321. doi:10.1103/PhysRevB.75.165321
32. Hu, G. C.; Zuo, M. Y.; Li, Y.; Ren, J. F.; Xie, S. J. *Appl. Phys. Lett.* **2014,** *104,* 033302. doi:10.1063/1.4862970
33. Hu, G.; He, K.; Xie, S.; Saxena, A. *J. Chem. Phys.* **2008,** *129,* 234708. doi:10.1063/1.3041773
34. Xie, S. J.; Ahn, K. H.; Smith, D. L.; Bishop, A. R.; Saxena, A. *Phys. Rev. B* **2003,** *67,* 125202. doi:10.1103/PhysRevB.67.125202
35. Mujica, V.; Roitberg, A. E.; Ratner, M. *J. Chem. Phys.* **2000,** *112,* 6834. doi:10.1063/1.481258
36. Hu, G. C.; Wei, J. H.; Xie, S. J. *Appl. Phys. Lett.* **2007,** *91,* 142115. doi:10.1063/1.2790076
37. Datta, S. *Electronic Transport in Mesoscopic Systems;* Oxford University Press: New York, NY, U.S.A., 1995; p 148.
38. Ferry, D.; Goodnick, S. M. *Transport in Nanostructures;* Cambridge University Press: Cambridge, United Kingdom, 1997; p 169.
39. Xie, S. J.; Zhao, J. Q.; Wei, J. H.; Wang, S. G.; Mei, L. M.; Han, S. H. *Europhys. Lett.* **2000,** *50,* 635. doi:10.1209/epl/i2000-00317-0
40. Moodera, J. S.; Meservey, R.; Hao, X. *Phys. Rev. Lett.* **1993,** *70,* 853. doi:10.1103/PhysRevLett.70.853
41. Hao, X.; Moodera, J. S.; Meservey, R. *Phys. Rev. B* **1990,** *42,* 8235. doi:10.1103/PhysRevB.42.8235
42. Zhou, J.; Shi, Q. W.; Wu, M. W. *Appl. Phys. Lett.* **2004,** *84,* 365. doi:10.1063/1.1640805
43. Sadeghi, N.; Ketabi, S. A.; Shahtahmassebi, N.; Abolhassani, M. R. *J. Supercond. Novel Magn.* **2015,** *28,* 2203. doi:10.1007/s10948-015-3004-y
44. Sun, S.-J. *Eur. Phys. J. B* **2009,** *72,* 423. doi:10.1140/epjb/e2009-00371-4
45. Wang, H.; Li, Y.; Li, D.-m.; Cui, B.; Liu, D.-S. *Phys. Chem. Chem. Phys.* **2016,** *18,* 503. doi:10.1039/C5CP05789B
46. Papaconstantopoulos, D. A. *Handbook of the Band Structure of Elemental Solids;* Plenum: New York, NY, U.S.A., 1986; pp 163–169.
47. Fert, A. *J. Phys. C* **1969,** *2,* 1784. doi:10.1088/0022-3719/2/10/311
48. Velev, J. P.; Duan, C.-G.; Burton, J. D.; Smogunov, A.; Niranjan, M. K.; Tosatti, E.; Jaswal, S. S.; Tsymbal, E. Y. *Nano Lett.* **2009,** *9,* 427. doi:10.1021/nl803318d
49. Gajek, M.; Bibes, M.; Fusil, S.; Bouzehouane, K.; Fontcuberta, J.; Barthélémy, A.; Fert, A. *Nat. Mater.* **2007,** *6,* 296. doi:10.1038/nmat1860
50. Yin, Y. W.; Raju, M.; Hu, W. J.; Weng, X. J.; Li, X. G.; Li, Q. *J. Appl. Phys.* **2011,** *109,* 07D915. doi:10.1063/1.3564970
51. Yoo, J.-W.; Chen, C.-Y.; Jang, H. W.; Bark, C. W.; Prigodin, V. N.; Eom, C. B.; Epstein, A. J. *Nat. Mater.* **2010,** *9,* 638. doi:10.1038/nmat2797
52. Li, B.; Kao, C.-Y.; Yoo, J.-W.; Prigodin, V. N.; Epstein, A. J. *Adv. Mater.* **2011,** *23,* 3382. doi:10.1002/adma.201100903
53. Aviram, A.; Ratner, M. A. *Chem. Phys. Lett.* **1974,** *29,* 277. doi:10.1016/0009-2614(74)85031-1
54. Metzger, R. M.; Chen, B.; Höpfner, U.; Lakshmikantham, M. V.; Vuillaume, D.; Kawai, T.; Wu, X.; Tachibana, H.; Hughes, T. V.; Sakurai, H.; Baldwin, J. W.; Hosch, C.; Cava, M. P.; Brehmer, L.; Ashwell, G. J. *J. Am. Chem. Soc.* **1997,** *119,* 10455. doi:10.1021/ja971811e
55. Stokbro, K.; Taylor, J.; Brandbyge, M. *J. Am. Chem. Soc.* **2003,** *125,* 3674. doi:10.1021/ja028229x
56. Chen, X. D.; Yageneh, S.; Qin, L. D.; Li, S. Z.; Xue, C.; Braunschweig, A. B.; Schartz, G. C.; Ratner, M. A.; Mirkin, C. A. *Nano Lett.* **2009,** *9,* 3974. doi:10.1021/nl9018726
57. Ng, M.-K.; Lee, D.-C.; Yu, L. *J. Am. Chem. Soc.* **2002,** *124,* 11862. doi:10.1021/ja026808w
58. Yu, Z. G.; Song, X. *Phys. Rev. Lett.* **2001,** *86,* 6018. doi:10.1103/PhysRevLett.86.6018
59. Hu, G. C.; Zhang, Z.; Zhang, G. P.; Ren, J. F.; Wang, C. K. *Org. Electron.* **2016,** *37,* 485. doi:10.1016/j.orgel.2016.07.032
60. Dalgleish, H.; Kirczenow, G. *Phys. Rev. B* **2006,** *73,* 235436. doi:10.1103/PhysRevB.73.235436
61. Rao, J.; Fan, X.; Ma, L.; Zhou, H.; Zhao, X.; Zhao, J.; Zhang, F.; Zhou, S.; Xue, D. *J. Appl. Phys.* **2015,** *117,* 17C725. doi:10.1063/1.4914962
62. Thingna, J.; Wang, J.-S. *Europhys. Lett.* **2013,** *104,* 37006. doi:10.1209/0295-5075/104/37006
63. Zhu, L.; Yao, K. L.; Liu, Z. L. *Chem. Phys.* **2012,** *397,* 1. doi:10.1016/j.chemphys.2011.09.009
64. Hu, G. C.; Wang, H.; Ren, J. F.; Xie, S. J.; Timm, C. *Org. Electron.* **2014,** *15,* 118. doi:10.1016/j.orgel.2013.10.028
65. Rammer, J. *Quantum Transport Theory;* Westview Press: Boulder, CO, U.S.A., 2004.

BEILSTEIN JOURNAL OF NANOTECHNOLOGY

Electronic structure, transport, and collective effects in molecular layered systems

Torsten Hahn*[1], Tim Ludwig[2], Carsten Timm[2] and Jens Kortus[1]

Full Research Paper

Open Access

Address:
[1]Institute of Theoretical Physics, TU Freiberg, Leipziger Str. 23, D-09599 Freiberg, Germany and [2]Institute of Theoretical Physics, Technische Universität Dresden, 01062 Dresden, Germany

Email:
Torsten Hahn* - torstenhahn@fastmail.fm

* Corresponding author

Keywords:
electron correlation; electronic structure; quantum transport; spin transport

Beilstein J. Nanotechnol. **2017,** *8,* 2094–2105.
doi:10.3762/bjnano.8.209

Received: 10 February 2017
Accepted: 08 September 2017
Published: 06 October 2017

This article is part of the Thematic Series "Towards molecular spintronics".

Guest Editor: G. Salvan

Abstract

The great potential of organic heterostructures for organic device applications is exemplified by the targeted engineering of the electronic properties of phthalocyanine-based systems. The transport properties of two different phthalocyanine systems, a pure copper phthalocyanine (CoPc) and a flourinated copper phthalocyanine–manganese phthalocyanine (F_{16}CoPc/MnPc) heterostructure, are investigated by means of density functional theory (DFT) and the non-equilibrium Green's function (NEGF) approach. Furthermore, a master-equation-based approach is used to include electronic correlations beyond the mean-field-type approximation of DFT. We describe the essential theoretical tools to obtain the parameters needed for the master equation from DFT results. Finally, an interacting molecular monolayer is considered within a master-equation approach.

Introduction

Implementing molecular spintronics requires the understanding and the ability to modify and control charge-transport characteristics of organic molecules. Thus a solid understanding of the basic effects that govern the transport characteristics in the desired material is required for the development of further devices. Examples were demonstrated for a wide variety of applications including molecular spin filters [1], single-molecule or thin-film-based field-effect transistors [2-4], as well as potential candidates for memory devices utilizing organometallic complexes of tetracyanoquinodimethane (TCNQ) [5,6]. At interfaces between different organic materials interesting physical phenomena appear, in most cases due to (partial) charge transfer between the materials. One example is the formation of a two-dimensional metallic interface between insulating organic crystals [7,8]. Other effects are metal-insulator transitions or superconductivity which were reported for organic charge-transfer crystals realized by a combination of strongly electron-accepting and strongly electron-donating molecules [9,10].

Recently, a heterostructure of manganese phthalocyanine (MnPc) and structurally similar fluorinated copper phthalocyanine (F_{16}CoPc), has demonstrated the occurrence of hybridization [11]. It was proved that a local charge transfer which affects only the transition-metal centers changes the charge state of the transition metal and is directly related to a change of its magnetic moment. Further studies indicated that the Co $3d_{3r^2-z^2}$ orbital is filled due to the charge transfer at the interface to MnPc. Experiments and theory showed that a bulk material can be formed that maintains the charge and spin transfer between the two molecules [12]. Similar observations were made for organic molecules combined with the strong acceptor molecule F_4TCNQ. In general all of the fabricated heterostructures revealed new low-energy optical excitations originating from hybrid states. These states are of special importance for the transport characteristics of the hybrid materials. In contrast to other organic molecules, the hybrid dimer states close to the Fermi level in the the picene/F_4TCNQ compound excite a very asymmetric *I–V* curve with a pronounced diode-like forward/reverse current behavior. Additinally the effect of an applied gate voltage is greatly enhanced [13].

The electronic structure of free molecules or molecular assemblies will be substantially modified if the molecular material comes in contact with metal substrates. The formation of hybrid states at the metal-organic interface due to the different chemical potentials of the materials induces a wide range of effects and strongly depends on the microscopic details of the interface. The question arises of how the substrate interactions change the electronic structure of the molecular material and whether favorable properties for envisaged applications can be realized. Another important aspect for transport and potential applications are electronic interactions and correlations, which can be very strong in the confined molecular orbitals. Approaches beyond mean-field-type approximations are required for the treatment of correlation effects such as Coulomb blockade and the Kondo effect [14]. Such interactions not only occur within a single molecule but also between neighboring molecules in a film [15], where they can lead to ordering phenomena.

Our paper is organised as follows. First we will present the methodical background and results of our theoretical investigations on different phthalocyanine heterostructures by using the DFT-NEGF approach. In the second part we present our approach to combine DFT calculations and the master equation approach to quantum transport. Finally we present results of this new approach to describe tunnelling effects in monolayers.

DFT-NEGF transport theory

The ground-state electronic structure of the molecules was investigated using the all-electron DFT NRLMOL program package, which achieves a high level of numerical accuracy (see [16,17] and references therein). For the exchange correlation, GGA/PBE [18] was used and in all calculations dispersion correction utilizing the DFT-D2 method [19] was included. The geometry of the molecules was optimized using a gradient approach, the relaxation was terminated once all atomic were below 0.05 eV/Å. We applied the NEGF method for the self-consistent calculation of the electronic transport properties as implemented in the GPAW code [20,21] to investigate the *I–V* characteristics of our model devices. For the transport calculations, the electronic structure is obtained by DFT calculations using the common approach of constructing a model device for which the molecule of interest together with additional electrode atoms (scattering region, see below Figure 2e) are sandwiched between two semi-infinite metallic electrodes. We use at least three additional Au(111) layers at each side of the molecule to construct the scattering region, followed by a further geometry-optimization step, where the topmost two gold layers together with the attached molecules are allowed to relax. For the scattering region as well as for the leads, a localized double-ζ polarized basis set was used. The whole system can be subject to an external bias and/or gate voltage. The electronic structure of the scattering region and therefore the *I–V* curves are calculated self-consistently in the presence of such external fields.

The key facts of the DFT-NEGF method where already given in [13] and a detailed discussion of the method can be found in the cited literature and the references therein [22,23].

Ground state molecular properties

Important effects arise from interactions between the organic molecules and metallic contacts. These interactions may substantially alter the electronic structure of the organic material and needs to be carefully investigated [24]. In the following, we present DFT results for model systems were two phthalocyanine systems are in contact with Au(111) and Ni(111) surfaces.

We have investigated a F_{16}CoPc/MnPc heterostructure, which exhibits ground-state charge and spin transfer. We compare the results to a CoPc/CoPc reference structure, which does not show spin and charge transfer effects in the ground state. For both organic materials, we assume β-stacking [25].

The selected Au surface is known to form metal–organic contacts with medium interactions [26]. On the other hand, pure Ni surfaces are known to have a very high reactivity that sometimes lead to decomposition of the deposited organic material [27,28]. The reactivity of the Ni contact can be reduced by inserting a single layer of graphene between the organic molecule and the metal surface.

The model systems used here were built by first relaxing the F_{16}CoPc/MnPc and CoPc/CoPc molecular stacks on top of five-layer metal slabs. In a second step, the model device was built by adding a second metal slab on top of the organic material, with subsequent relaxation. The distance between the second contact and the organic material was systematically varied and the structure with the lowest total energy was used for the transport calculations.

In Figure 1, we show the results for the two organic systems between Au(111) surfaces. The electronic properties of both systems are altered due to the interaction with the gold surface. While in the contact-free CoPc/CoPc stack, the cobalt atoms couple antiferromagnetically, yielding an $S = 0$ system, the interaction with the gold surface reduces the Co moment due to a charge transfer from the metal surface. Qualitatively, the same effect is observed for the F_{16}CoPc/MnPc stack. Again, charge is transferred from the Au surface to the Co atom, in agreement with experimental results [29]. Figure 1c,d shows the respective plots of the density of states as obtained from the DFT calculations. While the electronic structure of CoPc and F_{16}CoPc is qualitative similar after surface contact, the manganese center in the F_{16}CoPc/MnPc yields a larger local magnetic moment and more strongly occupied metal 3d states close to the Fermi level. Both structures show some asymmetry between the spin-up and spin-down DOS.

Results and Discussion

Transport through phthalocyanine heterostructures

The ground state calculation results are reflected in the corresponding I–V curves shown in Figure 2a,b together with plots of the spin polarization of the current as a function of the bias voltage in Figure 2c,d. As expected, the resulting I–V curves show pronounced non-linear behavior in both cases and one can identify features in both curves that reflect distinct electronic states of the material. A second important result is the fact that the spin polarization of the current depends strongly on the applied bias voltage. While for the CoPc/CoPc system the spin polarization vanishes with increasing bias voltage, the F_{16}CoPc/MnPc stack shows maxima of the spin polarization at approximately $V_{bias} = \pm 0.5$ V of over 60% and the polarization does not vanish for larger bias voltages.

The same methodology is applied to the second model system, where the two different molecular stacks are in contact with magnetic Ni(111) leads. The quantity of interest for possible applications is the tunnel magnetoresistance (TMR), which can be obtained directly from I–V calculations with parallel and antiparallel magnetization of the Ni leads. The very strong interaction with the ignoble Ni surface leads, however, to a complete loss of the molecular properties of the organic material. For this reason, we introduce a single layer of graphene be-

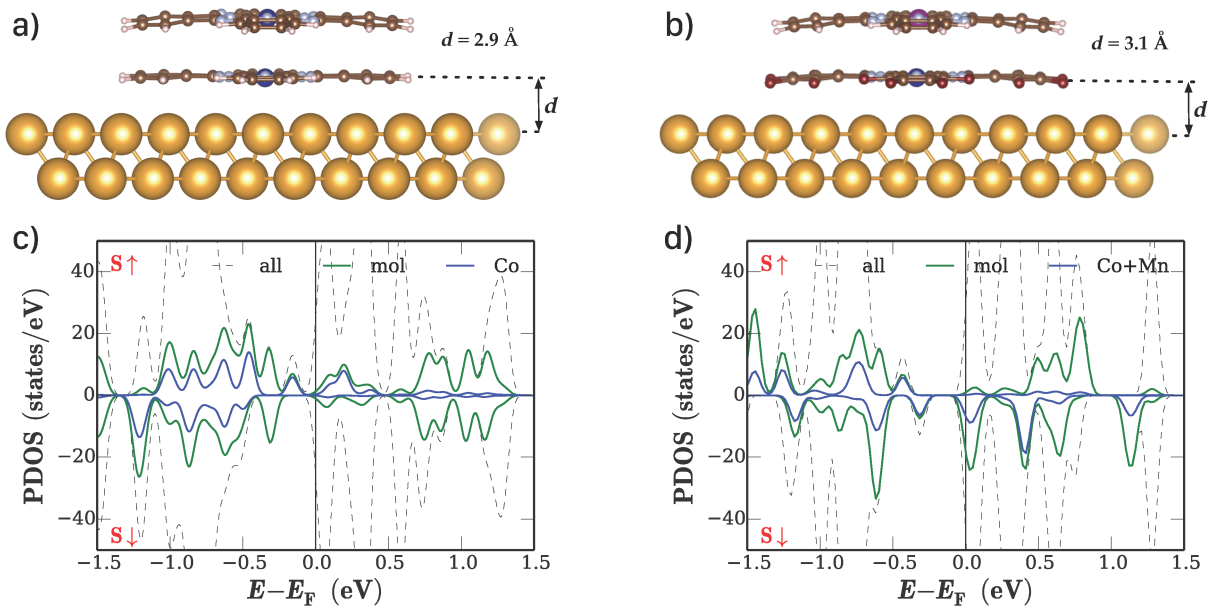

Figure 1: Results of DFT calculations for phthalocyanine stacks on fcc-Au(111) surfaces: relaxed geometries of a) the CoPc/CoPc stack and b) the F_{16}CoPc/MnPc stack. c), d) Density of states (DOS) of the molecule-Au(111) interfaces as obtained from the calculations. The overall DOS as well as the projections onto the molecule and metal centers are shown.

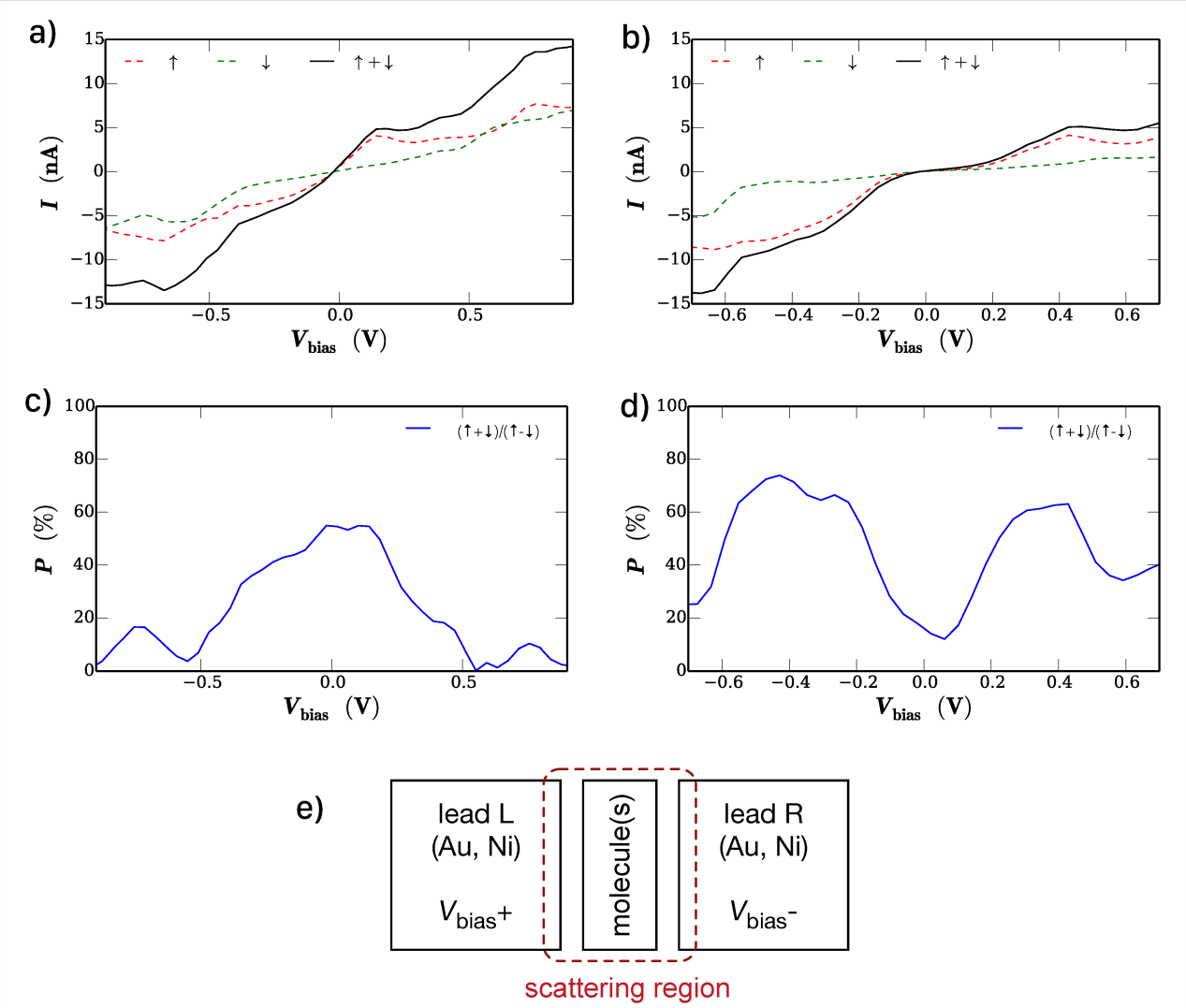

Figure 2: *I–V* curves calculated within the DFT-NEGF method for the sandwich structure a) CoPc/CoPc and b) F_{16}CoPc/MnPc. c), d) Spin polarization of the current as a function of the bias voltage. e) Schematic drawing of the used device configuration for the DFT-NEGF transport calculations.

tween the nickel surfaces and the molecular material on both sides of the device. Based on this layout, which is shown in Figure 3a,b, it was possible to obtain device structures for which the geometry of the Pc/Pc stacks was preserved during relaxation. Contrary to the direct deposition on a gold surface, the additional graphene layer effectively decouples the molecular stacks from the reactive Ni surface and preserves the electronic structure of the molecular material. The DOS for both systems is shown in Figure 3c,d.

The corresponding TMR is shown in Figure 4a,b. The DFT-NEGF methodology produces qualitative different results for the two material systems. Apart from increased values at very low bias voltages, the CoPc/CoPc stack exhibits a rather constant TMR of approximately 4%. On the other hand, the F_{16}CoPc/MnPc system shows significantly higher TMR values than the CoPc/CoPc system. Another interesting feature of the F_{16}CoPc/MnPc stack is the fact that the TMR changes sign depending on the applied bias voltage, which demonstrates the effect of the molecular properties on the observed current and ultimately on the TMR effect. It was already validated experimentally in [30] that the tunneling through single CoPc molecules on ferromagnetic Fe thin film exhibits pronounced spin dependence.

These investigations suggest the possibility of versatile applications in spintronic devices. The calculations on model systems with gold contacts show that it is possible to obtain spin-polarized currents from both phthalocyanine-based devices. However, the F_{16}CoPc/MnPc heterostructure yields a stronger spin polarization of the current, which is predicted not to vanish for high bias voltages. The investigated prototypical TMR device

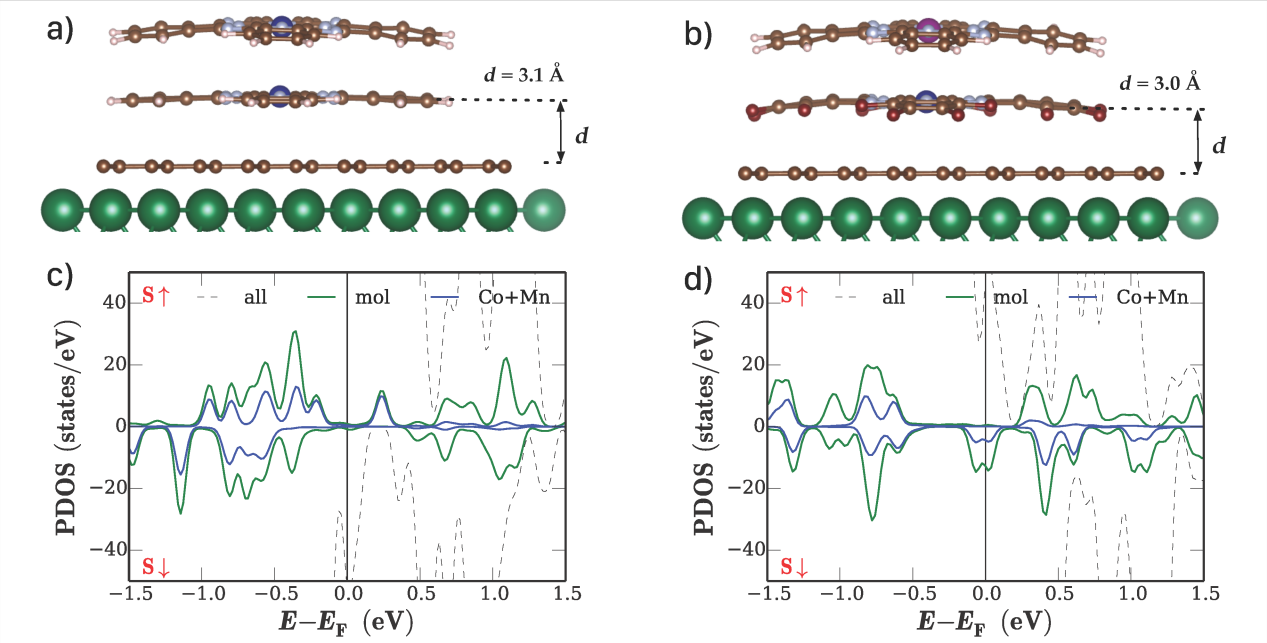

Figure 3: Results of DFT calculations for phthalocyanine stacks on fcc-Ni(111) surfaces: relaxed geometries of a) the CoPc/CoPc stack and b) the F_{16}CoPc/MnPc stack. c), d) DOS of the molecule-Au(111) interfaces as obtained from the calculations. The overall DOS as well as the projections onto the molecule and metal centers are shown.

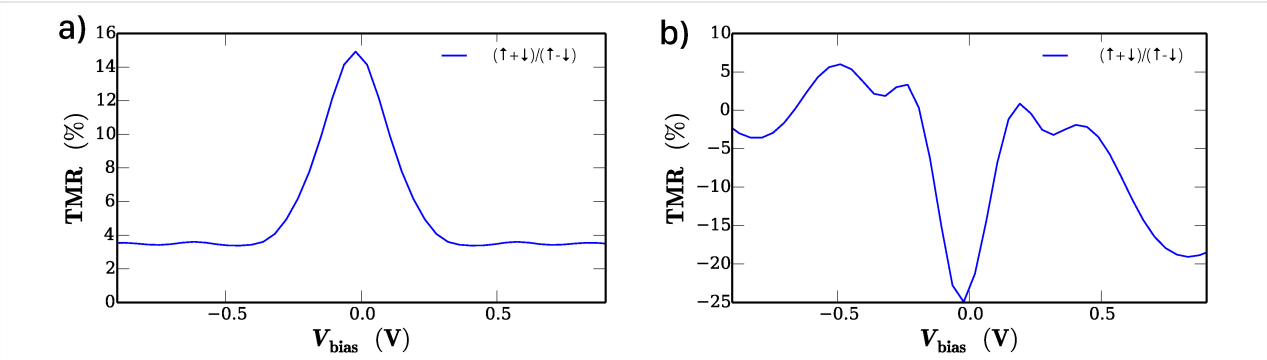

Figure 4: Calculated TMR for the sandwich structure a) CoPc/CoPc and b) F_{16}CoPc/MnPc on Ni(111). The TMR as a function of the bias voltage is obtained from the spin-polarized current within the DFT-NEGF method.

yields a qualitatively consistent picture. The predicted TMR for the F_{16}CoPc/MnPc heterostructure is by a factor of 2–3 larger than the TMR of the pure CoPc device, depending on the applied bias voltage. Our results make the F_{16}CoPc/MnPc material system a more promising candidate for applications. In principle the experiments presented in [31] did show that application specific design of transport properties is possible by variation of the stack size of CoPc molecules. The use of different types of phthalocyanines as suggested in this work seems to open a new path to design transport properties.

The DFT-NEGF as a standard approach for the investigation of transport properties of model device structures gives reasonable information on whether a specific materials combination is suitable for applications. However, one has to keep in mind that the electronic structure used as input is derived from ground-state DFT results and thus has the limitations inherent to the DFT method. To provide a more comprehensive picture, especially in situations where the electronic correlations are strong, it is necessary to apply techniques that permit a treatment of molecular interactions beyond the mean-field-like DFT approach.

DFT combined with the master equation

An improved treatment of electronic correlation is relevant especially for weakly hybridized molecular systems since the electrons are confined to relatively small molecular orbitals so that electron–electron interactions dominate. DFT typically gives reasonable results for the spatial structure of orbitals,

whereas energy levels are not always well reproduced. Even if the energies are reasonable, the magnitude of the tunneling currents through nanoscale devices are often strongly overestimated [32-35]. The origins of these problems are threefold: First, tunneling under a finite bias is a non-equilibrium situation that is not well described by standard DFT, which is a method for the ground state. In principle, excited states and time-dependent effects can be treated using time-dependent density functional theory and time-dependent current density functional theory [36,37]. However, this is complicated by the lack of good approximate exchange-correlation functionals for transport calculations [38] and by the high computational cost. Second, standard functionals for DFT do not describe strongly correlated systems particularly well. Third, NEGFs can describe tunneling (hybridization) exactly but naturally lead to perturbative approximations for interactions.

The master-equation (ME) approach focuses on the many-body state of the molecular system and traces out the degrees of freedom of the electrodes, e.g., the top and bottom Au or Ni electrodes discussed in the previous sections or the tip and the substrate in an STM setup. We are here interested in the latter situation. The ME is an equation of motion for the reduced density operator ρ_{mol} of the molecule [14,39-53]. The ME approach is complementary to NEGFs in that it allows to treat the interactions within the molecule exactly but lends itself to approximate expansions in the tunneling between the molecule and the leads. The method is thus powerful for strong interactions but weak hybridization between the molecules and the electrodes (STM tip and substrate).

The ME approach requires the formal separation of the system into the molecule and the electrodes, where the connection between them is expressed by a bilinear tunneling Hamiltonian $H_t = \sum_{\mathrm{ij}} \left(t_{\mathrm{ij}} c_{\mathrm{i}}^{\dagger} d_{\mathrm{j}} + \mathrm{H.c.} \right)$. Here, t_{ij} are tunneling amplitudes and $c_{\mathrm{i}}^{\dagger}$ $\left(d_{\mathrm{j}}^{\dagger} \right)$ are electronic creation operators for the molecule (the electrodes). The derivation of tunneling amplitudes t_{ij} from a fundamental interacting Hamiltonian has been studied intensively [54-59] but is still not completely solved [60]. For STM, the tunneling amplitudes describing tunneling between the tip and the molecule or the substrate depend on the tip position.

It is highly desirable to obtain realistic, system-specific tunneling amplitudes based on DFT. While the combination of DFT with NEGFs is integrated in existing packages, not much work has been done for DFT combined with the ME. In the following, we outline the main steps needed for such an approach and illustrate the feasibility by showing results for CoPc on graphene. The Hamiltonian reads $H = H_{\mathrm{leads}} + H_{\mathrm{mol}} + H_t$, where

$$H_{\mathrm{leads}} = \sum_{\alpha \mathbf{k} \sigma} \omega_{\alpha \mathbf{k}} a_{\alpha \mathbf{k} \sigma}^{\dagger} a_{\alpha \mathbf{k} \sigma} \tag{1}$$

describes the tip ($\alpha = T$) and the substrate ($\alpha = S$). Both are modeled as non-interacting electron gases with DOS $D_{\alpha\sigma}(\xi)$ and chemical potentials μ_{α}. $a_{\alpha \mathbf{k} \sigma}^{\dagger}$ creates an electron in lead α with wave vector $\mathbf{k}$, spin σ, and energy $\omega_{\alpha \mathbf{k}}$ (taking $\hbar = 1$). The molecular part is

$$\begin{aligned} H_{\mathrm{mol}} = & \sum_{\nu \sigma} e_{\nu} c_{\nu \sigma}^{\dagger} c_{\nu \sigma} + \frac{1}{2} \sum_{\nu} U_{\nu} n_{\nu} \left(n_{\nu} - 1 \right) \\ & + \frac{1}{2} \sum_{\nu \neq \nu'} U_{\nu \nu'} n_{\nu} n_{\nu'} + \frac{1}{2} \sum_{\nu \neq \nu'} J_{\nu \nu'} \mathbf{S}_{\nu} \cdot \mathbf{S}_{\nu'}, \end{aligned} \tag{2}$$

where $c_{\nu \sigma}^{\dagger}$ creates an electron in the molecular orbital ν with spin $\boldsymbol{\sigma}$ and single-particle energy e_{ν}, $n_{\nu} \equiv c_{\nu \uparrow}^{\dagger} c_{\nu \uparrow} + c_{\nu \downarrow}^{\dagger} c_{\nu \downarrow}$ is the corresponding number operator, and $\mathbf{S}_{\nu} \equiv \sum_{\sigma \sigma'} c_{\nu \sigma}^{\dagger} \left(\sigma_{\sigma \sigma'} / 2 \right) c_{\nu \sigma'}$ is its spin operator in terms of the vector of Pauli matrices, $\boldsymbol{\sigma}$. U_{ν} and $U_{\nu\nu'} = U_{\nu'\nu}$ describe the intraorbital and interorbital Coulomb interactions, respectively, and $J_{\nu\nu'} = J_{\nu'\nu}$ is the Hund-rule coupling. The orbital energies e_{ν} are shifted by the electric potential, which is controlled by the bias voltage $V = (\mu_T - \mu_S)/e$.

The eigenenergies and eigenstates of H_{mol} satisfy $H_{\mathrm{mol}} |n\rangle = \varepsilon_n |n\rangle$. Only the differences between molecule and electrode energies enter the final results and it is useful to keep the molecular energies unchanged and instead shift the chemical potentials. A simple estimate is given by Datta et al. [23], who model tip and substrate as capacitor plates. For fixed molecular energies the chemical potentials are then $\mu_T = \eta e V$ and $\mu_S = (\eta - 1) eV$, where $\eta \equiv z_{\mathrm{mol}}/z_{\mathrm{tip}}$. Here, z_{mol} is the distance to the molecule and z_{tip} the distance to the tip, both measured from the substrate. Thus η can in principle be varied in the range $0 < \eta < 1$. Better approximations taking account of the actual geometry are of course possible.

Finally, the tunneling between the molecule, the tip, and the substrate is described by

$$\begin{aligned} H_t = & \sum_{\alpha = T,S} \sum_{\mathbf{k} \nu \sigma} \frac{1}{\sqrt{N_{\alpha}}} \left(t_{\alpha \mathbf{k} \nu \sigma} \alpha_{\alpha \mathbf{k} \sigma}^{\dagger} c_{\nu \sigma} + \mathrm{H.c.} \right) \\ & + \frac{1}{\sqrt{N_T N_S}} \sum_{\mathbf{k} \mathbf{k}' \sigma} \left(t_{T \mathbf{k} S \mathbf{k}' \sigma} \alpha_{T \mathbf{k} \sigma}^{\dagger} a_{S \mathbf{k}' \sigma} + \mathrm{H.c.} \right), \end{aligned} \tag{3}$$

where the first term corresponds to tunneling between the molecule and lead α, while the second corresponds to direct tunneling between tip and substrate. The numbers N_{α} of sites in lead α drop out of the physical results.

For calculating the stationary current under an arbitrary tip–substrate bias voltage, we employ the sequential-tunneling approximation, i.e., we expand the ME up to the first non-vanishing order in the tunneling amplitudes. The derivation is standard, see, e.g., [45,47-53]. It starts from the exact von Neumann equation for the full density operator of the tip–molecule–substrate system. Taking the trace over the tip and substrate degrees of freedom, one obtains a ME for the reduced density operator $\rho_{\rm mol}$. The ME is then expanded up to second order in $t_{\alpha\mathbf{k}\nu\sigma}$. For the stationary state, off-diagonal components of $\rho_{\rm mol}$ in the eigenbasis of $H_{\rm mol}$ (i.e., coherences) vanish if the system is non-magnetic or all magnetic axes (applied magnetic field, magnetization, easy anisotropy axis) are parallel. Then one obtains rate equations for the diagonal components, i.e., for the probabilities of molecular states,

$$\frac{\mathrm{d}}{\mathrm{d}t}\rho_{\rm mol}^{nn} = \sum_m \left(R_{m\to n}\,\rho_{\rm mol}^{mm} - R_{n\to m}\,\rho_{\rm mol}^{nn} \right), \tag{4}$$

where m and n label molecular eigenstates and

$$R_{n\to m} = 2\pi \sum_{\alpha\nu\sigma} |t_{\alpha\nu\sigma}|^2\, D_{\alpha\sigma}\left(\xi_{mn,\alpha}\right) \Big(f\left(\xi_{mn,\alpha}\right) \left|C_{nm}^{\nu\sigma}\right|^2 + \left[1 - f\left(\xi_{mn,\alpha}\right)\right] \left|C_{mn}^{\nu\sigma}\right|^2 \Big), \tag{5}$$

with $\xi_{mn,\alpha} \equiv \varepsilon_n - \varepsilon_m - \mu_\alpha$ are transition rates for sequential tunneling. We have assumed the tunneling amplitudes to be independent of the wave vector $\mathbf{k}$. The matrix elements $C_{nm}^{\nu\sigma}$ are defined as $C_{nm}^{\nu\sigma} \equiv \langle n | c_{\nu\sigma} | m \rangle$. Finally, the current is

$$I_\alpha = \mp e \sum_{mn} \left(n_n - n_m\right) R_{m\to n}^{\alpha}\, \rho_{\rm mol}^{mm}, \tag{6}$$

where the upper (lower) sign pertains to $\alpha = T\,(S)$, n_n denotes the occupation number in the eigenstate $|n\rangle$, and the rates $R_{m\to n}^{\alpha}$ contain only terms involving lead α.

We now turn to the determination of the model parameters from DFT. At least two different charge states must contribute to obtain sequential tunneling but more charge states can be relevant, in particular for large bias voltages. Furthermore, for any charge state, certain orbitals will contribute to sequential tunneling. Their relative energies for the same charge is usually well described by DFT. Energy differences between states with N and $N-1$ electrons are best obtained from the ionization energies of the N-electron systems. The DOS $D_{\alpha\sigma}(\xi)$ of the tip and the substrate are standard quantities obtained from band-structure calculations.

The calculation of the tunneling amplitudes $t_{\alpha\nu\sigma}$ is our main concern. We start by considering the molecule–substrate interface. The approach uses DFT to calculate the KS orbitals and eigenvalues and the KS potential of the free substrate, of the free molecule, and of both combined. Similarly to [55,61], we write the Hamiltonian as

$$H_{\rm KS} = \int \mathrm{d}^3 r\, \Psi^\dagger(\mathbf{r}) \left[-\frac{\nabla^2}{2m} + V_{\rm KS}(\mathbf{r}) \right] \Psi(\mathbf{r}), \tag{7}$$

where $V_{\rm KS}$ is the KS potential for molecule and substrate combined. We now split the field operator Ψ into two parts according to

$$\Psi(\mathbf{r}) = \Psi_S(\mathbf{r}) + \Psi_{\rm mol}(\mathbf{r}), \tag{8}$$

$$\Psi_S(\mathbf{r}) = \sum_{\mathbf{k}\sigma} a_{S\mathbf{k}\sigma}\, \phi_{S\mathbf{k}\sigma}(\mathbf{r}), \tag{9}$$

$$\Psi_{\rm mol}(\mathbf{r}) = \sum_{\nu\sigma} c_{\nu\sigma}\, \phi_{{\rm mol},\nu\sigma}(\mathbf{r}), \tag{10}$$

where the $\phi_{S\mathbf{k}\sigma}(\mathbf{r})$ $\left(\phi_{{\rm mol},\nu\sigma}(\mathbf{r})\right)$ are KS orbitals from the calculation for the substrate (molecule) alone. Each set by itself forms a complete basis of the space of single-particle wave functions. Taken together, they are thus overcomplete so that the decomposition in Equation 8 is not unique. To cure this problem, we only include a (typically small) number of relevant molecular orbitals in $\Psi_{\rm mol}$ and throw out the same number or more of high-energy orbitals from Ψ_S. Which ones these are is irrelevant for the low-energy physics. The remaining wave functions are linearly independent. However, the KS orbitals for the molecule and those for the substrate are not orthogonal. This would make the tunneling amplitudes ill-defined, as we shall see, and we therefore orthonormalize the states. Since our purpose is to identify the orbitals as molecule and substrate states, we demand that the orthonormalized states deviate minimally from the (input) states of the molecule and substrate alone. This is achieved by Löwdin orthonormalization [62,63]. The resulting orbitals are denoted by $\widetilde{\phi}_{{\rm mol},\nu\sigma}$ and $\widetilde{\phi}_{S\mathbf{k}\sigma}$ and the corresponding fermion operators by $\widetilde{c}_{\nu\sigma}$ and $\widetilde{a}_{S\mathbf{k}\sigma}$.

The KS Hamiltonian (Equation 7) is not diagonal in the new basis. Generally, there are off-diagonal components within the sector of molecular states, within the sector of substrate states, and between the two. For the molecular sector, the off-diagonal matrix elements $\langle \widetilde{\phi}_{{\rm mol},\nu\sigma} | H_{\rm KS} | \widetilde{\phi}_{{\rm mol},\nu'\sigma} \rangle$ describe the mixing of molecular states due to the presence of the substrate. The coupling to the substrate also leads to a change of the diagonal

matrix elements. In principle, all these matrix elements can be absorbed into the model Hamiltonian H_{mol}. In the substrate sector, the off-diagonal matrix elements $\langle\tilde{\phi}_{S\mathbf{k}\sigma}|H_{\mathrm{KS}}|\tilde{\phi}_{S\mathbf{k}'\sigma}\rangle$ affect the local DOS at the surface. These effects on the molecule and the substrate lead to higher-order corrections on top of the sequential-tunneling approximation and are neglected to leading order.

The tunneling amplitudes between molecule and substrate are given by $t_{S\mathbf{k}\nu\sigma} \equiv \langle\tilde{\phi}_{S\mathbf{k}\sigma}|H_{\mathrm{KS}}|\tilde{\phi}_{\mathrm{mol},\nu\sigma}\rangle$. The additional approximation of **k**-independent tunneling amplitudes in Equation 5 requires us to average over **k** or, if the dependence is seen to be weak, choose a representative substrate state.

The orthonormalization of states is crucial: If we had worked with non-orthonormalized wave functions, adding a supposedly irrelevant constant C to the Hamiltonian H_{KS} in Equation 7 would change $t_{S\mathbf{k}\nu\sigma}$ by $C\langle\phi_{S\mathbf{k}\sigma}|\phi_{\mathrm{mol},\nu\sigma}\rangle \neq 0$. Then the rates (Equation 5) and, consequently, all observables would depend on C. This problem already appears in the seminal paper of Slater and Koster [64]. Using orthonormalized states avoids the ambiguity.

For the tunneling amplitudes between the molecule and the tip, $t_{T\mathbf{k}\nu\sigma}$, and between the substrate and the tip, $t_{T\mathbf{k}S\mathbf{k}'\sigma}$, one can use an analogous procedure, with one important modification. It is unfeasible to perform a DFT calculation for every relevant tip position for the full tip–molecule–substrate system. Instead, we take the sum of the KS potentials obtained separately for the substrate, the molecule, and the tip (translated to any tip position of interest) as an approximation for the full KS potential $V_{\mathrm{KS}}^{\mathrm{full}}$. This neglects the interaction of the molecule with substrate and tip for the purpose of calculating the tip–molecule tunneling amplitudes and is valid for weak hybridization. The tip–molecule tunneling amplitudes are finally calculated as

$$t_{T\mathbf{k}\nu\sigma} \equiv \left\langle\tilde{\phi}_{T\mathbf{k}\sigma}\middle|H_{\mathrm{KS}}^{\mathrm{full}}\middle|\tilde{\phi}_{\mathrm{mol},\nu\sigma}\right\rangle, \tag{11}$$

where

$$H_{\mathrm{KS}}^{\mathrm{full}} = \int \mathrm{d}^3 r \Psi^{\dagger}(\mathbf{r})\left[-\frac{\nabla^2}{2m} + V_{\mathrm{KS}}^{\mathrm{full}}(\mathbf{r})\right]\Psi(\mathbf{r}) \tag{12}$$

and $\tilde{\phi}_{T\mathbf{k}\sigma}(\mathbf{r})$ is a properly orthonormalized tip wave function. The calculation of the tip–substrate amplitudes is analogous to the case of the tip–molecule amplitudes, with the molecular wave functions $|\tilde{\phi}_{\mathrm{mol},\nu\sigma}\rangle$ replaced by the substrate wave functions $|\tilde{\phi}_{S\mathbf{k}\sigma}\rangle$.

For illustration, we show in Figure 5a the absolute value squared $|t_T|^2$ of the tunneling amplitude between the tip and the highest occupied molecular orbital (HOMO), in this case of CoPc, as a function of the lateral position (x,y) for fixed height $z = 0.64$ nm. The tip was approximated by a single hydrogen 1s orbital for simplicity. The substrate was taken to be a graphene monolayer for simplicity, intended as a decoupling layer as discussed in section 'DFT-NEGF transport theory'. The symmetry of the HOMO is clearly visible and is not noticeably reduced by the hybridization with the substrate. Figure 5b shows the absolute value squared $|t_{TS}|^2$ of the direct tunneling amplitude between the tip and a representative low-energy substrate state, specifically the Bloch state at the K point localized on one of the two sublattices, modified by the Löwdin orthonormalization with respect to the CoPc HOMO and the tip. The ampli-

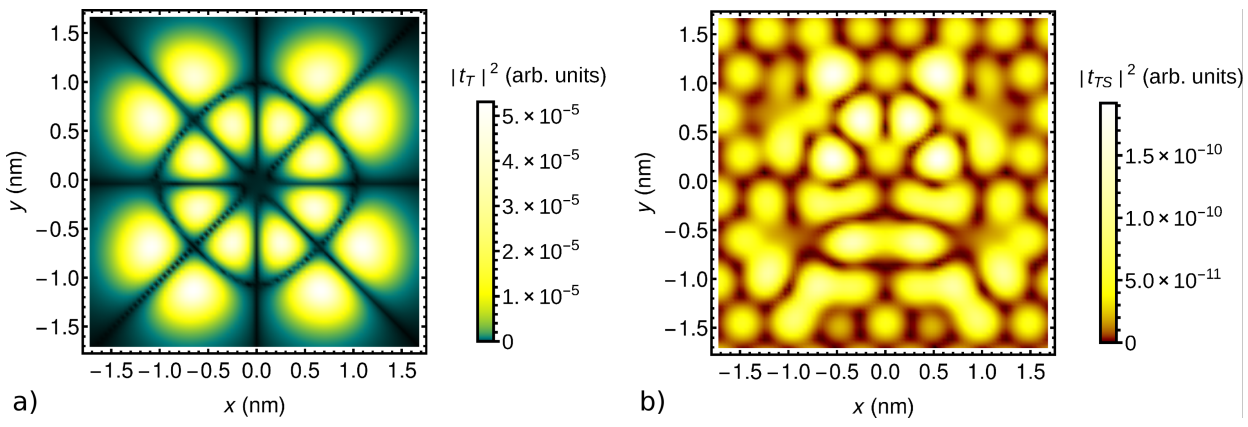

Figure 5: Absolute value squared of the tunneling amplitude a) between the STM tip and a CoPc HOMO on a graphene substrate and b) between the tip and a representative low-energy Bloch-type substrate state, as functions of the lateral position (x,y) for fixed height $z = 0.64$ nm.

tude is enhanced where large weights of the substrate and CoPc orbitals coincide. The enhancement signifies coherent tunneling from the tip through the molecule to the substrate. Note, however, that the tip–substrate amplitude t_{TS} is small compared to the tip–molecule amplitude t_T for the present height z.

Tunneling through monolayers

Many molecules form highly ordered self-assembled monolayers on appropriate substrates [65-70]. Sandwich structures of monolayers contacted by conducting materials at the top and bottom are of interest for applications and also from a fundamental point of view since non-local interactions between molecules are relevant. The combination of interactions with a bias voltage perpendicular to the monolayer can lead to interesting non-equilibrium properties. The fabrication of the top contact has proved to be difficult since the technique must be sufficiently gentle not to damage the molecular layer. One successful technique involves rolled-up nanolayers [71-78].

An advanced theoretical description extending the mean-field-type description within the DFT-NEGF approach requires a method that can deal with strong interactions in systems far from equilibrium, and the prime candidate is again the ME approach discussed in Section 'DFT combined with the master equation', ideally using parameters from DFT calculations. The non-local interaction adds another level of complication [15,79]. In the sequential-tunneling and diagonal approximation described above, this interaction can be treated essentially exactly using Monte Carlo simulations [15]. The main idea is to use the sequential-tunneling rates, which are analogous to Equation 5 and uniform throughout the monolayer, to determine the probabilities of local Monte Carlo updates. Importantly, these rates depend on the total occupation of the neighboring sites through the nearest-neighbor Coulomb interaction. Note that the rates do not satisfy detailed balance for nonzero bias voltages.

A simple model system consisting of a square lattice with a single spinful orbital per site and with very strong intraorbital and arbitrary nearest-neighbor Coulomb interactions has recently been studied by two of us [15]. There, the molecules have been assumed to be symmetric, which would for example be appropriate for a CoPc layer. In the present work, we consider a minimal model for a layer of dimers such as F_{16}CoPc/MnPc [11,12] sandwiched between electrodes. F_{16}CoPc/MnPc has a twofold spin degenerate HOMO so that a model with a single orbital per site with interactions should be reasonable. The main difference from the previously studied case [15] is the asymmetry of the molecule. The asymmetry can be modeled by assuming different tunneling probabilities between the molecular orbital and the two electrodes. In the following, we analyze how such an asymmetry affects observables and compare to the symmetric case. For details of the theory we refer to [15].

The main parameters of the model are the on-site energy E_d, the nearest-neighbor Coulomb repulsion U_1, and the bias voltage V. The on-site Coulomb repulsion U_0 is set to infinity, excluding double occupation. Results are plotted as functions of ratios E_d/U_1 and eV/U_1. The ratio $\Gamma_{\text{top}}/\Gamma_{\text{bottom}}$ of the tunneling rates $\Gamma_\alpha \propto |t_\alpha|^2$ is taken to equal 0.5. We here restrict ourselves to the limit of zero temperature. In this limit, the transition rates are step functions of the molecular energy level E_d and of the bias voltage V. Consequently, all observables are also step functions.

Regions that contain a piece of the $V = 0$ axis or touch that axis at their boundary have rates that are the same as for an equilibrium model in the limit of $T \to 0$. The stationary state is thus the equilibrium state for $T \to 0$, i.e., the ground state. Since the model is of Ising type, with the modification of the two-fold (spin) degeneracy of the occupied single-site states, this ground state is known to be the completely occupied state for $E_d/U_1 < -4$, a state with checkerboard charge order for $-4 < E_d/U_1 < 0$, and the completely empty state for $E_d/U_1 > 0$. The other simple limiting case pertains to sufficiently large bias voltage $|V|$. In this limit, all sequential-tunneling rates are nonzero and are independent of the occupation of the neighboring sites. Thus the layer decouples into independent sites. Moreover, forward and backward rates are always equal, $R_{n\to m} = R_{m\to n}$, so that the system is equivalent to a model at infinite temperature. For the other regions, we have performed Monte Carlo simulations as in [15].

Figure 6a shows the average imbalance $\langle |n_A - n_B| \rangle$ between the occupations n_A and n_B of the two checkerboard sublattices, for the case of $\Gamma_{\text{top}}/\Gamma_{\text{bottom}} = 0.5$. For comparison, we show the corresponding results for symmetric contacts, $\Gamma_{\text{top}}/\Gamma_{\text{bottom}} = 1$, in Figure 6b [15]. Figure 7 shows the average current per site for both cases. Evidently, there is a phase with checkerboard charge order and vanishing current for both values of the asymmetry. It extends the equilibrium checkerboard ordered phase to nonzero bias voltages V. We next note that $\Gamma_{\text{top}} \neq \Gamma_{\text{bottom}}$ breaks the symmetry between positive and negative bias. The current reaches a larger value for positive bias, the device thus acts as a (rather poor) rectifier. This is expected. Much more interestingly, we find two regions, in the lower right quadrant of Figure 6a, where checkerboard order coexists with a nonzero current. Such a checkerboard conducting phase was predicted in [15]. However, for the symmetric contacts considered there, it only occurs for degeneracies of the occupied sites of at least 4. Such a large degeneracy is hard to realize. The new results show that for a very moderate asymmetry of the device, the spin degeneracy of 2 is already sufficient to stabilize this interesting

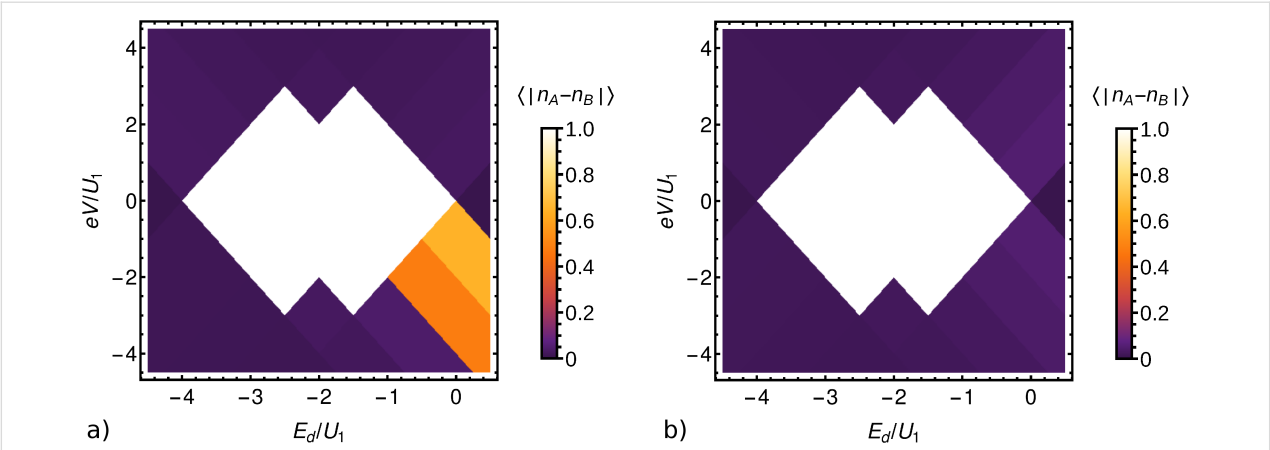

Figure 6: Average imbalance $\langle |n_A - n_B| \rangle$ between the occupations n_A and n_B of the two checkerboard sublattices for a) asymmetric tunneling, $\Gamma_{top}/\Gamma_{bottom} = 0.5$, and b) symmetric tunneling, $\Gamma_{top}/\Gamma_{bottom} = 1$ [15], both for a degeneracy of 2 of occupied single-site states.

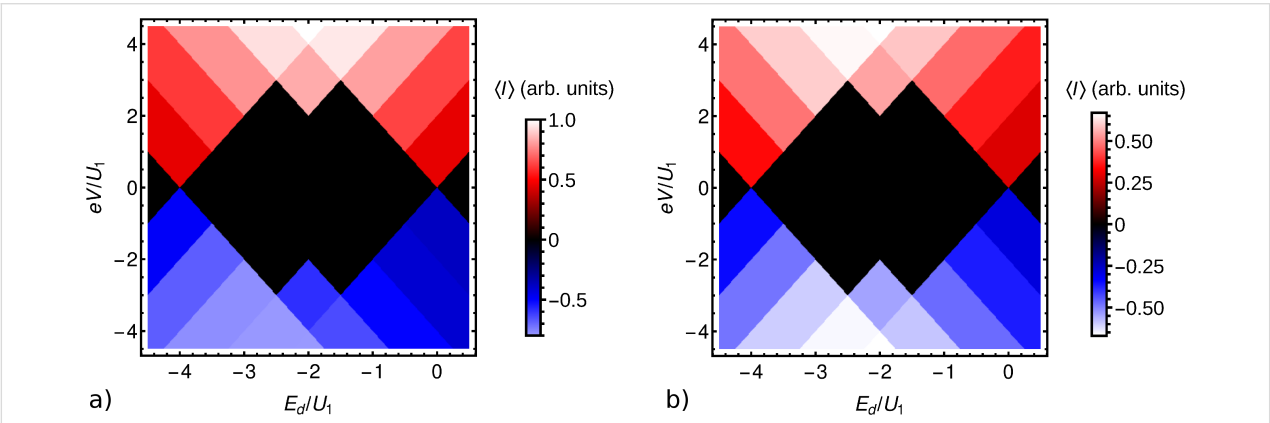

Figure 7: Average current $\langle I \rangle$ per site for a) asymmetric tunneling, $\Gamma_{top}/\Gamma_{bottom} = 0.5$, and b) symmetric tunneling, $\Gamma_{top}/\Gamma_{bottom} = 1$ [15], both for a degeneracy of 2 of occupied single-site states.

phase. In this phase, tunneling takes place only through one sublattice, which has an average occupation between 0 and 1, while the other sublattice is empty. According to Figure 6a, it occurs for negative bias voltages, which correspond to electrons tunneling out of the bottom electrode into the molecules. This is the junction with the larger tunneling rate Γ_{bottom}. Thus the asymmetry favors in-tunneling from the bottom electrode. Since increasing the degeneracy of the occupied sites also favors the occupied state and this can stabilize the checkerboard conducting phase [15], it is plausible that the asymmetric tunneling has the same effect.

Conclusion

In this contribution, we have discussed and illustrated approaches to transport calculations for molecular systems sandwiched between conducting electrodes. In the first part, we have reported on the transport properties of two different phthalocyanine structures. Our studies using the standard DFT-NEGF approach show that both structures exhibit transport properties that may be useful for device applications. A reasonable spin polarization of the current through model devices with non-magnetic Au(111) leads is predicted. For F_{16}CoPc/MnPc heterostructure, this polarization is more robust at higher bias voltages, which qualifies this hybrid material as the better candidate for a possible spin-filter application. Devices with magnetic Ni(111) contacts yield TMR values of 4% for the pure CoPc system and up to 18% for the F_{16}CoPc/MnPc heterostructure at bias voltages relevant for applications. In the second part, we point out that the DFT-NEGF approach becomes questionable if electronic correlations in the molecule are strong, and introduce an alternative approach based on combining DFT with the ME. We discuss how a model suitable for ME calculations could be constructed on the basis of DFT calculations and a first proof-of-concept implementation of coupling DFT and ME is presented. Unlike for the well established NEGF, a lot of work remains to be done, however this could lead to a new way

to investigate transport in strongly correlated materials. Finally, we show how strong Coulomb interactions between different molecules in a monolayer sandwiched between electrodes can be treated within a ME approach. This method is applied to asymmetric molecular systems such as F_{16}CoPc/MnPc. Besides the expected current rectification, it is found that the asymmetry can lead to a non-equilibrium conducting state with checkerboard charge order.

Acknowledgements

The authors thank S. Diehl, C. Hess, J. Marino, M. Knupfer and T. Vojta for useful discussions and the ZIH Dresden for providing computational resources. Financial support by the Deutsche Forschungsgemeinschaft, through Research Unit FOR 1154, Towards Molecular Spintronics, and HA5070/3, is gratefully acknowledged.

References

1. Herrmann, C.; Solomon, G. C.; Ratner, M. A. *J. Am. Chem. Soc.* **2010,** *132,* 3682–3684. doi:10.1021/ja910483b
2. Wang, J.; Wang, H.; Yan, X.; Huang, H.; Yan, D. *Appl. Phys. Lett.* **2005,** *87,* 093507. doi:10.1063/1.2037204
3. Wang, H.; Wang, J.; Huang, H.; Yan, X.; Yan, D. *Org. Electron.* **2006,** *7,* 369–374. doi:10.1016/j.orgel.2006.04.004
4. Yoshida, K.; Hamada, I.; Sakata, S.; Umeno, A.; Tsukada, M.; Hirakawa, K. *Nano Lett.* **2013,** *13,* 481–485. doi:10.1021/nl303871x
5. Potember, R. S.; Poehler, T. O.; Cowan, D. O. *Appl. Phys. Lett.* **1979,** *34,* 405–407. doi:10.1063/1.90814
6. Reda, T.; Collings, A. F.; Barton, C.; Lukins, P. *J. Phys. Chem. B* **2003,** *107,* 13774–13781. doi:10.1021/jp034836a
7. Chu, C. W.; Harper, J. M. E.; Geballe, T. H.; Greene, R. L. *Phys. Rev. Lett.* **1973,** *31,* 1491. doi:10.1103/PhysRevLett.31.1491
8. Wen, S.; Deng, W.-Q.; Han, K.-L. *Chem. Commun.* **2010,** *46,* 5133–5135. doi:10.1039/c0cc00955e
9. Coleman, L. B.; Cohen, M. J.; Sandman, D. J.; Yamagishi, F. G.; Garito, A. F.; Heeger, A. J. *Solid State Commun.* **1973,** *12,* 1125–1132. doi:10.1016/0038-1098(73)90127-0
10. Seo, H.; Hotta, C.; Fukuyama, H. *Chem. Rev.* **2004,** *104,* 5005–5036. doi:10.1021/cr030646k
11. Lindner, S.; Knupfer, M.; Friedrich, R.; Hahn, T.; Kortus, J. *Phys. Rev. Lett.* **2012,** *109,* 027601. doi:10.1103/PhysRevLett.109.027601
12. Friedrich, R.; Lindner, S.; Hahn, T.; Loose, C.; Liebing, S.; Knupfer, M.; Kortus, J. *Phys. Rev. B* **2013,** *87,* 115423. doi:10.1103/PhysRevB.87.115423
13. Hahn, T.; Liebing, S.; Kortus, J. *Nanoscale* **2014,** *6,* 14508–14513. doi:10.1039/C4NR02455A
14. Andergassen, S.; Meden, V.; Schoeller, H.; Splettstoesser, J.; Wegewijs, M. R. *Nanotechnology* **2010,** *21,* 272001. doi:10.1088/0957-4484/21/27/272001
15. Ludwig, T.; Timm, C. *Phys. Rev. B* **2016,** *94,* 155444. doi:10.1103/PhysRevB.94.155444
16. Pederson, M. R.; Porezag, D. V.; Kortus, J.; Patton, D. C. *Phys. Status Solidi B* **2000,** *217,* 197–218. doi:10.1002/(sici)1521-3951(200001)217:1<197::aid-pssb197>3.0.co;2-b
17. Porezag, D.; Pederson, M. R. *Phys. Rev. A* **1999,** *60,* 2840–2847. doi:10.1103/PhysRevA.60.2840
18. Perdew, J. P.; Burke, K.; Ernzerhof, M. *Phys. Rev. Lett.* **1996,** *77,* 3865–3868. doi:10.1103/PhysRevLett.77.3865
19. Grimme, S. *J. Comput. Chem.* **2006,** *27,* 1787–1799. doi:10.1002/jcc.20495
20. Chen, J.; Thygesen, K. S.; Jacobsen, K. W. *Phys. Rev. B* **2012,** *85,* 155140. doi:10.1103/PhysRevB.85.155140
21. Enkovaara, J.; Rostgaard, C.; Mortensen, J. J.; Chen, J.; Dułak, M.; Ferrighi, L.; Gavnholt, J.; Glinsvad, C.; Haikola, V.; Hansen, H. A.; Kristoffersen, H. H.; Kuisma, M.; Larsen, A. H.; Lehtovaara, L.; Ljungberg, M.; Lopez-Acevedo, O.; Moses, P. G.; Ojanen, J.; Olsen, T.; Petzold, V.; Romero, N. A.; Stausholm-Møller, J.; Strange, M.; Tritsaris, G. A.; Vanin, M.; Walter, M.; Hammer, B.; Häkkinen, H.; Madsen, G. K. H.; Nieminen, R. M.; Nørskov, J. K.; Puska, M.; Rantala, T. T.; Schiøtz, J.; Thygesen, K. S.; Jacobsen, K. W. *J. Phys.: Condens. Matter* **2010,** *22,* 253202. doi:10.1088/0953-8984/22/25/253202
22. Meir, Y.; Wingreen, N. S. *Phys. Rev. Lett.* **1992,** *68,* 2512–2515. doi:10.1103/PhysRevLett.68.2512
23. Datta, S.; Tian, W.; Hong, S.; Reifenberger, R.; Henderson, J. I.; Kubiak, C. P. *Phys. Rev. Lett.* **1997,** *79,* 2530–2533. doi:10.1103/PhysRevLett.79.2530
24. Li, Z.; Li, B.; Yang, J.; Hou, J. G. *Acc. Chem. Res.* **2010,** *43,* 954–962. doi:10.1021/ar9001558
25. Birnbaum, T.; Hahn, T.; Martin, C.; Kortus, J.; Fronk, M.; Lungwitz, F.; Zahn, D. R. T.; Salvan, G. *J. Phys.: Condens. Matter* **2014,** *26,* 104201. doi:10.1088/0953-8984/26/10/104201
26. Lindner, S.; Treske, U.; Knupfer, M. *Appl. Surf. Sci.* **2013,** *267,* 62–65. doi:10.1016/j.apsusc.2012.06.104
27. Rosei, F.; Schunack, M.; Naitoh, Y.; Jiang, P.; Gourdon, A.; Laegsgaard, E.; Stensgaard, I.; Joachim, C.; Besenbacher, F. *Prog. Surf. Sci.* **2003,** *71,* 95–146. doi:10.1016/s0079-6816(03)00004-2
28. Rocha, A. R.; Garcia-Suárez, V. M.; Bailey, S. W.; Lambert, C. J.; Ferrer, J.; Sanvito, S. *Nat. Mater.* **2005,** *4,* 335–339. doi:10.1038/nmat1349
29. Lindner, S.; Treske, U.; Grobosch, M.; Knupfer, M. *Appl. Phys. A: Mater. Sci. Process.* **2011,** *105,* 921–925. doi:10.1007/s00339-011-6648-x
30. Brede, J.; Atodiresei, N.; Kuck, S.; Lazić, P.; Caciuc, V.; Morikawa, Y.; Hoffmann, G.; Blügel, S.; Wiesendanger, R. *Phys. Rev. Lett.* **2010,** *105,* 047204. doi:10.1103/PhysRevLett.105.047204
31. Chen, X.; Fu, Y.-S.; Ji, S.-H.; Zhang, T.; Cheng, P.; Ma, X.-C.; Zou, X.-L.; Duan, W.-H.; Jia, J.-F.; Xue, Q.-K. *Phys. Rev. Lett.* **2008,** *101,* 197208. doi:10.1103/PhysRevLett.101.197208
32. Krstić, P. S.; Dean, D. J.; Zhang, X.-G.; Keffer, D.; Leng, Y. S.; Cummings, P. T.; Wells, J. C. *Comput. Mater. Sci.* **2003,** *28,* 321–341. doi:10.1016/s0927-0256(03)00116-2
33. Evers, F.; Weigend, F.; Koentopp, M. *Phys. Rev. B* **2004,** *69,* 235411. doi:10.1103/PhysRevB.69.235411
34. Toher, C.; Filippetti, A.; Sanvito, S.; Burke, K. *Phys. Rev. Lett.* **2005,** *95,* 146402. doi:10.1103/PhysRevLett.95.146402
35. Sai, N.; Zwolak, M.; Vignale, G.; Di Ventra, M. *Phys. Rev. Lett.* **2005,** *94,* 186810. doi:10.1103/PhysRevLett.94.186810
36. Vignale, G.; Kohn, W. In *Electronic Density Functional Theory: Recent Progress and New Directions;* Dobson, J. F.; Vignale, G.; Das, M. P., Eds.; Plenum Press, 1996; pp 199 ff.
37. Marques, M. A. L.; Ullrich, C. A.; Nogueira, F.; Rubio, A.; Burke, K.; Gross, E. K. U. *Time-Dependent Density Functional Theory. Lecture Notes in Physics;* Springer, 2006.

38. Arulmozhiraja, S.; Coote, M. L. *J. Chem. Theory Comput.* **2012,** *8,* 575–584. doi:10.1021/ct200768b
39. Nakajima, S. *Prog. Theor. Phys.* **1958,** *20,* 948–959. doi:10.1143/PTP.20.948
40. Zwanzig, R. *J. Chem. Phys.* **1960,** *33,* 1338. doi:10.1063/1.1731409
41. Tokuyama, M.; Mori, H. *Prog. Theor. Phys.* **1976,** *55,* 411–429. doi:10.1143/PTP.55.411
42. Hashitsume, N.; Shibata, F.; Shingū, M. *J. Stat. Phys.* **1977,** *17,* 155–169. doi:10.1007/BF01040099
43. Schoeller, H.; Schön, G. *Phys. Rev. B* **1994,** *50,* 18436–18452. doi:10.1103/PhysRevB.50.18436
44. König, J.; Schoeller, H.; Schön, G. *Europhys. Lett.* **1995,** *31,* 31. doi:10.1209/0295-5075/31/1/006
45. Breuer, H.; Petruccione, F. *The Theory of Open Quantum Systems;* Oxford University Press, 2002.
46. Bruus, H.; Flensberg, K. *Many-Body Quantum Theory. Condensed Matter Physics;* Oxford University Press, 2004.
47. Mitra, A.; Aleiner, I.; Millis, A. J. *Phys. Rev. B* **2004,** *69,* 245302. doi:10.1103/PhysRevB.69.245302
48. Koch, J.; von Oppen, F.; Oreg, Y.; Sela, E. *Phys. Rev. B* **2004,** *70,* 195107. doi:10.1103/PhysRevB.70.195107
49. Elste, F.; Timm, C. *Phys. Rev. B* **2005,** *71,* 155403. doi:10.1103/PhysRevB.71.155403
50. Timm, C.; Elste, F. *Phys. Rev. B* **2006,** *73,* 235304. doi:10.1103/PhysRevB.73.235304
51. Timm, C. *Phys. Rev. B* **2008,** *77,* 195416. doi:10.1103/PhysRevB.77.195416
52. Timm, C. *Phys. Rev. B* **2011,** *83,* 115416. doi:10.1103/PhysRevB.83.115416
53. Sobczyk, S.; Donarini, A.; Grifoni, M. *Phys. Rev. B* **2012,** *85,* 205408. doi:10.1103/PhysRevB.85.205408
54. Bardeen, J. *Phys. Rev. Lett.* **1961,** *6,* 57–59. doi:10.1103/PhysRevLett.6.57
55. Prange, R. E. *Phys. Rev.* **1963,** *131,* 1083–1086. doi:10.1103/PhysRev.131.1083
56. Zawadowski, A. *Phys. Rev.* **1967,** *163,* 341–351. doi:10.1103/PhysRev.163.341
57. Appelbaum, J. A.; Brinkman, W. F. *Phys. Rev.* **1969,** *186,* 464–470. doi:10.1103/PhysRev.186.464
58. Caroli, C.; Combescot, R.; Nozières, P.; Saint-James, D. *J. Phys. C: Solid State Phys.* **1971,** *4,* 916. doi:10.1088/0022-3719/4/8/018
59. Feuchtwang, T. E. *Phys. Rev. B* **1974,** *10,* 4121–4134. doi:10.1103/PhysRevB.10.4121
60. Patton, K. R. *arXiv.org, e-Print Arch., Condens. Matter* **2010,** 1007.1238.
61. Appelbaum, J. A. *Phys. Rev.* **1967,** *154,* 633–643. doi:10.1103/PhysRev.154.633
62. Löwdin, P.-O. *J. Chem. Phys.* **1950,** *18,* 365–375. doi:10.1063/1.1747632
63. Mayer, I. *Int. J. Quantum Chem.* **2002,** *90,* 63–65. doi:10.1002/qua.981
64. Slater, J. C.; Koster, G. F. *Phys. Rev.* **1954,** *94,* 1498–1524. doi:10.1103/PhysRev.94.1498
65. Bigelow, W. C.; Pickett, D. L.; Zisman, W. A. *J. Colloid Sci.* **1946,** *1,* 513–538. doi:10.1016/0095-8522(46)90059-1
66. Scheffler, M.; Smykalla, L.; Baumann, D.; Schlegel, R.; Hänke, T.; Toader, M.; Büchner, B.; Hietschold, M.; Hess, C. *Surf. Sci.* **2013,** *608,* 55–60. doi:10.1016/j.susc.2012.09.017
67. Smykalla, L.; Shukrynau, P.; Korb, M.; Lang, H.; Hietschold, M. *Nanoscale* **2015,** *7,* 4234–4241. doi:10.1039/C4NR06371F
68. Poirier, G. E.; Tarlov, M. J.; Rushmeier, H. E. *Langmuir* **1994,** *10,* 3383–3386. doi:10.1021/la00022a004
69. Vuillaume, D.; Boulas, C.; Collet, J.; Davidovits, J. V.; Rondelez, F. *Appl. Phys. Lett.* **1996,** *69,* 1646–1648. doi:10.1063/1.117444
70. Whitesides, G. M.; Boncheva, M. *Proc. Natl. Acad. Sci. U. S. A.* **2002,** *99,* 4769–4774. doi:10.1073/pnas.082065899
71. Prinz, V. Y.; Seleznev, V. A.; Gutakovsky, A. K.; Chehovskiy, A. V.; Preobrazhenskii, V. V.; Putyato, M. A.; Gavrilova, T. A. *Physica E* **2000,** *6,* 828–831. doi:10.1016/s1386-9477(99)00249-0
72. Schmidt, O. G.; Eberl, K. *Nature* **2001,** *410,* 168. doi:10.1038/35065525
73. Bof Bufon, C. C.; Cojal González, J. D.; Thurmer, D. J.; Grimm, D.; Bauer, M.; Schmidt, O. G. *Nano Lett.* **2010,** *10,* 2506–2510. doi:10.1021/nl1010367
74. Thurmer, D. J.; Bof Bufon, C. C.; Deneke, C.; Schmidt, O. G. *Nano Lett.* **2010,** *10,* 3704–3709. doi:10.1021/nl1022145
75. Bof Bufon, C. C.; Arias Espinoza, J. D.; Thurmer, D. J.; Bauer, M.; Deneke, C.; Zschieschang, U.; Klauk, H.; Schmidt, O. G. *Nano Lett.* **2011,** *11,* 3727–3733. doi:10.1021/nl201773d
76. Müller, C.; Bof Bufon, C. C.; Navarro Fuentes, M. E.; Makarov, D.; Mosca, D. H.; Schmidt, O. G. *Appl. Phys. Lett.* **2012,** *100,* 022409. doi:10.1063/1.3676269
77. Grimm, D.; Bof Bufon, C. C.; Deneke, C.; Atkinson, P.; Thurmer, D. J.; Schäffel, F.; Gorantla, S.; Bachmatiuk, A.; Schmidt, O. G. *Nano Lett.* **2013,** *13,* 213–218. doi:10.1021/nl303887b
78. Bof Bufon, C. C.; Vervacke, C.; Thurmer, D. J.; Fronk, M.; Salvan, G.; Lindner, S.; Knupfer, M.; Zahn, D. R. T.; Schmidt, O. G. *J. Phys. Chem. C* **2014,** *118,* 7272–7279. doi:10.1021/jp409617r
79. Leijnse, M. *Phys. Rev. B* **2013,** *87,* 125417. doi:10.1103/PhysRevB.87.125417

License and Terms

BEILSTEIN JOURNAL OF NANOTECHNOLOGY

Ester formation at the liquid–solid interface

Nguyen T. N. Ha[*1], Thiruvancheril G. Gopakumar[*2], Nguyen D. C. Yen[1], Carola Mende[3], Lars Smykalla[1], Maik Schlesinger[4], Roy Buschbeck[3], Tobias Rüffer[3], Heinrich Lang[3], Michael Mehring[4] and Michael Hietschold[1]

Full Research Paper

Open Access

Address:
[1]Solid Surfaces Analysis Group, Institute of Physics, Technische Universität Chemnitz, D-09107 Chemnitz, Germany, [2]Department of Chemistry, Indian Institute of Technology Kanpur, Kanpur 208016, India, [3]Inorganic Chemistry, Institute of Chemistry, Technische Universität Chemnitz, D-09107 Chemnitz, Germany, and [4]Coordination Chemistry, Institute of Chemistry, Technische Universität Chemnitz, D-09107 Chemnitz, Germany

Email:
Nguyen T. N. Ha[*] - thi-ngoc-ha.nguyen@physik.tu-chemnitz.de;
Thiruvancheril G. Gopakumar[*] - gopan@iitk.ac.in

* Corresponding author

Keywords:
on-surface reaction; scanning tunneling microscopy; trimesic acid; undecan-1-ol

Beilstein J. Nanotechnol. **2017,** *8,* 2139–2150.
doi:10.3762/bjnano.8.213

Received: 13 April 2017
Accepted: 19 September 2017
Published: 12 October 2017

This article is part of the Thematic Series "Towards molecular spintronics".

Guest Editor: G. Salvan

Abstract

A chemical reaction (esterification) within a molecular monolayer at the liquid–solid interface without any catalyst was studied using ambient scanning tunneling microscopy. The monolayer consisted of a regular array of two species, an organic acid (trimesic acid) and an alcohol (undecan-1-ol or decan-1-ol), coadsorbed out of a solution of the acid within the alcohol at the interface of highly oriented pyrolytic graphite (HOPG) (0001) substrate. The monoester was observed promptly after reaching a threshold either related to the increased packing density of the adsorbate layer (which can be controlled by the concentration of the trimesic acid within the alcoholic solution via sonication or extended stirring) or by reaching a threshold with regards to the deposition temperature. Evidence that esterification takes place directly at the liquid–solid interface was strongly supported.

Introduction

On-surface reactions are a widespread class of chemical reactions taking place on a surface or at an interface involving active participation of two-dimensional molecular entities. This participation is usually beyond the role of just being a solid support for the reactants.

Using scanning tunneling microscopy (STM) it is possible to actively study the elementary processes of on-surface reactions. Different types of reactions such as Ullmann coupling, imine coupling, boronic anhydridation reaction, etc. have been explored on surfaces [1-14]. In the publication by Hla et al. [1]

the reaction of two single iodobenzene molecules towards one biphenyl molecule (an Ullmann reaction) on the edge of a monoatomic step of a Cu(111) substrate surface has been thoroughly investigated. In addition to the imaging, the tunnel tip was active in promoting the reaction by local energy transfer to and local transport of the reactants. Endothermal on-surface reactions of a whole molecular monolayer can be initiated by a corresponding heating process after deposition. STM imaging in different stages of the reaction has been demonstrated in such cases where the molecular entities changed their appearance due to structural and electronic changes during different reaction steps. Examples for this are the polymerization reaction of brominated copper-2,3,7,8,12,13,17,18-octabromo-5,10,15,20-tetraphenylporphyrin ($CuTPPBr_8$) at an Au(111) substrate [2] or the polymerization of 1,3,6,8-tetrabromopyrene on Cu(111) and Au(111) substrates [3]. Characteristic for all these studies is that they are performed at an almost ideal monocrystalline surface in ultra-high vacuum (UHV).

On the other hand, solid–liquid interfaces are much more often encountered in real world applications ranging from heterogeneous catalysis to biomembranes. Heating is in such cases usually limited by the boiling of the liquid phase, and other means to initiate on-surface reactions are often required.

Here we present a chemical reaction (esterification) between trimesic acid (benzene-1,3,5-tricarboxylic acid; TMA) dissolved in an alcoholic solvent (undecan-1-ol or decan-1-ol) on a highly oriented pyrolytic graphite (HOPG) (0001) substrate. The reaction proceeds without catalyst and is controlled by the solute concentration at the interface as well as deposition temperature. To the best of our knowledge, such a study has not yet been performed by other researchers. Ball and stick models of all the molecules used in the study are illustrated in the Figure 1.

Esterification is a chemical reaction which finds application in several areas like biology (synthesis of drug molecules), the food industry (artificial flavors and fragrances), and textiles (polyesters) [15]. The most common route of esterification starts from a carboxylic acid and an alcohol in the presence of dehydrating agents [16]. The reaction proceeds typically slow and highly reversible without a catalyst. Dehydrating agents like sulfuric or sulfonic acid [15], or milder ones like dicyclohexylcarbodiimide [17], triphenylphosphane and diazenedicarboxylate [18] are used for esterification from organic acids. In UHV, an on-surface esterification of benzene-1,4-diboronic acid and triphenylene-2,3,6,7,10,11-hexol to a 1,3,2-dioxaborole heterocycle has been studied by Zwaneveld et al. [19].

Trimesic acid (TMA) has become the "drosophila melanogaster molecule" for studies of self-assembly at crystalline surfaces both under UHV conditions [20] and at the solid–liquid interface [21-27]. Nath et al. showed the coadsorption of TMA with alcohols at an alcohol/graphite interface [26,27]. Although an ester formation is expected when mixing alcohol and acid, in situ ester formation was not found in their experiments under ambient conditions [27]. Molecular mixture at solid−liquid interfaces could possibly initiate chemical reactions and be monitored in situ with scanning tunneling microscopy (STM). Metal complexation reactions, polymerizations [28-30] and photochemical dimerization [31] are shown to be initiated at the solid–liquid interface. Initial efforts have been made to perform chemical reactions leading to covalently stabilized adlayers at metal crystal/UHV interfaces [2,10-12]. However, the size of covalently linked domains is often limited in UHV due to low diffusion of the components forming the adlayers. This problem may be easily circumvented at solid–liquid interfaces due to the high dynamics of reactants in solution. Furthermore, in this case, defects in the adsorbate layer are more often self-repaired.

Results

A typical STM image of the coadsorption pattern of TMA and undecan-1-ol is shown in Figure 2a. This is consistent with the reported linear pattern (LP) of alcohol and TMA coadsorbed on

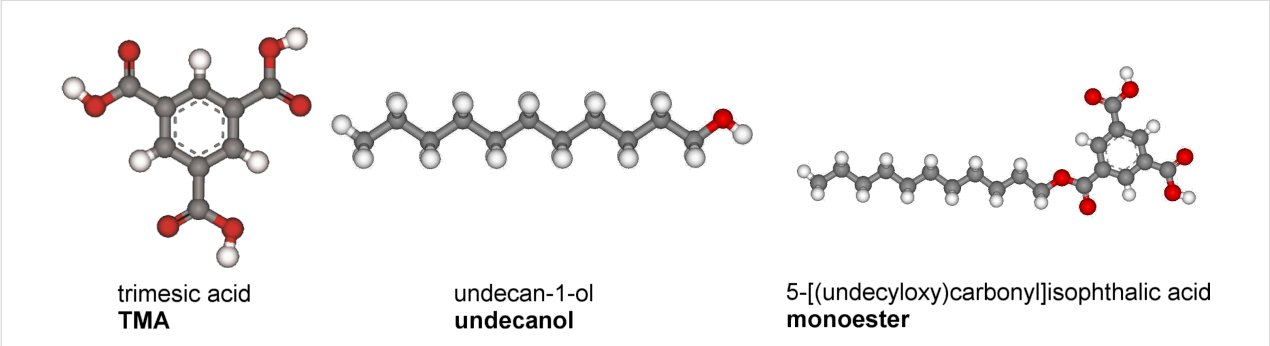

Figure 1: Molecular structures of the molecules involved in the study and shortened forms of their names (in bold).

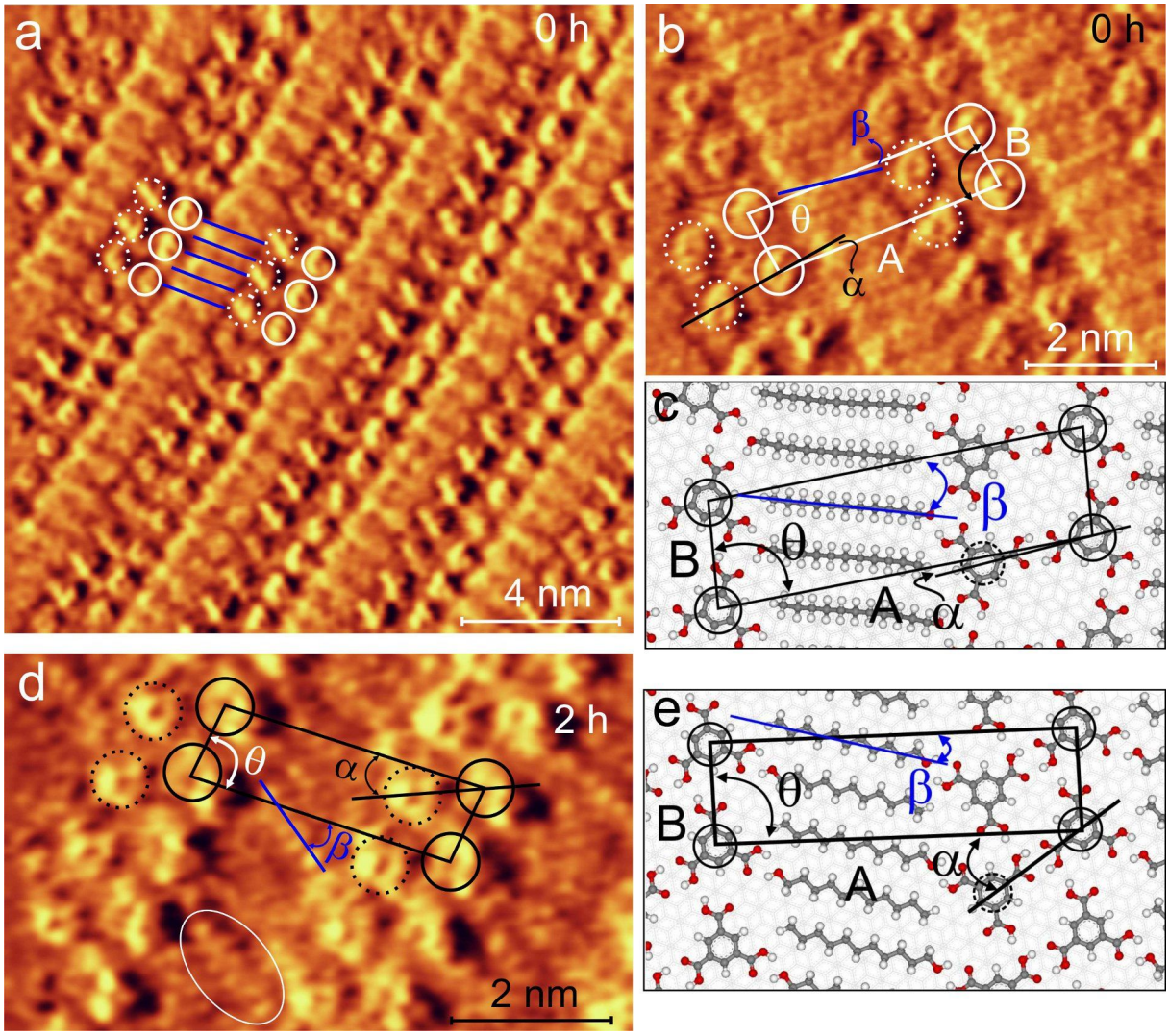

Figure 2: a) STM constant height image (1.2 V, 1 nA) of a TMA–undecanol linear pattern (LP0) formed on HOPG (0001) from solution without previous sonication. The LP0 consists of alternating TMA dimer tapes (dashed and full-line circle pairs) between lamellas of undecan-1-ol (blue lines); (a) is reproduced from [25], copyright 2013 Elsevier. b) A magnified section of LP0: the unit cell (parallelogram) contains two TMA and two undecanol molecules; A and B are unit cell parameters and θ is the angle embedded between them. β is the angle between the molecular axis of the undecanol back bone and the long axis of the unit cell. α describes the relative orientation of the TMA dimer with respect to the long axis of unit cell. c) Dreiding force field optimized geometric model (initial geometry based on experiments) of the LP0. d) STM constant height image (1.2 V, 1 nA) of TMA–undecanol LP2 structure formed on HOPG (0001) from solution sonicated for 2 h and the corresponding Dreiding force field optimized geometry (e). The white oval in (d) shows a submolecularly resolved undecyl chain part of undecanol.

the HOPG (0001) surface [26,27]. TMA interacts with undecanol via noncovalent hydrogen bonding and forms the observed LP. We call this structure LP0, where 0 indicates no previous sonication of the solution. The pattern consists of undecanol lamella (blue lines in Figure 2a [25]) and the TMA dimer tapes, which are represented by the pairs of full-line and dashed circles in Figure 2a. A magnified section of the linear pattern is shown in Figure 2b. The typical donor–acceptor double hydrogen bonds govern the interaction between TMA molecues within the TMA dimer tapes [26,27]. The unit cell parameters of this LP are A ≈ 35 Å and B ≈ 10 Å. Within the unit cell, TMA dimers form an angle of α ≈ 8° with respect to the long side of the unit cell (A). The angle θ (≈ 84°) is the angle between the unit cell vectors and β (≈ 6°) describes the relative orientation of the undecanol chain with respect to the long side A of the unit cell.

A Dreiding force field optimized structure (based on the initial geometry from experiments) of the linear pattern shown in Figure 2c is comparable with the adsorption geometry of TMA and undecanol observed in the LP. The adsorption geometry of TMA, the standard dimer hydrogen bonding motifs via carboxy

groups between TMA molecules and their interaction with undecanol are discernible. The orientation of the zig-zag plane of the alkyl chain of undecanol is assumed to be perpendicular to surface according to Nath et al. [26,27]. The geometric parameters obtained from the simulations fit fairly well with the experiments, except for β (see Supporting Information File 1 for details). It has been shown that alkyl chains organize on HOPG in a zig-zag manner at well-defined sites [32,33]. Therefore, the difference in β observed between simulation and experiments is attributed to the interaction between molecules and the substrate, which is not included in the actual model. However, it considers the intermolecular interactions within the adlayer quite reasonably as revealed by the resemblance of the TMA dimer and undecanol lamella with the experiment.

The structures of LP formed from solutions sonicated for a longer time (at least 2 h) are noticeably different from LP0. The LP from the solution sonicated for 2 h (LP2) is shown in Figure 2d and the corresponding optimized geometry in Figure 2e. The angle between unit cell parameters A (≈34 Å) and B (≈10 Å) of LP2 remains nearly the same θ (83°) as for LP0. However, the relative orientation of the TMA dimer with respect to the long side of the unit cell in LP2 (α ≈ 23°) is clearly different from LP0 (α ≈ 8°). Additionally, undecanol molecules are tilted steeper (β ≈ 37°) compared to LP0. As a consequence, the packing density of LP2 is slightly larger than that of LP0. Undecanol molecules (one of them marked with an oval in Figure 2d) show clearly a substructure for its zig-zag plane which is parallel to the substrate.

A comparison of energetics from force field calculations (see Supporting Information File 1 for details) shows that the structure which corresponds to LP0 is energetically more favorable than LP2. This is in agreement with a previous report, where theoretical calculations showed the same result [26,27]. That is, the most favorable structure expected for TMA coadsorbed from an untreated solution in undecanol is LP0 without any external triggers. The solubility of TMA in undecanol increases upon sonication. From this solution, TMA molecules will be repelled more easily when exposed to a clean surface (HOPG) and therefore their concentration at the interface increases. UV–vis studies have confirmed such a direct correlation between sonication time and concentration (see Supporting Information File 1). Previous reports have also shown that TMA forms high packing density structures only when deposited from relatively high concentration solutions in phenyloctane and fatty acids [23-25]. That is, the energetically less favorable structure (LP2) is triggered by an external control parameter – the excess concentration at the interface.

When the sonication time is increased to 4 h, the corresponding structure LP4 (Figure 3a) quite resembles LP0 except for the

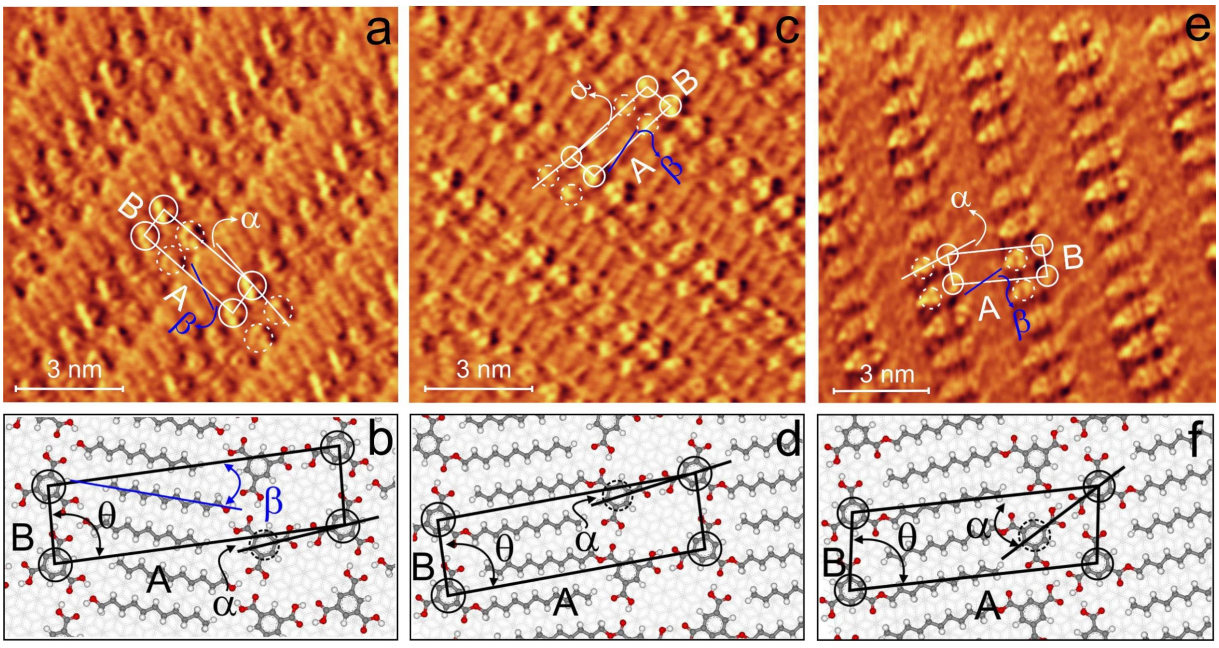

Figure 3: STM constant height image (1.2 V, 1 nA) of linear pattern LP4 (a), monoester type-I (c), and monoester type-II (e) deposited from a TMA–undecanol solution sonicated for 4 h. The unit cell is depicted by a parallelogram in STM images and A and B are the corresponding unit cell parameters. The blue line indicates the orientation of undecanol (a) or undecyl chains of the ester molecule (c, e) with respect to the long side of the unit cell within the lamella. Force field optimized geometries of the linear pattern (b) and patterns formed by monoesters (d, f). In the models, solid circles indicate TMA (TMA head group in the case of ester) at the corners of the unit cells and dashed circles indicate the second TMA (TMA head group) of the dimer pair.

orientation of the undecanol with respect to the TMA dimer (β ≈ 33°). In addition to LP4, two further close-packed structures are observed from solutions sonicated longer than 4 h (Figure 3c,e). The significant difference of these structures compared to LP4 is the shorter A-axis (a ≈12–18% reduction compared to LP0 and LP2). The geometric parameters corresponding to these structures are listed in Table 1. These additional structures cannot be interpreted in terms of coadsorption of individual TMA and undecanol molecules but of a reaction product of them which should be the corresponding monoester (this assumption will be justified later in this paper). We address these compact patterns as ester patterns in the following sections. To verify the decrease in A for the ester pattern, we have analyzed a split image (ester pattern and graphite in the same frame). The imaged graphite lattice is used as reference to scale the images and it clearly shows here that the magnitude of A is ≈31 Å (see Supporting Information File 1 for the split image).

There are two ester patterns visible on the surface which are slightly different in their value of A and significantly differ for the relative orientation of the head groups of the monoester (α; dimer formed by the TMA group of ester) and undecyl lamella (β; with respect to the long side of unit cell). We refer to the ester at the interface with A ≈ 31 Å as ester4-type-I and with A ≈ 28 Å as ester4-type-II in the following sections. The Dreiding force field optimized geometries of these ester structures (based on the initial geometry from the experiment) are shown in Figure 3d,f. The adsorption geometries of type-I and type-II esters (except β) are comparable with the experiments. The relative orientation of the head group of TMA and undecyl chain of the ester patterns resembles LP0 and LP2. This is very likely connected with the original linear patterns from which each type of these ester patterns has developed. Ester4-type-I has a lower packing density than ester4-type-II, which also holds for LP0 and LP2. Further geometrical details of the simulation are provided in Supporting Information File 1.

The optimized structure corresponding to LP0 (Figure 2c) shows that within the linear pattern even closer packing is not possible. This is hindered by steric repulsion between the methyl end groups of undecanol and the hydrogen atoms of the C–H groups of TMA. A closer packing is only possible via reorganization of TMA dimers as seen in LP2 or via a gauche isomer of undecanol parallel to the surface. However, the undecanol molecules are observed as linear features in the STM images, which is consistent with their linear zig-zag geometry. That is, the observed decrease in A could be explained only by the replacement of TMA and undecanol by the corresponding monoester at the interface. The theoretically calculated distance between neighboring molecules in ester patterns is 19–24% shorter than that in various LPs. This is consistent to the observed reduction of ≈12–18% in A for the ester pattern compared to LPs. That is, ester formation only can further increase the packing density. The geometric pattern of the ester molecules here resembles the adsorption structure of hexadecyl ester on a Au(111) surface [34].

We then further extended the sonication time up to 8 h. Both ester pattern type-I and type-II are obtained from solutions sonicated for 6 and 8 hours as well. The structure of these ester patterns remains nearly unchanged when the sonication time is increased. However, the A value of LP increases slightly as the time of sonication increases, whereas the other geometrical parameters (e.g., B, θ) remain nearly unchanged. As a result, the packing density of LP decreases slightly with increasing sonication time. It is to be noted that the distances between TMA dimers in the dimer tape of LP and the dimer of TMA head groups in ester pattern type-I and type-II remain the same for all sonication times. That is, the dimers are always intact and with

Table 1: Unit cell parameters A, B, and θ orientation angles α, β, and molecular packing densities of different linear patterns (LP) and monoester patterns formed after sonication or stirring. PD is packing density (molecules/nm^2).

Sonication time (h)	0	2	4		Synthesized monoester
Stirring time (h)	0	10	15		
	LP0	LP2	LP4	Ester4[d]	Ester pattern
A (Å)[a]	35	34	36	31 (28)	29
B (Å)[a]	10	10	10	10 (10)	10
θ (°)[b]	84	83	86	83 (83)	83
α (°)[b]	8	23	8	4 (25)	25
β (°)[b]	6	37	33	7 (27)	28
PD[c]	0.58	0.61	0.54	0.65 (0.71)	0.65

[a]Distances may have an error of ±2 Å, [b]angles may have an error of ±2°, [c]PDs may have an error of ±0.2 nm^{-2}, [d]the numbers in parenthesis correspond to values for type-II monoester (see Figure 2e).

sonication only their relative orientation with respect to the TMA tape changes in different structures (Table 1).

Practically the same ester patterns are observed also for two alternative preparation methods: prolonged magnetic stirring for about 15 h or increasing the substrate temperature to 60–80 °C during deposition. As an example, the STM image of TMA–monoundecyl ester type-I obtained from the TMA–undecanol solution stirred for 15 h is shown in Figure 4.

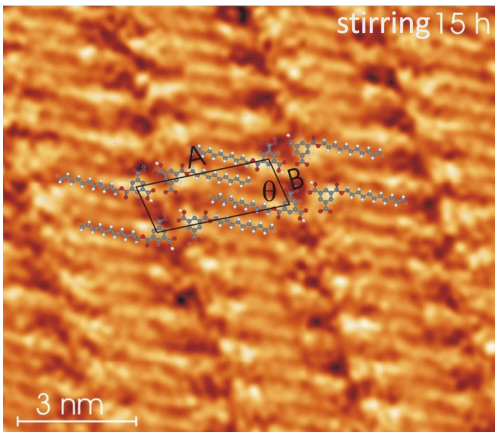

Figure 4: STM constant current image (1.1 V, 1 nA) of TMA–monoundecyl ester type-I obtained from a TMA–undecanol solution stirred for 15 h. The corresponding unit cell parameters of the above pattern are A = 29 ± 1 Å, B = 10 ± 1 Å.

The ester pattern observed after increasing the substrate temperature during deposition (subsequent STM was carried out at room temperature) is shown in Figure 5. The unit cell parameter A = 3.0 ± 0.1 nm and the angle of the undecanol alkyl chain with respect to A, β = 16 ± 3°, are obtained from the STM images. With respect to most of the structural parameters, the patterns correspond (see Table 1) to that observed for sonication and stirring. This type of preparation procedure has been previously reported and leads also to an increased concentration in the deposited solution due to enforced evaporation as well as to an increased mobility of the molecules [35].

Figure 6 shows simulated constant height mode STM images obtained from a calculated local density of states (LDOS) of the free monoester molecule. Both HOMO and LUMO show a strong intensity close to the location of TMA and binding to the alkane chain. Such a characteristic feature can be observed also in the experimental STM images of Figure 4 and Figure 5. Of course, most of the details from the calculation cannot be expected to be well reproduced in an experimental STM images due to the approximation of isolated molecules neglecting the adsorbate–substrate interaction as well as various effects of the tip and the environment on the imaging.

To further prove that the patterns observed at high sonication/stirring time and high substrate temperature really show deposited monoester molecules, we have studied the self-assembly of the synthesized monoester (see Supporting Information File 1) dissolved in undecanol as a reference experiment. The monoester was synthesized according to literature [36]. Figure 7 shows a self-assembled pattern of the synthesized monoester deposited at the HOPG–undecanol interface (the concentration of the solution should be considerable less than 8×10^{-3} M (there were sediments of molecules at the

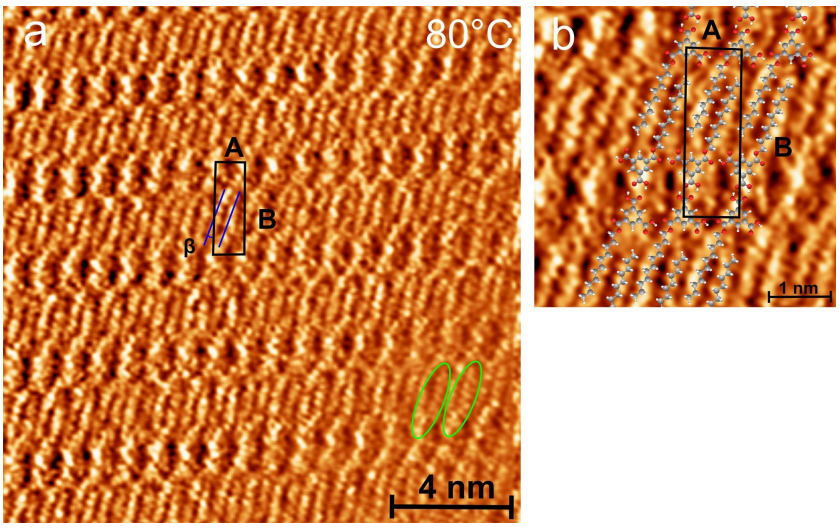

Figure 5: STM constant height images (1.2 V, 1.3 nA) of monoester obtained from a TMA–undecanol solution on HOPG (0001) deposited at ≈60–80 °C. (a) The parallelogram depicts the unit cell of the ester pattern where A and B are the corresponding unit cell parameters. (b) The force-field-optimized geometry of the monoester pattern overlaid on the STM image (5 × 5 nm^2).

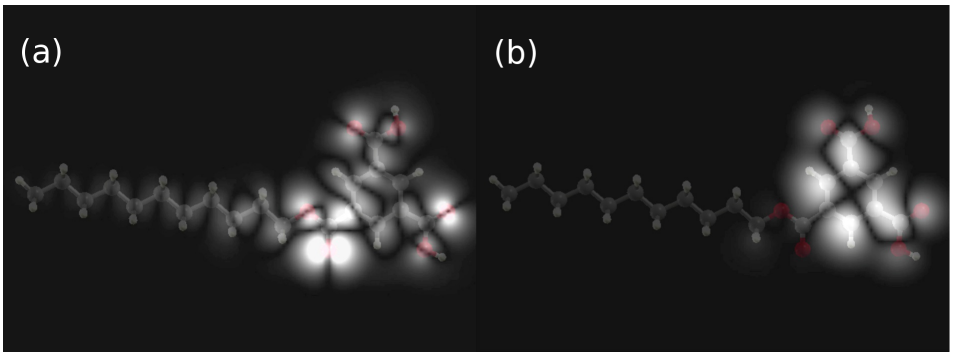

Figure 6: Simulation of the STM constant height mode images (HOMO (a) and LUMO (b)) of a single monoester molecule.

bottom of the vial). The circles depict the location of TMA groups of the synthesized monoester. A and B are the unit cell parameters and θ is the angle between them. α depicts the angle between the molecular unit cell axis A and the pair formed by TMA groups of adjacent monoesters. These quantities are indicated in Table 1. The geometrical parameters of the synthesized monoester pattern obtained here are in excellent agreement with those observed for ester type-II formed from the TMA–undecanol solutions at high sonication or stirring time or enhanced substrate temperature. This experiment establishes that the observed close packed patterns (ester type-I and -II) obtained at the TMA–undecanol interface from solutions at high sonication/stirring time and high substrate temperature are made of monoester molecules.

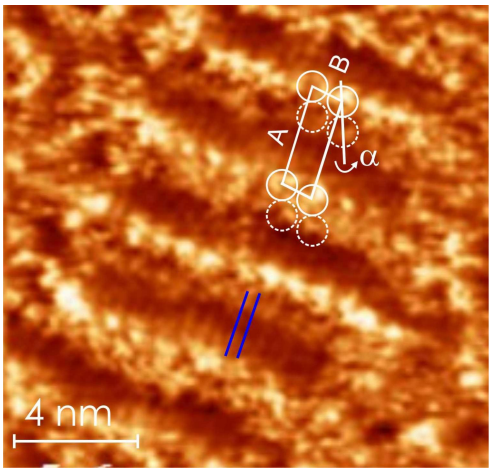

Figure 7: STM constant height image (1.2 V, 1 nA) of the linear pattern of the synthesized monoester at the HOPG–undecanol interface (A = 3.1 ± 0.1 nm; B = 1.0 ± 0.1 nm; α = 23 ± 1°). The triangular features indicated with circles correspond to the TMA head groups and blue lines indicate alkyl chains of synthesized monoester molecules. The orientation of the alkyl chain adopts an angle of ≈2° with respect to the A axis (indicated as β in other images). According to the calculation it is expected that the alkyl chain of synthesized monoester should be almost parallel to the A axis.

To better understand the general behavior of ester formation in aliphatic alcohols, we have investigated the ester formation using decan-1-ol as an alternative solvent. Details of the LPs formed at different sonication times in this solution are provided in Supporting Information File 1. As in the case of undecanol, at low sonication times, for LPs of coadsorbed TMA and the alcohol molecules are formed. Different types of monoesters (type-I and type-II) are observed from solutions that were sonicated for four hours. After esterification, the packing density of LPs decreases as the sonication time increases. These results are all very similar to those obtained for the undecanol–TMA mixture. This shows that the concentration driven LPs and ester formation are very likely common for TMA and long chain alcohols such as decanol and undecanol.

Discussion

Generally, esterification is a reversible process (Scheme 1) and the yield is low without dehydrating agents [15-18]. To increase the yield, Le Chatelier's principle is commonly used; that is, the concentration of one of the reactants is increased. This is supported by the molecular collision theory. The higher the molecular concentration, the more collisions of suitable pairs of molecules can take place. The successful collisions should have also sufficient activation energy transferred at the moment of impact to break the existing bonds and to form new ones, resulting in the reaction products.

Scheme 1 shows a proposed reversible esterification route with a dimer intermediate of TMA and undecanol to TMA–monoundecyl ester. The possible formation of TMA–monoundecyl ester and water from a TMA–undecanol dimer in the gas phase (see energy diagram in Figure 8) was simulated. To simulate the reaction path and energy barrier, a "nudged elastic band" calculation was done using DFT with the program code GPAW [37]. The molecule was placed in a large box with non-periodic boundary conditions and 7 Å of vacuum in each direction. The starting and end geometry (reactants and

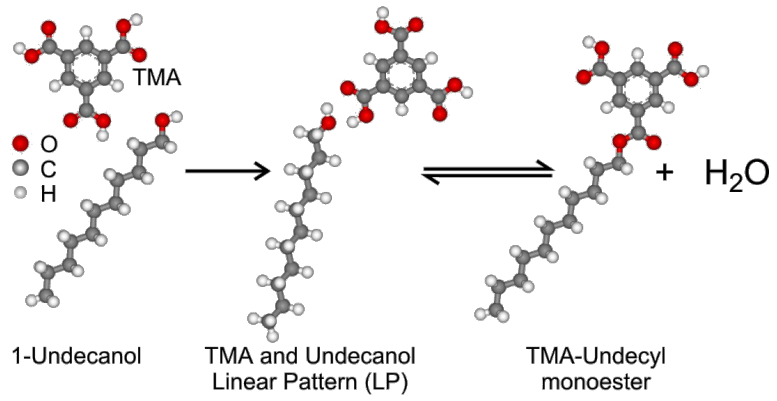

Scheme 1: Proposed scheme of ester formation from TMA and undecanol via an intermediate dimer.

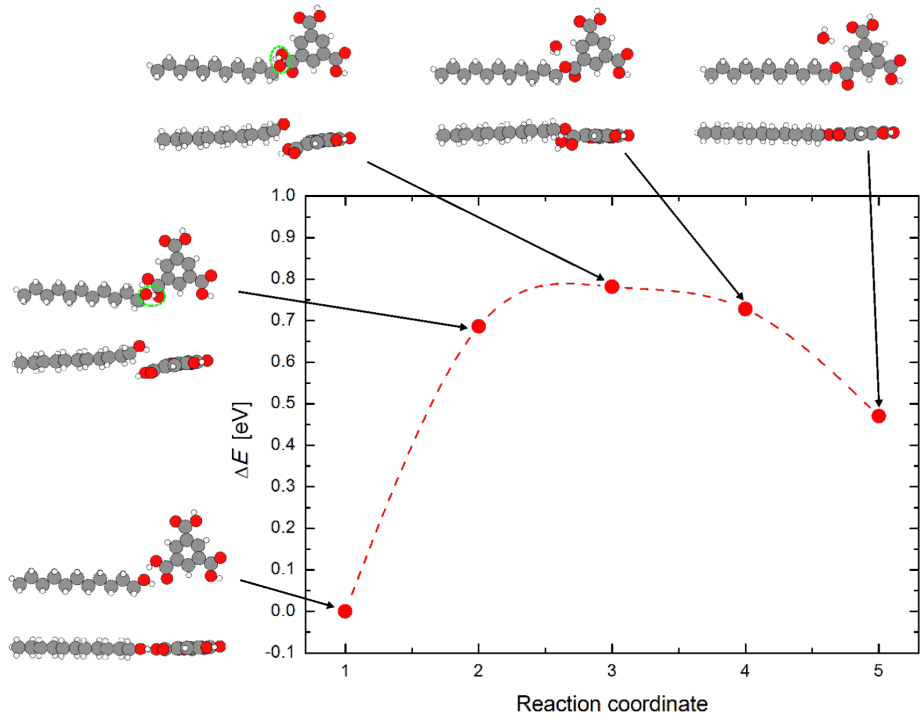

Figure 8: Energy diagram of the reaction path of TMA and undecanol to form TMA–undecyl ester and water for isolated molecules (gas phase) calculated using DFT (PBE). The corresponding geometry of the molecules in the simulation is shown for each energy point marked in the reaction path. The "flat approach" (almost 2-dimensional) as shown in the simulation for the free molecules is strongly supported by the underlying crystal surface in the experiments.

products) are first optimized separately, then three intermediate geometries are interpolated and the whole path of five reaction steps is relaxed together to find the lowest energy barrier. The XC-functional PBE [38], a LCAO dzp basis set, and default values for the self-consistency cut off were used. The starting and end geometry (reactants and products) are first optimized separately, then three points are interpolated and the whole path is relaxed together to find the lowest energy barrier.

The formation energy calculated for the monoester from undecanol and TMA is, $E_{ester} - (E_{TMA} + E_{undecanol} - E_{water}) \approx$ 470 meV with a reaction barrier of ≈800 meV. It is interesting to note that the reaction mechanism shows several intermediate steps that involve a nearly planar geometry of TMA and undecanol before the monoester formation. Therefore, we suggest that the coadsorption pattern (LP) allows the reactants to approach each other already in a quite favorable relative orienta-

tion for a subsequent reaction. That is the "flat approach" (almost 2-dimensional) necessary as shown in the simulation as the free molecules correspond fairly well also to the experimental situation of the on-surface reaction considered experimetally. The equilibrium that is established between ester and TMA–undecanol dimers at the interface can be influenced if excess reactants are offered at the interface. That is, monoester formation can be controlled by varying the concentration of the acid. By increasing the sonication time and stirring, the concentration of TMA is increased in the solution. Furthermore, when this solution is applied on a fresh HOPG surface, the additional TMA molecules within the solution tend to become preferentially accumulated at the interface. This increase in the concentration of TMA and the interface, together with its flat adsorption geometry (templated by the planar substrate surface), favors the esterification reaction to proceed forward.

Typically, the formation of an ester is promoted at high temperature. The effect of changing the temperature on the equilibrium, and thereby changing the heat in the system, can be understood by including heat energy in the reaction formula either on the side of reactants or the products. According to Le Chatelier's principle, an increased temperature would then favor the forward reaction of esterification similar to increasing the relative concentration of the reactant. Enhanced temperature can also result in an increased evaporation of water that is created in this reaction, thereby removing it and pulling the equilibrium to the side of the ester. On the other hand, aqueous systems help the equilibrium to be established in the reverse direction by providing an excess of the water needed for the hydrolysis. The temperature influence on a chemical reaction at the liquid–solid interface by STM is also reported by Hipps et al., that is, the formation of an ester promoted by high temperatures [39].

There remain three possible hypotheses concerning the origin of the ester or the location of esterification, respectively: 1) The ester molecules originate all from the solution (either as contamination or as the result of an esterification in the bulk liquid phase); 2) the seed molecules for the ordered adsorbed ester pattern originate from the solution but around them further esterification takes place at the interface; or 3) the esterification observed here is a typical on-surface reaction.

Concerning 1): ESIMS analysis (see Supporting Information File 1) showed some traces of the ester after sufficiently long sonication time due to an initiated reaction in the bulk of the solution. Furthermore, taking into account the detection limit of the method, there should be sufficient preexisting ester molecules in the droplet to enable a complete coverage of the substrate by an ester monolayer (ester pattern). Nevertheless, this hypothesis can be ruled out, since there is a threshold (for sonication/stirring time as well as deposition temperature) to find the monoester pattern. The threshold indicates a critical concentration of TMA in the solution within three different experimental approaches: sonication, stirring, and deposition at enhanced temperature. If the ester formed in the solution would be the origin of the ester pattern, then this pattern should be observed at lower sonication or stirring time or deposition temperature as well. We also note that sonicated solutions retained for several days (12 days) did not show any ester pattern (see Supporting Information File 1 for details of this experiment). This indicates a finite lifetime for the higher concentrated (possibly super-saturated) solution after which we observe only a linear pattern of TMA and undecanol (and no ester pattern). This would not be the case if the ester pattern originates from ester formed due to sonication within the solution.

Furthermore, the reference experiment with a solution of the monoester (which definitely had a much higher concentration of monoester molecules than the solutions discussed for the case 1) did verify the corresponding adsorption pattern but did not lead to a comparatively large ordered area of the pattern as had been found in the previous experiments (TMA–undecanol with 4 h sonication). Evidently, only some growth directly on the substrate could explain the experimental findings, and hypothesis 1) can be ruled out completely.

Concerning 2): There would definitely always be sufficient monoester molecules available in the solution – especially after the corresponding treatments (sonication, stirring or heating, respectively) to enable single-molecule adsorption with a subsequent growth process around a seed molecule coming from the solution. However, once again, such a process cannot explain the threshold behavior found in the deposition experiments here.

Concerning 3): An on-surface reaction can explain the concentration thresholds found which shifts the reaction balance towards the production of the ester by effectively increasing the concentration on the surface. This leads to an increased packing density of the coadsorbed reaction partners. Furthermore, their mutual arrangement, especially in the LP2 pattern, creates a good precondition for the final reaction initiated by something as a two-dimensional pressure. This drives the adjacent reaction partners even closer to each other with increasing packing density. Furthermore, the simulated reaction path of TMA–monoundecyl ester (Figure 8) does not only illustrate this statement, but also nicely shows how the role of the supporting planar substrate dramatically reduces the amount of mutual spatial configurations of the reaction partners in a very favorable way. We note that no other assembly (particularly any disordered phase) than the well-ordered LP and ester patterns

are observed at the interface of all solutions. As observed using ESIMS, the sonicated solutions possess minor amounts of monoester, diester and decarboxylation products. If these products would be the origin of the assembly at the interface, one should expect only a disordered phase, which is not the case in the experiments. Possible sonochemistry products formed in the solutions are most likely stabilized within the solutions and do not appear at the interface. After these discussions, hypotheses 1) and 2) can be ruled out and 3) is assumed as summarized in Figure 9.

As an outlook, we suggest to use appropriate diols to create covalently bound 2-dimentional networks made of the corresponding polyesters. For the present system based on TMA, this could lead to 3- and/or 6-fold symmetric networks in contrast to 4-fold symmetric networks which have been already fabricated based on porphyrines.

Conclusion

In summary we have investigated the molecular self-assembly from a solution of TMA in undecanol at the HOPG–undecanol interface. Above a critical concentration of TMA, which can be controlled by the time of sonication/stirring of the mixture of TMA and undecanol, a monoester is formed at the interface. A similar result was also observed by increasing the deposition temperature. To prove this assumption, we have also investigated the self-assembly of presynthesized monoester molecules at the undecanol–HOPG interface and observed a very similar pattern as obtained before. The monoester formation has been interpreted as an on-surface reaction. We believe that this result will initiate further work towards covalently bound ultra-thin surface coatings.

Experimental

TMA (0.05 g) and undecanol (7.5 mL, Aldrich, 98%) were mixed leading to a clear solution and a sediment of excess TMA at the bottom. Next, these samples were sonicated (1–8 h) or stirred (1–30 h). Afterward, the mixtures were either centrifuged or allowed to rest undisturbed for one day. From the optically clear supernatant 2 µL were put on a freshly cleaved HOPG (0001) basal plane substrate and in situ investigated using STM mechanically cut Pt(80)/Ir(20) tips. During imaging, the tip apex is introduced into the droplet deposited at the HOPG substrate. The figure captions of the STM images contain the imaging parameters for tunnel bias and current, respectively.

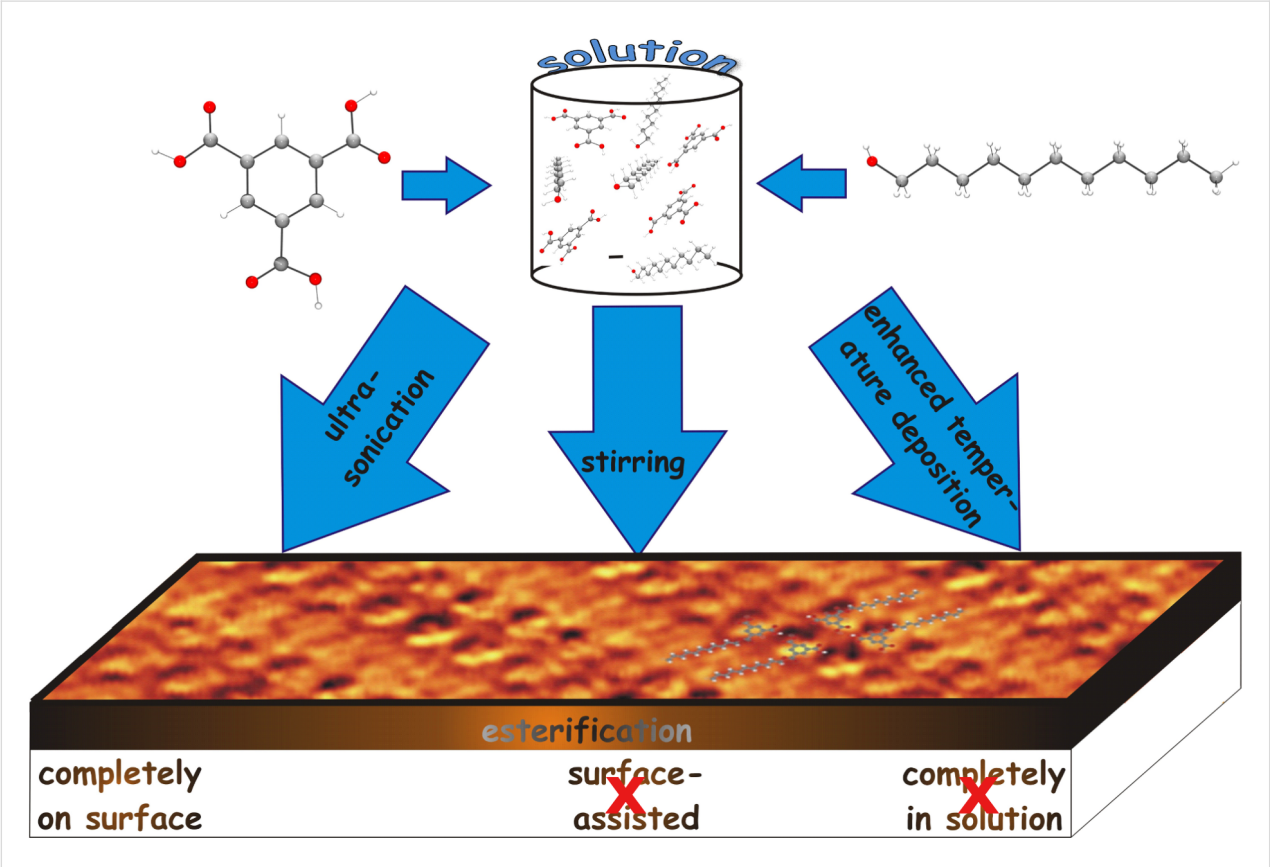

Figure 9: Three possible hypotheses for the formation of the monoester from TMA and undecanol.

The HOPG (0001) substrate was preheated up to 60–80 °C, then a droplet of 2 µL of unprocessed TMA–undecanol solution was applied on this preheated substrate. The sample was kept at that temperature for 10 min and then the substrate was cooled down to room temperature for STM imaging.

DFT calculations were carried out using the grid-based projector augmented wave method (GPAW) [37]. The PBE exchange-correlation functional [38] and the LCAO mode [37] with the standard double-zeta-polarized (dzp) basis set of atomic orbitals was used. The reaction path was modeled by a "nudged elastic band" (NEB), whereby each step was fully relaxed.

Supporting Information

Supporting Information File 1

Additional experimental results.
Dreiding force field calculations of different types of linear patterns of TMA and monoester on graphite double layer, UV–vis spectra as a function of sonication and concentration for different sonication times, a split image of the ester pattern and graphite, the synthesized monoester assembly pattern at the HOPG–undecanol interface, NMR and ESIMS spectra of the synthesized TMA–monoundecyl ester, evidence of self-assembly out of a solution of TMA in decanol controlled by concentration, ESIMS data of the ultrasonicated solution of TMA and undecanol-1, and the time-dependent evolution of LP and ester pattern.
[http://www.beilstein-journals.org/bjnano/content/supplementary/2190-4286-8-213-S1.pdf]

Acknowledgements

The authors thank for the financial support from the DFG Research Unit 1154 "Towards Molecular Spintronics".

References

1. Hla, S.-W.; Bartels, L.; Meyer, G.; Rieder, K.-H. *Phys. Rev. Lett.* **2000,** *85,* 2777–2780. doi:10.1103/PhysRevLett.85.2777
2. Smykalla, L.; Shukrynau, P.; Korb, M.; Lang, H.; Hietschold, M. *Nanoscale* **2015,** *7,* 4234–4241. doi:10.1039/C4NR06371F
3. Pham, T. A.; Song, F.; Nguyen, M.-T.; Li, Z.; Studener, F.; Stöhr, M. *Chem. – Eur. J.* **2016,** *22,* 5937–5944. doi:10.1002/chem.201504946
4. Ciesielski, A.; El Garah, M.; Haar, S.; Kovaříček, P.; Lehn, J.-M.; Samorì, P. *Nat. Chem.* **2014,** *6,* 1017–1023. doi:10.1038/nchem.2057
5. Yu, Y.; Lin, J.; Wang, Y.; Zeng, Q.; Lei, S. *Chem. Commun.* **2016,** *52,* 6609–6612. doi:10.1039/C6CC02005D
6. Tanoue, R.; Higuchi, R.; Enoki, N.; Miyasato, Y.; Uemura, S.; Kimizuka, N.; Stieg, A. Z.; Gimzewski, J. K.; Kunitake, M. *ACS Nano* **2011,** *5,* 3923–3929. doi:10.1021/nn200393q
7. Plas, J.; Waghray, D.; Adisoejoso, J.; Ivasenko, O.; Dehaen, W.; De Feyter, S. *Chem. Commun.* **2015,** *51,* 16338–16341. doi:10.1039/C5CC06970J
8. Sun, J.; Zhou, X.; Lei, S. *Chem. Commun.* **2016,** *52,* 8691–8694. doi:10.1039/C5CC09276K
9. Plas, J.; Ivasenko, O.; Martsinovich, N.; Lackinger, M.; De Feyter, S. *Chem. Commun.* **2016,** *52,* 68–71. doi:10.1039/C5CC07557B
10. Walch, H.; Gutzler, R.; Sirt, T.; Eder, G.; Lackinger, M. *J. Phys. Chem. C* **2010,** *114,* 12604–12609. doi:10.1021/jp102704q
11. Zhong, D.; Franke, J.-H.; Podiyanachari, S. K.; Blömker, T.; Zhang, H.; Kehr, G.; Erker, G.; Fuchs, H.; Chi, L. *Science* **2011,** *334,* 213–216. doi:10.1126/science.1211836
12. Dienstmaier, J. F.; Gigler, A. M.; Goetz, A. J.; Knochel, P.; Bein, T.; Lyapin, A.; Reichlmaier, S.; Heckl, W. M.; Lackinger, M. *ACS Nano* **2011,** *5,* 9737–9745. doi:10.1021/nn2032616
13. Dienstmaier, J. F.; Medina, D. D.; Dogru, M.; Knochel, P.; Bein, T.; Heckl, W. M.; Lackinger, M. *ACS Nano* **2012,** *6,* 7234–7242. doi:10.1021/nn302363d
14. Liu, C.; Yu, Y.; Zhang, W.; Zeng, Q.; Lei, S. *Chem. – Eur. J.* **2016,** *22,* 18412–18418. doi:10.1002/chem.201603547
15. Riemenschneider, W.; Bolt, H. M. *Esters, Organic. Ullmann's Encyclopedia of Industrial Chemistry;* Wiley-VCH, 2005. doi:10.1002/14356007.a09_565.pub2
16. Fischer, E.; Speier, A. *Chem. Ber.* **1895,** *28,* 3252–3258. doi:10.1002/cber.189502803176
17. Neises, B.; Steglich, W. *Angew. Chem., Int. Ed.* **1978,** *17,* 522–524. doi:10.1002/anie.197805221
18. Mitsunobu, O.; Yamada, M. *Bull. Chem. Soc. Jpn.* **1967,** *40,* 2380–2382. doi:10.1246/bcsj.40.2380
19. Zwaneveld, N. A. A.; Pawlak, R.; Abel, M.; Catalin, D.; Gigmes, D.; Bertin, D.; Porte, L. *J. Am. Chem. Soc.* **2008,** *130,* 6678–6679. doi:10.1021/ja800906f
20. Griessl, S.; Lackinger, M.; Edelwirth, M.; Hietschold, M.; Heckl, W. M. *Single Mol.* **2002,** *3,* 25–31. doi:10.1002/1438-5171(200204)3:1<25::AID-SIMO25>3.0.CO;2-K
21. Lackinger, M.; Griessl, S.; Heckl, W. M.; Hietschold, M.; Flynn, G. W. *Langmuir* **2005,** *21,* 4984–4988. doi:10.1021/la0467640
22. Li, Z.; Han, B.; Wan, L. J.; Wandlowski, T. *Langmuir* **2005,** *21,* 6915–6928. doi:10.1021/la0507737
23. Ha, N. T. N.; Gopakumar, T. G.; Gutzler, R.; Lackinger, M.; Tang, H.; Hietschold, M. *J. Phys. Chem. C* **2010,** *114,* 3531–3536. doi:10.1021/jp907781a
24. Ha, N. T. N.; Gopakumar, T. G.; Hietschold, M. *J. Phys. Chem. C* **2011,** *115,* 21743–21749. doi:10.1021/jp111640t
25. Ha, N. T. N.; Gopakumar, T. G.; Hietschold, M. *Surf. Sci.* **2013,** *607,* 68–73. doi:10.1016/j.susc.2012.08.008
26. Nath, K. G.; Ivasenko, O.; Miwa, J. A.; Dang, H.; Wuest, J. D.; Nanci, A.; Perepichka, D. F.; Rosei, F. *J. Am. Chem. Soc.* **2006,** *128,* 4212–4213. doi:10.1021/ja0602896
27. Nath, K. G.; Ivasenko, O.; MacLeod, J. M.; Miwa, J. A.; Wuest, J. D.; Nanci, A.; Perepichka, D. F.; Rosei, F. *J. Phys. Chem. C* **2007,** *111,* 16996–17007. doi:10.1021/jp0762774
28. Nandi, G.; Chilukuri, B.; Hipps, K. W.; Mazur, U. *Phys. Chem. Chem. Phys.* **2016,** *18,* 20819–20829. doi:10.1039/C6CP04454A
29. De Feyter, S.; De Schryver, F. C. *J. Phys. Chem. B* **2005,** *109,* 4290–4302. doi:10.1021/jp045298k
30. Okawa, Y.; Aono, M. *Nature* **2001,** *409,* 683–684. doi:10.1038/35055625

31. Abdel-Mottaleb, M. M. S.; De Feyter, S.; Gesquière, A.; Sieffert, M.; Klapper, M.; Müllen, K.; De Schryver, F. C. *Nano Lett.* **2001,** *1,* 353–359. doi:10.1021/nl010034k
32. Groszek, A. J. *Proc. R. Soc. London, Ser. A* **1970,** *314,* 473–498. doi:10.1098/rspa.1970.0019
33. Bléger, D.; Kreher, D.; Mathevet, F.; Attias, A.-J.; Schull, G.; Huard, A.; Douillard, L.; Fiorini-Debuischert, C.; Charra, F. *Angew. Chem., Int. Ed.* **2007,** *119,* 7548–7551. doi:10.1002/ange.200702376
34. Klymchenko, A. S.; Furukawa, S.; Müllen, K.; Van der Auweraer, M.; de Feyter, S. *Nano Lett.* **2007,** *7,* 791–795. doi:10.1021/nl0700752
35. Nguyen, D. C. Y.; Smykalla, L.; Nguyen, T. N. H.; Rüffer, T.; Hietschold, M. *J. Phys. Chem. C* **2016,** *120,* 11027–11036. doi:10.1021/acs.jpcc.6b03409
36. Ahn, S.; Matzger, A. J. *J. Am. Chem. Soc.* **2012,** *134,* 3208–3214. doi:10.1021/ja210933h
37. Larsen, A. H.; Vanin, M.; Mortensen, J. J.; Thygesen, K. S.; Jacobsen, K. W. *Phys. Rev. B* **2009,** *80,* 195112–195122. doi:10.1103/PhysRevB.80.195112
38. Perdew, J. P.; Burke, K.; Ernzerhof, M. *Phys. Rev. Lett.* **1996,** *77,* 3865–3868. doi:10.1103/PhysRevLett.77.3865
39. Friesen, B. A.; Bhattarai, A.; Mazur, U.; Hipps, K. W. *J. Am. Chem. Soc.* **2012,** *134,* 14897–14904. doi:10.1021/ja304431b

License and Terms

BEILSTEIN JOURNAL OF NANOTECHNOLOGY

The interplay between spin densities and magnetic superexchange interactions: case studies of mono- and trinuclear bis(oxamato)-type complexes

Azar Aliabadi[1], Bernd Büchner[1,2], Vladislav Kataev[*1] and Tobias Rüffer[*3]

Review

Open Access

Address:
[1]Leibnitz Institute for Solid State and Materials Research, IFW Dresden, Helmholtzstrasse 20, D-01069 Dresden, Germany, [2]Institut für Festkörperphysik, TU Dresden, Zellescher Weg 16, D-01062 Dresden, Germany and [3]Department of Inorganic Chemistry, Faculty of Natural Sciences, TU Chemnitz, Strasse der Nationen 62, D-09111 Chemnitz, Germany

Email:
Vladislav Kataev[*] - v.kataev@ifw-dresden.de; Tobias Rüffer[*] - tobias.rueffer@chemie.tu-chemnitz.de

* Corresponding author

Keywords:
bis(oxamato); bis(oxamidato); copper(II); electron nuclear double resonance; electron paramagnetic resonance; magnetic superexchange interactions; pulsed electron–electron double resonance; spin density distribution

Beilstein J. Nanotechnol. **2017,** *8,* 2245–2256.
doi:10.3762/bjnano.8.224

Received: 21 February 2017
Accepted: 06 October 2017
Published: 27 October 2017

This article is part of the Thematic Series "Towards molecular spintronics".

Guest Editor: G. Salvan

Abstract

For future molecular spintronic applications the possibility to modify and tailor the magnetic properties of transition-metal complexes is very promising. One of such possibilities is given by the countless derivatization offered by carbon chemistry. They allow for altering chemical structures and, in doing so, to tune magnetic properties of molecular spin-carrying compounds. With emphasis on the interplay of the spin density distribution of mononuclear and magnetic superexchange couplings of trinuclear bis(oxamato)-type complexes we review on efforts on such magneto-structural correlations.

Introduction

The flexibility of carbon chemistry together with the structural variety of coordination chemistry offers unique possibilities to design new coordination complexes. This includes the potential of metalloligands for a metallosupramolecular perspective [1-7]. The genesis of this field with respect to modern developments of molecular magnetism has been comprehensively reviewed recently [8]. The multidisciplinarity of the field is vividly demonstrated by reference to, for example, electro- and/or photoswitchable complexes as active magnetic components for future applications in information processing and data storage [8]. To that development, namely the design of novel metalloligands for the synthesis of multinuclear, multidimensional and multifunctional magnetic materials we did already contribute. For example, we reported on the first chiral bis(oxamato)-type metalloligand [9], later on used by Ferrando-Soria et al. for the design of the first chiral single-chain magnets

(SCMs) [10]. Additionally, we reported how to introduce the redox-active anthrachinone functionality into bis(oxamato)-type metalloligands [11], later on adapted for the design of higher nuclear complexes that could potentially act as molecular magnetic capacitors [12], or we reported to which extent a ferrocene group in multinuclear bis(oxamato)-type complexes is suited to vary magnetic properties with respect to its oxidation state [13].

Among many different types of metalloligands [8], the already mentioned archetypal bis(oxamato)-type complexes (type **II**, Scheme 1) are just one, but a very versatile, representative. From their precursors, usually the diethyl ester of *N,N*'-bridged organodiyl(oxamic acid) denoted as type-**I** molecules in Scheme 1, type-**II** complexes are comparatively easily accessible. The first example for such a type-**I** molecule was reported by Gaade in 1936 [14], while the capability of type-**II** complexes to act as metalloligands has been reported for the first time by Monoyama et al. [15] in 1976. Intriguingly, this first report of type-**II** complexes stated that "[…]The oxamide moiety bridging two metal ions […] serve as a pathway through which electron spin interactions takes place and their copper complexes […] are magnetically subnormal[…]" [15]. The beauty of this "bottom-up" approach, i.e., the addition of transition-metal complex fragments and transition-metal salts to type-**II** metalloligands to obtain discrete trinuclear and 1D polynuclear complexes (type **III** and **IV**, Scheme 1), respectively, or the synthesis of multifunctional 2D and 3D networks with potential applications in information storage, nanotechnology, molecular electronics and spintronics was impressively brought into bloom by O. Kahn himself and his school later on [5,8,16-18]. Type-**III** complexes are of interest because, for example, the determination of their magnetic properties, in particular their magnetic superexchange couplings, is an estimate of the magnetic properties of higher nuclear complexes [5,8,16-18]. As a strict orthogonality of magnetic orbitals cannot be achieved for higher nuclear complexes derived out of type-**II** complexes, they always possess an antiferromagnetic superexchange coupling. However, an alternative strategy is offered when heterometallic type-**IV** complexes combine paramagnetic metal ions with a large and a small spin quantum number. In such a case the magnetic ground state will be ferrimagnetic. In doing so, Kahn and his school [19,20] gave access to the first SCMs, see above, a class of magnetic material that exhibits a slow relaxation of the magnetization below the blocking temperature.

Oxamato-based SCMs, especially when equipped with further redox-switchable functionalities, are regarded as novel materials for the design of molecular spintronic devices [8,17,18]. Into such devices [21,22] diamagnetic molecules [23] and even individual single-molecule magnets (SMMs) [24] were already successfully integrated, and spin-organic field-effect transistors [25] or spin-organic light-emitting diodes [26] were developed. Although it remains puzzling to understand the spin-polarized transport phenomena of spintronic devices in detail, we focused on the synthesis of type-**III** complexes as models of SMMs with the aim to deposit them as thin films on surfaces. Already in 2006, we reported on the deposition of thin films of a type-**III** complex by spin coating [27], although the surface roughness of the thin films prevented any reliable characterization by magneto-optical Kerr effect (MOKE) spectroscopic studies. Spectroscopic MOKE measurements of such thin films would be, from a rather fundamental point of view but also with respect to potential applications of SMMs and SCMs, very interesting as magneto-optical effects are used in various optoelectronic devices [28]. It took us roughly a decade to understand how to tailor type-**III** complexes to engineer from

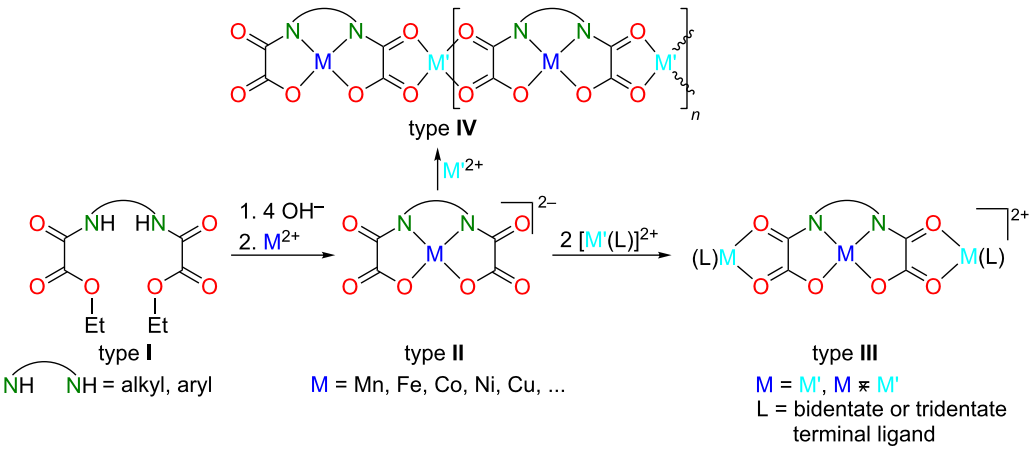

Scheme 1: Chemical structures of type **I**–**IV** species and principal synthetic strategy to obtain type **II**–**IV** complexes. Additionally coordinated apical donors of the metal ions are not displayed.

them smooth thin films them suitable for spectroscopic MOKE studies [29], but this odyssey is not content of this review.

Along with these efforts we became interested in possibilities to strengthen and to tailor the *J* couplings of type-**III** complexes as well as to identify their magnetic superexchange pathway itself. Such an understanding is one prerequisite for the rational design of new molecular multifunctional magnetic materials for material science applications. Moreover, it would be fascinating if electron spin resonance (ESR) spectroscopic studies could give access to the spin density distribution of type-**II** complexes as an experimentally achievable measure of the magnetic superexchange couplings of type-**III** complexes and of related higher nuclear magnetic materials. There are already reports of spin and electron density distribution studies by polarized neutron and high-resolution X-ray diffraction measurements, respectively, for a ferrimagnetic type-**IV** coordination polymer [30,31]. Both studies revealed formidable direct experimental evidence that "[…]the oxamato bridge […] exhibits spin delocalization, responsible for exchange coupling along the chains[…]" [31], as anticipated by Monoyama et al. [15]. The electron density study pointed out that there is a larger spin delocalization along the N⋯C⋯O compared to the O⋯C⋯O part of an individual oxamato-bridging unit [31]. This was understood as an indication that the magnetic superexchange pathway preferably went along the N⋯C⋯O part. Consequently, the authors did conclude according to O. Kahn [32], that "[…]Replacing all O atoms of an oxalate group by N atoms (or even better by S atoms) should therefore induce higher exchange J couplings[…]" and that comparative and systematic studies should be carried out including oxamato-, oxamidato- and thiooxalato-bridged complexes to better understand the magnetic superexchange interactions mechanisms and to classify them topologically [31]. In the following we aim to review on efforts to determine the spin density distribution of mononuclear type-**II** and related complexes by ESR spectroscopy as a measure of the magnetic superexchange interactions of their related trinuclear type-**III** complexes.

Review

The concept

The spin density of the N⋯C⋯O part exceeds significantly the one of the O⋯C⋯O part of type-**IV** complexes, as demonstrated experimentally [30,31]. Hypothetically, this situation can be assumed for type-**III** complexes as well. Moreover, one could hypothetically assume that the spin densities of the N atoms and the paramagnetic metal ions of type-**II** complexes as precursors of type-**III** complexes are a direct measure of the magnitude of *J* couplings. Hence, the larger the spin densities at the N atoms and the smaller at the metal ions of type-**II** type complexes, the larger the magnitude of *J* couplings of corresponding type-**III** complexes and vice versa. Spin densities or the spin density distribution, respectively, of paramagnetic transition-metal complexes can be determined by making use of ESR spectroscopy. This method in its continuous wave [33] and, in particular, in the microwave-pulse versions [34-41] has a long history of applications in this research field. By now ESR has become an established method along with neutron diffraction (ND) and nuclear magnetic resonance (NMR) spectroscopies since it does not require large amounts of a sample as is the case for ND, and often offers a better sensitivity than NMR spectroscopy. One possibility to investigate the electron spin density by ESR is, as nicely described in [33], the fabrication of single crystals composed of the paramagnetic complex of interest co-crystallized in the host lattice of a corresponding and structural analogous diamagnetic complex, which usually should be even isomorphic. The single crystals itself should be large enough in order to be able to manipulate them reliably. In an initial study we co-crystallized a Cu(II)-containing type-**II** complex in the host lattice of the corresponding Ni(II) complex [42]. In doing so, we managed to obtain diamagnetically diluted single crystals. X-band ESR studies gave access to all components of the g-factor tensor, the tensors of on-site ^{Cu}A and transferred ^{N}A hyperfine interactions [42]. The orientation of the single crystals within the ESR spectrometer is of crucial importance, as for certain orientations the spectra become complicated due to small ^{63,65}Cu hyperfine couplings overlapped by ^{14}N quintets. Especially in case of arbitrary B_0 orientation the N atoms are not magnetically equivalent and this may result in less resolved triplets of triplets for the ^{14}N hyperfine patterns [42]. The obtained experimentally derived spin density distribution of the Cu(II)-containing type-**II** complex compares excellently with values derived out of quantum chemical calculations [42]. In a subsequently performed study we investigated seven different Cu(II)-containing type-**II** complexes and determined their spin density distribution by X-, Q-, and W-band ESR studies [9]. With the access to Q- and W-band ESR spectrometers the fabrication of diamagnetically diluted single crystals is not a prerequisite anymore to extract the required information. Instead, diamagnetically diluted powders could be shown to be sufficient for this purpose [9], since at Q- and especially at W-band frequencies the powder pattern of the ESR spectrum arising due to the g-factor anisotropy is much better resolved. We demonstrated that the higher the tetrahedral distortion of the CuN_2O_4 coordination units of type-**II** complexes is, the larger is the spin density at the Cu(II) ions and the smaller it is at the N atoms. Consistently, our study strongly suggests that the magnitude of the *J* coupling of a certain type-**III** complex is larger, the smaller the spin density at the Cu(II) ion and the larger at the N atoms of the corresponding type-**II** complexes are [9].

Now, we turn towards the pairs of structurally related mononuclear complexes displayed in Figure 1 and to compare the obtained results with the one reported for the combination of **2@1**. As Figure 1 illustrates, we successively replaced O atoms with N–R units. If otherwise identical to type-**III** complexes the trinuclear complexes derived out of **4**, **6**, **8** and **10** should have larger *J* couplings according to [31]. Furthermore, in case that the interplay between the spin density distribution of mononuclear and the *J* couplings of trinuclear complexes is of general validity, the spin densities at the Cu(II) ions should decrease and those of the N_{aryl} atoms should increase when going from of **2** over **4** to **6**, **8** and **10**.

Fabrication of diamagnetically diluted single crystals

Single crystals of **2@1**, **4@3**, **6@5**, **8@7**, and **10@9** (Figure 1) required for the ESR studies could be obtained in the same way as those of the individual complexes. There are no additional arrangements to be made. It seems likely, that the isostructural Ni(II) and Cu(II) complexes should be isomorphic as well in order to obtain diamagnetically diluted single crystals. Based on our experiments performed so far we cannot verify this further but aim to indicate that **9** and **10** crystallized in different monoclinic space groups, although their measures were nearly identical [43]. Furthermore we reported that single crystals of **6@5** were too small to be suitable for ESR studies, although both complexes could be crystallized individually in form of very large single crystals [43]. Additionally we noticed with surprise [44], that the crystallization of a mixture of the complexes **1**–**4** resulted in the formation of **2@1** together with **4@3** as a remarkable example for the supramolecular recognition of isostructural complexes (Figure 2). For a better comprehension, Table 1 reports on selected crystallographic data of **1**–**10**.

Experimental determination of spin densities

The relevant interactions that determine the parameters of the Cu(II) ESR spectrum can be described by the following standard Hamiltonian [9,43,45]:

$$\begin{aligned}\mathcal{H} = {} & \mu_B \vec{B}_0 \boldsymbol{g} \vec{S} + \vec{S} \boldsymbol{A}^{Cu} \vec{I}^{Cu} \\ & + \sum_{i=1}^{3(\text{for } 1),\,4(\text{for } 2,3)} \vec{S} \boldsymbol{A}^{N_i} \vec{I}^{N_i} \\ & + g_N \mu_N \vec{B}_0 \left(\sum_{i=1}^{4} \vec{I}^{N_i} + \vec{I}^{Cu} \right).\end{aligned} \tag{1}$$

Here, the first term represents the Zeeman interaction of an electron spin *S* with an external magnetic field B_0, while $\boldsymbol{g}$ and μ_B stand for the g-tensor and the Bohr magneton, respectively. The hyperfine (HF) interaction between the electron spin *S* of Cu(II) and the ^{63}Cu, ^{65}Cu and ^{14}N nuclear spins I^{Cu} and I^{N} is described by the second and the third term, respectively. Here, $\boldsymbol{A}^{Cu}$ and $\boldsymbol{A}^{N}$ are the on-site Cu and transferred N HF coupling tensors, respectively. The last term describes the nuclear Zeeman interaction of the ^{63}Cu, ^{65}Cu and ^{14}N nuclear spins I^{Cu} and I^{N} with the external magnetic field B_0, which is not included for the modelling of continuous wave (CW) ESR spectra. Finally, g_N and μ_N denote the nuclear *g*-factor and the nuclear magneton, respectively. CW ESR measurements were performed at room temperature with a Bruker EMX spectrometer operating at the X-band (10 GHz) frequency. ESR spectra

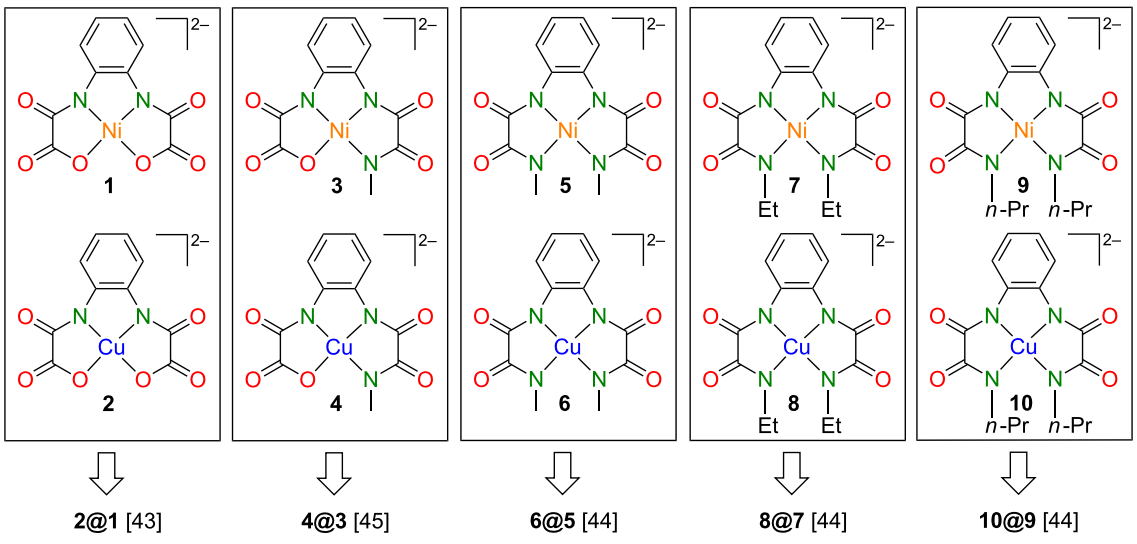

Figure 1: Chemical structures of reviewed pairs of diamagnetic Ni(II) and the corresponding Cu(II) complexes.

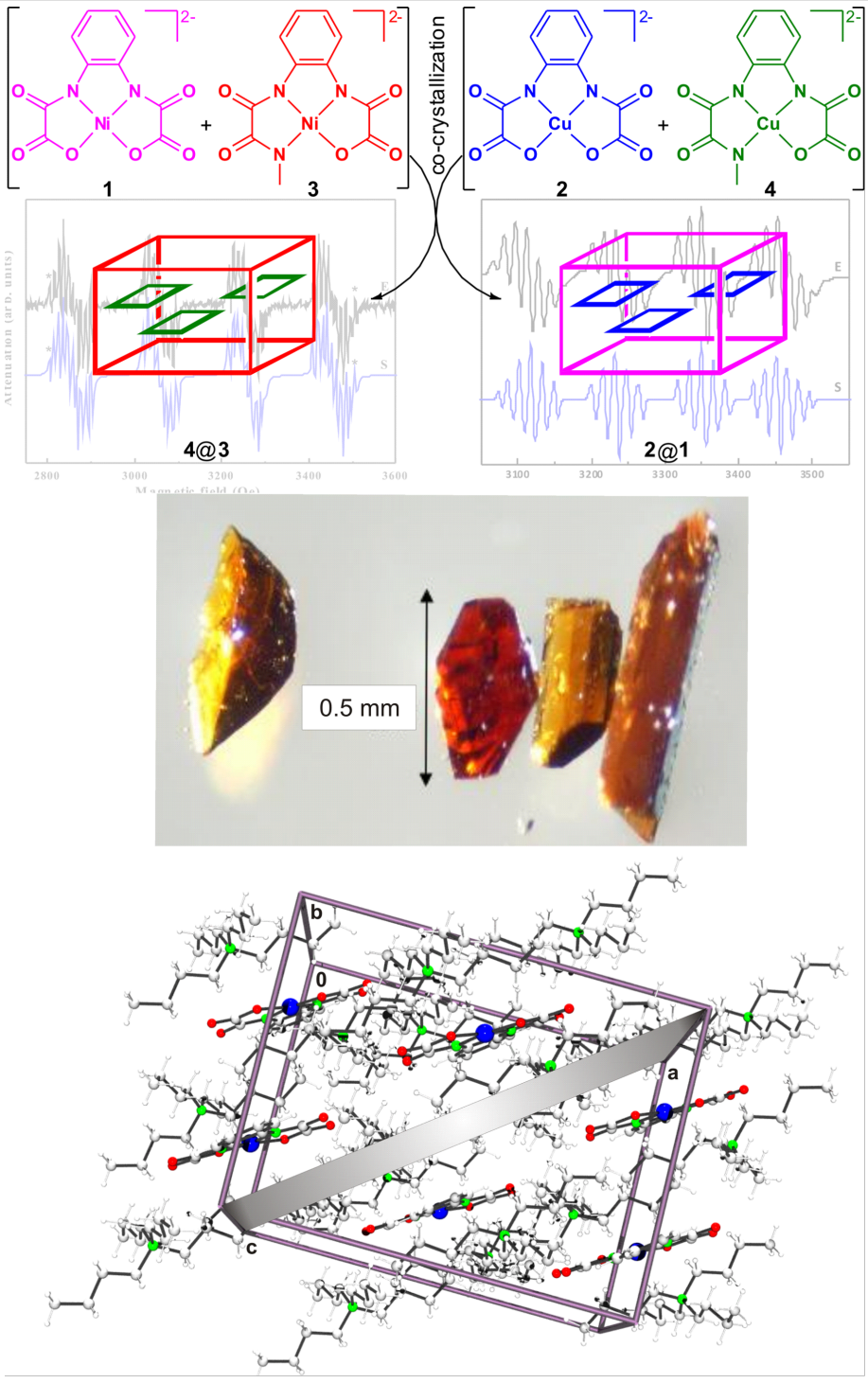

Figure 2: Top: Schematic representation of the successful co-crystallization of a mixture of two different Cu(II) (**2**, **4**) and two different Ni(II) containing complexes (**1**, **3**). Middle: Single crystals of diamagnetically diluted **4@3** (left) and **2@1** (right). Reproduced with permission from [44], copyright 2013 The Royal Society of Chemistry. Bottom: Cut-off of the crystal structure of **1**, displaying the orientation of the complex fragments with respect to the (101) plane. Color code: Cu (blue), O (red), N (green), C (light grey), H (white), cell truncate (purple) and (101) plane (grey).

were processed using the Win-ESR® software package [46]. Isotropic ESR parameters of the studied compounds were obtained from measurements of the samples dissolved in MeCN at a concentration of 1 mM. The angular dependence of the ESR spectra of the single crystals under study (Figure 1) was measured by rotation of the magnetic field B_0 in the plane perpendicular to the molecular plane to obtain anisotropic ESR parameters. A standard manually controlled goniometer from

Table 1: Selected crystallographic data of **1**–**10**.

	unit cell parameters						volume (Å^3)	crystal system	space group
	a (Å)	*b* (Å)	*c* (Å)	α (°)	β (°)	γ (°)			
1 [30]	18.5088(4)	17.1731(4)	14.2230(4)	90.0	91.997(3)	90.0	4518.1(2)	monoclinic	C_2/c
2 [30]	18.5716(9)	17.2023(7)	14.1556(5)	90.0	91.897(4)	90.0	4519.9(3)	monoclinic	C_2/c
3 [30][a]	11.3391(3)	13.9271(4)	15.9078(5)	97.566(3)	95.666(3)	110.349(3	2306.5(1)	triclinic	$P\bar{1}$
4 [30][a]	34.213(1)	13.3036(4)	19.7816(5)	90.0	90.0	90.0	9003.8(4)	orthorhombic	$Pna2_1$
5 [29]	10.7141(4)	14.4059(5)	15.4535(6)	99.540(3)	90.910(3)	102.522(3)	2292.9(2)	triclinic	$P\bar{1}$
6 [29]	10.583(13)	14.534(3)	15.609(15)	98.444(11)	91.564(9)	102.01(1)	2318.8(5)	triclinic	$P\bar{1}$
7 [29]	24.3834(7)	13.4528(3)	15.9421(4)	90.0	110.328(3)	90.0	4903.7(2)	monoclinic	C_2/c
8 [29]	24.396(5)	13.432(3)	15.919(3)	90.0	109.80(3)	90.0	4908(2)	monoclinic	C_2/c
9 [29]	13.5126(5)	14.7246(4)	25.4056(7)	90.0	95.567(3)	90.0	5031.0(3)	monoclinic	$P2_1$
10 [29]	13.4875(6)	14.6748(7)	25.6140(12)	90.0	95.346(4)	90.0	5047.6(4)	monoclinic	$P2_1/c$

[a]**3** was crystallographically characterized as $[n\text{-Bu}_4\text{N}]_2[\text{Ni(opooMe)}]\cdot 1.25\text{H}_2\text{O}$, while **4** was characterized as $[n\text{-Bu}_4\text{N}]_2[\text{Cu(opooMe)}]$ [44], although **3** and **4** were crystallized under identical conditions. As a consequence the isostructural compounds **3** and **4** are not isomorphic. Single crystals of **4@3** were checked to correspond to the measures reported for **3**.

Bruker was used for this purpose with the sample attached to a quartz-rod sample holder.

As an example, experimental and simulated X-band ESR spectra of **4@3** at 90° orientation ($B_0 \perp$ molecular plane) reported in [45] are shown in Figure 3. This preferred orientation can be judged conveniently when performing a crystallographic face-indexation of the diamagnetically diluted single crystals (Figure 2). The spectra consist of a quartet of groups of lines owing to the on-site HF coupling of an electron spin of S(Cu(II)) = 1/2 to its own nuclear spin $I(^{63,65}\text{Cu}) = 3/2$. Each group further represents a subset of lines arising due to a transferred HF-coupling with the ^{14}N nuclear spins $I(^{14}\text{N}) = 1$ of the N donor atoms. Due to a large line width, the lines from the transferred HF coupling of an individual N-donor atom are not well resolved. For B_0 parallel to the molecular plane the line groups overlap because of the small ^{63}Cu HF coupling constant, $A_\perp^{\text{Cu}}$, in this direction. Therefore, the extraction of the coupling parameters gets very difficult. Indeed, an estimate of $A_\perp^{\text{Cu}}$ can be obtained by using the relation $A_{\text{iso}} = \left(2A_\perp + A_{||}\right)/3$, where the isotropic HF constant A_{iso} was determined from a measurement in liquid solution [43,45].

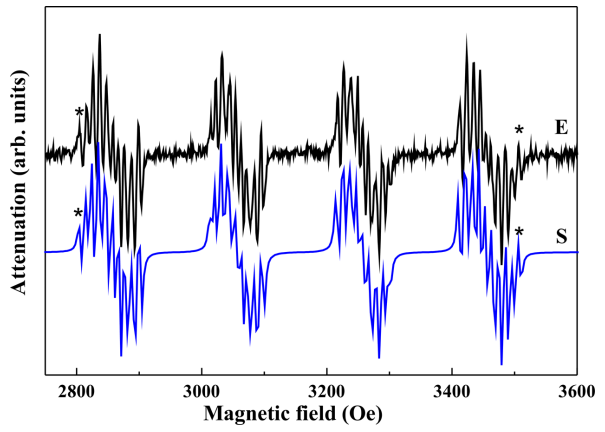

Figure 3: Experimental (E) and simulated (S) X-band ESR spectra of **4@3** at 90° orientation ($B_0 \perp$ molecular plane). Reproduced with permission from [45], copyright 2012 The Royal Society of Chemistry.

The principal values of the on-site A^{Cu} HF tensor, the g-tensor and the averaged principal values of the transferred HF tensor for one individual N donor have been determined by the modeling of the spectra. For the modeling, the Hamiltonian in Equation 1 was adopted and the following assumptions have been made [43,45]:

$$\begin{aligned} g_x &= g_y = g_\perp \\ g_z &= g_{||} \\ A_x &= A_y = A_\perp < A_z = A_{||}. \end{aligned} \tag{2}$$

The respective tensor axes of g, A^{Cu} and A^{N} are shown in Figure 4.

Furthermore, pulse Davies electron nuclear double resonance (ENDOR) experiments with an X-band ESR spectrometer Elexsys E580 (Bruker) equipped with the CF935 cryostat and the temperature control unit ITC503 from Oxford Instruments were performed on **8@7** at a temperature of 20 K to obtain additional insights into the HF coupling and to determine the HF tensor of the individual N donor atoms. Conventional ESR experiments do not allow for obtaining such information. The pulse Davies ENDOR technique is based on the detection of the electron spin echo (ESE) [34,39]. The microwave (mw) pulse

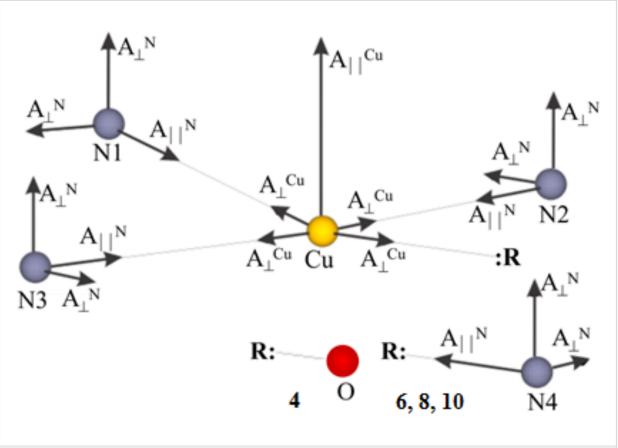

Figure 4: Scheme of the principal axes of the Cu and N HF tensors and the g-tensor. Reproduced with permission from [43], copyright 2015 The Royal Society of Chemistry.

sequence of this technique consists of three pulses π–τ–π/2–τ–π–ESE that define three periods of the evolution of the spin system (preparation, mixing and detection periods). Changes in the population of the nuclear energy levels induced during the application of an additional radiofrequency pulse in the megahertz range between the first and the second mw pulse reduce the intensity of the ESE signal. Such reductions are measured as a function of the radiofrequency. As an example, experimental and simulated ENDOR spectra of **8@7** at different orientations of the crystal in the magnetic field are shown in Figure 5 [43]. The 0° orientation corresponds to the direction of B_0 along the $g_{||}$-axis of the g-tensor, and the 90° orientation represents the perpendicular direction. The lengths of the first (inversion) π-pulse, and the detection π/2 and π pulses were set to 400 ns, and 16 ns and 32 ns, respectively. The length of the intervening radiofrequency pulse was 7 μs.

The lines in the ENDOR spectrum that arise from the HF coupling of the Cu spin with the nuclear spins of the individual N donor atoms are well resolved. Peaks from protons (^{1}H) located at the low frequency part of the spectra can be identified as well. The principal values of the transferred HF tensor of the individual N donor atoms have been obtained from the simulation of the spectra according to the Hamiltonian in Equation 1, taking into account the HF interaction between the ^{14}N nuclear spins $I(^{14}N) = 1$ of four N-donor atoms and the unpaired electron at the central Cu(II) ion under the assumptions of Equation 2. The values of the g-factor and the on-site HF coupling tensors for Cu(II) were taken from the CW ESR results. The obtained nitrogen HF tensors can be grouped in two groups A and B, and C and D, which were associated with two N_{aryl} and two N_{alkyl} donor atoms, respectively [43]. The values of the tensor components in each pair of groups are quite close. The difference between the groups is considerable. However, the

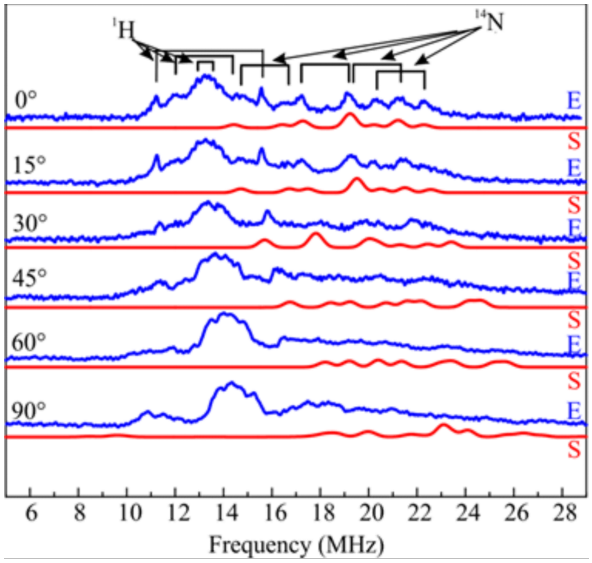

Figure 5: Experimental (E) and simulated (S) Davies ENDOR spectra of **8@7** at (ν = 9.56 GHz, T = 20 K) at six different orientations of the single crystal in the external magnetic field. The 0° orientation corresponds to the direction of B_0 along the $g_{||}$-axis of the g-tensor, and the 90° orientation represents the perpendicular direction. Reproduced with permission from [43], copyright 2015 The Royal Society of Chemistry.

ENDOR measurements indicate some difference in the HF parameters also within each group, which is not evident in the CW ESR results. However, due to a low signal-to-noise (S/N) ratio and the overlap of the lines arising from ^{14}N and protons (^{1}H) in some orientations, the accuracy of the determination of the N HF tensors with the ENDOR technique was still limited (see below). Possible reasons for the low S/N ratio could be a long duration of the pulse sequence used and temperature instabilities due to sample heating by the radio frequency pulse. In this respect the pulsed electron–electron double resonance (PELDOR) detected NMR (EDNMR) technique turns out to be advantageous as it has a shorter duration of the pulse sequence [38,41]. By performing EDNMR experiments at a higher frequency a possible overlap of a signal by the so-called central hole in the EDNMR spectrum can be avoided and a better separation of the lines from ^{14}N and ^{1}H can be achieved. Therefore, EDNMR experiments have been carried out to verify and refine the HF tensor for the individual N donor atoms of **8@7**, and to accurately determine HF tensor for the individual N donor atoms of **10@9**.

The EDNMR technique uses the excitation of forbidden ESR transitions with the selection rules $\Delta m_S = \pm 1$ and $\Delta m_I = \pm 1$ to measure HF interactions. In this approach, nuclear transition frequencies are measured by exciting two areas within the inhomogeneously broadened ESR line with two mw pulses (preparation and probe pulses). The application of the preparation mw

pulse with a frequency $\omega_{mw}^{(1)}$ corresponding to the low field forbidden transition saturates allowed transitions. These saturations manifest themselves as holes in the ESR line. The pattern of holes is recorded via the integral of the free induction decay (FID) after the selective probe pulse of frequency $\omega_{mw}^{(2)}$ while varying the frequency difference $\Delta\omega_{mw} = \omega_{mw}^{(1)} - \omega_{mw}^{(2)}$ giving thus the EDNMR spectrum.

In our experiments reported in [47] the EDNMR spectra of **8@7** and **10@9** at different orientations of the single crystals were recorded with a Q-band ESR spectrometer Elexsys E580 (Bruker) at a temperature of 20 K. The length of the preparation and probe mw pulses were set to 6 µs and 400 ns, respectively. The time delay between these two pulses amounted to 8 µs. Figure 6 shows the experimental and modeled EDNMR spectra of single crystals of **8@7** at different orientations of the single crystals. 0° and 90° orientations correspond to B_0 being parallel and perpendicular to the normal of the molecular plane, respectively. ^{14}N HF lines are well resolved in all orientations with a substantially better S/N ratio as compared to the pulsed ENDOR spectra of **8@7**. This improvement can be explained by the different relaxation paths involved in the two experiments and the smaller number of pulses in the EDNMR protocol. The EDNMR spectra have been modeled with the same approach as used for the analysis of the ENDOR spectra. All experimental lines located in a frequency range of 10–35 MHz are reasonably well reproduced in the simulation and therefore can be assigned to the system of one electron spin $S = 1/2$ of Cu(II) coupled to the ^{14}N nuclear spins $I(^{14}N) = 1$ of four N donor atoms in the studied complexes. The additional lines located at higher frequencies can arise when other nuclear spins are coupled to the electron spins [47]. At the Q-band frequency, which corresponds to a magnetic field of approximately 1 T, the proton (^{1}H) Larmor frequency is ca. 50 MHz. Therefore protons probably also contribute to the line in the EDNMR spectra around 50 MHz.

Like the ENDOR results, the obtained HF tensors indicate two different groups of N ligands classified as groups A and B for **8**. The same observation is obtained for **10** as well. The ^{14}N HF constants for group A are close to those of **2** [9]. Therefore, group A could be assigned to N_{aryl} nitrogen donor atoms while group B, with smaller ^{14}N HF constants, corresponds to the N_{alkyl} nitrogens of **8** and **10**, respectively.

Estimates of the electron spin densities

In our works [43,45] as well as in [9], two different models introduced by Maki and McGarvey [48] and Morton and Preston [49] were followed to calculate the spin densities on the Cu(II) ion and N donor atoms of Cu(II) complexes from experimentally obtained HF coupling constants. In the approach of

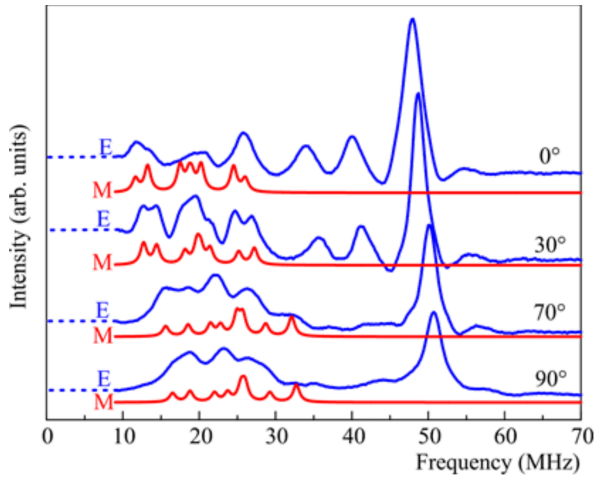

Figure 6: Experimental (E) and modeled (M) EDNMR spectra of **8@7** at the Q-band frequency, at T = 20 K and at four orientations of the crystal in the external magnetic field B_0. 0° and 90° correspond to B_0 being parallel and perpendicular to the normal of the molecular plane, respectively. Reprinted with permission from [47], copyright 2015 American Chemical Society.

Maki and McGarvey [48], the perpendicular and the parallel Cu HF coupling constants for a complex containing a Cu(II) ion surrounded by four ligands in a square planar configuration are derived and expressed as:

$$A_{\parallel} = P\left(-\kappa - \frac{4}{7}\alpha^2 + \Delta g_{\parallel} + \frac{3}{7}\Delta g_{\perp}\right), \quad (3)$$

$$A_{\perp} = P\left(-\kappa + \frac{2}{7}\alpha^2 + \frac{11}{14}\Delta g_{\perp}\right). \quad (4)$$

In these expressions, $P\kappa$ is the Fermi contact term with $P(^{63}\text{Cu}) = \mu_B g_e \mu_n \gamma \cdot \langle r^3 \rangle_{3d} = 1164$ MHz, that is, the dipolar HF coupling parameter of the unpaired electron [50], and $\Delta g_{\parallel,\perp} = g_{\parallel,\perp} - 2.0023$. The parameter α^2 is a covalency parameter that describes the in-plane metal–ligand σ-bonding. The value of α^2 represent the spin density on the Cu(II) ion (ρ^{Cu} (total)) and was determined by using Equations 1 and 2, and experimentally obtained Cu HF coupling constants for the complexes under study. Furthermore, the procedure of Morton and Preston [49] was used to calculate the spin density on the N donor atoms and the Cu(II) ion. The values obtained for the spin density on the Cu(II) ion were compared with those deduced by the procedure of Maki and McGarvey [48].

According to Morton and Preston [49], the isotropic and anisotropic HF coupling constants for unit spin density on the corresponding s- and p-, d- and f-orbitals have been obtained,

respectively. Spin densities on the copper and nitrogen s-orbitals for our complexes are derived as the ratio of the isotropic HF coupling constants obtained experimentally and the theoretical isotropic HF parameters A_0^{Cu} = 5995 MHz and A_0^N = 1811 MHz for unit spin density [49]. The spin density on the p- and d-orbitals of N and Cu, respectively, is proportional to the dipolar HF coupling constant $A_{dip} = A_{iso} - A_{\perp}$. These contributions are calculated as the ratio of the respective A_{dip} derived from the experimental values and the theoretical anisotropic HF parameters 138.8 MHz and 1197 MHz, which are calculated for unit spin density on the nitrogen p- and copper d-orbitals [49], respectively.

Results of electron spin density measurements

Obtained results of experimentally determined spin density distributions via the approaches by Maki and McGarvey [48] and Morton and Preston [49] according to the above described procedure are summarized in Figure 7. Furthermore and for comparison, DFT-calculated values of **2**, **4**, **6**, **8** and **10** are given as well. One can notice that the experimentally determined spin densities of the Cu(II) ions of **8** and **10** are very similar and exceed the value reported for **2**, while for **4** a lower value compared to **2** was determined. Thus, experimentally obtained data do not follow the suggested tendency that replacing the O donor by N_{alkyl} donor atoms results in a lower spin density on Cu(II) and in higher spin densities at the N_{aryl} donor atoms (Figure 7).

As pointed out in [43], larger HF parameters of tensors A–B (see above) associated with N_{aryl} donor atoms generally indicate a larger spin density r on N_{aryl} as compared to that on N_{alkyl} donor atoms, which reveal smaller parameters of the associated HF tensor C. Surprisingly the HF tensor D, which is also related to N_{alkyl}, appears to be similar to A–B. This could be a result of an overestimate of the anisotropy of the HF couplings ($A_{\parallel} - A_{\perp}$) due to the still somewhat limited accuracy of the performed ENDOR experiments.

In order to demonstrate that the spin densities of abovementioned N donor atoms are indeed different, we carried out additional pulse EDNMR studies of **8** and **10** [47] (Figure 6). The result of this study revealed unambiguously that the spin densities of the N_{aryl} donor atoms of **8** and **10** are significantly larger compared to those of the N_{alkyl} donor atoms (Figure 8). Moreover, it could be demonstrated that all four N donor atoms of both **8** and **10** possess different spin densities, as revealed by quantum chemical calculations (Figure 7, Figure 8 and [43]). The EDNMR experiments did, however, not allow for the determination of the spin densities at the Cu(II) ions of **8** and **10**. In order to give a rough estimate for a comparative discussion, they have been calculated as described in Figure 8. According to the much lower spin density of Cu(II) in mononuclear **8** (ca. 57%) compared to **10** (ca. 66%) we expected a significantly higher J value for trinuclear **11** compared to **12**. However, the opposite situation has been determined experimentally (Figure 8 and [43]). This counterintuitive result has been explained by considering both differences of the local geometries of the terminal and central Cu(II) ions of **8** and **10**.

We already noticed with surprise the differences of the coordination behavior of the terminal $[Cu(pmdta)]^{2+}$ complex fragments to binuclear bis(oxamidato)-type complexes as represented by **8** and **10** compared to type-**II** complexes displayed in Scheme 1 [43]. The different coordination behavior is expected to have an impact on the magnetic superexchange coupling pathways in corresponding trinuclear complexes. As a consequence, we realized that there are further parameters to be considered when deriving a conclusion whether the spin densi-

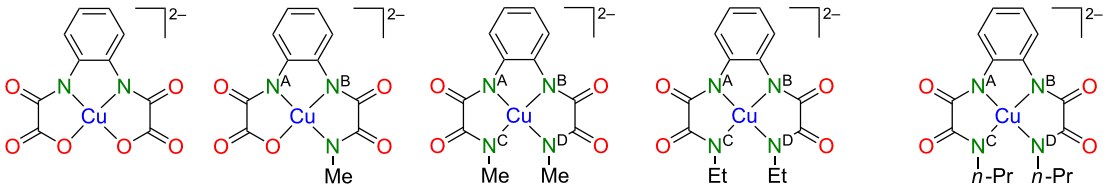

spin density at	**2** [43]		**4** [45]		**6** [44]		**8** [44]		**10** [44]	
	calc.[a]	exp.[b]	calc.[a]	exp.[b]	calc.[c]	exp.[b]	calc.[c]	exp.[b]	calc.[b,c]	exp.[a,c]
Cu	55	71.0/54.6	53.9	68/51	52.5/51.1	-	52.2/51.0	74/57.1	52.0/50.5	74/57.5
N_{aryl}	15	10.3/14.5	11.8^{A},14.8^{B}	10.5/9.5	$13.7^{A/B}$/14.7^{A},14.0^{B}	-	$13.8^{A/B}$/14.7^{A},13.9^{B}	8.9/9.3	$13.8^{A/B}$/14.4^{A},14.0^{B}	8.9/8.2
O/N_{alkyl}	7	10.3/14.5	7.7,8.8	10.5/9.5	8.9^{C}/8.4^{D}	-	$8.8^{C/D}$/9.1^{C},8.7^{D}	8.9/9.3	$8.8^{C/D}$/9.4^{C},9.2^{D}	8.9/8.2

Figure 7: Selected values of calculated versus experimentally determined spin densities of **2**, **4**, **6**, **8**, and **10**. a) Data refer to geometry optimized fragments only. b) The first/second entry refers to data obtained according to the approaches by Maki and McGarvey [48]/Morton and Preston [49]. c) The first/second entry refer to data obtained for geometry optimized complex fragments or to data obtained by using complex geometries from crystallographic characterization, respectively. For further data of **4** cf. [44]. Reproduced with permission from [43], copyright 2015 The Royal Society of Chemistry.

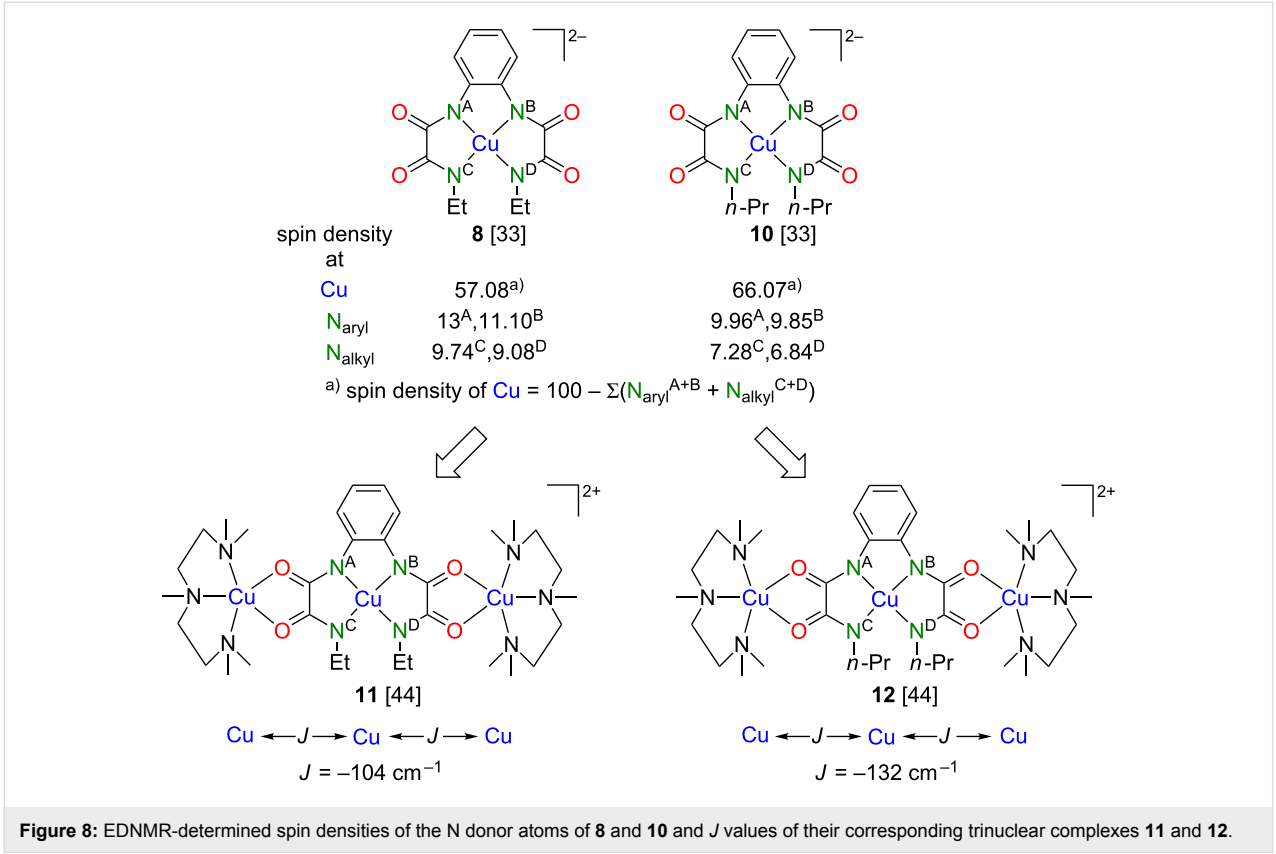

Figure 8: EDNMR-determined spin densities of the N donor atoms of **8** and **10** and *J* values of their corresponding trinuclear complexes **11** and **12**.

ties of mononuclear type-**II** or bis(oxamidato) complexes could be a measure of *J* values of their corresponding trinuclear complexes. In this context we note, that determination of the spin densities from the HF parameters should be considered as a reasonable method to obtain qualitative estimates and tendencies to be compared and discussed together with the DFT results and to be critically evaluated with respect to geometrical features of the studied molecular complexes. In particular, the approach of Maki and McGarvey [48] implies a square planar geometry of the molecule, a condition that is not always fulfilled. A limitation of the model by Morton and Preston [49] is that it presumes calculation of the HF constants for a free atom. With this in mind, it is indeed reasonable to conclude that the transfer of the spin density from the metal ions to the bonding ligands is certainly an important but not yet the decisive factor that determines the strength of the superexchange interactions in the trinuclear complexes **11** and **12**. In this particular case, it is most likely the steric factors that eventually yield the stronger antiferromagnetic exchange interaction in **12** as compared to **11**.

This presentation of our results should not end without reference to further studies of such diamagnetically diluted single crystals. We have recently shown the means of manipulating and enhancing the electron spin coherence of **2@1** and **10@9** at different temperatures by applying special microwave pulse sequences in an ESR experiment [51]. We aim to obtain with such experiments further insights into an understanding of mononuclear type-**II** and bis(oxamidato) complexes with respect to their electron spin dynamics, spin coherence and relaxation processes as well as their possible applications in molecular electronic devices.

Conclusion

Is there an interplay between the spin density distribution of mononuclear bis(oxamato) type-**II** and related complexes and the magnetic superexchange interactions of their related trinuclear type-**III** complexes? Our results support this hypothesis, although they clearly indicate that many further experiments are required to establish this interplay. For example, the O donor atoms of type-**II** complexes should be all substituted by N_{alkyl}, or alternatively by S donor atoms. Such substitutions are expected [32] to modify the spin density distribution of the mononuclear building blocks to a much higher extent compared to our here reported initial studies. As the transfer of the spin density along the bridging groups is a prerequisite for supermagnetic exchange couplings, such a modification of the mononuclear complexes should result in higher *J* couplings accordingly. Here, the specifics of the bonding geometry and its implications for the superexchange interactions have to be considered seriously.

On the other hand, we reported to which extent the materials made available, especially the diamagnetically diluted single crystals, prompted us to apply complex pulse ESR techniques for a better understanding of the physical properties of our compounds. This progress leads to the request for advanced types of materials. It would be thus challenging to replace the paramagnetic terminal $[Cu(pmdta)]^{2+}$ complex fragments of **11** and **12** by diamagnetic $[Zn(pmdta)]^{2+}$. Such heterotrinuclear Zn(II)Cu(II)Zn(II) complexes would allow us to determine the spin density distribution of the central building blocks "in action", that is, when contributing to magnetic exchange couplings especially in the case that the Zn(II)Cu(II)Zn(II)-type complexes are isomorphic to **11** and **12**. On first of such efforts we already report in this Thematic Series, namely the synthesis and characterization of heterotrinuclear Cu(II)Ni(II)Cu(II) bis(oxamidato)-type complexes [52].

Acknowledgements

This work was supported by the Deutsche Forschungsgemeinschaft through the Focused Research Unit FOR1154 "Towards Molecular Spintronics". We express our gratitude to numerous co-workers and partners, whose contribution is acknowledged in the author list of the original works reviewed in this article.

References

1. Fujita, M.; Yakazi, J.; Ogura, K. *J. Am. Chem. Soc.* **1990,** *112,* 5645–5647. doi:10.1021/ja00170a042
2. Constable, E. C. *Prog. Inorg. Chem.* **1994,** *42,* 67–138.
3. Lehn, J.-M. *Supramolecular Chemistry: Concepts and Perspectives;* VCH: Weinheim, Germany, 1995. doi:10.1002/3527607439
4. Kahn, O. *Adv. Inorg. Chem.* **1995,** *43,* 179–259. doi:10.1016/S0898-8838(08)60118-X
5. Pardo, E.; Ruiz-García, R.; Cano, J.; Ottenwaelder, X.; Lescouëzec, R.; Yournaux, Y.; Loret, F.; Julve, M. *Dalton Trans.* **2008,** 2780–2805. doi:10.1039/b801222a
6. Steel, P. J. *Chem. N. Z.* **2011,** *75,* 194–197.
7. Huang, S.-L.; Lin, Y.-J.; Li, Z.-H.; Jin, G.-X. *Angew. Chem., Int. Ed.* **2014,** *53,* 11218–11222. doi:10.1002/anie.201406193
8. Ferrando-Soria, J.; Vallejo, J.; Castellano, M.; Martinez-Lillo, J.; Pardo, E.; Cano, J.; Castro, I.; Lloret, F.; Ruiz-Garcia, R.; Julve, M. *Coord. Chem. Rev.* **2017,** *339,* 17–103. doi:10.1016/j.ccr.2017.03.004
9. Bräuer, B.; Weigend, F.; Fittipaldi, M.; Gatteschi, D.; Reijerse, E. J.; Guerri, A.; Ciattini, S.; Salvan, G.; Rüffer, T. *Inorg. Chem.* **2008,** *47,* 6633–6644. doi:10.1021/ic702460t
10. Ferrando-Soria, J.; Cangussu, D.; Eslava, M.; Yournaux, Y.; Lescouëzec, R.; Julve, M.; Lloret, F.; Pasan, J.; Ruiz-Perez, C.; Lhotel, E.; Paulsen, C.; Pardo, E. *Chem. – Eur. J.* **2011,** *17,* 12482–12494. doi:10.1002/chem.201101459
11. Rüffer, T.; Bräuer, B.; Meva, F. E.; Walfort, B. *Dalton Trans.* **2008,** 5089–5098. doi:10.1039/b804382e
12. Castellano, M.; Barros, W. P.; Acosta, A.; Julve, M.; Lloret, F.; Li, Y.; Journaux, Y.; de Munno, G.; Armentato, D.; Ruiz-Garcia, R.; Cano, J. *Chem. – Eur. J.* **2014,** *20,* 13965–13975. doi:10.1002/chem.201403987
13. Abdulmalic, M. A.; Aliabadi, A.; Petr, A. K.; Krupskaya, Y.; Kataev, V.; Büchner, B.; Hahn, T.; Kortus, J.; Yeche, N.; Klauss, H.-H.; Rüffer, T. *Organometallics* **2013,** *32,* 5988–6003. doi:10.1021/om4005115
14. Gaade, W. *Recl. Trav. Chim. Pays-Bas* **1936,** *55,* 325–330. doi:10.1002/recl.19360550408
15. Monoyama, K.; Ojima, H.; Monoyama, M. *Inorg. Chim. Acta* **1976,** *20,* 127–132. doi:10.1016/S0020-1693(00)94103-3
16. Dul, M.-C.; Pardo, E.; Lescouëzec, R.; Journaux, Y.; Ferrando-Soria, J.; Ruiz-García, R.; Cano, J.; Julve, M.; Lloret, F.; Cangussu, D.; Pereira, C. L. M.; Stumpf, H. O.; Pasán, J.; Ruiz-Pérez, C. *Coord. Chem. Rev.* **2010,** *254,* 2281–2296. doi:10.1016/j.ccr.2010.03.003
17. Grancha, T.; Ferrando-Soria, J.; Castellano, M.; Julve, M.; Pasán, J.; Armentato, D.; Pardo, E. *Chem. Commun.* **2014,** *50,* 7569–7585. doi:10.1039/C4CC01734J
18. Castellano, M.; Ruiz-García, R.; Cano, J.; Ferrando-Soria, J.; Pardo, E.; Fortea-Pérez, F. R.; Stiriba, S.-E.; Barros, W. P.; Stumpf, H. O.; Cañadillas-Delgado, L.; Pasán, J.; Ruiz-Pérez, C.; de Munno, G.; Armentato, D.; Yournaux, Y.; Lloret, F.; Julve, M. *Coord. Chem. Rev.* **2015,** *303,* 110–138. doi:10.1016/j.ccr.2015.05.013
19. Pei, Y.; Verdaguer, M.; Kahn, O.; Sletten, J.; Renard, J. P. *Inorg. Chem.* **1987,** *26,* 138–143. doi:10.1021/ic00248a027
20. Pei, Y.; Journaux, Y.; Kahn, O. *Inorg. Chem.* **1988,** *27,* 399–404. doi:10.1021/ic00275a031
21. Xiong, Z. H.; Wu, D.; Vardeny, Z. V.; Shi, J. *Nature* **2004,** *427,* 821. doi:10.1038/nature02325
22. Dediu, V.; Murgia, M.; Matacotta, F. C.; Barbanera, S.; Taliani, C. *Solid State Commun.* **2002,** *122,* 181. doi:10.1016/S0038-1098(02)00090-X
23. Göhler, B.; Hamelbeck, V.; Markus, T. Z.; Kettner, M.; Hanne, G. F.; Vager, Z.; Naaman, R.; Zacharias, H. *Science* **2011,** *331,* 894. doi:10.1126/science.1199339
24. Urdampilleta, M.; Klyatskaya, S.; Cleuziou, J.-P.; Ruben, M.; Wernsdorfer, W. *Nat. Mater.* **2011,** *10,* 502. doi:10.1038/nmat3050
25. Reichert, T.; Saragi, T. P. I. *Appl. Phys. Lett.* **2011,** *98,* 063307. doi:10.1063/1.3554388
26. Nguyen, T. D.; Ehrenfreund, E.; Vardeny, Z. V. *Science* **2012,** *337,* 204. doi:10.1126/science.1223444
27. Bräuer, B.; Zahn, D. R. T.; Rüffer, T.; Salvan, G. *Chem. Phys. Lett.* **2006,** *432,* 226–229. doi:10.1016/j.cplett.2006.10.070
28. Sugano, S.; Kojima, N. *Magneto-Optics;* Springer: Berlin, Germany, 2000. doi:10.1007/978-3-662-04143-7
29. Abdulmalic, M. A.; Fronk, M.; Bräuer, B.; Zahn, D. R. T.; Salvan, G.; Meva, F. E.; Rüffer, T. *J. Magn. Magn. Mater.* **2016,** *419,* 17–28. doi:10.1016/j.jmmm.2016.06.002
30. Baron, V.; Gillon, B.; Cousson, A.; Mathoniere, C.; Kahn, O.; Grand, A.; Öhrström, L.; Delley, B.; Bonnet, M.; Boucherle, J.-X. *J. Am. Chem. Soc.* **1997,** *119,* 3500–3506. doi:10.1021/ja9641620
31. Pillet, S.; Souhassou, M.; Mathonière, C.; Lecomte, C. *J. Am. Chem. Soc.* **2004,** *126,* 1219–1228. doi:10.1021/ja030279u
32. Kahn, O. *Angew. Chem., Int. Ed. Engl.* **1985,** *24,* 834–850. doi:10.1002/anie.198508341
33. Kirmse, R.; Stach, J. *ESR-Spektroskopie. Anwendungen in der Chemie;* Akademie-Verlag: Berlin, Germany, 1985.
34. Mims, W. B. *Phys. Rev. B* **1972,** *5,* 2409–2419. doi:10.1103/PhysRevB.5.2409
35. Bekauri, P. I.; Berulava, B. G.; Khakhanashvili, O. G.; Sanadze, T. I. *Phys. Lett. A* **1967,** *24,* 156–158. doi:10.1016/0375-9601(67)90739-6
36. Bekauri, P. I.; Berulava, B. G.; Sanadze, T. I.; Khakhanashvili, O. G. *Sov. Phys. - JETP* **1967,** *25,* 292–296.

37. Sanadze, T. I.; Khutsishvili, G. R. *Sov. Phys. - JETP* **1969,** *29,* 248–251.
38. Wacker, T.; Schweiger, A. *Chem. Phys. Lett.* **1991,** *186,* 27–34. doi:10.1016/0009-2614(91)80187-3
39. Davies, E. R. *Phys. Lett. A* **1974,** *47,* 1–2. doi:10.1016/0375-9601(74)90078-4
40. Mims, W. B. *Proc. R. Soc. London, Ser. A* **1965,** *283,* 452–457. doi:10.1098/rspa.1965.0034
41. Schosseler, P.; Wacker, T.; Schweiger, A. *Chem. Phys. Lett.* **1994,** *224,* 319–324. doi:10.1016/0009-2614(94)00548-6
42. Bräuer, B.; Rüffer, T.; Kirmse, R.; Griebel, J.; Weigend, F.; Salvan, G. *Polyhedron* **2007,** *26,* 1773–1775. doi:10.1016/j.poly.2006.09.075
43. Abdulmalic, M. A.; Aliabadi, A.; Petr, A.; Krupskaya, Y.; Katave, V.; Büchner, B.; Zaripov, R.; Vavilova, E.; Voronkova, V.; Salikov, K.; Hahn, T.; Kortus, J.; Meva, F. E.; Schaarschmidt, D.; Rüffer, T. *Dalton Trans.* **2015,** *44,* 8062–8079. doi:10.1039/C4DT03579H
44. Abdulmalic, M. A.; Aliabadi, A.; Petr, A.; Kataev, V.; Rüffer, T. *Dalton Trans.* **2013,** *42,* 1798–1809. doi:10.1039/C2DT32259E
45. Abdulmalic, M. A.; Aliabadi, A.; Petr, A.; Krupskaya, Y.; Kataev, V.; Büchner, B.; Hahn, T.; Kortus, J.; Rüffer, T. *Dalton Trans.* **2012,** *41,* 14657–14670. doi:10.1039/c2dt31802d
46. *Win-ESR®,* Version 2.3; ESR Division, Bruker Instruments, Inc., 1998.
47. Aliabadi, A.; Zaripov, R.; Abdulmalic, M. A.; Vavilova, E.; Voronkova, V.; Rüffer, T.; Kataev, V.; Salikov, K.; Büchner, B. *J. Phys. Chem. B* **2015,** *119,* 13762–13770. doi:10.1021/acs.jpcb.5b03987
48. Maki, A. H.; McGarvey, B. R. *J. Chem. Phys.* **1958,** *29,* 31–34. doi:10.1063/1.1744456
49. Morton, J. R.; Preston, K. F. *J. Magn. Reson.* **1978,** *30,* 577–582. doi:10.1016/0022-2364(78)90284-6
50. McGarvey, B. R. *J. Phys. Chem.* **1967,** *71,* 51–66. doi:10.1021/j100860a007
51. Zaripov, R.; Vavilova, E.; Khairuzhdinov, I.; Salikhov, K.; Voronkova, V.; Abdulmalic, M. A.; Meva, F. E.; Weheabby, S.; Ruffer, T.; Büchner, B.; Kataev, V. *Beilstein J. Nanotechnol.* **2017,** *8,* 943–955. doi:10.3762/bjnano.8.96
52. Abdulmalic, M. A.; Weheabby, S.; Meva, F. E.; Aliabadi, A.; Kataev, V.; Schleife, F.; Kersting, B.; Rüffer, T. *Beilstein J. Nanotechnol.* **2017,** *8,* 789–800. doi:10.3762/bjnano.8.82

License and Terms

BEILSTEIN JOURNAL OF NANOTECHNOLOGY

Adsorption of iron tetraphenylporphyrin on (111) surfaces of coinage metals: a density functional theory study

Hao Tang*[1], Nathalie Tarrat[1], Véronique Langlais[1] and Yongfeng Wang[2]

Full Research Paper

Open Access

Address:
[1]CEMES/CNRS, 29 rue Jeanne Marvig, P.O. Box 94347, 31055 Toulouse CEDEX 4, France and [2]Key Laboratory for the Physics and Chemistry of Nanodevices, Department of Electronics, Peking University, Beijing 100871, China

Email:
Hao Tang* - tang@cemes.fr

* Corresponding author

Keywords:
activation barrier; density functional theory; iron tetraphenylporphyrin; spin switch; spin states

Beilstein J. Nanotechnol. **2017,** *8,* 2484–2491.
doi:10.3762/bjnano.8.248

Received: 28 February 2017
Accepted: 02 November 2017
Published: 23 November 2017

This article is part of the Thematic Series "Towards molecular spintronics".

Guest Editor: G. Salvan

Abstract

The adsorption of the iron tetraphenylporphyrin (FeTPP) molecule in its deckchair conformation was investigated on Au(111), Ag(111) and Cu(111) surfaces by performing spin-polarized density functional theory (DFT) calculations taking into account both van der Waals (vdW) interaction and on-site Coulomb repulsion. The deckchair conformation of the molecule favours intermolecular π–π-type interactions in a less densely packed monolayer than the saddle conformation. The activation barrier between the two stable magnetic states (high spin, $S = 2$ and intermediate spin, $S = 1$) of the molecule in vacuum disappears upon adsorption on the metal surfaces. The high-spin state of physisorbed FeTPP is stable on all adsorption sites. This result reveals that an external permanent element such as a STM tip or an additional molecule is needed to use FeTPP or similar molecules as model system for molecular spin switches.

Introduction

Porphyrins, phthalocyanines and their transition-metal (TM) complexes are largely investigated in surface science as reported in detail by Gottfried [1]. The nature of the central metal atom greatly determines the electronic, magnetic, catalytic properties of these molecules. Once adsorbed on metallic surfaces, these properties could be significantly modified due to the interaction between the central macrocycle of these molecules and the substrate. Among these complexes, iron tetraphenylporphyrin (FeTPP) is particularly attractive for molecular spintronics due to its magnetic bistability. Indeed, the Fe^{2+} centre ($4s^0 3d^6$) can have three magnetic states, i.e., low-spin state (LS, $S = 0$), intermediate state (IS, $S = 1$) and high-spin state (HS, $S = 2$). While the LS ground state is mostly observed in sixfold-coordinated molecular complexes, the ground state of square planar fourfold-coordinated Fe porphyrin can be either IS or HS depending on the functional groups, characterization method or approximation used [2-7]. The main difference between these two stable magnetic states is essentially associated to the strength of the ligand field. The modification of the coordination sphere of the metallic centre is thus necessary to manipu-

late its spin state. Most of such manipulations have been achieved by coordinating an additional small molecule (e.g., NO, CO) or atom (Cl) in order to modify the coordination number [8-11]. Only few reversible manipulations of spin were achieved without additional ligand, as the one shown by N. Lin et al. on a single FeTPP molecule junction in a scanning tunnelling microscope (STM) [12]. In this junction, the line shape of zero-bias resonance of the adsorbed FeTPP molecule reversibly varies by adjusting the tip to surface distance, i.e., by mechanically squeezing the molecule. Density functional theory (DFT) calculations reveal that the spin state of the Fe centre undergoes a switch from $S = 2$ to $S = 1$ associated with a conformational change by passing from a saddle shape to a planar shape in the presence of the STM tip.

To the best of our knowledge, the stability as well as the activation barrier between HS and IS FeTPP have not yet been investigated. In this paper, a brief analysis of the free FeTPP molecule conformations is presented at first, together with an evaluation of the activation barrier between these conformations. The magnetic switch barrier is then evaluated for the C_{2h} conformation. Second, the monolayer of this molecule on (111) surfaces of Au, Ag and Cu is investigated. At the end, the relationship between the substrate and the coordination sphere of Fe is discussed in terms of molecule–surface interaction, charge transfer and work function modification.

Results and Discussion

Free molecule and conformations

The ideal D_{4h} symmetry, exhibiting the phenyl rings perpendicular to the planar central macrocycle (Figure 1a), does not correspond to the equilibrium state for the free FeTPP molecule. By rotating these peripheral rings, symmetry reductions down to S_4, D_{2d} or C_{2h} could be obtained with energies lower than that of the D_{4h} conformation. The central macrocycle is slightly deformed in the twisted conformation (S_4) (Figure 1c) or more significantly deformed in the saddle (D_{2d}) (Figure 1b) or deckchair (C_{2h}) shape (Figure 1d). In fact, the D_{4h} conformation corresponds to an average of these three conformations. The saddle conformation (D_{2d}) has the lowest energy, while the twisted conformation (S_4) is higher in energy by 0.04 eV. The C_{2h} conformation is intermediate with an energy of 0.02 eV higher than D_{2d}. Two magnetic states were found for each of these conformations in our calculations. The ground state of these three conformations is HS, the IS state being higher by 0.11 eV for S_4, and by 0.04 eV for D_{2d} and C_{2h} (Table 1). Note that the IS state was found as ground state in some other calculated results [6,7]. The difficulty for obtaining a proper description of the fundamental state of Fe porphyrin is well known. This is a result of the competition between electron correlation, spin–orbital coupling and the on-site Coulomb repulsion [13].

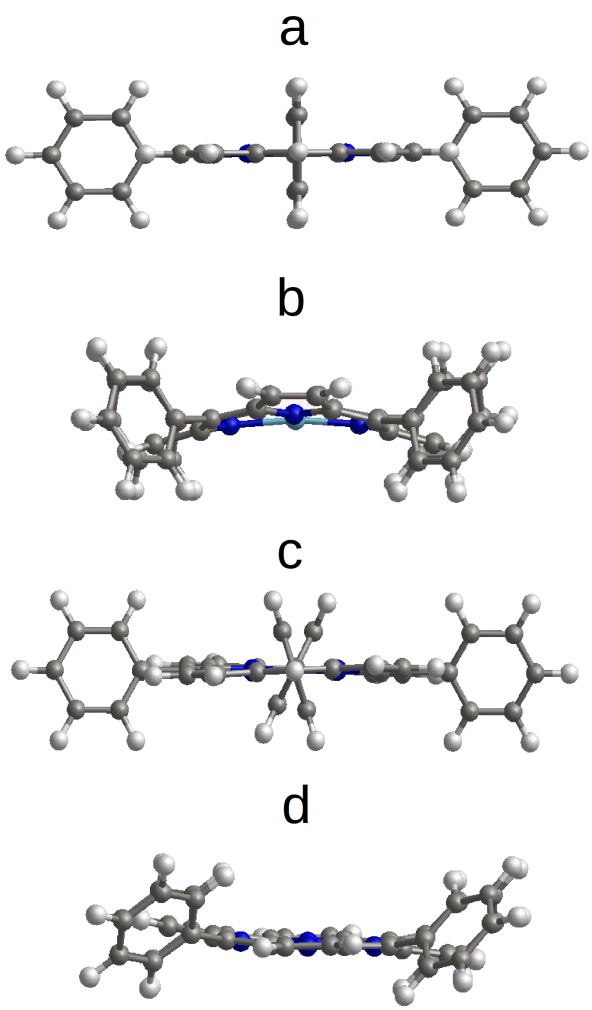

Figure 1: Low-symmetry FeTPP conformations: a) ideal (D_{4h}); b) saddle (D_{2d}); c) twist (S_4); d) deckchair (C_{2h}).

Table 1: Relative energy, E_0, and magnetic moment, μ, of S_4, D_{2d} and C_{2h} conformations in the states $S = 1$ and $S = 2$. The reference energy is that of the HS D_{2d} conformation.

	twist (S_4)	saddle (D_{2d})	deckchair (C_{2h})
HS ($S = 2$), E_0 (eV)	0.04	0	0.02
μ (μ_B)	3.94	3.94	3.94
IS ($S = 1$), E_0 (eV)	0.15	0.04	0.06
μ (μ_B)	2.03	2.03	2.03

The activation barriers to switch between the three non-ideal conformations have been calculated (free molecules in vacuum) by using the nudged elastic band (NEB) method [14,15] (Figure 2). The barriers between the different conformations are 0.037 eV from S_4 to D_{2d}, 0.077 eV from D_{2d} to S_4, 0.074 eV from D_{2d} to C_{2h} and 0.055 eV for C_{2h} to D_{2d}.

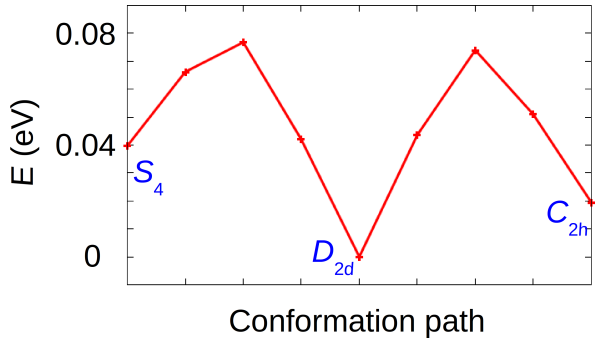

Figure 2: Activation energy to pass from the twist form (S_4) to the saddle shape (D_{2d}) and from the saddle shape to the deckchair conformation (C_{2h}).

Intermolecular interactions

The D_{2d} conformation is the most extensively studied for both the single molecule and molecules in self-assembled 2D islands [16-18]. In these assemblies, FeTPP forms a close-packed arrangement involving T-type interactions, i.e., the four phenyl rings of one molecule point their extremities perpendicularly towards the phenyl of the neighbouring FeTPP molecules (Figure 3a). In this configuration the central macrocycle has a saddle shape conformation (D_{2d}) with the H atoms of two pyrrole groups (along the axis perpendicular to the figure) pointing upward and the H atoms of the other two pyrrole groups (along the horizontal axis in the plane of the figure) pointing downward (Figure 1b). In a less close-packed arrangement, the interaction between neighbouring FeTPP molecules is of π–π type. In the latter, all phenyl rings of a FeTPP molecule are parallel to the phenyl groups of neighbouring molecules (Figure 3b). The H atoms of two pyrrole rings (along the axis perpendicular to the figure) remain nearly in the same plane, while in one pyrrole group (the left one along the horizontal axis in the plane of the figure), the H atoms point upward and the H atoms of the pyrrole group at the opposite side (the right one along the horizontal axis in the plane of the figure) point downward (Figure 1d). In this second case, the macrocycle adopts a deckchair form (C_{2h}). These conformations have been identified in sub-molecular resolution STM images on a Au(111) surface as shown in the work of N. Lin et al. [16] for the saddle conformation (twofold symmetry) and in the work of Gopakumar et al. [11] for the planar conformation (fourfold symmetry). The distance between the Fe centre of neighbouring molecules is about 14 Å in both cases and is consistent with a commensurate epitaxial mesh of (5 0; 3 6) on the Au(111) surface. T-type and π–π-type arrangements could also be distinguished by comparing the size of the void spaces between the molecules and their relative orientation as suggested in [18].

Activation barrier between magnetic states

The saddle-shape conformation (D_{2d}) has already been extensively reported in the literature [16-19]. Hence, we focus on the deckchair conformation (C_{2h}) (Figure 3b). In order to evaluate the activation barrier of the free molecule between HS and IS states of this conformation, the energy of a series of intermediate images has been calculated (Figure 4). From these calculations, the activation energy from IS to HS (respectively, from HS to IS) was found to be 0.02 eV (respectively, 0.07 eV) with a Fe–N bond length of 2.059 Å in HS and 2.003 Å in IS. This is in accordance with the expected trend of a larger Fe–N distance in HS than in IS [2]. For the transition state, this length is about

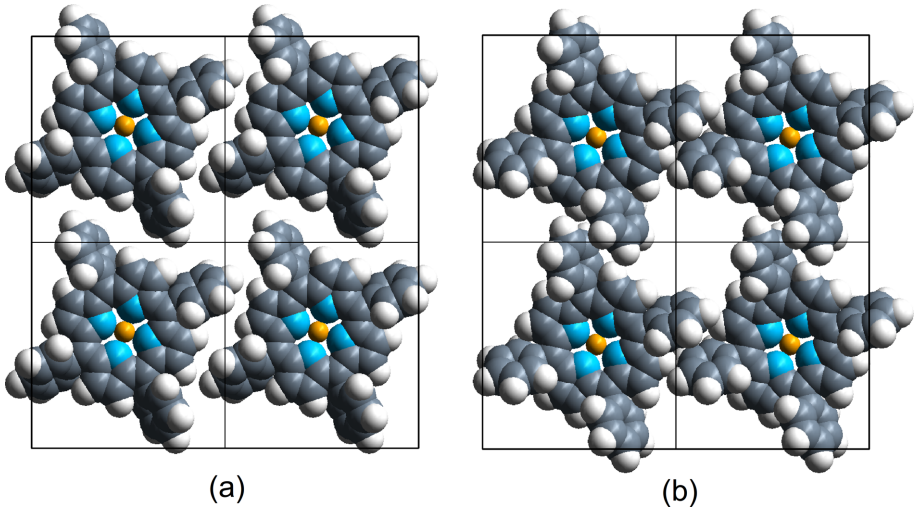

Figure 3: a) T-type (saddle conformation) and b) π–π-type (deckchair conformation) arrangements of FeTPP in 2D assemblies.

2.026 Å. Therefore, for a free FeTPP molecule in C_{2h} conformation, the identification of this transition state clearly confirmed the existence of two stable states, HS and IS.

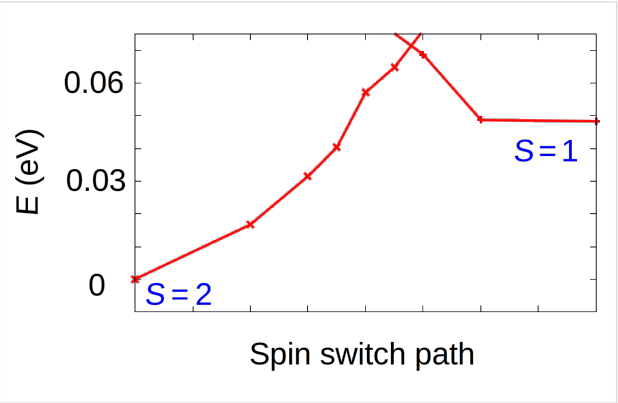

Figure 4: calculated activation barrier between HS (S = 2) and IS (S = 1) of a FeTPP molecule in C_{2h} conformation.

Adsorption configurations and spin states on Au(111)

The deckchair form (C_{2h}) molecule adsorbed on Au(111) also presents two magnetic states (HS, $S = 2$ and IS, $S = 1$) (Table 2). The most stable adsorption site is hollow-fcc in the HS state, which will be used as reference for the total energy comparison from now on. At the three other adsorption sites (hollow-hcp, top and bridge), the energy is higher by 0.04 eV. The magnetic moment of HS state is 4.18 ± 0.05 μ_B for these four sites. At hollow-fcc, the IS state energy is found to be higher by 0.07 eV than the HS state, while at the three other sites (hollow-hcp, top and bridge) the IS energies are 0.10 eV larger than the reference. The magnetic moment of the IS state on these sites is 2.24 ± 0.02 μ_B. The molecule–surface distance is defined as the difference between the average z-values of C and N atoms in the macrocycle of FeTPP and the average z-values of the Au atoms of the top layer of the slab. This distance is 3.63 ± 0.06 Å independent of the magnetic state. However, the Fe-to-surface distance, $d_{Fe\text{-}surface}$, is significantly different. In the HS state this distance is 3.17 ± 0.03 Å, and in the IS state this distance is 3.48 ± 0.04 Å. This difference indicates a stronger attractive interaction between the Fe atom and the surface in the HS state. The Fe–N bond length, $d_{Fe\text{-}N}$, is slightly increased to 2.075 ± 0.002 Å in the HS state (respectively, slightly decreased to 2.002 ± 0.002 Å in the IS state) by comparison with the free molecule bond length. Furthermore, the side view of the central porphyrin macrocycle of the HS shows a deformation with the Fe atom pointing out of the plane formed by the four N atoms of the pyrrole rings (downwards to the surface) (Figure 5a). This deformation creates a square-based pyramid environment for the coordination sphere around the Fe atom, which also favours the HS state.

Table 2: Relative energy, E_0, magnetic moment, μ, and Fe–surface distance, $d_{Fe\text{-}surface}$, of FeTPP (in deckchair conformation) adsorbed on Au(111) surface in the HS and IS states. The reference is HS at the hollow-fcc site.

	top	bridge	hollow-fcc	hollow-hcp
HS ($S = 2$), E_0 (eV)	0.04	0.04	0.00	0.04
μ (μ_B)	4.23	4.13	4.13	4.13
$d_{Fe\text{-}surface}$ (Å)	3.15	3.20	3.14	3.17
IS ($S = 1$), E_0 (eV)	0.10	0.10	0.07	0.10
μ (μ_B)	2.26	2.24	2.22	2.23
$d_{Fe\text{-}surface}$ (Å)	3.44	3.52	3.43	3.46

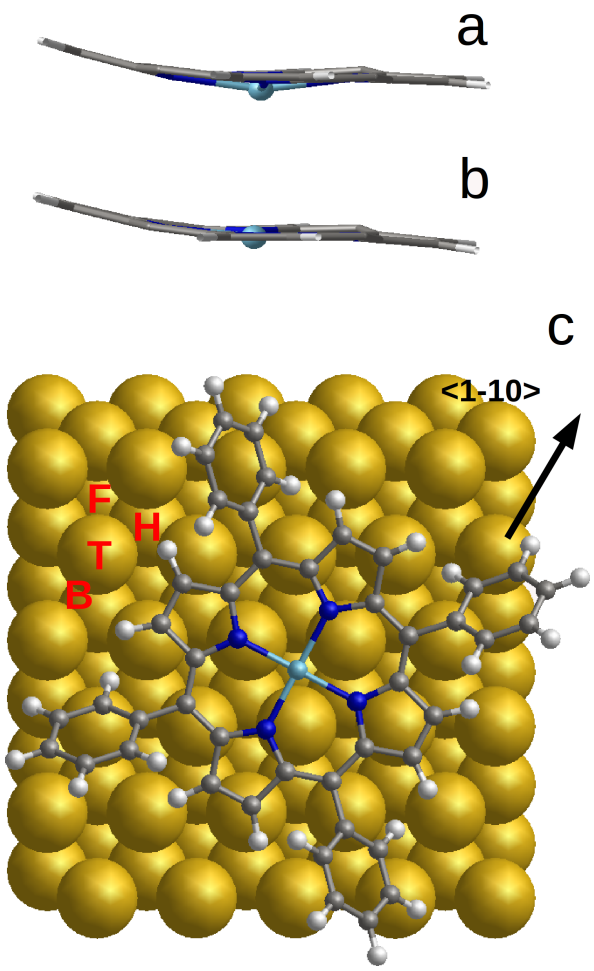

Figure 5: Conformation of the central porphyrin core in a) HS state; b) IS state (phenyl rings were omitted for clarity). In c) example of FeTPP adsorbed on fcc site of Au(111) on which the positions of the top (T), bridge (B), fcc (F) and hcp (H) sites are indicated. The optimized molecule is oriented along the <1−10> direction.

The activation energy between the HS and IS states of FeTPP adsorbed on Au(111) has been evaluated. To do so, the NEB method was employed for FeTPP adsorbed on fcc site from HS ($S = 2$) to IS ($S = 1$) (Figure 6). While the activation energy

from HS to IS (energy difference) is found to be 0.08 eV, no energy barrier was found to pass from IS to HS, indicating that the IS state is unstable when the molecule is adsorbed on Au(111). The fact that IS state was obtained during the geometrical optimization can be explained by a very flat potential energy surface (PES) around this configuration or by an activation barrier that is too small to be identified with the computational precision we used. Based on these results, the HS seems to be the only stable state for the adsorbed FeTPP in the deckchair conformation (C_{2h}). In the following we check the strength of different interactions involved in the adsorption of this HS FeTPP on the Au(111) surface as well as the charge transfer, work function modification and the projected density of states (PDOS) variations.

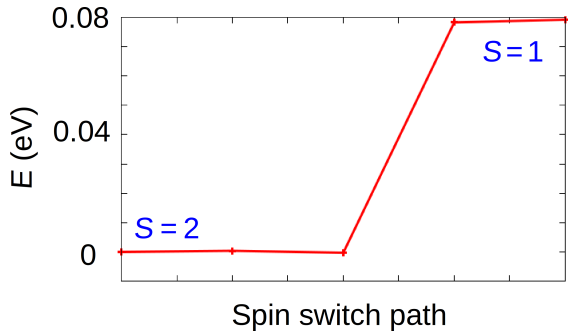

Figure 6: Calculated activation barrier between HS (S = 2) and IS (S = 1) of FeTPP (C_{2h} conformation) adsorbed at the hollow-fcc site of Au(111).

In the reference configuration (HS, fcc), the adsorption energy is calculated to be −1.86 eV while the vdW contribution is found to be −1.70 eV. This small energy difference confirms the physisorption of FeTPP on Au(111). The molecule–surface distance of 3.63 ± 0.06 Å is consistent with the presence of the four peripheral phenyl rings acting as spacer that mitigate the coupling between the central macrocycle and the surface. X-ray standing wave measurements (XSW) on 3,4,9,10-perylene tetracarboxylic dianhydride (PTCDA) and on diindoperylene (DIP) on Au(111) report distances slightly lower (3.27 Å and 3.22 Å, respectively) [20,21]. The deformation energy of the adsorbed FeTPP is found to be +1.08 eV (0.03 eV for the gold surface), while the intramolecular vdW energy is −3.12 eV.

The charge transfer defined as the difference between the number of valence electron in the adsorbed molecule and in the free molecule in vacuum, $\Delta q = q_{\text{adsorbed molecule}} - q_{\text{free molecule}}$, was investigated through a Bader charge analysis [22]. The FeTPP molecule is positively charged by transferring 0.24e from the molecule to the Au(111) surface at the hollow-fcc site, but also at the bridge and hollow-hcp sites. At the top site, due to the direct coordination between the Fe and the Au atom, the transfer is slightly larger with 0.29e. The variation of partial charge on Fe (Δq_{Fe}) is a loss of about 0.04e (0.06e for HS on top site). The sign of this variation is the same as the molecule–surface charge transfer.

As shown in [16], the Fe centre contributes to electronic states around the Fermi level. We compare here the spin-resolved density of states projected (PDOS) onto the d-orbitals of Fe in the HS state before and after adsorption (with FeTPP adsorbed at the fcc site of Au(111) surface) (Figure 7). In these cases, only one orbital (d_{z2}) is doubly occupied (by both majority and minority spin). The four other orbitals (d_{xy}, d_{xz}, d_{yz} and d_{x2_y2}) are occupied by majority spin, but unoccupied by minority spin. These four singly occupied orbitals confirm the spin multiplicity of S = 2 for the HS state. As displayed in Figure 7, the charge transfer from FeTPP to the Au(111) surface does not disturb the distribution of d-orbitals around the Fermi level.

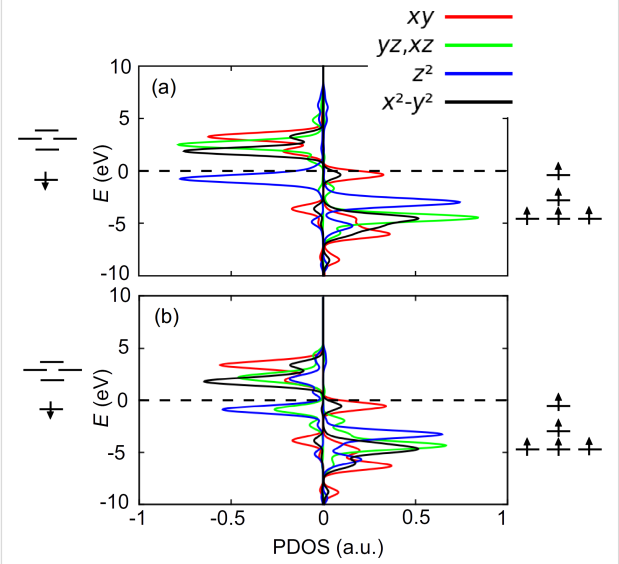

Figure 7: Spin-resolved PDOS on d-orbitals of the Fe atom of HS FeTPP (a) at the fcc site of Au(111) and (b) in the free molecule.

The work function $\Phi = E_{\text{pot}} - E_{\text{Fermi}}$ on uncovered Au(111) was calculated with E_{pot} being the local potential at the middle of vacuum of the simulation cell. The evaluated value of 5.14 eV is in good agreement with the experimental one (5.35 eV) [23]. After the adsorption, the work function was reduced to 4.19 eV. This value is consistent with that measured on copper phthalocyanine (CuPc) adsorbed on Au(111) [24].

Adsorption on Ag(111) and Cu(111) surfaces

It is well known for large organic molecules such as PTCDA or DIP that their interaction with coinage-metal surfaces are different and the binding strength increases in the form of

Au < Ag < Cu while the molecule–surface distance decreases [20,21]. In order to verify this trend for FeTPP, calculations were performed on fcc, hcp, top and bridge sites of Ag(111) and Cu(111) surfaces (Figure 8).

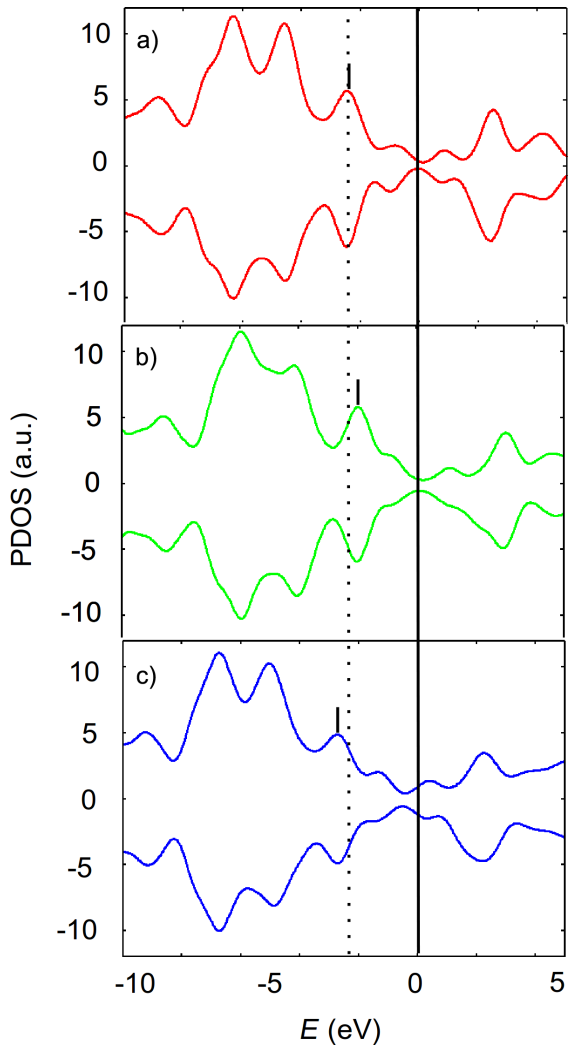

Figure 8: Spin-resolved PDOS of FeTPP. a) free molecule (red), adsorbed on fcc site of b) Au(111) (green), c) on Ag(111) (blue). The shift of PDOS on Cu(111) is similar to that on Ag(111).

The adsorption energy for HS FeTPP on Ag(111) is −4.99 ± 0.01 eV with a molecule–surface distance of $d_{\text{FeTPP-Ag(111)}}$ = 3.06 ± 0.01 Å and an Fe–surface distance of $d_{\text{Fe-Ag(111)}}$ = 2.82 ± 0.01 Å. On Cu(111), the adsorption energy of HS FeTPP is −4.85 ± 0.02 eV with a molecule–surface distance of $d_{\text{FeTPP-Cu(111)}}$ = 2.82 ± 0.05 Å and an Fe–surface distance of $d_{\text{Fe-Cu(111)}}$ = 2.48 ± 0.04 Å. The adsorption energies on these two surfaces are significantly larger than those on Au(111). The main reason is the molecule–surface vdW contribution, which is overestimated [25] on Ag(111) and Cu(111) (−6.32 eV and −6.42 eV, respectively when adsorbed on fcc site). As mentioned in the computational details, the C_6 parameter for Au was optimized on a model system in such a manner that it represents about one third of the standard value. For calculations on Ag(111) and Cu(111), we did not optimize this parameter. As the weak molecule–surface interaction on Au(111) is sufficient to stabilize the HS state of the adsorbed FeTPP molecule, we did not expect a contrary result on Ag(111) and Cu(111) surfaces.

The Bader charge analyses result in a negatively charged FeTPP molecule on Ag(111), with 0.60 ± 0.02 electron being transferred from the surface to the molecule in the HS state. The Fe centre has only gained (0.02 ± 0.01)*e*. This charge variation does not modify the magnetic state of the adsorbed molecule. The same trend was observed on Cu(111), with an average of (0.66 ± 0.08)*e* being transferred from the surface to the molecule in HS state, and 0.04 electron gain on the Fe centre.

Upon FeTPP adsorption, the work function of the Ag(111) surface (respectively, Cu(111) surface) is found to be reduced from 4.41 eV (4.77 eV) for the bare substrate to 3.71 eV (4.36 eV) for the covered surface. The same trends were reported for the adsorption of benzene on Ag(111) [26] and on Cu(111) [23]. From this study, we can conclude that all three tested (111) surfaces exhibit the same trend of a lowered work function upon molecular adsorption. Nevertheless, we have found that the charge transfer on Au(111) occurred in opposite direction than that on Cu(111) and Ag(111). This result is perfectly reflected in the comparison of the PDOS of the free molecule and of the adsorbed molecule. By adsorbing the FeTPP molecule on Au(111), the occupied electronic states of the molecule are shifted towards the Fermi level, thus facilitating the charge transfer from the molecule to the substrate. By adsorbing on Ag(111) and Cu(111), the unoccupied molecular states are shifted towards the metal Fermi level, thus facilitating the charge transfer from the substrate to the molecule. These shifts explain the direction of the charge transfer.

In summary, by performing spin-polarized DFT and NEB calculations, we have identified two stable magnetic states of the free FeTPP molecule in its deckchair conformation (C_{2h}). The two states (HS and IS) were separated by an activation barrier of 0.07 eV to pass from S = 2 to S = 1 and an activation barrier of 0.02 eV to pass from S = 1 to S = 2. However, when this molecule is adsorbed on Au(111) in a monolayer, the IS state is no longer stable as the activation barrier from S = 1 to S = 2 disappears. The most stable magnetic state on Au(111), HS, has an adsorption energy of −1.83 ± 0.02 eV with a contribution of vdW interactions of −1.70 eV, and the central porphyrin macrocyle is at a distance of 3.63 ± 0.06 Å above the surface. These physisorption characteristics were confirmed by a

small charge transfer (0.24*e*) from the molecule to the surface. By changing from Au(111) to Ag(111) and to Cu(111) surfaces, the adsorption energy increases and the molecule–surface distance decreases as expected. However, these quantities cannot be compared quantitatively since we have used an optimized C_6 parameter for Au and standard DFT-D2 parameter for Ag and Cu. Qualitatively, the amount of charge transfer was slightly increased to 0.60*e* from Ag(111) to FeTPP and to 0.64*e* from Cu(111) to the molecule. In spite of these charge transfers, the partial charge on the Fe centre remains almost unchanged, i.e., 0.1*e* on Au(111), 0.02*e* on Ag(111) and 0.04*e* on Cu(111). Due to molecular adsorption, the work function of Au(111) was reduced by 0.95 eV, this reduction being 0.71 eV on Ag(111) and 0.41 on Cu(111).

Conclusion

In this study, we have focused our investigation on the deckchair conformation (C_{2h}) of the FeTPP molecule, which favours π–π-type interactions in self-assembled monolayers on Au(111), Ag(111) and Cu(111) surfaces. In spite of the presence of two stable magnetic states in the free molecule, only the high-spin ($S = 2$) state is stable when adsorbed on metal. These results show that the physisorption of FeTPP on coinage metal surfaces is strong enough to modify the ligand-field environment of Fe. This result reveals that an external permanent element such as a STM tip or an additional molecule is needed to use FeTPP or similar molecules as model system for molecular spin switches.

Method and Computational Details

Spin-polarized DFT calculations were performed using a slightly modified version of the Vienna ab initio simulation package VASP [27-30]. Projector-augmented wave (PAW) pseudo-potential [31,32], as well as the exchange–correlation functional proposed by Perdew–Burke–Ernzerhof (PBE) in the framework of the generalized gradient approximation [33,34] were employed. The van der Waals dispersive interaction correction according to Grimme's DFT-D2 method [35] was considered for inter- and intra-molecular interactions as well as molecule–surface interactions. The C_6 parameter was optimized in a model system on Au(111) in such a manner that its value is about three times smaller than the standard C_6 [36]. This smaller value is due to the screening effect similar to that demonstrated by Tkatchenko et al. [37]. In addition, the DFT-D2 correction was not applied in the metal slabs as no significant improvement has been demonstrated [37,38]. The kinetic cut-off energy for the plane-waves basis was set to 410 eV for Au, 460 eV for Ag and 500 eV for Cu. For the FeTPP/Au(111) system, a simulation supercell of (14.76 Å × 15.33 Å × 27.51 Å) containing 120 Au atoms (30 atoms × 4 layers) and 77 atoms for the Fe-TPP molecule ($C_{44}H_{28}N_4Fe$) was used. This dimension is (14.73 Å × 15.30 Å × 27.45 Å) for Ag(111) and (17.81 Å × 15.42 Å × 25.18 Å) for Cu(111) for which each atomic layer contains 48 atoms (4 × 48 = 192 Cu atoms in the slab). The Brillouin zone sampling in reciprocal space was restricted to the Γ point. The validity of this restriction was tested on the reference configuration (FeTPP at the hollow-fcc site of Au(111)) with a (5 × 5 × 1) Monkhorst–Pack *k*-point mesh. This comparison gives a difference lower than 1% for the total energy and the bond length. The difference in density of states and local electrostatic potential (including dipole interaction correction) are not noticeable. DFT + U method as proposed by Dudarev [39] was used to take into account the on-site d-electron correlation of the central Fe atom. For this purpose, the Coulomb repulsion parameter U was set to 4 eV and the exchange parameter J was set to 1 eV (as in [11]). The convergence condition of the self-consistent electronic loops was set to 10^{-6} eV, while the atomic positions were relaxed until the forces reached a value lower than 0.01 eV/Å. The atoms of the two bottom layers of the metal slab were kept fixed at their bulk positions and all other atoms were allowed to relax without any constraint. The adsorption energy was determined as $E_{ads} = E_{tot} - E_{slab} - E_{mol}$ where E_{tot} is the total energy of the system containing a FeTPP molecule on a Au/Ag/Cu (111) slab, E_{mol} is the energy of the FeTPP molecule in vacuum and E_{slab} is the total energy of the 4-layer metal slab.

Acknowledgements

This work was granted access to the HPC resources of CALMIP supercomputing centre under the allocations p0686 and p1303.

References

1. Gottfried, J. M. *Surf. Sci. Rep.* **2015,** *70,* 259–379. doi:10.1016/j.surfrep.2015.04.001
2. Collman, J. P.; Hoard, J. L.; Kim, N.; Lang, G.; Reed, C. A. *J. Am. Chem. Soc.* **1975,** *97,* 2676–2681. doi:10.1021/ja00843a015
3. McGarvey, B. R. *Inorg. Chem.* **1988,** *27,* 4691–4698. doi:10.1021/ic00299a004
4. Mispelter, J.; Momenteau, M.; Lhoste, J. M. *J. Chem. Phys.* **1980,** *72,* 1003–1012. doi:10.1063/1.439266
5. Hu, C.; Noll, B. C.; Schulz, C. E.; Scheidt, W. R. *Inorg. Chem.* **2007,** *46,* 619–621. doi:10.1021/ic0620182
6. Liao, M.-S.; Scheiner, S. *J. Chem. Phys.* **2002,** *116,* 3635. doi:10.1063/1.1447902
7. Liao, M.-S.; Scheiner, S. *J. Chem. Phys.* **2002,** *117,* 205. doi:10.1063/1.1480872
8. Hieringer, W.; Flechtner, K.; Kretschmann, A.; Seufert, K.; Auwärter, W.; Barth, J. V.; Görling, A.; Steinrück, H.-P.; Gottfried, J. M. *J. Am. Chem. Soc.* **2011,** *133,* 6206–6222. doi:10.1021/ja1093502
9. Seufert, K.; Auwärter, W.; Barth, J. V. *J. Am. Chem. Soc.* **2010,** *132,* 18141–18146. doi:10.1021/ja1054884
10. Seufert, K.; Bocquet, M.-L.; Auwärter, W.; Weber-Bargioni, A.; Reichert, J.; Lorente, N.; Barth, J. V. *Nat. Chem.* **2011,** *3,* 114–119. doi:10.1038/nchem.956

11. Gopakumar, T. G.; Tang, H.; Morillo, J.; Berndt, R. *J. Am. Chem. Soc.* **2012,** *134,* 11844–11847. doi:10.1021/ja302589z
12. Kuang, G.; Zhang, Q.; Lin, T.; Pang, R.; Shi, X.; Xu, H.; Lin, N. *ACS Nano* **2017,** *11,* 6295–6300. doi:10.1021/acsnano.7b02567
13. Bhandary, S.; Schüler, M.; Thunström, P.; di Marco, I.; Brena, B.; Eriksson, O.; Wehking, T.; Sanyal, S. *Phys. Rev. B* **2016,** *93,* 155158. doi:10.1103/physrevb.93.155158
14. Mills, G.; Jónsson, H.; Schenter, G. K. *Surf. Sci.* **1995,** *324,* 305–337. doi:10.1016/0039-6028(94)00731-4
15. Henkelman, G.; Uberuaga, B. P.; Jónsson, H. *J. Chem. Phys.* **2000,** *113,* 9901–9904. doi:10.1063/1.1329672
16. Wang, W.; Pang, R.; Kuang, G.; Shi, X.; Shang, X.; Liu, P. N.; Lin, N. *Phys. Rev. B* **2015,** *91,* 045440. doi:10.1103/physrevb.91.045440
17. Buchner, F.; Flechtner, K.; Bai, Y.; Zillner, E.; Kellner, I.; Steinrück, H.-P.; Marbach, H.; Gottfried, J. M. *J. Phys. Chem. C* **2008,** *112,* 15458–15465. doi:10.1021/jp8052955
18. Buchner, F.; Kellner, I.; Hieringer, W.; Görling, A.; Steinrück, H.-P.; Marbach, H. *Phys. Chem. Chem. Phys.* **2010,** *12,* 13082–13090. doi:10.1039/c004551a
19. Janet, J. P.; Zhao, Q.; Ioannidis, E. I.; Kulik, H. J. *Mol. Simul.* **2017,** *43,* 327–345. doi:10.1080/08927022.2016.1258465
20. Duhm, S.; Gerlach, A.; Salzmann, I.; Bröker, B.; Johnson, R. L.; Schreiber, F.; Koch, N. *Org. Electron.* **2008,** *9,* 111–118. doi:10.1016/j.orgel.2007.10.004
21. Bürker, C.; Ferri, N.; Tkatcenko, A.; Gerlach, A.; Niederhausen, J.; Hosokai, T.; Duhm, S.; Zegenhagen, J.; Koch, N.; Schreiber, F. *Phys. Rev. B* **2013,** *87,* 165443. doi:10.1103/physrevb.87.165443
22. Tang, W.; Sanville, E.; Henkelman, G. *J. Phys.: Condens. Matter* **2009,** *21,* 084204. doi:10.1088/0953-8984/21/8/084204
23. Witte, G.; Lukas, S.; Bagus, P. S.; Wöll, C. *Appl. Phys. Lett.* **2005,** *87,* 263502. doi:10.1063/1.2151253
24. Huang, Y. L.; Wruss, E.; Egger, D. A.; Kera, S.; Ueno, N.; Saidi, W. A.; Kucko, T.; Wee, A. T. S.; Zojor, E. *Molecules* **2004,** *19,* 2969–2992. doi:10.3390/molecules19032969
25. Hu, Z.-X.; Lan, H.; Ji, W. *Sci. Rep.* **2014,** *4,* 5036. doi:10.1038/srep05036
26. Zhou, X.-L.; Castro, M. E.; White, J. M. *Surf. Sci.* **1990,** *238,* 215–225. doi:10.1016/0039-6028(90)90079-N
27. Kresse, G.; Hafner, J. *Phys. Rev. B* **1993,** *47,* 558. doi:10.1103/physrevb.47.558
28. Kresse, G.; Hafner, J. *Phys. Rev. B* **1994,** *49,* 14251. doi:10.1103/physrevb.49.14251
29. Kresse, G.; Furthmüller, J. *Comput. Mater. Sci.* **1996,** *6,* 15. doi:10.1016/0927-0256(96)00008-0
30. Kresse, G.; Furthmüller, J. *Phys. Rev. B* **1996,** *54,* 11169. doi:10.1103/physrevb.54.11169
31. Blöchl, P. E. *Phys. Rev. B* **1994,** *50,* 17953. doi:10.1103/physrevb.50.17953
32. Kresse, G.; Joubert, D. *Phys. Rev. B* **1999,** *59,* 1758. doi:10.1103/physrevb.59.1758
33. Perdew, J. P.; Burke, K.; Ernzerhof, M. *Phys. Rev. Lett.* **1996,** *77,* 3865. doi:10.1103/physrevlett.77.3865
34. Perdew, J. P.; Burke, K.; Ernzerhof, M. *Phys. Rev. Lett.* **1997,** *78,* 1396. doi:10.1103/physrevlett.78.1396
35. Grimme, S. *J. Comput. Chem.* **2006,** *27,* 1787. doi:10.1002/jcc.20495
36. Sławińska, J.; Dabrowski, P.; Zasada, I. *Phys. Rev. B* **2011,** *83,* 245429. doi:10.1103/PhysRevB.83.245429
37. Ruiz, V. G.; Liu, W.; Tkatchenko, A. *Phys. Rev. B* **2016,** *93,* 035118. doi:10.1103/physrevb.93.035118
38. Chiter, F.; Nguyen, V. B.; Tarrat, N.; Benoit, M.; Tang, H.; Lacaze-Dufaure, C. *Mater. Res. Express* **2016,** *3,* 046501. doi:10.1088/2053-1591/3/4/046501
39. Dudarev, S. L.; Botton, G. A.; Savrasov, S. Y.; Humphreys, C. J.; Sutton, A. P. *Phys. Rev. B* **1998,** *57,* 1505. doi:10.1103/physrevb.57.1505

License and Terms